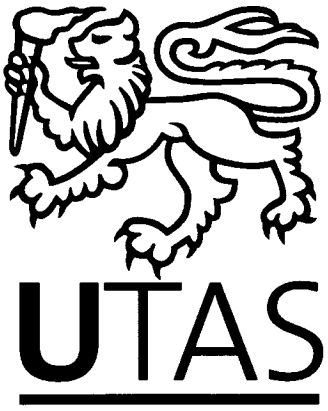

University of Tasmania
School of Mathematics and Physics

Interstellar masers as evolutionary tracers of high-mass star formation

by

Shari Lyndal Breen, B.Sc.(Hons.)

Submitted in fulfilment of the requirements for the
Degree of Doctor of Philosophy

University of Tasmania October 2010

To my beautiful friends Alistair and Timmy. I miss the 'cuddles', being told that I am wrong, the hair styles, the laughter, your smiles and sharp wits; you are both with me always.

I am a better person for knowing you both, you taught me not to take things too seriously (among other things not particularly applicable to radio astronomy....), a valuable lesson and one which I wouldn't have made it through my Ph.D. without.

Declaration

This thesis contains no material which has been accepted for the award of any other higher degree or graduate diploma in any tertiary institution. To the best of my knowledge and belief, this thesis contains no material previously published or written by any other person, except where due acknowledgement has been made in the text, nor does it contain any material that infringes copyright.

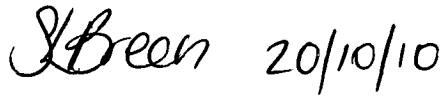

Shari Lyndal Breen

Authority of access

This thesis may be made available for loan. Copying of any part of this thesis is prohibited for one year from the date this statement was signed; after that time limited copying is permitted in accordance with the *Copyright Act 1968*.

S Breen 20/10/10

Shari Lyndal Breen

Abstract

Determining an evolutionary clock for high-mass star formation is a much sought after result in astrophysics, as it will allow comprehensive quantitative studies of the formation of high-mass stars to be completed. We have carried out detailed studies of a large number of sources suspected of undergoing high-mass star formation and have found that common masers transitions can be very helpful in determining their relative evolutionary stage.

We present new observations of 22 GHz water masers and 12.2 GHz methanol masers, completed with the Australia Telescope Compact Array and the Parkes radio telescope, respectively. Hundreds of maser sources are reported here for the first time. From the large samples, we are able to confidently report detection statistics, as well as characteristics of the source populations. Analysis of the maser velocities, flux densities, luminosities and variability are presented.

We have investigated the relative evolutionary phases of high-mass star formation associated with the presence or absence of combinations of the 22 GHz water and 12.2 GHz methanol masers that we detect, along with the locations of 6.7 GHz methanol and main-line OH masers. The locations of the different maser species have been compared with the positions of 1.2 mm dust clumps, molecular data, radio continuum, GLIMPSE point sources and Extended Green Objects. Comparison between the characteristics of coincident sources has revealed strong evidence for an evolutionary sequence for the different maser species in high-mass star formation regions. We present our proposed sequence for the presence of the common maser species associated with young high-mass stars, along with the data supporting our arguments.

Insights into the characteristics and physical conditions associated with the different relative evolutionary stages are presented. We find a general trend whereby both the water and methanol masers increase in luminosity as they evolve. Further to this, we find evidence that the methanol and water masers increase in velocity range as they evolve, implying that the gas volume conducive to the maser emission also increases with evolution. The rate of increase of the 12.2 GHz methanol maser luminosity and velocity range is lower than that of their 6.7 GHz counterparts. We find evidence to suggest that water maser sources also

increase in luminosity less rapidly than 6.7 GHz methanol maser sources. We additionally find evidence to suggest that the increase in luminosity and velocity range of water maser sources 'turns over' towards the later stages of evolution, presumably decreasing until the maser emission ceases. We find no evidence for the methanol masers to show a similar decrease in either luminosity or velocity range, implying that they cease emitting much more abruptly.

Comparisons with mid-infrared data show that the masers themselves are more sensitive to evolutionary changes than the associated mid-infrared emission.

Preface

The work presented in this thesis is largely my own, but has been carried out in close collaboration with my supervisors; Simon Ellingsen and James Caswell. Here I detail other, or more significant, contributions that have been made to some chapters of this work and by whom they were made.

- **Chapter 3:** This chapter is closely based on the publication Breen et al. (2007) with the addition of a section of Bains et al. (2009) which was written by me. The original search for water masers made with the 26 m Mount Pleasant radio telescope was submitted as partial fulfillment of my honours project (Breen, 2005) (as stated in the text). However, the followup observations carried out with the Australia Telescope Compact Array (ATCA), and all subsequent analysis is further work that has not been previously submitted as part of any degree.

  The ATCA observations presented in this chapter were executed by Melanie Johnston-Hollitt and Cliff Senkbeil. The majority of the data analysis and interpretation was carried out by me in close collaboration with Simon Ellingsen, but with two significant exceptions. Simon Wotherspoon made significant contributions to the statistical analysis presented in this chapter, specifically the fitting of the generalized linear models to the data. Simon Ellingsen carried out the comparison between the detected water masers and GLIMPSE point sources and wrote the majority of the section in the paper that corresponds to Section 3.4.2.

- **Chapter 4:** This chapter shows few deviations from the paper Breen et al. (2010a). The 12.2 GHz Parkes observations that are presented in this chapter were carried out by myself, Simon Ellingsen, James Caswell and Ben Lewis. Simon Ellingsen compared the locations of the masers with GLIMPSE point sources, and he also produced Fig. 4.7.

- **Chapter 5:** The 22 GHz water maser observations presented in this chapter were carried out by myself and James Caswell.

- **Chapter 6:** This chapter is essentially that published in Breen et al. (2010b). The 22 GHz observations presented were carried out by James Caswell and Chris Phillips prior to the commencement of my Ph.D. Data collected in 2003 were processed by James Caswell, and the data collected in 2004 were processed by me. James Caswell made some significant contributions to the text, and in particular, wrote the majority of the section that presents the comments on individual sources in the paper which corresponds to Section 6.3.1.

  The majority of the analysis (subsequent to that of the original data) was carried out by me, with the exception of the comparison with GLIMPSE point sources which was carried out by Simon Ellingsen. The text presented in Section 6.4.7 that relates to the comparison with GLIMPSE point sources was written by Simon and I jointly. Comparison, analysis and text relating to 'Extended Green Objects' in Section 6.4.7 was completed by myself.

- **Chapter 7:** The 12.2 GHz observations presented in this chapter were targeted towards 6.7 GHz methanol maser sources detected in the Methanol Multibeam Survey and have been used in advance of their publication. The 12.2 GHz follow observations were carried out by Simon Ellingsen, James Caswell, Ben Lewis and myself.

Acknowledgements

I have many people that I am thankful to for their support throughout the course of my Ph.D. candidature. Above all else, I am extremely grateful to my supervisor, Simon Ellingsen. I don't think that either of us thought that I would be where I am now at the beginning of my Honours project in 2005, but I am very glad that I am, and a lot of the credit has to go to him. I quite literally wouldn't have, and couldn't have, done this without him.

I would also like to thank my co-supervisor, James Caswell, for his immense knowledge and the patient way in which he delivers it. I am also appreciative to him for smiling at 'lovely water masers', and in doing so, allowing me to feel like there was nothing abnormal about such practices!

I am also grateful to the University of Tasmania and the Australia Telescope National Facility for financial support.

At times when my supervisors where momentarily detained I leaned on my 'surrogate supervisors'; Andrew Walsh and Jim Lovell. You have both fulfilled the jobs that I forced you into beautifully, copping some of the pain but none of the credit. Thank you.

Kate Brooks and Lisa Harvey-Smith have offered me good advice and encouragement throughout my Ph.D. for which I am very grateful.

A lot of time throughout my Ph.D. was spent at observatories, and I have to say that these times were some of the highlights. A big thank you to all the observatory staff at the Hobart 26 m radio telescope, as well as those at the ATCA and Parkes, for making observing so enjoyable. Special mentions go to: Brett and Eric at Hobart; Robin, Jamie, Balt, Meg and Chris at the ATCA; and Jannette, Anne, Shirley, Stacy, John R., Geena, Brett A., Brett D. and Brett P. at Parkes.

I spent many hundreds of hours observing for the MMB survey, although it never felt like so much time had passed since my co-observers were always amazing. I have made many friends in the long hours of close confinement in the Parkes control room, especially, Jimi Green, Adam Avison, Maxim Voronkov, Gary Fuller and the super lovely Lyshia Quinn (in addition to the people already mentioned).

I would also like to thank the entire Maths and Physics department for making my work environment what it was. In particular, thanks to Karen Bradford for being my 'Hobart mother' and friend, providing me with constant support. Thanks also to my fellow students for being fun, encouraging and understanding and especially to Anita Titmarsh who has gone above and beyond the call of duty, proof reading the majority of this thesis.

Finally, I would like to thank my friends and family for their immense love and support throughout my 8 years at University.

Contents

List of Figures

List of Tables

1

Introduction

The process through which high-mass stars (M > $\sim$8$M_{\odot}$) form is one of the hottest topics in modern astrophyics, with implications for fields as diverse as galactic evolution and the epoch of reionization. We are yet to realise a unified theory of star formation or the mechanism through which high-mass stars are able to form. One of the difficulties is the lack of sequential signposts in identifying different evolutionary stages of star formation, especially during the early stages while the young stellar objects are still embedded in their natal molecular clouds.

A common phenomenon observed in active high-mass star forming regions is the presence of interstellar masers, particularly emission from the OH, water and methanol molecules. They are relatively common and intense making them one of the best, if not *the* best signposts of young high-mass star formation regions. Observing interstellar masers allows us to probe stars at very early stages of formation and because these masers arise at radio frequencies, they are relatively unaffected by the dense, optical-obscuring gas and dust present at these earliest stages. Masers have long been regarded as powerful probes of the kinematics of star formation regions, but we are only recently beginning to be able to use masers to investigate aspects such as the physical conditions through comparison of observational data and maser pumping theories. Different maser species trace different physical conditions and have been hypothesised to signpost different evolutionary phases of high-mass star formation (e.g. Ellingsen et al. 2007).

I have investigated the presence or absence of water, OH and methanol masers associated with a large number of sources suspected of undergoing high-mass star

formation. Many observations were carried out to complete this project, utilizing data from the Australia Telescope National Facility's Australia Telescope Compact Array (ATCA) and Parkes 64 m radio telescope and the University of Tasmania 26 m Mount Pleasant radio telescope. Specifically, the 22 GHz transition of water, 22 GHz radio continuum and 12.2 GHz methanol masers have been searched for and we have uncovered a large number of new sources. Data collected through this series of observations has then been combined with published data (e.g. 6.7 GHz methanol masers, OH maser sources, 1.2 mm dust clumps, molecular data and mid-infrared sources) for these sources, in order to compare the characteristics of sources associated with different combinations of maser species. Throughout this work an emphasis has been placed on investigating the relative evolutionary phases that the different maser species are tracing and into gaining insight into the physical conditions that are associated with the presence or absence of the common maser species in high-mass star formation regions.

An introduction to the radio telescopes, data reduction and visualisation packages, the statistical analysis used throughout this work, as well as a brief summary of each of the chapters, are presented in the sections that follow.

1.1 The radio telescopes

1.1.1 The University of Tasmania 26 m Mount Pleasant radio telescope

The University of Tasmania 26 m Mount Pleasant radio telescope is the largest of three radio telescopes located at the Mount Pleasant Observatory, located about 20 km from Hobart, Tasmania. The 26 m radio telescope is located at latitude 42° 48' 18" S, longitude 147° 26' 21" E. The telescope was donated to the University of Tasmania in the 1980s by National Aeronautics and Space Administration (NASA) and moved to Mount Pleasant in 1985 from Orroral Valley where it was part of their deep space network. For this reason the telescope has an unusual X-Y mount (aligned East-West) which was required for the telescope to move rapidly, especially directly overhead, in order to maintain view of the satellites

it was tracking. The traditional telescope Azimuth-Elevation mount does not allow the tracking of objects overhead, but in general are more desirable as they are more compact, keeping the telescope lower to the ground and allowing better pointing accuracy.

The telescope is a prime focus instrument and has multiple receivers mounted on a movable platform, allowing the observations of frequencies between 600 MHz and 22 GHz. Both the 12 GHz and 22 GHz receivers where used in order to complete this work and are part of the multi-frequency receiver which is cryogenically cooled with liquid Helium to a temperature of around -250°C. This dramatically enhances the receiver's sensitivity as it decreases the thermal noise.

While few observations using the Mount Pleasant telescope are presented in this work, many hours of preparatory observations for the majority of the projects were completed. These observations allowed the feasibility of observation strategies to be completed, but also allowed us to gain an idea of the number of detections and the kinds of results to expect from our proposed projects. Furthermore, they allowed us to use allocated time on the Australia Telescope National Facility instruments to be used in the most efficient manner, allowing us to observe large sample sizes which ultimately have lead an increase in science results.

1.1.2 The Australia Telescope National Facility

The Australia Telescope National Facility (ATNF) is a division of the CSIRO, which includes the ATNF headquarters located at Marsfield in Sydney, as well as the Parkes, Paul Wild and Mopra Observatories, located near Parkes, Narrabri and Coonabarabran, respectively (and are all located within NSW, Australia). The ATNF facilities operate under a semester based system with two application deadlines per year. Gaining time on these instruments is highly competitive since oversubscription rates are generally high, so time is prioritised according to rankings awarded by the Time Allocation Committee.

The Parkes 64 m radio telescope

The Parkes 64 m radio telescope is operated by the ATNF and is located about 380 km west of Sydney. The telescope is located at latitude latitude 32° 59' 54"

S, longitude 148° 15' 49" E. The surface of the dish is high precision aluminum millimeter wavepanels to a diameter of 17 m, perforated aluminum plate out to 45 m and then galvanized steel mesh out to 64 m. The telescope is a prime focus antenna with an azimuth-elevation mount. Parkes has receivers with allows observations between the frequencies of 0.44 and ~26 GHz.

Observations presented in Chapters 4 and 7 use the Ku-band receiver, operating at ~12 GHz. At this frequency the low efficiency of the outer panels of the telescope mean that it can be regarded as a ~55 m telescope.

The Australia Telescope Compact Array

The Australia Telescope Compact Array (ATCA) is an array of six, 22 m antennas. Located about 500 km north-west of Sydney, the telescopes are situated at the Paul Wild Observatory and, like Parkes, are operated by the ATNF. The six antennas are located at a latitude of 30° and can be placed at stations along the 6 km track aligned east-west, as well as a 214 m northern spur. The location of the ATCA allows for full *uv*-coverage at high angular resolution for sources south of declinations of −24°. However, snap-shot observations of sources up to a declination of +48° are attainable, with perhaps the most problematic range of declinations being those close to a declination of zero degrees where the synthesized beam becomes highly elongated due to the East-West orientation of the array baselines.

The ATCA operates between frequencies of 1.3 and 105 GHz. In Chapters 3, 5 and 6, ATCA observations of spectral line and continuum data at 22 GHz, are presented.

1.2 Data reduction software

A number of data reduction and visualization packages have been used throughout Chapters 3 - 7. One of the most frequently used packages MIRIAD (Sault, Teuben & Wright, 1995) which is a radio interferometry data reduction package, widely used for the reduction of both continuum and spectral line data collected chiefly with the ATCA. MIRIAD can be used for all stages of data reduction, from loading

the data files, through to imaging fields, and extracting the required information from the images.

The images produced from the interferometric observations using MIRIAD were inspected using kvis which is part of the Karma package of visualisation tools. Kvis is a tool which not only displays images and movies, but also allows multiple data sets to be loaded and displayed such that contours of one image can be overlaid on another, line profiles of multiple images can be overlaid. Images can also be annotated and exported from this package.

For single dish data, ASAP (ATNF Spectral line analysis package) has been used for data reduction. This package was produced by the ATNF to reduce data from their single dish antennas, but has been adapted to reduce data from other antennas, such as the Mount Pleasant 26 m radio telescope. ASAP is based on the AIPS++ package and the user interface uses an object oriented ipython interactive shell. Due to this, scripting the data reduction process in python is relatively simple, allowing data reduction to be carried out very efficiently. ASAP is very flexible and allows for non-standard data reduction to be carried out with relative ease which was important in reducing the data presented in Chapters 4 and 7.

1.3 Statistical analysis

A number of the discoveries presented in this thesis are a result of the statistical analysis of the characteristics associated with the large data sets. Throughout, the statistical analysis package 'R' (R Development Core Team, 2006) has been used for this purpose. As well as standard statistical tests such as t-tests, chi-sqared tests and linear regression, slightly less widely applied analysis such as fitting Binomial generalized linear models (GLM) have been used. Since there are a number of cases where we have observations of masers towards either 1.2 mm dust clump data (Mookerjea et al., 2004; Hill et al., 2005) or molecular data (e.g. Bains et al., 2006), the fitting of GLMs to the data allows the characteristics of the sources associated with the masers to be compared with sources devoid of the maser species. Furthermore, GLMs do not require the tested variables to be independent and they allow for the prediction of future outcomes from the

analysis of the predictors.

GLMs have been used to investigate the properties of the molecular gas and dust in the regions with associated maser emission. They have been fitted to the maser presence/absence data using associated source properties (such as ^{13}CO and 1.2 mm dust clump properties reported by Bains et al. (2006) and Mookerjea et al. (2004); Hill et al. (2005) respectively), as predictors. A Binomial GLM predicts the probability, p_i, of finding a maser in the i^{th} clump, in terms of the clump properties x_{1i} x_{2i} $x_{3i} \ldots x_{mi}$. The model takes the form

$$\begin{aligned} y_i &\sim \text{Bin}(1, p_i) \\ \log\frac{p_i}{1-p_i} &= \beta_0 + \beta_1 x_{1i} + \beta_2 x_{2i} + \ldots + \beta_m x_{mi} \end{aligned}$$

where y_i is the maser presence or absence in the i^{th} clump and β_0, β_1, $\beta_2 \ldots \beta_m$ are the regression coefficients to be estimated.

To test the significance of individual clump properties all possible single term models can be fitted, and compared by analysis of deviance to the null model consisting of only an intercept. Stepwise model selection based on the Akaike Information Criteria (AIC) (Burnham & Anderson, 2002) was used to select the most parsimonious model with the greatest predictive power. The AIC is a trade off between goodness of fit and model complexity and is defined as

$$AIC = -2(\text{max log likelihood}) + 2(\text{number of parameters})$$

with the preferred model being the model with the lowest AIC (Venables & Ripley, 2002).

For ease of comparison between the data sets box plots were commonly created for each of the clump properties. The solid horizontal line in each of these plots represents the median of the data. The box represents the 25^{th} to the 75^{th} percentile, while the vertical line from the top of the box represents data from the 75^{th} percentile to the maximum value and the vertical line from the bottom of the box represents data from the 25^{th} percentile to the minimum value. Extreme values are classified as outliers, and represented by dots, if their range from the 25th or 75th percentile (in the case of the minimum and maximum values of

clump properties, respectively) is greater than 1.5 times that of the interquartile range.

1.3.1 An example of GLM analysis

Here we step through an example of were a GLM has been fitted to a data set in Chapter 3, Section 3.4.4. In this case, particular portions of a giant molecular cloud have been searched for both water masers and 1.2 mm dust clump emission. A comparison between the locations of the water masers with the 1.2 mm dust clumps shows, not surprisingly, that each of the water masers is coincident with a 1.2 mm dust clump. In order to determine if there is any differences between the properties of the 1.2 mm dust clumps with associated water maser emission, compared to those without, we have fitted a binomial GLM to the water maser presence/absence data, using the 1.2 mm dust clump properties (e.g. radius, mass etc.) as predictors.

Firstly, we fit all possible single term models to see if any of the clump properties alone can be used as an indicator of the likelihood of water maser presence. Basically, this is just a test of the hypothesis that the stated single term model provides no better fit than the null model which consists only of an intercept. In other words, this tests looks for a relationship between the y-values (e.g. values of 1.2 mm dust clump radius) and whether or not there is an associated water maser, i.e. to determine whether or not there is a slope between the two groups of data (the dust clumps with masers and those without). Table 3.13 gives the results of this analysis. The most important value in this table is the p-value. For example, for the dust clump property radius, the resultant p-value is 3.787e–07 which means that the null hypothesis can be rejected. From this we can assert that there is a statistically significant difference between the 1.2 mm dust clump measurements for sources with associated water masers compared to those without.

The second major piece of analysis is the stepwise model selection. Our model selection method tries to include as few of the dust clump properties as possible, while maintaining the ability to predict whether or not there is an associated water maser. This process is begun by adding in all of the predictors and then

deleting the one that causes the least reduction in the 'goodness of fit' (and so on), a process called backward elimination. Continuing the explanation of our former example (Chapter 3, Section 3.4.4), the results of this analysis are located in Table 3.14. In this table the only dust clump property presented is the dust clump radius. This does not indicate that the other dust clump properties are not related to the presence of the water masers, but rather, that the inclusion of these other properties failed to increase the predictive properties of the model. As stated in Section 3.4.4, the estimated regression relation is

$$\log\frac{p_i}{1-p_i} = -11.477 + 9.174x_{radius},$$

where x_{radius} is the radius of the 1.2 mm dust clump in pc.

Since there is only one predictor included in this model, the physical implications are easily determined, as discussed in Section 3.4.4. In the case where such a model has two or more terms, these implications become harder to decipher. In such cases, coefficients should not by considered individually, but instead as a whole. For instance, a hypothetical equation that includes a positive coefficient for radius but a negative coefficient for mass, may give an indication that the masers are associated with the big clumps that perhaps have slightly lower densities than the other considered sources.

1.4 Thesis summary

Chapter 2 contains a review of the literature, and necessary background information.

In Chapter 3 I present a complete survey for water maser towards portions of the G 333 giant molecular cloud (covering a total area of almost half a square degree). Comparisons between the locations of the water and methanol masers with ^{13}CO and 1.2 mm dust clumps as well as infrared data are completed. From these data, a predictive model for water masers associated with 1.2 mm dust clumps was formed. This Chapter is essentially that presented in Breen et al. (2007) with the addition of Section 6.4 from Bains et al. (2009).

Chapter 4 presents observations of 12.2 GHz methanol masers observed towards 6.7 GHz methanol masers associated with 1.2 mm dust clumps observed by Hill et al. (2005). The properties of these sources (such as the presence or absence of emission from the 12.2 GHz transition of methanol, as well as the properties of the associated 1.2 mm dust clumps) were compared with the locations of 8 GHz radio continuum emission (Walsh et al., 1998), OH masers (Caswell, 1998) and mid-infrared point sources and statistical analysis of these data have resulted in an evolutionary sequence for masers in high-mass star formation regions, placing quantitative estimates on the relative lifetimes for the first time. This work is that presented in Breen et al. (2010a).

Chapter 5 contains water maser observations carried out with the ATCA towards the majority of the 404 1.2 mm dust clumps presented in Hill et al. (2009). The 1.2 mm dust clumps with and without associated water masers are then compared to the predetermined probabilities of water maser presence using the model of Breen et al. (2007) (also see Chapter 3). Discussion of the current model for water maser presence associated with 1.2 mm dust clumps is given, and using the larger sample, refinements to this model are offered. In addition, comparison between the locations of the detected water masers with other maser species, radio continuum data and mid-infrared sources is carried out.

Chapter 6 presents water maser observations towards a statistically complete sample of $\sim$200 OH masers (Caswell, 1998) and a sample $\sim$100 methanol masers Caswell, Kramer & Reynolds (2009). Detection statistics as well as some analysis of water maser variability, peak velocity comparisons between the different maser species and associations with 22 GHz radio continuum and mid-infrared sources are presented. This work is that published in Breen et al. (2010b).

Chapter 7 contains 12.2 GHz observations towards all of the 6.7 GHz methanol masers detected in the Parkes Methanol Multibeam (MMB) south of declination $-20°$. This is the largest search for 12.2 GHz methanol maser ever completed, gaining a full sample of these masers in the southern hemisphere, south of $-20°$. Detection statistics free from biases are derived for the first time along with numerous results uncovered from the comparison between the two methanol maser transitions, along with the characteristics of the sources that they are associated with.

Chapter 8 discusses all the individual projects together and here a conclusion is made using the combined results of Chapters 3 - 7. Along with the scientific implications of the numerous results given in Chapters 3 - 7, an updated evolutionary timeline for the common maser species in high-mass star formation regions is given.

2

High-mass star formation, interstellar masers and evolutionary tracers

In this chapter, a review of the literature relevant to the work contained in this thesis is presented. While an effort was made to include major works that have contributed to our knowledge of high-mass star formation, associated interstellar masers and different evolutionary tracers, due to the breadth of the topics covered it has not been possible to include everything. Due to this, only necessary background information is given along with a number of examples of supporting publications from the literature.

2.1 The formation of high-mass stars

The characteristics of our Galaxy, as well as those throughout the Universe, have been dramatically influenced by high-mass stars. Throughout their short lifetimes, they infuse their immediate environments with immense amounts of energy through their powerful outflows, ultraviolet radiation, and finally, as energetic supernovae. Their eventual demise as supernovae also allows them to inject heavy elements into the interstellar medium. The important role that high-mass stars play throughout the universe is undeniable and yet little is known about the mechanism through which they are able to form. Furthermore, through their study we hope to gain greater understanding of what is causing the low star formation efficiency in our Galaxy. And in particular, determine what is regulating the star

formation rate (e.g. supersonic turbulent flows (e.g. Mac Low & Kleesen, 2004) or magnetic fields that are supporting the molecular cloud against gravitational collapse (e.g. Shu, Adams & Lizano, 1987)).

The study of high-mass stars is hindered by the fact they they form in clusters, deeply embedded in high density gas and dust. This means that high-mass stars are highly obscured by their natal material, dramatically limiting their observation, since they they are inaccessible at optical, and often near-infrared wavelengths. Their formation in clusters also adds further complication since each member of the cluster can be at different evolutionary stages, as well as in a different mass range. Due to the conditions in which these influential objects are born, the best tracers of their existence are limited to radio wavelengths (through observations of UCHII regions, masers), sub-mm dust continuum, far-infrared and mid-infrared wavelengths. Furthermore, these objects are rare (due to the steep dependence on mass in the initial mass function), evolve quickly and are located at relatively far distances. All of these facts have contributed to our lack of understanding of these sources.

While aspects of the way high-mass stars form is still under debate, the process that results in the formation of isolated low-mass stars is reasonably well understood, and the basic model of accretion (Shu, Adams & Lizano, 1987) is generally accepted. For stars greater than $\sim$8 $M_{\odot}$, the Kelvin-Helmholtz time (the time it takes for the core to begin converting gravitational potential energy into heat) will be less that the free-fall time (the time scale of collapse). This implies that fusion begins before the object has stopped collapsing. The radiation pressure in these objects is great enough to stop spherical accretion, but since we know that stars with greater masses exist, there has to be a mechanism which allows them to acquire it.

Some (e.g. Bally & Zinnecker, 2005) have suggested that higher-mass stars form via mergers, or coalescence, of lower-mass stars. This theory is supported by the fact that high-mass stars are seen to form in clusters, whereas isolated low-mass stars are known. The problem with this scenario is that high-mass star formation would be restricted to the centres of large stellar clusters with very high densities; densities that are rarely present in any known clusters (Bonnell, Bate & Zinnecker, 1998).

The most widely accepted model for high-mass star formation is based on a 'scaled-up' version of the low-mass model, but with a few alterations. In order for the stars to gain enough mass to be considered high-mass stars, they must undergo much higher accretion rates through a disk which allows the radiation pressure to be overcome (e.g. Tan & McKee, 2004; Krumholtz et al., 2009).

Although the basic mechanisms through which low- and high-mass stars form are expected to be similar, the formation of high-mass objects occurs over shorter timescales due to the increased density and energy. In this model, the star is created through the collapse of a core that is embedded within a clump that is in turn embedded in a molecular cloud. A schematic of the hierarchical structure of this process is presented in Fig. 2.1. As the embedded young star is forming, it accretes matter allowing it to gain mass, some of which is lost by through bipolar outflows or jets (which also allows angular momentum to momentum to be shed). There is growing evidence that (at least for some stars) the initial collapse of the core which will go on to form stars is 'triggered' by one of several mechanisms: these are discussed in Section 2.1.4.

Kurtz (2006) summarises the formation of high-mass stars through the accretion model as follows:

- Gravitational collapse of the material in a molecular cloud occurs on the free-fall time scale of 10^5 years.
- A core forms when enough matter has collapsed, evolving on the Kelvin-Helmholtz time scale of 10^4 years.
- The density of the core increases, the core becomes optically thick and the energy released in the gravitational collapse begins to heat the core.
- Nuclear reactions begin and produce ultraviolet radiation which ionises the surrounding material.
- Depending on the density of the heated core, the UCHII region that is created by the ultraviolet radiation can remain an UCHII region or evolve into a less compact HII region, with the possibility of extended emission.

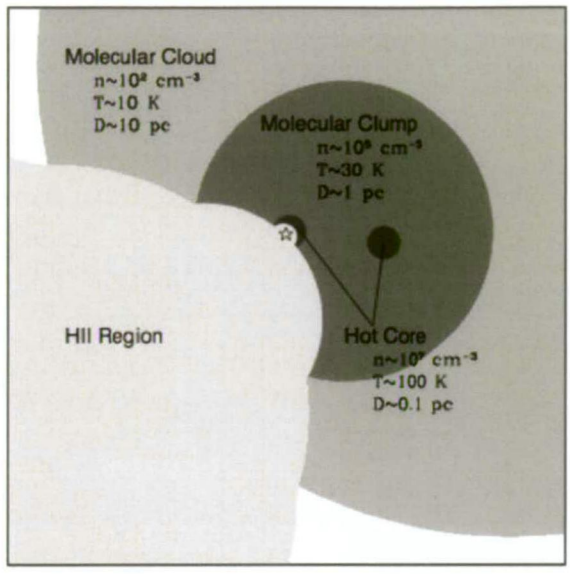

Figure 2.1: *Schematic diagram of the hierarchical structures within molecular clouds (taken from Kim & Koo (2001)). This illustration shows that molecular clouds have clumps which have cores. High-mass stars form within the hot cores, creating an UCH*II *region which is initially small but can become very extended as the source evolves.*

A brief discussion of the each of the 'phases' of high-mass star formation are presented in the following sub-sections. Further discussion is presented in Section 2.3 which includes information of the best traces of the formation during these stages.

2.1.1 Giant molecular clouds

Giant Molecular Clouds (GMCs) form the largest structures within our Galaxy. Their size and structure is varied, but often fall in the range 20 - 100 pc, with masses in the range 10^4 - 10^6 $M_\odot$ (e.g. Beuther et al., 2007). GMCs are formed when gas and dust accumulate under their own gravity, allowing them to become more than a thousand times denser than the interstellar gas that surrounds them. Their composition is mainly molecular hydrogen although they also contain varied amounts of some heavier elements and molecular gas.

The average density and temperature of a GMC is usually of the order of

$\sim 10^2$ cm^{-3} and $\sim$10 K respectively. The velocity dispersions of GMCs are typically only a few km s^{-1} which can largely be attributed to turbulence within the clouds. Measurements of magnetic fields in molecular clouds have shown that they typically have field strengths of the order of several tens of μG (e.g. Bourke et al., 2001).

The structure of a GMC is typically highly non-uniform, composed of high density and lower density regions and much higher density cores (which are the locations where star formation originates). The high-density, star forming regions of GMCs can be easily identified by sub-mm dust continuum emission (e.g. Mookerjea et al., 2004) and high density molecular-line tracers (e.g. Lo et al., 2009). These cores are discussed further in the next section.

The stars that are forming in these 'stellar nurseries' eventually cause the dissipation of the surrounding gas and dust through heating, stellar winds and other disruptions that they impart into their immediate environments. The net result of their action may quench further star formation, or alternatively, trigger a new generation of star formation (see Section 2.1.4 for further discussion of this).

2.1.2 Cold and Hot cores

Preceding the hot core phase in the high-mass star formation sequence is, not surprisingly, the cold core phase. Garay et al. (2004) identified four such objects from 1.2 mm dust continuum emission. Their derived sizes, temperatures and masses (radius = 0.2 - 0.3 pc, temperature $\leq$ 17 K, and mass = 4 $\times$ 10^2 - 2 $\times$ 10^3 $M_\odot$), combined with their lack of mid- or far-infrared counterparts highlighted their potential to eventually collapse and form high-mass stars. Since then, other 1.2 mm dust continuum surveys have found many more cold core candidates (e.g. Hill et al., 2005). These objects are often found embedded in infrared dark clouds (IRDCs) (e.g. Rathborne et al., 2010); extinction features identified against the bright Galactic mid-infrared emission.

As these cold, dense cores collapse and heat up they reach the hot core phase. Observational evidence for this stage was recognised $\sim$20 years ago (e.g Cesaroni et al., 1991; Cesaroni, Walmsley & Churchwell, 1992). During this stage,

temperatures of $\geq$ 100 K are experienced along with densities $\geq 10^7$ cm^{-3} and a multitude of molecular lines are observable, including transitions that require high levels of excitation.

Since hot cores are found to be internally heated (e.g. Cesaroni et al., 1998), based on temperature gradients peaking near the center of the cores, they are now accepted as a stage of high-mass star formation that precedes the onset of a detectable UCHII region. Supporting evidence for this comes from the associated masers that are present during this phase, some of which have been seen to be tracing disks and bipolar outflows (e.g. Torrelles et al., 1998) which is consistent with the characteristics expected during this phase. Molecular line surveys have also frequently shown line wings when targeting hot cores, indicative of both infall and outflows (e.g. Fuller, Williams & Sridharan, 2005; Purcell et al., 2006).

2.1.3 HII regions

HII regions are created when the young high-mass star begins ionising its surroundings by emitting ultraviolet photons, creating an expanding bubble around the object. These sources are classified by their size and emission measure as per the values listed in Table 2.1. For many years, UCHII regions were considered as one of the earliest detectable stages of high-mass star formation, but in recent years, advances in this field have allowed the identification of the other earlier phases already mentioned.

Wood & Churchwell (1989) found 75 UCHII regions in the first large survey of these objects and noted that this number was inconsistent with the expected observable lifetime of these objects (of $< 3 \times 10^4$ years). Wood & Churchwell (1989) further noted five different source morphologies (43 % unresolved, 20 % cometary, 16 % core-halo, 4 % shell, and 17 % irregular or multiply peaked).

The UCHII phase was considered the transition phase between the hot molecular core and the compact HII regions, until Gaume et al. (1995) identified the first hypercompact HII region. It has been postulated that this new class of object was present prior to an UCHII region (e.g. Beuther & Shepherd, 2005). However, it is not yet clear if the hypercompact HII regions represent an evolutionary stage that preceeds the UCHII region, or alternatively represents a different class of

Table 2.1: *Physical parameters of HII regions (Kurtz, 2005).*

Class of region	Size (pc)	Density (cm^{-3})	Emis. Meas. ($pc\ cm^{-6}$)	Ionised mass $M_\odot$
Hypercompact	$\leq$0.03	$\geq 10^6$	$\geq 10^10$	$\sim 10^{-3}$
Ultracompact	$\leq$0.1	$\geq 10^4$	$\geq 10^7$	$\sim 10^{-2}$
Compact	$\leq$0.5	$\geq 5\times 10^3$	$\geq 10^7$	$\sim$1
Classical	$\sim$10	$\sim$100	$\sim 10^2$	$\sim 10^5$
Giant	$\sim$100	$\sim$30	$\sim 5\times 10^5$	10^3-10^6
Supergiant	>100	$\sim$10	$\sim 10^5$	10^6-10^8

object. Kurtz (2006) remark that from the typical sizes of UCHII and hypercompact HII regions may indicate that hypercompact HII regions just represent the ionised gas around a single star where as an UCHII region corresponds to a cluster of stars.

These hypercompact HII regions are classified by their small sizes and large emission measures (see Table 2.1). Kurtz (2005) comment that UCHII regions typically show radio recombination line widths of 30 - 40 km s^{-1}, while those detected towards hypercompact HII regions often show much broader line widths (e.g. Sewilo et al., 2004). Since the first hypercompact HII region was identified by Gaume et al. (1995), the list of known examples of this class of sources has grown (e.g. Murphy et al., 2010; Sewilo et al., 2008).

2.1.4 Triggered star-formation

Evidence for the evolution of one high-mass star causing the birth of a new generation of high-mass stars is growing (so called 'triggered star formation'). Elmegreen (1998) summarized three three distinct mechanisms through which triggered star formation could occur:

- compression of pre-exsisting clumps via, e.g., propagating shock waves created by expanding supernova ('globule squeezing');

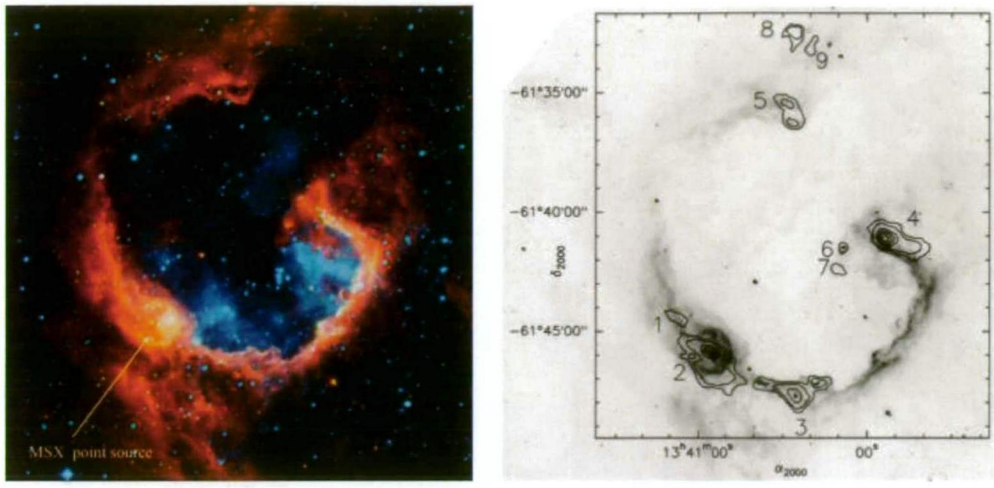

Figure 2.2: *Images of RCW 79 showing a superimposed image of the 8 μm image from GLIMPSE (orange) and the Hα image from SuperCOSMOS (turquoise) on the left, and 1.2 mm dust continuum emission on the right (Zavagno et al., 2006).*

- gas accumulating into a dense shell or ridge that causes the gravitational collapse into cores ('collect and collapse');
- gravitational instabilities induced by clouds colliding ('cloud-cloud collisions').

In 'collect and collapse' an expanding HII region sweeps up a dense shell of molecular material which can result in its fragmentation into clumps. Further disturbances can then trigger the collapse of the created clumps which results in star formation. Zavagno et al. (2006) shows one of a growing number of sources where there is evidence for 'collect and collapse' induced star formation around the Galactic HII region RCW 79. Fig. 2.2 shows both a superimposed 8 μm GLIMPSE image and Hα image of the HII region and a 1.2 mm dust continuum image. The comparison of these images shows that there is a layer of cold dust that traces the edge of the ionized region that has fragmented into clumps. In some of these clumps there is evidence for active high-mass star formation (as traced by masers and compact HII regions).

The observational evidence of triggered star formation is mounting. However it is clear that events such as expanding HII regions that can trigger star-

formation, can also disrupt star formation by causing the dispersion of gas and dust.

2.2 Interstellar masers

Interstellar masers are key tools for investigating the formation of high-mass stars. The masers reside in the dusty molecular envelope or torus of a high-mass star in its early stage of formation, and are a sensitive probe for discovering stars in this embryonic state when the star is not visible because of obscuration from the dust. Many species and transitions of interstellar masers have been detected towards high-mass star formation regions, but the most common and strong transitions are from OH, methanol and water molecules. Analyses carried out in this thesis is limited to main-line OH, 6.7 and 12.2 GHz methanol (Class II transitions) and 22 GHz water masers. Due to this, the review of the literature is mostly limited to these transitions, along with some discussion of Class I methanol maser transitions.

Detailed studies of selected maser sites have been made comparing OH with water, and OH with methanol (Forster & Caswell, 1989, 1999; Caswell, 1997; Caswell, Vaile & Forster, 1995). These studies suggest that the maser spots of all species are usually contained inside a region of diameter less than 30 mpc ($= 0.93\ 10^{15}$ m $= 0.93\ 10^{17}$ cm $\approx$ 6200 au $\approx$ 0.1 light year), corresponding to an angular diameter of about 1 arcsec at a typical distance of 6 kpc. Positional precision of about 1 arcsec is therefore needed to establish whether masers of different species originate from the same site.

Within many star formation regions, on a larger scale of 100 mpc or more, the Forster & Caswell (1989) and Caswell (1997) studies revealed many instances where a number of maser sites are present in a small cluster, often with different combinations of maser species present. There has been considerable speculation that the various combinations are indicative of massive young stars at a different evolutionary stage, or in a different mass range (e.g. Ellingsen et al., 2007), since the different masers are known to trace different physical conditions (e.g. Cragg, Sobolev & Godfrey, 2002).

To date progress has been slow towards the overall goal of utilizing masers

as tools to study star formation, however, the pace of advancement has recently accelerated. The proliferation of complementary high-resolution observations of star formation regions at millimetre through mid-infrared wavelengths means that this trend is likely to continue. Ideally, we would like to use masers to probe the physical conditions in the regions where they arise and the recent advancements in quality, unbiased survey data will aid enormously in this way.

In the following sections, particulars about the common maser species that are detected towards high-mass star formation regions are presented. Further, more specific information is presented at the introductions of Chapters 3 - 7.

2.2.1 OH masers

The discovery of the first interstellar maser was from the OH line by Weaver et al. (1965), who announced the discovery of 'mysterium'. Since their discovery, they have commonly been thought to reside in the compressed zone just outside the expanding HII region (e.g. Cook, 1968; Baart & Cohen, 1985) which is in agreement with the model of Elitzur & de Jong (1978). Cragg, Sobolev & Godfrey (2002) support the idea that OH masers are pumped by infrared radiation from warm dust (chiefly, although line-overlap is also required), just like Class II methanol masers, and suggest that it is the difference in the chemistry of the cores which decides whether emission from one or both species is seen.

Main-line OH maser emission at 1665 and 1667 MHz are by far the strongest and most populous of the OH maser lines, but other excited and satellite-line OH transitions exists in star formation regions, e.g. 1612, 1720, 6030, 6035, 13441 MHz. Caswell & Haynes (1987) found, in observations towards more than 100 southern OH sources, that the 1665 MHz transition is usually stronger than the 1667 MHz transition (typically by a factor of 3) and that it is detected towards 90 % of the 1665 MHz sources. Interferometric observations of Caswell (1998) confirmed that the two strong transitions were coincident to within an arcsec.

On comparing the locations of UCHII regions with OH and water masers, Forster & Caswell (1989) found from the association statistics that OH masers are associated with a later phase of high-mass star formation than water masers, making them an excellent evolutionary probe.

OH masers typically show velocity ranges of $\sim$9 km s^{-1} (Caswell, 1998) and have not been detected with any extreme high-velocity components, suggesting that they are not associated with high-velocity outflows. However, Argon, Reid & Menten (2003) presents evidence that weak OH masers can be produced in outflows.

OH masers are commonly circularly polarised, in fact there are numerous example of sources being 100 % circularly polarised. Zeeman splitting can therefore act to increase the inferred velocity ranges of these sources, since for example, the 1665 MHz line is split by 3 km s^{-1} in a magnetic field of 5 mG (Caswell, 1998). Magnetic fields of a few mG are common in star formation regions (Caswell, 2001; Fish et al., 2003) but fields of up to 40 mG have been observed (Fish & Reid, 2007). By using VLBI techniques, magnetic fields can be mapped over OH maser sites, allowing them to be probed on scales to far less than an arcsec (e.g. Caswell, Kramer & Reynolds, 2009).

Interestingly, the 1667 MHz seems to always be the dominant line in OH megamasers and sometimes the 1665 MHz line is not detected at all (Darling & Giovanelli, 2002), in direct contrast with OH masers detected in our Galaxy. Zeeman splitting has also been observed in OH megamasers, allowing magnetic fields to be probed (e.g. Robishaw, Quataert & Heiles, 2008).

OH masers in our Galaxy show variability of up to a factor of two over a period of years, but some sources appear to remain stable over the course of $\sim$20 years (e.g. Caswell, 1998). Some sources have exhibited quite rapid variations, although show generally similar emission at each epoch with changes to the relative amplitudes of components (e.g. Clegg & Cordes, 1991). Robishaw, Quataert & Heiles (2008) notes that some OH maser sources that have been observed with strong magnetic fields (both in our Galaxy and in OH megamasers) were undergoing flaring activity, suggesting that variability in OH masers may correlate with strong magnetic fields.

Caswell (1998) presents a catalogue of more than 200 OH masers detected in a combination of targeted observations and a complete search between longitudes 312° to 356°. This catalogue of OH masers will provide useful comparisons with complete methanol (Green et al., 2009) and water (Walsh et al., 2008) maser surveys that will cover the same regions. However, much is already known about the

association of OH masers with other maser species since these sources have been the common targets for other maser surveys. Methanol masers in the 6.7 GHz transition are associated with about 80 % of OH sites and a comparable number is seen with water masers. However, the statistics relating to the number of water and methanol masers that are devoid of OH emission are not well determined.

2.2.2 Methanol masers

The first detection of methanol maser emission was in a series of 25 GHz transitions by Barrett, Schwartz & Walters (1971) towards Orion A. Later, Menten et al. (1986) showed that these sources were relatively common in the vicinities of high-mass stars. To date, more than 50 transitions of methanol masers have been detected towards star formation regions (Müller, Menten & Mäder, 2004, and references therein).

Methanol masers are broken into two classes, reflecting their different locations with respect to the star formation region (Menten, 1991a) which is now understood to reflect their different pumping mechanisms. Class I sources are believed to be ccollisionally excited, where as Class II sources undergo radiative excitation from infrared photons. Below we discuss briefly the characteristics of each of these classes of methanol masers.

Class II methanol masers

Class II methanol masers have been detected in more than 20 transitions (Müller, Menten & Mäder, 2004, and references therein), none of which are as common or strong, or as extensively studied as the 12.2 and 6.7 GHz transitions. Due to this, and the fact that these are the two transitions that are investigated in this thesis, the discussion that follows is focused only on these two transitions.

From soon after the discovery of the relatively strong and wide-spread Class II methanol maser transition at 12.2 GHz (2_0–3_{-1} E) by Batrla et al. (1987), methanol masers have been considered as excellent tracers of star formation regions, appearing to be coincident with OH masers and UCHII regions. An early search for 12.2 GHz maser sources towards sites located in the southern hemisphere confirmed their close association with star formation regions (Norris et al.,

1987).

In observations towards known star formation regions in the northern hemisphere during 1991, Menten (1991b) discovered even stronger emission from methanol masers in the 6.7 GHz (5_1–6_0 A^+) transition. Menten (1991b) noted that all of the detected 6.7 GHz sources had 12.2 GHz counterparts and therefore suggested that this new transition belonged to the Class II maser group. Later observations of Class II masers showed that the sources were indeed closely associated with UCHII regions as well as OH masers (e.g Caswell, Vaile & Forster, 1995). These observations showed that the 6.7 GHz transition was even more wide-spread than the 12.2 GHz methanol masers.

Cragg, Sobolev & Godfrey (2005) showed through maser modelling that the physical conditions that are required to produce luminous class II methanol masers in the 6.7 and 12.2 GHz transitions are similar. While there is a large amount of overlap in the conditions for the two transitions (as shown in Fig. 2.3), they do not cover exactly the same regions of parameter space. Given that there is a large fraction of 6.7 GHz methanol masers devoid of 12.2 GHz methanol maser counterparts, the physical conditions in these regions must be close to the point where the 12.2 GHz masers switch on or off.

The 6.7 and 12.2 GHz methanol maser transitions are two of the strongest detected towards star formation regions and both are known to trace an early evolutionary stage of high-mass star formation (Ellingsen, 2006). Complementary observations of these two strong methanol maser transitions are especially useful in probing the physical conditions of the environments in which they arise, as they are known to typically be co-spatial to within a few milliarcseconds (Moscadelli et al., 2002) especially where the spectra at the two transitions are similar (Norris et al., 1993).

Interferometric observations by Norris et al. (1993) showed that the 6.7 GHz methanol masers were frequently distributed along lines or arcs, suggesting that they may be associated with shock fronts, jets or edge on protoplanetary disks. Observations for 6.7 GHz methanol masers towards low-mass stars have failed to discover any luminous emission (Minier et al., 2003; Xu et al., 2008). These sources therefore have an important role to play in understanding high-mass star formation, regions with which they are exclusively associated. Class II methanol

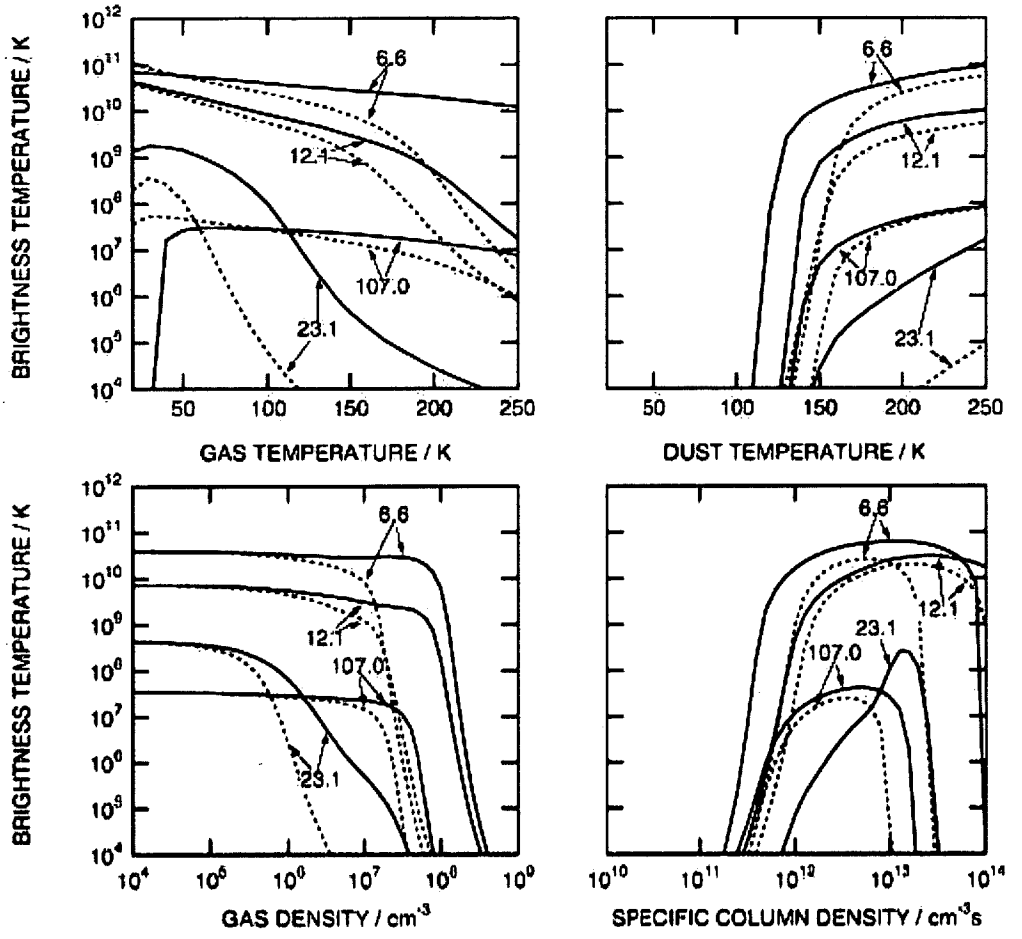

Figure 2.3: *Methanol maser models for four of the Class II transitions of methanol masers from Cragg, Sobolev & Godfrey (2005) showing the effects that parameter variation has on the maser brightness temperature. Calculations are presented for two differed collision rates: PFD collision data (solid lines) and propensity rules (dashed).*

masers require warm temperatures of ~150 K, and dense environments (10^{6-7} cm^{-3}) (e.g. Müller, Menten & Mäder, 2004), characteristics commonly found in high-mass star formation regions.

From high-sensitivity, interferometric observations for these sources, it has been found that they are not associated with energetic outflows (unlike water masers) and as such their velocities are reliably near that of the systemic velocity of the regions they are tracing (e.g. Caswell, 2009). This is particularly helpful as it allows kinematic distances to the high-mass star formation regions to be calculated. Furthermore, since masers at 6.7 and 12.2 GHz exclusively trace sites of high-mass star formation, they are restricted to locations within the spiral arms, making them excellent candidates for tracing Galactic structure through parallax measurements. For example, through parallax measurements of 18 masers, Reid et al. (2009) have uncovered details of the structure of our Galaxy which have allowed them to present a new prescription for the calculation of more accurate kinematic distances.

In general, neither the 6.7 or 12.2 GHz masers show extreme levels of variability, which is typically limited to less than about 20 % over months to years (e.g Caswell et al., 1995b). Variations of factors of two or more are very rare (e.g. Caswell et al., 2010) and the vast majority of these methanol maser sources are recognisable in spectra taken over two or more epochs. Some sources however, show variability with remarkable periodicity (e.g Goedhart et al., 2009, 2005a,b; Goedhart, Gaylard & van der Walt, 2004).

Multiwavelength observations of a sample of 6.7 GHz methanol masers (Walsh et al., 1998, 1999, 2003) found that 6.7 GHz methanol masers were commonly offset from UCHII regions, but are usually associated with the peaks of 1.2 mm dust continuum emission (Hill et al., 2005). These findings support the idea that the 6.7 GHz methanol masers are associated with a generally early evolutionary stage of high-mass star formation, typically emitting prior to the onset of a strong UCHII region. Molecular line observations targeting these sources (Purcell et al., 2006, 2009) showed that most of the sources associated with the 6.7 GHz methanol masers showed emission suggestive of them being hot cores, leading to the suggestion that the sources are internally heated. Furthermore, many of the thermal line profiles showed signatures indicative of infall or outflow, additional

evidence of ongoing star formation.

A complete survey for 6.7 GHz methanol masers, the Methanol Multibeam Survey (MMB) has been carried out with the Parkes radio telescope (see Section 7.2 or Green et al. (2009) for more extensive details), pinpointing sites of high-mass star formation. The MMB survey constitutes the most sensitive large scale search for the strong widespread emission exhibited from the 6.7 GHz methanol maser transition. Observations of the large portion of the Galactic plane visible to the Parkes radio telescope have now been completed (Caswell et al., 2010; Green et al., 2010). Sources detected in this manner will form an important catalogue of sources that will be the targets for future studies.

Class I methanol masers

Class I methanol masers are collisionally excited via shocks from outflows (e.g Voronkov et al., 2006) or cloud-cloud interactions (e.g. Mehringer & Menten, 1996). These masers are found within the vicinity of high-mass stars, but are generally offset from UCHII regions and strong infrared sources (e.g. Cyganowski et al., 2009), as shown in Fig. 2.4. More than 20 transitions of methanol have been detected as Class I masers (e.g. Müller, Menten & Mäder, 2004) and the common ones include a series of transitions near 25 GHz, as well as 36, 44, 84 and 95 GHz. Other transitions have also been detected in the vicinity of high-mass stars, such as at the 9.9 GHz transition (Voronkov et al., 2010a).

High detection rates of Class I sources have been detected towards EGOs; sources that show dominant, extended emission in the 4.5 μm band of GLIMPSE (Cyganowski et al., 2009; Chen, Ellingsen & Shen, 2009). Cyganowski et al. (2008) suggest that these EGOs are produced by shock-excited H_2 and CO and are therefore regions that show characteristics consistent with those expected to harbor Class I emission.

Ellingsen (2006) proposed that Class I methanol masers are associated with a generally early evolutionary stage of high-mass star formation than Class II sources. From this conclusion Ellingsen et al. (2007) placed Class I sources as the earliest detectable common maser type on their evolutionary diagram (see Fig. 2.9). With the benefit of new data, Voronkov et al. (2010a) find evidence to suggest that Class I sources actually outlast the stage where the common Class II

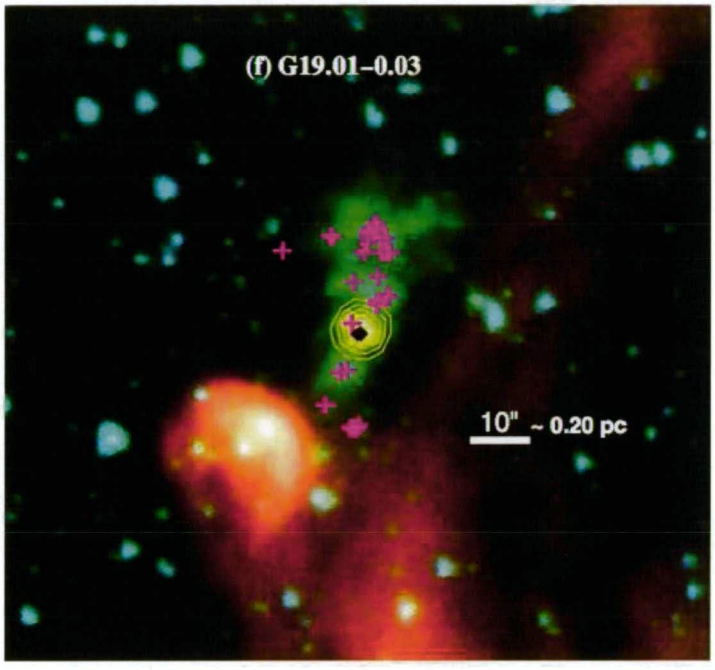

Figure 2.4: *Three-colour GLIMPSE images of G 19.01–0.03 (Cyganowski et al., 2009) where 8.0 μm is shown in red, 4.5 μm is shown in green and 3.6 μm is shown in blue. Overlaid are the positions of the Class II methanol masers at the 6.7 GHz transition (black diamonds) and Class I methanol masers at the 44 GHz transition (magenta crosses). Yellow contours show the extent of the 24 μm MIPSGAL emission.*

maser transition at 6.7 GHz is present, finding a significant overlap in time with the presence of OH maser emission which is known to trace a later evolutionary stage (Forster & Caswell, 1989). The authors find evidence to suggest that shocks created by expanding HII regions are able to excite Class I transitions.

Early observations of Class I methanol masers showed relatively simple spectra, often with only one spectral feature. Since multiple transitions were often found at the same velocity, it was suggested that all of the detected transitions arose from the same volume of gas. More recently, some Class I methanol maser sources have been detected with high velocity features extending to 30 km s^{-1} from the peak emission (Voronkov et al., 2010b), consistent with their association with outflows. Recently, Class I sources have also been detected towards both low and intermediate mass stars (Kalenskii et al., 2010).

2.2.3 Water masers

Water masers have been regarded as one of the best indicators of star formation since soon after their first detection in Sgr B2, Orion and W 49 in 1969 (Cheung et al., 1969). Water masers have several advantages over either methanol or OH masers, particularly that they are the most populous and strongest of the maser species detected towards star formation regions. The 22 GHz $6_{1,6} \rightarrow 5_{2,3}$ rotational transition of water is the brightest spectral line at radio wavelengths. Other water maser transitions have been observed, particularly in higher frequency vibrational transitions, chiefly towards evolved stars (e.g. Menten & Melnick, 1989).

The nature of the sources that the water maser emission is tracing are even more puzzling than other species of maser emission. Water masers have been detected towards both low- and high-mass star formation regions (e.g. Furuya et al., 2003) as well as towards active galactic nuclei and in the envelopes of asymptotic giant branch stars (e.g. Deacon et al., 2007). Water masers are produced by collisional excitation and the proposed model of Elitzur et al. (1989) is generally supported. The physical conditions required to produce water maser excitation are high densities (10^7-10^9 cm^{-3}) and temperatures of a few 100 K (Elitzur, Hollenbach & McKee, 1989), both of which are seen in the inner parts of circumstellar disks around young stellar objects and in regions of shocked gas (Torrelles et al.,

2002). Emission from this transition often exhibits significantly greater temporal variability than is commonly observed in other interstellar maser species such as OH and methanol (Brand et al., 2003; Felli et al., 2007).

It has commonly been thought that water masers are most prolific at an early stage of stellar evolution. However, targeted observations towards sites of high-mass star formation tend to discover many isolated water masers that can be only partly accounted for by very young sites preceding OH maser excitation. Other offset positions indicate the additional occurrence of water masers towards lower mass stars, evolved stars, or in high velocity fragments that have travelled far from the initial site. In the latter case, maser spots from individual fragments are sometimes ephemeral, and disappear on a timescale as short as months, but are often replaced by generally similar emission in the same region, although at a slightly different position and velocity.

To date there have been relatively few large scale unbiased surveys for water masers. Searches have focused on high-mass star formation regions, typically targeting UCHII regions selected on the basis of *IRAS* colours (e.g. Churchwell et al., 1990) or other maser species (e.g. Batchelor et al., 1980; Caswell et al., 1983b; Beuther et al., 2002). Due to this, the known sample of water masers lacks the completeness that has been acheived in both 6.7 GHz methanol masers (e.g. Caswell et al., 2010; Green et al., 2010) and main line OH masers (e.g. Caswell, 1998). This, coupled with the fact that the positions of the majority of southern hemisphere water masers are not known to sub-arcsecond accuracy, means that relatively little is known about water maser associations with infrared and molecular sources. To combat these biases in the known sample of water maser emission, two relatively small but highly sensitive complete searches (Caswell & Breen, 2010; Caswell, Breen & Ellingsen, 2010) have been carried out with the ATCA. In addition to these, a large-scale single-dish survey for water masers has recently been completed over 100 degrees of the Southern Galactic Plane (Walsh et al., 2008) and the survey results are expected to be released within the coming year.

Palagi et al. (1993) investigated the *IRAS* counterparts to all of the water masers known north of the declination cut off of –30 degrees up to 1988 (~500 sources). On the basis of the colours of the nearest *IRAS* source, within a radius

of 2 arcmin, Palagi et al. (1993) concluded that 52 % of the water maser sources were associated with star formation regions, while 45 % were associated with late type stars. The large number of associations with late type stars is slightly concerning, but can be attributed to a combination of the chance coincidences in such a large search radius, the adopted colour classification schemes and the tendency for the early water maser searches to biased against high-mass stars in the early stages of formation. In contradiction with Palagi et al. (1993), Garay & Lizano (1999) proposed that the detection of water masers almost guarantees a site of high-mass star formation. While this is true for the vast majority of instances, no definitive study has shown the percentage of the total population of water masers that are associated with high-mass, low-mass or evolved stars.

Water maser emission detected towards low-mass stars is generally weaker and even more variable than water maser emission that is detected towards high-mass stars (Claussen et al., 1996). The population of water masers towards lower mass stars is not well understood, and the mass range of objects that can be associated with water maser emission is not currently well constrained.

Water masers towards high-mass star formation regions

The majority of the early searches for water masers were targeted towards sites of OH maser emission and yielded very high detection rates (e.g. Johnston et al., 1972; Caswell et al., 1974; Batchelor et al., 1980; Caswell et al., 1983a,b, 1989). These searches were so successful that some even suggested that there may be a one-to-one relationship between the two maser species. Others, with the benefit of better spatial resolution but with the drawback of being limited to only a few strong sources (such as W3(OH), W49N and W51), suggested that OH and water masers may not be closely related (e.g. Mader, Johnston & Moran, 1978) although noted that sites of OH maser emission were still one of the best places to detected water maser emission.

Water maser searches towards infrared targets were also popular, and achieved similar detection rates to the early OH maser targeted searches. Jaffe, Gusten & Downes (1981) found 42 far-infrared sources in the Galactic longitude range 10° to 16°. Water maser observations targeting these objects yielded a detection rate of almost 60 % and therefore lead to the suggestion that far-infrared sources were

an even better place to detect water maser sources than UCHII regions or OH maser sites. Attempts to make targeted searches on the basis of infrared colours have achieved mixed results. Churchwell et al. (1990) achieved a high success rate (discussed below), while a search by Palla et al. (1993) only detected water masers towards 5 % of the sources searched.

Churchwell et al. (1990) targeted a sample of 84 UCHII regions and sources with similar infrared colours for ammonia and water maser emission. The authors found water masers towards 67 % of the sources searched. Hofner & Churchwell (1996) present high resolution images of 21 of the Churchwell et al. (1990) sources, and compare these with the images of the associated UCHII regions. They find that the water masers appear in different regions with respect to the associated UCHII region depending on the classification of the UCHII region morphology. On average, Hofner & Churchwell (1996) find that the separation between the UCHII peak emission and the associated water maser sources to be almost 3 arcsec. In the case of cometary UCHII regions, the water maser sources are found in front of the cometary arc (e.g. Fig. 2.5), where as for non-cometary sources, the water maser emission is projected against the UCHII emission.

Codella et al. (1994) showed that water masers can be associated with diffuse HII regions, but at a much lower rate of detected than that found towards less evolved UCHII regions and suggest that water masers are associated with about one-sixth of the lifetime of HII regions. This is consistent with the expectation that the evolution of the UCHII region will destroy the associated maser emission (e.g. Caswell, 2001).

VLBI measurements of water masers have uncovered details about the regions that the sources are tracing, and proper motion studies have uncovered important characteristics; such as the distance to the Galactic Center (Reid et al., 1988). Furthermore, high angular resolution studies of water maser have shown that the water maser trace a number of specific regions in high-mass star formation regions. These are as follows: (1) in the rotating disk around the young stellar object (e.g. Torrelles et al., 1998); (2) in the high velocity bipolar outflows that originate from the young stellar object (e.g. Genzel et al., 1981; Torrelles et al., 1998; Hofner & Churchwell, 1996); (3) in the bow shocks created by the outflows and expanding shells (e.g. Hofner & Churchwell, 1996).

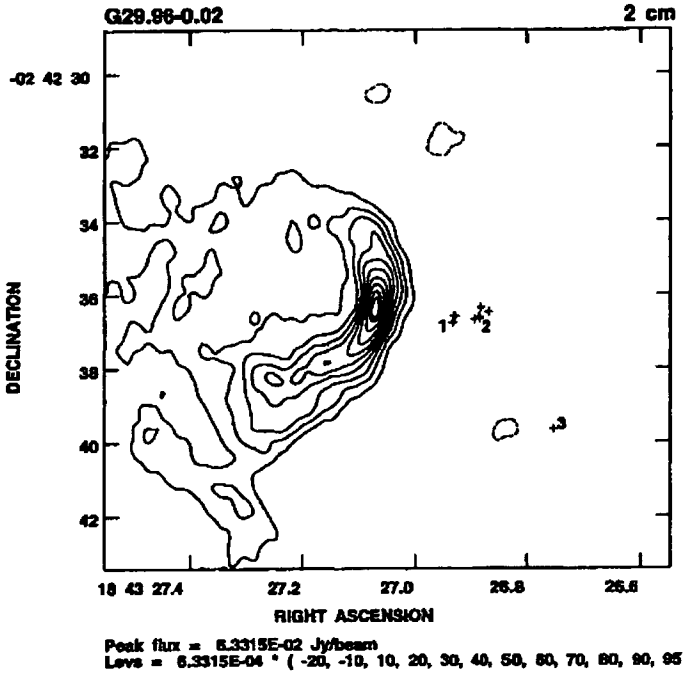

Figure 2.5: *2cm continuum map of cometary UCH*II *region G 29.96–0.02 overlaid with the location of the water maser emission (crosses) (Hofner & Churchwell, 1996).*

The maser emission from the 22 GHz transition of water detected towards high-mass star formation regions has been noted for its ability to vary dramatically in flux density on relatively short time scales from only months after the discovery of the emission (Knowles et al., 1969). Sullivan (1971) proposed that the variability in the water maser emission could be explained by a change in any, or a combination of three factors; (1) changes in the pump power, (2) a change in the density of water molecules in the $6_{1,6}$ and $5_{2,3}$ rotational states, or (3) a change in the path length, which can be influenced by turbulence, density, temperature or passing shock fronts. Since then, other investigations attempting to quantify this behaviour have been attempted (e.g. White & Macdonald, 1979; Comoretto et al., 1990; Valdettaro et al., 2001; Brand et al., 2003; Felli et al., 2007) but the exact process that results in the observed variability is still largely unknown. Batchelor et al. (1980) show that only slightly more than half of the water maser features that they observed varied less than a factor of two over a period of less than a year.

Two long-term water maser monitoring projects have been completed over 13 and 20 years (Brand et al., 2003; Felli et al., 2007, respectively) and have both found that the most persistent water maser features occur at velocities close to the velocity of the associated molecular cloud (see Fig. 2.6). Brand et al. (2003) found that the higher luminosity young stellar objects (as determined from the *IRAS* sources that the masers are associated with) were generally associated with stronger and more stable water maser emission. The authors also suggest that some water maser sources exhibit periodic, long-term variations which may be a consequence of periodic variations in the jets that are emanating from the associated young stellar object. Brand et al. (2003) also show that some features show either acceleration or deceleration between 0.02 and 1.8 km s^{-1} yr^{-1} which may be explained (depending on the nature of the source of the water maser emission) by rotation of the disk, changes in the velocity of the outflow or precession of the outflows. Caswell (2004a) similarly noted an apparent acceleration of some of the high-velocity features that he detected in water masers in NGC 3576. Caswell (2004a) notes that this acceleration implies that the ejected outflow material must still be close to its origin, otherwise a deceleration would be expected.

Water masers have been noted on many occasions to exhibit high velocity

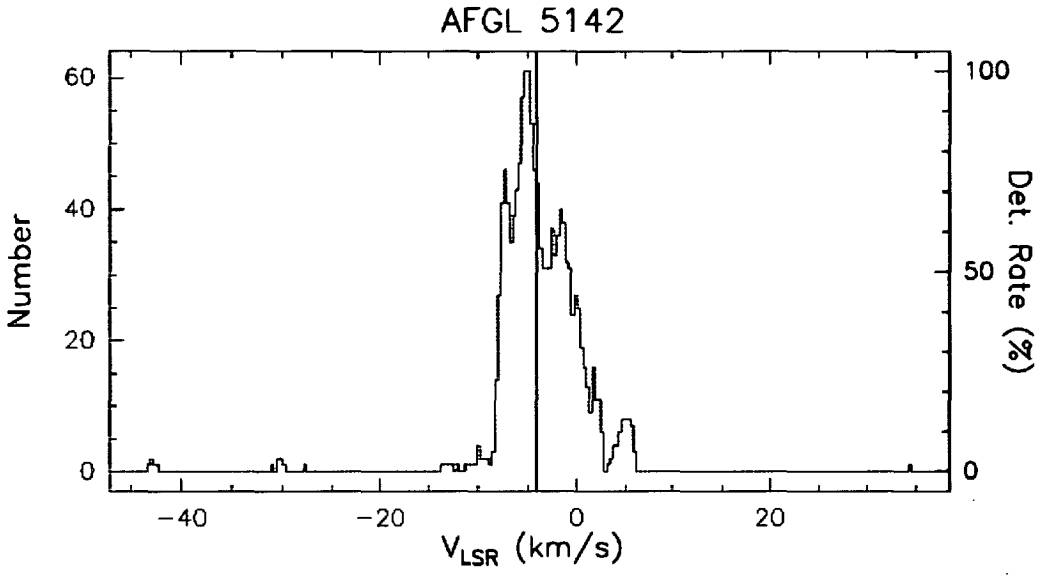

Figure 2.6: *Rate of occurrence plot for water maser AFGL 5142 from Felli et al. (2007). The vertical line shows the velocity of the associated thermal molecular gas.*

features and emission more than 100 km s^{-1} from the systemic velocity is not considered unusual (e.g. Batchelor et al., 1980). Given the close association between a number of water masers with outflows (e.g. Genzel et al., 1981) from young stellar objects, it is not difficult to explain the tendency for water masers to show much wider velocity ranges than e.g. 6.7 GHz methanol masers which are never associated with strong outflows (Caswell et al., 1995a). Even water masers that are not directly associated with outflows, but rather expanding shells which often show remarkable symmetry in blue and red-shifted emission, can show comparatively broad velocity ranges.

Brand et al. (2003) suggest that water masers that are associated with higher luminosity sources are more likely to excite emission over large velocity ranges but that the emission that dominates the spectrum is likely to be close to the velocity of the associated molecular cloud. On comparison between the water maser peak velocities and that of associated ammonia emission, Churchwell et al. (1990) found that the distribution was skewed towards there being more blue-shifted water maser sources, as shown in Fig. 2.7. Zinchenko, Mattila & Toriseva (1995) compared the velocity of the peak of the water maser with the associated

CS emission for 27 water masers and found that the mean difference in velocity in -8.4 ± 4.3 km s^{-1} which they suggest means that the water maser emission is preferentially beamed in the direction of its movement relative to the parent molecular cloud.

Water masers more often show high-velocity emission that is blue-shifted than red-shifted (e.g. Batchelor et al., 1980; Caswell, 2004a). Caswell (2004a) suggest two possible explanations; (1) weak continuum emission from the central object is seen to be amplified by the blue-shifted outflowing water if the two are closely aligned to the observers line of sight, or (2) variations in temperature and density can occur along the outflow and therefore the different paths could promote the maser emission from one end. For a number of sources displaying the high-velocity emission, the peak of the water maser emission is close to systemic, however a number of exceptions to this have been identified in a growing number of water masers that fall into a distinct class of objects that are dominated by highly blue-shifted outflows (e.g. Goss et al., 1977; Caswell, 2004a; Caswell & Phillips, 2008; Caswell & Breen, 2010; Caswell, Breen & Ellingsen, 2010). Caswell & Breen (2010) suggests that these sources may represent an early evolutionary stage, explaining the preponderance of sources identified in recent complete searches compared to sources presented in the literature (which have historically been biased towards more evolved sources). Further supporting evidence for this is that the sources that are dominated by strong blue-shifted emission are rarely accompanied by OH maser emission (Caswell & Phillips, 2008; Caswell & Breen, 2010).

2.3 Evolutionary tracers of high-mass star formation regions

The idea that the presence, absence or intensity of certain properties associated with high-mass star formation regions can give an indication on the relative evolutionary stage of star formation is not a new one. In particular, from soon after the discovery of interstellar masers, it has been suggested that these masers are associated with a particular evolutionary phase of star formation (e.g. Lo, Burke

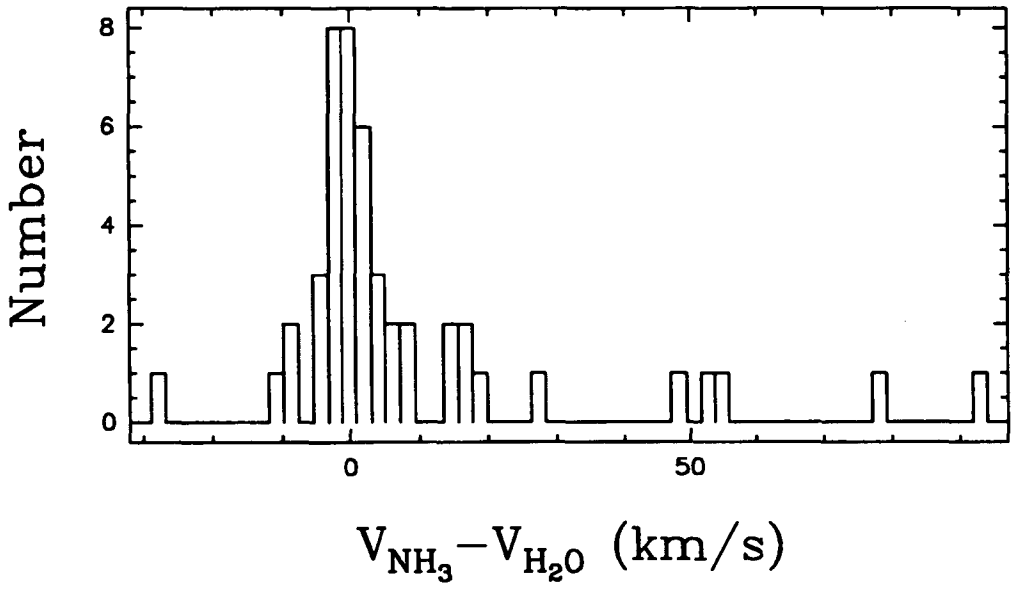

Figure 2.7: *Distribution of the difference between the water maser peak velocity and the velocity of the associated ammonia emission Churchwell et al. (1990).*

& Haschick, 1975; Genzel & Downes, 1977). The possibility that different properties of high-mass star formation regions can be used as sequential signposts of the evolution of the region, has received increasing attention in recent years as complementary data for these regions at high angular resolution are becoming more prevalent.

Many other tracers of high-mass star formation have been considered as potential evolutionary probes. Obviously, the presence of centimeter radio continuum emission is a good indicator of a certain evolutionary stage, after the ignition of the central object (and are therefore limited to the later stages of formation). Other tracers include: thermal molecular lines, including widespread and readily detectable spectral lines such as ammonia; and properties of infrared data, particularly in the mid-infrared regime. The deciphering of the evolutionary status of high-mass objects is enormously aided by studies employing the use of data of more than one wavelength. Considering at least one tracer in conjunction with another, unlocks tremendous scope for advances in this matter.

A number of works investigate the evolution of high-mass star formation re-

gions, and a basic evolutionary scenario for high-mass stars is pretty well excepted. A broad evolutionary sequence is based on the combined conclusions of many investigations, including Kim & Koo (2001); Minier et al. (2003); Fuller, Williams & Sridharan (2005); Kurtz (2006); Purcell et al. (2006); Zinnecker & Yorke (2007); Longmore et al. (2007, 2008); Purcell et al. (2009); Lo et al. (2009), is as follows:

- **Cold molecular clouds.** High-mass stars form within dense regions of cold gas and dust within molecular clouds. At these earliest stages of formation, the size of the regions that will go onto form stars is about 10 pc, and can be traced by simple quiescent molecules whose production is not dependent on temperature (e.g. CO, CS, HNC, HCN, HCO^+, etc.). At this stage, temperatures of less than around 20 K are expected very little dust continuum or free-free emission would be detectable.

- **Cold dense cores.** In the 'second stage' of formation, the dense regions within the cold dusty molecular clouds collapse under self gravity to cores with sizes of $\sim$1 pc. Cold dense cores can be detected through tracers such as millimeter dust continuum emission, infrared dark clouds, strong emission from N_2H^+ and NH_3. At this stage moderate depletion of HCO^+ and high levels of CO and CS depletion would be expected.

- **Hot molecular cores.** The mass of the objects increase through accretion and/or mergers. As the temperature and density of gas increases, molecules collide and stick to the grain surface allowing the production of new saturated molecules.

  In the hot molecular core phase sources have sizes of $\sim$0.1 pc. The heating of the central object, along with the presence of outflows, encourages the production of more complex molecules. One of the best tracers of this phase are masers, particularly methanol (although this is based largely on biased data and water masers are also likely to be very prevalent at this stage). Other good tracers of this outflow phase include CH_3OH, SiO, SiO_2, SO, SO_2, H_2CS, HCO^+.

- **UCHII regions.** Within the hot molecular core, and UCHII region forms as the ultraviolet radiation from the embedded star ionises the surrounding material. In the beginning of this process, the size of this region is ~0.1 pc and temperatures are 100 - 300 K. This stage is well traced by the detection of radio continuum, masers and strong infrared radiation. However, as the UCHII region expands as the source evolves, to become a HII region that can reach sizes of ~10 pc across, maser emission ceases and complex molecules are destroyed.

Fig. 2.1 presents a schematic of the hierarchical structure within molecular clouds and has been taken from Kim & Koo (2001). Also shown on this figure are the approximate densities and temperatures present during each of the stages. Fig. 2.8 presents an illustration of the proposed evolutionary scenario of a cluster of high-mass stars (Purcell, 2006). This illustration presents a clear but simplistic view of the basic evolutionary scenario by assuming that all high-mass stars forming in a given cluster will be at the same evolutionary stage. The proposed evolutionary sequence of Purcell (2006) can now be expanded upon by testing it on large groups of sources over a wide variety of wavelengths. The transition periods between each of the phases should be further investigated to better understand the intermediate phases. Masers and other spectral lines are excellent candidates for tracing, in particular, the hot core phase on shorter timescales.

Spectral lines have several advantages over other tracers of high-mass star formation as a number of transitions are bright and relatively widespread. Only spectral lines are able to probe: the kinematics of the regions that they are tracing; the physical conditions in the immediate vicinities in which they arise; the chemical composition of the high-mass star formation regions; and these characteristics combined can provide information about the relative evolutionary stages of the high-mass star formation regions, especially in the hot core phase, where a multitude of molecular lines are prevalent.

Progress has been made in tracing the different evolutionary stages of high-mass star formation in different wavelengths. Below we summarise some of the major results from evolutionary investigations, including the use of masers, thermal lines, radio continuum and infrared data.

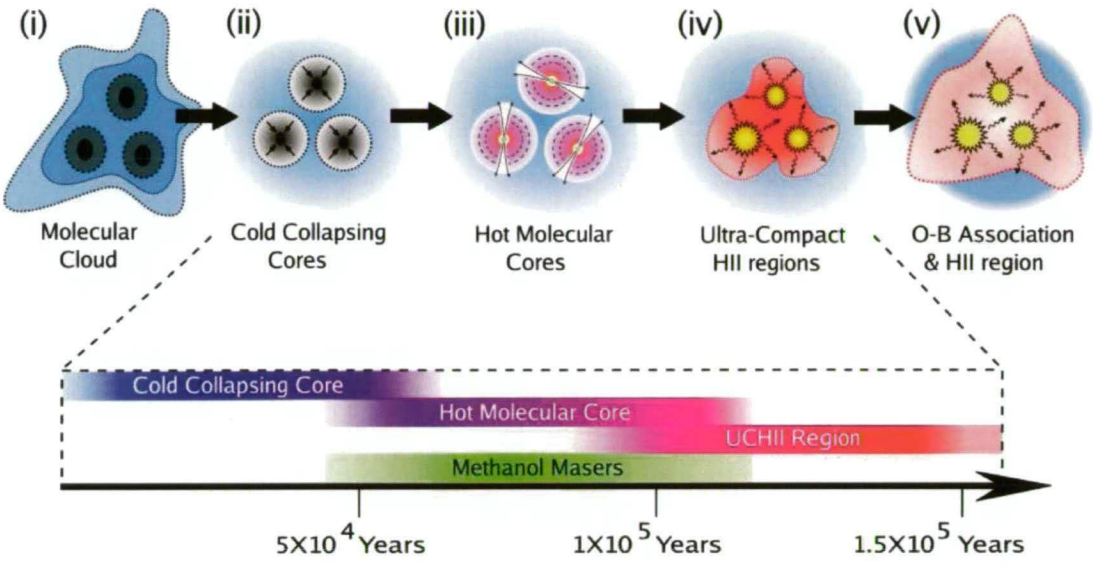

Figure 2.8: *Illustration showing the proposed evolutionary scenario of a cluster of high-mass stars (Purcell, 2006). The five evolutionary phases (as listed by Purcell (2006)) are as follows: (i) Massive stars are born in dense knots of cold gas and dust at the heart of giant molecular clouds; (ii) These knots collapse into cores under self gravity and increase in mass, via mergers or accretion; (iii) Heat and outows from the central protostar evaporate simple ices from the dust grains, driving a rich time-dependent chemistry and leading to the production of complex hydrocarbons in a hot core; (iv) UV-radiation from the young embedded stars creates a bubble of ionised gas, creating an UCHII region which subsequently expands (v), destroying the complex molecules.*

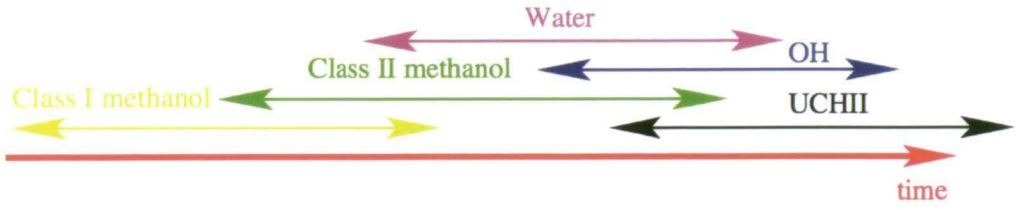

Figure 2.9: *'Straw man' diagram of the evolutionary sequence for the common maser species detected towards high-mass star formation regions from Ellingsen et al. (2007).*

2.3.1 Masers as evolutionary signposts of high-mass star formation

To date, there have been numerous proposed scenarios for the evolutionary phase that masers are tracing, with some more specifically addressing the relative stages that the individual common maser species are tracing. Based on the knowledge that different maser species are tracing different physical conditions (e.g. Cragg, Sobolev & Godfrey, 2005), the probability that the different maser species could provide us with a reliable sequential clock for the relative evolutionary stages of high-mass star formation (although restricted to the phase where masers are present) is considered high by some (e.g. Ellingsen et al., 2007). Fig. 2.9 presents a proposed evolutionary sequence for the common maser species in high-mass star formation regions of Ellingsen et al. (2007).

Historically, individual studies of combinations of the common maser species in high-mass star formation regions have uncovered mixed, and sometimes contradictory evolutionary results. However, until recently, observations had typically been limited to highly biased surveys with poor sensitivities and positional accuracies or to small number of well studied 'special' sources. Some exceptions are true, particularly the early studies with the VLA, but although overcoming sensitivity and positional uncertainties, these observations were still strongly biased towards particular groups of sources.

A VLA study of both OH and water maser emission in high-mass star formation regions was carried out by Forster & Caswell (1989). These observations targeted sites of known OH maser emission. Forster & Caswell (1989) proposed

that the size and complexity of a maser cluster, comprising of water and OH maser spots, may indicate the relative evolutionary stage of the exciting star. Furthermore, they propose an evolutionary scenario whereby the water masers appear first and are then closely followed by OH maser emission (from comparison with their radio continuum data) and suggest that this phase lasts 10^5 years. Caswell et al. (1983b) suggested that the ratio of water to OH maser intensity may change systematically with age and therefore could be a useful diagnostic in determining the evolutionary stage of the masing region.

Walsh et al. (1997) targeted 535 *IRAS*-selected objects for 6.7 GHz methanol maser emission. High resolution followup observations (Walsh et al., 1998) of both the detected 6.7 GHz methanol masers and radio continuum observations conducted at 8 GHz, found that the majority of 6.7 GHz methanol masers were most likely present before a detectable associated UCHII region. Furthermore, from this large sample the authors found that the methanol maser emission is likely to be quickly destroyed as the UCHII region evolves. Caswell (1997) compared the locations of excited OH masers with 6.7 GHz methanol masers and UCHII regions and found that there was a striking trend whereby the UCHII regions are preferentially associated with the sources exhibiting excited OH masers, further supporting the hypothesis that methanol masers are present at a very early evolutionary stage of high-mass star formation.

The investigation of the relative locations of OH, water and methanol masers as well as radio continuum by Garay & Lizano (1999) led to the conclusion that water masers appear in the earliest stages of high-mass star formation, during the rapid accretion phase, while 6.7 GHz methanol masers are seen later as the protostar forms a detectable UCHII region and the OH masers appear in the latest stages in the compressed circumnebular shell. The masers diminish as the UCHII evolves into a diffuse HII region Codella et al. (1994). There is however much room for error in these simplistic determinations as the age calculations are often crude. There are also numerous examples of sources where all three maser species are seen at the same time, and hence evolutionary stage of the star's formation.

Comparisons made by Beuther et al. (2002) between the locations of water and 6.7 GHz methanol masers with centimeter radio continuum showed that six out

of the 22 water maser they detect are coincident with radio continuum, whereas this is true for only 3 of the 18 observed 6.7 GHz methanol masers. The difference in the detection statistics of the two maser species with associated UCHII regions, they claim, suggests that the methanol masers are more sensitive to the ignition of the central object and thereby ceasing the emission of the methanol maser emission at an earlier evolutionary phase than the water maser sources. Drawing firm conclusions about these results is difficult since the sample size is relatively small.

An investigation of the association between a statistically complete sample of 6.7 GHz methanol masers with GLIMPSE and *MSX* sources by Ellingsen (2006) uncovered further evidence for an evolutionary sequence for the different maser species in high-mass star formation regions. Towards these objects, OH (Caswell, 1998), Class I methanol masers in the 95.1 GHz transition (Ellingsen, 2005), and water masers (Hanslow, 1997) have also been searched, allowing for a comparison in the infrared properties associated with the different combinations of maser sources. Ellingsen (2006) found evidence that suggested that the 6.7 GHz methanol masers with associated 95.1 GHz methanol maser emission were likely to be younger than the 6.7 GHz methanol masers with associated OH masers. If these results are representative of all methanol masers that are considered either Class I or Class II objects, then this implies that Class I sources are present at the earliest evolutionary stages, followed by Class II sources and then finally OH masers.

A recent study by Fontani, Cesaroni & Furuya (2010) investigated the evolutionary phases that both Class I and Class II methanol masers as well as water masers, are tracing. This study saw the completion of new 6.7, 44 and 95.1 GHz observations of methanol masers, which were compared to the water maser observations of Palla et al. (1991) (which had targeted the same *IRAS* selected sources). All of the mentioned observations were carried out with various single dish instruments. On the basis of age estimates of the targeted *IRAS* sources, Fontani, Cesaroni & Furuya (2010) reports that there is no evidence to suggest that Class I methanol masers are present at an earlier evolutionary phase than the Class II sources, instead favouring a scenario where the phenomena triggering the maser emission become more prominent throughout the evolution process; an

explanation that accounts for the higher detection rate of both the Class I and Class II methanol masers in the more evolved *IRAS* sources. One of the problems with this conclusion is that the different sensitivities of the observations of the different maser transitions. For example, if the maser species increased in flux density as the sources evolved (which we certainly find evidence for in the case of water masers and both 6.7 and 12.2 GHz methanol masers in Chapters 4, 5 and 7) then the observations of Fontani, Cesaroni & Furuya (2010) are much more sensitive to younger sources in the 6.7 GHz methanol maser transition that either of the Class I transitions. If the sensitivity of the Class I observations was comparable to that of the 6.7 GHz observations, a very different result might be seen, with the possibility of more detections of Class I sources associated with the less evolved sources.

Specific characteristics of the different maser species may additionally lend insight into the evolutionary stage, as well as the physical conditions that the different maser species are tracing. Water masers have long shown evidence of a close association with energetic outflows (e.g Hofner & Churchwell, 1996; Genzel et al., 1981). Recent high sensitivity systematic observations of Caswell & Breen (2010) detected 32 water masers within two portions of the Galactic plane covering almost half a square degree each. These observations showed a surprising preponderance of water maser sources with highly blue-shifted emission. Investigation by Caswell & Breen (2010) lead to a suggestion that these water masers represent a population of sources that are tracing a very early evolutionary stage, perhaps even preceding the stage where 6.7 GHz methanol masers are seen.

2.3.2 Other spectral lines as evolutionary signposts of high-mass star formation

A number of spectral lines have been proposed as good evolutionary clocks for high-mass star formation, and here we note a number of the significant works that have contributed to this knowledge.

Longmore et al. (2007) observed the 24 GHz radio continuum along with (1,1), (2,2), (4,4) and (5,5) transitions of NH_3 towards 21 hot molecular cores traced by 6.7 GHz methanol maser emission. Emission from NH_3 was detected

towards all of the regions targeted, and radio continuum at 24 GHz was detected towards just over half of them. Longmore et al. (2007) split their sources into four groups as follows: (1) isolated ammonia cores; (2) ammonia cores with associated methanol masers; (3) ammonia cores with associated methanol masers as well as radio continuum; and (4) ammonia cores with continuum only. The authors found that the linewidths of the detected ammonia emission increased from group (1) to group (3) and then reduces slightly for group (4), showing that the isolated ammonia cores are the most quiescent. Comparison by Longmore et al. (2007) of their sources with 8 GHz radio continuum sources detected by Walsh et al. (1998) revealed that all of the 24 GHz continuum sources that were devoid of continuum emission at 8 GHz had associated ammonia emission, whereas of those with associated 8 GHz emission, only two of the sources had associated ammonia emission, indicating that cores associated with continuum emission at both frequencies are more evolved that those that are detectable at only 24 GHz. They conclude that the physical properties of the ammonia cores vary according to their association with either methanol maser emission, continuum emission or both and suggest that the cores in each of the groups are at different evolutionary phases and proposed an evolutionary trend from most quiescent to most evolved as follows:

- isolated ammonia cores
- ammonia (1,1) cores associated with only methanol maser emission
- ammonia (1,1) cores associated with both 24 GHz radio continuum emission and 6.7 GHz methanol masers
- ammonia (1,1) cores associated with 24 GHz continuum emission only
- ammonia cores with 8 and 24 GHz continuum emission.

Purcell et al. (2006) finds that the CH_3CN and HCO^+ lines are more luminous and have larger linewidths when detected towards sources which harbor both UCHII regions and methanol maser emission than sources exibiting only methanol maser emission. Purcell et al. (2009) found that this result could be extended to include other molecules, such as N_2H^+, HCN, HNC and CH_3OH.

Purcell et al. (2009) further suggested that thermal CH_3OH could be used as a crude evolutionary clock, especially in the case of single dish observations, as it is particularly enhanced compared to the other species in the more evolved sources.

Fuller, Williams & Sridharan (2005) searched for infall signatures towards 77 sources they believed were high-mass protostellar object candidates, by targeting HCO^+, H_2CO, and $H^{13}CO^+$ observations towards these sources. From the line profiles, these observations resulted in the identification of 22 infalling candidate sources. It is shown therefore, that particular line characteristics can indicate the particular evolutionary stages.

2.3.3 Infrared characteristics at particular evolutionary stages

Cyganowski et al. (2008) compiled a catalogue of GLIMPSE sources that showed dominant, extended emission in the 4.5 μm band and dubbed these sources 'Extended Green Objects' (EGOs). These sources were suggested to be tracing outflows from high-mass young stellar objects while the sources are still actively accreting and followup observations presented in Cyganowski et al. (2009) show strong evidence to support this hypothesis. These followup observations revealed a high detection rate of 6.7 GHz methanol masers towards these sources, as well as outflow signatures. EGOs are therefore potentially excellent tracers of outflows that are likely powered by active accretion.

Chambers et al. (2009) also suggests that particular infrared properties can be suggestive of the evolutionary stage of high-mass star formation. In particular, Chambers et al. (2009) postulate that IRDCs that are associated with either EGOs (regions of enhanced 4.5 μm emission, indicating shocked gas), or 24 μm point sources, are actively undergoing star formation and are therefore at a later evolutionary stage than the cores that are embedded within IRDCs that show neither infrared signature. The authors test this theory by comparing the sizes, density and the prevalence of maser species of the two categories of sources and find that the sources that they expect to be more evolved have smaller sizes, higher densities and a higher association rate with both methanol and water masers.

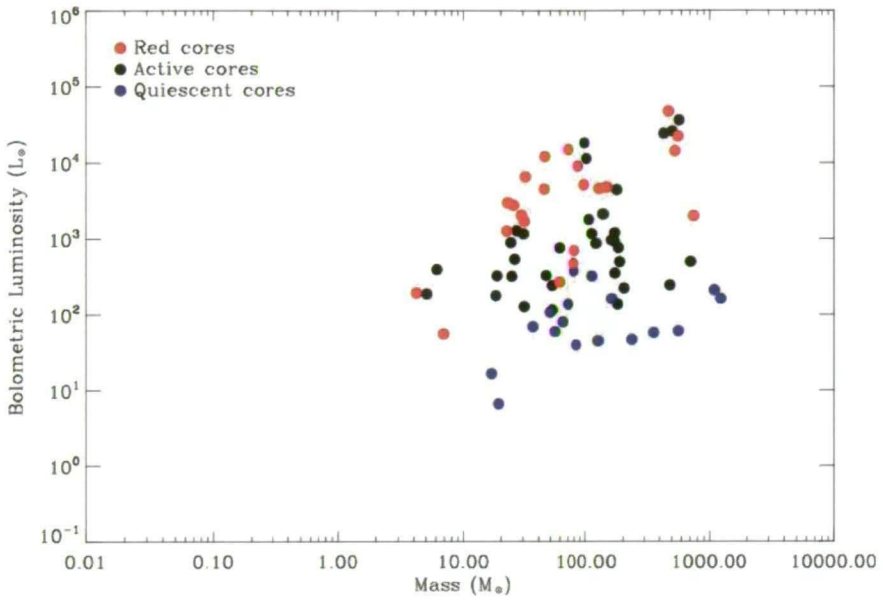

Figure 2.10: *Comparison between the derived bolometric luminosity and the mass of the cores from Rathborne et al. (2010) showing that the luminosity increases from the quiescent cores to the active cores and finally to the red cores.*

From observations of 24, 60-100 μm and submillimeter continuum data towards IRDCs, Rathborne et al. (2010) was able to separate 190 cores into five categories indicative of their relative evolutionary stages. Of these cores, 79 are classified as 'quiescent' (meaning that they have no associated 3-8 or 24 μm emission); 32 as 'intermediate' (indicating that the cores are associated with either EGOs or 24 μm point sources); 38 'active' (associated with both EGOs and 24 μm point sources); 35 'red' (associated with dominate 8.0 μm emission); and 'blue' (associated with bright 3.5 μm emission). Comparing that derived temperatures, luminosities and masses of the cores indicated that the quiescent cores, while colder and less luminous than the active cores, have similar masses. This trend is shown in Fig. 2.10. The authors therefore suggest that the differences in temperature and luminosity are reflecting the different evolutionary stages of the sources. They therefore propose an evolutionary sequence from least to more evolved as follows: quiescent, intermediate, active, red.

3

Masers associated with the G 333 giant molecular cloud

3.1 Introduction

Interstellar masers from water (e.g. Valdettaro et al., 2001), OH (e.g. Caswell, 1998) and methanol (e.g. Pestalozzi, Minier & Booth, 2005; Caswell et al., 2010; Green et al., 2010) transitions have been detected towards hundreds of star formation regions in our Galaxy, with many of these showing emission from more than one species. While there have been a number of large-scale untargeted searches for OH (Caswell, Haynes & Goss, 1980; Caswell, 1998) and methanol (Ellingsen et al., 1996; Szymczak et al., 2002; Caswell et al., 2010; Green et al., 2010), previous searches for water masers in star formation regions have typically targeted ultracompact HII regions selected on the basis of *IRAS* (Infrared Astronomy Satellite) colours (e.g. Churchwell, Walmsley & Cesaroni, 1990), or other sources believed to be high-mass young stellar objects (e.g. Beuther et al., 2002).

Until recently, extensive untargeted surveys for water masers in the Galactic Plane had been avoided primarily because at a frequency of 22 GHz telescope beam sizes are approximately one-third the size of those at 6.7 GHz, the frequency of the strongest methanol maser transition, and hence require approximately an order of magnitude more pointings to completely search target regions. An extensive sensitive search for 6.7 GHz methanol masers in the Southern Galactic

Plane (covering 924 square degrees) has now been completed and is producing first survey results (Caswell et al., 2010; Green et al., 2010), when the Northern Hemisphere component has been completed, this survey will cover the entire Galactic plane within a latitude of $|b| < 2°$ (1440 square degrees). A slightly less sensitive search for 22 GHz water masers over a 90 square degree region is nearing completion (Walsh et al., 2008). This survey constitutes the first such extensive search for water masers in the Galactic plane and has been carried out with the 22 m Mopra radio telescope. The use of a relatively small single dish telescope has allowed this large search region to be covered in a timely manner, discovering an unprecedented number of water masers, but presents some difficulties in identifying the locations of highly variable searches in followup observations. Recently, three regions covering approximately 0.5 square degrees each have been completely searched for 22 GHz water masers with the ATCA (Caswell & Breen, 2010; Caswell, Breen & Ellingsen, 2010) with a high sensitivity. These searches have revealed a high density of water masers within the regions searched. Approximately half of the 59 sources detected in Caswell & Breen (2010); Caswell, Breen & Ellingsen (2010) are below the detection limit of the more extensive search carried out by (Walsh et al., 2008).

Here we present followup observations of water masers detected in an untargeted search by Breen (2005) within the giant molecular cloud (GMC) complex associated with RCW 106 (the G 333.2–0.6 GMC). The GMC is located at a distance of 3.6 kpc (Lockman, 1979) and was discovered by Gillespie et al. (1977) during observations of molecular clouds associated with southern Galactic HII regions in the J=1–0 transition of CO. These observations uncovered a number of bright HII regions along a line which is almost parallel to the Galactic plane including one of the brightest infrared sources in our Galaxy, *IRAS* 16183–4958 (Becklin et al., 1973), which is associated with the HII region G 333.6–0.2.

The GMC is roughly centred on $l \sim 333°$, $b \sim -0.5°$ (α_{j2000}=16:21, δ_{j2000}=–50:20) and extends approximately 1.2 x 0.6 degrees on the sky (or approximately 90 pc x 30 pc at an assumed distance of 3.6 kpc (Bains et al., 2006)). This region passes through the ring of molecular clouds that circle the Galaxy at around 5 kpc from its centre (e.g. Simon et al., 2001) and exhibits a diverse range of molecular regions, bright HII regions, GLIMPSE (*Spitzer* Galactic Legacy Infrared Mid-

Plane Survey Extraordinaire) point sources, *IRAS* and *MSX* (Midcourse Space Experiment) sources, all of which are embedded in a larger region of diffuse atomic and molecular gas.

Observations of the ^{13}CO J=1–0 transition at 110 GHz by Bains et al. (2006) showed the velocity structure of the region to contain five primary velocity components, with the dominent feature centred on $v_{\rm LSR} \sim -50$ km s^{-1}. Bains et al. (2006) showed that it is likely that at least five distinct molecular clouds lie along the line-of-sight (see Section 3.3.1). For this reason the G 333.2–0.6 GMC is refered to as the main cloud, showing emission over the velocity range –35 km s^{-1} to –65 km s^{-1}. Analysis of the integrated ^{13}CO data using the CLUMPFIND algorithm of Williams, de Geus & Blitz (1994) identified 61 ^{13}CO clumps within the main cloud. The ^{13}CO emission takes the form of a string of knots with the clumps arranged along an axis aligned NW to SE (Bains et al., 2006).

This GMC has been the focus of numerous observations in recent times, including far-infrared (FIR) observations of the dust continuum at 150 and 210 μm which identified 23 emission peaks with dust temperatures between 20 and 40 K (Karnik et al., 2001). The region was also observed by Mookerjea et al. (2004) who used SIMBA (SEST IMaging Bolometer Array) on the Swedish European Southern Observatory Submillimetre Telescope (SEST) to obtained a 1.2 mm dust continuum image of the region. Mookerjea et al. (2004) identified 95 dust emission peaks (or clumps), half of which have *MSX* counterparts. Observations of a multitude of molecular lines towards detected HII regions and *IRAS* sources indicate probable ongoing star formation (Mookerjea et al., 2004). These observations, like those of Bains et al. (2006) have identified that the GMC has a linear clumpy structure.

Complete surveys of the GMC region have been carried out by Ellingsen et al. (1996) for 6.7 GHz methanol masers and Caswell, Haynes & Goss (1980) for 1665 and 1667 MHz OH masers. These surveys resulted in the detection of nine methanol and six OH masers within the region surveyed in ^{13}CO by Bains et al. (2006). Five water masers have also been detected within this region in targeted searches made by Johnston et al. (1972), Caswell et al. (1974), Batchelor et al. (1980) and Braz & Scalise (1982).

The original survey for water masers by Breen (2005) covered two distinct

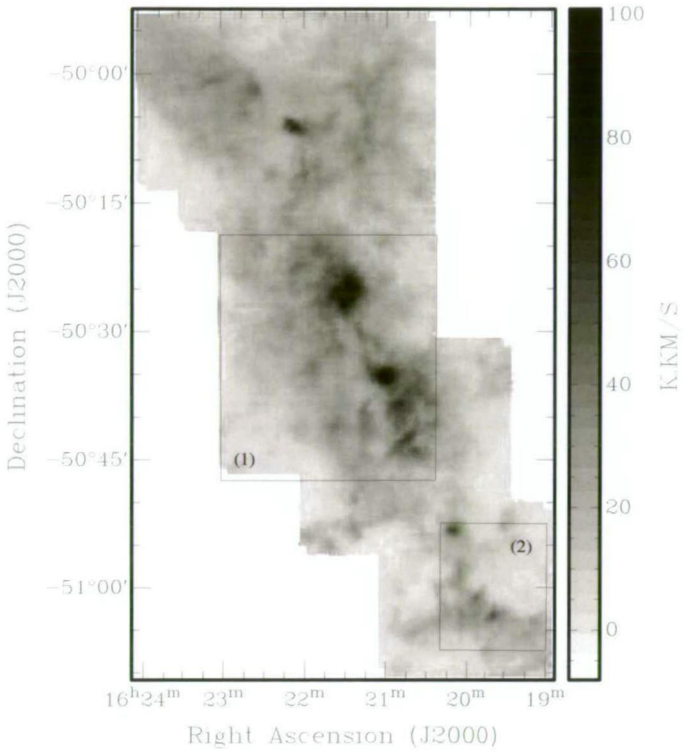

Figure 3.1: *Integrated ^{13}CO emission observed by Bains et al. (2006) with the two regions surveyed for water masers overlaid.*

regions within the GMC. The first (hereafter Region 1) is a 0.50 × 0.42 degree area centered on l ∼ 333, b ∼ –0.5°. This region encompasses much of the high density gas and dust regions identified by Karnik et al. (2001), Mookerjea et al. (2004) and Bains et al. (2006) in the central section of the GMC. Region 1 contains one previously detected 22 GHz water maser, G 333.13–0.43, discovered by Caswell et al. (1974). The second region (hereafter Region 2) covers a 0.28 × 0.24 degree area of the GMC and is approximately centred on well-known optically visible HII region RCW 106. This region contains two previously detected water masers. The extent of the two regions compared to the integrated ^{13}CO emission are shown in Fig. 3.1.

The GMC is the focus of an ongoing project to characterise the turbulence in the molecular cloud and compare this to the star formation efficiency in or-

der to attain a relationship between the two. Commencing in 2004 a multitude of millimetre molecular line transitions (including ^{13}CO (Bains et al., 2006), $C^{18}O$ (Wong et al., 2008), CS, $C^{34}S$, C_2H, HCN, $H^{13}CN$, HCO^+, $H^{13}CO^+$, HNC, CH_3OH and SiO (Lo et al., 2009)) have been observed by the Delta Quadrant Survey Team at the University of New South Wales[1] (UNSW). Interstellar masers require special physical conditions and the different species are generally thought to trace particular evolutionary phases of the high-mass star formation process. Through combining information on all the strong and common interstellar maser transitions with millimetre molecular line and other existing infrared and millimetre continuum data we aim to better understand the evolutionary phases traced by each type of maser.

3.2 Observations & Data processing

3.2.1 Initial survey observations

The initial blind survey for water masers were carried out in 2005 by Breen (2005). The specifications and characteristics of this search are listed below.

The primary search for 22 GHz water masers towards the G 333.2–0.6 GMC was undertaken between 2005 April-November using the University of Tasmania's 26-m radio telescope at Mount Pleasant. The observations were made with a cryogenically cooled receiver that detects both left and right circularly polarized signals and has a typical system equivalent flux density of 2000-2200 Jy in good weather at elevations above about 40 degrees. At 22 GHz the telescope has a 2.2-arcmin half power beam width (HPBW) and at the time of the observations the measured RMS pointing errors were $\sim$1 arcminute. The data were recorded using a 2-bit auto-correlation spectrometer configured with 2048 spectral channels per polarisation over a 32-MHz bandwidth, which was centred on an LSR velocity of approximately –40 km s^{-1}. The observations covered a velocity range of 430 km s^{-1} with a spectral resolution of 0.25 km s^{-1}. The two regions were surveyed using an equilateral triangle pattern with each pointing separated by 1.1 arcminutes (half of the HPBW) from all adjacent grid points. Each pointing

[1]http://www.phys.unsw.edu.au/astro/mopra/dqs.php

was observed for a total onsource integration time of 10 minutes. The water maser G 333.608–0.215, discovered by Johnston et al. (1972), was observed at the beginning of each observing session to test the system and ensure consistency. Although it is not located in either of the survey regions we have included it in the nine masers detected in this survey.

The weather conditions in which the observations were made varied substantially, and in general, the data for Region 1 were taken under much more favourable conditions. In order to minimize atmospheric and telescope pointing effects all observations were made above an elevation of 40 degrees. Data affected by poor weather conditions were reobserved (in some cases on multiple occasions), however a small percentage of the data has a significantly poorer sensitivity. The observations of Region 1 required approximately 750 pointings while Region 2 was much smaller containing just under 300 pointings. After box car smoothing over 5 channels and averaging the two polarisations together the majority (78 percent) of the data taken in Region 1 had an RMS noise level of less than 1 Jy while the remaining (22 percent of) data in this region was subject to an RMS noise level of between 1 Jy and 2 Jy. This equates to a 5σ detection limit of 5 Jy over the majority of the region, with a maximum of 10 Jy in the worst affected pointings. In Region 2 only 35 percent of pointings have an RMS noise level of less than 1 Jy and the remaining 65 percent had an RMS noise of up to 5 Jy. This equates to a 5σ detection limit between 5 and 25 Jy, hence our ability to detect weaker masers within Region 2 is greatly reduced.

For each detected water maser additional observations consisting of a 5-point grid (centred on the preliminary position) were made to locate the emission more accurately. The position was determined by fitting a 2D circular Gaussian (with the same HPBW as the telescope) to the relative amplitudes of the strong emission in the maser spectra observed in the 5-point grid. Positions determined in this manner are accurate to approximately 1 arcminute, which is insufficient to allow meaningful comparison with millimetre and infrared observations of the region.

3.2.2 ATCA observations

In order to obtain accurate positions for the detected water masers we were granted two sessions of Australia Telescope Compact Array (ATCA) director's time. Preliminary observations of the masers detected in the Mount Pleasant survey were made on 2006 June 19 with the ATCA in the 1.5D configuration. The observations were centred on a frequency of 22.238 GHz with the correlator configured to record 256 spectral channels across a 16-MHz bandwidth. These observations failed to detect one of the water masers discovered in the Mount Pleasant survey (G 333.29–0.38), most likely due to temporal variability.

Further observations were made with the ATCA in the 6A configuration on 2006 July 16 & 17. In this array configuration the minimum baseline length is 337 m and the maximum is 5939 m. The observations were centred on 22.236 GHz and the correlator sampled two orthogonal linear polarisations, each processed to give a 512 channel spectrum across an 8-MHz bandwidth. Each of the maser sites detected in the earlier ATCA observations (8 in total) were observed in a series of three minute cuts over a range of hour-angles. Observations of one of the phase calibrators MRC B1613–586 or MRC B1646–50 were made for a duration of 90 seconds before and after every two maser observations (i.e. every 6 minutes). PKS B1934–638 was used as the primary flux calibrator and at 22.236 GHz has an assumed flux density of 0.83 Jy. PKS B1253–055 was used for bandpass calibration. These ATCA observations were made using reference pointing, and as arcsecond accurate positions were obtained in the initial ATCA observations all of the maser sites were close to the centre of the primary beam. Over the two days each source was observed a total of eight times, equivalent to a total on-source integration time of 24 minutes.

The data were processed using the `miriad` software package (Sault, Teuben & Wright, 1995) applying the standard techniques for ATCA spectral line and continuum observations. Continuum sources which were located away from the centre of the primary beam have had their flux densities corrected to account for beam attenuation. The frequency resolution, after Hanning smoothing, was 0.038 MHz or 0.50 km s^{-1}. The RMS noise in a single spectral channel in the final data cubes was approximately 0.15 Jy and the signal-to-noise ratio of the final

spectra was about 20:1 in the worst case. The RMS noise level in the continuum images was typically around 0.02 Jy/beam. These observations have enabled us to determine the positions of the water masers to an accuracy of approximately 0.5 arcseconds.

3.3 Results

A search of two regions near the G 333.2–0.6 giant molecular cloud resulted in the detection of nine 22 GHz water masers, five of which are new detections (Table 3.1), as well four 22 GHz continuum sources (see Section 3.3.2). Fig. 3.2 shows the positions of all the detected water masers overlaying the integrated ^{13}CO emission observed by Bains et al. (2006), while Fig. 3.3 shows the maser locations on a three colour GLIMPSE image of the GMC. Comparison of the water maser locations with the other maser species, the integrated ^{13}CO emission and the three colour GLIMPSE image shows that in general the water masers originate very close to the higher density molecular gas and warm dust, near the main axis of star formation within the molecular cloud. In contrast the methanol masers tend to be offset from this axis, close to the interface between the intense mid-infrared emission and the larger molecular cloud (Ellingsen, 2006).

Spectra of the detected water masers are shown in Figs. 3.4 and 3.5. The spectra have been produced by integrating the emission in the ATCA image cubes for each source. The only exception is water maser G 333.29–0.38 for which the Mount Pleasant spectrum is shown. The positional accuracy of sources detected in the ATCA observations is approximately 0.5 arcseconds and we have used three significant figures after the decimal place in their Galactic coordinate names. For the source only detected in the Mount Pleasant component of the survey we are only justified in using 2 significant figures and have done so throughout the chapter. Comments on each maser can be found in Section 3.3.1. The newly detected water masers (Fig. 3.4), with one exception have a peak flux density less than 50 Jy, while the previously detected sources (Fig. 3.5), again with one exception, have peak flux densities greater than 100 Jy.

Walsh et al. (2008) present survey results of a region that covers the same areas that we have surveyed as part of the HOPS (H_2O Southern Galactic Plane

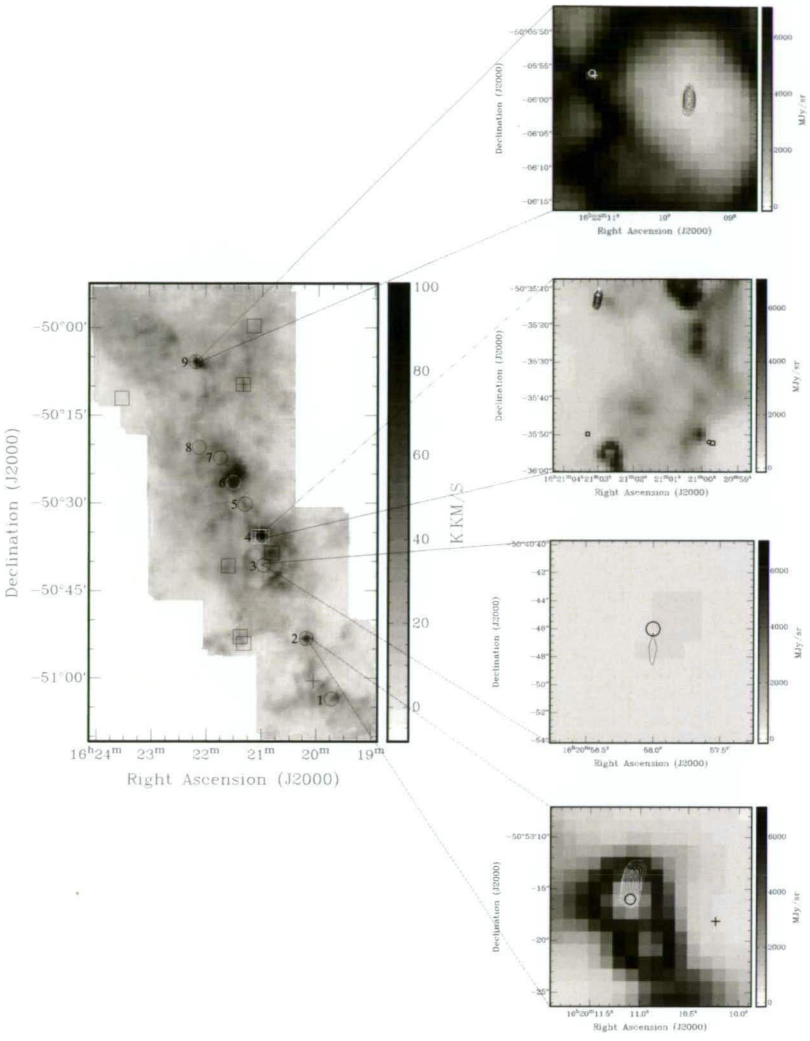

Figure 3.2: *The main image shows the integrated ^{13}CO emission observed by Bains et al. (2006) with the positions of water (circle), methanol (square) and OH (cross) masers overlaid (note that the most central OH maser in the main image is in fact two OH sources close together as shown in the second sub-image). Also overlaid are the water maser source numbers as shown in Table 3.1. The positions of the methanol and OH masers have also been obtained from ATCA observations and have a similar positional accuracy to the water maser positions (Caswell, 1998; Ellingsen, 2005). In the main image, the size of the shapes is much larger than the positional accuracy, however, the four sub-images (of water masers 9, 4, 3 and 2 respectively) show the positions of the maser species and indicate the positional accuracy of these masers overlaid on a 8.0 μm GLIMPSE image of the region. Also overlaid on the sub-images are the 22 GHz continuum contours detected in our ATCA observation. The first contour in each case is at the 5σ level for the continuum image and they increase in factors of $\sqrt{2}$. Details of the continuum sources can be found in Table 3.3.*

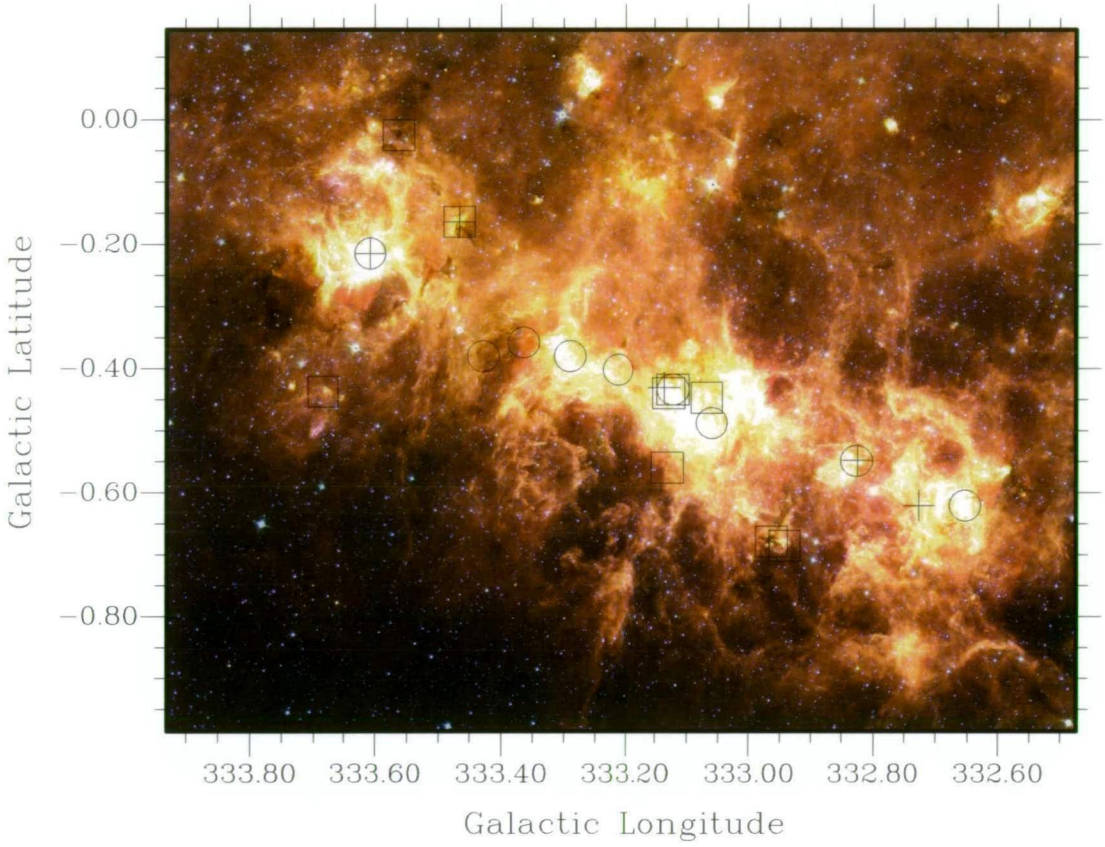

Figure 3.3: *Three colour GLIMPSE image of the GMC where red=8.0 μm green=5.8 μm and blue=3.6 μm. The positions of the nine water masers detected in this survey are represented by circles, positions of the methanol masers observed by Ellingsen (2005) are represented by squares and the positions of the OH masers observed by Caswell (1998) are represented by crosses. Water maser sources 1-9 are numbered in order of increasing Galactic Longitude.*

Table 3.1: *22 GHz water masers detected within the survey regions. Column 1 gives the water maser source number (which is used in later tables), column 9 indicates whether or not each maser was detected in the ATCA observation and column 10 gives the water maser references. ATCA positions are quoted for all water masers with the exception of G 333.29-0.38 (source number 6). References: * = new source; 1 = Caswell et al. (1974); 2 = Kaufmann et al. (1976); 3 = Braz & Scalise (1982) 4 = Johnston et al. (1972).*

Source number	Water maser (l, b)	Right Ascension (J2000)	Declination (J2000)	Peak Flux (Jy)	Peak Vel. wrt LSR (km s^{-1})	Velocity Range (km s^{-1})	epoch	ATCA detection?	Ref
1	G 332.653–0.621	16:19:43.569	–51:03:37.06	28.9	–45.3	–59,–43	2006 July	yes	2
2	G 332.826–0.549	16:20:11.089	–50:53:16.07	239.4	–59.1	–69,–45	2006 July	yes	3
3	G 333.060–0.488	16:20:58.002	–50:40:46.32	64.3	–8.7	–13,5	2006 July	yes	*
4	G 333.121–0.434	16:20:59.762	–50:35:51.55	161.1	–57.7	–60,–46	2006 July	yes	1
5	G 333.221–0.402	16:21:17.913	–50:30:17.99	9.6	–52.0	–58,–48	2006 July	yes	*
6	G 333.29–0.38	16:21:30.4	–50:26:34	7	–49.0	–51,–47	2005 June	no	*
7	G 333.364–0.358	16:21:44.319	–50:22:21.08	3.2	–52.6	–55,–49	2006 July	yes	*
8	G 333.428–0.380	16:22:07.539	–50:20:34.29	12.4	4.1	–6,6	2006 July	yes	*
9	G 333.608–0.215	16:22:11.060	–50:05:55.98	103.3	–49.2	–64,–38	2006 July	yes	4

Survey) search that has been carried out with the Mopra radio telescope in 2006 December. The Walsh et al. (2008) observations were of comparable but much more uniform sensitivity. The authors present two additional water masers that were not detected by us; 332.73–0.63 and 333.03–0.44, while we detect three sources that were not identified by them (sources 6, 7 and 8). It is not surprising that our source 6 (G 333.29–0.38) was not detected in the HOPS observations since we failed to detect any emission in out followup ATCA observations. In Chapter 6 we present two epochs of water maser observations that showed that 16 % of sources were only detectable on one epoch. If we add the two additional water maser sources detected by Walsh et al. (1998) to the sources that we detected in our survey regions (i.e. a total of 10 sources), it is evident that the percentage of sources only detected in one region is much higher in this region at 50 %. It is therefore evident that a number of the water masers in this region are variable, but it is not clear that they are more variable than the much larger sample of sources presented in Chapter 6. Given that the water maser observations presented in Chapter 6 are of a much higher sensitivity (5-σ of $\sim$0.2 Jy) the higher incidence of non-detectability is likely to be due to our poorer sensitivity since some sources would not need to vary by much to fall below our detection limits.

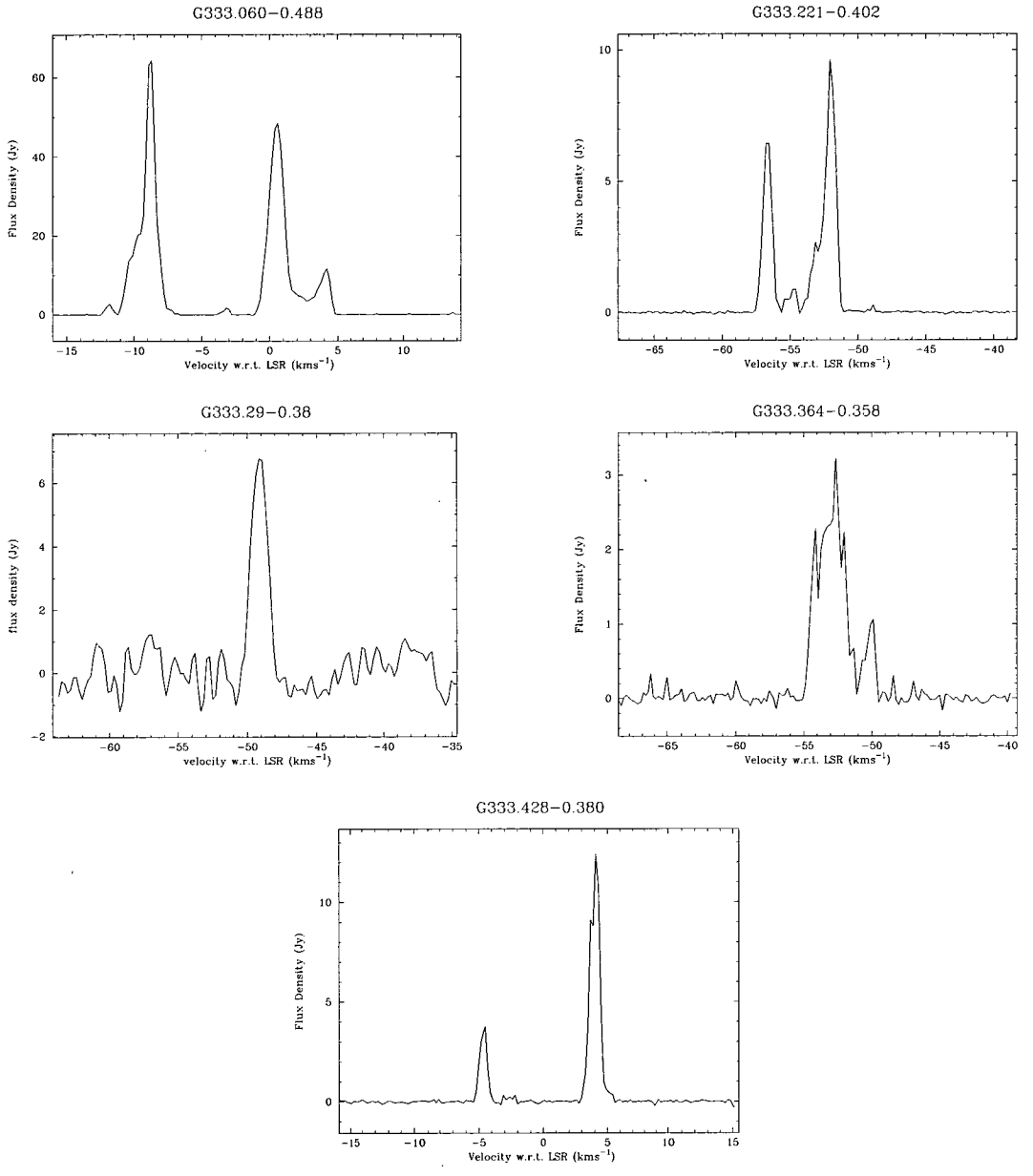

Figure 3.4: *Spectra of the 22 GHz water maser sources discovered in this survey. All of the spectra presented are from the ATCA observations with the exception of G 333.29–0.38 which is from the Mount Pleasant observations.*

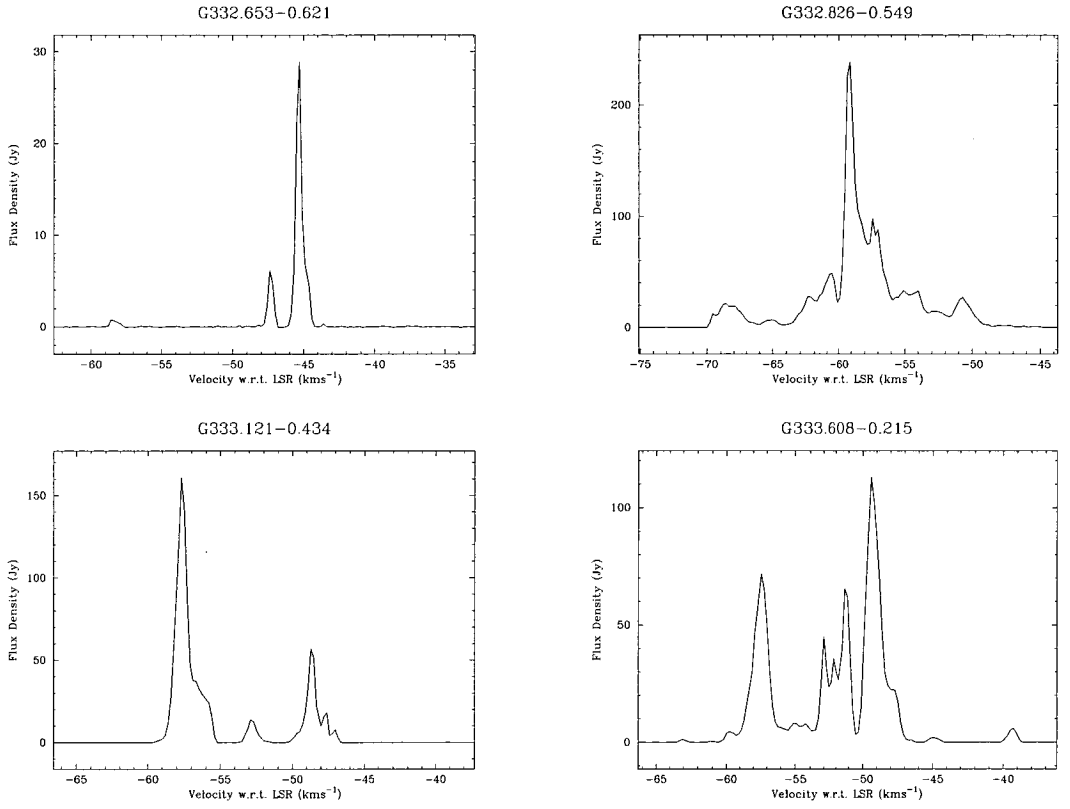

Figure 3.5: *ATCA spectra of the 22 GHz water maser sources detected in the search that have been previously discovered.*

The 6.7 GHz methanol masers sites in this region have previously been searched for associated 22 GHz water maser emission by Hanslow (1997) who detected emission towards a number of sources (G 332.942–0.686, G 333.121–0.434, G 333.128–0.440, G 333.130–0.560, G 333.234–0.062 and G 333.466–0.164) in the G 333.2–0.6 giant molecular cloud. Three of these (G 332.942–0.686, G 333.234–0.062 and G 333.466–0.164) lie outside the regions of our untargeted search. While of the other three, only G 333.121–0.434 was detected in the current work. It appears that the emission attributed to G 333.128–0.440 by Hanslow (1997) is in fact associated with G 333.121–0.434, while that associated with G 333.130–0.560 was not detectable at the epoch of our search. Because of the uncertainty in the position of the water masers detected by Hanslow (1997) and the possibility that some may result from an unassociated strong source detected in a sidelobe, in Figs. 3.2 & 3.3 we have only marked those water masers detected in our current survey.

In addition to the nine water masers that we present, we made a one-time detection with the 26-m Mount Pleasant radio telescope of a water maser right on the edge of the field of observations with coordinates G 333.22–0.20. Subsequent observations showed no detectable emission and as a result we do not include it in the list of water masers that we detect. This emission consisted of a single velocity feature at –87 km s^{-1} of around 6 Jy. We believe that this emission was actually a detection of the strong water maser G 333.234–0.062 detected by Hanslow (1997). Hanslow (1997) reported G 333.234–0.062 to consists of multiple velocity features with the most prominent observed at –86 km s^{-1}, with a flux density of 108 Jy.

The majority of the water masers we detected have exhibited variability of up to a factor of 10 on a time scale of several months. This type of variability is common in water masers and a survey of water maser emission towards main-line OH masers in star formation regions by Batchelor et al. (1980) found that about 60 percent of water masers exhibited variability of up to a factor of two over an eight month period, while the remaining 40 percent exhibited more extensive variability. Given that our initial observations were made in varying weather conditions with comparitively poor pointing accuracy it is difficult to quantify the absolute variations accurately. However, because the water masers have multiple spectral components we are able to determine that variability has occurred by

examining the relative amplitudes. Water masers associated with low mass stars are typically both weaker and more variable than those associated with high mass stars (Claussen et al., 1996). So we would expect our observations to be more likely to detect masers associated with high-mass star formation, than those associated with less luminous objects. Variability is also a likely explanation as to why one of the masers detected in the survey with the 26-m Mount Pleasant radio telescope were not detected in the final observations made with the ATCA 6-8 months later.

We have compared the positions of the water masers that we detected with GLIMPSE, *IRAS* and *MSX* sources, as well as 1.2 mm dust clumps (Mookerjea et al., 2004), FIR sources (Karnik et al., 2001), ^{13}CO emission (Bains et al., 2006), CS emission (N. Lo, private communication) and other maser species (these CS data have since been published (Lo et al., 2009)). The relative positional accuracy of each of these datasets differs, some having significantly poorer positional accuracy than our ATCA observations. We consider a water maser to be associated with a GLIMPSE, *IRAS*, *MSX* or FIR source if it is within a radius of 2, 30, 5 or 60 arcseconds respectively. For water maser G 333.29–0.38 we use more relaxed positional constraints as its position is much less accurately known. For this source we consider the water maser to be associated if it is within 5, 90, 40 or 60 arcseconds of a GLIMPSE, *IRAS*, *MSX* or FIR source respectively. We consider a water maser to be associated with a ^{13}CO, CS or 1.2 mm dust continuum clump if its position falls within the radius of the ^{13}CO, CS or 1.2 mm dust clumps. We have used the clump radii reported by Bains et al. (2006) and Mookerjea et al. (2004) for the ^{13}CO and 1.2 mm dust clumps, respectively. In the case of the CS data we have considered that a water maser falls within the radius of a given CS clump if it lies within emission that has a value of flux density per beam which surpasses a 5σ level. The velocity ranges of the ^{13}CO and CS clumps correlate well with the velocity ranges of the associated masers (see Tables 3.7 and 3.9). Table 3.2 summarises all associations.

Of the nine water masers that we detect, four are associated with a GLIMPSE point source, three are associated with an *IRAS* source, two are associated with an *MSX* source, five are associated with a FIR clump (Karnik et al., 2001) and seven are associated with a 1.2 mm dust clump (Mookerjea et al., 2004). All of

the water masers detected in this survey either lie within a ^{13}CO clump identified by Bains et al. (2006) or an identifiable emission peak of the ^{13}CO data. In addition all of the water masers, for which CS data of the GMC was available, are associated with CS emission peaks covering a comparable velocity range to the masers.

3.3.1 Individual sources

Comments on the nine water masers that we detect can be found in Section 3.3.1. Refer to Table 3.1 for a summary of each of the sources. Figs 3.2 and 3.3 show the positions of the water masers overlaying the integrated ^{13}CO emission (Bains et al., 2006) and a three colour GLIMPSE image of the GMC (also showing the locations of 6.7 GHz methanol masers (Ellingsen, 2005) and main-line OH masers (Caswell, 1998)), respectively.

Possible associations with a foreground cloud

Bains et al. (2006) found that the mean velocity profile of the ^{13}CO emission averaged over their field of observations exhibited five distinct velocity features (see Fig. 3.6), while only the brightest velocity feature was attributed to the G 333.2–0.6 GMC. This most prominent feature is also the broadest feature and spans a velocity range of –35 km s^{-1} to –65 km s^{-1}. The additional four velocity features seen in Fig. 3.6 are centred on velocities of –105, –90, –70 and –10 km s^{-1}. Bains et al. (2006) plotted the kinematic distance versus the LSR velocity at the centre of the GMC and found that for the clouds at –10, –50, –70, –90, –105 km s^{-1} the associated distances were approximately 1, 3.5, 4.5, 5.5 and 6.5 kpc.

Water masers 1, 2, 4-7 and 9 have velocities which are comparable to the broadest feature of velocity profile observed by Bains et al. (2006) and as such we associate these masers with the main cloud. The velocity ranges of water masers 3 and 8 indicate that they are probably associated with a foreground cloud (or clouds) located at a distance of 1 kpc. Water maser 3 is separated by less than an arcsecond from the 22 GHz continuum source G 333.060-0.489, indicating that the two are likely to be associated. This means that like water maser 3 this continuum source is likely to be associated with a foreground cloud.

Visual inspection of the ^{13}CO data of Bains et al. (2006) shows that at velocities of approximately –10 km s^{-1} emission is restricted to a small range of right ascensions and declinations and is elongated almost perpendicular to the axis of the main GMC. Water maser 3 lies within this emission that is located at a distance of approximately 1 kpc. From the ^{13}CO data, it appears unlikely that water maser 8 is associated with the same cloud (as maser 3), as the ^{13}CO emission associated with this maser does not overlap with the ^{13}CO emission associated with water maser 3. Also, the spatial separation between these masers is significant.

Comments on individual sources

1. *G 332.653–0.621:* This water maser was discovered by Kaufmann et al. (1976), who observed it to have a peak flux density of 58 Jy at a velocity of –47 km s^{-1} in 1975. Subsequent observations by Batchelor et al. (1980) during 1977 May showed a single maser feature at –44 km s^{-1} and a slightly weaker intensity of 30 Jy. We measured the peak flux density to be 29 Jy at –45 km s^{-1}, similar to the observations made in 1977. No OH or 6.7 GHz methanol masers have been detected associated with this water maser (Caswell, Haynes & Goss, 1980; Ellingsen et al., 1996).

This source is offset from the HII region G 332.663–0.621 identified by Huang et al. (1999) by 35 arcseconds at a position angle of 58° and is situated within the RCW 106 complex. *IRAS* source *IRAS* 16158–5055 is located 11 arcseconds away from this maser and has colours typical of an ultra-compact HII region. This maser is separated from the centre of the nearest ^{13}CO clump by 35 arcseconds and is 45 arcseconds from the centre of the 1.2 mm dust emission peak identified by Mookerjea et al. (2004) at position angles of –79° and –83° respectively.

2. *G 332.826–0.549:* This maser was discovered by Braz & Scalise (1982) in 1980 April, who reported it to have a peak flux density of 250 Jy at –70.8 km s^{-1}. We found the intensity peak of the maser to be 239 Jy at –59.1 km s^{-1} with emission covering a range of more than a 20 km s^{-1}. While the velocity range over which emission has been observed has remained roughly constant since the maser's discovery, the relative intensities and velocity of the strongest emission have not, for example observations made by Braz & Scalise (1982) in 1981 May

showed a peak at –62 km s^{-1} of 198 Jy.

This maser appears to be associated with the *MSX* source G 332.8269–00.5489 which is offset by 5 arcseconds and may be also associated with *IRAS* 16164–5046 which is located 29 arcseconds away, as well as a FIR source (Karnik et al., 2001). The maser is probably associated with a ^{13}CO clump identified by Bains et al. (2006) and a 1.2 mm dust emission peak identified by Mookerjea et al. (2004), which are separated from the maser by 11 arcseconds and 8 arcseconds respectively. This maser is located about 2 arcminutes from the peak of the RCW 106B complex which is centered on 16:20 –50:52 and is offset from the peak of the 22 GHz continuum source detected in our ATCA observations by 2 arcseconds. The water maser is separated from the OH maser G 332.826-0.548 (Caswell, 1998) by 8 arcseconds (see fourth sub-image of Fig. 3.2).

3. *G 333.060–0.488:* This maser exhibits several spectral features over an 18 km s^{-1} velocity range, with the most intense having a flux density of 64 Jy at –8.7 km s^{-1}. This source was first observed at Mount Pleasant on 8 August 2005 when the feature at –8.7 km s^{-1} was approximately 6.5 Jy and the secondary feature at about 0 km s^{-1} was 3 Jy, implying a variation of a factor of 10 over an 11 month period. The velocity of this maser is comparable to one of the secondary features of the velocity profile of the GMC observed by (Bains et al., 2006) (see Fig. 3.6). This maser is likely part of a different molecular cloud located along the line of sight at a distance of approximately 1 kpc (see Section 3.3.1).

The ATCA observations detected a 22 GHz continuum source offset from the water maser source by about an arcsecond (see third sub-image of Fig. 3.2). The water maser source appears to be associated with GLIMPSE point source G 333.0600–00.4888.

4. *G 333.121–0.434:* This source was discovered by Caswell et al. (1974) in 1973 June. Subsequent observations made in 1976 August by Batchelor et al. (1980) showed a decline in the –51 km s^{-1} peak, while improved sensitivity uncovered additional spectral features. We observed the current peak intensity to be 161 Jy at –57.7 km s^{-1} with emission covering the velocity range –60 to –46 km s^{-1}. The most prominent feature exhibited variation by a factor of two over a nine-month period.

This source is located within the RCW 106A structure and is offset from

two OH masers by about 50 arcseconds (Caswell, 1998). The 6.7 GHz methanol maser G 333.121–0.434 (Ellingsen, 2005) is separated from the water maser by less than an arcsecond and emission is seen over a similar velocity range to the water maser. This maser falls within FIR, ^{13}CO and 1.2 mm dust clumps with angular separations of 59, 40 and 47 arcseconds from the centre of the respective clumps. We detected a 22 GHz continuum source separated from the water maser by approximately 50 arcseconds which may be associated with the two OH masers observed by Caswell (1998) (see second sub-image of Fig. 3.2).

5. *G 333.221–0.402:* The peak flux density of this maser has remained approximately constant over the course of our observations, however, initial observations made in 2005 August showed only one spectral feature, while observations with the ATCA on 2006 July detected four additional peaks. While three of these features can be explained by the improved sensitivity offered by the ATCA the remaining secondary peak of approximately 7 Jy should have been detected in initial observations, suggesting this maser exhibits some variability.

This water maser appears to be associated with GLIMPSE point source G 333.2205–00.4024 and is separated from the centre of the nearest ^{13}CO clump by 33 arcseconds. This source falls within 10 arcseconds of the centre of a 1.2 mm dust clump and 42 arcseconds from the centre of a FIR source detected by Karnik et al. (2001).

6. *G 333.29–0.38:* This water maser was discovered on 2005 June 26 when it was detected in both polarisations and in adjacent spectra, however, when follow-up observations were made during 2005 September and October the peak flux density of the maser was less than 1 Jy. The earlier observations showed the maser to have a single spectral feature of approximately 7 Jy at –49 km s^{-1}, comparable to the velocity of the HII region, GAL 333.3–00.4, (Huang et al., 1999) which is situated 17 arcseconds away and has a velocity of –52.1 km s^{-1}. The *MSX* source G 333.2898–00.3898 may be associated with the maser as the sources are separated by 33 arcseconds, less than the maser positional uncertainty of 1 arcminute. At the time of the observations made with the ATCA the peak flux density of this maser was less than the 5σ detection limit of 0.75 Jy.

7. *G 333.364–0.358:* A decline in the peak flux density has been observed since this maser was discovered on 2005 August 25. In the initial observations a

peak flux density of 9 Jy was observed compared to the final observations made with the ATCA where a peak flux of 3.2 Jy was recorded. This source is separated from the centre of the nearest ^{13}CO clump by 47 arcseconds and the centre of a FIR source detected by Karnik et al. (2001) by 37 arcseconds.

8. *G 333.428–0.380:* This maser consists of two main spectral features at velocities of –4.5 and 4.1 km s^{-1} with flux densities of 4 Jy and 12.4 Jy respectively. A decrease in the flux density of the primary feature has been observed since observations made during 2005 April when it had a peak flux density of 26 Jy. This is the only maser detected in our survey for which there is no *IRAS*, *MSX*, 1.2 mm dust or other maser species within 2 arcminutes. There is however a nearby ^{13}CO emission peak located at about 40 arseconds from the maser. Like water maser G 333.060–0.488, the velocity of this maser indicates that it probably belongs to another molecular cloud located at a distance of approximately 1 kpc (Bains et al., 2006) (see Section 3.3.1).

9. *G 333.608–0.215:* This is one of the earliest southern hemisphere water masers to be discovered and was first detected by Johnston et al. (1972) who observed a primary feature at –49 km s^{-1} and a secondary feature at –57 km s^{-1}. Observations in 1976 August by Batchelor et al. (1980) found a 100 Jy peak at –52 km s^{-1}. We detected emission over a 26 km s^{-1} velocity range with the most intense feature of 103 Jy at –49.2 km s^{-1} and a decline in the –52 km s^{-1} feature to about 38 Jy. There is an associated OH maser observed by Caswell (1998) which is displaced from the water maser by less than an arcsecond and shows emission over a velocity range of –48 km s^{-1} to –36km s^{-1} (see first sub-image of Fig. 3.2).

This maser is offset by 15 arsec from the well known HII region G 333.6–0.2 which is almost totally obscured at optical wavelengths but is one of the brightest objects at longer wavelengths. This maser is probably associated with an *IRAS* source, FIR source, ^{13}CO clump, CS emission and 1.2 mm dust clump.

3.3.2 22 GHz continuum sources

Four radio continuum sources were detected in the ATCA observations. Their properties are summarised in Table 3.3 and are shown in the sub-images of

Table 3.2: *Summary of all possible associations. Details of GLIMPSE,* IRAS, MSX, *FIR, 1.2 mm dust,* ^{13}CO *and CS sources can be seen in Tables 3.4, 3.5, 3.6, 3.10, 3.7 and 3.9. y indicates the presence of an association, n indicates that there is no association, * indicates the* ^{13}CO *emission peaks that we identify that were outside the velocity range of clump analysis carried out by Bains et al. (2006) and - indicates that no data over a similar velocity to the respective water masers was available.*

Source number	GLIMPSE	*MSX*	*IRAS*	FIR	1.2 mm dust	^{13}CO	CS	Methanol maser	OH maser
1	n	n	y	n	y	y	y	n	n
2	y	y	y	y	y	y	y	n	n
3	n	n	n	n	y	y*	-	n	n
4	y	n	n	y	y	y	y	y	n
5	n	n	n	y	y	y	y	n	n
6	y	y	n	y	y	y	y	n	n
7	y	n	n	n	n	y	y	n	n
8	n	n	n	n	n	y*	-	n	n
9	n	n	y	y	y	y	y	n	y

Fig. 3.2. As there is no high resolution, low frequency continuum data available for the region, spectral indices (and therefore likely source mechanisms) could not be determined.

G 333.826–0.549 This is the strongest radio continuum source detected in our ATCA observations and its peak is located within 2 arcseconds of the water maser G 332.826–0.549. The nearest infrared source is *IRAS* 16164–5046, with which it is possibly associated.

G 333.060–0.489 This is the weakest continuum source that we detected. The source is spatially coincident with GLIMPSE point source G 333.0600–00.4888 as well as the water maser G 333.060–0.488. As the separation between the continuum source and the near-by water maser is less than an arcsecond it seems likely that the two are associated. As this water maser (source number 3) is probably associated with a foreground cloud (see Section 3.3.1) and not the main GMC, it is likely that this continuum source also belongs to the foreground cloud.

G 333.135–0.432 This continuum source, while not associated with any water masers, does appear to be associated with two OH masers observed by Caswell (1998) (shown in Fig. 3.2). There is no associated infrared source.

Table 3.3: *22 GHz continuum sources. Column 1 is the source number of the nearest water maser, Columns 2-4 give the position of the continuum source, column 5 gives the peak of the continuum source in mJy/beam, column 6 gives the total flux density of the continuum source in mJy and column 7 gives the angular separation between the continuum source and the nearest water maser source.*

Source number	Continuum Source (l, b)	Right Ascension (J2000)	Declination (J2000)	F_{Peak} (mJy/beam)	Total Flux Density (mJy)	Separation from maser (arcsec)
2	G 332.826–0.549	16:20:11.089	–50:53:14.07	948	1180	2
3	G 333.060–0.489	16:20:58.002	–50:40:47.32	91	126	1
4	G 333.135–0.432	16:21:03.017	–50:35:12.54	720	901	50
9	G 333.605–0.212	16:22:09.605	–50:05:59.98	13000	15500	15

G 333.605–0.212 This continuum source is coincident with the *MSX* source G 333.6046–00.2124 and *IRAS* source *IRAS*16183–4958. These infrared sources are separated from the the peak of the continuum emission by 1.3 and 5.8 arcseconds respectively. This source is offset from the nearest water maser that we observe by about 15 arcseconds. The peak and integrated flux densities for this source were erroneously reported by Breen et al. (2007) to be 567 mJy/beam and 631 mJy, those reported in Table 3.3 are now correct and are corroborated by independent observations presented in Chapter 6.

3.4 Discussion

3.4.1 Association with other maser species

To our knowledge, this is the first high-mass star formation complex for which untargeted searches have been made in all of main-line OH, 6.7 GHz methanol and 22 GHz water masers. Previous targeted searches for water masers towards known 6.7 GHz methanol masers achieved detection rates of around 50 percent (Szymczak, Pillai & Menten, 2005). In contrast we find that only 25 percent of the 6.7 GHz methanol masers that fall within our survey region have an an associated water maser. We additionally find that only 11 percent of the water masers that we detect have an associated methanol maser which implies that targeted water

maser searches towards 6.7 GHz methanol masers is not be the most efficient way to increase the number of known water masers. This notion is supported by the results of extensive water maser observations presented in Chapter 6 which shows that a high number of 'extra' water maser sources were detected within the OH and methanol maser target fields. It also supports the hypothesis that water masers may be the most prevelant species within star formation regions as our relatively insensitive survey has detected twice as many water masers as either 6.7 GHz methanol or OH in the corresponding regions.

3.4.2 Association with infrared sources

Ellingsen (2006) found that approximately two-thirds of 6.7 GHz methanol masers have an associated GLIMPSE point source, and less than 10 percent of sources are not associated with mid-infrared emission (at the sensitivity of the GLIMPSE observations). A search of the GLIMPSE catalogue reveals four of the water maser sources detected (all of them new discoveries) have an associated GLIMPSE point source within 2 arcseconds. The details of these GLIMPSE point sources are summarized in Table 3.4. Of the remaining five water masers, the four previously detected sources are all clearly projected against regions of bright mid-infrared emission (see Fig. 3.3). Ellingsen (2006) suggested that a search for 6.7 GHz methanol masers towards GLIMPSE point sources meeting the criteria [3.6]–[4.5] > 1.3 mag and 8.0 μm magnitude < 10 would detect more than 80 percent of this class of maser. From Table 3.4 it can be seen that three of the four GLIMPSE point sources associated with water masers satisfy these criteria. We compared the [3.6]–[4.5] colours of the GLIMPSE sources associated with water masers with the colours of GLIMPSE sources associated with 6.7 GHz methanol masers (see fig. 16 of Ellingsen). The colours of the sources associated with water masers are clustered in the less red end of the range observed in the methanol associated sources. The idea that different maser species may trace different phases of the high-mass evolutionary sequence is not new, however, it has been receiving renewed attention lately, as sensitive, high-resolution observations at sub-millimetre through mid-infrared wavelengths become more readily available. Ellingsen (2006) looked at this question in some detail and we will not repeat the

arguments here. However, the striking difference between the relative location of the water and methanol masers in the G 333.2–0.6 GMC, and the less red colours of the water maser associated GLIMPSE sources supports the hypothesis that 6.7 GHz methanol masers may trace a generally earlier evolutionary phase than water masers. The very small water maser sample size prevents us from drawing any firm conclusions, however, it suggests that comparison of the properties of GLIMPSE sources associated with water and methanol masers may provide useful insights relating to this question.

The top and bottom inset images in Fig. 3.2 each show a ring of diffuse 8.0 μm emission surrounding a darker region. We have closely examined the GLIMPSE images of these regions. In the case of the southern most region (associated with the water maser G 333.826–0.549) it is clear that this is the result of a known image artifact that is present in some GLIMPSE sources where saturation occurs. An explanation for the northern most source (associated with the water maser G 333.608–0.215) is not as clear. The ring like structure seen in the 8.0 μm is similarly seen in the other GLIMPSE bands with radius decreasing with wavelength and the point where the dip in flux density per steradian occurs is close to the GLIMPSE saturation level. Interestingly, the *MSX* images of the region show a similar structure, warranting further observations of this source at both radio and infrared wavelengths to better understand its nature.

Three of the nine water masers detected in this survey (all previously known sources) have an *IRAS* source within 30 arcseconds. Two of the water masers that we observe have an associated *MSX* source. The details of these *IRAS* and *MSX* sources are presented in Table 3.5.

Karnik et al. (2001) detected 23 FIR sources in a survey of the GMC at 150 and 210 μm. Of the six most luminous of these sources, five have associated water masers (see Table 3.6 for details).

3.4.3 Association with molecular gas and dust clumps

^{13}CO clump associations

Bains et al. (2006) produced CLUMPFIND fits of the GMC using the 2D ^{13}CO data integrated over the velocity range –65 km s^{-1} to –35 km s^{-1} which covers

Table 3.4: *Water masers with GLIMPSE point source associations, here IRAC bands 1, 2, 3 and 4 correspond to 3.6 μm, 4.5 μm, 5.8 μm and 8.0 μm. Column 1 gives the water maser source number (see Table 3.1 for details), column 2 is the associated GLIMPSE point source, column 3 gives the angular separation between the GLIMPSE point source and the water maser source and colums 4 to 7 show the magnitudes of IRAC bands 1, 2, 3 and 4 for each of the GLIMPSE point sources, while column 8 gives the [3.6]–[4.5] colour for each.*

Source number	GLIMPSE point source (l, b)	Separation (arcsec)	IRAC band 1	Magnitude (mag) IRAC band 2	IRAC band 3	IRAC band 4	[3.6]–[4.5] colour (mag)
3	G 333.0600–00.4888	1.3	11.964	10.633	9.258	-	1.331
5	G 333.2205–00.4024	1.8	8.973	7.434	6.368	5.895	1.539
6	G 333.3639–00.3574	0.8	11.263	9.780	8.560	7.551	1.483
7	G 333.4285–00.3809	2.0	14.233	13.373	-	-	0.860

Table 3.5: *Possible infrared and water maser source associations. Column 1 gives the water maser source number (see Table 3.1 for details), column 2 shows the closest* IRAS *source within 2 arcminutes of the water masers, column 3 gives the angular separation between the water maser sources and the* IRAS *source, column 4 is the closest* MSX *source to within 1 arcminute and column 5 gives the angular separation between the* MSX *source and water maser source.*

Source number	*IRAS* source	Separation (arcsec)	*MSX* source	Separation (arcsec)
1	16158–5055	11		
2	16164–5046	29	G332.8269–00.5489	5
6	-		G333.2898–00.3898	33
9	16183–4958	20		

Table 3.6: *Separation from FIR sources, detected at 150 and 210 μm. Positions given are of the peak of the 210 μm (Karnik et al., 2001). Columns are as follows; 1 is the maser source number, 2 is the FIR source number quoted by Karnik et al. (2001), 3 and 4 are the Right Ascension and Declination of the clumps, 5 gives the angular separation between the water maser and the peak of the FIR source, columns 6 and 7 give the FIR source's peak flux densities at 150 and 210 μm respectively and column 8 gives the source luminosity.*

Source number	FIR source number	Right Ascension (J2000)	Declination (J2000)	Separation (arcsec)	150 μm Flux Density (Jy)	210 μm Flux Density (Jy)	Luminosity (10^3 $L_\odot$)
2	S11	16:20:06.0	−50:53:19	48	15380	7790	411
4	S15	16:20:57.9	−50:34:55	59	20811	10009	482
5	S18	16:21:20.3	−50:29:43	42	2180	1043	115
6	S20	16:21:29.8	−50:25:57	37	15572	8015	460
9	S23	16:22:08.9	−50:05:28	35	27841	11555	921

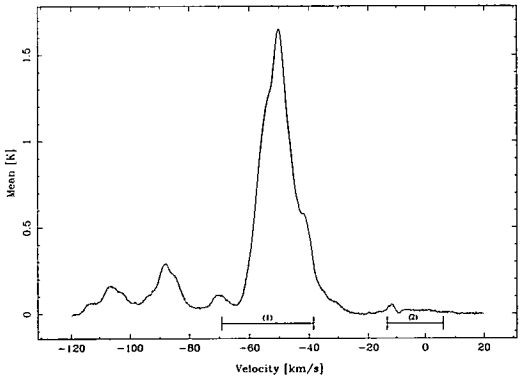

Figure 3.6: *The mean velocity profile of the ^{13}CO emission averaged over the entire field of observations from Bains et al. (2006). Overlaid are the velocity ranges of the water masers. (1) indicates the total velocity range of the seven water masers with comparable velocity ranges; maser sources 1, 2, 4, 5, 6, 7 and 9, while (2) indicates the velocity ranges of maser sources 3 and 8.*

the most prominent feature of the velocity profile seen in Fig. 3.6. Seven of the nine water masers that we detect fall within the velocity range analysed by Bains et al. (2006) and all of these masers fall within a ^{13}CO clump that they identify.

We obtained the ^{13}CO data of Bains et al. (2006) in the velocity range –120 km s^{-1} to 20 km s^{-1} which has allowed us to identify additional ^{13}CO emission peaks (or possible clumps) which may be associated with the two masers not coincident with a clump identified by Bains et al. (2006), G 333.060–0.488 and G 333.428–0.380. These emission peaks, like their associated water masers, have velocity ranges which fall outside that analysed by Bains et al. (2006). Water masers G 333.060–0.488 and G 333.428–0.380 show emission over a comparable velocity range of a secondary feature seen in the ^{13}CO emission (Fig. 3.6).

Details of the ^{13}CO clumps identified by Bains et al. (2006) and the ^{13}CO emission peaks that we identify along with their associated water maser sources are summarized in Table 3.7, while clump properties identified by Bains et al. (2006) are presented in Table 3.8. The velocity ranges of the ^{13}CO clumps or emission peaks have been obtained from visual inspection of the data. The ^{13}CO emission peaks have more extensive velocity ranges than the associated water maser emission in all cases with the exception of water masers G 333.060–0.488 and G 333.428–0.380. Interestingly these two water masers have similar velocity ranges which place them both at a distance of around 1 kpc (see Section 3.3.1). In the majority of cases the velocity of the peak flux density of the water masers are within a few km s^{-1} of the velocity of the associated peak ^{13}CO emission. In Chapter 6 we similarly conclude that a significant fraction of the water masers show peak emission near the systemic velocity of the region, however, it is clear that there are many exceptions to this, with a number of sources showing their peak emission in excess of 10 km s^{-1} from the systemic velocity.

Associations with CS emission

The GMC has been mapped in CS emission by the Delta Quadrant Survey Team as part of the ongoing project at University of New South Wales. CS emission is sensitive to higher densities and as a result the mapped region is less extensive than that covered in the ^{13}CO mapping (and was obtained in advance of publication as a result of correspondence with N. Lo from UNSW, these data have since

Table 3.7: *Water maser sources with nearby ^{13}CO clumps identified by Bains et al. (2006) (over velocity range -65 km s^{-1} to -35 km s^{-1}) or emission peaks as identified by visual inspection of the data used by Bains et al. (2006). Column 1 is the water maser source number (see Table 3.1 for details), columns 2 and 3 give the velocity range and the velocity of the peak emission of the water maser, column 4 gives the ^{13}CO clump number from Bains et al. (2006) if applicable, columns 5 and 6 show the right ascension and declination of the ^{13}CO clump or alternatively the ^{13}CO emission we identified from the ^{13}CO data from Bains et al. (2006), columns 7 and 8 give the velocity range and the velocity of the ^{13}CO emission peak as we have identified and column 9 is the separation between the centre of the clump that Bains et al. (2006) reported or the emission peak that we identified. The velocity ranges of the additional emission peaks that we identify as being associated with water masers 3 and 8, indicate that they are probably located along the line of sight at a distance of approximately 1 kpc (Bains et al., 2006).*

Source number	Velocity Range (km s^{-1})	Peak Velocity (km s^{-1})	^{13}CO source number	Right Ascension (J2000)	Declination (J2000)	Velocity Range (kms^{-1})	Peak Velocity (kms^{-1})	Separation (arcsec)
1	–59,–43	–45.3	9	16:19:40	–51:03:27	–60,–43	–50	35
2	–69,–45	–59.1	7	16:20:11	–50:53:27	–65,–44	–55	11
3	–13,5	–8.7	-	16:20:58	–50:40:39	–9,–2	–6	8
4	–60,–46	–57.7	1	16:21:03	–50:35:27	–64,–45	–51	40
5	–58,–48	-52.0	14	16:21:21	–50:30:03	–57,–40	–52	33
6	–58,–47	–49.0	2	16:21:31	–50:26:51	–58,–45	–52	23
7	–55,–49	-52.6	22	16:21:42	–50:21:39	–67,–42	–51	48
8	–6,6	4.1	-	16:22:05	–50:21:02	–1,10	6	40
9	–64,–38	–49.2	5	16:22:08	–50:06:27	–61,–32	–46	42

Table 3.8: *Properties of the ^{13}CO clumps (Bains et al., 2006). Column 1 is the number of the associated water maser source, column 2 is the ^{13}CO clump number (Bains et al., 2006), column 3 is the integated flux density of the clump peak, column 4 is the ^{13}CO clump peak in terms of antenna temperature, column 5 is the clump radius, column 6 is the ^{13}CO column density and column 7 is the total LTE molecular mass.*

Source number	^{13}CO Clump	Integrated Flux (10 K km s^{-1})	Peak (K)	Radius (pc)	N(^{13}CO) (10^{16} cm^{-2})	Mass (10^3 M$_\odot$)
1	9	10.5	13.3	1.7	6.6	4.6
2	7	12.0	14.4	1.8	6.2	5.0
4	1	18.5	46.0	2.6	10.1	16.0
5	14	8.8	15.7	1.8	6.9	5.5
6	2	15.8	41.4	2.4	10.3	14.4
7	22	8.9	25.0	2.2	7.6	8.7
9	5	13.8	27.4	2.2	7.9	9.5

Table 3.9: *Water masers sources with nearby CS emission peaks. Column 1 is the water maser source number, columns 2 and 3 give the velocity range and velocity of emission peak, columns 4 and 5 are the right ascension and declination of the CS emission peak, columns 6 and 7 show the velocity range and the emission peak of the CS emission and column 8 shows the angular separation between the water maser source and the CS emission peak.*

Source number	Velocity Range (kms^{-1})	Velocity Peak (kms^{-1})	CS Right Ascension (J2000)	Clump Declination (J2000)	Velocity Range (kms^{-1})	Peak Velocity (kms^{-1})	Separation (arcsec)
1	–59,–43	–45.3	16:19:40	–51:03:30	–56,–44	–50	33
2	–69,–45	–59.1	16:20:11	–50:53:19	–61,–51	–55	4
4	–60,–46	–57.7	16:21:03	–50:34:56	–61,–44	–53	63
5	–58,–48	–52.0	16:21:22	–50:30:46	–57,–48	–51	45
6	–58,–47	–49.0	16:21:29	–50:26:31	–58,–45	–51	12
7	–55,–49	–52.6	16:21:41	–50:23:19	–55,–45	–49	69
9	–64,–38	–49.2	16:22:08	–50:06:17	–58,–39	–47	40

been published (Lo et al., 2009)). This means that CS data was not available for two of the positions of the detected water masers. We inspected the data over a velocity range of –80 km s^{-1} to –20 km s^{-1} and identified CS emission peaks near all of the seven water masers for which CS data was available. The details of these emission peaks and their associated water masers are summarized in Table 3.9.

Unlike the ^{13}CO emission, CS emission is observed over a smaller velocity range than the associated water maser emission, however like the ^{13}CO emission the velocity of the peak flux density of the water masers correlates to within a few km s^{-1} with the velocity of the CS emission peaks. The association of the water masers with CS emission indicates that the water masers are probably associated with massive star formation (Bronfman, Nyman & May, 1996).

Association with 1.2 mm dust clumps

Seven of the water masers that we detect are associated with a 1.2 mm dust emission peak observed by Mookerjea et al. (2004) and the properties of the dust clumps are summarized in Table 3.10. Mookerjea et al. (2004) identified 95 1.2 mm dust clumps within the GMC and 73 of these fall within our observed regions. A statistical analysis of the 1.2 mm clumps that fall within the observed regions is presented in Section 3.4.4.

3.4.4 ^{13}CO and 1.2 mm dust clump analysis

In order to investigate the properties of the molecular gas and dust in the regions with associated water maser emission we have fitted a Binomial generalized linear model (GLM) (McCullagh & Nelder, 1989) to the maser presence/absence data using ^{13}CO and 1.2 mm dust clump properties reported by Bains et al. (2006) and Mookerjea et al. (2004) respectively, as predictors. Details of this method are presented in Chapter 1, Section 1.3. In the case of the ^{13}CO clumps the properties considered were the integrated flux densities of the clump peaks (10 K km s^{-1}), the peak flux in terms of antenna temperature (K), clump radius (pc), ^{13}CO column density (10^{16} cm^{-2}) and the total LTE molecular mass calculated from the ^{13}CO data. In the case of the 1.2 mm dust clump analysis the properties F_{peak} (mJy/beam), radius (pc), total integrated flux density (F_ν) in Jy, mass ($M_\odot$) and

Table 3.10: *Maser sources with nearby 1.2 mm dust clumps identified by Mookerjea et al. (2004). Column 1 is the water maser source number, column 2 is the dust clump number, columns 3 and 4 give the right ascension and declination of the dust clump, column 5 is the angular separation between the water maser and associated dust clump, column 6 gives the peak flux density for the clump, column 7 gives the clump radii, column 8 is the total integrated flux densities of the clumps, column 9 gives the estimated mass of the clumps assuming a temperature of 40 K and column 10 gives the column density.*

Source number	1.2 mm dust source	Right Ascension (J2000)	Declination (J2000)	Separation (arcsec)	F_{peak} (mJy/beam)	Radius (pc)	F_v (Jy)	Mass ($M_\odot$)	n_{H_2} (10^4 cm^{-3})
1	MMS84	16:19:38.9	−51:03:28	45	2499	1.48	21.9	2871	2.45
2	MMS68	16:20:11.9	−50:53:17	8	12460	1.70	36.1	5548	2.56
3	MMS51	16:20:52.1	−50:40:51	56	348	1.11	2.7	1029	0.73
4	MMS39	16:21:03.7	−50:35:23	47	8925	1.19	32.6	4584	6.18
5	MMS33	16:21:18.6	−50:30:25	10	1095	0.90	3.5	1325	1.76
6	MMS29	16:21:32.7	−50:27:12	44	6502	1.27	24.7	9281	4.38
9	MMS5	16:22:10.1	−50:06:06	14	40013	1.88	129.5	15936	5.44

n_{H_2} (10^4 cm^{-3}) where investigated as predictors. For ease of comparison between the data sets box plots were created for each of the clump properties. Box plots of each of the clump properties of both the ^{13}CO clumps and the 1.2 mm dust clumps are shown in Figs. 3.7 and 3.9 respectively.

^{13}CO clump results

Fits of the single term addition Binomial model to the ^{13}CO clump properties reported by Bains et al. (2006), showed an increasing probability of the presence of a maser was associated with all of the tested factors (the integrated flux density of the clump peak, ^{13}CO clump peak in terms of antenna temperature, clump radius, ^{13}CO column density and the total LTE molecular mass calculated from the ^{13}CO data). This means that any of the clump properties (in isolation) gives an indication of the likelihood of maser presence. Table 3.11 gives a summary of the single term addition Binomial model. The same information is shown graphically in Fig. 3.7 which clearly illustrates that for all clump properties there is a difference between the ^{13}CO clumps that have an associated water maser and those that do not. In general the ^{13}CO clumps with associated water masers are

Table 3.11: *Analysis of deviance table for the single term models (using ^{13}CO clump properties), showing the AIC and the deviance together with the associated likelihood ratio statistic and p-value for the test of the hypothesis that the stated single term model provides no better fit than the null model consisting only of an intercept.*

Predictor	AIC	Deviance	LRT	p-value
none	39.098	37.098		
Integrated	28.774	24.774	12.325	0.000447
Peak	33.093	29.093	8.005	0.004664
Radius	34.063	30.063	7.035	0.007994
Density	34.615	30.615	6.483	0.010892
Mass	35.265	31.265	5.833	0.015729

bigger, denser, brighter and more massive.

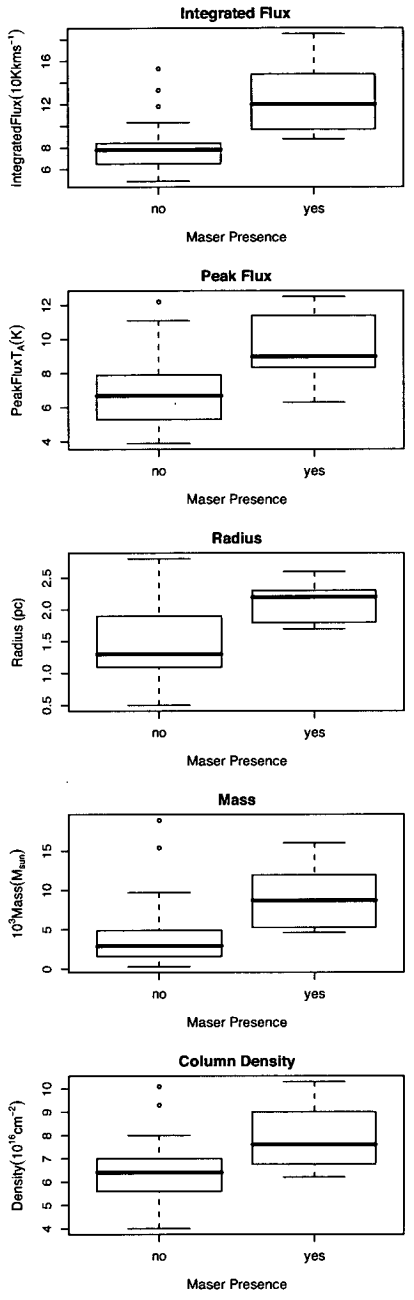

Figure 3.7: *Box plots of each of the ^{13}CO clump properties split into the categories of yes and no, referring to water maser presence and absence respectively.*

Table 3.12: *Summary table for the Binomial regression model of the ^{13}CO data, showing for each predictor the estimated coefficient and its standard error, and the standardised z-value and p-value for the test of the hypothesis that β_i=0.*

Predictor	Estimate	Std. Error	z value	p-value
Intercept	–21.2018	9.0538	–2.342	0.0192
Integrated	1.3037	0.5041	2.586	0.0097
Radius	8.0589	5.0069	1.610	0.1075
Mass	–1.2290	0.6153	–1.997	0.0458

The most parsimonious model for predicting maser presence involved the integrated flux density of the clump peak, clump radius and the total LTE molecular mass calculated from the ^{13}CO data. This means that if the integrated flux density of the peak, radius and mass is known for a ^{13}CO clump then a probability of maser presence can be determined. The estimated regression relation is

$$\log\frac{p_i}{1-p_i} = -21.2018 + 1.3037x_{integrated} + 8.0589x_{radius} - 1.2290x_{mass},$$

where $x_{integrated}$, x_{radius} and x_{mass} represent clump properties integrated flux density of the clump peak (10 K km s^{-1}), radius (pc) and mass (10^3 M$_\odot$). The full regression summary is shown in Table 3.12.

Setting the threshold probability of the ^{13}CO clump model at 0.5 (i.e. a value greater than 0.5 suggests a water maser will be associated with a clump, while a lower value suggests no water maser), we find the misclassification rates to be low. Of the 40 ^{13}CO clumps that fall in our observation regions which correspond the the main part of the GMC (-65 km s$^{-1}\leq$ v$_{\rm LSR}$ ≤ -35 km s^{-1}), seven have an associated water maser while our model predicts that five of these have an associated water maser and returns a false-negative for the remaining two clumps. There are 33 clumps within the survey regions that do not have associated water masers, our model predicts that 31 of these do not have associated water masers but returns a false-positive for the remaining two clumps.

1.2 mm dust clump results

In terms of the 1.2 mm dust clump properties, fits of the single term addition Binomial model showed an increasing probability that the presence of a maser was associated with increasing value of all of the clump properties reported by Mookerjea et al. (2004). Table 3.13 gives a summary of the single term addition. This means that any one of the clump properties may give an indication of the likelihood of maser presence. There is a significant difference between the clumps with associated water masers and those without, evident from Fig. 3.9. Clumps with associated masers are bigger, denser, more massive and have higher flux densities than clumps where we see no associated water maser.

The most parsimonious model for predicting maser presence involved only the radius of the 1.2 mm dust clumps. This equation allows the probability of maser presence to be predicted knowing only the radius of a 1.2 mm dust clump. The estimated regression relation is

$$\log\frac{p_i}{1-p_i} = -11.477 + 9.174x_{radius},$$

where x_{radius} is the radius of the 1.2 mm dust clump in pc. The regression summary of this model is shown in Table 3.14.

Table 3.13: *Analysis of deviance table for the single term models (using the 1.2 mm dust clump properties), showing the AIC and the deviance together with the associated likelihood ratio statistic and p-value for the test of the hypothesis that the stated single model provides no better fit than the null model consisting only of an intercept.*

Predictor	AIC	Deviance	LRT	p-value
none	48.130	46.130		
$\mathbf{F}_{peak}$	28.088	24.088	22.042	2.668e–06
Radius	24.330	20.330	25.800	3.787e–07
$\mathbf{F}_{v}$	25.428	21.428	24.702	6.693e–07
Mass	27.467	23.467	22.663	1.930e–06
Density	39.969	35.969	10.160	0.001435

The misclassification rates for the model, given a probability of 0.5 of maser presence within a given clump are again low in predicting the clumps that have no associated water maser. Of the 73 1.2 mm dust clumps that fall within our survey region, seven have an associated water maser, while 66 do not. Our model predicts that 65 of the 66 clumps with no associated water maser will not have an associated water maser and returns a false-positive result for the remaining clump. The model predicts that of the seven clumps that have an associated water maser only four will have an associated water maser and returns a false-negative

Table 3.14: *Summary table for the Binomial regression model, showing for each predictor the estimated coefficient and the standardised z-value and p-value for the test of the hypothesis that $\beta_i=0$.*

Predictor	Estimate	Std. Error	z value	p-value
Intercept	–11.477	3.537	–3.245	0.00118
Radius	9.174	3.163	2.900	0.00373

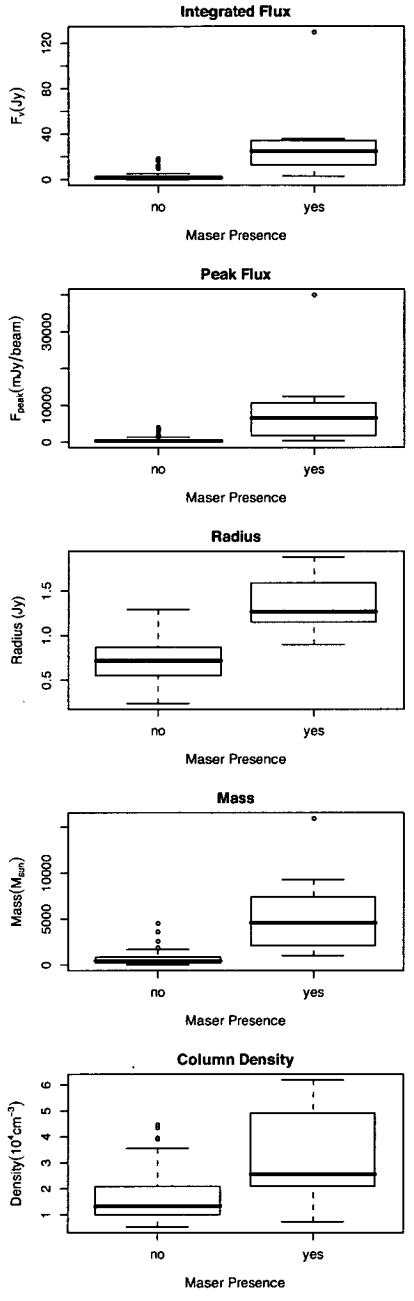

Figure 3.8: *Box plots of the 1.2 mm dust clump properties split into the categories of yes and no, referring to water maser presence and absence respectively.*

for the remaining three clumps.

As this model is only concerned with clump radius it is easy to illustrate its physical implications. By setting the probability of maser presence to be 0.5, for example, we are able to determine that the corresponding clump radius is approximately 1.25 pc. This means that all 1.2 mm dust clumps with a radius of 1.25 pc or greater have a probability of 0.5 or more of having an associated water maser.

3.5 Methanol masers associated with 1.2 mm dust and ^{13}CO clumps

We have repeated the analysis carried out with water masers associated with ^{13}CO and 1.2 mm dust clumps, this time investigating the properties of the ^{13}CO and 1.2 mm dust clumps associated with 6.7 GHz methanol masers (Ellingsen, 2005). Comparison of the locations of the methanol masers with the molecular gas and dust data showed that all 5 of the methanol masers that lie within the regions surveyed by Bains et al. (2006) and Mookerjea et al. (2004) are associated with both molecular gas and dust emission peaks. In the regions completely searched for both methanol masers and ^{13}CO clumps there are 56 ^{13}CO clumps with no associated methanol masers and 5 ^{13}CO clumps with associated methanol masers. In the case of the 1.2 mm dust clumps there are 90 clumps with no associated methanol masers and 5 with associated methanol masers. A GLM was fitted to the maser presence/absence data. ^{13}CO and 1.2 mm dust clump properties were used as predictors and are as for the analysis with water masers in Section 3.4.4.

The significance of all individual clump properties we tested by fitting all possible single term models and compared by analysis of deviance to the null model consisting only of an intercept. There is an increased likelihood of methanol maser presence associated with ^{13}CO clumps with increasing values of integrated flux density and column density. In the case of the 1.2 mm dust clumps, we find that there is and increased likelihood of methanol maser presence associated with increasing values of column density, radius and mass. Box plots of each of the clump properties of the ^{13}CO and 1.2 mm dust clumps are shown in Fig. 3.9.

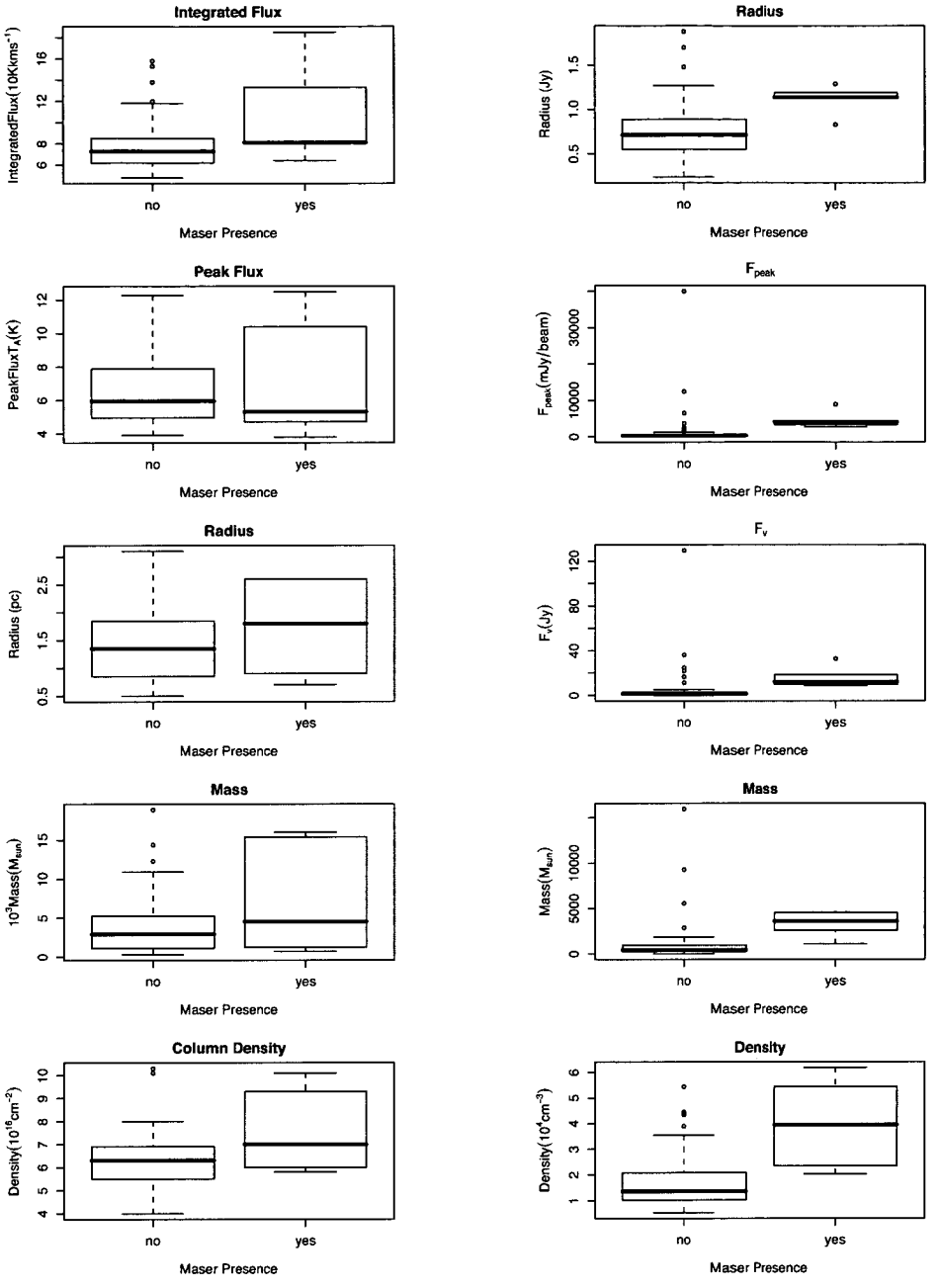

Figure 3.9: *Box plots of the ^{13}CO (left) and 1.2 mm dust (right) clump properties split into the categories of yes and no, referring to methanol maser presence and absence respectively.*

Stepwise model selection based on the Akaike Information Criteria (Burnham & Anderson, 2002) was used to select the simplest model with the greatest predictive powers. In the case of the ^{13}CO analysis the estimated regression relation is

$$\log\frac{p_i}{1-p_i} = -5.56 + 1.47x_{integ} - 1.53x_{peak},$$

where p_i is the probability of methanol maser presence in the i^{th} clump, x_{integ} represents the integrated flux density of the clump peak (10 K kms^{-1}), x_{peak} represents the clump peak in terms of antenna temperature (K).

The estimated regression relation for methanol maser presence associated with 1.2 mm dust clumps is

$$\log\frac{p_i}{1-p_i} = -94.55 + 0.00151x_{Fpeak} + 78.3x_{radius} - 2.24x_{Fv} - 0.000836x_{mass} + 10.7x_{density},$$

where p_i is the probability of methanol maser presence in the i^{th} clump, x_{Fpeak} is the peak flux density per beam of the clump (mJy/beam), x_{radius} is the clump radius (pc), x_{Fv} is the integrated flux density (Jy), x_{mass} is clump mass in units of solar masses and $x_{density}$ is column density (10^4 cm^{-3}).

These models have encouraging misclassification rates, although could benefit from some refinements by testing a larger sample. In particular, the ^{13}CO model for methanol maser presence predicts that nearly all of the ^{13}CO clumps have a very low probability of methanol maser presence although it does predict that the clumps with associated methanol masers have a slightly higher probability of methanol maser presence than those clumps without associated methanol masers. The 1.2 mm dust clump model has better predictive properties, if we set the probability threshold to 0.5 (i.e. those clumps with a value greater than 0.5 suggests the presence of a methanol maser, while a lower value suggests no methanol maser) the model correctly predicts 89 of the 90 clumps within the region with no associated methanol masers and predicts 3 of the 5 clumps with associated methanol masers correctly.

3.6 Summary

Regions within the GMC associated with RCW 106 have been surveyed for 22 GHz water masers by Breen (2005). We have followed up the detections from this survey from the ATCA which have resulted in the detection of nine water masers (five of these being new detections) and four 22 GHz continuum sources. All of the water masers that we observed have exhibited some level of variability over the 11 month course of these observations. The most extensive temporal variability was observed in water maser G 333.060–0.488, which showed a variation in peak flux density of a factor of 10 over the observational period. The GMC has previously been searched for 6.7 GHz methanol masers (Ellingsen et al., 1996) and main-line OH masers (Caswell, Haynes & Goss, 1980). In addition to the nine water masers detected there are four 6.7 GHz methanol masers (Ellingsen et al., 1996) and three OH masers (Caswell, Haynes & Goss, 1980) within the regions surveyed here. All of the three species of masers have sub-arcsecond positional accuracy which allows a comparison of the relative positions of the respective maser species. The water masers that we detect lie along the main axis of star formation within the GMC while the methanol masers are located near the periphery. We find there to be little overlap between the sites of the different maser species, in fact there are only two associations with other maser species. There is one association with a 6.7 GHz maser and one association with an OH maser.

Four of the new water maser detections are associated with GLIMPSE point sources, of similar colours to those associated with detected 6.7 GHz methanol masers. There is a slight bias for the water maser associated sources to be less red. This coupled with the relative positions of the water masers and the 6.7 GHz methanol masers with respect to the main axis of star formation lends support to the hypothesis that 6.7 GHz methanol masers trace an earlier evolutionary phase than water masers.

All of the water masers are associated with a ^{13}CO emission peak that we identify or a clump reported by Bains et al. (2006). Statistical investigation of the ^{13}CO (Bains et al., 2006) and 1.2 mm dust (Mookerjea et al., 2004) clumps shows that there is a strong increase in likelihood of water maser detection with

increased clump radius, mass, density and brightness. We find that the ^{13}CO and 1.2 mm dust clumps associated with the methanol masers have high values of clump radius, mass, density and brightness, although are generally not as extreme than as associated with the water masers. After fitting a GLM to the maser presence data using the clump properties of Bains et al. (2006) and Mookerjea et al. (2004) as predictors we obtained the simplest models with the greatest maser predictive power. In the case of the 1.2 mm dust clumps our model uses only clump radius to predict the likelihood of the clump having an associated water maser. However the model generated for ^{13}CO clumps takes into account radius, integrated flux density of the clump peak and mass. These models have a low misclassification rate and may allow more efficient targeted searches for water masers (where appropriate ^{13}CO or 1.2 mm data is available) than those previously conducted towards other species of masers or mid-infrared sources. While our survey was of comparatively small scale, we believe that the results are indicative of the likelihood of occurrence of water masers with respect to ^{13}CO and 1.2 mm dust clumps.

Observations of ^{13}CO clumps and 1.2 mm dust clumps within the G 333.2–0.6 GMC that do not fall within the regions already surveyed will allow us to test and refine our predictive models. Additional observations towards ^{13}CO clumps and 1.2 mm dust clumps which are not part of the G 333.2–0.6 GMC will allow us to determine models with more highly accurate predictive properties and lower standard errors (see Chapter 5). As more data for the G 333.2-0.6 GMC in other molecular line transitions becomes avaliable, analysis similar to what we have undertaken here will be carried out. The multitude of data becoming available for the G 333.2-0.6 GMC, ranging from complete searches of water, methanol and main-line OH masers to many molecular line transitions as well as 1.2 mm dust continuum emission, provides us with a unique opportunity to continue our investigation of the relative evolutionary stages that different maser species may be tracing.

We have tested the model for water maser presence in 1.2 mm dust clumps on a large catalogue of 1.2 mm dust clumps (Hill et al., 2005). The ATCA has been used to search for water masers towards almost 300 of the 1.2 mm dust clumps presented in this catalogue. These observations, detection statistics, comparison

with the computed probability of water maser presence, as well as a refinement to the current model are presented in Chapter 5.

4

12 GHz methanol masers associated with 1.2 mm dust clumps: Quantifying high-mass star formation evolutionary schemes

4.1 Introduction

To date there have been several searches for 12.2 GHz methanol maser emission towards 6.7 GHz methanol maser emission (e.g. Caswell et al., 1995b; Błaszkiewicz & Kus, 2004). Caswell et al. (1995b) targeted their search for 12.2 GHz methanol masers towards 238 6.7 GHz methanol masers that had been detected towards sites of OH masers and achieved a detection rate of 55 per cent. Błaszkiewicz & Kus (2004) directed their observations at 12.2 GHz towards 6.7 GHz methanol masers that were observed towards a sample of *IRAS* (Infrared Astronomy Satellite) selected sources (Szymczak et al., 2000) as well as 6.7 GHz methanol masers that were detected in a blind search that had relatively poor positional accuracy and sensitivity (Szymczak et al., 2002).

Searches such as those by Caswell et al. (1995b) and Błaszkiewicz & Kus (2004) have shown that 12.2 GHz methanol maser emission is only rarely brighter than the associated 6.7 GHz methanol maser emission. This coupled with the fact that there have been no serendipitous detections of 12.2 GHz masers without

a 6.7 GHz counterpart mean that it is unlikely that an unbiased Galactic survey would uncover many, if any, more 12.2 GHz methanol masers than would be yielded from a search targeted towards 6.7 GHz methanol maser sources.

Recently, a small subset of the strong 6.7 GHz methanol masers from the sources observed by Hill et al. (2005) at 1.2 mm, were searched for the presence of 12.2 GHz methanol masers with the University of Tasmania 26 m Mount Pleasant radio telescope (Lewis, 2007). Lewis (2007) detected 17 12.2 GHz methanol masers towards the 27 sites searched with a detection limit of $\sim$4 Jy. Hill et al. (2005) observed 131 regions that were suspected of undergoing massive star formation, using the presence of previously identified 6.7 GHz methanol masers and/or an ultracompact HII region to select these regions. A total of 404 1.2 mm dust clumps were identified, with 113 of these associated with 6.7 GHz methanol masers, 35 of which are associated with radio continuum emission (Walsh et al., 1998).

Statistical analysis by Lewis (2007) of the properties of 1.2 mm dust clumps associated with 6.7 GHz methanol maser emission with and without 12.2 GHz methanol masers showed that those 1.2 mm dust clumps with both 6.7 GHz and 12.2 GHz were less massive and less dense than the 1.2 mm clumps that were associated with only 6.7 GHz methanol maser emission. Comparison between the 6.7 GHz methanol masers with detected 12.2 GHz with those with no detectable 12.2 GHz maser emission, showed that 12.2 GHz methanol masers were preferentially found at those 6.7 GHz methanol maser sites with associated OH emission (to a better than 95 per cent confidence). As OH masers are expected to trace a generally later stage of star formation (Forster & Caswell, 1989; Caswell, 1997) than 6.7 GHz methanol masers. As the sample size of the Lewis (2007) observations was small, was subject to a 6.7 GHz flux density bias and had relatively poor sensitivity, the aim of the current work was to confirm these results by testing a large sample with a much lower 12.2 GHz detection limit.

Here we present a targeted search for 12.2 GHz methanol masers, with a greatly increased sample size and sensitivity (c.f. Lewis (2007)), towards 112 known 6.7 GHz methanol masers which have been previously targeted for 1.2 mm dust continuum emission (Hill et al., 2005). Statistical analysis of the 1.2 mm dust clumps devoid of either methanol maser transition and those associated with

12.2 GHz and/or 6.7 GHz methanol maser sources has been carried out, with a particular emphasis on the investigation of the relative evolutionary stage each class of source is tracing.

6.7 GHz sources in this sample that fall south of declination –20 degrees have also been include in the search for 12.2 GHz methanol maser emission that is presented in Chapter 7.

4.2 Observations & Data Reduction

We have searched 112 6.7 GHz methanol masers, towards which Hill et al. (2005) observed 1.2 mm dust clump continuum emission, for the presence of associated 12.2 GHz methanol maser emission. Observations were carried out with the Australia Telescope National Facility (ATNF) Parkes 64-m radio telescope during 2008 June 20 - 25. Follow-up observations of two sources were made on 2008 December 7 using an identical set-up to the observations carried out in 2008 June. The observations were made with the Ku-band receiver which detected two orthogonal linear polarizations and had typical system temperatures of 205 and 225 Jy for the respective polarizations throughout the observations. The Parkes multibeam correlator was configured to record 8192 channels over 16-MHz for each of the recorded linearly polarized signals. This configuration yielded a useable velocity coverage of $\sim$290 km s^{-1} and a spectral resolution of 0.08 km s^{-1}, after Hanning smoothing. The Parkes radio telescope has rms pointing errors of $\sim$10 arcsec and at 12.2 GHz the telescope has a half power beam width of 1.9 arcmin.

All sources were observed at a fixed frequency of 12178-MHz (i.e. with no Doppler tracking), which alleviated the requirement for a unique reference observation to be made for each of the source positions. Instead, all the spectra collected each day were combined to form a sensitive reference bandpass by taking the median value of each channel. The noise contribution to the quotient spectrum from such a reference is negligible and means that the theoretical radiometer noise is achieved for each observation.

As the bandpass is not constant throughout an observing session, observing in this mode introduced ripples into the quotient spectra. This was overcome

by subtracting a running median over 100 channels from the baseline. As the maser lines are much narrower than 100 channels this has little effect on emission spectra but may have an adverse effect on absorption features which are of a comparable width. Our ability to detect absorption is therefore reduced and in most cases where we do detect absorption it appears narrower and weaker than it would have been if we had employed a more traditional, but less efficient, observing method. In order to determine the absorption characteristics of the sources, spectra where absorption features were detected were boxcar smoothed over 20 channels, decreasing our spectra resolution to 0.26 km s^{-1} and resulted in a typical rms noise of $\sim$0.04 Jy.

Data were reduced using ASAP (ATNF Spectral Analysis Package). Alignment of velocity channels was carried out during processing. Absolute flux density calibration was achieved by observing PKS B1934-638 each day which has an assumed flux density of 1.825 Jy at 12178-MHz (Sault, 2003). Each target was observed for 10 minutes, and once the polarizations were averaged yielded a typical rms noise of 0.11 Jy corresponding to a 5-σ detection limit of 0.55 Jy. For weak sources (of comparable strength to our detection limit), individual polarizations were inspected as a further check on the reliability of the detection. The adopted rest frequency was 12.178597 GHz (Müller, Menten & Mäder, 2004).

4.3 Results

Our search, for 12.2 GHz methanol masers, targeted 112 6.7 GHz methanol maser sites and resulted in the detection of 68 12.2 GHz methanol masers, equating to a detection rate of 60 per cent. A search of the literature (e.g. Pestalozzi, Minier & Booth, 2005; Błaszkiewicz & Kus, 2004; Caswell et al., 1995b) reveals that 29 of these are new detections. A number of the 12.2 GHz methanol masers that have been previously observed, particularly the stronger ones, were discovered prior to Błaszkiewicz & Kus (2004); Caswell et al. (1995b) by others (e.g. Gaylard, MacLeod & van der Walt, 1994; Caswell et al., 1993). However, direct comparison of the majority of these sources are complicated by large positional uncertainties, pointing offsets and the limited velocity ranges covered in the observations.

Table 4.1 summarizes information on the targeted 6.7 GHz methanol masers

(Caswell, 2009; Minier et al., 2003; Walsh et al., 1998, 1997; Caswell et al., 1995a; Szymczak et al., 2002), associated 12.2 GHz methanol masers that we detect, along with the 1.2 mm dust clump (Hill et al., 2005) that each methanol maser site is associated with. For the majority of sources, precise positions for the 6.7 GHz methanol maser sources have been determined with the Australia Telescope Compact Array to an accuracy better than 1 arcsec. There are five instances where two methanol masers are associated with the same dust clump, therefore our observations targeted a total of 106 1.2 mm dust clumps. Spectra of the detected 12.2 GHz methanol masers are shown in Fig. 4.1 and are presented in order of Galactic longitude except for where vertical alignment of nearby sources was necessary to highlight where features of a source were also detected at nearby positions. Comments on some individual sources can be found in Section 4.3.1. The absorption features that we detect are presented in Table 4.2.

Table 4.1: *Targeted 6.7 GHz methanol masers, detected 12.2 GHz methanol masers and associated 1.2 mm dust clump that they are associated with. Column 1 gives the Galactic coordinates for each methanol maser source, derived from the position of the 6.7 GHz methanol maser, columns 2 and 3 give the 6.7 GHz methanol maser right ascension and declination. References for each 6.7 GHz methanol maser position are represented by the superscript number at the end of the source name where 1: Caswell (2009), 2: Minier et al. (2003), 3: Walsh et al. (1998), 4: Walsh et al. (1997), 5: Caswell et al. (1995a), 6: Szymczak et al. (2002), α: James Caswell, private communication; see also note in comments on sources for G 034.246+0.134 and G 035.025+0.350. References for previously detected 12.2 GHz methanol masers are listed after the 6.7 GHz methanol maser references and are separated by a comma and contained within brackets to avoid confusion, here 7: Caswell et al. (1995b), 8: Błaszkiewicz & Kus (2004), *: new detection. Columns 4 - 10 list the 6.7 GHz peak flux density (Jy), peak velocity (km s^{-1}), velocity range (km s^{-1}) (nb. where the source reference is Walsh et al. (1998) the velocity range has been taken from Walsh et al. (1997) where available and Pestalozzi et al. (2005) if not), 12.2 GHz peak flux density (Jy), peak velocity (km s^{-1}), velocity range (km s^{-1}) and integrated flux density (Jy km s^{-1}). The 5-σ detection limit and velocity range covered at 12.2 GHz is presented for sources where we detect no 12.2 GHz emission, in these cases the 5-σ detection limit is presented in column 7 and is preceded by a <, and the velocity ranges observed are listed in column 9. $^{\beta}$ indicates a source that was previously observed by Caswell et al. (1995b) but we do not detect. Column 11 indicates if the methanol maser sites have been searched for the presence of an associated OH maser by Caswell (1998), – indicates that no suitable data were found, n indicates that the site has been searched but no source was detected and y indicates that there is an OH maser within 2 arcsec of the 6.7 GHz methanol maser. The dust clump (Hill et al., 2005) that the methanol masers are coincident with are listed in column 12, a $^{\#}$ after the source name indicates sources that were not included in the statistical analysis, for details see Section 4.3.2.*

Methanol maser (l, b) (degrees)	RA (J2000) (h m s)	Dec (J2000) (^{o} ′ ″)	$S_{6.7}$ (Jy)	$Vp_{6.7}$	$Vr_{6.7}$	$S_{12.2}$ (Jy)	$Vp_{12.2}$	$Vr_{12.2}$	$I_{12.2}$	OH	Dust clump (l, b) (degrees)
G 189.778+0.345[1]	06 08 35.28	+20 39 06.7	15	6	2,6	<0.75		−163,125		–	G 189.78+0.34
G 192.600−0.048[1,(*)]	06 12 53.99	+17 59 23.7	72	5.0	2,6	0.47	3.6	3.4,3.7	0.1	–	G 192.60−0.05

Table 4.1: – continued

Methanol maser (l, b) (degrees)	RA (J2000) (h m s)	Dec (J2000) (° ′ ″)	$S_{6.7}$ (Jy)	$Vp_{6.7}$	$Vr_{6.7}$	$S_{12.2}$ (Jy)	$Vp_{12.2}$	$Vr_{12.2}$	$I_{12.2}$	OH	Dust clump (l, b) (degrees)
G 206.543–16.355[2]	05 41 44.15	–01 54 44.9	1.5	–1		< 0.6		–165,123		–	G 206.54–16.35
G 213.705–12.597[1,(7)]	06 07 47.87	–06 22 57.0	337	12	8,13	14	12.7	12.2,13.3	6.0	y	G 213.61–12.6
G 259.939–0.041[3]	08 35 31.086	–40 38 23.96	2.5	–1.3		<0.55		–180,108		n	G 259.94–0.04#
G 269.153–1.128[1]	09 03 33.46	–48 28 02.6	1.6	16	7,16	<0.75		–179,109		n	G 296.15–1.13
G 269.456–1.467[3,(*)]	09 03 14.848	–48 55 11.25	4.5	56		1.4	56.0	55.9,56.3	0.4	n	G 296.45–1.47
G 270.255+0.835[1]	09 16 41.51	–47 56 12.1	0.6	3.9	3,5	<0.75		–179,109		n	G 270.25+0.84
G 284.352–0.419[1,(7)]	10 24 10.89	–57 52 38.8	1.7	3.3	3,11	<0.80[β]		–176,112		n	G 284.35–0.42#
G 287.371+0.644[1,(*)]	10 48 04.40	–58 27 01.7	80	–1.8	–3,0	49	–2.0	–2.5,–1.0	20.2	y	G 287.37+0.65
G 290.374+1.661[1]	11 12 18.10	–58 46 21.5	0.6	–24.2	–28,–22	<0.6		–174,115		y	G 290.37+1.66#
G 290.411–2.914[3,(*)]	10 57 33.987	–62 59 03.13	2.4	–16.2	–17,–15	1.5	–16.1	–16.2,–15.8	0.4	n	G 290.40–2.91
G 291.274–0.709[1,(7)]	11 11 53.35	–61 18 23.7	100	–29.6	–31,–28	3.1	–29.1	–30.1,–28.7	2.4	y	G 291.27–0.70
G 291.579–0.431[1]	11 15 05.76	–61 09 40.8	0.7	14.5	11,16	<0.6		–173,115		y	G 291.58–0.53#
G 291.582–0.435[1]	11 15 06.61	–61 09 58.3	1.7	10.5	8,11	<0.6		–173,115		n	G 291.58–0.53#
G 293.827–0.746[3]	11 32 05.606	–62 12 25.43	3.6	36.7	35,39	<0.56		–173,115		n	G 293.82–0.74
G 293.942–0.874[4,(*)]	11 32 42.091	–62 21 47.51	3.6	41.0		2.1	41.1	40.9,41.3	0.6	n	G 293.942–0.876
G 294.511–1.621[1]	11 35 32.25	–63 14 43.2	12	–10.2	–14,–9	<0.55		–172,116		y	G 294.52–1.60
G 294.990–1.719[1]	11 39 22.88	–63 28 26.4	18	–12.3	–13,–11	<0.55		–172,116		n	G 294.989–1.720
G 298.262+0.739[3]	12 11 47.655	–61 46 21.14	11	–30.2	–31,–29	<0.55		–172,116		y	G 298.26+0.7
G 299.013+0.128[1]	12 17 24.60	–62 29 03.7	7	18.4	18,20	<0.56		–171,117		y	G 299.02+0.1
G 300.504–0.176[1]	12 30 03.58	–62 56 48.7	4.7	7.5	4,11	<0.55		–170,118		y	G 300.51–0.1
G 301.136–0.226[1]	12 35 35.14	–63 02 32.6	1.2	–39.8	–41,–37	<0.52		–146,142		y	G 301.14–0.2
G 302.032–0.061[1]	12 43 31.92	–62 55 06.7	11	–35.3	–43,–33	<0.6		–170,118		n	G 302.03–0.06
G 305.199+0.005[1,(*)]	13 11 17.20	–62 46 46.0	2.3	–42.8	–45,–38	0.7	–42.6	–42.7,–41.4	0.1	n	G 305.192–0.006
G 305.200+0.019[1,(*)]	13 11 16.93	–62 45 55.1	44	–33.1	–38,–29	10.6	–31.8	–33.2,–31.6	8.8	y	G 305.200+0.02
G 305.202+0.208[1,(7)]	13 11 10.49	–62 34 38.8	20	–43.9	–47,–43	3.5	–43.9	–45.0,–43.6	1.8	y	G 305.21+0.21
G 305.208+0.206[1,(7)]	13 11 13.71	–62 34 41.4	320	–38.3	–42,–34	1.7	–36.5	–40.5, –35.7	0.9	y	G 305.21+0.21
G 305.248+0.245[1]	13 11 32.47	–62 32 09.1	4	–32.0	–36,–28	<0.60		–169,119		n	G 305.248+0.245

Table 4.1: – continued

Methanol maser (l, b) (degrees)	RA (J2000) (h m s)	Dec (J2000) (° ′ ″)	$S_{6.7}$ (Jy)	$Vp_{6.7}$	$Vr_{6.7}$	$S_{12.2}$ (Jy)	$Vp_{12.2}$	$Vr_{12.2}$	$I_{12.2}$	OH	Dust clump (l, b) (degrees)
G 305.362+0.150[1]	13 12 35.86	−62 37 17.9	3	−36.5	−38,−35	<0.55		−169,119		y	G 305.361+0.151
G 305.366+0.184[1,(7)]	13 12 36.74	−62 35 14.7	2.5	−33.8	−35,−33	3.3	−34.1	−34.4,−33.6	1.6	n	G 305.362+0.185
G 305.563+0.013[α,(*)]	13 14 26.90	−62 44 29.4	4.5	−37.3	−42,−32	1.6	−37.1	−41.6,−35.7	1.4	n	G 305.552+0.013
G 305.799−0.245[1]	13 16 43.23	−62 58 32.9	0.7	−39.5	−40,−36	<0.55		−168,120		y	G 305.81−0.25
G 306.322−0.334[1]	13 21 23.01	−63 00 29.5	1.2	−24.4	−25,−22	<0.55		−168,120		y	G 306.33−0.3
G 309.921+0.479[1,(7)]	13 50 41.78	−61 35 10.2	635	−59.8	−65,−54	179	−59.7	−61.3,−57.7	108.5	y	G 309.92+0.4
G 318.948−0.196[1,(7)]	15 00 55.39	−58 58 52.8	690	−34.7	−39,−31	140	−34.4	−35.5,−32.0	91.0	y	G 318.92−0.68
G 323.740−0.263[1,(7)]	15 31 45.45	−56 30 50.1	3000	−51.1	−58,−45	420	−48.7	−52.6,−47.8	785.1	y	G 323.74−0.3
G 330.953−0.182[1]	16 09 52.37	−51 54 57.6	7	−87.6	−90,−87	<0.55		−156,132		n	G 330.95−0.18
G 331.278−0.188[1,(7)]	16 11 26.59	−51 41 56.7	190	−78.2	−87,−77	76	−78.7	−83.1,−77.7	58.8	y	G 331.28−0.19[#]
G 332.653−0.621[1]	16 19 43.51	−51 03 39.9	7.1	−50.6	−52,−49	<0.54		−130,158		n	G 332.648−0.606
G 332.726−0.621[1,(*)]	16 20 03.00	−51 00 32.5	2.7	−49.5	−57,−44	0.5	−47.3	−47.4,−47.2	0.1	y	G 332.73−0.62
G 000.212−0.001[1,(*)]	17 46 07.63	−28 45 20.9	3.5	49.2	41,50	0.8	49.5	49.1,49.7	0.5	n	G 0.21−0.00
G 000.315−0.201[1,(*)]	17 47 09.13	−28 46 15.7	41.2	18	14,27	2.4	18.3	17.8,18.5	1.0	n	G 0.32−0.20
G 000.316−0.201[1]	17 47 09.33	−28 46 16.0	1.3	21	20,22	<0.55		−120,168		n	G 0.32−0.20
G 000.496+0.188[1,(*)]	17 46 03.96	−28 24 52.8	10	0.8	−12,2	18	1.1	−9.5,1.5	15.6	y	G 0.49+0.19
G 000.546−0.852[1,(7)]	17 50 14.35	−28 54 31.1	50	13.8	8,20	3.9	18.5	16.1,19	2.1	y	G 0.55−0.85
G 000.836+0.184[1]	17 46 52.86	−28 07 34.8	8.1	3.5	2,4	<0.52		−115,173		n	G 0.83+0.18
G 001.147−0.124[3]	17 48 48.467	−28 01 11.81	4	−20.8	−21,−15	<0.51		−115,173		n	G 1.14−0.12
G 002.536+0.198[1,(*)]	17 50 46.47	−26 39 45.3	40	3.2	2,20	3.7	7.0	3.4,7.2	2.6	n	G 2.54+0.20
G 005.900−0.430[1]	18 00 40.86	−24 04 20.8	5.3	10	4,11	<0.55		−113,175		n	G 5.90−0.42
G 006.610−0.082[1,(*)]	18 00 54.03	−23 17 03.1	10.8	0.7	0,1	10.7	0.9	0.5,1.4	4.7	n	G 6.60−0.08[#]
G 008.139+0.226[1]	18 03 00.75	−21 48 09.9	3.5	20	19,21	<0.55		−112,176		n	G 8.13+0.22
G 008.669−0.356[1,(*)]	18 06 18.99	−21 37 32.2	8.5	39.3	39,40	0.3	39.5	39.4,39.6	0.05	y	G 8.68−0.36
G 008.683−0.368[1,(7)]	18 06 23.49	−21 37 10.2	70	42.9	40,46	8.4	44.2	41.0,45.5	11.6	y	G 8.686−0.366
G 009.619+0.193[1,(*)]	18 06 14.92	−20 31 44.3	72	5.5	5,7	0.4	5.8	5.7,5.9	0.1	y	G 9.62+0.19
G 009.621+0.196[1,(7)]	18 06 14.67	−20 31 32.4	5000	1.3	−4,9	401	1.4	−3.0,5.8	202.8	y	G 9.62+0.19
G 009.986−0.028[1,(*)]	18 07 50.12	−20 18 56.5	28	47.1	40,52	1.0	47.1	44.3,47.3	0.5	n	G 9.99−0.03

Table 4.1: – continued

Methanol maser (l, b) (degrees)	RA (J2000) (h m s)	Dec (J2000) (^{o} ′ ″)	$S_{6.7}$ (Jy)	$Vp_{6.7}$	$Vr_{6.7}$	$S_{12.2}$ (Jy)	$Vp_{12.2}$	$Vr_{12.2}$	$I_{12.2}$	OH	Dust clump (l, b) (degrees)
G 010.287–0.125[1]	18 08 49.36	–20 05 59.0	27	5.0	4,6	<0.52		–111,178		n	G 10.284–0.126
G 010.299–0.146[1]	18 08 55.54	–20 05 57.5	3.5	20	19,21	<0.54		–111,178		n	G 10.29–0.14
G 010.323–0.160[1,(*)]	18 09 01.46	–20 05 07.8	126	10	4,14	2.3	10.3	5.1,12.6	1.8	n	G 10.32–0.15
G 010.444–0.018[1,(7)]	18 08 44.88	–19 54 38.3	14.8	73.2	68,79	6.5	72.0	68.0,73.7	10.1	y	G 10.44–0.01
G 010.473+0.027[1,(7)]	18 08 38.20	–19 51 50.1	120	75.0	58,77	12.4	75.1	73.7,76.7	9.1	y	G 10.47+0.02
G 010.480+0.033[1]	18 08 37.88	–19 51 16.0	9.7	65.0	58,66	<0.55		–111,178		y	G 10.47+0.02
G 010.627–0.384[1,(7)]	18 10 29.22	–19 55 41.1	3.1	4.6	–6,7	1.4	4.6	4.0,6.6	0.8	n	G 10.62–0.38
G 010.629–0.333[1]	18 10 17.98	–19 54 04.8	4.2	–7.5	–13,1	<0.54		–111,178		n	G 10.62–0.33
G 011.497–1.485[1,(*)]	18 16 22.13	–19 41 27.1	167	6.7	4,17	29	9.0	6.0,17.1	15.8	n	G 11.49–1.48
G 011.904–0.141[1,(7)]	18 12 11.44	–18 41 28.6	56	42.8	40,45	17	43.0	42.1,44.0	8.2	y	G 11.903–0.140
G 011.936–0.150[1]	18 12 17.29	–18 40 02.6	1.9	48.5	47,50	<0.76		–111,178		n	G 11.93–0.14
G 011.936–0.616[1,(7)]	18 14 00.89	–18 53 26.6	41	32.2	30,44	4.3	39.8	31.5,42.4	4.4	n	G 11.93–0.61
G 011.992–0.272[3]	18 12 51.197	–18 40 39.7	0.6	59.5	59,61	<0.75		–110,179		n	G 11.99–0.27
G 012.025–0.025[1,(7)]	18 12 01.86	–18 31 55.7	85	107.7	105,112	14	108.6	107.8,109.4	8.8	n	G 12.02–0.03
G 012.202–0.120[1]	18 12 42.93	–18 25 11.8	1.7	26.4	26,27	<0.75		–111,178		n	G 12.18–0.12
G 012.209–0.102[1]	18 12 39.92	–18 24 17.9	9.2	19.8	16,22	<0.75		–111,178		n	G 12.20–0.09
G 012.681–0.182[1,(7)]	18 13 54.75	–18 01 46.6	450	57.6	50,61	8	57.1	55.6,60.3	7.6	y	G 12.68–0.18
G 012.889+0.489[1,(7)]	18 11 51.39	–17 31 29.6	27	39.3	28,42	19	39.4	38.9,40.2	8.7	y	G 12.88+0.48
G 012.909–0.260[1,(7)]	18 14 39.53	–17 52 00.0	300	39.9	35,47	16	39.4	38.5,40.6	14.0	y	G 12.90–0.26
G 014.60+0.01[3,(*)]	18 17 01.139	–16 14 38.88	1.2	23.2	22,28	0.6	24.7	24.6,24.7	0.1	n	G 14.60+0.01
G 015.034–0.677[1,(7)]	18 20 24.78	–16 11 34.6	28	21.2	20,24	21	23.4	21.2,23.7	12.1	y	G 15.03–0.67
G 016.58–0.05[3,(7)]	18 21 09.132	–14 31 48.69	22	59.3	52,69	2.2	65.9	59.2,68.7	2.2	y	G 16.58–0.05
G 016.86–2.15[3]	18 29 24.411	–15 16 04.12	24	14.8	14,19	<0.53		–108,180		y	G 16.86–2.15
G 019.609–0.234[α]	18 27 37.99	–11 56 37.6	0.4	40.1	36,43	<0.53		–107,181		y	G 19.607–0.234
G 019.612–0.134[3,(7)]	18 27 16.524	–11 53 38.49	18	56.2	50,61	1.3	50.5	50.2,55.1	0.8	–	G 19.61–0.1
G 021.880+0.014[3]	18 31 01.749	–09 49 01.13	5.5	20.6	17,22	<0.52		–106,182		–	G 21.87+0.01
G 022.356+0.066[3,(*)]	18 31 44.128	–09 22 12.40	10.0	80.0	77,88	1.0	81.4	81.4,81.5	0.1	–	G 22.35+0.06
G 023.257–0.241[3,(*)]	18 34 31.259	–08 42 46.84	6.0	64.0	63,66	0.9	64.9	63.8,65.9	0.7	–	G 23.25–0.24

Table 4.1: – continued

Methanol maser (l, b) (degrees)	RA (J2000) (h m s)	Dec (J2000) (° ′ ″)	$S_{6.7}$ (Jy)	$Vp_{6.7}$	$Vr_{6.7}$	$S_{12.2}$ (Jy)	$Vp_{12.2}$	$Vr_{12.2}$	$I_{12.2}$	OH	Dust clump (l, b) (degrees)
G 023.437–0.184[1,(7)]	18 34 39.25	–08 31 38.5	45	103.0	101,108	3.3	104.0	103.6,105.3	1.4	y	G 23.43–0.18
G 023.440–0.182[1,(7)]	18 34 39.18	–08 31 25.3	25	96.6	94,100	9	97.5	96.1,107.3	16.0	–	G 23.43–0.18
G 024.790+0.083[3]	18 36 12.571	–07 12 11.31	63	113.3	106,115	<0.52		–104,184		y	G 24.78+0.08
G 024.850+0.087[3,(*)]	18 36 18.398	–07 08 52.09	24	109.7	109,115	1.8	110.1	107.7,110.7	1.2	–	G 24.84+0.08
G 025.650+1.050[3]	18 34 20.913	–05 59 40.44	90	41.7	38,43	<0.51		–104,184		–	G 25.65+1.04
G 025.710+0.044[3,(8)]	18 38 03.148	–06 24 14.80	355	95.5	89,101	144	95.6	89.3,100.4	107.7	–	G 25.70+0.04
G 025.826–0.178[3,(*)]	18 39 03.631	–06 24 09.64	36	91.5	89,94	25	90.9	90.0,92.1	14.7	–	G 25.83–0.18
G 028.146–0.005[1,(7)]	18 42 42.59	–04 15 36.5	61	101.2	99,105	20	101.3	99.9,104.1	11.9	–	G 28.14–0.00
G 028.201–0.049[1]	18 42 58.08	–04 13 56.2	3.5	98.9	94,100	<0.52		–103,185		y	G 28.20–0.04
G 028.282–0.359[3,(*)]	18 44 13.270	–04 18 02.99	1.1	40.4		0.7	41.0	40.8,41.0	0.1	–	G 28.28–0.35
G 028.305–0.387[3,(*)]	18 44 21.988	–04 17 38.42	66	81.0	79,93	8	81.9	80.8,83.0	7.9	–	G 28.31–0.38
G 029.865–0.043[3,(7)]	18 45 59.588	–02 44 57.60	12	101.2	95,105	21	100.4	99.9,102.1	10.1	–	G 29.86–0.04
G 029.956–0.016[3,(7)]	18 46 03.763	–02 39 19.69	158	95.7	95,102	51	96.6	91.2,98.5	45.0	–	G 29.96–0.02B
G 029.979–0.047[3,(7)]	18 46 12.974	–02 38 58.05	14	98.2	97,105	6.6	98.3	96.5,103.9	4.9	–	G 29.978–0.050
G 030.591–0.042[3]	18 47 18.886	–02 06 07.00	0.6	43.2	36,49	<0.55		–102,186		–	G 30.59–0.04
G 030.704–0.068[3]	18 47 36.801	–02 00 48.99	66	88.0	85,90	<0.55		–102,186		–	G 30.705–0.065
G 030.760–0.052[3,(7)]	18 47 39.729	–01 57 21.92	75	91.8	88,95	1.7	91.3	90.7,91.8	0.9	–	G 30.769–0.048
G 030.818–0.057[3,(7)]	18 47 46.984	–01 54 19.61	10	101.2	91,110	0.5	108.1	108.0,108.1	0.1	–	G 30.81–0.05
G 030.898+0.162[3,(*)]	18 47 09.133	–01 44 10.29	40	101.8		14	101.7	99.3,102.1	13.5	–	G 30.89+0.16
G 031.061+0.094[3]	18 47 41.342	–01 37 21.31	16	16.2	15,17	<0.5		–102,186		–	G 31.06+0.09
G 031.282+0.062[3,(7)]	18 48 12.385	–01 26 22.60	83	110.0	102,113	15	110.4	105.1,113.0	25.8	–	G 31.28+0.06
G 031.411+0.307[3,(7)]	18 47 34.314	–01 12 47.14	9	103.4	90,108	1.5	95.7	94.1,95.8	0.6	y	G 31.41+0.30
G 033.13–0.09[5,(7)]	18 52 07.2	+00 08 06	12.4	73	71,81	0.35	73.3	72.9,73.3	0.1	–	G 33.13–0.09
G 034.246+0.134[α,(7)]	18 53 21.46	+01 13 54	10.6	55.4	55,63	1.3	61.2	61.0,61.8	0.8	–	G 34.24+0.13
G 035.025+0.350[α,(*)]	18 54 00.66	+02 01 18	36	44.3	40,47	0.7	42.2	42.0,43.4	0.2	–	G 35.02+0.35
G 037.47–0.11[6,(*)]	19 00 06.7	+03 59 27	12.5	58.4	54,64	2.0	63.0	58.6,63.1	1.2	–	G 37.475–0.106
G 049.470–0.371[1,(*)]	19 23 37.90	+14 29 59.4	9.2	64.0	55,76	2.0	57.8	57.0,64.0	1.2	–	G 49.472–0.366
G 049.489–0.369[1,(7)]	19 23 39.83	+14 31 05.0	26	56.1	55,61	4.8	56.2	55.6,57.3	2.1	–	G 49.49–0.37

4.3.1 Comments on individual sources

G 192.600–0.048 : The weak 12.2 GHz methanol maser emission towards this 6.7 GHz methanol maser is one of the two weakest of our detections. The emission has a peak flux density of 0.47 Jy, which corresponds to a 4.7-σ detection. Furthermore, the velocity of the 12.2 GHz emission is 3.6 km s^{-1}, close to the peak of the 6.7 GHz methanol maser at 5 km s^{-1}, well within the full velocity range of the associated 6.7 GHz methanol maser.

G 284.352–0.419 : Caswell et al. (1995b) detected a 0.7 Jy 12.2 GHz methanol maser towards this 6.7 GHz methanol maser in 1992. We detect no hint of emission at 12.2 GHz and expect that this is due to source variability. Due to this we have excluded this source from our statistical analysis.

G 290.374+1.661 : Observations in 2008 June detected marginal 12.2 GHz emission toward this 6.7 GHz methanol maser outside the velocity range of the 6.7 GHz maser emission at a peak velocity of –35.1 km s^{-1} of 0.6 Jy. Follow-up observations carried out in 2008 December uncovered no detectable 12.2 GHz emission. We have therefore listed this source as having no associated 12.2 GHz emission but have removed this source from our statistical analysis to avoid the possibility that we have misclassified this source.

G 291.579–0.431 : During the 2008 June observations we detected weak 12.2 GHz methanol maser emission towards this source. The velocity of the detected emission was within the velocity range of the 6.7 GHz methanol maser emission, however, since the detection was less than 5-σ the source was re-observed in 2008 December and resulted in no detectable emission. As for G 290.374+1.661, we have removed this source and the associated 1.2 mm dust clump from our statistical analysis.

G 305.208+0.206 : Observations towards 6.7 GHz methanol maser G 305.208+0.206 as well as near-by G 305.202+0.208, offset by 22 arcsec, were carried out in adjacent observations. The relative amplitudes of the detected emission at these two positions suggest that all of the emission is associated with G 305.208+0.206; however, the peak of the 12.2 GHz emission is at the peak velocity of nearby G 305.202+0.208 and observations by Caswell et al. (1995b) also indicate that there is 12.2 GHz emission associated with each 6.7 GHz methanol maser source.

Table 4.2: *Absorption features that we detect at 12.2 GHz towards 6.7 GHz methanol masers. The first three columns in this table are as in Table 4.1. Column 4 indicates whether or not emission at 12.2 GHz was detected, followed in columns 5 to 7 by the flux density of the absorption, peak velocity (where the peak corresponds to the minimum in the absorption trough) and velocity range of the 12.2 GHz absorption features that we detect.*

Methanol maser (l, b) (degrees)	RA (J2000) (h m s)	Dec (J2000) (° ′ ″)	12 GHz emission ?	Abs. Flux Density (Jy)	Peak Velocity (km s^{-1})	Velocity Range (km s^{-1})
G 206.543–16.355[2]	05 41 44.15	–01 54 44.9	n	–0.3	9	8,11
G 269.153–1.128[1]	09 03 33.46	–48 28 02.6	n	–0.3	10	8,12
G 301.136–0.226[1]	12 35 35.14	–63 02 32.6	n	–0.2	–39	–42,–37
G 305.200+0.019[1]	13 11 16.93	–62 45 55.1	y	–0.2	–34	–40,–26
G 305.208+0.206[1,(7)]	13 11 13.71	–62 34 41.4	y	–0.4	–40	–49,–30
G 318.948–0.196[1,(7)]	15 00 55.39	–58 58 52.8	y	–0.5	–37	–39,–27
G 323.740–0.263[1,(7)]	15 31 45.45	–56 30 50.1	y	–0.6	–47	–58,–43
G 331.278–0.188[1,(7)]	16 11 26.59	–51 41 56.7	y	–0.4	–77	–91,–75
G 000.496+0.188[1]	17 46 03.96	–28 24 52.8	y	–0.3	3	–14,6
G 008.669–0.356[1]	18 06 18.99	–21 37 32.2	y	–0.4	37	34,50
G 008.683–0.368[1,(7)]	18 06 23.49	–21 37 10.2	y	–0.4	37	36,48
G 010.444–0.018[1,(7)]	18 08 44.88	–19 54 38.3	y	–0.3	70	63,77
G 010.627–0.384[1,(7)]	18 10 29.22	–19 55 41.1	y	–0.5	–1	–5,3
G 011.936–0.616[1,(7)]	18 14 00.89	–18 53 26.6	y	–0.5	39	27,46
G 012.025–0.025[1,(7)]	18 12 01.86	–18 31 55.7	y	–0.3	113	103,116
G 012.909–0.260[1,(7)]	18 14 39.53	–17 52 00.0	y	–0.3	37	32,47
G 016.86–2.15[3]	18 29 24.411	–15 16 04.12	n	–0.2	19	17,21
G 023.437–0.184[1,(7)]	18 34 39.25	–08 31 38.5	y	–0.7	101	90,109
G 023.440–0.182[1,(7)]	18 34 39.18	–08 31 25.3	y	–0.6	101	91,112
G 025.710+0.044[3,(8)]	18 38 03.148	–06 24 14.80	y	–1.7	94	84,100
G 025.826–0.178[3]	18 39 03.631	–06 24 09.64	y	–0.3	94	86,95
G 028.305–0.387[3]	18 44 21.988	–04 17 38.42	y	–0.3	85	76,87
G 029.956–0.016[3,(7)]	18 46 03.763	–02 39 19.69	y	–0.4	100	90,108
G 029.979–0.047[3,(7)]	18 46 12.974	–02 38 58.05	y	–0.3	100	93,108
G 030.704–0.068[3]	18 47 36.801	–02 00 48.99	n	–0.4	91	89,95
G 030.818–0.057[3,(7)]	18 47 46.984	–01 54 19.61	y	–0.4	97	94,99
G 030.898+0.162[3]	18 47 09.133	–01 44 10.29	y	–0.4	105	95,106
G 031.282+0.062[3,(7)]	18 48 12.385	–01 26 22.60	y	–0.9	109	100,116
G 031.411+0.307[3,(7)]	18 47 34.314	–01 12 47.14	y	–0.2	99	96,101

We suggest that either pointing errors or unfavourable weather conditions have resulted in the relative amplitudes of the emission towards the two sources being affected. Both of these methanol maser sites are located within the one dust clump.

G 305.366+0.184, G 000.496+0.188, G 029.865-0.043 : These sources all have stronger 12.2 GHz methanol maser emission than the values for their 6.7 GHz counterparts as shown in Table 4.1. As masers are intrinsically variable, measurements of the 6.7 GHz methanol maser flux density would need to be taken at the same epoch as the 12.2 GHz methanol masers to be certain that this was not a result of source variability.

G 034.246+0.134 and G 035.025+0.350 : The positions for these sources were determined with the ATCA with a large declination uncertainty of ±15 arcsec (James Caswell, private communication) owing to the highly elongated beam for sources near declination 0°.

G 049.489-0.369 : We observed this source towards a position offset from the true position by ~66 arcsec (58 percent of the HPBW). We therefore expect that the flux density of this source is underestimated by approximately a factor of two.

4.3.2 Statistical analysis

In order to determine if there are any differences between 1.2 mm dust clumps without associated 6.7 GHz methanol masers, those associated with 6.7 GHz methanol masers only and those associated with both 6.7 and 12.2 GHz methanol maser emission, we carried out a statistical analysis following the method used in Chapter 3 to investigate water maser presence towards ^{13}CO clumps and 1.2 mm dust clumps. Additionally, the possibility of a relationship between dust clump properties and OH maser presence as well as peak 6.7 GHz methanol maser luminosity values and the presence of detectable radio continuum were investigated. Due to the difficulty in determining meaningful uncertainties for many of the tested source characteristics, all values have been equally weighted and assumed to be error free in all subsequent statistical analysis.

Of the 404 1.2 mm dust clump sources listed by Hill et al. (2005), 26 were excluded from our statistical analysis as they were either missing a value for one or

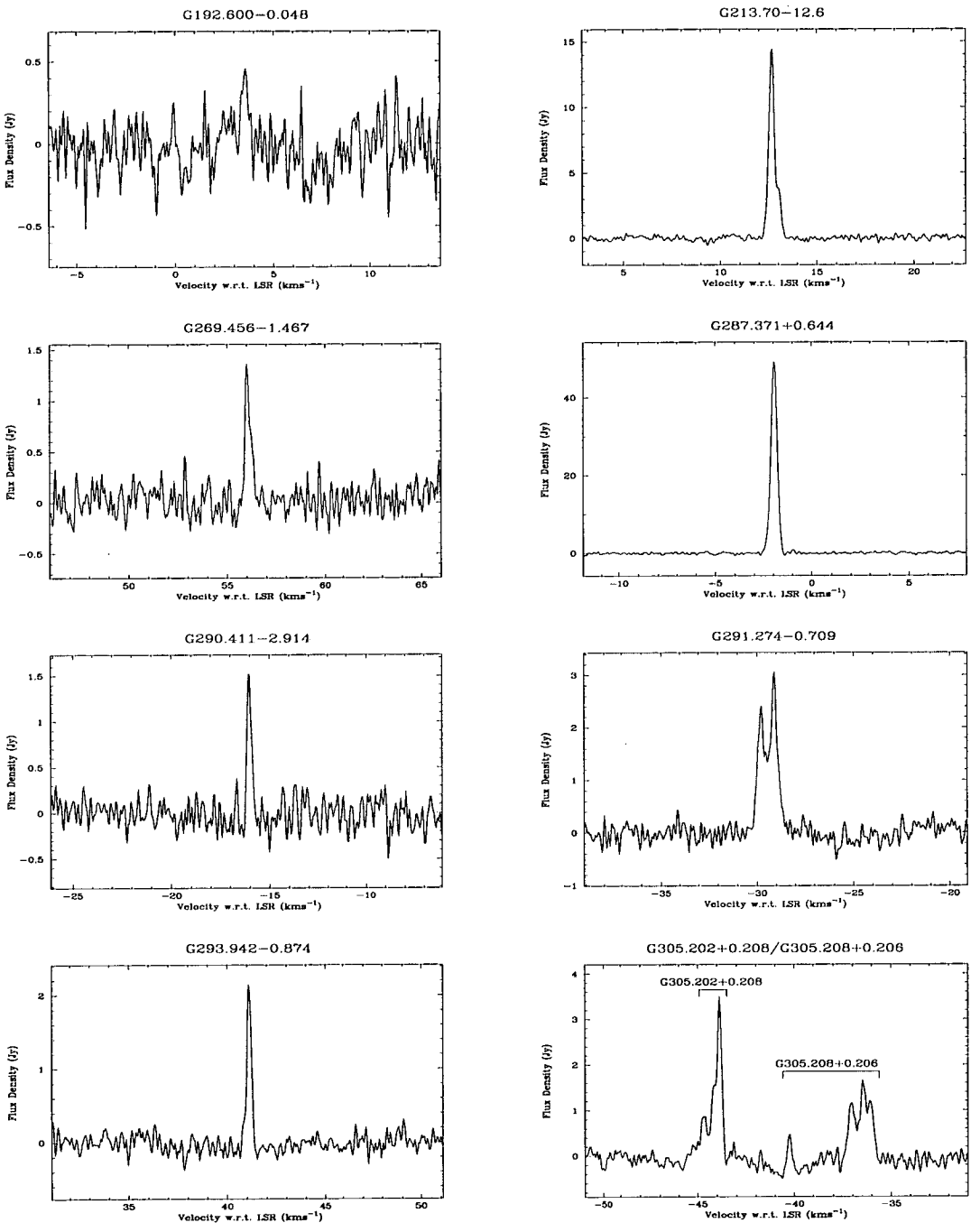

Figure 4.1: *Spectra of all the 12.2 GHz methanol masers detected in the search towards 6.7 GHz methanol masers.*

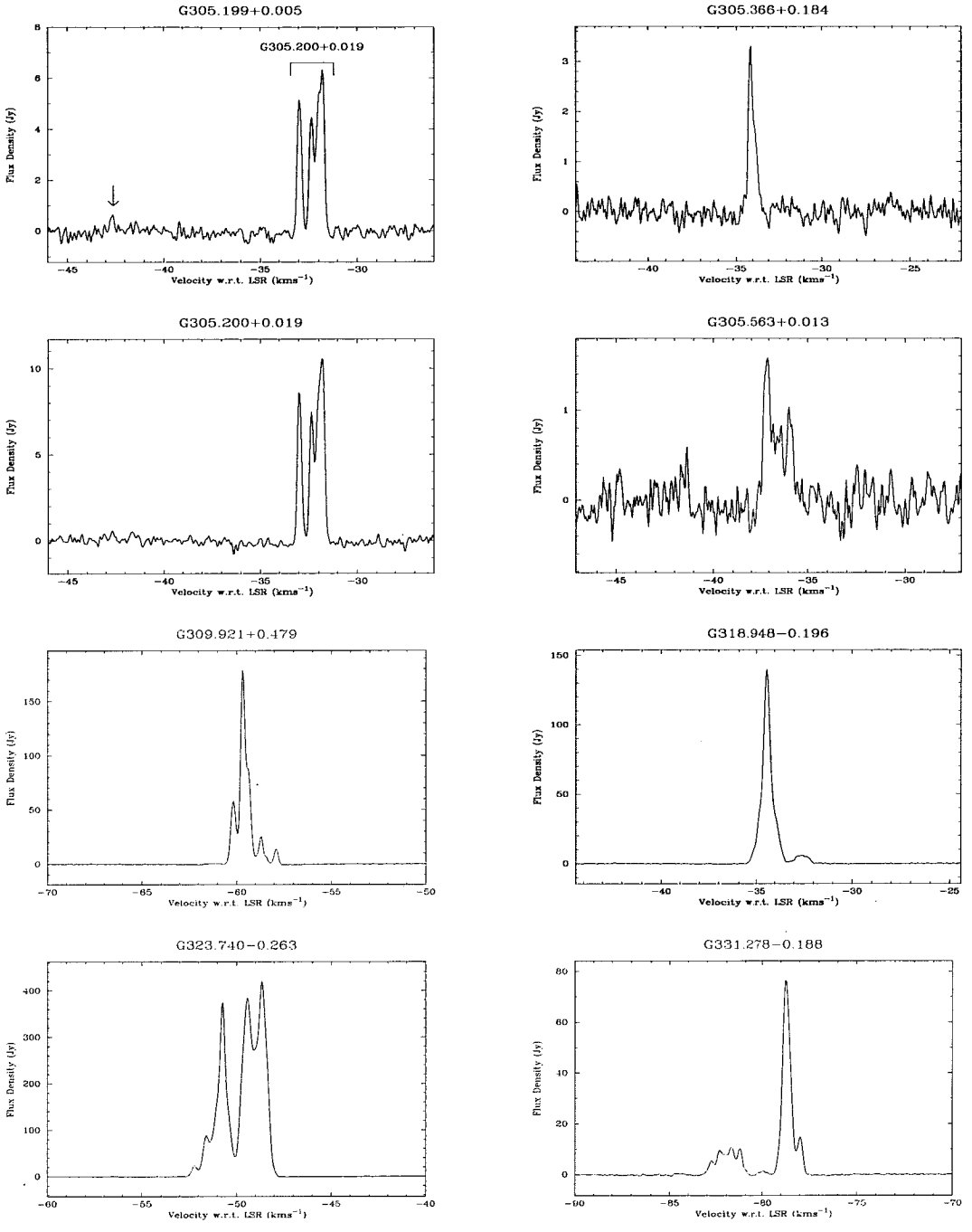

Figure 4.1: – continued

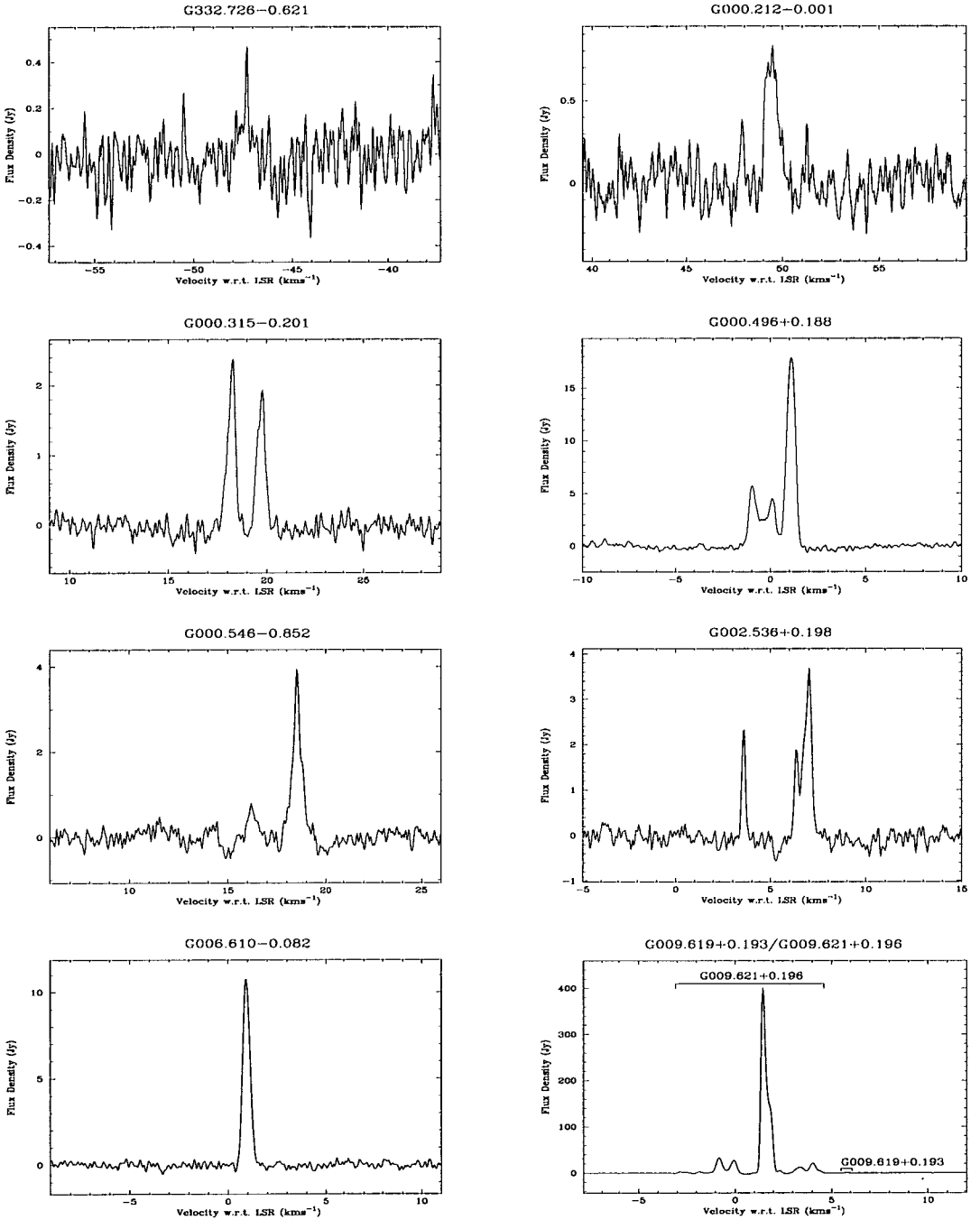

Figure 4.1: – continued

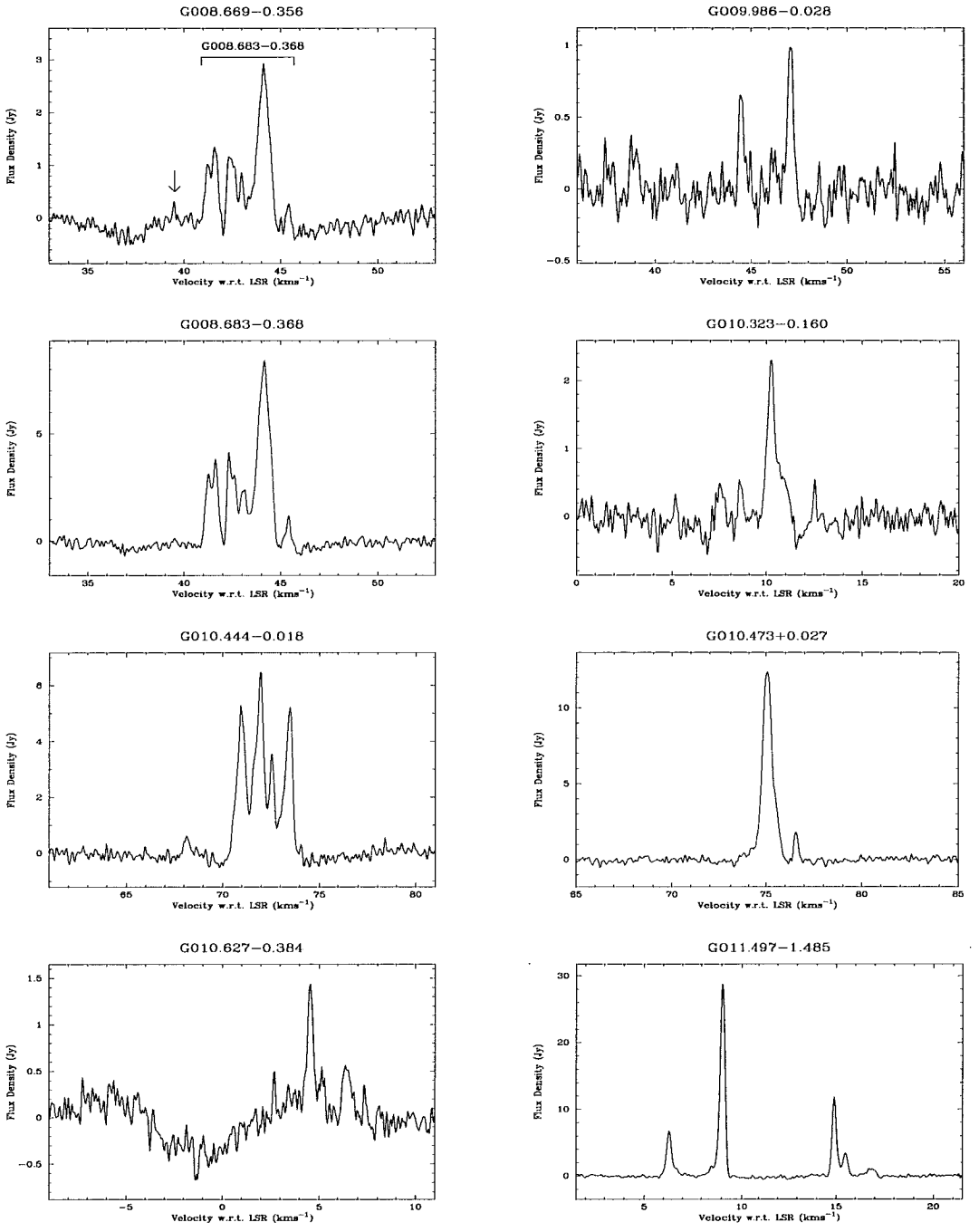

Figure 4.1: – continued

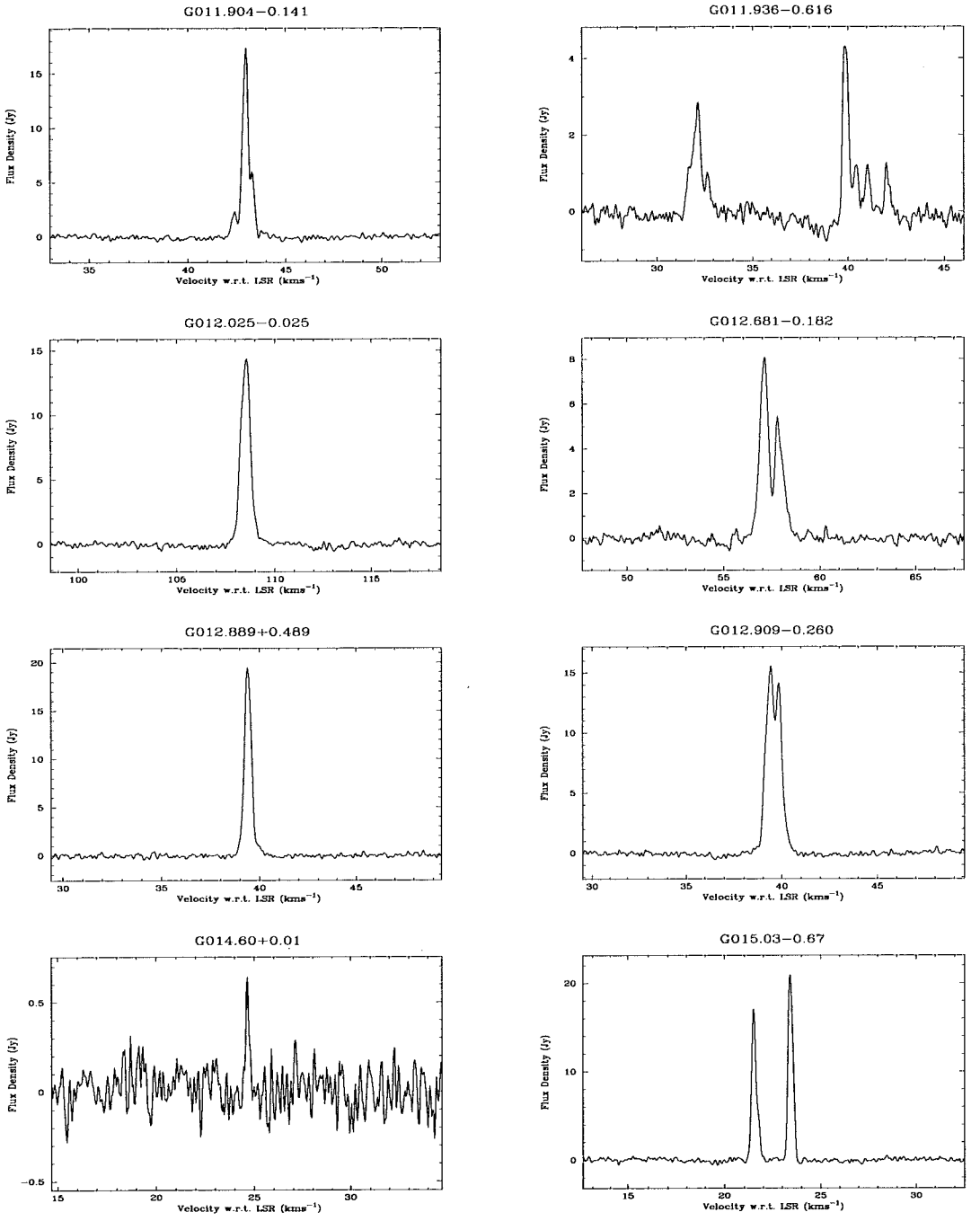

Figure 4.1: – continued

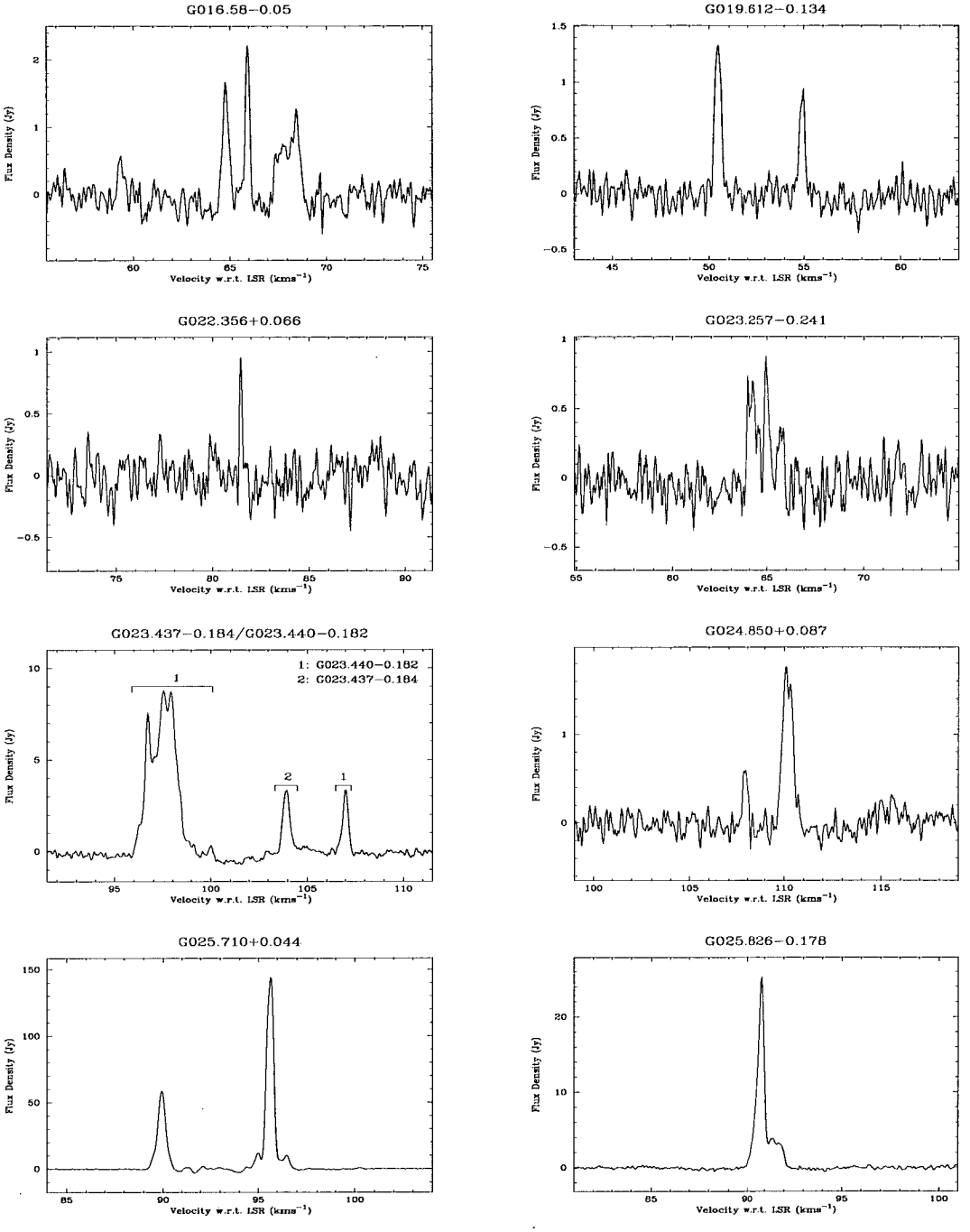

Figure 4.1: – continued

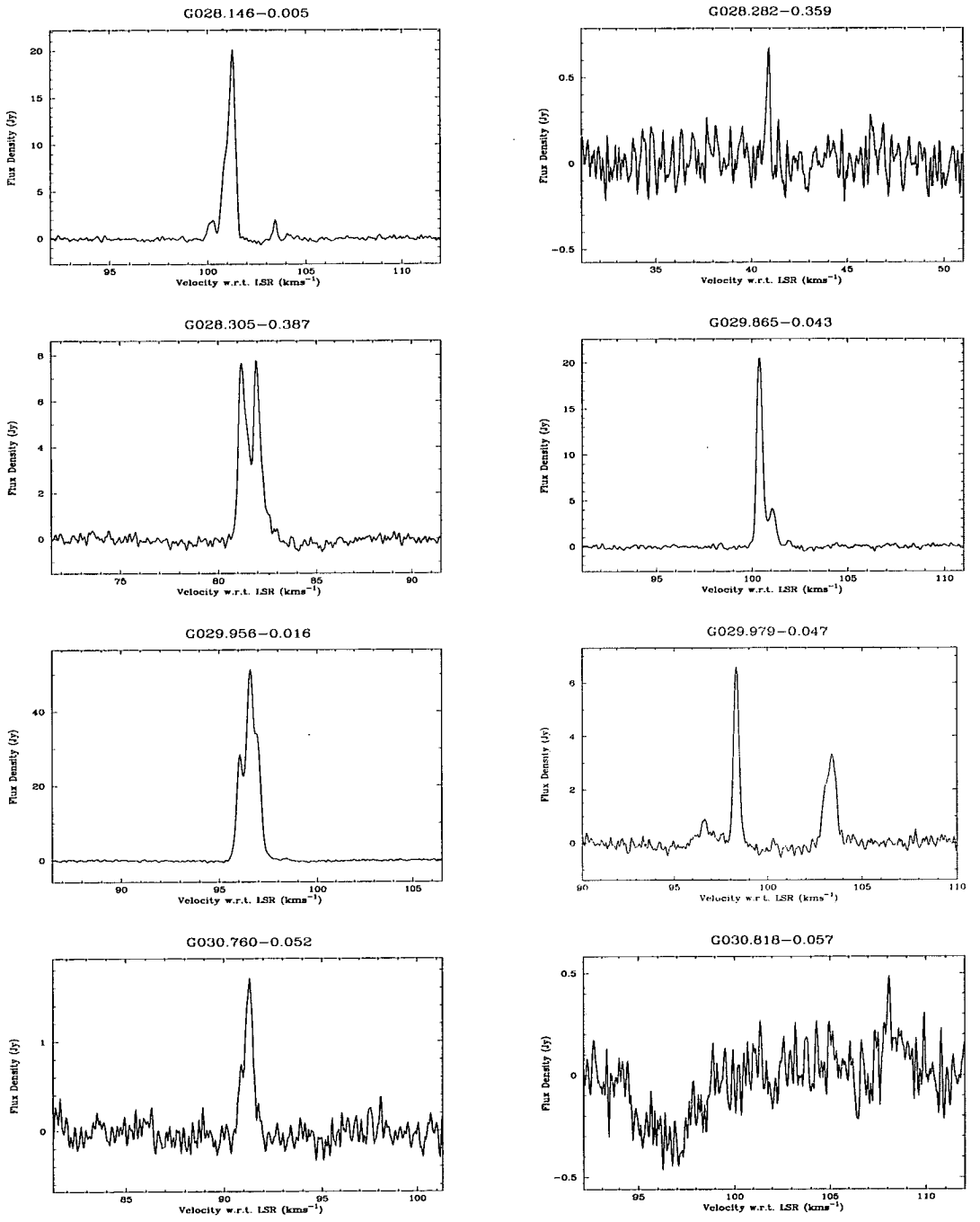

Figure 4.1: – continued

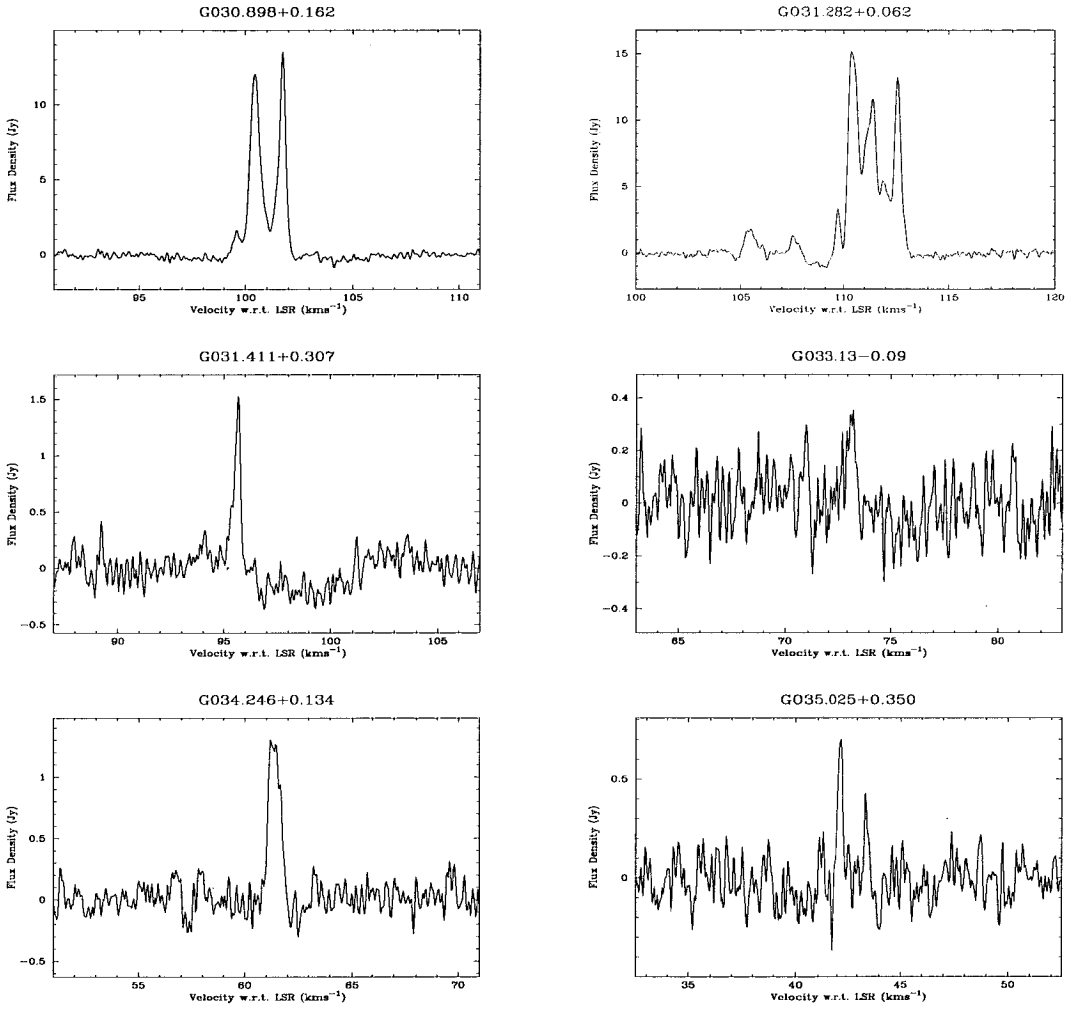

Figure 4.1: – continued

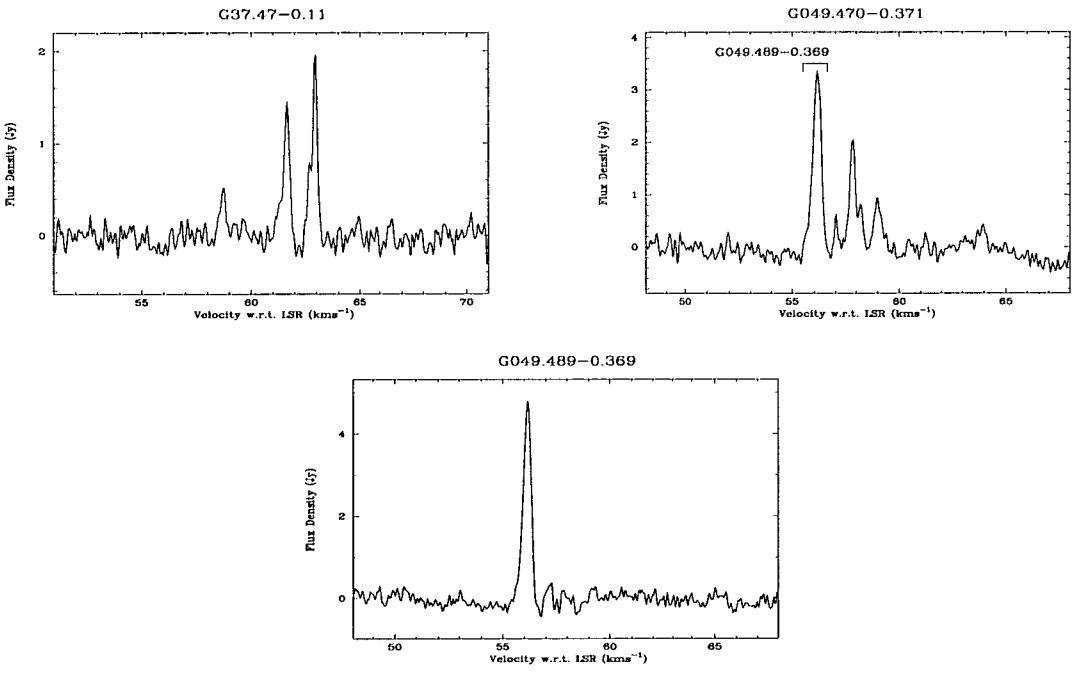

Figure 4.1: - continued

more of the dust clump properties to be tested, or were listed by Hill et al. (2005) as having mass values that are uncharacteristic of massive star formation regions. To investigate whether statistically significant relationships exist between the dust clump properties and the associated methanol masers the dust clumps were split into groups depending upon the presence or absence of specific associated phenomena. Four different categorizations were tested, specifically:

- dust clumps with and without associated 6.7 GHz methanol maser emission;
- dust clumps with 6.7 GHz methanol maser emission with and without associated 12.2 GHz methanol maser emission;
- dust clumps with and without detectable radio continuum;
- dust clumps associated with more luminous 6.7 GHz methanol masers together with those associated with less luminous methanol maser sources (sources in this group were split into presence/absence data at the median value of 6.7 GHz peak luminosity, i.e. presence meaning the 1.2 mm dust

clump is associated with a 6.7 GHz methanol maser with a peak luminosity greater than the median value and vice versa for the absence data).

A Binomial generalized linear model (GLM) (McCullagh & Nelder, 1989) was then fitted to the maser presence/absence data using the dust clump properties as predictors for each of the four groups. The significance of each individual clump property was tested by fitting all possible single term models, and compared by analysis of deviance to the null model consisting of only an intercept. Stepwise model selection based on the Akaike Information Criteria (AIC) (Burnham & Anderson, 2002) was used to select the simplest model with the greatest predictive power and is a trade-off between goodness of fit and model complexity.

For each of the 1.2 mm dust clumps (Hill et al., 2005), all of the derived clump properties in each of the four groups were tested: the integrated flux density (Jy), peak flux density (Jy beam^{-1}), source full width at half maximum (FWHM) (arcsec), distance (kpc), mass ($M_{\odot}$), radius (pc) and H_2 number density (cm^{-3}). In the following sections we consider p-values of less than 0.05 to be statistically significant (i.e. the hypothesis that the single term model provides no better fit than the null model consisting only of an intercept is rejected when the p-value is less than 0.05). Individual p-values, detailed tables and box plots relating to all subsequent statistical analysis are presented in Appendix 4.6.1. A summary of the main results from the statistical analysis is presented in Section 4.3.3.

Hill et al. (2009) used spectral energy distribution (SED) modelling to determine a statistically probable range of values for temperature, mass and luminosity for around half of the Hill et al. (2005) sample. We have not incorporated the data from Hill et al. (2009) as it is only a subset of the sample of Hill et al. (2005) and appears to be biased towards including a large fraction of the more evolved sources. Hill et al. (2009) commented that a large fraction of the 1.2 mm dust clumps with no associated methanol masers or radio continuum do not have *MSX* counterparts. As a result, a number of these sources were initially included in the sample but were later excluded as the models were poorly constrained (Hill et al., 2009). Furthermore, 50 of the 1.2 mm dust clumps in Hill et al. (2009) are associated with 8 GHz radio continuum emission compared with 71 sources in the complete sample of Hill et al. (2005). Hill et al. (2009) find that the masses of sources calculated using their SED method are similar to those presented in Hill

et al. (2005) with both publications showing that the "MM-only" sources are the least massive, followed by the sources associated with 6.7 GHz methanol masers, and then the sources with radio continuum and finally the sources associated with both radio continuum and 6.7 GHz methanol maser emission. This means that even though the masses in Hill et al. (2005) were calculated using a constant temperature of 20 K the calculated masses are not significantly different from the masses presented in Hill et al. (2009) which were calculated using temperatures that were determined from their SED modelling.

For all dust clump properties with near/far distance ambiguities we have used the values calculated at the near distance. While it is often considered that, where distance ambiguities exist, the near distance is statistically more likely to be correct than the far distance (e.g. Sobolev et al., 2005), Xu et al. (2009) suggest that using the far distances results in a better correlation between the locations of methanol masers with respect to the spiral arms of the Galaxy. In order to insure that the assumption that sources are more likely to be located at the near distance did not introduce any significant bias, the distribution of dust clump properties mass and radius of Hill et al. (2005) was compared to the distribution of dust clump properties observed by Mookerjea et al. (2004). Mookerjea et al. (2004) carried out 1.2 mm dust clump observations towards the G333 giant molecular cloud (GMC) associated with RCW106. This GMC is located at a distance of 3.6 kpc (Lockman, 1979), and all clump properties were calculated at this distance. ^{13}CO observations towards the G333 GMC (Bains et al., 2006) showed that, while there was emission detected along the line-of-sight, the brightest broadest feature seen in the mean velocity profile could be attributed to the target GMC. It is therefore likely that the majority of the dust clumps observed by Mookerjea et al. (2004) have been correctly assigned the distance of the GMC, introducing little bias in the clump property distributions. Comparison between the distributions of dust clump mass and radius of the dust clumps from Hill et al. (2005) with the dust clumps of Mookerjea et al. (2004) has shown that the distribution of the clump properties at the near distances of Hill et al. (2005) are similar to the distribution of the clump properties of Mookerjea et al. (2004). We therefore expect that our assumption that the near distances are correct will introduce no gross bias into our statistical analysis. Peak luminosities of the 6.7 GHz methanol

masers were calculated using the 6.7 GHz methanol maser peak flux density (as integrated flux densities are not readily available) and the near kinematic distance of the maser sources as used in Hill et al. (2005).

In Section 4.3.2 only 101 of the 1.2 mm dust clumps sources with associated 6.7 GHz methanol masers are considered. Five 1.2 mm dust clumps were removed from the observed sample of 106 dust clumps with associated 6.7 GHz methanol masers for the following reasons; G 259.94–0.04 and G 331.28–0.19 have some clump properties missing, the 6.7 GHz methanol maser associated with G 284.35–0.42 had previously had a 12.2 GHz counterpart observed by Caswell et al. (1995b) that we failed to detect, G 291.58–0.53 and G 290.374+1.661 were excluded because we detected marginal 12.2 GHz emission towards these sources in 2008 June; but not 2008 December making these sources impossible to classify and G 6.60–0.08 because Hill et al. (2005) suggest that the derived mass of this source is uncharacteristic of massive star formation regions and were therefore doubtful that it is located at the near distance.

1.2 mm dust clumps with and without 6.7 GHz methanol masers

Although the observations of Hill et al. (2005) were primarily targeted towards sites of known 6.7 GHz methanol masers, many additional 1.2 mm dust clumps were detected in the fields of the observations and have no associated 6.7 GHz methanol maser, allowing us to determine if there is any statistically significant difference between those dust clump sources with and those without associated methanol masers. The combined sample size for this analysis is 378. Fits of the single term addition Binomial model showed an increasing probability of the presence of 6.7 GHz methanol masers associated with increasing values of dust clump integrated flux density, peak flux density, FWHM, mass and radius. This means that any one of them can give an indication of the likelihood of having an associated 6.7 GHz methanol maser. Results of the single term additions are given in Table 4.3.

The simplest model with the greatest predictive power contains the four dust clump properties: integrated flux density, peak flux density, FWHM and density. The estimated regression relation is

$$\log\frac{p_i}{1-p_i} = -2.677 - 0.295x_{\text{Integrated}} + 1.172x_{\text{Peak}} + 0.030x_{\text{FWHM}} + 0.00000143x_{\text{Density}}$$

where $x_{\text{Integrated}}$ is the 1.2 mm dust clump integrated flux density, x_{Peak} is the peak flux density, x_{FWHM} is the source FWHM, x_{Density} is the H_2 number density and p_i is the probability of finding a 6.7 GHz methanol maser towards the i^{th} 1.2 mm dust clump. The regression summary of this model is shown in Table 4.4.

However, the misclassification rate for this model is relatively high. Setting the threshold probability to 0.5 the model misclassifies almost two thirds of the 1.2 mm dust clumps with associated 6.7 GHz methanol masers as having no associated methanol masers and, while lowering the probability threshold allows more of the methanol maser associated 1.2 mm dust clumps to be correctly classified, it results in a marked increase in the number of 1.2 mm dust clumps with no associated methanol masers wrongly classified as having an associated methanol source. A likely explanation for this is that all of the properties involved in the regression model show a significant overlap in the range of values for the 1.2 mm dust clump with and without associated methanol maser sources (see Fig. 4.8) thereby leading to the misclassification of many sources. However, it is also possible that some of the assumptions made by Hill et al. (2005) in calculating the dust clump properties (like uniform temperature) could account for this. Therefore, a reliable predictive model of 6.7 GHz methanol maser presence towards 1.2 mm dust clumps requires more accurately determined dust clump properties and additional information, possibly from other wavelengths. This is in contrast to water maser associations with 1.2 mm dust clumps, for which in Chapter 3 we found a promising model that was based on only 1.2 mm dust clump radius.

Bains et al. (2009) compared the locations of 6.7 GHz methanol masers (Ellingsen, 2005) with both ^{13}CO (Bains et al., 2006) and 1.2 mm dust clumps (Mookerjea et al., 2004) and used an identical statistical analysis to investigate the differences between the clumps with associated methanol masers and those without. Bains et al. (2009) found that 1.2 mm dust clumps with associated methanol masers had larger radii, mass and H_2 number densities than those clumps with no associated 6.7 GHz methanol masers. The results of Bains et al.

(2009) seem to be in contradiction to the results that we find here: that there is no statistical difference between the 1.2 mm dust clumps H_2 number densities for sources with associated 6.7 GHz methanol masers compared to those sources with no associated 6.7 GHz methanol masers. However, this apparent discrepancy can be explained by the consideration of a few differences between the data sets. Comparison of the distribution of 1.2 mm dust clumps from Hill et al. (2005) and Mookerjea et al. (2004) uncovers the first such difference. Mookerjea et al. (2004) observed 95 1.2 mm dust clumps within a GMC having H_2 number densities in the range 0.5 to 6 $\times$ 10^4 cm^{-3}. These observations had a residual noise limits of 23 mJy for the majority of the observed region and up to 50 mJy for the northern-most section of the GMC. In comparison, Hill et al. (2005) observed a number of individual sources at a range of Galactic longitudes with slightly higher residual noise of 50 mJy for the majority of sources and up to $\sim$150 mJy for some sources. The H_2 number densities derived for the 404 1.2 mm dust clumps by Hill et al. (2005) are all in the range 1.4 $\times$ 10^3 to 1.9 $\times$ 10^6 cm^{-3}, a much large range than observed by Mookerjea et al. (2004).

In Chapter 3 we produced a three color GLIMPSE image of the GMC and showed that the central section of the GMC is dominated by bright mid-infrared emission, tracing a relatively later evolutionary stage of massive star formation. The majority of the 1.2 mm dust clumps observed by Mookerjea et al. (2004) are also aligned along this section of the GMC, meaning that the majority of the 1.2 mm dust sources will also be more evolved. Also in Chapter 3 we showed that the methanol masers within the region were located towards the periphery of the GMC away from the bright mid-infrared emission associated with the central axis of star formation, supporting the idea that methanol masers trace an early evolutionary stage of massive star formation. As Hill et al. (2005) targeted many of their observations towards methanol masers we expect that the majority of sources observed will be at an earlier evolutionary phase than the majority of sources observed by Mookerjea et al. (2004).

The density of the 1.2 mm dust sources found to be associated with methanol masers in the GMC (Bains et al., 2009) have densities that would fall in the lower end of the range of the H_2 number densities we find associated with 6.7 GHz methanol masers. The small sample size of Mookerjea et al. (2004) (and therefore

Bains et al. (2009)) limits our ability to meaningfully compare the results of Bains et al. (2009) with what we find here. Furthermore, if the difference in the nature of the 1.2 mm target sources of Hill et al. (2005) and Mookerjea et al. (2004) as well as the differing sensitivities of these two sets of observations are considered it is not surprising that the results differ; and therefore this difference cannot be considered a contradiction.

1.2 mm dust clumps and 6.7 GHz methanol maser luminosity

Dust clumps associated with more luminous methanol masers and dust clumps associated with 6.7 GHz methanol masers with lower luminosities were compared to determine if there was any statistically significant dependance on 6.7 GHz methanol maser luminosity. The 101 1.2 mm dust clumps with appropriate data and associated 6.7 GHz methanol masers were split into two groups at the median value of 6.7 GHz methanol maser peak luminosity and the two groups were compared. In addition to the dust clump properties (Hill et al., 2005) the significance of the presence of an associated OH maser was tested in regions common with the complete search for OH masers carried out by Caswell (1998) (this incorporates $\sim$70 per cent of the complete sample). Fits of the single term addition Binomial model to the 1.2 mm dust clump properties showed an increasing probability of more luminous 6.7 GHz methanol masers being associated with dust clump sources that have bigger radii, higher mass, lower densities and are located at further distances. A summary of the single term addition Binomial model can be found in Table 4.5 and is represented graphically in the form of box plots in Fig. 4.9.

In order to determine if OH masers are preferentially associated with more luminous 6.7 GHz methanol masers we then fitted a Binomial model to the presence or absence of an OH maser. For this analysis only the sources that fell within the range of the complete search of Caswell (1998) were considered. We found that there is a greatly increased chance of finding an OH maser associated with the more luminous 6.7 GHz methanol masers, the p-value of 0.012, corresponding to a confidence level of 98.8 per cent.

The tendency for the more luminous 6.7 GHz methanol masers to be associated with 1.2 mm dust clumps with lower H_2 number densities was further

investigated to see if there was an overall trend present in the data. Figure 4.2 shows the log of the 6.7 GHz peak luminosity versus the log of the H_2 number density of the associated 1.2 mm dust clump. We have used the technique of linear regression and have found that there is a statistically significant negative slope in the distribution, with a weak correlation (correlation coefficient of 0.46) between the data points. The null hypothesis that there is zero slope in the data can be rejected (p-value of 1.16e-06). The line of best fit has the equation

$$\log(6.7\text{ GHz lum}) = -0.85[0.16](\log(\text{H}_2\text{density})) + 6.25[0.75],$$

where '6.7 GHz lum' is the peak luminosity of the 6.7 GHz methanol maser and 'H_2density' is the H_2 number density of the associated 1.2 mm dust clumps and the numbers contained in the square brackets are the standard errors of the slope and the y intercept respectively. It is likely that at least some of the scatter present in the distribution of data points can be explained by the use of the near kinematic distances which are prone to errors. A further contributer is likely to be the variable nature of the maser sources (see e.g. Goedhart, Gaylard & van der Walt, 2004).

The most parsimonious model produced by fitting a GLM to the high and low 6.7 GHz methanol maser luminosity associated dust clumps includes both the dust clump FWHM and the distance. The estimated regression relation is

$$\log\frac{p_i}{1-p_i} = -3.184 + 0.017x_{\text{FWHM}} + 0.489x_{\text{Distance}},$$

where x_{FWHM} is the FWHM of the 1.2 mm dust clump and x_{Distance} is the distance to the source. The regression summary of this model, including an estimate of errors is shown in Table 4.6.

The accuracy of this model was tested on the data and when the threshold of probability was set to 0.5 the misclassification rates were found to be promising. Of the 51 1.2 mm dust clumps with 6.7 GHz methanol masers with high luminosities, the model correctly predicts that 38 of these 1.2 mm dust clumps will have associated methanol masers with high luminosities, but falsely predicts that the remaining 13 clumps will have associated low luminosity methanol masers.

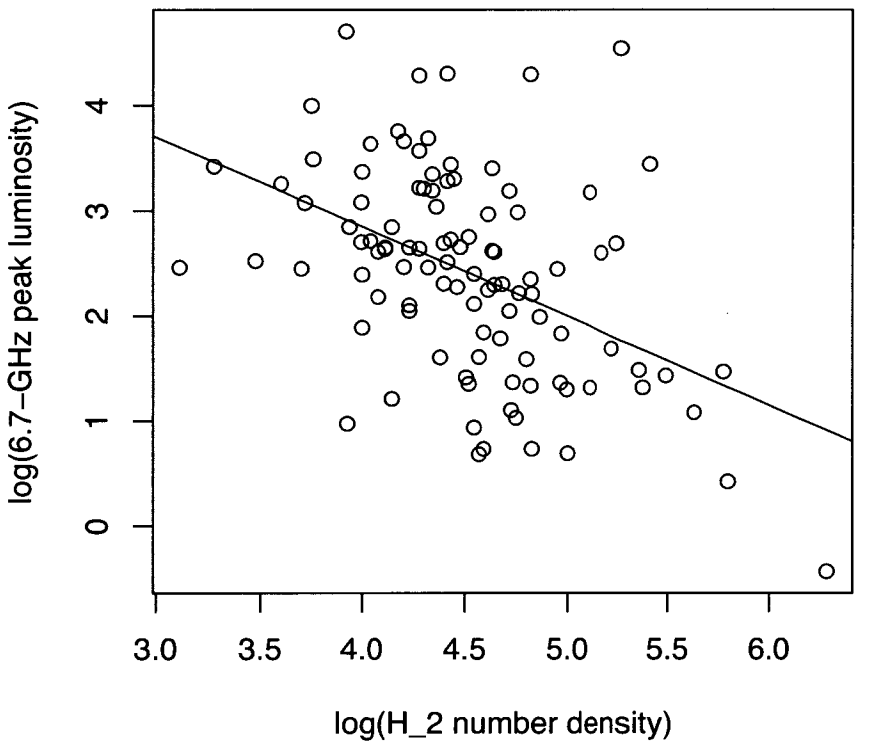

Figure 4.2: *Log of 6.7 GHz peak luminosity versus the H_2 number density of the associated dust clump in cm^{-3}. The line of best fit is also plotted.*

Of the 50 1.2 mm dust clumps with associated low luminosity methanol masers the model predicts 39 correctly and falsely predicts that 11 will have highly luminous associated 6.7 GHz methanol masers. It is likely that these misclassification rates can be explained by a combination of the fact that we are using 6.7 GHz peak luminosity, rather than the more appropriate value of 6.7 GHz integrated luminosity, the fact that the calculated luminosities are sensitive to errors in the adopted kinematic distances and the fact that there are a number of sources with similar 6.7 GHz peak luminosities around the median value.

1.2 mm dust clumps with associated 6.7 GHz methanol masers with and without 12.2 GHz methanol masers

The properties of the 1.2 mm dust clumps associated only with 6.7 GHz methanol masers were compared to 1.2 mm dust clumps associated with both 6.7 and 12.2 GHz methanol masers; the sample size for this analysis was 101 dust clumps (those that were excluded are shown in column 12 of Table 4.1 and discussed in Section 4.3.2). Fits of the single term Binomial model show that there is a statistically significant increase in the likelihood of finding a 12.2 GHz methanol maser associated with increasing 6.7 GHz methanol maser flux density, 6.7 GHz methanol maser peak luminosity and decreasing values of 1.2 mm dust clump density. The results of the single term additions are in Table 4.7. The significance of the presence of an OH maser associated with the 6.7 GHz methanol masers was tested on the sample within the search region for OH masers of Caswell (1998) (this incorporates ~70 per cent of the complete sample). This resulted in a p-value of 0.025, meaning that 12.2 GHz methanol masers are preferentially found towards 6.7 GHz methanol masers with associated OH masers.

The luminosity of the 12.2 GHz methanol masers were investigated to determine if individual source luminosity had any relationship with either the association with 8 GHz radio continuum or the luminosity of the associated radio continuum. We found that there is no relationship between either the presence of an associated radio continuum source or the luminosity of associated radio continuum and the luminosity of the associated 12.2 GHz methanol maser.

The luminosities of the 12.2 GHz methanol masers were compared to the H_2 number densities of the 1.2 mm dust clump using the same method as for

6.7 GHz peak luminosity in Section 4.3.2. Figure 4.3 shows a plot of the data overlaid with the line of best fit. We find that there is a very weak correlation in this data set, with a correlation coefficient of 0.25. Similarly to Fig. 4.2, we expect that the largest contributions to the scatter in Fig. 4.3 are the use of the kinematic distances and maser variability. However, there is an overall negative slope in the data that is statistically significant, the p-value is 0.05 meaning that the null hypothesis that there is zero slope can be rejected. The line of best fit has the equation

$$\log(12.2\text{ GHz lum}) = -0.56[0.28](\log(\text{H}_2\text{density})) + 4.16[1.23],$$

where '12.2 GHz lum' is the integrated luminosity of the 12.2 GHz methanol maser and the 'H_2density' is the H_2 number density of the associated 1.2 mm dust clumps and the numbers contained in the square brackets are the standard errors of the slope and the y intercept respectively.

The most parsimonious model produced by fitting a GLM to the 12.2 GHz methanol maser presence/absence data, includes only the value of the 6.7 GHz peak flux density. The estimated regression relation is

$$\log\frac{p_i}{1-p_i} = -0.41058 + 0.03571 x_{6.7\text{GHzFlux}},$$

where $x_{6.7\text{GHzFlux}}$ is the flux density of the 6.7 GHz methanol maser peak in Jy. The regression summary of this model, including an estimate of errors is shown in Table 4.8. The physical implication of this model is that 6.7 GHz methanol masers with peak flux densities of $\sim$11.5 Jy have a probability of 0.5 of having a 12.2 GHz methanol maser counterpart with a flux density >0.55 Jy, with the probability increasing with increasing values of 6.7 GHz methanol maser flux density and decreasing for lower values.

For the 63 dust sources that do have associated 6.7 and 12.2 GHz methanol masers the model predicts (when the probability threshold is set to 0.5) that 44 of the 6.7 GHz methanol masers will have associated 12.2 GHz methanol maser emission and wrongly predicts that the remaining 19 will not have associated 12.2 GHz methanol maser emission. Applying the model to the 38 6.7 GHz

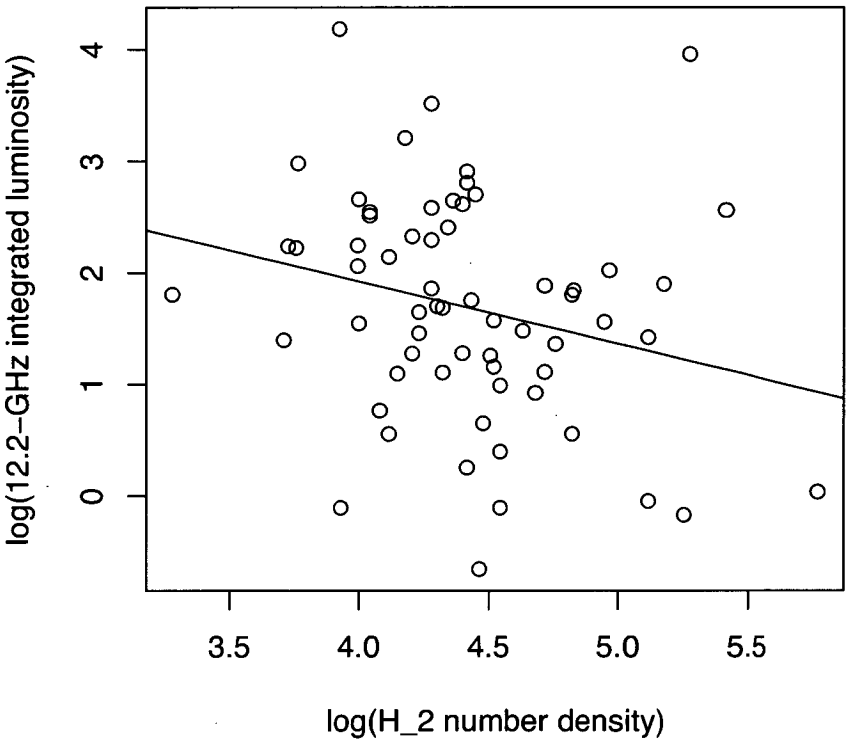

Figure 4.3: *Log of 12.2 GHz integrated luminosity versus the H_2 number density of the associated dust clump in cm^{-3}. The line of best fit is also plotted.*

methanol masers with no detectable 12.2 GHz emission, the model predicts 29 of these correctly and falsely expects the remaining 9 to have associated 12.2 GHz methanol maser emission.

This analysis was then repeated after limiting the sample to sources where the associated 6.7 GHz methanol maser was stronger than 9 Jy (more than 16 times our detection limit of 0.55 Jy). This was done to determine if the results of the analysis of the full sample was due to a sensitivity bias that may have been introduced by the fact that 12.2 GHz methanol masers are usually weaker than their associated 6.7 GHz emission. Caswell et al. (1995b) found that the median ratio of 12.2 to 6.7 GHz methanol maser intensity was 1:9 (taking into account 12.2 GHz non-detections) which we have doubled and adopted as the 6.7 GHz methanol maser cut off threshold. Therefore, methanol masers with peak flux densities of less than 9 Jy were removed from the sample, leaving 61 dust clumps, and the statistics were recalculated. The removal of the weaker 6.7 GHz methanol maser sources had little effect on the results of the statistics with the 1.2 mm dust clump density, 6.7 GHz methanol maser peak luminosity and flux density remaining the only properties showing statistically significant differences.

Statistical analysis of 1.2 mm dust clumps with and without 8 GHz radio continuum

In order to determine if there was any difference between the properties of 1.2 mm dust clumps with and without detectable radio continuum we also fitted a Binomial GLM to the radio continuum presence/absence data. 378 1.2 mm dust clumps were used in this analysis, 71 of which have detectable radio continuum (Hill et al., 2005, and references therein). Fits of the single term Binomial model showed that all tested 1.2 mm dust clump properties, with the exception of distance, were statistically significant. In the case of 1.2 mm integrated and peak flux densities, radius, mass and FWHM, increasing values of the dust clump properties showed a greater likelihood of being associated with detectable radio continuum, whereas in the case of the H_2 number density it is the smaller values that show an increased likelihood of associated radio continuum. Results of the single term additions are in Table 4.10 and that data is shown in the form of box

plots in Fig. 4.12.

4.3.3 Summary of statistical results

Here we briefly summarize the main results from the statistical analysis carried out in the previous section, Section 4.3.2:

- 1.2 mm dust clumps with associated methanol masers have higher values of integrated and peak flux densities, mass and radius than those with no associated 6.7 GHz methanol maser.

- 1.2 mm dust clumps with associated 6.7 GHz methanol masers with high peak luminosities are more likely to be associated with OH masers and have larger values of mass and radius and lower values of density than those clumps that are associated with 6.7 GHz methanol masers with low luminosities.

- 1.2 mm dust clumps associated with both 6.7 and 12.2 GHz methanol masers are more likely to be associated with OH masers and have lower densities than 1.2 mm dust clumps with just 6.7 GHz methanol maser associations.

- The luminosity of 12.2 GHz methanol masers is not dependent on either the presence of associated radio continuum, or the luminosity of associated radio continuum.

- 6.7 GHz methanol masers with 12.2 GHz methanol maser counterparts have larger flux densities and higher peak luminosities than 6.7 GHz methanol masers with no 12.2 GHz counterpart and this is not likely to be a result of a sensitivity bias.

- 1.2 mm dust clumps with associated radio continuum have higher values of mass, radius, peak and integrated flux density and lower values of density than clumps without detectable radio continuum.

4.4 Discussion

4.4.1 Comparison between 6.7 and 12.2 GHz methanol masers

We have made a preliminary investigation of the relative intensities and velocity ranges of the 6.7 and 12.2 GHz methanol maser sources within this sample. Detailed analysis of these properties, as well as spectral structure, will be carried out in a subsequent paper which will present 12.2 GHz observations towards all 6.7 GHz methanol masers detected in the southern hemisphere component of the Parkes Methanol Multibeam (MMB) Survey (Green et al., 2009). The MMB survey for 6.7 GHz methanol masers is the most sensitive survey yet undertaken for young high-mass stars in the Galaxy and is complete within 2 degrees of the Galactic plane.

Investigation of the peak flux densities of the 6.7 and 12.2 GHz methanol maser associations reveals that there are three instances where the flux density of the 12.2 GHz methanol maser is stronger than the reported values of the associated 6.7 GHz methanol maser emission. Given that interstellar masers are intrinsically variable it is likely that in at least some of these instances the 6.7 GHz methanol masers are now stronger than their reported values from several years prior to the 12.2 GHz methanol maser observations.

We have made a comparison of the 6.7 and 12.2 GHz methanol maser peak flux densities (where emission was detected at both frequencies) and find that the median ratio of 12.2 to 6.7 GHz methanol flux density is 1:5.9 with an average ratio of 1:3.1. We additionally find that the most extreme ratios of 12.2 to 6.7 GHz methanol maser peak flux density are 1:180 and 1:0.56, highlighting the fact that when the 12.2 GHz emission is stronger it is only marginally stronger. In comparison, Caswell et al. (1995b) found a median ration of 12.2 to 6.7 GHz methanol maser peak flux density of 1:5.4.

We have compared the ratio of 6.7 to 12.2 GHz peak flux density to both the peak luminosity of the 6.7 GHz methanol maser and the integrated luminosity of the 12.2 GHz methanol masers. We find that there is a general trend whereby the 6.7 GHz methanol masers with high peak luminosities have higher ratios of 6.7 to

12.2 GHz methanol maser flux density (i.e. the more luminous 6.7 GHz methanol masers have relatively weaker emission at 12.2 GHz). Comparison between source flux density ratios and 12.2 GHz methanol maser luminosities calculated from the integrated flux densities of the 12.2 GHz methanol maser sources show the complementary trend (i.e. the less luminous 12.2 GHz methanol masers have relatively stronger emission at 6.7 GHz).

Plots of the flux density ratios versus 6.7 GHz peak luminosity and 12.2 GHz integrated luminosity are shown in Figs 4.4 and 4.5 to demonstrate our results quantitatively. We have used linear regression to show that the trends in the data are statistically significant. For the 6.7 GHz peak luminosity, we find a slope of 0.25 with a standard error of 0.08 and a p-value of 0.003 which allows us to reject the null hypothesis that there is zero slope. The correlation coefficient between the points is 0.36 which is classified as a weak correlation. For the 12.2 GHz integrated luminosity we find a slope of −0.15 with a standard error of 0.07 and a p-value of 0.03 which similarly means that the slope of the line is statistically significant and non-zero. The correlation coefficient is 0.27 which also corresponds to a weak correlation between the data points. The significant scatter present in both data sets are likely to be due to a combination of a few factors. The first is that the calculated luminosities are heavily dependent on the derived kinematic distances for the sources, which in many instances have large ambiguities. We have assumed the near distances for sources here as for all previous analysis which, for some sources, may introduce large errors into the calculated source luminosities. It is also likely that the 6.7 GHz methanol maser flux densities reported in the literature would not correspond to the true flux density of these sources if measured at the time of the 12.2 GHz methanol maser observations. We therefore expect that source variability also contributes to the scatter in Figs 4.4 and 4.5. It is expected that these influences will have an effect on our data; however, we would expect that they would act to weaken trends not acting in a systematic way to strengthen them. It is therefore likely that accurate distance measurements and single epoch observations of both methanol maser transitions would result in a more tightly correlated relationship, but, this is something for future investigation.

In Section 4.3.2 we showed that the 6.7 GHz peak luminosity increases with

decreasing dust clump density. We also show that centimetre radio continuum emission is preferentially found towards lower density dust clumps, which suggests that the dust clump density decreases as the source evolves (see Section 4.4.3 for a more detailed discussion of our results and their implications for an evolutionary sequence for high-mass star formation). These results (and others) combined suggest that the 6.7 GHz methanol peak luminosity increases as the high-mass star formation it is associated with evolves. That the average ratio of 6.7 to 12.2 GHz peak flux density increases as the 6.7 GHz peak luminosity increases implies that the rate of increase of the 12.2 GHz peak flux density as the source evolves is less than that for the 6.7 GHz transition. Modeling of methanol masers by Cragg et al. (2005) shows that the 6.7 GHz transition is essentially always stronger than the 12.2 GHz transition and our results suggest that as the underlying star formation region evolves the relative intensity of the 6.7 GHz transition increases more quickly. In particular, figures 2 & 3 of Cragg et al. (2005) show that the intensity of the 12.2 GHz transition decreases more rapidly with increasing gas temperature than the 6.7 GHz transition does, which is consistent with an evolutionary trend for the 6.7 to 12.2 GHz flux density ratio to increase.

Inspection of the velocity ranges of the 6.7 GHz methanol masers as well as their associated 12.2 GHz methanol maser emission has shown that of the 68 12.2 GHz methanol masers that we observed, 49 sources show the peak of their emission at the same velocity as the 6.7 GHz methanol maser, to within the spectral resolutions of the respective observations. For the remaining 16 sources we find the 12.2 GHz peak velocity within the velocity range of the detectable 6.7 GHz methanol maser emission and is coincident with a secondary 6.7 GHz methanol maser feature. In the majority of cases we find that the 12.2 GHz methanol masers have narrower velocity ranges than the 6.7 GHz methanol maser counterparts. The average velocity range of the 6.7 GHz methanol masers with associated 12.2 GHz methanol masers is 9 km s^{-1} and the average velocity range of the 12.2 GHz methanol masers that we observe is 3.4 km s^{-1}. The median value of 12.2 GHz velocity range of the sources that we observed is 5.4 km s^{-1} which is remarkably similar to the median value of the 131 sources reported by Caswell et al. (1995b) as 5 km s^{-1}.

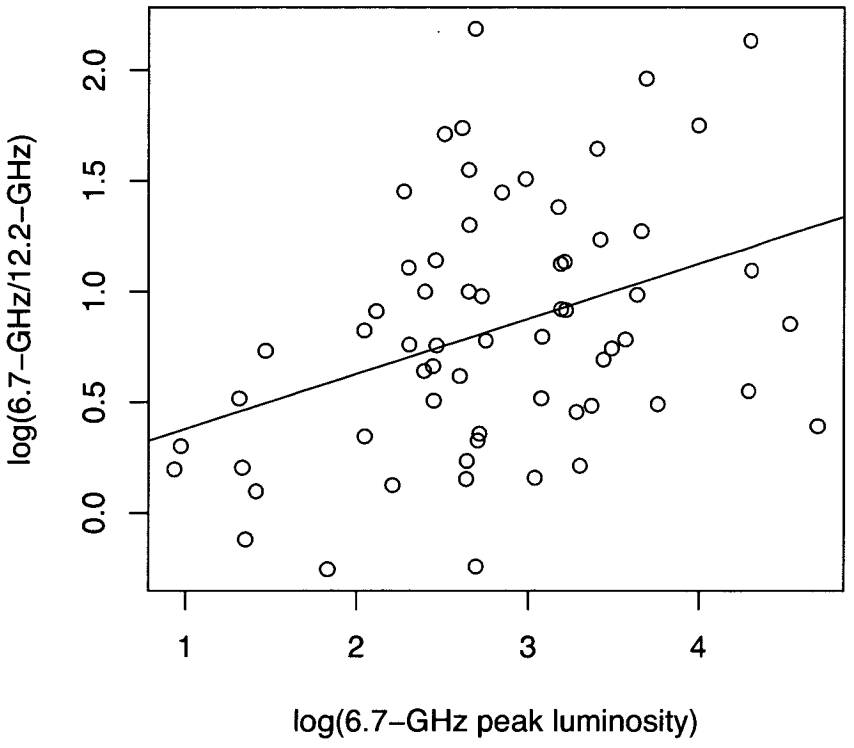

Figure 4.4: *Log of the 6.7 GHz methanol maser peak flux density divided by the 12.2 GHz methanol maser peak flux density versus the log of the 6.7 GHz peak luminosity, overlaid with the line of best fit.*

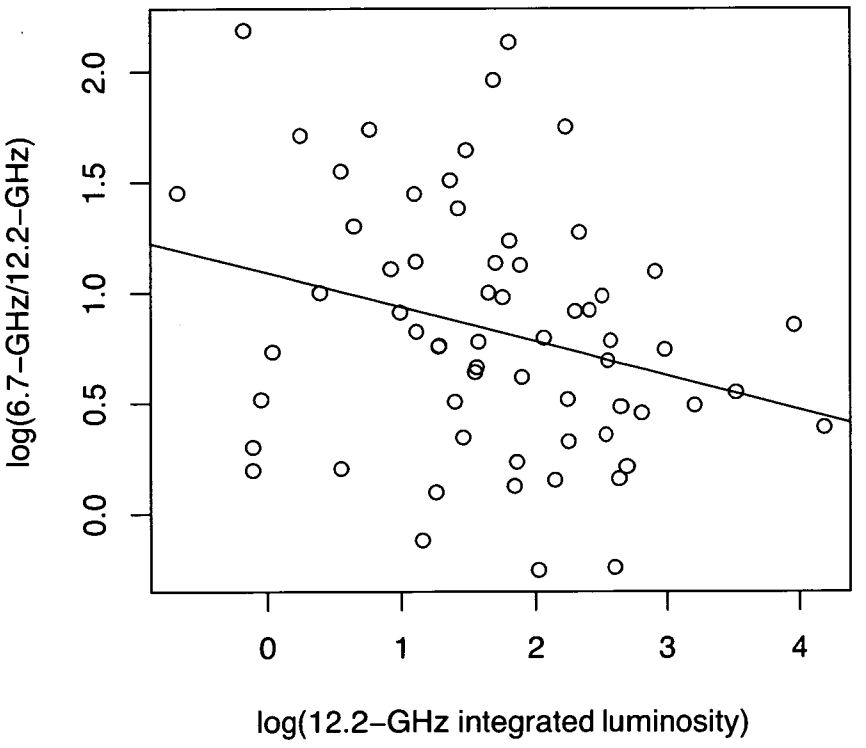

Figure 4.5: *Log of the 6.7 GHz methanol maser peak flux density divided by the 12.2 GHz methanol maser peak flux density versus the log of the 12.2 GHz integrated luminosity, overlaid with the line of best fit.*

4.4.2 Absorption at 12.2 GHz

29 of our target 6.7 GHz methanol masers show absorption at 12.2 GHz, of which 24 also show 12.2 GHz maser emission. In comparison Caswell et al. (1995b) detected 19 absorption spectra toward 238 6.7 GHz methanol masers. We suspect that absorption accompanying emission in some cases may be an artifact of out processing method (see Section 4.2).

4.4.3 Evolutionary sequence for sources

The relatively large number of class II methanol maser sources in our Galaxy (esimated to be of order 1000), means that they must be associated with objects covering a range of stellar masses and also have an appreciable "lifetime". It is generally assumed that the properties of the masers and the complementary data at different wavelengths will depend upon both the age of the source and its mass. At present we do not have sufficient information to disentangle these two factors. Circumstantial evidence can sometimes be used to infer one or the other as the primary factor. However, some of the attributes ascribed to evolutionary factors may be partially, or even largely mass related (and vice versa).

Purcell et al. (2009) propose that the difference between radio-loud and radio-quiet massive young stellar objects (YSOs) may be attributed to evolution, with the radio-loud sources corresponding to a later stage of evolution. Our statistical comparison between 1.2 mm dust clumps with associated radio continuum from ultra-compact (UC) HII regions at 8 GHz and those without has shown that 1.2 mm dust clumps with detectable radio continuum in general have bigger radii, masses, flux densities as well as lower H_2 number density. We therefore propose that these 1.2 mm dust clump properties give an indication of comparative stages of evolution (i.e. sources with larger radii, masses, flux densities and smaller H_2 number densities are more likely to be at a later stage of evolution than sources which have smaller values of radii, mass, flux density and larger values of density). Purcell et al. (2009) similarly found that YSOs with associated 8 GHz radio continuum are more massive than those without detectable radio continuum.

The evolutionary interpretation of the results of the statistics is contingent on the assumption that a large number of the 1.2 mm dust clump sources with no

detectable radio continuum will go on to form massive stars. While it is likely that some of the 1.2 mm dust clumps without associated radio continuum are 'failed' cores and will not form massive stars, we know that a large number of them will do so, since they exhibit other tracers that are indicative of massive star formation such as methanol masers (Caswell, 2009; Minier et al., 2003; Walsh et al., 1998, 1997; Caswell et al., 1995a; Szymczak et al., 2002) and ammonia (Longmore et al., 2007). Hill et al. (2009) concluded from investigation of a subset of the Hill et al. (2005) sample that the 1.2 mm dust clumps with no overt signs of massive star formation displayed similar characteristics to those 1.2 mm dust clumps associated with known massive star formation regions. Therefore, as the number of sources in this sample is large we believe that the possibility of the inclusion of some 'failed' cores is inevitable, but the number will be few and so will have little effect on our statistics.

Longmore et al. (2007) detected 24 GHz continuum emission towards some of the 1.2 mm dust clump sources where no 8 GHz continuum emission was detected by Walsh et al. (1998). It is therefore likely that some of the sources that we have classified as having no associated continuum emission are in fact associated with radio continuum from hyper-compact (HC) HII regions which are often optically thick at centimetre wavelengths and are associated with an earlier evolutionary phase of massive star formation than UCHII regions. According to Longmore et al. (2007), this means that sources with detectable radio continuum at 24 GHz and not 8 GHz are part of another class of object that is more evolved than sources with no detectable radio continuum and less evolved than sources with detectable continuum at centimetre wavelengths. This distinction also means that we have not introduced any bias into our analysis by not accounting for sources that are in the HCHII region stage.

Interpretation of the relative evolution of sources associated with the different maser properties can be made by comparing the 1.2 mm dust clump properties associated with these sources to the results of the analysis with UCHII regions. We find that 1.2 mm dust clumps with associated 6.7 GHz methanol masers have higher flux densities, radii and mass than those with no associated 6.7 GHz methanol maser. This suggests that 6.7 GHz methanol masers are present prior to any significant change in source density that occurs along side the formation

of UCHII regions. However, the 1.2 mm dust clump observations of Hill et al. (2005) have a relatively low resolution (24") and so only reflect the large scale structures. Hence significant changes in source structure and physical conditions are likely to be occurring on smaller spatial and temporal scales, but these will only be revealed by higher resolution observations of the dust properties.

Our analysis of 6.7 GHz methanol maser peak luminosity and 6.7 GHz methanol masers associated with 1.2 mm dust clumps shows that methanol masers with high peak luminosities are more likely to be associated with 1.2 mm dust clumps of larger mass and clump radii and lower H_2 number densities than 6.7 GHz methanol masers with lower peak luminosities. While we find that there is no statistical difference between the flux densities of 1.2 mm dust clump sources with varying levels of 6.7 GHz methanol maser peak luminosity, we find that the properties of the 1.2 mm dust clumps associated with 6.7 GHz methanol masers with high luminosities are similar to those 1.2 mm dust clumps that are associated with a later stage in evolution. We additionally find that more luminous 6.7 GHz methanol masers are more likely to be associated with OH masers which are known to trace a generally later evolutionary phase of massive star formation than isolated methanol masers (e.g. Forster & Caswell, 1989; Caswell, 1997). Therefore we expect that there is a trend between 6.7 GHz methanol maser peak luminosity and evolutionary phase, with the more luminous 6.7 GHz methanol maser peaks tending towards a later phase in evolution than 6.7 GHz methanol masers with low peak luminosities. This important result will deserve further investigation using luminosities that have been calculated from integrated maser flux densities.

We find that 1.2 mm dust clump sources associated with both 6.7 and 12.2 GHz methanol masers are more likely to have lower densities than the sources which are associated with only the 6.7 GHz maser transition of methanol. Pumping models of methanol masers (e.g. Cragg, Sobolev & Godfrey, 2005) predict that the 6.7 and 12.2 GHz transitions are inverted over very similar ranges of parameter space. The absence of 12.2 GHz masers associated with a large fraction of 6.7 GHz sources (40 %) implies that the physical conditions are commonly close to the point where the 12.2 GHz masers switch on or off. Cragg, Sobolev & Godfrey (2005) also find that 6.7 GHz methanol masers can exist at higher den-

sities than 12.2 GHz methanol masers, consistent with the results of our analysis. We also find that 12.2 GHz methanol masers are more likely to be associated with 6.7 GHz methanol masers with higher flux densities and peak luminosities. This result is not surprising as all previous observations of both 12.2 and 6.7 GHz methanol masers have shown that the 12.2 GHz emission is rarely brighter than the associated 6.7 GHz methanol maser emission. However, when we lessened the chance of a sensitivity bias by removing all of the weak 6.7 GHz methanol masers from our analysis, we find that our results do not change. This means that there is likely to be a delay between when the 6.7 GHz methanol maser 'switches on' and when the 12.2 GHz methanol maser 'switches on'. Furthermore, 12.2 GHz methanol masers are more likely to be found toward 6.7 GHz methanol masers with associated OH masers. We therefore suggest the 12.2 GHz methanol masers are present sometime after the onset of 6.7 GHz methanol maser emission.

van der Walt (2005) estimates the lifetime of 6.7 GHz methanol masers to be in the range 2.5×10^4 to 4.5×10^4 years, combining this with our detection rate of associated 12.2 GHz methanol masers we expect that the corresponding lifetime of 12.2 GHz methanol masers will be in the range 1.5×10^4 to 2.7×10^4 years. This inference assumes that 12.2 GHz methanol masers are never without associated 6.7 GHz methanol maser emission. However, given that previous searches have not resulted in serendipitous detections of 12.2 GHz methanol masers without accompanying 6.7 GHz methanol maser emission and the fact that the current search and previous searches (Caswell et al., 1995b; Błaszkiewicz & Kus, 2004) have shown that 12.2 GHz methanol maser emission is only rarely brighter that the associated 6.7 GHz maser emission, this is not an unreasonable assumption.

While our simplified evolutionary results appear to be self consistent and reliable the full picture is likely to be more complex. We found that 1.2 mm dust clumps with detectable radio continuum have larger radii, masses, flux densities and smaller H_2 number densities and suggest that these properties can be used to give an indication of the probable evolutionary stage. However, it is likely that some of the more massive dust clumps will go on to form higher mass stars and are therefore more likely to have detectable radio continuum earlier than some of the less massive cores. Furthermore the flux density of the radio continuum will depend on the dust fraction and the type of star that the 1.2 mm dust clump is

associated with.

The H_2 number densities of the 1.2 mm dust clumps are central to a number of our evolutionary arguments. There are several factors that directly affect the accurate determination of this quantity. Both the 1.2 mm dust clump mass and radius rely heavily on the accuracy of the distance measurements. However, it would be unlikely that the susceptibility of the radius and mass to errors would have a systematic effect that resulted in the strengthening of a relationship between radius and some other property, such as maser presence - it would be much more likely to dilute such a relationship. We therefore believe that the only effect that potential errors in the determined 1.2 mm dust clump radius (and therefore the H_2 number density) would have on our statistics is to weaken true relationships rather than falsely cause correlations between properties.

Hill et al. (2005) adopted a constant temperate of 20 K to calculate the masses of the 1.2 mm dust clumps. Hill et al. (2009) have shown that in the vast majority of cases this is an overestimate but that the distribution of masses is similar to that found in Hill et al. (2005). As we expect less evolved 1.2 mm dust clumps to be colder than the more evolved sources that show detectable 8 GHz radio continuum emission, errors introduced by the assumption of a constant temperature would result in the less evolved sources having underestimated masses relative to the more evolved sources. Therefore, the use of accurate temperature measurements would strengthen our finding that more evolved sources have lower H_2 number densities. Due to this dependance however, we are unable to separate the effects that the H_2 number density and temperature have on the evolutionary phase and expect that temperature would also play a large role in indicating the relative evolutionary phase of the sources.

As Hill et al. (2005) targeted their observations towards sources suspected of undergoing massive star formation, there is a possibility that an unbiased search would result in a distribution of source properties that differs from this sample. However, as discussed in Section 4.3.2 the distribution range of the 1.2 mm dust clump properties from the targeted sample of Hill et al. (2005) greatly exceeds the distribution range from the unbiased search of a GMC (Mookerjea et al., 2004). Furthermore, as the number of serendipitous detections of 1.2 mm dust clumps within the fields of targeted objects is large (253), the likelihood of biases being

introduced by the targeted nature of this sample is low.

Another point that needs to be considered is that a dust clump is unlikely to form only one star. Some of the confusion in our predictive models can be explained by the fact that often, there are clusters of stars forming within the one dust clump, at different evolutionary stages and with different mass ranges. This fact is evident in our sample because there are multiple instances where there is more than one 6.7 GHz methanol maser within the one dust clump.

Combining all of our statistical analyses we find that as the 1.2 mm dust clump becomes more massive (n.b. this is mostly likely a consequence of the relatively underestimated masses of the less evolved sources, a consequence of the constant temperature assumption, rather than a real increase in mass as discussed above), and increases in radius and flux density, a weak 6.7 GHz methanol maser forms. Then, as the clump becomes less dense and continues to increase in mass, radius and flux density, the 6.7 GHz methanol maser increases in flux density and the 12.2 GHz methanol maser forms. At this stage the detection of associated OH masers and 8 GHz radio continuum becomes more likely. We therefore propose the following scenario for evolutionary sequence of sources from less evolved to more evolved: (i) 1.2 mm dust clumps with no associated methanol maser emission or 8 GHz radio continuum, (ii) 1.2 mm dust clumps with associated 6.7 GHz methanol masers, (iii) 1.2 mm dust clumps with associated methanol maser emission at both 6.7 and 12.2 GHz. 8 GHz radio continuum is observed toward 29 of our sample of 112 methanol masers and we find that 19 of these also have associated 12.2 GHz methanol maser emission (this is not statistically significant p-value=0.24 from a chi-sqared test). We therefore postulate that 8 GHz radio continuum generally becomes detectable toward the end of the 6.7 GHz methanol maser only stage, prior to the onset of 12.2 GHz methanol maser emission if the mass of the star is sufficiently large.

In Fig. 4.6 we present our proposed evolutionary sequence for masers in massive star formation regions. We have used the evolutionary sequence presented in Ellingsen et al. (2007) as a starting point, adjusted it according to our new data, and placed quantitative estimates on the relative lifetimes of the different species using additional maser observations (e.g. Caswell, 2009). The estimates of the lifetimes of the different maser species have been extrapolated from the 6.7 GHz

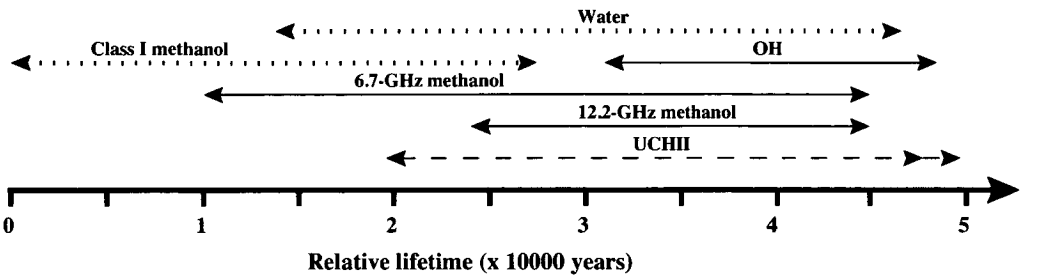

Figure 4.6: *Evolutionary sequence for masers associated with massive star formation regions. Lifetimes represented by dotted lines indicate that they have been estimated from the literature along with unpublished data. The lifetime of the UCH*II *region is represented by a dashed line as the onset of radio continuum emission is particularly dependent on the mass of the associated star. The double arrow head on the far end of the UCH*II *region lifetime is to show that it will persist past the end of the range of the plot.*

methanol maser lifetime of van der Walt (2005) and detection statistics for the different maser species.

6.7 & 12.2 GHz methanol maser association with radio continuum

There are 29 1.2 mm dust clumps that are associated with both methanol maser emission and 8 GHz radio continuum within our sample. 19 of these sources are associated with both 6.7 and 12.2 GHz methanol maser emission while the remaining 10 are associated with only 6.7 GHz methanol masers. We have compared these two groups of sources in order to determine if there are any differences in the 1.2 mm dust clump properties. We find that the clumps with both 12.2 and 6.7 GHz methanol masers have large FWHM (p-value 0.01), lower densities (p-value 0.07) and higher 6.7 GHz methanol maser peak luminosity and peak flux densities. We have also investigated the 8 GHz radio continuum luminosities (calculated from the flux densities given in Walsh et al. (1998)) and found that there is no difference between either the flux density or the luminosity of the continuum between those sources with associated 12.2 GHz methanol masers and those without. This implies that the presence of an associated 12.2 GHz maser is much more reliant on suitable densities rather than either the presence or strength of an associated radio continuum source. In general, however, 1.2 mm

dust clumps with associated radio continuum emission are more likely to satisfy the density ranges for emission from the 12.2 GHz methanol maser transition.

4.4.4 Association with GLIMPSE point sources

Positions of the 6.7 GHz methanol masers were compared to the positions of infrared point sources listed in the GLIMPSE point source catalogue as well as the GLIMPSE archive. As most methanol maser positions are known to a high precision we assume an association between the GLIMPSE sources and the methanol masers if they lie within 2 arcsec of each other. We find that 90 of the methanol masers that we observe lie within the regions covered by GLIMPSE of which 51 (57 %) are associated with either a GLIMPSE point source or GLIMPSE archive source. Ellingsen (2006) found 68 % of a sample of 56 methanol masers had associated GLIMPSE sources. The difference in detection rates is not statistically significant.

Fig. 4.7 shows a plot of the [3.6]–[4.5] μm versus [5.8]–[8.0] μm colours of the GLIMPSE point sources associated with the methanol masers in our sample. For sources to be present on this plot they needed to have flux density measurements for all four of the IRAC bands, limiting the number of 6.7 GHz methanol maser associated GLIMPSE sources in the plot to 13, 8 of which are also associated with 12.2 GHz methanol maser emission. Similarly to Ellingsen (2006), we find that the GLIMPSE sources associated with the methanol masers lie above the majority of the comparison sources in our colour-colour plot.

We have compared the colours of the GLIMPSE sources associated with both 6.7 and 12.2 GHz methanol masers with those associated with only 6.7 GHz methanol masers and find that there is no statistically significant difference between them. We will not be able to determine if this is a consequence of our small sample size or rather a real effect, until we can compare the colours for a larger number of sources. However, if our results are representative then this implies that the masers themselves are much more sensitive to evolutionary changes than is the associated infrared emission of wavelengths < 10 μm.

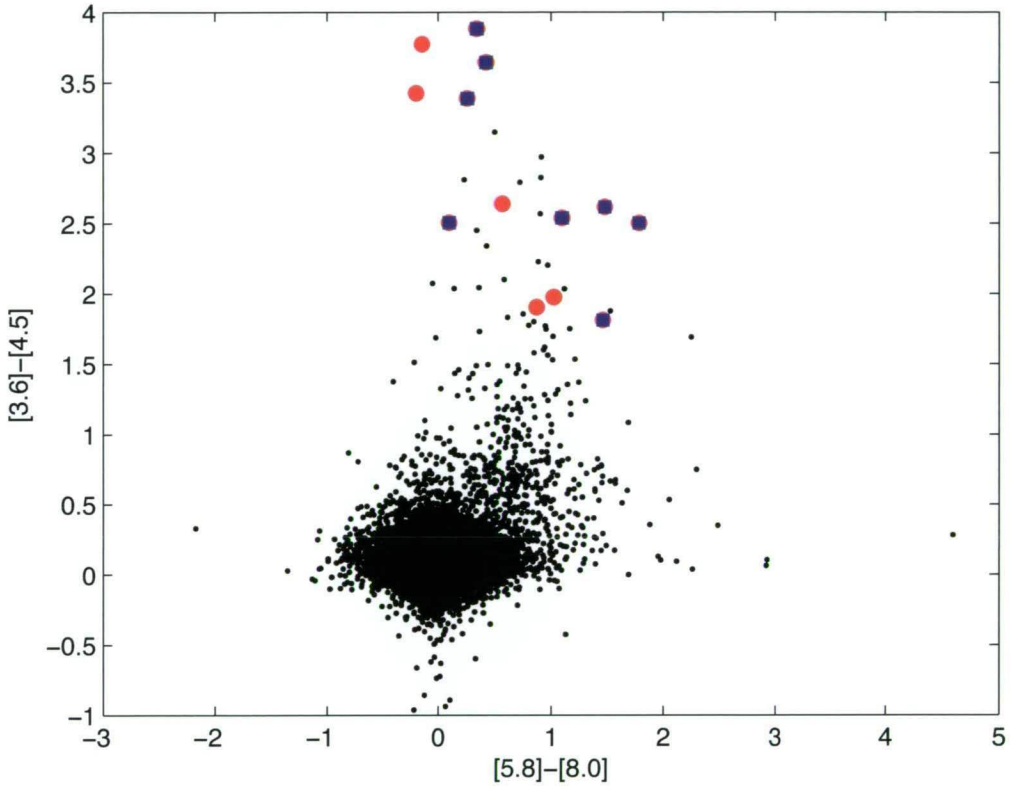

Figure 4.7: *Colour-colour plot of GLIMPSE point source data. Methanol maser sources showing both 6.7 and 12.2 GHz emission are represented by blue squares and sources with only the 6.7 GHz methanol maser transition are represented by the red circles. The black dots represent all of the GLIMPSE point sources within 30 arcmin of* $l = 326.5°$, $b = 0.0°$.

4.5 Summary

We have searched 112 known 6.7 GHz methanol masers for associated 12.2 GHz methanol maser emission with the ATNF Parkes 64-m radio telescope. We have detected 12.2 GHz methanol masers towards 68 of these sources; a detection rate of 60 percent. We estimate the life-time of 12.2 GHz methanol maser emission to be of the order of 2.1×10^4 years. We find that for the majority of sources, the peak velocity of the 12.2 GHz methanol maser emission is the same as the 6.7 GHz methanol maser and, for the remainder, the 12.2 GHz peak emission is coincident with a secondary feature present in the 6.7 GHz methanol maser spectrum. Comparison between the peak flux densities of the respective methanol maser transitions has shown that median ratio of 6.7 to 12.2 GHz peak flux density is 1:5.9, similar to previous searches. We additionally find that the ratio of 6.7 to 12.2 GHz methanol maser peak flux density has some dependence on 6.7 GHz methanol maser luminosity, with the more luminous 6.7 GHz sources having comparatively weaker 12.2 GHz methanol maser emission and vice versa.

All of the target sources have previously been observed at 1.2 mm for dust continuum emission (Hill et al., 2005). We have carried out statistical analysis of the dust clump properties of sources in the following four subgroups compared the 1.2 mm dust clump properties: dust clumps with and without associated 6.7 GHz methanol maser emission; dust clumps associated with highly luminous 6.7 GHz methanol masers compared with those of low luminosity; dust clumps associated with 6.7 GHz methanol maser emission with and without associated 12.2 GHz methanol maser emission; and dust clumps with and without associated radio continuum. Our statistics show that there are many differences between the sources that fall into these subgroups; consistent with the different source combinations and characteristics being associated with different stages of massive star formation. An evolutionary scenario for the common maser species associated with high-mass star formation regions is presented.

The positions of the 6.7 GHz methanol masers have been compared to sources in the GLIMPSE point source catalogue. We find that 57 per cent of the 6.7 GHz methanol masers that lie within the GLIMPSE regions are associated with a GLIMPSE point source. Comparison between the GLIMPSE colours associated

with sources that exhibit emission at both 6.7 and 12.2 GHz and those exclusively at 6.7 GHz has shown that there is little difference between the colours of the associated point sources.

We will present detailed investigation of the relative intensities and velocity ranges of 12.2 GHz methanol masers detected towards the 6.7 GHz methanol masers detected in the southern hemisphere component of the MMB survey (Green et al., 2009) in a subsequent paper. The near simultaneous observations of hundreds of 6.7 and 12.2 GHz methanol masers collected from the MMB survey and follow-up observations will be used to make a detailed investigation of the range and distribution of the intensity ratio for these two transitions. Combining this with our evolutionary studies we will obtain unique insight into the changes in physical conditions responsible for the presence/absence of the different maser methanol transitions.

Our results relating to the evolution of star formation regions will be independently tested in the future through comparison between the unbiased sample of 6.7 GHz methanol masers observed in the MMB survey Green et al. (2009), followup observations at 12.2 GHz and 870 μm dust sources observed as part of ATLASGAL (APEX Telescope Large Area Survey of the Galaxy)[1].

4.6 Appendix

4.6.1 Details relating to statistical analysis

In this section we present the tables and box plots relating to the statistical analysis that is presented in Section 4.3.2. All of the statistical analysis (including the production of box plots) was completed using the R statistical analysis package[2]. See Section 1.3 for a more comprehensive description of the statistical methods adopted in our analysis.

Box plots have been used as a way of presenting the data as they are a useful

[1] http://www.mpifr-bonn.mpg.de/div/atlasgal/

[2] R Development Core Team (2006). R: A language and environment for statistical computing. R Foundation for Statistical Computing, Vienna, Austria. ISBN 3-900051-07-0, URL http://www.R-project.org.

Table 4.3: *Analysis of deviance table for the single term models; 1.2 mm dust clumps with and without 6.7 GHz methanol*

Predictor	Deviance	AIC	LRT	Pr(Chi)
none	455.47	457.47		
Integrated	429.24	433.24	26.23	3.034e-07
Peak	417.15	421.15	38.32	6.008e-10
FWHM	417.91	421.91	37.56	8.881e-10
Distance	453.23	457.23	2.24	0.1343038
Mass	445.21	449.21	10.26	0.0013616
Radius	443.27	447.27	12.20	0.0004782
Density	455.36	459.36	0.11	0.7370057

tool for displaying differences between populations. They can instantly hilight the distribution of the data as the separation between the different parts of the box have specific meanings. The solid line in the in each of these plots represents the median of the data. The box represents the 25^{th} to the 75^{th} percentile, while the vertical line from the top of the box represents data from the 75^{th} percentile to the maximum value and the vertical line from the bottom of the box represents data from the 25^{th} percentile to the minimum value. Extreme values, or outliers, are represented by dots and are defined as points that exceed 1.5 times the interquartile range in separation from either the 25^{th} or $75th$ percentile.

Table 4.4: *Summary table for the Binomial regression model of 1.2 mm dust clumps with and without 6.7 GHz methanol masers, showing for each predictor the estimated coefficient and the standardised z-value and p-value for the test of the hypothesis that* $\beta_i = 0$.

Predictor	Estimate	Std. Error	z value	p-value
Intercept	–2.677e+00	3.244e-01	-8.251	< 2e-16
Integrated	–2.952e-01	7.338e-02	–4.023	5.75e-05
Peak	1.172e+00	2.744e-01	4.271	1.94e-05
FWHM	2.994e-02	6.427e-03	4.659	3.18e-06
Density	1.434e-06	6.876e-07	2.085	0.0370

Table 4.5: *Analysis of deviance table for the single term models, dust clumps with and without highly luminous 6.7 GHz methanol masers.*

property	Deviance	AIC	LRT	Pr(Chi)
none	140.006	142.006		
Integrated	139.777	143.777	0.229	0.632381
Peak	139.690	143.690	0.316	0.574197
FWHM	137.791	141.791	2.215	0.136674
Distance	117.717	121.717	22.289	2.345e-06
Mass	135.027	139.027	4.979	0.025657
Radius	121.923	125.923	18.083	2.115e-05
Density	131.441	135.441	8.564	0.003428
6.7 Maser flux	95.731	99.731	44.275	2.854e-11

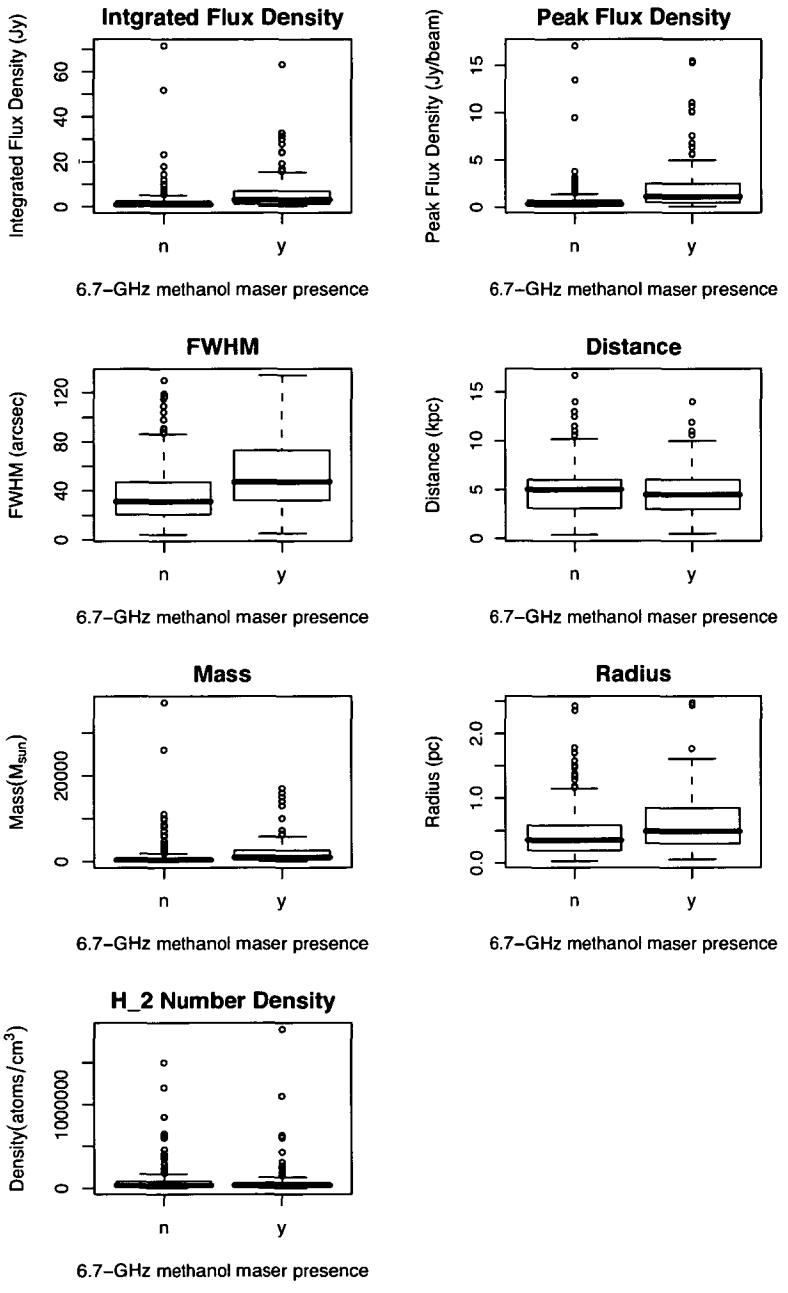

Figure 4.8: *Box plots of the 1.2 mm dust clump properties split in the categories of yes and no, referring to the presence or absence of 6.7 GHz methanol maser emission respectively. There is a statistically significant difference between the two categories in the 1.2 mm dust clump integrated flux density, peak flux density, mass, radius and source FWHM. This information is the graphical display relating to the information in Table 4.3.*

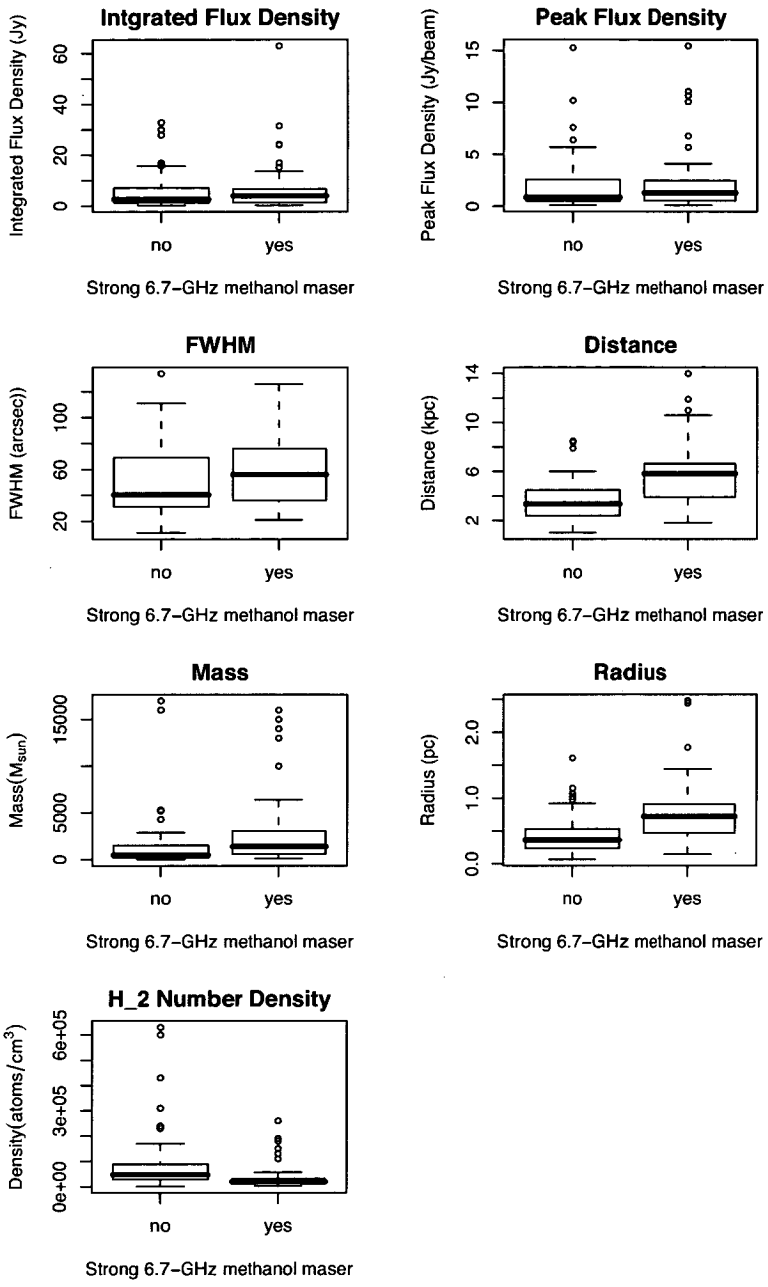

Figure 4.9: *Box plots of the 1.2 mm dust clump properties split in the categories of yes and no, referring to the presence of 6.7 GHz methanol maser emission with high and low luminosities respectively. There is a statistically significant difference between the two categories in the 1.2 mm dust clump mass, radius and H_2 number density. This information is the graphical display relating to the information in Table 4.5.*

Table 4.6: *Summary table for the Binomial regression model of 1.2 mm dust clumps with luminous 6.7 GHz methanol masers and those with less luminous 6.7 GHz methanol masers, showing for each predictor the estimated coefficient and the standardised z-value and p-value for the test of the hypothesis that $\beta_i=0$.*

Predictor	Estimate	Std. Error	z value	p-value
Intercept	-3.183923	0.823230	-3.868	0.00011
FWHM	0.017130	0.008611	1.989	0.04665
Distance	0.488554	0.121787	4.012	6.03e-05

Table 4.7: *Analysis of deviance table for the single term models, dust clumps with 6.7 GHz methanol masers with and without 12.2 GHz methanol. This analysis includes not only the 1.2 mm dust clump properties, but also both the peak flux density and luminosity of the associated 6.7 GHz methanol maser.*

Predictor	Deviance	AIC	LRT	Pr(Chi)
none	133.763		135.763	
Integrated	133.345	137.345	0.417	0.51821
Peak	133.342	137.342	0.421	0.51655
FWHM	131.321	135.321	2.442	0.11814
Distance	133.588	137.588	0.175	0.67568
Mass	133.559	137.558	0.205	0.65090
Radius	133.573	137.573	1.190	0.27529
Density	130.732	134.732	3.031	0.08171
6.7 GHz lum	113.790	117.790	19.973	7.853e-06
6.7 GHz flux	107.800	111.800	25.963	3.481e-07

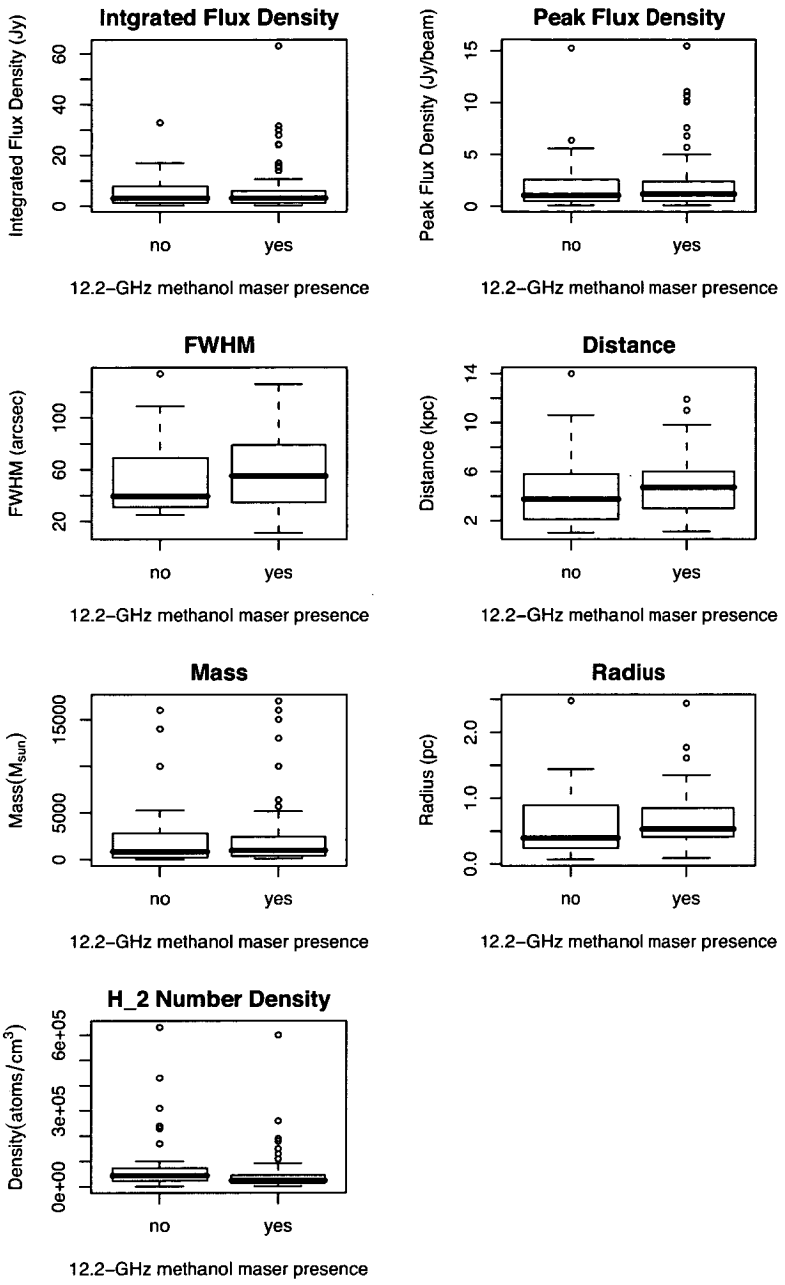

Figure 4.10: *Box plots of the 1.2 mm dust clump properties split in the categories of yes and no, referring to the presence or absence of 12.2 GHz methanol maser emission. There is a statistically significant difference between the two categories in the 1.2 mm dust clump H_2 number density. This information is the graphical display relating to some of the information in Table 4.7.*

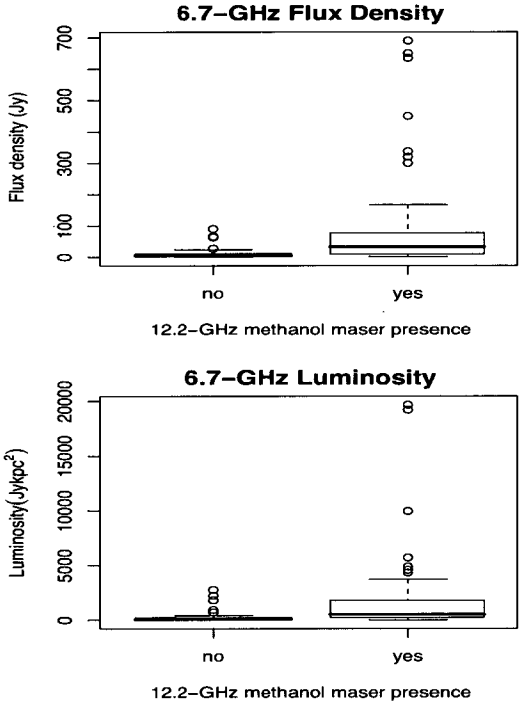

Figure 4.11: *Box plots of the 6.7 GHz methanol maser properties split in the categories of yes and no, referring to the presence or absence of 12.2 GHz methanol maser emission. The differences in the two populations is highly significant in the case of both the 6.7 GHz methanol maser peak flux density and peak luminosity. The three points with the most extreme values for either property have been removed to allow the distribution to be seen. This information is the graphical display relating to some of the information in Table 4.7.*

Table 4.8: *Summary table for the Binomial regression model of 1.2 mm dust clumps with associated 6.7 GHz methanol masers with and without a 12.2 GHz methanol maser counterpart, showing for each predictor the estimated coefficient and the standardised z-value and p-value for the test of the hypothesis that β_i=0.*

Predictor	Estimate	Std. Error	z value	p-value
Intercept	-0.41058	0.29388	-1.397	0.16238
6.7 GHz flux	0.03571	0.01180	3.027	0.00247

Table 4.9: *Analysis of deviance table for the single term models, dust clumps with 6.7 GHz methanol masers with and without 12.2 GHz methanol. Data associated with 6.7 GHz with peak flux densities less than 9 Jy have been removed. The results of the single term models applied to the full data set are shown in Table 4.7.*

Predictor	Deviance	AIC	LRT	Pr(Chi)
none	60.925	62.925		
Integrated	60.428	64.428	0.496	0.481075
Peak	59.637	63.637	1.287	0.256532
FWHM	59.856	63.856	1.069	0.301177
Distance	59.343	63.343	1.582	0.208483
Mass	60.924	64.924	0.0003	0.986207
Radius	60.342	64.342	0.581	0.445201
Density	55.748	59.748	5.177	0.022894
6.7 GHz Lum	55.136	59.136	5.789	0.016130
6.7 GHz Flux	53.484	57.484	7.440	0.006377

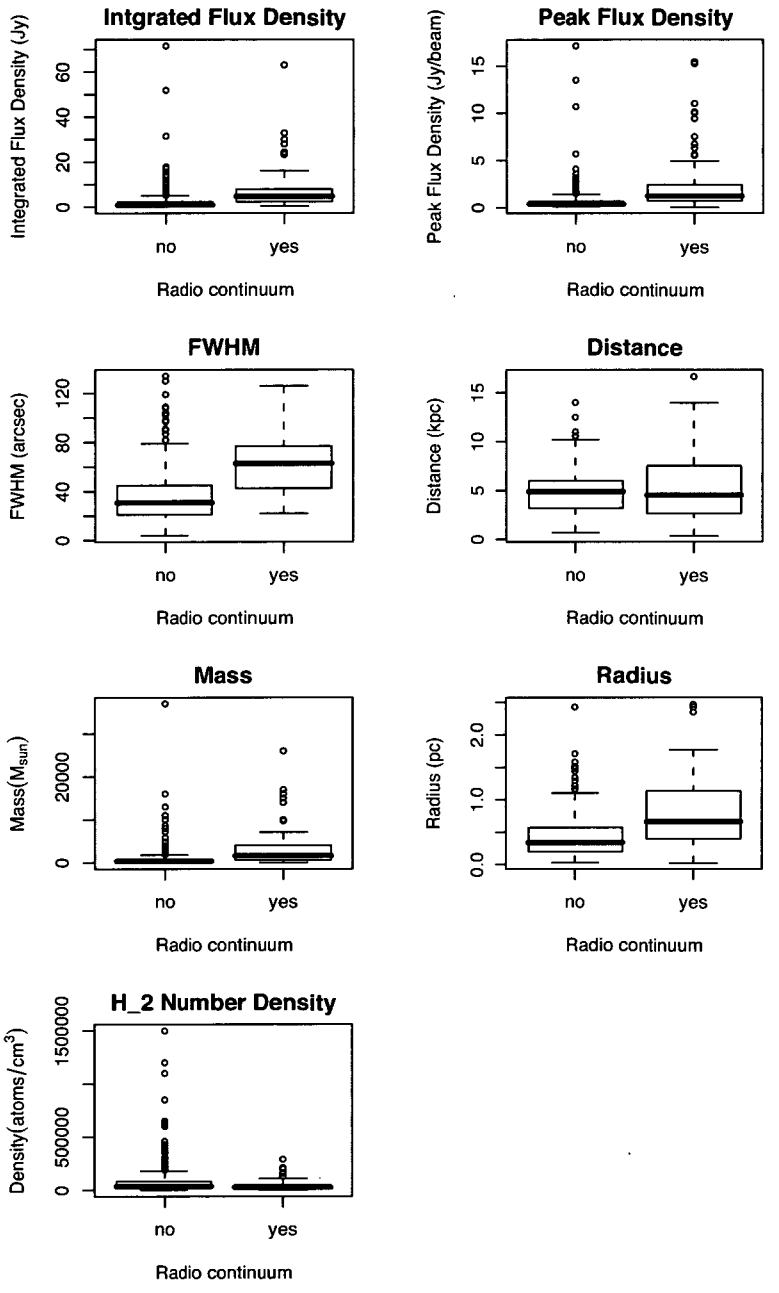

Figure 4.12: *Box plots of the 1.2 mm dust clump properties split in the categories of yes and no, referring to the presence or absence of detectable radio continuum emission. There is a statistically significant difference between the two categories in all 1.2 mm dust clump properties with the exception of distance. The results of the single term models applied to the full data set are shown in Table 4.10.*

Table 4.10: *Analysis of deviance table for the single term models, dust clumps with and without associated 8 GHz radio continuum.*

Predictor	Deviance	AIC	LRT	Pr(Chi)
none	365.19	367.19		
Integrated	340.56	344.56	24.63	6.941e-07
Peak	330.03	334.03	35.17	3.025e-09
FWHM	305.12	309.12	60.07	9.145e-15
Distance	363.24	367.24	1.96	0.161618
Mass	339.94	343.94	25.26	5.023e-07
Radius	320.32	324.32	44.88	2.096e-11
Density	355.57	359.57	9.63	0.001919

5

The association between water masers and 1.2 mm dust clumps

5.1 Introduction

Large-scale, unbiased surveys for water masers are hindered by the large amounts of time required, the susceptibility to poor weather conditions and the intrinsic variability of the sources which requires high positional precision in either the initial observations, or rapid follow up observations. Targeted searches are therefore popular, although these have been traditionally biased towards more evolved sources (as traced by e.g. *IRAS* sources or OH masers).

Previous attempts have been made to model water maser presence towards high-mass star formation regions, with the aim of gaining a more complete sample of water maser sources. These attempts have used particular observable properties of the high-mass star formation regions to make these predictions. Palla et al. (1991) modelled the probability of water maser presence on the basis of *IRAS* far-infrared colours. This model was tested by Palla et al. (1993) and resulted in a detection rate of only around of 5%. This disappointing result is most likely due to the poor spatial resolution of the *IRAS* observations (30 arcseconds at 100 μm) which results in significant source confusion in crowded high-mass star formation regions and demonstrates the need for high-resolution complementary data in the formulation of such models.

A recent systematic search for water masers of almost half a square degree

near the G 333.2–0.6 giant molecular cloud (presented in Chapter 3) revealed a strong relationship between water maser presence and the bigger, brighter, more massive and dense 1.2 mm dust clumps identified by Mookerjea et al. (2004), within the giant molecular cloud. From these observations, we have produced what appears to be a reliable statistical model for predicting which 1.2 mm dust clumps will and will not have an associated water maser. While the likelihood of water maser presence increases with increasing values of all of the dust clump properties tested, the simplest model with the greatest predictive properties was found to only include the dust clump radius. This model predicts that all 1.2 mm dust clumps of radius 1.25 pc (or higher) have a probability of 0.5 (or higher) of having an associated water maser.

While the model presented in Chapter 3 is promising, the water maser survey observations on which this model was derived, were of comparatively low sensitivity (detection limit of $\sim$5 Jy or more in some regions). This combined with the fact that the sample size was small, presented an opportunity for the model to be tested and refined on a much larger sample. Hill et al. (2005) presents a catalogue of 404 1.2 mm dust clumps, a large but manageable sample, perfect for a targeted water maser search to test the current model.

A model relating the properties of 1.2 mm dust clumps to the presence/absence of water masers represents a unique tool for investigating questions such as the mass range of the stars that produce luminous water masers and the evolutionary phase they trace. The primary aim of this project is to test and further refine the model developed in Chapter 3.

Hill et al. (2005) targeted their 1.2 mm dust continuum observations towards 131 regions that were suspected of undergoing massive star formation, using the presence of previously identified methanol masers and/or ultracompact HII regions to select these regions. The observations were carried out using the SIMBA instrument on SEST (the 15 m Swedish ESO Submillimetre telescope) and detected emission directly associated with all but 20 of the methanol masers and nine of the UCHII regions targeted.

We have used the model for water maser presence associated with 1.2 mm dust clumps presented in Chapter 3 to determine the probability of water maser presence in each of the 404 1.2 mm dust clumps presented in Hill et al. (2005)

(that have a measurement for radius). Comparatively few (58 of the 294 dust clumps that we observed with the ATCA) of the 1.2 mm dust clumps presented in Hill et al. (2005), have a calculated probability of water maser presence of greater than 0.1 (using the model presented in Chapter 3).

Chapter 4 presents 12.2 GHz methanol maser observations targeting a number of these dust sources. This search for 12.2 GHz methanol masers, constitutes a near-complete sample within the sample of Hill et al. (2005) sources, since no strong 12.2 GHz emission is expected in regions lacking 6.7 GHz methanol maser emission. Since a number of the sources presented in Hill et al. (2005) are contained within the regions searched for OH maser emission by Caswell (1998), a large subset of the 1.2 mm dust clumps have been searched for OH masers. In this Chapter, new 22-GHz water maser observations completed with the ATCA towards many of the Hill et al. (2005) sample are presented.

In some instances, data presented in Chapter 6 are used, rather that carrying out repeat observations and likewise observations of Forster & Caswell (1989) and Caswell & Breen (2010) are used wherever possible. However, since many of the 1.2 mm dust clumps are located near other dust clumps, even in the case where one of those dust clumps is associated with a previously reported water maser, they were often observed again since they were located within the field of nearby dust clumps.

5.2 Observations and data reduction

5.2.1 Observations

The feasibility of this study was tested with observations using the 26 m Mount Pleasant radio telescope. All 404 1.2 mm dust clumps given in Hill et al. (2005) were targeted in these observations during 2007. An estimated 150 water maser sources were detected within the regions. An effort was made to locate the origin of the emissions by observing four-point grids around each of the targets and fitting a 2D-Gaussian to the relative amplitudes of the emission detected in each. Given the immense success in detecting water maser sources, together with the impossible task of confidently disentangling nearby sources and associating them

Table 5.1: *ATCA observations: epochs and array configurations.*

array	epoch
H75	2007 October 9, 10
6D	2007 November 26
H214	2007 December 7
H214	2008 July 12, 13
6B	2008 August 15, 16, 17

with the 1.2 mm dust clumps (especially given the limited pointing accuracy of the instrument), we proposed to observe the sources with the ATCA. Using the ATCA has several advantages, foremost of which are the ability to obtain accurate positions and gain much greater sensitivity.

ATCA observations were carried out in four different array configurations over five epochs; these are listed in Table 5.1. For some sources observed by Hill et al. (2005), observations at 22 GHz are not presented (individual dust clumps sources not targeted are listed in Table 5.7), and the particular reasons are as follows:

- A small number of sources presented in Hill et al. (2005) have no reported radius (21 dust clump sources). This information is needed to calculate the probability of water maser presence. Since observations of these sources would add nothing to the current model for water maser presence they were assigned as a low priority and due to this have not been observed.

- Observations of sources located near to a declination of zero degrees are especially troubling at the ATCA. Due to this, all 1.2 mm dust clump sources within ± 2 degrees of the equatorial plane (35 dust clump sources) were excluded from the sample, with the intention of carrying out these observations with the VLA (a proposal for these observations has been accepted and is awaiting observation). In order to combat problems observing sources close to declination zero degrees, an effort was made to observe all sources within declinations ± 8 degrees in hybrid configurations, significantly increasing the achieved *uv*-coverage. Unfortunately, even tak-

ing these precautions has not allowed for data with sufficiently good quality to be obtained for all sources. In a number of instances, the relatively poor *uv*-coverage, combined with very strong nearby water maser sources, have resulted in such strong side-lobe responses that the data is rendered unusable. In these cases the respective sources have been removed from our statistics (10 sources).

- 1.2 mm dust clump sources located north of +10 degrees were not observed with the ATCA and are to be observed in the VLA sample (30 dust clump sources, but one of these has also been counted in the 'no radius measurement' group).

- Observations completed with the ATCA at one epoch (2007 November) were taken under extremely poor weather conditions (more details about these observations are give in Section 5.2.1), and have had to be excluded (16 dust clumps).

In total, 294 1.2 mm dust clumps were searched for water maser presence with the ATCA. For all observations the field of view of the telescope is almost 5 arcmin, and the HPBW is 2.3 arcmin. Observations were carried out in groups of relatively nearby sources, decreasing overheads and allowing reference pointing observations to be carried out effectively. Pointings were carried out on a strong continuum source, located within ~20 degrees of the target sources, approximately every hour. Using this method, the pointing accuracy is usually good to 5 arcsec, compared to about 20 arcsec when no pointing observations are carried out.

Targets were observed in a series of cuts, interspersed with phase calibration observations. The general observation strategy differed depending on the array and weather conditions, but in general, nearby sources were grouped together and bracketed by phase calibration observations carried out on a compact continuum source, located not more than 10 degrees from the targets. The time spent observing the targets and the time between phase calibration was tailored to most efficiently observe the targets in the allocated time on the ATCA. The average strategy was to observe each target field for 10 minutes, over five cuts, with phase calibration (onsource for 1.5 minutes) carried out every 10 minutes.

In general, these observations have allowed 5-σ detections to be made at 150 - 200 mJy in the central section of the beam. For some sources, integration times were adjusted depending on the scheduled time allotment, and due to this the sensitivity limit may be either slightly lower or slightly higher.

On each observing day, observations of a bandpass calibrator were completed. Two different sources were used; PKS B1253–055 and PKS B1921–293, both are strong at 22 GHz and are usefully at high elevations near the beginning and end of the time that the Galactic plane is visible, respectively. Primary flux calibration is with respect to observations of PKS B1934–638, which were also carried out daily.

Details of the the observations carried out in each of the array configurations are given below. Descriptions of the correlator configurations (and therefore spectral resolution and velocity coverage), individual observation strategies are also given in this section. Note that none of the data were smoothed.

H75

The first series of observations were carried out in the most compact ATCA configuration, H75 (see Table 5.2 for baseline lengths). Primarily, observations of sources located near declinations of zero degrees were intended for this array configuration, but we were able to observe some additional, early rising sources in a Director's time allocation prior to our scheduled time on 2007 October 9.

For these observations the correlator was configured to record 1024 channels across a bandwidth of 16 MHz for a single polarisation. This correlator configuration allowed for a channel spacing of 0.21 km s^{-1}, corresponding to a velocity resolution of 0.25 km s^{-1}. The velocity coverage of these observations was just over 200 km s^{-1}.

In these observations, target sources were observed for 10 minutes each, over a series of five cuts (in general) spread over several hours. Observations of a phase calibrator source were carried out every 8 - 14 minutes.

Table 5.2: *H75 configuration. Spacings between each pair of the antennas are given in metres.*

	CA02	CA03	CA04	CA05	CA06
CA01	31	77	43	82	4408
CA02		46	31	77	4378
CA03			55	89	4332
CA04				46	4378
CA05					4378

6D

The next epoch of observations were made in a 6D configuration. The baseline lengths for this 6 km array are given in Table 5.3. For these observations the correlator was configured to record 512 channels over a bandwidth of 32 MHz for a single polarisation. We made this change in correlator configuration, as from our first series of observations, it was clear that for some sources we were unable to observe the full extent of the velocity range of the emission. In these observations we made a sensible compromise, forgoing additional spectral resolution for twice the bandwidth. The resultant velocity coverage is over 400 km s^{-1} and the spectral resolution is 1.0 km s^{-1} in these observations.

Prior to carrying out these observations, the weather conditions were very poor and we were experiencing periods of rain. Due to this the observation schedule was altered to include fairly rapid switching between the target sources and phase calibration observations. Throughout the observations it was clear that the phase stability was terrible and upon processing the data it was found that the data quality was so bad that it could not be reliably used. Many of the dust clumps that were observed on this epoch, were subsequently observed during the H214 or 6B observations (31 dust clumps). Therefore, as previously described, 16 dust clump sources which were observed only at this epoch have been omitted from the analysis carried out in this chapter. The specific dust clump sources that this affected are given in Table 5.7.

Table 5.3: *6D configuration. Spacings between each pair of the antennas are given in metres.*

	CA02	CA03	CA04	CA05	CA06
CA01	367	1163	2449	2526	5878
CA02		796	2082	2158	5510
CA03			1286	1362	4714
CA04				77	3429
CA05					3352

H214

Water maser observations were carried out in this hybrid configuration over two epochs (see Table 5.4 for baseline lengths). The first epoch was during 2007 December and included only one source (G 213.705–12.597) which was observed as part of a multifrequency study of the masers associated with nearby star formation region Mon R2. Due to this the adopted correlator configuration for these observations were very different for this source, using a bandwidth of 4 MHz and 1024 channels. In this configuration the velocity coverage is limited to ~50 km s^{-1}, but the spectral resolution is increased to 0.06 km s^{-1}.

The main series of observations carried out in this array configuration were completed in 2008 July. Although scheduled with the intention of observing only those sources near a declination of zero degrees, a number of hours of Director's time were awarded on 2008 July 12 and 13 from LST 6h. This allowed a number of the dust sources with right ascensions chiefly less than 13h to additionally be observed.

The correlator configuration for the main program of observations was identical to that used in the observations carried out in the 6B and 6D configurations. That is, 512 channels were recorded over a 32 MHz bandwidth, for a single polarisation, giving a velocity coverage in excess of 400 km s^{-1} and a spectral resolution of 1.0 km s^{-1}.

The average strategy for these observations was to observe each source for

Table 5.4: *H214 configuration. Spacings between each pair of the antennas are given in metres.*

	CA02	CA03	CA04	CA05	CA06
CA01	92	230	144	247	4500
CA02		138	82	216	4408
CA03			132	240	4270
CA04				138	4378
CA05					4383

12-14 minutes over 6-7 cuts of 2 minutes each spaced over several hours. Phase calibrator observations were completed approximately every 13 minutes.

6B

The final series of observations was carried out in a 6B array in 2008 August. The baseline lengths for this configuration are presented in Table 5.5. These observations included a large proportion of the dust clump sources that were targeted, as the time allocated on the ATCA was quite large and also included a number of hours of Director's time on either side of the scheduled time on each day. Due to this, we were able to split the time up into essentially two observing sessions per day, filling the first with early rising sources, and the second with the later rising sources, and were still able to achieve sufficient *uv*-coverage to confidently position any detected sources.

The correlator was configured as for the observations carried out in the H214 and 6D array observations, giving a velocity coverage of more than 400 km s^{-1}, and a spectral resolution of 1.0 km s^{-1}.

Similar to the other observations, the observing strategy for observations in this array saw sources observed as a series of 2 minute cuts spaced over several hours. On average, sources were observed seven times, giving onsource integration times of 14 minutes. Observations of a phase calibrator were conducted approximately every seven minutes.

Table 5.5: *6B configuration. Spacings between each pair of the antennas are given in metres.*

	CA02	CA03	CA04	CA05	CA06
CA01	949	2219	2755	2969	5969
CA02		1270	1806	2020	5020
CA03			536	750	3750
CA04				214	3214
CA05					3000

5.2.2 Data reduction

All ATCA data were reduced using the MIRIAD software package (Sault, Teuben & Wright, 1995), applying the standard techniques for ATCA spectral line observations. Image cubes of the entire primary beam and usable velocity range were produced for each source. The flux densities of sources that were located away from the centre of the primary beam have been corrected to account for beam attenuation using the MIRIAD task 'linmos'. Both vector and scalar average spectra of the calibrated *uv*-data were inspected for each of the targets and cross checked with the emission identified in each of the image cubes. Spectra for each of the detected sources were produced by integrating the emission in the image cubes. The typical resultant rms noise in each spectrum was 25 - 40 mJy for sources located near the centre of the beam.

The typical synthesised beam sizes experienced in each of the array configurations are listed in Table 5.6. In both of the hybrid configurations (H75 and H214), data from antenna six was not included in the data reduction.

5.3 Results

Hill et al. (2005) presented a catalogue of 404 1.2 mm dust clumps. Towards 294 of these clumps, we present water maser data and compare our detections with the derived probability of water maser presence using the model presented

Table 5.6: *Size of the synthesised beam in each of the array configurations*

array	beam size (arcsec)
H75	28x24
H214	13x8
6B	1.7x0.5

in Chapter 3. Most of the water maser data presented are new observations, however, where appropriate, data from Chapter 6 has been used, in addition to data presented in Caswell & Breen (2010) and Forster & Caswell (1989).

Table 5.8 shows the targeted 1.2 mm dust clumps, along with their calculated probability of water maser presence, followed by the water maser data. We find a total of 165 water maser sources towards 128 of the 1.2 mm dust clumps. Spectra of each of the water masers that we detect are presented in Fig. 5.1 and are essentially ordered as the 1.2 mm dust clumps presented in Hill et al. (2005) (in order of increasing right ascension) unless there was a need for nearby sources to be vertically aligned. For the majority of sources, a velocity range of 200 km s^{-1} is shown, however, this has been reduced to 100 km s^{-1} for sources observed in the H75 configuration of the ATCA (which were carried out with a smaller bandwidth) and for one source, G 213.705–12.597, a velocity range of 40 km s^{-1} is shown (this source was observed with 4 MHz bandwidth). Confusion from strong nearby sources are marked on the individual spectra, except where they are present as features of negative intensities.

A number of the sources that we detect have been previously presented in the literature (e.g. Johnston et al., 1972; Caswell et al., 1974; Kaufmann et al., 1976; Genzel & Downes, 1977; Batchelor et al., 1980; Braz & Scalise, 1982; Braz & Epchtein, 1983; Caswell et al., 1989; Hofner & Churchwell, 1996, and references therein). However, the majority of these observations were conducted 20 or more years ago, with relatively poor positional accuracy. When combined with the often extreme variable nature of water maser sources, the task of identifying our sources with those in the literature is therefore fraught with difficulties. Since the

only certain way to match up sources with those in the literature is by position, we only compare our detections with observations of comparable positional accuracy.

Several of the sources that we detect have been observed in interferometric observations (e.g. Caswell & Breen, 2010; Caswell & Phillips, 2008; Forster & Caswell, 1989, Chapter 6), allowing us to compare our positions and therefore assessing our positional uncertainties. In general, our positional agreement with previous observations is excellent, sometimes better than 0.5 arcsec but consistently within 2 arcsec. In Chapter 6, a more extensive assessment of the positional uncertainties of those water masers showed that perhaps the largest contributor to the uncertainty was the tendency for the water maser spots to be spread out and the difference between measuring a slightly different feature at a different epoch. Here we similarly find that this is the case, and therefore expect the positional uncertainties of the water masers that we present to be accurate to 2 arcsec.

Another facet of this assessment allowed us to determine the effect that the synthesised beam has on the positional accuracy of the sources. As can be seen in Table 5.6, the beam sizes resulting from the hybrid configurations are much larger than that of the more extended 6B array. Comparisons with other measurements shows that even when the beam is large, accurate positions can be derived, since it is rarely the case that two sources show emission at the same velocities and are spatially separated by less than a synthesised beam. The much smaller beam of the 6B array has allowed for some water maser sites to be broken up into individual components, although it is likely the case that very close companions are intimately associated with the same exciting source.

There is an excellent correspondence between the locations of the detected water masers and the 1.2 mm dust sources. The vast majority of the detected water masers lie within the emission associated with one of the targeted 1.2 mm dust clumps. Four sources that are an exception to this are discussed in Section 5.3.2.

Table 5.7: *1.2 mm dust clumps (Hill et al., 2005) that have been excluded from our target list and/or subsequent analysis. Columns 1-3 and 5-7 give the dust clump name, followed by the right ascension and declination. The reason for the exclusion of each clump are contained in columns 4 and 8. A detailed description of these reasons are given in Section 5.2, but briefly; 'radius' means that no dust clump radius measurement was given; 'North' indicates that the sources lie in the northern hemisphere; 'dec0' indicates that the sources were excluded due to their close proximity to a declination of zero degrees; 'dec0f' indicates sources that were observed but failed due their proximity to declination zero degrees; and '6D' indicates sources that were observed in very poor weather conditions.*

Dust clump			Reason	Dust clump			Reason
Name	RA	Dec		Name	RA	Dec	
(l, b)	(J2000)	(J2000)		(l, b)	(J2000)	(J2000)	
(degrees)	(h m s)	(° ′ ″)		(degrees)	(h m s)	(° ′ ″)	
G 183.34+0.59	05:51:06.0	+25:45:46	North,radius	G 30.908+0.137	18:47:15.5	−01:44:18	dec0
G 189.78+0.34	06:08:34.5	+20:38:51	North	G 30.869+0.116	18:47:15.5	−01:47:06	dec0
G 189.03+0.76	06:08:40.1	+21:31:00	North	G 30.59−0.04	18:47:18.9	−02:06:07	dec0
G 189.028+0.805	06:08:45.3	+21:31:48	North	G 30.924+0.092	18:47:26.7	−01:44:42	dec0
G 188.79+1.02	06:09:06.5	+21:50:27	North	G 30.760−0.027	18:47:34.2	−01:56:41	dec0
G 192.581−0.042	06:12:52.9	+18:00:35	North	G 31.41+0.30	18:47:34.3	−01:12:47	dec0
G 192.60−0.05	06:12:54.0	+17:59:23	North	G 30.682−0.072	18:47:35.4	−02:02:07	dec0
G 192.594−0.045	06:12:54.0	+17:59:47	North	G 30.78−0.02	18:47:35.8	−01:55:13	dec0
G 206.535−16.356	05:41:42.7	−01:54:23	dec0	G 30.705−0.065	18:47:36.0	−02:01:05	dec0
G 206.54−16.35	05:41:45.4	−01:55:51	dec0	G 30.76−0.05	18:47:37.9	−01:57:45	dec0
G 259.94−0.04	08:35:31.5	−40:38:28	radius	G 30.769−0.048	18:47:38.5	−01:56:57	dec0
G 284.295−0.362	10:24:03.0	−57:47:58	radius	G 30.740−0.060	18:47:39.2	−01:58:41	dec0
G 304.890+0.636	13:08:13.5	−62:10:20	radius	G 30.749−0.048	18:47:39.6	−01:53:53	dec0
G 304.906+0.574	13:08:23.8	−62:13:56	radius	G 31.094+0.111	18:47:41.3	−01:35:05	dec0
G 304.919+0.542	13:08:31.9	−62:15:48	radius	G 30.716−0.082	18:47:41.3	−02:00:33	dec0
G 305.952+0.555	13:08:34.2	−62:15:00	radius	G 30.729−0.078	18:47:41.3	−01:59:45	dec0
G 304.952+0.522	13:08:35.4	−62:17:00	radius	G 31.06+0.09	18:47:41.3	−01:37:21	dec0
G 304.933+0.546	13:08:38.8	−62:15:32	radius	G 30.81−0.05	18:47:46.5	−01:54:16	dec0
G 304.942+0.550	13:08:43.3	−62:15:16	radius	G 31.065+0.051	18:47:50.9	−01:38:17	dec0
G 305.242+0.225	13:11:30.3	−62:33:24	6D	G 31.119+0.029	18:48:01.6	−01:36:01	dec0
G 305.355+0.194	13:12:30.5	−62:34:43	radius	G 31.28+0.06	18:48:12.4	−01:26:23	dec0
G 305.513+0.333	13:13:46.0	−62:25:37	radius	G 31.256+0.061	18:48:09.7	−01:27:50	dec0
G 305.533+0.360	13:13:55.2	−62:23:53	radius	G 31.40−0.26	18:49:33.1	−01:29:04	dec0
G 305.538+0.340	13:13:58.7	−62:25:05	radius	G 31.388−0.266	18:49:34.2	−01:29:44	dec0
G 305.519−0.040	13:14:06.1	−62:47:53	radius	G 32.80+0.19	18:50:30.7	−00:02:00	dec0
G 305.776−0.251	13:16:31.5	−62:59:02	6D	G 33.13−0.09	18:52:08.0	+00:08:10	dec0
G 331.28−0.19	16:11:26.9	−51:41:57	radius	G 33.92+0.11	18:52:50.2	+00:55:28	dec0
G 332.646−0.647	16:19:48.3	−51:02:00	6D	G 34.256+0.155	18:53:18.2	+01:14:57	dec0
G 332.695−0.609	16:19:51.7	−51:01:20	6D	G 34.24+0.13	18:53:21.7	+01:13:37	dec0
G 332.701−0.587	16:19:47.4	−51:00:08	6D	G 35.57+0.07	18:56:01.2	+02:22:59	dec0f
G 332.827−0.552	16:20:12.0	−50:53:20	radius	G 35.586+0.061	18:56:03.9	+02:23:23	dec0f
G 6.620−0.10	18:00:59.2	−23:17:02	6D	G 35.575+0.048	18:56:05.5	+02:22:27	dec0f
G 10.359−0.149	18:09:03.5	−20:02:54	6D	G 35.05−0.52	18:57:09.0	+01:39:05	dec0
G 10.575−0.347	18:10:14.5	−19:57:17	radius	G 49.459−0.317	19:23:24.9	+14:30:56	North
G 12.112−0.125	18:12:33.1	−18:30:05	6D	G 49.458−0.330	19:23:27.7	+14:30:33	North
G 12.855−0.226	18:14:25.5	−17:53:52	radius	G 49.465−0.324	19:23:27.1	+14:31:04	North
G 18.15−0.28	18:25:01.3	−13:15:35	6D	G 49.456−0.354	19:23:32.6	+14:29:52	North
G 18.142−0.297	18:25:03.5	−13:16:15	6D	G 49.482−0.355	19:23:35.9	+14:31:04	North
G 18.165−0.293	18:25:05.1	−13:14:55	6D	G 49.472−0.366	19:23:37.1	+14:30:16	North
G 18.177−0.296	18:25:07.3	−13:14:23	6D	G 49.533−0.338	19:23:38.2	+14:34:16	North

Table 5.7: – continued

Dust clump Name (l, b) (degrees)	RA (J2000) (h m s)	Dec (J2000) (^{o} ′ ″)	Reason	Dust clump Name (l, b) (degrees)	RA (J2000) (h m s)	Dec (J2000) (^{o} ′ ″)	Reason
G 18.30–0.39	18:25:42.2	–13:10:32	6D	G 49.513–0.356	19:23:39.8	+14:32:40	North
G 19.70–0.27	18:27:55.5	–11:52:39	6D	G 49.528–0.348	19:23:39.8	+14:33:44	North
G 15.028–0.710	18:20:31.4	–16:12:51	radius	G 49.49–0.37	19:23:39.8	+14:31:05	North
G 16.871–2.154	18:29:24.2	–15:15:34	radius	G 49.488–0.385	19:23:43.1	+14:30:32	North
G 16.86–2.15	18:29:24.4	–15:16:04	6D	G 49.481–0.401	19:23:45.9	+14:29:44	North
G 16.883–2.188	18:29:33.1	–15:15:50	6D	G 49.465–0.417	19:23:47.5	+14:28:24	North
G 25.70+0.04	18:38:03.0	–06:24:01	dec0f	G 49.462–0.423	19:23:48.6	+14:28:08	North
G 28.231+0.367	18:42:43.1	–04:09:56	dec0f	G 49.474–0.420	19:23:49.2	+14:28:48	North
G 28.287+0.010	18:42:54.9	–04:07:40	dec0f	G 49.48–0.419	19:23:50.3	+14:29:28	North
G 29.912–0.045	18:46:05.0	–02:42:29	dec0f	G 49.536–0.395	19:23:50.3	+14:32:48	North
G 29.937–0.054	18:46:09.8	–02:41:25	dec0f	G 49.494–0.420	19:23:50.8	+14:29:52	North
G 29.945–0.059	18:46:11.5	–02:42:05	dec0f	G 49.508–0.409	19:23:50.8	+14:30:56	North
G 30.533–0.023	18:46:58.6	–02:07:27	dec0f	G 49.505–0.421	19:23:53.0	+14:30:24	North
G 30.855+0.149	18:47:07.0	–01:46:50	dec0	G 59.794+0.076	19:43:10.0	+23:44:59	North
G 30.89+0.16	18:47:08.6	–01:44:02	dec0	G 59.78–0.06	19:43:11.2	+23:44:03	North
G 30.894+0.140	18:47:13.4	–01:44:58	dec0				

Table 5.8: *Target 1.2 mm dust clumps, probability of water maser association, followed by a description of the water maser observations including any detections. Columns 1-3 give the 1.2 mm dust clump name followed by the right ascension and declination (Hill et al., 2005) and column 4 shows the calculated probability of water maser presence (using the model derived in Chapter 3). Column 5 gives information about the ATCA array configuration used in the water maser observations followed by the epoch. In some cases, data is taken from Chapter 6 which is marked in column 5 with a 'BCEP' followed by the year of the observations. This format is also followed for sources taken from Caswell & Breen (2010) (CB) and Forster & Caswell (1989) (FC). Columns 6-13 give details of the water masers detected towards the dust clumps (which in some cases is more than one source), as well as 5-σ detection limits where no source is detected, specifically; column 6: water maser Galactic coordinates; column 7: water maser right ascension; column 8: water maser declination; column 9: separation between water maser and 1.2 mm dust clump peak (arcsec); column 10: water maser peak flux density (Jy) or if preceded by '<' the 5-σ detection limit (mJy); column 11: velocity of the water maser peak emission (km s^{-1}); column 12: velocity range of either the detected emission, or the observed velocity range if no detection; and column 13: integrated flux density of the water maser emission (Jy km s^{-1}). Column 14 presents notes related to the sources, which in most cases are further discussed in Section 5.3.1.*

Dust clump					Water maser								
Name (l, b) (degrees)	RA (J2000) (h m s)	Dec (J2000) (° ′ ″)	prob.	array and epoch	Name (l, b) (degrees)	RA (J2000) (h m s)	Dec (J2000) (° ′ ″)	Sep. (″)	Sp (Jy)	Vp	Vr	Int	notes
G 213.61–12.6	06:07:47.9	–06:22:57	3.7E–4	H214dec07	G 213.705–12.597	06 07 47.85	–06 22 56.6	1	92	12	4,13	78	Mon R2
G 269.45–1.47	09:03:13.5	–48:55:22	0.15	H214jul08	G 269.461–1.471	09 03 15.01	–48 55 31.4	18	0.6	51	49,52	1.6	
				H214jul08	G 269.457–1.467	09 03 14.87	–48 55 12.6	24	0.8	66	56,69	1.7	
G 269.15–1.13	09:03:32.3	–48:28:00	1.2E–4	H214jul08	G 269.153–1.128	09 03 33.52	–48 28 03.0	12	26	7	6,16	40	
G 270.25+0.84	09:16:41.4	–47:55:46	4.1E–5	H214jul08	G 270.254+0.835	09 16 41.13	–47 56 11.3	25	98	9	4,17	199	
				H214jul08	G 270.257+0.834	09 16 41.62	–47 56 17.4	31	60	8	–2,48	227	
G 284.271–0.391	10:23:47.0	–57:48:38	8.5E–5	H214jul08					<155		–200,150		
G 284.307–0.376	10:24:04.0	–57:49:02	1.5E–3	H214jul08					<155		–200,150		
G 284.338–0.417	10:24:06.0	–57:52:06	5.4E–5	H214jul08					<400		–200,150		
G 284.35–0.42	10:24:10.0	–57:52:39	1.4E–4	H214jul08	G 284.351–0.418	10 24 10.92	–57 52 33.9	9	233	7	–32,61	847	

Table 5.8: – continued

Dust clump					Water maser							
Name (l, b) (degrees)	RA (J2000) (h m s)	Dec (J2000) (° ′ ″)	prob.	array and epoch	Name (l, b) (degrees)	RA (J2000) (h m s)	Dec (J2000) (° ′ ″)	Sep. (″)	Sp (Jy)	Vp	Vr	Int	notes
G 284.345–0.404	10:24:12.0	–57:51:42	1.5E–4	H214jul08					<280		–200,150		
G 284.341–0.389	10:24:14.0	–57:50:46	5.8E–3	H214jul08					<215		–200,150		
G 284.328–0.365	10:24:15.0	–57:49:10	4.9E–5	H214jul08	G 284.329–0.365	10 24 15.27	–57 49 09.4	2	0.8	1	–5,1	1.7	
G 284.384–0.441	10:24:18.0	–57:54:46	1.4E–4	H214jul08					<185		–200,150		
G 284.344–0.366	10:24:21.0	–57:49:42	1.5E–4	H214jul08					<156		–200,150		
G 284.352–0.353	10:24:27.0	–57:49:18	1.9E–3	H214jul08					<200		–200,150		
G 287.37+0.65	10:48:05.2	–58:26:40	3.1E–4	H214jul08	G 287.372+0.644	10 48 04.59	–58 27 01.4	22	5	–1	–21,7	12	
G 290.40–2.91	10:57:33.0	–62:58:54	9.4E–5	H214jul08	G 290.411–2.914	10 57 34.20	–62 59 02.4	12	12	–13	–32,8	100	
G 291.256–0.769	11:11:33.9	–61:21:22	1.8E–4	6Baug08	G 291.257–0.767	11 11 34.56	–61 21 16.8	7	2.1	–27	–28,–1	6.4	
				6Baug08	G 291.254–0.768	11 11 32.89	–61 21 14.9	10	1.7	–29	–29,–23	2.4	
G 291.256–0.743	11:11:38.3	–61:19:54	3.7E–4	6Baug08	G 291.256–0.739	11 11 39.22	–61 19 42.6	12	11	–25	–26,–24	13	
G 291.27–0.70	11:11:54.8	–61:18:26	0.046	H214jul08	G 291.274–0.709	11 11 53.46	–61 18 24.3	10	61	–32	–53,–4	148	
				H214jul08	G 291.271–0.719	11 11 49.82	–61 18 53.8	45	218	–94	–101,–19	705	BS
G 291.288–0.706	11:12:00.6	–61:18:34	1.6E–4	H214jul08	G 291.284–0.716	11 11 56.68	–61 19 00.9	57	730	–128	–136,–108	3789	clump edge, BS
G 291.302–0.693	11:12:09.4	–61:18:10	1.8E–4	6Baug08					<304		–200,150		
G 291.309–0.681	11:12:15.0	–61:17:38	7.0E–4	6Baug08	G 291.314–0.680	11 12 17.21	–61 17 44.2	17	8.4	–29	–32,–22	16	
G 290.37+1.66	11:12:16.1	–58:46:19	9.4E–5	BCEP03	G 290.374+1.661	11 12 17.98	–58 46 21.6	15	3.5	–12	–20,–10		
				BCEP03	G 290.384+1.663	11 12 22.53	–58 46 29.0	51	6	–38	–50,–35		
G 291.587–0.499	11:14:54.5	–61:13:32	0.69	6Baug08					<128		–200,150		
G 291.576–0.468	11:14:57.8	–61:11:40	8.3E–3	6Baug08					<267		–200,150		
G 291.572–0.450	11:14:58.9	–61:10:36	3.1E–4	6Baug08					<247		–200,150		
G 291.608–0.532	11:15:01.1	–61:15:56	0.19	BCEP03	G 291.610–0.529	11 15 02.58	–61 15 48.8	12	18	13	–66,20		
G 291.597–0.496	11:15:02.2	–61:13:40	0.59	6Baug08					<128		–200,150		
G 291.58–0.53	11:15:06.4	–61:09:38	5.3E–3	6Baug08	G 291.579–0.431	11 15 05.77	–61 09 39.5	6	120	11	–2,16	776	spread ∼2″
				6Baug08	G 291.579–0.434	11 15 05.19	–61 09 49.9	15	14.3	16.6	16,20	30	
G 291.630–0.545	11:15:08.9	–61:17:08	0.89	BCEP03	G 291.629–0.541	11 15 08.88	–61 16 54.8	13	70	11	8,16		
G 291.614–0.443	11:15:19.9	–61:11:08	5.9E–5	6Baug08	G 291.618–0.442	11 15 21.82	–61 11 09.3	14	0.7	15	0,15	2.4	slightly spread
				6Baug08	G 291.614–0.446	11 15 19.45	–61 11 15.2	8	0.3	7	7,8	0.2	
G 293.824–0.762	11:32:01.4	–62:13:18	2.3E–3	H214jul08					<1065		–200,150		
G 293.82–0.74	11:32:06.1	–62:12:22	6.3E–3	H214jul08	G 293.828–0.746	11 32 05.88	–62 12 26.1	4	1.5	59	15,68	9	
G 293.892–0.782	11:32:32.4	–62:15:42	2.3E–4	H214jul08					<115		–200,150		
G 293.95–0.8	11:32:42.0	–62:22:35	0.017	H214jul08	G 293.951–0.894	11 32 43.38	–62 23 07.1	34	15	35	29,51	28	
G 293.942–0.876	11:32:42.0	–62:21:55	0.012	H214jul08					<120		–200,150		
G 293.989–0.936	11:32:55.8	–62:26:11	0.038	H214jul08	G 293.993–0.931	11 32 58.42	–62 25 57.6	23	4.3	46	45,48	7	
G 294.52–1.60	11:35:31.0	–63:14:36	2.0E–5	H214jul08	G 294.512–1.621	11 35 32.44	–63 14 42.8	12	49	–14	–19,–9	182	
G 294.945–1.737	11:38:57.1	–63:28:46	2.4E–5	H214jul08					<710		–200,150		
G 294.97–1.7	11:39:09.0	–63:28:38	4.1E–5	H214jul08	G 294.977–1.734	11 39 14.25	–63 29 05.2	44	3.9	–7	–18,3	15	clump pos bad, BCEP
G 294.989–1.720	11:39:22.1	–63:28:30	2.6E–5	H214jul08	G 294.990–1.719	11 39 23.18	–63 28 27.5	8	25	–3	–12,–2	38	

Table 5.8: – continued

Dust clump					Water maser								
Name (l, b) (degrees)	RA (J2000) (h m s)	Dec (J2000) (° ′ ″)	prob.	array and epoch	Name (l, b) (degrees)	RA (J2000) (h m s)	Dec (J2000) (° ′ ″)	Sep. (″)	Sp (Jy)	Vp	Vr	Int	notes
G 298.26+0.7	12:11:45.4	−61:45:42	2.6E−4	H214jul08	G 298.259+0.748	12 11 46.72	−61 45 47.5	11	0.2	16	−29,16	0.3	
G 299.02+0.1	12:17:18.6	−62:28:40	0.035	H214jul08	G 299.013+0.128	12 17 24.65	−62 29 04.4	48	106	19	−3,30	164	clump pos bad
G 299.024+0.130	12:17:30.2	−62:29:04	2.3E−3	H214jul08					<184		−200,150		
G 300.455−0.190	12:29:37.3	−62:57:23	0.014	H214jul08					<157		−200,150		
G 300.51−0.1	12:30:02.0	−62:56:35	5.4E−3	H75oct07	G 300.504−0.176	12 30 03.60	−62 56 48.3	27	153	11	−37,16	421	
G 301.14−0.2	12:35:29.1	−63:01:32	0.010	H214jul08	G 301.136−0.226	12 35 34.92	−63 02 31.0	72	322	−50	−72,−23	1606	spread 5", clump pos bad
G 302.03−0.06	12:43:32.1	−62:55:06	3.4E−4	6Baug08					<111		−200,150		
G 305.145+0.208	13:10:40.5	−62:34:53	4.5E−5	H214jul08					<159		−200,150		
G 305.137+0.069	13:10:42.0	−62:43:13	1.0E−4	H214jul08	G 305.136+0.069	13 10 41.53	−62 43 12.7	3	1.2	−39	−40,−39	1.3	
				H214jul08	G 305.138+0.067	13 10 42.59	−62 43 20.4	8	4.2	−38	−39,−37	6	
				H214jul08	G 305.141+0.065	13 10 44.21	−62 43 27.3	21	0.5	−16	−71,−15	0.7	
G 305.201+0.241	13:11:08.3	−62:32:37	2.2E−5	H214jul08					<169		−200,150		
G 305.202+0.230	13:11:09.4	−62:33:17	2.8E−4	H214jul08					<158		−200,150		
G 305.20+0.02	13:11:12.3	−62:44:57	1.2E−3	H214jul08					<180		−200,150		
G 305.192−0.006	13:11:13.6	−62:47:29	8.5E−5	BCEP03	G 305.191−0.006	13 11 12.95	−62 47 27.7	5	25	31	28,36		
G 305.21+0.21	13:11:14.1	−62:34:45	0.02	H214jul08	G 305.208+0.206	13 11 13.60	−62 34 41.5	4	96	−39	−53,−30	425	
G 305.197+0.007	13:11:15.9	−62:46:41	1.8E−3	H214jul08	G 305.199+0.007	13 11 16.72	−62 46 37.6	7	16	−39	−42,1	40	
G 305.200+0.02	13:11:17.0	−62:45:53	4.1E−5	H214jul08					<314		−200,150		
G 305.226+0.275	13:11:19.8	−62:30:29	1.1E−4	6Baug08	G 305.223+0.275	13 11 18.50	−62 30 30.6	9	0.9	−36	−47,−34	2.8	
G 305.228+0.286	13:11:20.9	−62:29:48	3.4E−5	6Baug08					<115		−210,140		
G 305.238+0.261	13:11:26.7	−62:31:16	5.9E−4	6Baug08					<110		−210,140		
G 305.248+0.245	13:11:32.5	−62:32:12	1.6E−4	6Baug08	G 305.251+0.251	13 11 33.94	−62 31 47.2	27	0.8	−39	−42,−36	1.5	
G 305.233−0.023	13:11:35.8	−62:48:16	1.4E−4	6Baug08					<105		−210,140		
G 305.269−0.010	13:11:54.4	−62:47:19	8.5E−4	CB07	G 305.269−0.003	13 11 53.82	−62 46 55.6	24	0.8	−60	−83,−53		
G 305.358+0.203	13:12:31.6	−62:34:11	6.9E−3	6Baug08	G 305.359+0.200	13 12 32.12	−62 34 21.0	11	5	−85	−95,54	39	BS
G 305.362+0.185	13:12:34.7	−62:35:15	4.5E−4	6Baug08	G 305.366+0.184	13 12 36.75	−62 35 14.8	14	1.1	−17	−17,−16	1.1	
G 305.361+0.151	13:12:35.2	−62:37:15	9.4E−5	6Baug08	G 305.362+0.150	13 12 35.87	−62 37 18.9	6	120	−35	−41,−31	280	
G 305.37+0.21	13:12:36.3	−62:33:39	4.1E−4	6Baug08	G 305.368+0.212	13 12 36.21	−62 33 34.4	5	25	−33	−88,39	64	spread 2"
				6Baug08	G 305.369+0.212	13 12 37.04	−62 33 35.5	6	0.35	7	5,7	0.4	
G 305.340−0.172	13:12:38.1	−62:36:42	1.0E−4	6Baug08					<360		−210,140		
G 305.520−0.020	13:14:06.1	−62:46:41	5.9E−5	6Baug08					<135		−210,140		
G 305.549+0.002	13:14:20.0	−62:45:13	2.8E−4	6Baug08					<112		−210,140		
G 305.552+0.013	13:14:21.2	−62:44:33	1.6E−4	6Baug08					<162		−210,140		
G 305.552+0.012	13:14:22.4	−62:46:01	1.3E−3	6Baug08	G 305.553−0.012	13 14 22.79	−62 45 59.4	3	1.1	−44	−44,-7	3.8	
G 305.561+0.012	13:14:25.8	−62:44:32	4.8E−3	CB07	G 305.561+0.013	13 14 25.68	−62 44 30.0	2	0.7	−42	−48,−38		

Table 5.8: – continued

Dust clump					Water maser								
Name (l, b) (degrees)	RA (J2000) (h m s)	Dec (J2000) (^{o} ′ ″)	prob.	array and epoch	Name (l, b) (degrees)	RA (J2000) (h m s)	Dec (J2000) (^{o} ′ ″)	Sep. (″)	Sp (Jy)	Vp	Vr	Int	notes
G 305.581+0.033	13:14:35.1	−62:43:02	5.3E−3	6Baug08					<113		−210,140		
G 305.605+0.010	13:14:49.1	−62:44:24	1.8E−4	6Baug08					<111		−210,140		
G 305.81−0.25	13:16:43.2	−62:58:37	1.0E−3	BCEP03	G 305.799−0.245	13 16 42.92	−62 58 31.7	6	400	−26	−45,35		
G 305.833−0.196	13:16:58.3	−62:55:25	2.0E−4	6Baug08					<126		−210,140		
G 306.33−0.3	13:21:18.2	−63:00:43	4.5E−5	BCEP03	G 306.318−0.331	13 21 20.87	−63 00 22.7	27	2.1	−19 −24,−14			
G 306.319−0.343	13:21:18.2	−63:01:07	1.8E−5	H75oct07					<133		−10,−190		
G 306.343−0.302	13:21:32.3	−62:58:26	2.0E−5	6Baug08					<156		−200,150		
G 306.345−0.345	13:21:34.6	−62:59:54	2.0E−5	H75oct07	G 306.341−0.321	13 21 32.33	−62 59 36.9	23	0.7	−20	−22,−14	0.6	
G 309.917+0.494	13:50:38.2	−61:34:20	6.5E−5	6Baug08					<137		−200,150		
G 309.92+0.4	13:50:41.6	−61:35:15	0.025	6Baug08					<137		−200,150		
G 318.913−0.162	15:00:33.6	−58:58:05	4.9E−5	6Baug08	G 318.916−0.164	15 00 35.18	−58 58 06.4	19	0.2	−45	−46,−18	0.5	
G 318.92−0.68	15:00:55.3	−58:58:54	5.4E−5	BCEP04	G 318.948−0.196a	15 00 55.18	−58 58 51.6	3	9	−36	−44,−27		
				BCEP04	G 318.948−0.196b	15 00 55.33	−58 58 53.6	1	7	−38	−39,−21		
G 323.74−0.3	15:31:41.6	−56:30:11	1.6E−4	BCEP03	G 323.740−0.263	15 31 45.48	−56 30 49.6	50	140	−50	−72,−46		
G 330.95−0.18	16:09:48.8	−51:53:51	0.28	BCEP03	G 330.954−0.182	16 09 52.65	−51 54 54.6	73	240	−80	−150,70		
G 332.640−0.586	16:19:30.5	−51:02:40	3.4E−5	6Baug08					<144		−150,200		
G 332.648−0.606	16:19:38.1	−51:03:12	0.16	6Baug08	G 332.654−0.614	16 19 38.53	−51 03 38.3	26	1.4	−56	−57,−52	2.8	
				6Baug08	G 332.653−0.621	16 19 43.50	−51 03 36.6	57	40	−45	−52,−44	42	
G 332.73−0.62	16:20:02.7	−51:00:32	2.4E−5	6Baug08	G 332.725−0.621	16 20 02.95	−51 00 32.3	2	5	−8	−52,−5	8	
G 332.777−0.584	16:20:07.0	−50:56:48	3.1E−5	6Baug08					<143		−150,200		
G 332.627−0.511	16:20:07.0	−51:00:00	2.6E−5	6Baug08	G 332.737−0.620	16 20 05.92	−51 00 00.5	10	0.4	−52	−54,−51	0.7	
G 332.794−0.598	16:20:15.0	−50:56:40	6.5E−5	6Baug08					<143		−150,200		
G 0.204+0.051	17:45:54.3	−28:44:08	9.1E−3	6Baug08					<126		−150,200		
G 0.49+0.19	17:46:03.9	−28:24:58	5.9E−5	6Baug08	G 0.496+0.188	17 46 03.99	−28 24 51.7	6	0.5	0	−4,28	2.4	
				6Baug08	G 0.497+0.188	17 46 03.98	−28 24 50.1	8	1.0	−8	−13,0	3.6	
G 0.266−0.034	17:46:07.1	−28:41:28	9.1E−3	6Baug08					<131		−150,200		
G 0.21−0.00	17:46:07.7	−28:45:20	0.025	BCEP04	G 0.209−0.002	17 46 07.44	−28 45 32.1	13	2.2	39	18,42		
				BCEP04	G 0.212−0.002	17 46 07.86	−28 45 23.0	4	0.9	56	55,56		
G 0.497+0.170	17:46:08.2	−28:25:23	4.5E−5	6Baug08					<113		−150,200		
G 0.24+0.01	17:46:09.5	−28:43:36	0.91	6Baug08					<120		−150,200		
G 0.527+0.181	17:46:10.1	−28:23:31	9.4E−5	6Baug08	G 0.527+0.181	17 46 10.00	−28 23 30.9	1	1.0	−1	−42,0	1.2	
G 0.271+0.022	17:46:10.7	−28:41:36	3.3E−3	6Baug08					<131		−150,200		
G 0.26+0.01	17:46:11.4	−28:42:40	1.0	6Baug08	G 0.261+0.016	17 46 10.63	−28 42 17.6	25	1.5	37	35,38	2.5	
G 0.83+0.18	17:46:52.8	−28:07:35	1.8E−4	6Baug08	G 0.837+0.183	17 46 53.35	−28 07 34.3	7	0.5	−39	−39,−38	0.8	
				6Baug08	G 0.835+0.184	17 46 52.80	−28 07 35.8	1	1	6	−32,7	5	
G 0.331−0.164	17:47:00.0	−28:45:20	1.6E−3	6Baug08					<116		−150,200		
G 0.310−0.170	17:47:01.2	−28:45:36	9.4E−5	6Baug08	G 0.306−0.170	17 47 00.60	−28 45 45.4	12	0.6	11	10,12	0.7	

Table 5.8: – continued

Dust clump					Water maser								
Name (l, b) (degrees)	RA (J2000) (h m s)	Dec (J2000) (° ′ ″)	prob.	array and epoch	Name (l, b) (degrees)	RA (J2000) (h m s)	Dec (J2000) (° ′ ″)	Sep. (″)	Sp (Jy)	Vp	Vr	Int	notes
G 0.32–0.20	17:47:09.1	–28:46:16	1.0	BCEP04	G 0.316–0.201	17 47 09.29	–28 46 15.5	3	22	23	14,31		
G 0.325–0.242	17:47:20.1	–28:47:04	7.8E–5	6Baug08					<115		–150,200		
G 1.124–0.065	17:48:31.6	–28:00:31	2.2E–3	6Baug08					<240		–150,200		
G 1.134–0.073	17:48:34.7	–28:00:16	3.1E–4	6Baug08					<240		–150,200		
G 1.105–0.098	17:48:36.4	–28:02:31	4.1E–4	6Baug08					<137		–150,200		
G 1.13–0.11	17:48:41.9	–28:01:44	1.0	6Baug08	G 1.127–0.106	17 48 41.38	–28 01 38.7	9	5	–23	–24,–21	12	
G 1.14–0.12	17:48:48.5	–28:01:13	0.077	6Baug08	G 1.147–0.124	17 48 48.53	–28 01 11.3	2	43	–20	–23,–8	137	
G 0.55–0.85	17:50:14.5	–28:54:31	7.0E–4	6Baug08	G 0.546–0.851a	17 50 14.44	–28 54 30.1	1	499	34	15,44	1164	
				6Baug08	G 0.546–0.851b	17 50 14.39	–28 54 29.7	2	30	13	–67,105	280	wide vel range
				6Baug08	G 0.546–0.851c	17 50 14.51	–28 54 30.8	0	29	18	15,21	61	
G 0.549–0.868	17:50:18.8	–28:53:14	2.3E–4	6Baug08					<2645		–150,200		
G 0.627–0.848	17:50:24.9	–28:50:15	3.4E–5	6Baug08	G 0.627–0.838	17 50 22.69	–28 49 57.2	18	0.4	124	124,126	0.4	RS
G 0.600–0.871	17:50:26.7	–28:52:23	5.9E–05	6Baug08					<145		–150,200		
G 2.54+0.20	17:50:46.5	–26:39:45	4.4E–4	BCEP04	G 2.536+0.198	17 50 46.66	–26 39 44.9	2	30	25	–1,63		
G 5.48–0.24	17:59:04.6	–24:20:55	0.36	6Baug08					<136		–150,200		
G 5.504–0.246	17:59:07.5	–24:19:19	0.046	6Baug08	G 5.513–0.255	17 59 10.25	–24 19 17.6	38	0.2	22	18,23	0.4	on clump edge
G 5.89–0.39	18:00:31.0	–24:03:59	1.9E–3	BCEP03	G 5.886–0.392	18 00 30.52	–24 03 58.2	7	40	11	–10,23		
G 5.90–0.42	18:00:40.9	–24:04:21	4.4E–4	BCEP04	G 5.901–0.430	18 00 40.95	–24 04 19.6	2	3.9	14	–40,30		
G 5.90–0.44	18:00:43.9	–24:04:47	6.4E–4	BCEP04	G 5.897–0.445	18 00 43.90	–24 04 58.1	1	0.9	19	19,20		
G 6.53–0.10	18:00:50.9	–23:21:29	0.77	BCEP04	G 6.534–0.105	18 00 49.44	–23 21 40.2	23	0.5	22	6,23		
G 6.60–0.08	18:00:54.1	–23:17:02	1.1E–5	BCEP04	G 6.611–0.082	18 00 54.15	–23 17 00.8	1	7	6	–34,11		
G 8.127+0.255	18:02:52.8	–21:47:54	1.1E–4	6Baug08					<130		–140,210		
G 8.138+0.246	18:02:56.2	–21:47:38	1.5E–3	6Baug08					<130		–140,210		
G 8.13+0.22	18:03:00.8	–21:48:10	1.9E–3	6Baug08					<4256	–140,210			
G 5.948–1.125	18:03:26.3	–24:22:29	5.4E–5	6Baug08	G 5.947–1.127	18 03 26.61	–24 22 35.7	8	5	8	6,10	7	
G 5.975–1.146	18:03:34.5	–24:21:41	3.4E–5	6Baug08					<135		–140,210		
G 5.971–1.158	18:03:36.8	–24:22:13	7.8E–5	6Baug08					<135		–140,210		
G 5.97–1.17	18:03:40.9	–24:22:37	4.1E–4	6Baug08					<248		–140,210		
G 10.10+0.73	18:05:15.6	–19:50:55	1.4E–5	6Baug08					<129		–140,210		
G 9.62+0.19	18:06:14.8	–20:31:37	7.0E–4	BCEP03	G 9.620+0.194	18 06 14.97	–20 31 37.5	2	25	5	–30,50		
				BCEP03	G 9.622+0.195	18 06 14.88	–20 31 31.0	6	1.4	21	0,22		
G 8.68–0.36	18:06:18.9	–21:37:21	0.046	6Baug08	G 8.672–0.354	18 06 18.85	–21 37 19.9	1	8	3	–17,5	39	
				6Baug08	G 8.669–0.356a	18 06 19.04	–21 37 31.7	11	5	25	23,26	8	
				6Baug08	G 8.670–0.356	18 06 19.12	–21 37 29.7	9	1.2	31	30,32	1.4	
				6Baug08	G 8.669–0.356b	18 06 18.94	–21 37 32.2	11	10	32	31,35	20	
				6Baug08	G 8.667–0.357	18 06 18.95	–21 37 39.3	18	1.5	36	35,41	2.4	
				6Baug08	G 8.669–0.356c	18 06 19.03	–21 37 31.8	11	3.3	42	38,44	9	

Table 5.8: – continued

Dust clump					Water maser								
Name (l, b) (degrees)	RA (J2000) (h m s)	Dec (J2000) (° ′ ″)	prob.	array and epoch	Name (l, b) (degrees)	RA (J2000) (h m s)	Dec (J2000) (° ′ ″)	Sep. (″)	Sp (Jy)	Vp	Vr	Int	notes
G 8.686–0.366	18:06:23.5	–21:36:57	3.3E–3	6Baug08					<256		–140,210		
G 8.644–0.395	18:06:24.6	–21:40:01	1.6E–4	6Baug08					<120				
G 8.713–0.364	18:06:26.4	–21:35:29	0.011	6Baug08					<123				
G 8.735–0.362	18:06:28.7	–21:34:17	0.010	6Baug08	G 8.732–0.368	18 06 29.70	–21 34 36.4	24	1.4	50	31,52	6	
G 8.724–0.401a	18:06:36.1	–21:36:01	8.5E–5	6Baug08					<140		–140,210		
				6Baug08	G 8.727–0.395	18 06 35.08	–21 35 38.6	*	1.1	36	36,42	1.6	dust not listed?
G 8.724–0.401b	18:06:36.7	–21:37:05	4.1E–4	6Baug08					<113		–140,210		
G 8.718–0.410	18:06:37.3	–21:36:33	2.4E–5	6Baug08					<113		–140,210		
G 9.966–0.020	18:07:45.8	–20:19:47	3.1E–5	6Baug08					<128		–140,210		
G 9.99–0.03	18:07:50.4	–20:18:51	1.5E–3	6Baug08	G 9.986–0.028	18 07 50.12	–20 18 56.6	7	14	46	40,60	38	
G 10.001–0.033	18:07:53.2	–20:18:19	1.1E–4	6Baug08					<108		–140,210		
G 10.47+0.02	18:08:37.9	–19:51:41	0.99	BCEP03	G 10.473+0.027	18 08 38.30	–19 51 48.8	10	45	60	30,93		
				BCEP03	G 10.480+0.034	18 08 37.69	–19 51 12.4	29	12	64	63,65		BCEP no det. 04
G 10.44–0.01	18:08:44.9	–19:54:38	7.6E–3	BCEP04	G 10.455–0.018	18 08 45.01	–19 54 35.1	3	6	71	58,85		
G 10.287–0.110	18:08:45.9	–20:05:34	9.4E–5	6Baug08					<314		–140,210		
G 10.284–0.126	18:08:49.4	–20:05:58	7.1E–5	6Baug08	G 10.288–0.125	18 08 49.42	–20 05 58.0	0	0.9	17	16,18	1.1	
				6Baug08	G 10.287–0.125a	18 08 49.36	–20 05 58.6	1	1.6	13	13,17	3.9	
				6Baug08	G 10.287–0.125b	18 08 49.28	–20 05 59.5	2	0.5	6	5,7	0.7	
G 10.288–0.127	18:08:52.4	–20:05:58	5.4E–5	6Baug08					<110		–140,210		
G 10.29–0.14	18:08:55.5	–20:05:58	2.3E–4	6Baug08					<209		–140,210		
G 10.343–0.142	18:09:00.0	–20:03:34	3.1E–5	BCEP04	G 10.342–0.143	18 09 00.11	–20 03 35.8	2	4.8	8	–40,61		
G 10.32–0.15	18:09:01.5	–20:05:08	7.7E–4	BCEP04	G 10.323–0.160	18 09 01.57	–20 05 07.6	1	3.2	–3	–6,62		
G 10.146–0.314	18:09:14.2	–20:18:53	3.3E–3	6Baug08					<125		–140,210		
G 10.191–0.307	18:09:18.2	–20:16:21	4.5E–5	6Baug08					<158		–140,210		
G 10.148–0.331	18:09:18.2	–20:19:17	1.3E–3	6Baug08					<133		–140,210		
G 10.214–0.305	18:09:20.5	–20:15:01	9.4E–5	6Baug08	G 10.215–0.305	18 09 20.72	–20 15 01.0	3	0.6	16	2,8	2.6	
G 10.191–0.308	18:09:21.6	–20:16:21	4.5E–4	6Baug08					<158		–140,210		
G 10.15–0.34	18:09:21.6	–20:19:25	0.099	6Baug08					<135		–140,210		
G 10.213–0.326	18:09:25.0	–20:15:41	0.042	6Baug08					<268		–140,210		
G 10.188–0.344	18:09:26.2	–20:17:33	0.025	6Baug08					<114		–140,210		
G 10.133–0.378	18:09:26.7	–20:21:25	5.9E–4	6Baug08					<126		–140,210		
G 10.164–0.360	18:09:26.7	–20:19:17	0.95	6Baug08	G 10.157–0.366	18 09 27.04	–20 19 49.2	34	0.7	–22	–24,–22	1.1	
G 10.237–0.328	18:09:28.4	–20:14:29	7.8E–5	6Baug08					<121		–140,210		
G 10.206–0.350	18:09:29.6	–20:16:45	0.017	6Baug08					<269		–140,210		
G 10.184–0.370	18:09:31.3	–20:18:29	1.0E–4	6Baug08					<184		–140,210		
G 10.198–0.372	18:09:33.5	–20:17:49	5.9E–4	6Baug08					<141		–140,210		
G 10.138–0.419	18:09:34.6	–20:22:21	1.5E–4	6Baug08					<128		–140,210		
G 10.149–0.407	18:09:35.3	–20:21:25	4.9E–4	6Baug08					<128		–140,210		

Table 5.8: – continued

Dust clump					Water maser								
Name (l, b) (degrees)	RA (J2000) (h m s)	Dec (J2000) (^{o} ′ ″)	prob.	array and epoch	Name (l, b) (degrees)	RA (J2000) (h m s)	Dec (J2000) (^{o} ′ ″)	Sep. (″)	Sp (Jy)	Vp	Vr	Int	notes
G 10.165–0.403	18:09:36.4	–20:20:29	4.5E–4	6Baug08					<142		–140,210		
G 10.194–0.387	18:09:36.4	–20:18:29	5.8E–4	6Baug08					<192		–140,210		
G 10.186–0.404	18:09:39.2	–20:19:25	5.4E–5	6Baug08					<142		–140,210		
G 10.63–0.33B	18:10:15.7	–19:54:45	0.017	6Baug08					<123		–140,210		
G 10.62–0.33	18:10:18.0	–19:54:05	0.042	6Baug08					<180		–140,210		
G 9.88–0.75	18:10:19.0	–20:45:33	0.22	6Baug08	G 9.878–0.750	18 10 18.74	–20 45 38.4	7	0.9	31	23,31	1.8	
G 9.924–0.749	18:10:24.1	–20:43:09	4.1E–4	6Baug08					<114		–140,210		
G 10.62–0.38	18:10:29.4	–19:55:41	0.96	BCEP03	G 10.623–0.383	18 10 28.57	–19 55 49.4	14	350	2	–11,5		
G 10.620–0.441	18:10:41.1	–19:57:41	1.4E–4	6Baug08					<114		–140,210		
G 11.075–0.384	18:11:24.4	–19:32:04	7.7E–4	6Baug08					<115		–140,210		
G 11.11–0.34	18:11:31.8	–19:30:44	0.27	6Baug08					<114		–140,210		
G 11.117–0.413	18:11:35.8	–19:30:44	3.7E–4	6Baug08					<140		–140,210		
G 12.88+0.48	18:11:51.4	–17:31:30	0.025	6Baug08	G 12.889+0.489	18 11 51.46	–17 31 28.9	1	8	29	28,32	16	
G 11.948–0.003	18:11:52.9	–18:36:03	4.8E–3	6Baug08					<109		–140,210		
G 12.914+0.493	18:11:53.6	–17:30:02	1.4E–4	6Baug08	G 12.915+0.493	18 11 53.74	–17 29 58.8	4	2.7	33	31,34	3.9	
G 12.02–0.03	18:12:01.9	–18:31:56	6.4E–4	6Baug08					<120		–140,210		
G 11.902–0.100	18:12:02.1	–18:40:26	5.4E–5	6Baug08					<118		–140,210		
G 11.903–0.140	18:12:11.1	–18:41:27	0.027	BCEP03	G 11.903–0.142	18 12 11.41	–18 41 33.0	7	0.3	36	35,38		BCEP no det. 04
G 11.861–0.183	18:12:15.6	–18:44:58	4.5E–5	6Baug08					<121		–140,200		
G 11.93–0.14	18:12:17.3	–18:40:03	2.3E–4	6Baug08					<178		–140,200		
G 11.942–0.157	18:12:19.6	–18:39:54	3.2E–4	6Baug08	G 11.943–0.156	18 12 19.58	–18 39 52.0	2	4.9	41	7,94	25	
G 12.200–0.003	18:12:23.5	–18:22:49	0.059	6Baug08	G 12.199–0.033	18 12 23.43	–18 22 50.7	2	0.2	51	51,52	0.2	
G 11.956–0.177	18:12:25.7	–18:39:46	3.7E–5	6Baug08					<254		–140,210		
G 12.20–0.09	18:12:39.2	–18:24:17	1.0	6Baug08	G 12.209–0.102a	18 12 39.89	–18 24 17.7	10	63	22	12,29	199	
				6Baug08	G 12.209–0.102b	18 12 39.75	–18 24 17.7	8	75	0	–28,50	462	
				6Baug08	G 12.209–0.101	18 12 39.69	–18 24 16.2	7	0.7	–32	–34,–31	1.4	
G 11.942–0.256	18:12:41.6	–18:24:47	2.1E–4	6Baug08	G 12.203–0.107	18 12 40.22	–18 24 47.4	1	1.1	33	28,35	1.9	
G 12.18–0.12	18:12:42.7	–18:25:08	0.85	6Baug08					<208		–140,210		
G 12.216–0.119	18:12:44.4	–18:24:25	0.023	6Baug08					<293		–140,210		
G 11.99–0.27	18:12:51.2	–18:40:40	2.8E–4	6Baug08	G 11.991–0.272	18 12 51.20	–18 40 39.7	0	0.2	53	53,54	0.2	
G 12.43–0.05	18:12:56.4	–18:11:04	0.98	6Baug08	G 12.429–0.048	18 12 54.41	–18 11 10.8	29	0.3	–72	–74,–38	2.1	BS
G 12.68–0.18	18:13:54.7	–18:01:41	0.30	H75oct07	G 12.681–0.182	18 13 54.73	–18 01 46.5	6	565	60	53,64	668	
				H75oct07	G 12.670–0.177	18 13 52.42	–18 02 10.5	44	0.4	50	49,50	0.1	
G 11.94–0.62B	18:13:58.5	–18:54:21	1.9E–3	6Baug08	G 11.918–0.613	18 13 58.12	–18 54 20.2	5	49	40	21,45	122	
G 11.93–0.61	18:14:00.9	–18:53:27	2.3E–3	6Baug08					<149		–140,210		
G 12.722–0.218	18:14:07.6	–18:00:37	1.9E–3	6Baug08	G 12.720–0.218	18 14 07.35	–18 00 42.7	7	0.6	–36	–36,–35	0.9	BS
G 12.885–0.222	18:14:28.3	–17:52:08	4.9E–5	6Baug08					<121		–140,210		

Table 5.8: – continued

Dust clump					Water maser								
Name (l, b) (degrees)	RA (J2000) (h m s)	Dec (J2000) (° ′ ″)	prob.	array and epoch	Name (l, b) (degrees)	RA (J2000) (h m s)	Dec (J2000) (° ′ ″)	Sep. (″)	Sp (Jy)	Vp	Vr	Int	notes
G 12.892–0.226	18:14:30.0	–17:51:52	6.5E–5	6Baug08					<121		–140,210		
G 12.90–0.25B	18:14:34.3	–17:51:56	2.1E–3	6Baug08	G 12.901–0.241	18 14 34.43	–17 51 51.8	5	2.2	36	24,37	3.6	
G 12.859–0.272	18:14:36.1	–17:54:56	7.7E–4	6Baug08					<159		–140,210		
G 13.87+0.28	18:14:36.1	–16:45:44	0.029	6Baug08	G 13.874+0.281	18 14 35.83	–16 45 35.9	9	39	–43	–47,–14	155	BS
G 12.90–0.26	18:14:39.5	–17:52:00	0.025	6Baug08	G 12.907–0.261	18 14 39.45	–17 52 06.8	7	1.1	28	26,50	4.2	
				6Baug08	G 12.909–0.260	18 14 39.54	–17 52 00.0	1	2.2	27	26,38	3.9	
G 12.878–0.226	18:14:41.7	–17:54:24	7.8E–5	6Baug08					<153		–140,210		
G 12.897–0.281	18:14:42.9	–17:53:12	2.8E–5	6Baug08					<123		–140,210		
G 12.914–0.280	18:14:44.5	–17:52:16	3.4E–5	6Baug08					<161		–140,210		
G 12.938–0.272	18:14:45.7	–17:50:48	2.6E–5	6Baug08	G 12.939–0.271	18 14 45.58	–17 50 41.1	7	2.0	30	29,37	7	
G 11.49–1.48	18:16:22.1	–19:41:27	1.1E–4	BCEP04	G 11.498–1.486	18 16 22.32	–19 41 26.1	3	112	17	–3,21		
G 14.60+0.01	18:17:00.5	–16:14:44	1.3E–3	6Baug08	G 14.607+0.009	18 17 03.17	–16 14 41.6	40	2.5	27	4,27	2.8	
				6Baug08	G 14.610+0.012	18 17 02.72	–16 14 28.0	36	0.6	8	8,9	0.7	
				6Baug08	G 14.606+0.016	18 17 01.54	–16 14 32.1	19	0.5	21	17,39	1.2	
				6Baug08	G 14.604+0.017	18 17 01.14	–16 14 38.8	11	9	30	20,31	13	
G 10.84–2.59	18:19:12.6	–20:47:31	2.3E–4	6Baug08	G 10.843–2.593	18 19 12.51	–20 47 27.4	4	35	–81	–89,–73	127	BS
G 15.022–0.618	18:20:10.3	–16:10:35	4.9E–5	6Baug08					<231		–140,210		
G 14.987–0.670	18:20:17.6	–16:13:55	3.7E–5	6Baug08					<124		–140,210		
G 15.027–0.651	18:20:18.1	–16:11:15	1.6E–4	6Baug08	G 14.892–0.730	18 20 19.60	–16 10 38 .4	43	4.3	25	20,33	14	
G 15.054–0.641	18:20:19.2	–16:09:31	2.6E–5	6Baug08					<358		–140,210		
G 14.983–0.687	18:20:20.9	–16:14:35	2.1E–4	6Baug08					<199		–140,210		
G 15.012–0.671	18:20:20.9	–16:12:35	4.4E–4	6Baug08					<1000		–140,210		
G 15.03–0.67	18:20:23.1	–16:11:16	1.9E–3	6Baug08	G 15.028–0.672	18 20 23.02	–16 11 47.8	32	4.2	21	18,23	9	
G 14.99–0.70	18:20:23.1	–16:14:43	1.0E–4	6Baug08	G 14.985–0.696	18 20 23.16	–16 14 44.3	2	57	43	–20,72	327	spread
G 15.009–0.688	18:20:24.2	–16:13:15	4.2E–5	6Baug08					<235		–140,210		
G 15.005–0.695	18:20:25.3	–16:13:39	3.7E–5	6Baug08					<400		–140,210		
G 15.079–0.663	18:20:27.0	–16:08:51	1.0E–4	6Baug08					<171		–140,210		
G 15.016–0.702	18:20:28.1	–16:13:15	3.4E–5	6Baug08					<400		–140,210		
G 15.029–0.703	18:20:29.8	–16:12:35	2.8E–3	6Baug08					<400		–140,210		
G 15.089–0.673	18:20:30.3	–16:08:35	1.1E–4	6Baug08					<118		–140,210		
G 15.098–0.681	18:20:33.1	–16:08:19	5.4E–4	6Baug08					<173		–140,210		
G 16.580–0.079	18:21:14.6	–14:32:52	9.3E–4	6Baug08					<124		–140,210		
G 16.58–0.05	18:21:09.1	–14:31:49	3.3E–3	6Baug08	G 16.585–0.050a	18 21 09.05	–14 31 48.5	1	29	58	57,68	117	
				6Baug08	G 16.585–0.050b	18 21 08.97	–14 31 47.6	2	4.6	71	57,73	9	
G 18.087–0.292	18:24:56.0	–13:19:03	3.1E–5	H214jul08					<203		–120,230		
G 18.095–0.299	18:24:58.6	–13:18:47	7.1E–5	H214jul08					<203		–120,230		
G 18.105–0.304	18:25:00.8	–13:18:23	6.5E–5	H214jul08					<203		–120,230		

Table 5.8: – continued

Dust clump					Water maser								
Name (l, b) (degrees)	RA (J2000) (h m s)	Dec (J2000) (° ′ ″)	prob.	array and epoch	Name (l, b) (degrees)	RA (J2000) (h m s)	Dec (J2000) (° ′ ″)	Sep. (″)	Sp (Jy)	Vp	Vr	Int	notes
G 18.112–0.321	18:25:05.1	–13:18:31	3.1E–5	H214jul08					<390		–120,230		
G 19.61–0.1	18:27:16.3	–11:53:51	4.9E–4	H214jul08	G 19.613–0.134	18 27 16.60	–11 53 36.2	15	0.7	46	29,60	1.6	
G 19.607–0.234	18:27:38.2	–11:56:38	9.3E–4	H214jul08	G 19.610–0.234	18 27 38.11	–11 56 35.4	3	90	42	–5,81	477	spread
G 21.87+0.01	18:31:02.1	–09:49:14	3.7E–5	H214jul08	G 21.880+0.014	18 31 01.77	–09 49 00.1	15	11	21	17,29	35	
G 22.36+0.07B	18:31:43.2	–09:22:25	1.3E–3	H214jul08					<159		–120,230		
G 22.35+0.06	18:31:44.1	–09:22:12	8.5E–4	H214jul08	G 22.357+0.066	18 31 44.11	–09 22 11.8	0	9	88	75,90	31	
G 23.71+0.17	18:33:53.6	–08:07:15	2.8E–3	H214jul08	G 23.704+0.183	18 33 50.08	–08 07 15.2	52	0.6	111	111,112	0.8	clump edge
G 23.689+0.159	18:33:53.6	–08:08:43	8.5E–5	H214jul08					<203		–120,230		
G 24.450+0.489	18:34:07.6	–07:19:05	3.7E–5	H214jul08					<214		–120,230		
G 24.47+0.49	18:34:10.3	–07:17:45	8.3E–3	H214jul08					<186		–120,230		
G 25.65+1.04	18:34:20.9	–05:59:40	9.3E–4	H214jul08	G 25.650+1.050	18 34 20.84	–05 59 42.2	2	131	41	–21,56	321	
G 23.949+0.163	18:34:21.7	–07:54:45	5.9E–4	H214jul08	G 23.953+0.161	18 34 22.56	–07 54 37.4	15	0.4	48	41,50	0.7	clump edge
G 23.96+0.15	18:34:24.9	–07:54:53	4.8E–3	H214jul08	G 23.953+0.155	18 34 23.97	–07 54 48.2	15	0.8	66	65,74	1.5	
G 23.281–0.201	18:34:25.4	–08:40:23	9.4E–5	H214jul08					<182		–120,230		
G 23.268–0.210	18:34:25.9	–08:41:19	3.4E–4	H214jul08					<182		–120,230		
G 24.012+0.173	18:34:26.5	–07:51:09	4.5E–5	H214jul08					<183		–120,230		
G 23.976+0.150	18:34:27.6	–07:53:41	5.9E–5	H214jul08	G 23.980+0.149	18 34 28.17	–07 53 30.9	13	0.7	14	13,15	1.2	
G 23.960+0.137	18:34:28.7	–07:54:53	1.6E–5	H214jul08					<243		–120,230		
G 23.987+0.148	18:34:29.2	–07:53:09	8.5E–5	H214jul08					<244		–120,230		
G 23.25–0.24	18:34:31.3	–08:42:47	7.1E–5	H214jul08	G 23.257–0.240	18 34 31.25	–08 42 46.0	1	1.0	78	72,79	1.6	spread
G 24.016+0.150	18:34:31.9	–07:51:33	2.4E–5	H214jul08					<216		–120,230		
G 23.268–0.257	18:34:36.2	–08:42:39	1.6E–3	H214jul08					<187				
G 23.43–0.18	18:34:39.4	–08:31:33	0.016	H214jul08	G 23.436–0.184	18 34 39.25	–08 31 40.2	8	4.4	111	109,112	7	
G 23.409–0.228	18:34:45.6	–08:34:21	1.8E–4	H214jul08					<3225		–120,230		
G 23.420–0.235	18:34:48.4	–08:33:57	3.1E–4	H214jul08					<5000		–120,230		
G 23.319–0.298	18:34:50.7	–08:41:03	4.1E–4	H214jul08	G 23.320–0.298	18 34 50.62	–08 41 00.1	3	0.2	99	98,99	0.1	
G 23.754+0.095	18:36:06.1	–07:13:47	2.5E–3	H214jul08					<147		–120,230		
G 24.792+0.099	18:36:09.4	–07:11:39	6.9E–3	H214jul08					<173		–120,230		
G 24.78+0.08	18:36:12.6	–07:12:11	0.30	H214jul08	G 24.790+0.083	18 36 12.58	–07 12 11.6	1	54	113	35,127	162	spread, FC89
				H214jul08	G 24.792+0.082	18 36 13.13	–07 12 08.0	8	4.9	113	23,151	39	
G 24.84+0.08	18:36:18.4	–07:08:52	6.4E–4	H214jul08	G 24.850+0.087	18 36 18.40	–07 08 50.6	1	0.9	106	106,116	2.5	spread
G 24.850+0.082	18:36:19.5	–07:09:00	1.0E–4	H214jul08					<165		–120,230		
G 24.919+0.088	18:36:25.9	–07:05:08	0.046	H214jul08	G 24.921+0.083	18 36 27.25	–07 05 10.3	20	1.4	84	82,85	2.1	
				H214jul08	G 24.919+0.088	18 36 25.90	–07 05 08.1	0	6	42	35,53	20	
G 25.802–0.159	18:38:57.0	–06:24:53	6.4E–4	H214jul08					<152		–120,230		
G 25.83–0.18	18:39:03.6	–06:24:10	0.016	H214jul08	G 25.826–0.178	18 39 03.61	–06 24 10.3	0	38	95	80,123	87	

Table 5.8: – continued

Dust clump					Water maser								
Name (l, b) (degrees)	RA (J2000) (h m s)	Dec (J2000) (° ′ ″)	prob.	array and epoch	Name (l, b) (degrees)	RA (J2000) (h m s)	Dec (J2000) (° ′ ″)	Sep. (″)	Sp (Jy)	Vp	Vr	Int	notes
G 28.14–0.00	18:42:42.6	–04:15:32	2.5E–3	H214jul08					<158		–120,230		
G 28.20–0.04	18:42:58.1	–04:13:56	0.11	H75oct07	G 28.200–0.049	18 42 58.08	–04 13 57.7	2	8	96	57,100	11	
G 28.198–0.063	18:43:00.8	–04:14:28	1.8E–4	H75oct07					<311		–30,150		
G 29.193–0.073	18:43:02.4	–04:14:59	1.2E–4	H75oct07					<311	–30,150			
G 28.28–0.35	18:44:14.2	–04:17:59	5.9E–4	H214jul08					<266		–120,230		
G 28.31–0.38	18:44:22.0	–04:17:38	7.7E–4	H214jul08					<269		–120,230		
G 29.888+0.001	18:45:52.8	–02:42:29	3.1E–5	H214jul08					<356		–120,230		
G 29.889–0.006	18:45:54.4	–02:42:37	2.8E–4	H214jul08					<356		–120,230		
G 29.918–0.014	18:45:59.7	–02:41:17	4.5E–5	H214jul08					<328		–120,230		
G 29.86–0.04	18:46:00.2	–02:45:09	9.3E–4	H214jul08					<175		–120,230		
G 29.861–0.053	18:46:01.3	–02:45:25	3.4E–4	H214jul08					<175		–120,230		
G 29.853–0.062	18:46:02.4	–02:45:57	4.4E–4	H214jul08					<175		–120,230		
G 29.96–0.02B	18:46:04.0	–02:39:25	0.30	H214jul08	G 29.955–0.016	18 46 03.74	–02 39 22.3	5	63	99	80,115	340	
G 29.930–0.040	18:46:06.1	–02:41:25	4.1E–5	H75oct07					<7300		–30,150		
G 29.9687–0.033	18:46:08.8	–02:39:09	4.1E–4	H75oct07					<374		–30,150		
G 29.978–0.050	18:46:12.5	–02:39:09	0.016	H75oct07					<3035		–30,150		
G 30.716–0.082	18:47:41.3	–02:00:33	2.1E–3	H75oct07	G 30.718–0.083	18 47 41.74	–02 00 29.5	7	2.2	96	91,97	2.1	
G 35.02+0.35	18:54:00.5	+02:01:16	4.1E–4	FC89	G 35.025+0.250	18 54 00.59	+02 01 19.3	4	18.5	68.5			
G 35.575+0.010	18:56:13.5	+02:21:39	5.3E–3	H214jul08					<173		–120,230		
G 35.574+0.007	18:56:14.0	+02:21:15	1.1E–3	H214jul08					<173		–120,230		
G 35.58–0.03	18:56:22.4	+02:20:26	0.95	H75oct07	G 35.578–0.031	18 56 22.54	+02 20 27.4	3	12	52	42,57	17	
G 35.585–0.026	18:56:22.4	+02:20:58	5.9E–4	H75oct07					<435		–30,150		
G 35.564–0.037	18:56:22.4	+02:19:30	7.1E–5	H75oct07					<905		–30,150		
G 35.601–0.018	18:56:22.4	+02:22:02	7.6E–3	H75oct07					<2005		–30,150		
G 37.475–0.106	19:00:06.9	+03:59:39	1.2E–3	H214jul08	G 37.475–0.108	19 00 07.28	+03 59 34.7	7	0.2	52	51,58	0.4	
G 37.55–0.11	19:00:16.0	+04:03:15	0.27	H214jul08					<105		–120,230		

5.3.1 Individual sources

Here we draw attention to sources that we were unable to adequately describe in Table 5.8. Close neighbouring water masers are discussed, as well as sources with surprising velocities and intriguing histories. For some sources, associations with other maser species are also discussed.

G 213.705–12.597. This water maser is located in a nearby star formation region, Mon R2. Associated with this star formation region are many maser species, including 6.7 and 12.2 GHz methanol, main-line OH, and some excited OH maser transitions. Of particular interest is the excited OH maser at the 4765 MHz transition; these sources are very rare (only about 20 known in the Galaxy) and this source is by far the strongest know at this transition. Furthermore, the emission from this 4765 MHz OH maser undergoes phases of flaring activity that has not been seen in any other maser of this type (Smits, 2003; Smits, Cohen & Hutawarakorn, 1998).

G 284.351–0.418. This source is also presented in Chapter 6 as it is coincident with an OH maser (Caswell, 1998), although is named G 284.350–0.418, due to a slight difference in measured position effecting the rounded Galactic coordinates. In Chapter 6, spectra from two epochs are shown to display the typical level of variability seen in the water maser sources. When the 2003 and 2004 spectra are compared to that in the current chapter, it can be seen that the source has once again varied by a moderate level and has increased in peak flux density by about a factor of 2.

G 291.271–0.719, G 291.274–0.709 and G 291.284–0.716. This group of three sources are also listed in Chapter 6 since they all fall within the field of a target OH maser source. Caswell & Phillips (2008) also observed this group of sources, and remark that the strongest source, G 291.284–0.716, is a member of a distinct class of sources that are dominated by strong blue shifted outflows. In fact, maser emission has never been detected at the systemic velocity of the source (to a limit of 0.3 Jy in these observations), which is around 100 km s^{-1} from the detected emission. The location of G 291.284–0.716 with respect to the

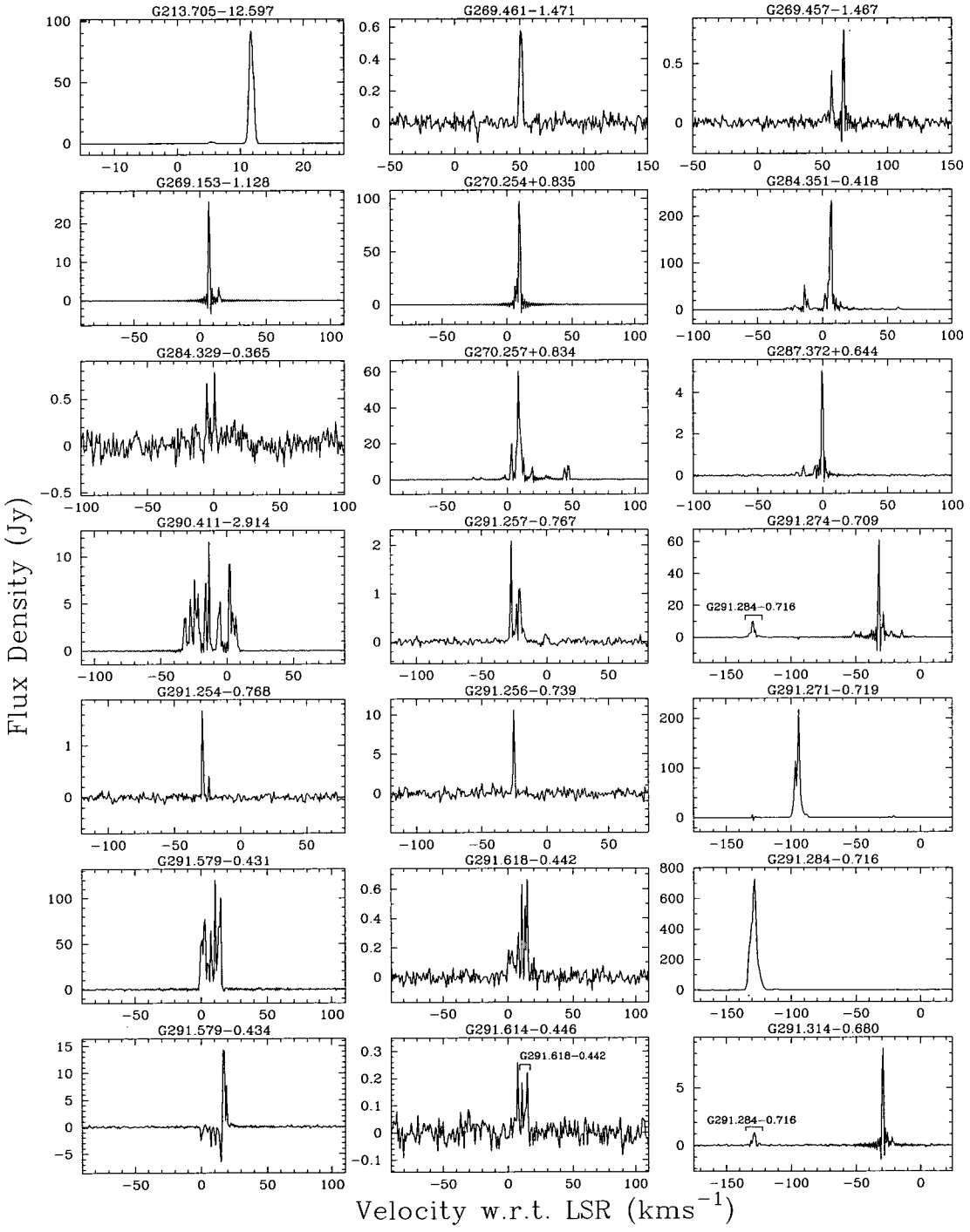

Figure 5.1: *Spectra of the 22-GHz water masers detected towards 1.2 mm dust clumps.*

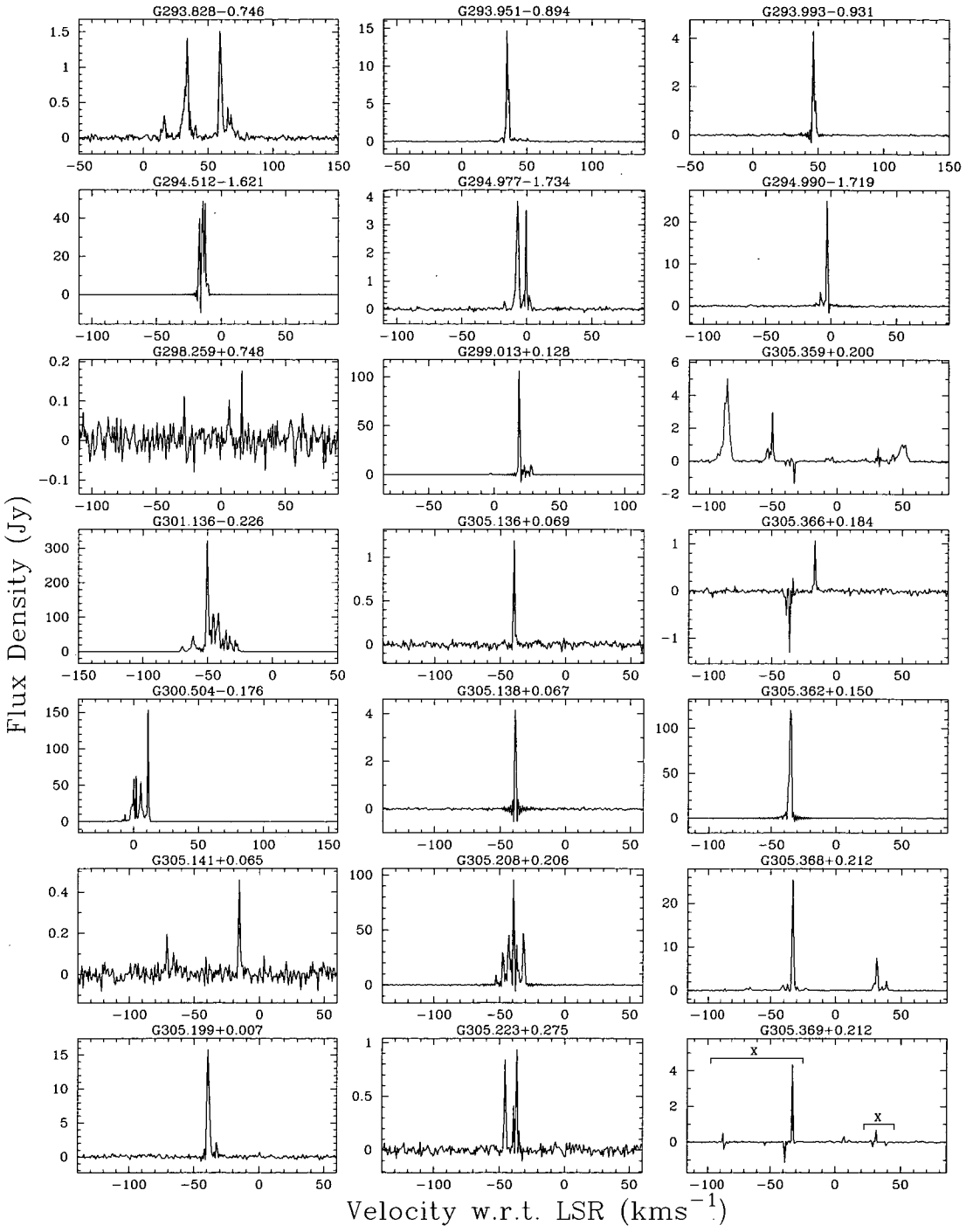

Figure 5.1: –continuued

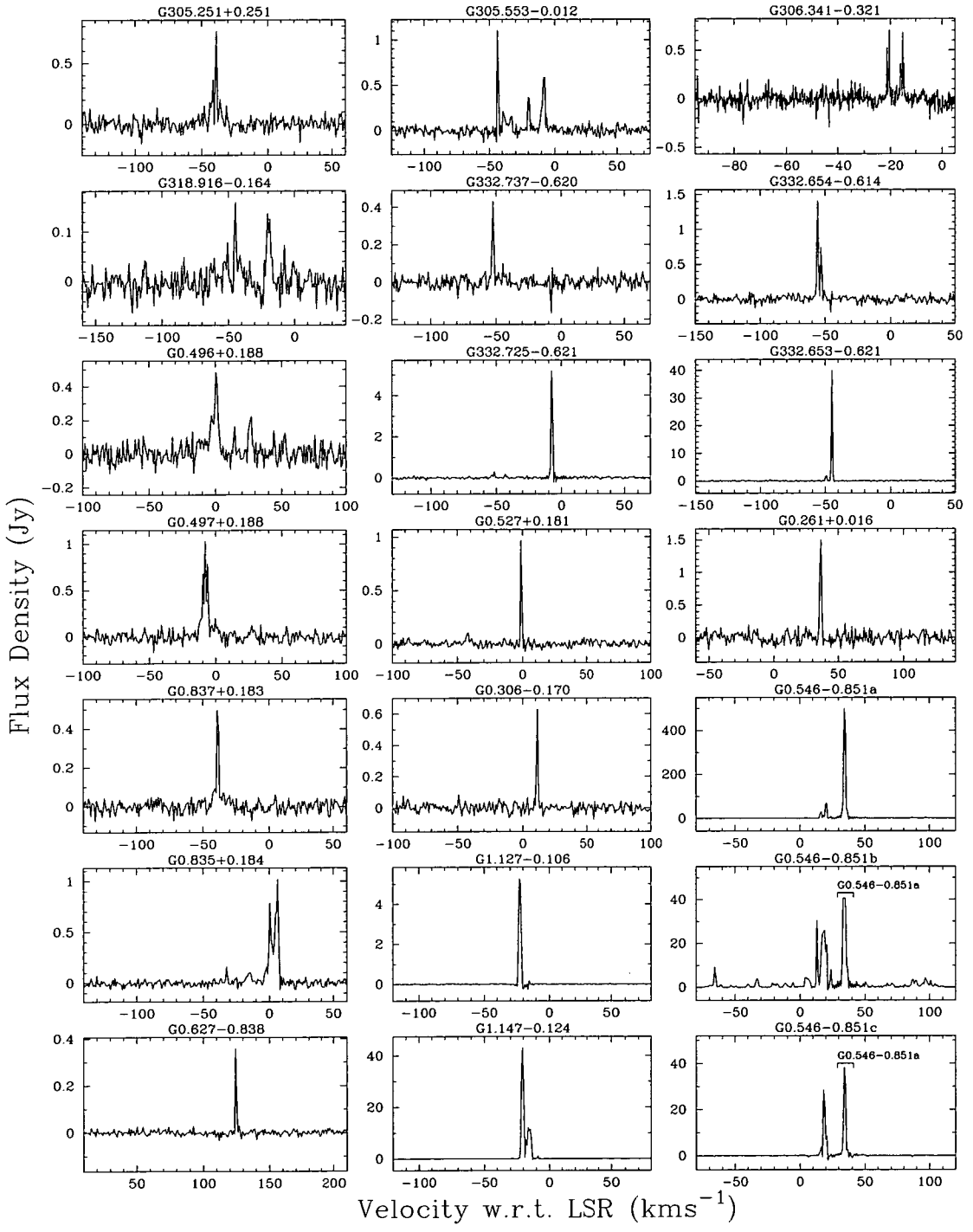

Figure 5.1: –continuued

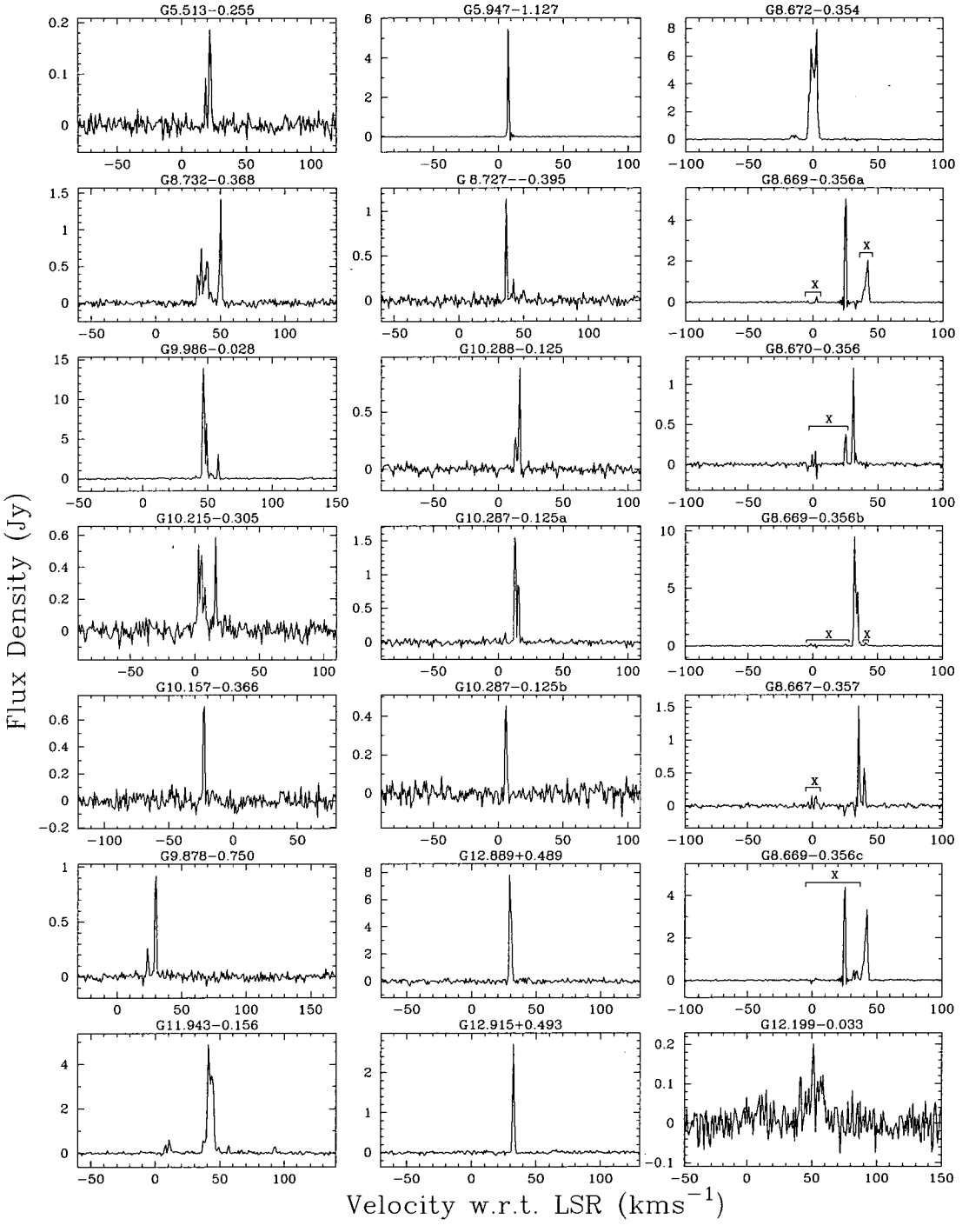

Figure 5.1: –continuued

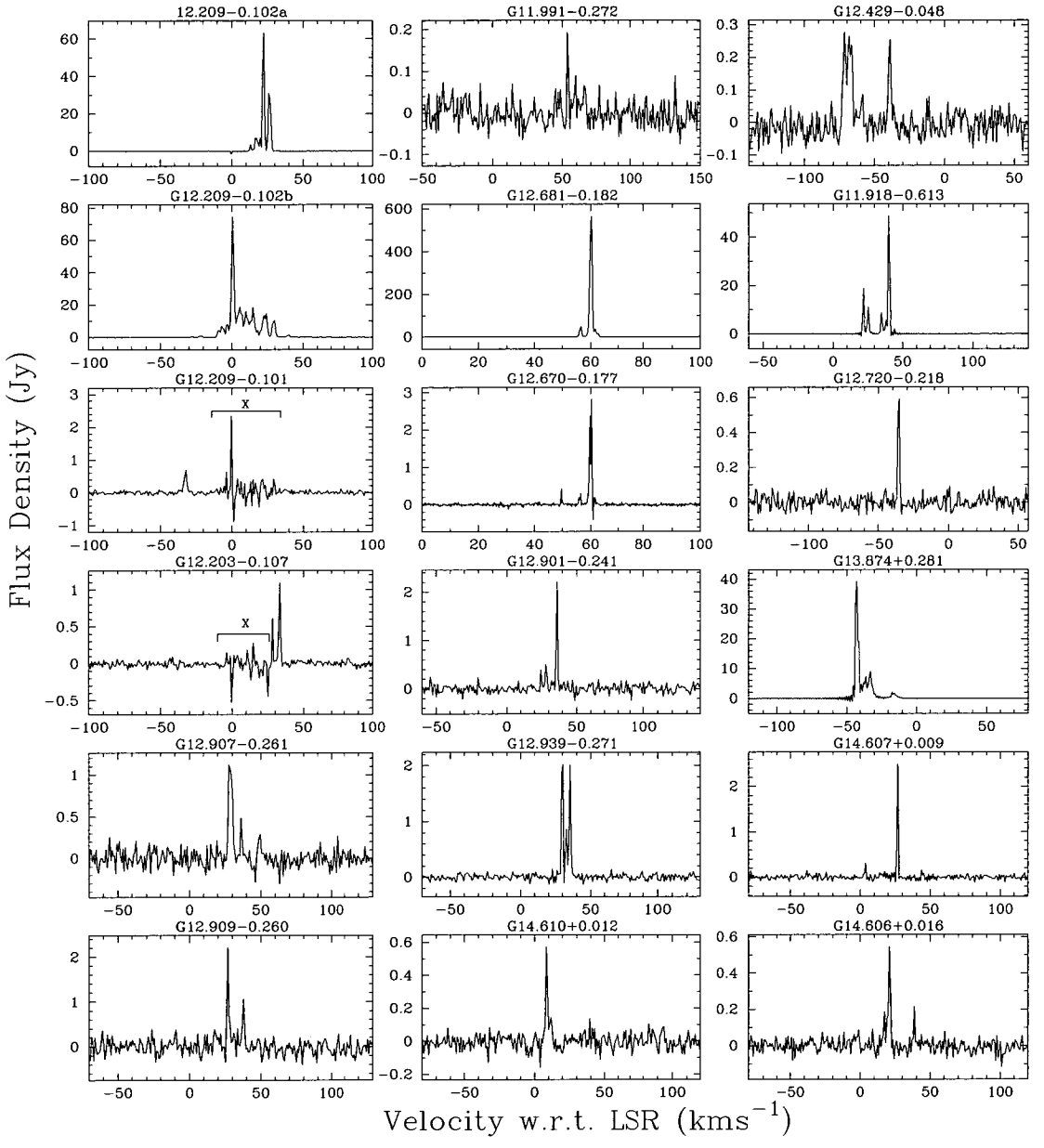

Figure 5.1: –continuued

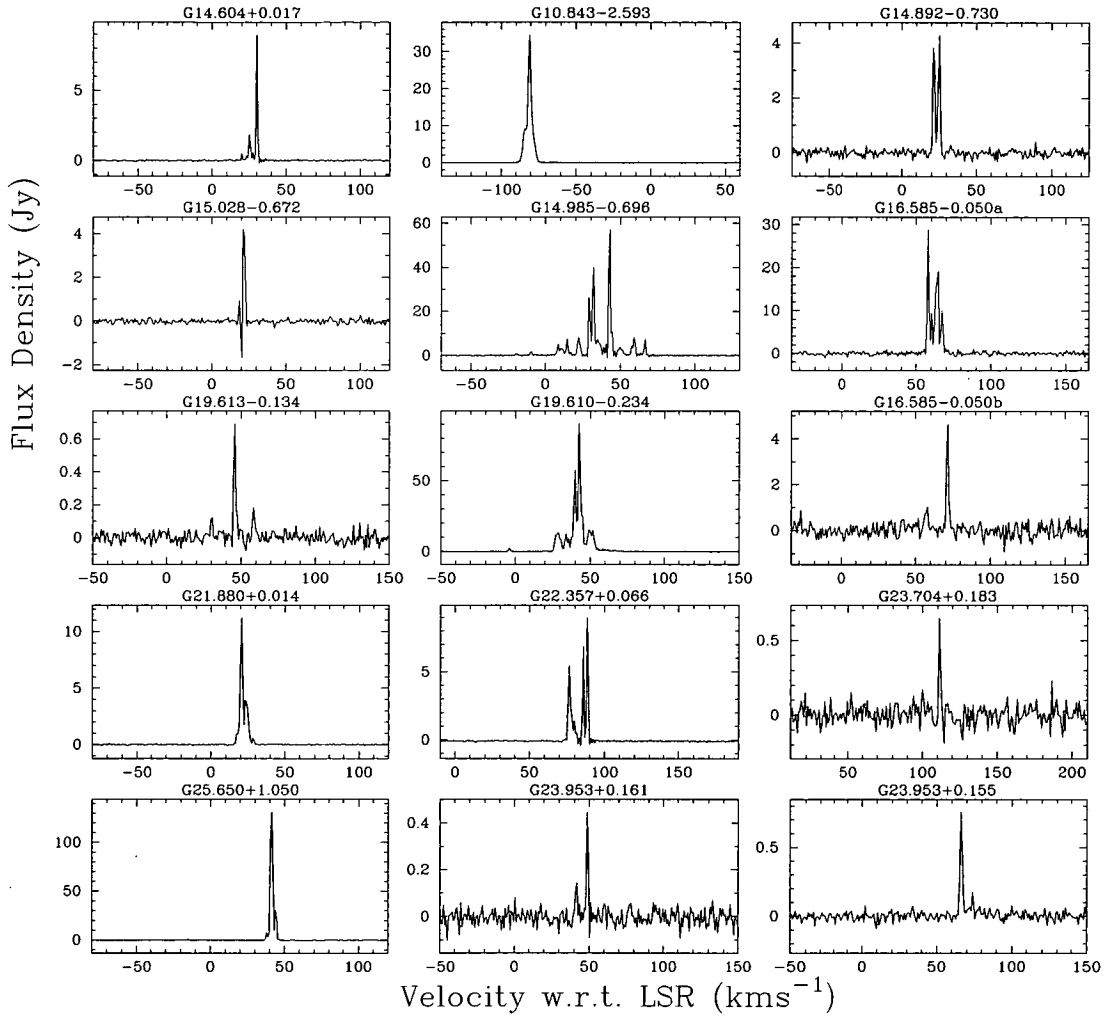

Figure 5.1: –continuued

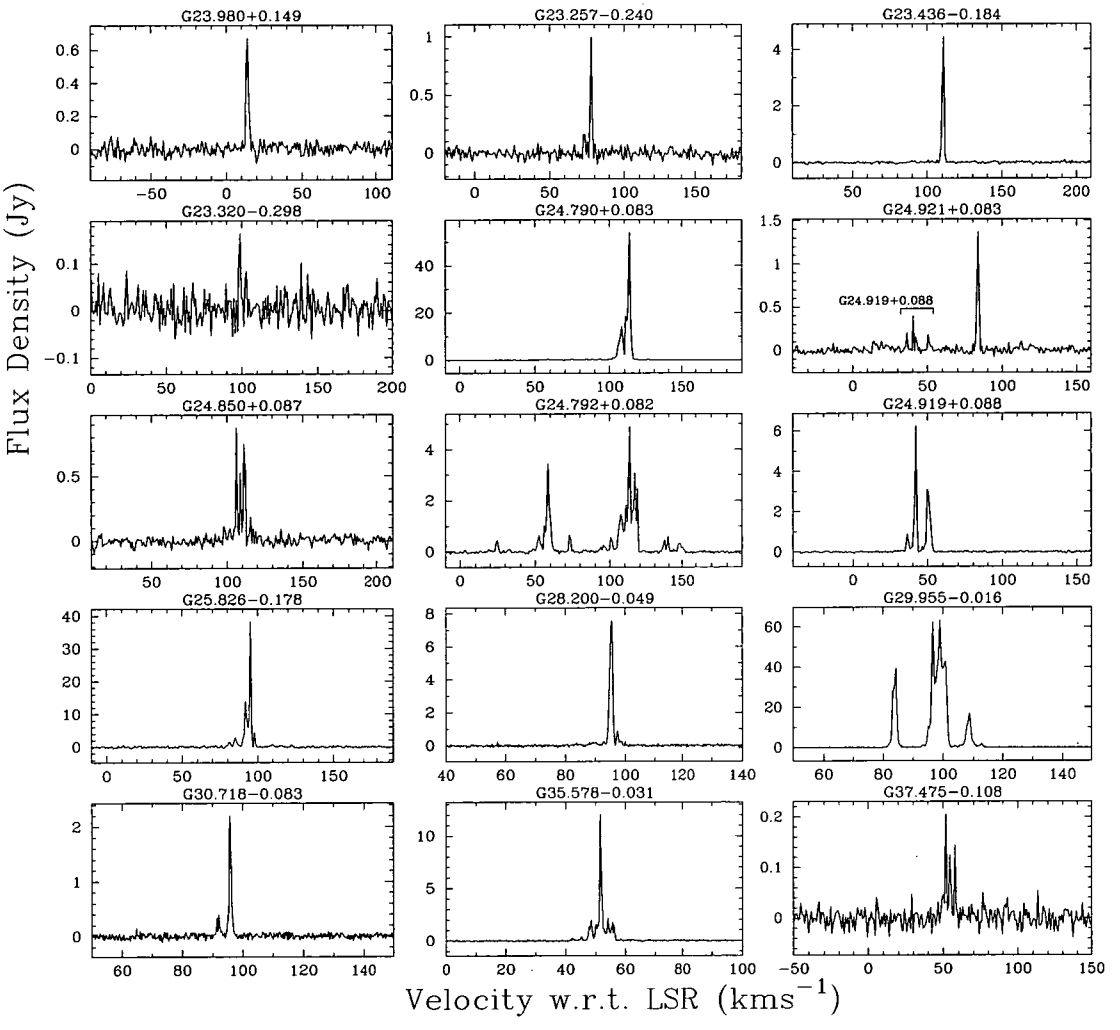

Figure 5.1: –continued

dust clump is very close to the edge of the 1.2 mm dust clump emission, unlike the majority of sources.

G 291.579–0.431 and G 291.579–0.434. G 291.579–0.431 shows emission spread over approximately 2 arcsec and in Table 5.8 we present the median of the positions measured for the individual features. This source is clearly separated from G 291.579–0.434, which is located more than 10 arcsec away.

G 301.136–0.226. As noted in Chapter 6, emission from this source is significantly spread. In the observations carried out in 2008 July, we observe individual maser components spread over almost 5 arcsec. An OH maser is located within the spread of the water maser emission (Caswell, 1998).

G 305.362+0.150. During the observations in 2008 August we detected a moderately strong water maser exhibiting one main spectral feature. In 2004 (presented in Chapter 6) an additional, broader feature of more than 100 Jy was also detected and has disappeared intervening interval.

G 0.546–0.851b. This water maser falls within a cluster of three distinct water maser sites and has a velocity range that exceeds 170 km s^{-1} . The emission extends almost symmetrically about the peak water maser emission.

G 5.513–0.255. Like G 291.284–0.716, this water masers lies unusually close to the edge of the 1.2 mm dust clump emission that was observed by Hill et al. (2005). No other similarities between the sources are evident. This sources is very weak and shows emission close to the likely systemic velocity of the region, while G 291.284–0.716 is very strong and is a dominant blue-shifted source.

G 8.727–0.395. This water maser is clearly projected against 1.2 mm dust continuum emission on inspection of the corresponding dust map of Hill et al. (2005), although no dust clump is reported at this position. It is likely that this source was omitted from the catalogue of Hill et al. (2005) in error.

G 10.473+0.027 and G 10.480+0.034. The observations presented in Table 5.8 have been taken from Chapter 6. Both of the sources were detected in observations carried out in 2003, but G 10.480+0.034 had fallen below the detection limits in 2004 (<0.2 Jy).

G 11.903–0.142. The observations presented in Table 5.8 have been taken from the observations carried out in Chapter 6, and similarly to G 10.480+0.034, this water maser was detected in 2003, but by 2004 the emission had fallen below our detection limits. Since the emission detected in 2003 had a peak flux density of 0.3 Jy, this is not surprising.

G 12.209–0.101, G 12.429–0.048, G 12.720–0.218 and G 13.874+0.281. These four well separated water maser sources all exhibit water maser emission at only negative velocities. From the velocities of nearby methanol masers, systemic velocities in this region of the sky would be expected to be between 20 - 60 km s^{-1}. Therefore these sources are all potential candidates for the class of sources that are dominated by blue-shifted emission.

5.3.2 Water masers with no apparent associated dust continuum emission

In addition to the water maser sources presented in Table 5.8 and Fig. 5.1, we detect several other sources which are of special interest. While an exhaustive attempt to search for water maser emission beyond the boundaries of the 1.2 mm dust clumps was not made, here we list a selection of the additional water maser sources that were identified.

Interestingly, we find four water maser sources that appear not to be associated with any 1.2 mm dust clump emission and these are presented in Table 5.9 and Fig. 5.2. Hill et al. (2005) detected 1.2 mm dust clump emission in the fields of all of the target 6.7 GHz methanol masers and UCHII regions, but for 20 of the methanol masers and 9 of the UCHII regions there is no spatially coincident dust continuum emission. Investigation by Hill et al. (2005) showed that these sources appeared to be no different to those where 1.2 mm dust continuum was detected.

Since the presence of 1.2 mm dust clump emission indicates the presence of cold, deeply imbedded sources, two of the possible explanations put forward by Hill et al. (2005) are that these sources are more evolved and hence no longer in the cold core phase, or, perhaps they are less massive.

We have investigated possible mid-infrared counterparts for these four sources by comparing their locations with products from the GLIMPSE survey. All are projected against regions of extended infrared emission, and two sources (G 19.612–0.120 and G 23.455–0.201) are coincident to within 1 arsec with a GLIMPSE point sources. Interestingly, the two sources with associated point sources are also associated with methanol masers. This suggests that these two sources may be located at the far distance and due to this were not detected in 1.2 mm dust continuum due to sensitivity limitations. The nature of the other two sources is more confusing and certainly warrants future investigation.

Unlike 6.7 GHz methanol masers, water masers have been detected towards both evolved and low-mass stars. Their presence in locations devoid of 1.2 mm dust continuum emission is therefore much more easily accounted for than methanol masers. Comments on each of these four water masers are given below.

G 305.248+0.195. This water maser is separated from the boundary of the nearest dust clump by more than an arcminute.

This source falls beyond the latitude range completely searched for the presence of water maser emission by Caswell & Breen (2010) which was focused on a region bound by a longitude range of G 305.0 - G 306.26 ° and ± 0.15° latitude. A total of 23 water maser sources were detected in this portion of the Galactic plane. Analysis of the masers found in this area, along with another region (longitude range of G 311.0 - G 312.18 ° and ± 0.15° latitude) showed a surprising preponderance of sources with highly blue-shifted emission. Investigation by Caswell & Breen (2010) led to a suggestion that these water masers represent a population of sources that are tracing a very early evolutionary stage, perhaps preceding the stage where 6.7 GHz methanol masers are seen.

Interesting, G 305.248+0.195 only shows emission at a blue-shifted velocity of –95 km s^{-1} (nearby methanol masers detected in the MMB survey exhibit peak velocities between –40 and –30 km s^{-1}), and therefore adds to the already high

number of blue-shifted sources in this region of the Galactic plane. However, the interpretation that such sources may be very young directly contradicts one of the suggestions given by Hill et al. (2005) as to why some sources are devoid of 1.2 mm dust continuum emission - that they are more evolved. Alternatively, it is possible that this water maser is associated with a low-mass object, although a high velocity feature > 50 km s^{-1} from the systemic velocity of the region would be unusual for a low-mass star.

G 19.612–0.120. This water maser is coincident with one of the methanol masers from Walsh et al. (1998) that were targeted by Hill et al. (2005), but is also offset from the boundary of the nearest dust clump by about an arcminute. Green et al. (2010) present evidence that suggest that this source is located at the far distance, which would limit the sensitivity of the 1.2 mm dust continuum observations, but not to the level where no detection of dust continuum emission would be expected.

G 23.397–0.219 and G 23.455–0.201. Both of these water masers fall within the one dust continuum emission map, but neither are directly associated with any detectable dust continuum emission. The first source is apparently solitary (i.e. without any associated UCHII region or 6.7 GHz methanol maser emission), but the second source appears to be coincident with an UCHII region reported by Walsh et al. (1998).

5.4 Discussion

5.4.1 Assessing the current model of water maser presence in 1.2 mm dust clumps

The model for water maser presence in 1.2 mm dust clumps that was derived in Chapter 3 has been used to calculate the probability of water maser detection for each of the dust clumps presented in Hill et al. (2005) that have dust clump radius measurements. For a number of dust sources presented in Hill et al. (2005) there is a near-far distance ambiguity. In these cases, we have assumed the near

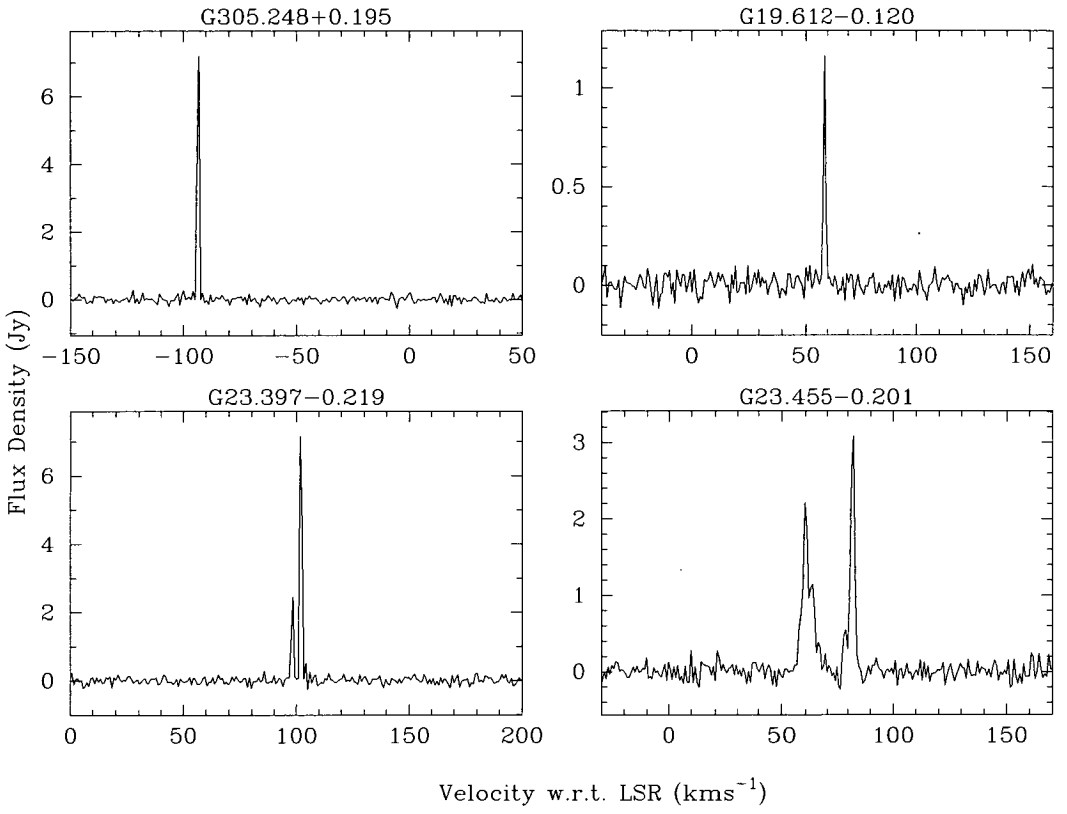

Figure 5.2: *Water maser sources with no associated 1.2 mm dust clump emission, detected within the target fields.*

Table 5.9: *Four water maser sources detected in the target fields that are not coincident with any detected 1.2 mm dust clump emission. Columns 1-7 give the: Water maser source name; water maser right ascension; declination; peak flux density (Jy); velocity of the water maser peak emission (km s^{-1}); velocity range (km s^{-1}); and the integrated flux density of the water maser emission (Jy km s^{-1}), respectively.*

Name (l, b) (degrees)	RA (J2000) (h m s)	Dec (J2000) (^{o} ' ")	Sp (Jy)	Vp	Vr	Int
G 305.248+0.195	13 11 34.84	–62 35 11.0	7	–93	–95,–92	9
G 19.612–0.120	18 27 13.55	–11 53 14.7	1.2	58	57,60	1.6
G 23.397–0.219	18 34 42.32	–08 34 43.3	7	102	97,106	14
G 23.455–0.201	18 34 44.89	–08 31 07.4	3.1	82	57,84	17

distance for consistency with analysis completed in other Chapters. A discussion of the choice of near distance over the far distance can be found in Chapter 4, Section 4.3.2. However, we note that in this instance this assumption is particularly hazardous, since the predictive model relates only to 1.2 mm dust clump radius which is highly influenced by the adopted distance measurement.

Using the model for water maser presence associated with 1.2 mm dust clumps, it was determined that only 58 of the 294 dust clumps considered in this analysis, had a probability of 0.01 or greater of having an associated water maser. Probabilities for individual dust clumps are presented in Table 5.8. Comparison between the calculated probability of water maser and the actual detections shows that the model described in Chapter 3 is promising. The average probability of water maser presence in the 128 1.2 mm dust clumps where water masers are detected is 0.10, and have a median value of 0.00081. In comparison, for the dust sources where we detect no water maser emission, the average probability of water maser presence is 0.027 and have a median value of 0.00026. An alternative description of these statistics is that, of the 27 of the 1.2 mm dust clumps which had a calculated probability of $\geq$0.1, 20 yielded water maser detections. If the considered probability is lowered to be $\geq$0.01 then the number of clumps is

increased to 58 and the number of clumps with detections is 39. It is therefore clear that the model is picking up a high detection rate for the sources with high calculated probabilities, however, given that we detect water maser towards 128 dust clumps, it is also clear that the model is failing to return high probabilities of water maser presence in just over half of the detected sources.

Given that the original model was derived from a sample of water masers that were detected in a complete search with a relatively high sensitivity limit ($\geq$5 Jy), the obvious property to investigate is the relative flux density of the detected water masers. It might be expected that there would be a trend whereby the water maser detections towards the 1.2 mm dust clumps with high association probabilities have higher flux densities, given the nature of the data on which the model was derived. The average flux density of the water maser sources detected towards dust clumps with a probability of 0.01 or higher (55 water maser sources) is 48 Jy and these sources have a median flux density of 6 Jy. In comparison, the average flux densities of the water masers detected towards clumps with a lower calculated probability is 33 Jy, with a median flux density of 3.5 Jy. It is possible, therefore, that the current model is biased towards predicting correctly the presence of the stronger sources, but more likely, is that the sources with very low probabilities are dominated by far distance sources which accounts for the lower average flux density.

Another obvious factor to consider is the high degree of dependence on distance measurements. Since the original model was derived from sources located within the one GMC with a well constrained distance measurement, the poorly determined distances towards most star formation regions did not affect the generation of this model. The model for water maser presence associated with dust clumps uses only the radius of the dust clump in order to calculate the probability. As previously discussed, we have assumed the near distance reported by Hill et al. (2005) for sources with distance ambiguities. It is clear that this is an unreliable assumption, especially since our search is of high sensitivity which reduces the likelihood of any significant detection dependence on distance. It would be expected that the split of near and far distance allocations should be approximately even (or maybe even favour the far distances due to the large volume). Inspection of the characteristics of some of the dust clump sources that

have low calculated probabilities, yet have associated water masers, shows that if the far distance was used the calculated probability would be high (in many cases >0.3). The increase in radius that results in a change from near to far distance does not result in a high probability in water maser presence in all of the dust clumps, especially those with no detected associated water masers.

If our assertion that the poorly constrained distance measurements are adversely effecting the predictive capabilities of the model is correct, then the distribution of the clump properties should support this. If, for example, we inspect the peak flux density of the 1.2 mm dust clumps with associated water masers and calculated probabilities of > 0.01, they should not be any different from the sample of 1.2 mm dust clumps with associated water masers and calculated probabilities of <0.01. But, they are in fact different. The average peak flux density of the clumps with calculated probabilities of >0.01 (and have associated water masers) is 2.8 Jy beam^{-1}, whereas the average of those clumps with lower than expected calculated probabilities (<0.01) is 1.4 Jy beam^{-1}. The most likely explanation for this is that a number of the 1.2 mm dust clumps which have low calculated probabilities, but yet have an associated water maser, are located at the far distance. This means that the seeming downfall of the model to allocate high probabilities to a number of the 1.2 mm dust clumps where we detect water masers may be eradicated if accurate distance measurements were obtained.

Figure 5.3 shows the distribution of the targeted 1.2 mm dust clumps throughout the Galactic plane. It became apparent upon inspection of the data presented in Table 5.8 and Fig. 5.3 that the water maser detection rate seemed to be higher for sources located at Galactic longitudes less than ~G 333. In fact, the water maser detection rate towards dust clumps located in the portion of the Galaxy between longitudes of G 213 - G 333 degrees is 55 % (51 of 93), compared with 38 % (77 of 201) for the longitude range G 0 - G 38 degrees. Although not covering exactly the same longitude ranges, it is curious to note that the detection rates of 12.2 GHz methanol masers in the longitude range G 270 - G 305 were significantly lower than in other parts of the Galaxy (see Chapter 7). If it were the relative distances that were effecting our detection rates then if anything we would expect to have a lower detection rate in the G 213 - G 333 region as we would expect relatively more dust clump detections in these regions. Since our maser observations

are of a high sensitivity we would expect a minimal detection rate dependence on distance. Caswell & Breen (2010) and Caswell, Breen & Ellingsen (2010) completed systematic searches for water masers within three regions of the Galactic plane. It is shown that there is a large difference in the water maser population densities within these regions, suggesting that local factors have an effect on the detection statistics. It is therefore possible that there are broader localised effects contributing to our detection statistics here. This warrants further investigation.

Water maser variability

Water masers are known to often exhibit extreme variability over relatively short timescales (e.g. Felli et al., 2007). The water maser observations presented in Chapter 6 were completed, in many cases, twice with the observation epochs separated by $\sim$10 months. Since the observations presented in this chapter were completed only once, we cannot directly determine the level which maser variability has affected our results. Instead, we derive predictions about the completeness of these observations by comparing this sample with the findings in Chapter 6.

In Chapter 6 we show that 17 % of the 253 water maser sources that were observed at two epochs were only detectable at one of these epochs. If we simply apply this percentage to the sample presented in this Chapter, it might be expected that $\sim$34 additional water maser sources would be detected if a second epoch of observations were conducted towards the target 1.2 mm dust clumps. Since we detect 165 water masers towards 128 1.2 mm dust clumps, we would perhaps expect that these additional sources be detected towards a further 26 1.2 mm dust clumps.

However, the situation is perhaps a little more complex than this. It is not clear if the role of variability would result in many more dust clumps being recognised as being associated with water masers, or alternatively that different water maser sources would be detected at different epochs towards the same dust clump. It is likely that both would be true, that is, that some number of water masers would be detected towards additional 1.2 mm dust clumps and that some additional/different water masers would be detected towards 1.2 mm dust clumps where we detected water masers.

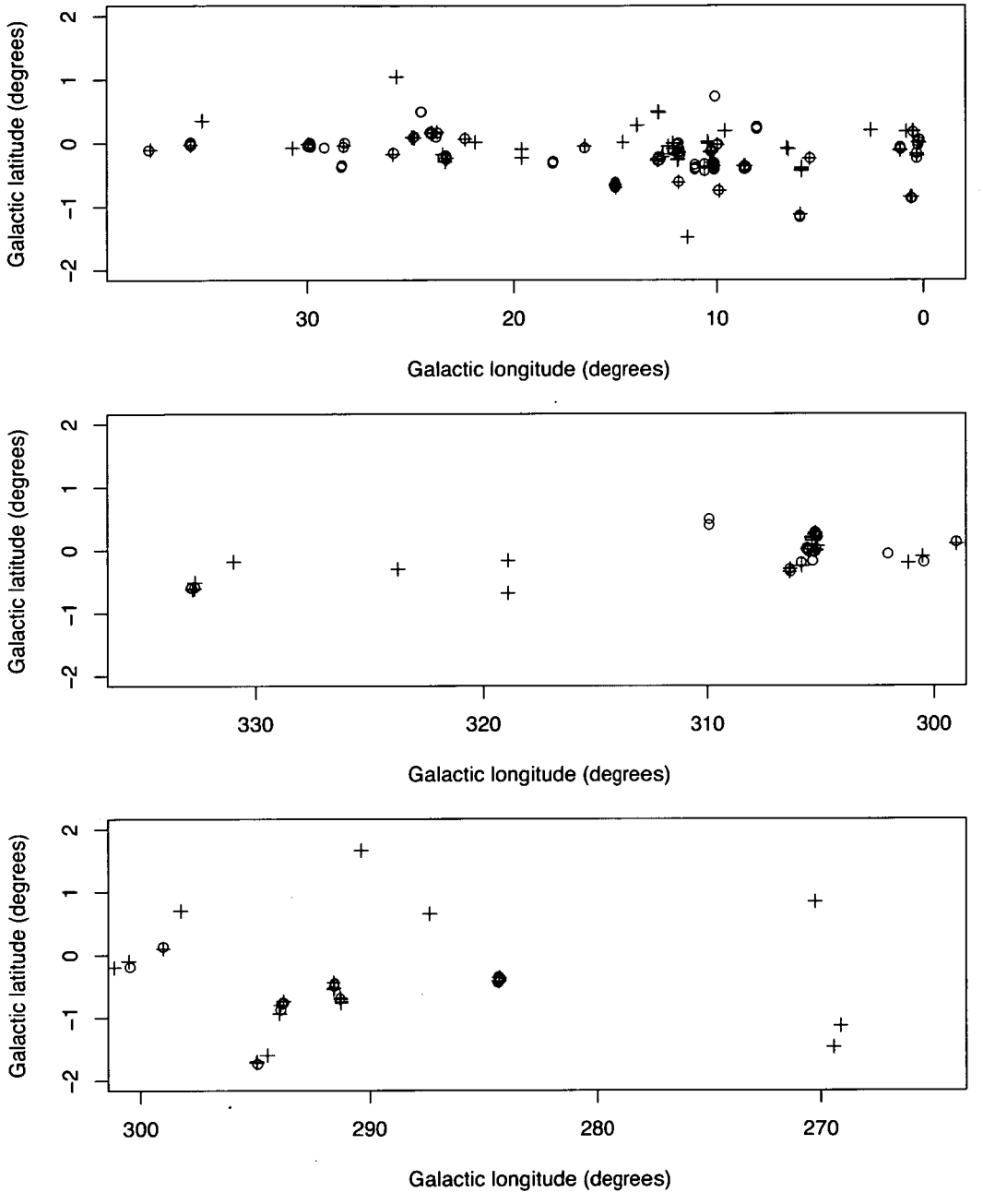

Figure 5.3: *Latitude versus longitude diagram of the targeted 1.2 mm dust clumps. The 1.2 mm dust clumps with associated water masers are shown by crosses and those with no detectable water maser counterpart are represented by circles. The three 1.2 mm dust clumps which lie beyond ±2 degrees of the Galactic plane have been excluded from these plots.*

5.4.2 Location of the water masers in the 1.2 mm dust clumps

Analysis of the locations of the water masers with respect to the 1.2 mm dust clump peak, as reported by Hill et al. (2005), shows that there is excellent correspondence between their locations. The 1.2 mm dust continuum maps of Hill et al. (2005) have 8 arcsec pixels, and the listed peak positions are just the central position of the peak pixel. On average, we find that the separation between the water maser positions and the associated dust clump peak is 13 arcsec and that the median separation is 8 arcsec. It is therefore likely that, in the majority of cases, the water masers are very closely associated with the peak 1.2 mm dust clump emission.

Fig. 5.4 shows a histogram of the separations between the dust clump peak and the detected water masers. An investigation of some of the water maser sources which are separated by more than ~25 arcsec from the dust clump peak, and especially those with separations >1 arcmin, has shown that in a number of these cases, there is an error in the position of the reported peak by Hill et al. (2005). Inspection of figure A1 of Hill et al. (2005) has shown that in some cases, the reported peak is clearly in error since it falls outside the area of dust clump emission or right near the boundary of the emission. For example, dust clump G 330.95–0.18 has a reported position that is 73 arcsec from the location of the water maser, but inspection of the 1.2 mm dust clump map shows that the maser is actually very close to the peak and that the reported dust clump peak is outside the visible portion of the clump. There are numerous examples where a similar thing is seen (e.g. dust clumps G 294.97–1.7, G 299.02+0.1 and G 301.14–0.2), but a more thorough investigation is needed to determine exactly how many sources are affected. Even though Hill et al. (2005) publish images of their 1.2 mm dust clumps, the resolution (and contrast) is insufficient to enable us to determine better positions independently. Given the obvious problems with some number of the dust clump peak positions which erroneously result in some of the most extreme separations between the peak of the clump and the associated water maser, it is likely that the actual average and median separations between the peak of the dust clumps and the associated water masers would be even smaller,

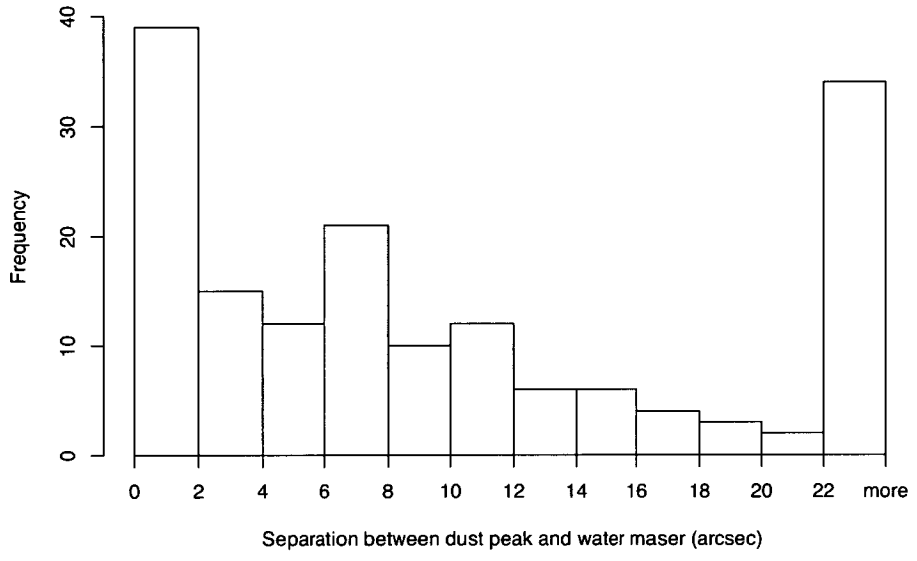

Figure 5.4: *Histogram of the angular separation between the reported 1.2 mm dust clump peak and the position of the water maser sources.*

perhaps comparable to the pixel size.

Fig. 5.5 shows a plot of the separation from the dust clump peak versus the peak flux density of the associated water masers. This figure shows, similarly to Fig. 5.4, that the bulk of the water maser sources are located near the peak of the associated 1.2 mm dust clumps. No strong trend is seen between the peak flux density and the separation between the dust clump peak position and the peak flux density of the associated water maser, but investigation of the 10 strong water masers that are located >16 arcsec from the dust clump peak shows that many of these have erroneously reported dust clump peak positions. Further investigation is therefore required, however, it is possible that most of the water masers that are located far from the dust clump peak are relatively weak.

5.4.3 Fitting Binomial general linear models to the new water maser and 1.2 mm dust clump data

While the current model for water maser presence in 1.2 mm dust clumps is promising, we have repeated the analysis carried out in Chapter 3 with the much

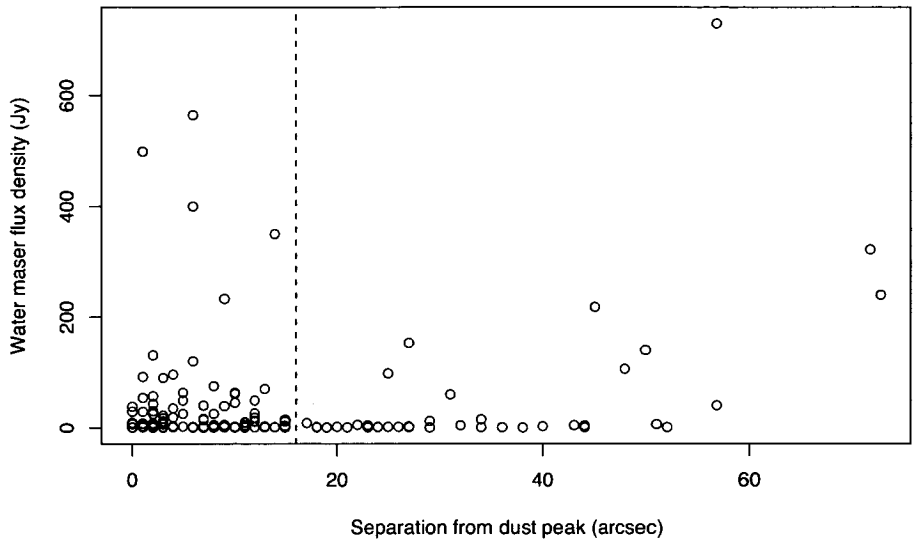

Figure 5.5: *Separation between the dust clump peak and the water masers associated with each of the dust clumps versus the water maser peak flux density. The vertical dashed line is marked at 16 arcsec.*

larger sample presented in this Chapter. It is important to remember, firstly, that the 1.2 mm dust clumps in this sample were not detected in a systematic manner (unlike the observations of Mookerjea et al. (2004) used in Chapter 3), although given the high number of additional 1.2 mm dust sources found within the fields of the target sources this is probably not detrimental to the analysis. The other thing that needs to be considered is the adoption of the near distance measurements for the sources where distance ambiguities exist.

We have fitted a Binomial generalized linear model to the water maser presence/absence data, using the 1.2 mm dust clump properties as predictors. For a more detailed description of this analysis method, see Chapter 1, Section 1.3. All but one of the targeted 1.2 mm dust clumps were included in this analysis. The source that has been excluded is G 6.60–0.08 as Hill et al. (2005) suggest that the derived mass of this source is uncharacteristic of massive star formation regions and were therefore doubtful that it is located at the near distance. For each of the 1.2-mm dust clumps, all of the derived clump properties were tested: the integrated flux density (Jy), peak flux density (Jy beam^{-1}), source full width at

half maximum (FWHM) (arcsec), distance (kpc), mass ($M_\odot$), radius (pc) and H_2 number density (cm^{-3}). As in other Chapters, in the following sections we consider p-values of less than 0.05 to be statistically significant (i.e. the hypothesis that the single term model provides no better fit than the null model consisting only of an intercept is rejected when the p-value is less than 0.05).

Fits of the single term addition Binomial model showed an increasing probability of the presence of water masers associated with increasing values of dust clump integrated flux density, peak flux density, FWHM, mass and radius. This result is similar to that found when investigating methanol masers (see Chapter 4), and means that any one of these dust clump properties can give an indication of the likelihood of finding an associated water maser. A summary of the results of the single term additions are given in Table 5.10. Box plots of each of the dust clump properties broken up into the categories of 'n' and 'y', referring to those clumps with no associated water maser, and those with an associated water maser, respectively, are presented in Fig. 5.6. These box plots show graphically the same information as the results of the single term additions; that lower values of the dust clump properties; integrated and peak flux density, FWHM, mass and radius, are associated with the 1.2 mm dust clump sources with no associated water maser emission, compared to those associated with water maser emission.

Stepwise model selection was used to create the simplest model with the greatest predictive power and this model contains the two dust clump properties; peak flux density and FWHM. The estimated regression relation is

$$\log\frac{p_i}{1-p_i} = -1.564 + 0.995x_{\rm Peak} + 0.012x_{\rm FWHM},$$

where $x_{\rm Peak}$ is the peak flux density, $x_{\rm FWHM}$ is the source FWHM, and p_i is the probability of finding a water maser towards the i^{th} 1.2-mm dust clump. The regression summary of this model is shown in Table 5.11. Unlike the previous model that was created in Chapter 3, this model does not contain radius.

The misclassification rates for this model are somewhat promising when the probability threshold is set to 0.5, it correctly predicts half (63 of 127) of the dust clump sources with associated water masers with have associated water masers, and it correctly predicts 144 of the 165 dust clumps with no associated

Table 5.10: *Analysis of deviance table for the single term models (using the 1.2 mm dust clump properties from Hill et al. (2005)), showing the deviance and the AIC together with the associated likelihood ratio statistic and* p*-value for the test of the hypothesis that the stated single model provides no better fit than the null model consisting only of an intercept.*

Predictor	Deviance	AIC	LRT	p-value
none	399.84	401.84		
integ	341.81	345.81	58.02	2.590e-14
peak	332.98	336.98	66.85	2.923e-16
fwhm	354.23	358.23	45.61	1.445e-11
dist	398.65	402.65	1.19	0.2761
mass	366.41	370.41	33.43	7.391e-09
radius	379.44	383.44	20.40	6.299e-06
density	399.66	403.66	0.18	0.6697

Table 5.11: *Summary table for the Binomial regression model, showing for each predictor the estimated coefficient and the standardised z-value and* p*-value for the test of the hypothesis that* $\beta_i = 0$.

Predictor	Estimate	Std. Error	z value	p-value
Intercept	-1.563746	0.271202	-5.766	8.12e-09
peak	0.994999	0.254413	3.911	9.19e-05
fwhm	0.011744	0.007242	1.622	0.105

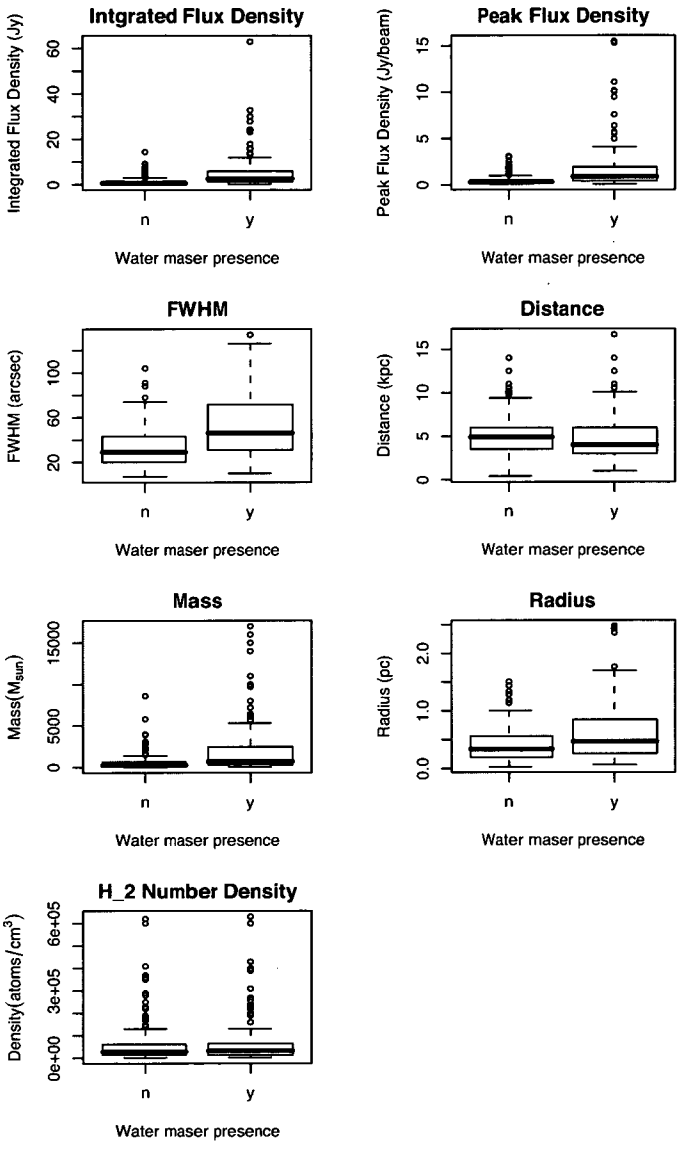

Figure 5.6: *Box plots of the 1.2-mm dust clump properties split in the categories of yes and no, referring to the presence of water maser emission. There is a statistically significant difference between the two categories in the 1.2 mm dust clump integrated and peak flux density, mass, FWHM and radius. This information is the graphical display relating to the information in Table 5.10. Note that source G 23.960+0.137 has been removed from these plots, since is is more than twice as dense as all of the other sources shown on the plot and therefore is an extreme outlier.*

water masers will have no associated water maser. It is easy to understand why such a model would fail on a high number of the dust clumps with associated water masers, since we know that these sources have higher peak flux densities on average, but as can be seen in Fig. 5.6, there is a large overlap in the range of values of this property between those clumps with associated water masers and those without. This is consistent with a number of dust clumps with associated water masers having apparently low peak flux densities, since they are located at the far distance. Therefore a peak flux density measurement that is scaled with reliable distance measurements may offer a promising model.

A new model based on 1.2 mm dust clump radius

Since the model for water maser presence presented in Chapter 3 uses only the dust clump radius to predict the probability of associated water maser presence, for comparison, a model using only dust clump radius has been produced from this new data. This was achieved by restricting the dust clump properties used to fit the GLM to only the dust clump radius. The resultant estimated regression relation is

$$\log\frac{p_i}{1-p_i} = -0.981 + 1.45x_{\text{radius}},$$

where x_{radius} is the radius of the 1.2 mm dust clump, and p_i is the probability of finding a water maser towards the i^{th} 1.2-mm dust clump. The regression summary of this model is shown in Table 5.12.

Since only one dust clump property is present in the regression relation, it is easy to determine the physical implications of the model. For example, if the probability of water maser presence is set to 0.5, the corresponding dust clump radius is 0.68 pc. This means that the model is saying that 1.2 mm dust clumps with a radius of 0.68 pc (or higher) have a probability of 0.5 (or higher) of having an associated water maser. In comparison, the model presented in Chapter 3 predicts that 1.2 mm dust clumps with radii greater than 1.25 pc for the same probability threshold of 0.5 will have associated water masers. The model produced with the current data, predicts that water masers are associated with much smaller dust clumps (about half the size), albeit relatively poorly. The

Table 5.12: *Summary table for the Binomial regression model using only dust clump radius, showing the estimated coefficient and the standardised z-value and* p*-value for the test of the hypothesis that* β_i*=0.*

Predictor	Estimate	Std. Error	z value	*p*-value
Intercept	-0.9814	0.2101	-4.670	3.01e-06
radius	1.4460	0.3544	4.081	4.49e-05

misclassification rates from this new model are poor, particularly in determining which clumps will have associated water masers (which it gets wrong two-thirds of the time).

It is clear that the influence of the poorly constrained distance measurements are having a large effect on our ability to model the water maser presence within the 1.2 mm dust clumps. However, the higher accuracy of the models in predicting the sources without associated water masers correctly, may indicate that there is a population of sources that are significantly far from the properties of the clumps that exhibit water masers that not even a change from near to far distance would boost them to a high probability of water maser presence.

5.4.4 Characteristics of the detected water masers

An extensive investigation of the characteristics of a large sample of water masers is carried out in Chapter 6 and here we present a much less detailed investigation with our primary goal being to determine if the samples show any difference in their properties.

Velocity ranges and flux densities of the complete sample

The average velocity range of the 165 water masers detected in this chapter is 26 km s^{-1} and they have a median velocity range of 13 km s^{-1}. In comparison, the average velocity range of the 379 water masers detected in Chapter 6 is 29 km s^{-1} and they have a median velocity range of 15 km s^{-1}. While these

numbers are quite similar, it is intriguing that velocity ranges of the sources that are potentially biased towards more evolved sources (those targeted towards a sample comprised of chiefly OH maser sites in Chapter 6) are, in general, larger than those detected towards the sample of dust clumps. In Chapter 7 we show evidence that suggests that both the 6.7 and 12.2 GHz methanol maser sources show an increase in velocity range as the sources evolve. Although complicated by the presence of high-velocity features, we have carried out a similar analysis on the water masers.

Further evidence to suggest that water masers presented in this chapter are less biased towards the more evolved sources (than is the case in Chapter 6) lies in the average and median flux density of the detected sources. In Chapter 6 we present evidence that suggests that the water masers increase in flux density as the sources evolve. The average flux density of the water masers detected towards the dust clumps is 39 Jy and they have a median of 4 Jy which are both lower than the average (57 Jy) and median (5 Jy) flux density of the sources presented in Chapter 6. This suggests that in the dust clump sample, we are sensitive to water masers over a broader range of evolutionary stages.

Association with other maser species and radio continuum

Hill et al. (2005) determined associations between their 1.2 mm dust clump sources with the 6.7 GHz methanol masers and UCHII regions (detected at 8 GHz) towards which their observations were targeted. We have made an investigation of the number of dust clumps, with and without associated water masers, that Hill et al. (2005) have designated as being 'mm-only' cores (i.e. sources without associated radio continuum emission or 6.7 GHz methanol masers), associated with 6.7 GHz methanol masers, associated with both 6.7 GHz methanol masers and radio continuum, and finally, those associated with only radio continuum. As in all of the statistical analysis in this chapter, all but one (which is missing values for some of the dust clump properties) of the 294 which were targeted for water masers have been included.

Table 5.13 shows a summary of the categories of dust clumps where we detect the water masers, as well as the water maser detection rate in each category. We find an overall water maser detection rate of 44 % towards the targeted dust

Table 5.13: *Summary of the number of dust sources that fall into the categories of 'mm-only' (those sources showing no associated methanol maser or radio continuum emission), those with associated methanol masers (meth), those with both methanol masers and radio continuum associations (meth+cont) and those with associated continuum (cont) from Hill et al. (2005). These numbers have been presented in two categories; those dust clumps with no detectable water maser emission, and those where we have detected water masers. The fourth column shows the water maser detection rate (%) in each of the categories.*

	No water	Water	Detection rate
'mm-only'	137	41	23
Meth	13	48	79
Meth+cont	5	25	83
Cont	10	14	58
Total	165	128	44

clumps, and that this number falls to 23 % for the 'mm-only' dust clump sources. The highest water maser detection rates are towards those dust clump sources that exhibit methanol maser emission, closely followed by those dust clumps showing only radio continuum emission. It can be seen that there are many more dust clump sources showing only water masers (41), than those showing only methanol masers (13). While some fraction of these 1.2 mm sources that show only methanol masers are likely to have associated water masers that were below our detection limits at the time of observation, it seems unlikely that this could be the case for all of them (by considering the statistics of detectability for the two epochs of water maser observations presented in Chapter 6). However, these sources will provide interesting targets for further water maser observations. Hill et al. (2005) suggests that these 'mm-only' cores may represent an earlier evolutionary phase than those sources showing methanol maser emission. If this is the case, these numbers certainly imply that water masers can be present even earlier than methanol masers. Supporting evidence for water masers having a longer lifetime than that of methanol masers is that water molecules are both more easily created and more robust than methanol, which is consistent with our interpretation.

An alternative explanation for the higher number of dust sources showing only water masers than only methanol masers is that a number of these additional water masers are associated with lower mass objects. Table 5.14 gives the average values of all of the 1.2 mm dust clump properties for sources associated with water masers. To allow a for a comparison, the average values are listed in the association categories; 'mm-only' (those sources showing no associated methanol maser or radio continuum emission), those with associated methanol masers (meth), those with both methanol masers and radio continuum associations (meth+cont) and those with associated continuum (cont) from Hill et al. (2005). It is evident from the values presented in this table that there are no obvious differences between the 'mm-only' sources compared with the other groups, other than the lower values of integrated and peak flux density, and FWHM. Comparing the properties of the dust clumps with associated water masers in the categories of 'mm-only' and those with methanol masers, shows that the main differences are that the sources with methanol masers are less dense and have brighter integrated

Table 5.14: *Average values of all of the 1.2 mm dust clump properties of sources that are associated with water masers, broken up into the association categories. Association categories are given in column 1, and are; 'mm-only' (those sources showing no associated methanol maser or radio continuum emission), those with associated methanol masers (meth), those with both methanol masers and radio continuum associations (meth+cont) and those with associated continuum (cont) from Hill et al. (2005). Average values of; the integrated flux density (Jy), peak flux density (Jy beam^{-1}), source full width at half maximum (FWHM) (arcsec), distance (kpc), mass ($M_{\odot}$), radius (pc) and H_2 number density (cm^{-3}), are given in columns 2-8, respectively.*

	Integ.	Peak	FWHM	Dist.	Mass	Radius	Density
'mm-only'	2.77	0.77	44.22	4.92	1295.56	0.53	60417.07
Meth	3.66	1.26	47.96	4.26	1188.55	0.47	97289.36
Meth+cont	12.89	4.66	74.96	5.20	4844.96	0.92	37392.00
Cont	5.27	1.78	63.64	5.84	2834.29	0.85	50050.00

and peak flux densities. These are consistent with the 'mm-only' water maser associated sources being younger than those in other categories.

We have investigated the water masers characteristics in each of the dust clump association categories. Table 5.15 presents the average and median values of both the water maser peak flux density and the velocity range. Like the methanol masers presented in Chapter 7, we find that there is a general gradient which tends from lower values of both flux density and velocity range for the probable younger sources to higher values for the more evolved sources. That is, those associated with 'mm-only' sources, to those with methanol masers, and then to those with methanol masers and radio continuum (Hill et al., 2005, Chapter 4). The exception to this trend is the last stage, where only radio continuum is seen.

If the numbers presented in Table 5.15 are representative of the larger population of water masers, then they imply that, while the water masers increase in flux density and velocity range as the sources evolve, towards the end of their lifetime this trend 'turns over' and they steadily decrease in both flux density

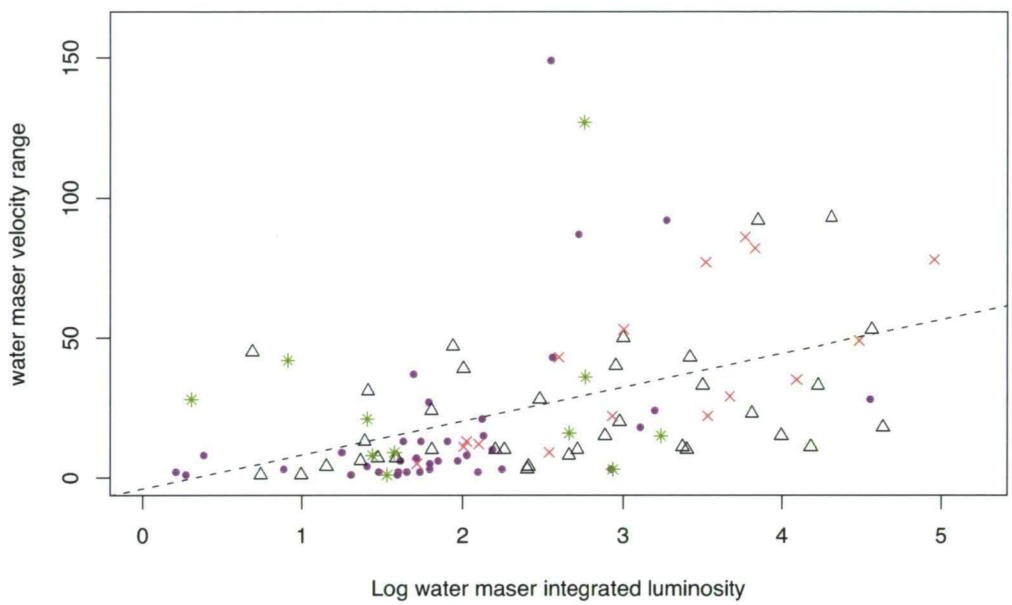

Figure 5.7: *Log of the integrated water maser luminosity versus the water maser velocity range. Shown on the plot are water sources that are associated with 'mm-only' sources (purple dots); water masers associated with methanol masers (black triangles); water masers associated with both methanol masers and 8 GHz radio continuum (red crosses); and water masers associated with only 8 GHz radio continuum (green stars). Overlaid is the line of best fit that corresponds to all of the water masers presented on the plot (linear regression gives; slope=12.11[2.37],* p-value= < *1.64e-06, and a correlation coefficient of 0.45).*

Table 5.15: *The average and median flux densities, and velocity ranges of all of the detected water masers. Water maser sources have been broken up into several categories, and are as for Table 5.13, with the addition of 'all sources' which shows the values for the entire sample.*

Water classification	Average flux density (Jy)	Median flux density (Jy)	Average vel range (km s^{-1})	Median vel range (km s^{-1})
all sources	39	4.4	26	13
'mm-only'	2	1.5	19	8
Meth	44	9	28	19
Meth+cont	107	18.5	42	23
Cont	9	1	26	17

and velocity range, presumably decreasing until the maser emission ceases. This is contrary to that seen in the case of methanol masers (Chapter 7), which seem not to experience any downwards trend, implying that they switch off much more abruptly.

In Fig. 5.7, the luminosities and velocity ranges of the water masers are presented, broken into the same categories of associations as in Table 5.13 and Table 5.15. It can be seen that there is a steady increase in both water maser luminosity and velocity range as you move through the association categories; 'mm-only'; to those with associated methanol masers; to those with both methanol masers and radio continuum. However, it is evident that there is significant overlap between the values within each association category. A high level of scatter is expected when considering water masers, since a number of sources show high velocity features and it is not clear that these are restricted to a certain evolutionary stage. Also shown on the plot are the sources that are associated with only 8 GHz radio continuum and these sources are scattered throughout the plot but none have large values of luminosity, and very few have large velocity ranges. These findings are consistent with those conclusions drawn from the average val-

Table 5.16: *Slopes and intercepts of the line of best fit of log integrated maser luminosity versus log of the H_2 number densities of the 1.2 mm dust clumps. Values for 6.7 and 12.2 GHz methanol masers are listed for comparison with the water maser values for comparison. Errors are presented in square brackets and follow the estimates of each value.*

Maser species	Slope	Intercept	Chapter
6.7 GHz	–0.72[0.25]	5.53[1.17]	7
12.2 GHz	–0.56[0.28]	4.16[1.23]	4
water	–0.43[0.07]	3.86[0.33]	current

ues that are presented in Table 5.15. Linear regression analysis of the full set of water masers (i.e. all of the association categories combined) shows that there is a statistically significant positive slope in the line of best fit and that there is a moderate correlation between data points.

Comparison between water maser luminosity and 1.2 mm dust clump H_2 number density

In Chapter 4 we show that the H_2 number density of the 1.2 mm dust clumps decreases as the sources evolve. In Figs 5.8 and 5.9 we present the log of the peak and integrated water maser luminosities versus the log H_2 number densities of the associated 1.2 mm dust clump. These plots show a slope that is consistent with our findings in Chapter 4 and those previously presented in this section - that the more luminous water masers are more evolved and that these are associated with the less dense 1.2 mm dust clumps and vice versa. Table 5.16 compares the computed slopes and intercepts of the line of best fit of the log luminosity 6.7 and 12.2 GHz methanol masers, along with the water masers versus the H_2 number densities of the associated clumps.

Inspection of the values listed in this table show firstly (as previously stated) that the 6.7 GHz methanol masers increase in flux density more rapidly as they

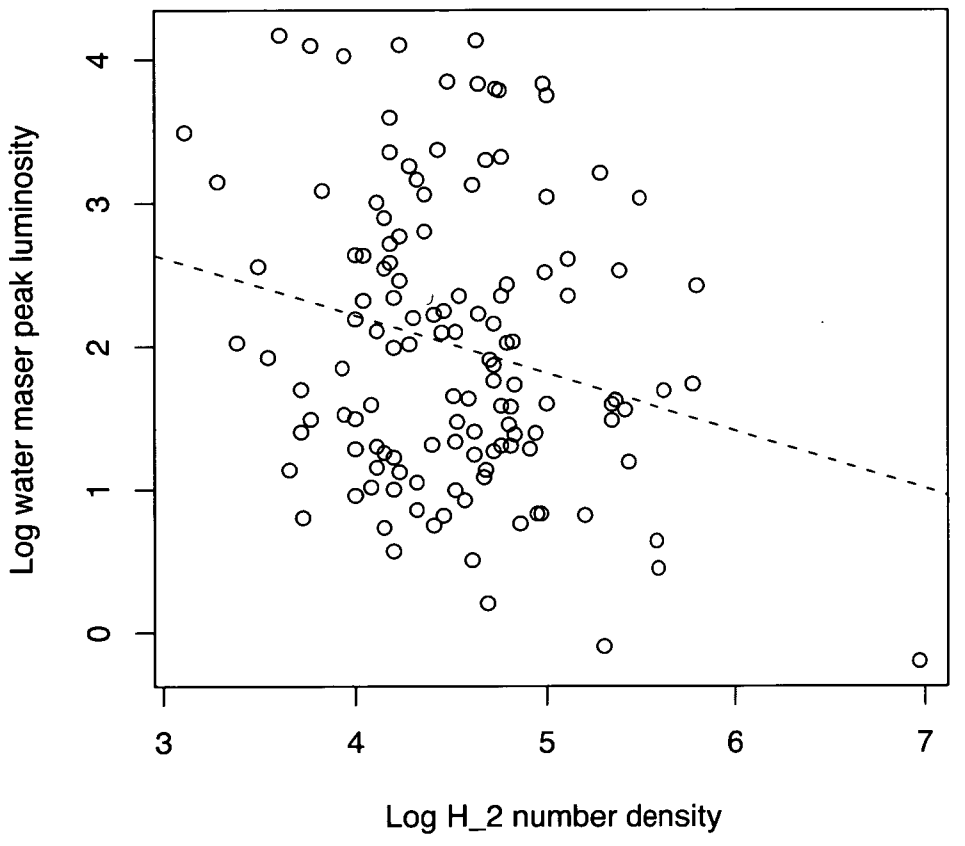

Figure 5.8: *Log water maser peak luminosity versus log of the H_2 number density of the associated 1.2 mm dust clump. The dashed line shows the line of best fit (which has a slope of −0.13[0.05] and an intercept of 4.79[0.11] and a correlation coefficient of 0.21).*

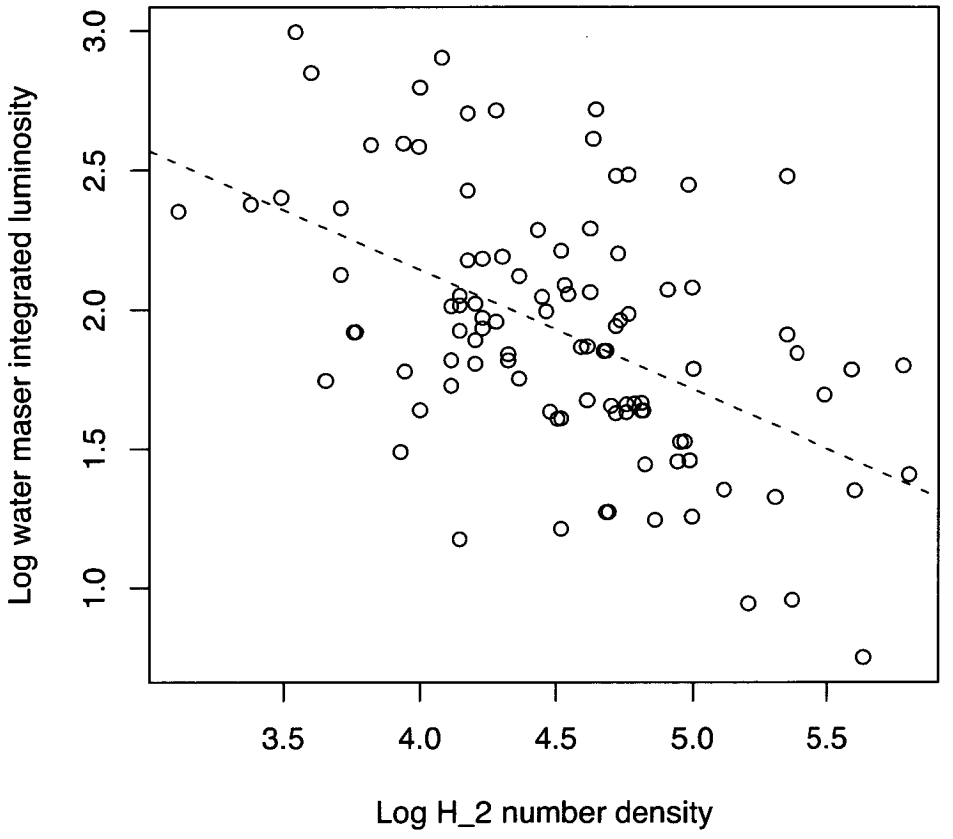

Figure 5.9: *Log water maser integrated luminosity versus log of the H_2 number density of the associated 1.2 mm dust clump. The dashed line shows the line of best fit (which has a slope of –0.43[0.07] and an intercept of 3.86[0.33] and a correlation coefficient of 0.50).*

evolve than the associated 12.2 GHz sources, and, as shown by the larger intercept, are generally stronger than the 12.2 GHz sources. Interestingly, the values associated with the water maser sources imply that the water masers also increase in flux density less rapidly than the 6.7 GHz methanol masers as they evolve and are also weaker in general at a given H_2 number density (than the sample of 6.7 GHz methanol masers). However, it is difficult to determine which of the maser species are present at the earliest evolutionary stage of high-mass star formation. While the water masers seem to be weaker than the 6.7 GHz methanol masers at a particular evolutionary stage, it is possible that the water masers spend a significant fraction of their lifetime as relatively weak sources.

5.5 Summary

The model for water maser presence in 1.2 mm dust clumps, as derived in Chapter 3, has been tested by targeting water maser observations towards 294 1.2 mm dust clumps. We find that there is a large number of water maser detections towards dust sources for which the computed probability of water maser presence in greater than 0.01, with a detection rate of 67 % towards these sources. However, since the number of clumps where we detect water maser (128) is higher than the number of clumps for which the probability of water maser presence is greater than 0.01 (58) it is clear the the model needs some refinement. However, some of this may be attributed to the adoption of the near kinematic distance for sources where distance ambiguities exist, since an assignment of the far distance would result in an inflated probability in a number of sources where water masers are detected.

In total, 165 water masers are detected towards 128 1.2 mm dust clumps, and an additional 4 water masers are detected towards no apparent 1.2 mm dust clump emission. A number of the water maser sources are detected here for the first time. Very few of the sources that had been previously detected and published in the literature have had accurately determined positions until now.

We have attempted to create a new model for water maser presence towards 1.2 mm dust clumps, but find that we are severely limited by distance uncertainties. Our analysis shows that the prospects of creating a reliable model for

water maser presence within 1.2 mm dust clumps is high when reliable distances can be assigned to the sources. Comparing the success of our model with that of Palla et al. (1991) shows that our model has a much higher detection rate in the sources that have large calculated probabilities of water maser presence.

A crude evolutionary implication of our derived model (in conjunction with the original model we present in Chapter 3), is that dust clumps with radii equal to 0.97±0.29 pc (calculated using the difference between the radii threshold implied from each model) have a 50 % chance of forming one or more sources that are able to excite water maser emission. Although a simplistic view, this further implies that the lifetime of the dust clump is approximately two times that of water masers.

Comparison between the 1.2 mm dust clump properties with and without associated water maser emission, shows similarly to results in Chapter 3, that the water masers are associated with the bigger, more massive sources with higher peak and integrated flux densities. There is a trend whereby the more luminous water masers are associated with 1.2 mm dust clumps with lower H_2 number densities than the less luminous water masers. This trend is also seen in the case of both 6.7 and 12.2 GHz methanol masers (Chapters 4 and 7).

Like the 6.7 and 12.2 GHz methanol masers presented in Chapter 7, we find that there is evidence for both the luminosity and the velocity range of the water masers to increase as the sources evolve. This implies that the gas volume conducive to the maser emission also increases with evolution. The water maser sources show evidence for this trend to 'turn over' towards the end of their lifetime, presumably showing a decline in both luminosity and velocity range until the emission ceases.

6

Water masers accompanying OH and methanol masers in star formation regions

6.1 Introduction

To date, the most extensive published unbiased survey for masers of the SFR variety completed in the Galactic plane is at the 1665 MHz transition of OH, presented as a catalogue reporting positions of arcsec accuracy for more than 200 masers (Caswell, 1998). Sensitive observations of 6.7 GHz methanol at these positions have already been made, with a detection rate of 80 % after high precision positions are compared (Caswell, 1998, 2009). Early 22 GHz water maser surveys with the Parkes radio telescope towards southern SFRs have been reported by Caswell et al. (1989) and references therein, with positions measured to about 10 arcsec accuracy. Until recent years, follow up observations to arcsec accuracy were restricted to northerly objects accessible to the VLA (Forster & Caswell, 1989, 1999). The availability of the 22 GHz frequency band at the ATCA has allowed us to search with high sensitivity and high positional precision for water masers towards the full sample of OH masers, as well as ~100 methanol maser sites.

6.2 Observations and data reduction

Water maser observations were made with the ATCA on two separate occasions. During the first epoch of observations (2003 October 4 and 5), OH maser sites from Caswell (1998) were targeted (see also Section 6.4.3) and during the second epoch (2004 July 25, 26 and 30) many water maser detections towards the OH masers were re-observed as well as a selected set of methanol masers (chiefly from Caswell, 2009). OH maser sources that were targeted in the first epoch but showed no detectable water maser emission were not observed at the second epoch, and only a few of the water maser sources that had previously been observed by Forster & Caswell (1989) with the VLA, and successfully confirmed during the first epoch, were reobserved.

Our first observations were made with an EW array yielding 10 baselines between 30 and 352 m (project c1190). The correlator sampled a single linear polarization, processed to give a 512-channel spectrum across a 32 MHz bandwidth. The observing strategy was to observe approximately 100 targets over each 12-h session. After initial calibration, the first 10 targets were observed for 1.5 min each, followed by a calibrator, and similarly for the remaining 90 targets. Then the cycle was repeated 2 more times, so as to provide for each source adequate uv-coverage, combined with a total integration time of 4.5 min. Primary flux calibration is relative to PKS B1934-638 and in general is expected to be accurate to ~20 %. PKS B1921-293 was used for bandpass calibration.

The AIPS reduction package was used for processing of the data collected in this first epoch, following the general procedure described in Caswell (1997). In the realignment of channels using the CVEL task, the adopted rest frequency was 22235.08 MHz, and the velocity scale was with respect to the local standard of rest (lsr). The channel separation was 0.84 km s^{-1} which, with uniform weighting of the correlation function, yields a final velocity resolution of 1.0 km s^{-1}. The quite coarse resolution was a compromise chosen in order to allow a large velocity coverage of more than 400 km s^{-1}. With this coverage, it was possible to recognise any high velocity features indicative of close association with outflows (for which the water masers are renowned).

Total intensity maps were then produced of the channels with maser emission

apparent in the scalar averaged spectrum, or in a vector averaged spectrum shifted to the location of the target OH or methanol maser emission. The rms noise in an individual channel image was typically 150 mJy. The synthesised beam has a halfpower width of approximately 8 arcsec in right ascension, but is larger in declination by a factor cosec(declination) as expected for an array aligned East-West with maximum baseline of 352 m.

Our second series of observations (project c1330) were made in similar fashion but with a different array configuration, H168. The correlator configuration, and therefore the spectral resolution and velocity coverage, was identical to that used in the 2003 observations. A few sample observations from this epoch were reduced, firstly with AIPS (as for the 2003 data), and secondly with `miriad` software package (Sault, Teuben & Wright, 1995). There was excellent agreement between data reduced in the respective data reduction packages. The full data set from this epoch were reduced using `miriad`, applying the standard techniques for ATCA spectral line and continuum observations. Image cubes of the entire primary beam and velocity ranges were produced for each source. The flux densities of sources that were located away from the centre of the primary beam have been corrected to account for beam attenuation. Spectra for each source detected at this epoch were produced by integrating the emission in the ATCA image cubes for each source. The typical resultant rms noise in each spectrum was 40 - 50 mJy. For the H168 array used in 2004, the synthesised beam was typically 13x9 arcsec.

The ATCA observations are most sensitive at the targeted positions, but provide useful measurements, albeit at lower sensitivity, of any other sources that happen to lie within the field of view of the primary beam; the full width to the first null is nearly 5 arcmin, and the HPBW is 2.29 arcmin = 137 arcsec.

6.3 Results

The search for 22 GHz water masers carried out with the ATCA in 2003 October and 2004 July towards 202 OH maser sites and 104 methanol maser sites (with no reported OH maser emission) resulted in the detection of 379 distinct water maser sites (Table 6.1). Spectra of all detected sources are shown in Fig. 6.1. For

Table 6.1: *22 GHz water masers detected towards sites of OH and methanol masers. Column 1 shows the source name in Galactic coordinates, column 2 and 3 give the right ascension and declination, column 4, 5 and 6 give the velocity of the water maser peak, velocity range and peak flux density in the 2003 observations, while columns 7, 8 and 9 give the velocity of the water maser peak, velocity range and peak flux density in the 2004 observations. A '–' in either column 6 or 9 indicates that no observations were made of the given source during the 2003 or the 2004 epoch, respectively, while the presence of a number preceded by a '<' indicates that there was no emission detected above the quoted threshold. For some complicated sources a 't' is present in either column 6 or 9 and this indicates that the exact nature of the detection is discussed in Section 6.3.1. Associations are given in column 10, where the presence of an 'o' denotes an OH maser, an 'm' denotes a methanol maser, a 'c' denotes the presence of a 22 GHz radio continuum source, a 'g' the presence of a GLIMPSE point source and the presence of a 'γ' indicates that the water maser source is outside the range of the GLIMPSE survey region. A '#' indicates that the proceeding associated source is strictly outside our association threshold but has been added through special circumstances. See Section 6.3 for a more extensive description.*

Water maser (l, b) (degrees)	RA (J2000) (h m s)	Dec (J2000) (° ′ ″)	Vpeak (km s^{-1}) 2003	Vrange (km s^{-1}) 2003	Speak (Jy) 2003	Vpeak (km s^{-1}) 2004	Vrange (km s^{-1}) 2004	Speak (Jy) 2004	Assoc.
G 240.316+0.071	07 44 51.94	−24 07 41.9	89	58,100	10			–	oγ
G 263.250+0.514	08 48 47.91	−42 54 27.1	19	17,21	3.0	20	17,21	0.7	omγ
G 284.350−0.418	10 24 10.60	−57 52 33.0	−4	−42,72	60	7	−78 ,71	102	oγ
G 285.260−0.067	10 31 24.57	−58 03 03.7	−28	−95,20	22	−92	−96,20	30	γ
G 285.263−0.050	10 31 29.64	−58 02 18.9	2	−59,50	1100	3	−36,63	1651	oγ
G 287.371+0.644	10 48 04.25	−58 27 00.7	1	−14,6	3.5	−1	−13,1	4.9	omγ
G 290.374+1.661	11 12 17.98	−58 46 21.6	−12	−20,−10	3.5	−47	−47,−33	0.26	omγ
G 290.384+1.663	11 12 22.53	−58 46 29.0	−38	−50,−35	6	−37	−41,−35	4.5	γ
G 291.270−0.719	11 11 49.67	−61 18 53.8	−102	−110,−23	65	−102	−109,−17	53	mγ
G 291.274−0.709	11 11 53.28	−61 18 24.1	−32	−51,14	60	−32	−59,−14	64	omγ
G 291.284−0.716	11 11 56.58	−61 19 01.1	−133	−142,−120	930	−133	−139,−120	701	γ
G 291.578−0.434	11 15 04.91	−61 09 50.7			<0.2	18	17, 27	16	γ
G 291.579−0.431	11 15 05.67	−61 09 41.0	12	−29,41	215	13	−31,22	608	omγ
G 291.581−0.435	11 15 06.17	−61 09 56.1	26	25,27	4.0			<0.2	mγ
G 291.610−0.529	11 15 02.58	−61 15 48.8	13	−66,20	18	12	−66,28	39	ocγ
G 291.627−0.529	11 15 10.18	−61 16 12.7	22	8,23	12	22	20,25	31	γ
G 291.629−0.541	11 15 08.88	−61 16 54.8	11	8,16	70	10	−2,21	46	γ
G 294.511−1.622	11 35 32.04	−63 14 44.3	−12	−20,−6	250	−12	−20,−4	112	omγ
G 294.976−1.733	11 39 13.77	−63 29 03.3			–	1	−17,5	2.2	γ
G 294.989−1.719	11 39 22.56	−63 28 25.1			–	−17	−18,−10	0.6	mγ
G 297.660−0.974	12 04 08.76	−63 21 37.3	29	−80,38	90	26	−79,82	75	o
G 299.012+0.125	12 17 24.05	−62 29 13.6			<0.2	−26	−27,−24	0.44	
G 299.013+0.128	12 17 24.58	−62 29 04.8	19	18,30	100	19	−1, 50	83	omcg
G 300.491−0.190	12 29 55.99	−62 57 33.8	24	23,25	2.3	25	22,25	1.6	

Table 6.1: – continued

Water maser (l, b) (degrees)	RA (J2000) (h m s)	Dec (J2000) (^{o} ′ ″)	Vpeak (km s^{-1}) 2003	Vrange (km s^{-1}) 2003	Speak (Jy) 2003	Vpeak (km s^{-1}) 2004	Vrange (km s^{-1}) 2004	Speak (Jy) 2004	Assoc.
G 300.504–0.176	12 30 03.42	–62 56 50.2	11	–37,14	180	11	–26,14	94	omg
G 300.968+1.143	12 34 52.51	–61 39 57.9	–61	–86,–42	70	–58	–86,–3	26	γ
G 300.971+1.143	12 34 54.34	–61 39 57.1			<3	–43	–46,–42	3.0	γ
G 301.136–0.225	12 35 34.76	–63 02 28.5			t	–47	–48,–41	17	
G 301.136–0.226a	12 35 34.93	–63 02 34.5	–29	–56,–18	80	–29	–31,–28	78	g
G 301.136–0.226b	12 35 34.84	–63 02 31.1			t	–45	–63,–43	92	(omc)
G 301.137–0.225	12 35 35.21	–63 02 30.6			t	–36	–40,–33	39	omc
G 305.191–0.006	13 11 12.95	–62 47 27.7	31	28,36	25	32	29,35	4.8	g
G 305.198+0.007	13 11 16.38	–62 46 37.4	–39	–42,–27	8	–35	–41,–24	3.5	
G 305.208+0.207	13 11 13.37	–62 34 40.0	–39	–43,–37	300	–39	–44,–38	235	om
G 305.361+0.150	13 12 35.61	–62 37 18.9	–43	–45,–28	250	–36	–44,–29	126	omg
G 305.799–0.245	13 16 42.92	–62 58 31.7	–26	–45,35	400	–34	–119,37	266	omg
G 306.318–0.331	13 21 20.87	–63 00 22.7	–19	–24,–14	2.1	–18	–23,–15	0.7	
G 307.805–0.456	13 34 27.32	–62 55 12.4	–13	–15,–7	1.4	–7	–11,–7	0.6	og
G 308.754+0.549	13 40 57.47	–61 45 42.4	–49	–50,–48	3.4	–49	–50,–48	0.7	omg
G 308.918+0.124	13 43 01.64	–62 08 48.9	–56	–66,–45	0.7	–61	–62,–49	1.5	om#
G 309.384–0.135	13 47 24.01	–62 18 11.4	–50	–57,–41	3.5	–50	–51,–48	2.2	omg
G 310.144+0.760	13 51 58.53	–61 15 40.6	–58	–60,–55	2.5	–58	–59,–57	1.6	omg
G 310.146+0.760	13 51 59.61	–61 15 39.7	–63	–64,–62	8			<0.2	
G 311.643–0.380	14 06 38.77	–61 58 22.7	35	18,50	320	36	8,56	167	omcg
G 312.106+0.278	14 08 46.06	–61 12 30.1			–	–54	–55,–53	0.6	g
G 312.109+0.262	14 08 49.45	–61 13 23.4			–	–48	–48,–47	0.43	mg
G 312.596+0.045	14 13 14.13	–61 16 57.6	–61	–62,–58	0.6	–59	–64,–56	1.5	m
G 312.599+0.046	14 13 15.19	–61 16 51.9	–75	–102,–58	2.7	–79	–96,–56	9	om
G 313.457+0.193	14 19 35.05	–60 51 54.2	–1	–2,0	1.9	45	–1,46	1.0	c
G 313.470+0.191	14 19 40.97	–60 51 46.2	–5	–10,–2	6	–6	–10,–1	4.5	omg
G 313.578+0.325	14 20 08.63	–60 41 59.0	–46	–58,–32	55	–47	–54,–32	46	omg
G 313.767–0.862	14 25 01.71	–61 44 57.2	–54	–56,–48	160	–54	–57,–36	162	omg
G 314.320+0.112	14 26 26.37	–60 38 29.4	–44	–70,–40	34	–45	–70,–40	16	om
G 316.360–0.361	14 43 11.07	–60 17 10.3	3	–4,21	30	3	–7,20	16	
G 316.361–0.363	14 43 12.22	–60 17 16.6	–3	–4,–1	6	–3	–7,–1	2.6	
G 316.412–0.308	14 43 23.22	–60 12 58.8	–22	–30,6	6	–20	–24,5	15	omcg
G 316.640–0.087	14 44 18.39	–59 55 10.7	–19	–104,–2	12	–15	–40,92	12	omg
G 316.763–0.011	14 44 56.32	–59 47 59.8	–47	–51,–33	60	–48	–49,–33	4.1	og
G 316.812–0.057	14 45 26.58	–59 49 14.1	–46	–47,–36	500	–46	–56,–11	408	om
G 317.429–0.561	14 51 37.72	–60 00 18.2	16	12,25	0.5	25	24,25	0.27	oc
G 317.429–0.556	14 51 36.75	–60 00 03.4	26	25,36	0.5	28	27,29	0.6	
G 318.044–1.404	14 59 08.61	–60 28 23.9	42	31,44	3.5	42	32,42	3.5	omγ
G 318.050+0.087	14 53 42.62	–59 08 52.3	–55	–61,–39	470	–48	–69,–38	50	omg
G 318.948–0.196a	15 00 55.18	–58 58 51.6	–41	–44,–28	5	–36	–44,–27	9	g
G 318.948–0.196b	15 00 55.33	–58 58 53.6			t	–38	–39,–21	7	omg
G 319.399–0.012	15 03 17.50	–58 36 11.4	–4.5	–20,1	10	–5	–7,2	3.8	oc
G 319.836–0.196	15 06 54.54	–58 32 58.6	–13	–23,0	9	–11	–19,0	2.8	omg
G 320.120–0.440	15 09 43.83	–58 37 06.3	–46	–70,–40	1.2	–46	–158,30	0.9	o
G 320.221–0.281	15 09 47.00	–58 25 47.6			<0.4	–73	–75,–72	0.7	
G 320.232–0.284	15 09 51.92	–58 25 38.0	–63	–70,–61	9	–67	–81,–72	2	om
G 320.233–0.284	15 09 52.50	–58 25 35.7	–60	–61,–58	3.5	–60	–61,–54	3.4	c
G 320.255–0.305	15 10 06.14	–58 26 00.8			–	–126	–144,–111	45	
G 320.285–0.308	15 10 18.88	–58 25 16.5			–	–69	–81,–56	15	g
G 321.028–0.484	15 15 50.90	–58 11 19.7	–60	–70,–55	2.5	–58	–70,–52	5	
G 321.033–0.483	15 15 52.60	–58 11 07.2	–60	–68,–58	3.6	–61	–64,–49	0.25	m
G 321.148–0.529	15 16 48.25	–58 09 50.1	–64	–66,–62	0.8	–97	–98,–61	1.6	omg
G 322.158+0.636	15 18 34.52	–56 38 24.7	–73	–81,–61	5	–76	–86,–65	2.7	om
G 322.165+0.625	15 18 39.74	–56 38 46.7	–40	–67,–36	9	–39	–67,–36	2.8	g
G 323.740–0.263	15 31 45.48	–56 30 49.6	–50	–72,–46	140	–50	–88,–42	70	omg
G 324.201+0.122	15 32 52.76	–55 56 04.9	–87	–100,–47	50	–87	–100,–48	14	o
G 324.716+0.342	15 34 57.41	–55 27 22.3	–55	–72,–47	10	–58	–81,–30	26	omg
G 326.662+0.521	15 45 02.73	–54 09 03.3	–39	–50,–34	256			–	m
G 326.665+0.553	15 44 55.82	–54 07 25.6			t	–42	–127,–39	16	g
G 326.670+0.554	15 44 57.03	–54 07 10.6	–42	–44,–40	26	–40	–48,8	101	o

Table 6.1: – continued

Water maser (l, b) (degrees)	RA (J2000) (h m s)	Dec (J2000) (^{o} ′ ″)	Vpeak (km s^{-1}) 2003	Vrange (km s^{-1}) 2003	Speak (Jy) 2003	Vpeak (km s^{-1}) 2004	Vrange (km s^{-1}) 2004	Speak (Jy) 2004	Assoc.
G 326.780–0.241	15 48 55.10	–54 40 38.6	–64	–66,–60	36	–66	–92,–52	18	og
G 326.859–0.676	15 51 13.82	–54 58 03.6			–	–103	–104,–103	0.42	mg
G 327.119+0.511	15 47 32.56	–53 52 39.3	–87	–90,–80	25	–88	–89,–57	19	omg
G 327.291–0.578	15 53 07.65	–54 37 07.2	–56	–80,–39	400	–63	–84,–36	668	omg
G 327.391+0.200	15 50 18.31	–53 57 06.1			–	–86	–92,–86	0.40	mg
G 327.402+0.445	15 49 19.32	–53 45 13.8	–80	–83,–68	230	–81	–84,–69	195	o#mcg
G 327.581–0.077	15 52 29.50	–54 02 51.6			–	–101	–102,–95	1.0	
G 327.594–0.095	15 52 38.19	–54 03 11.5			–	–99	–102,–91	0.8	g
G 327.619–0.111	15 52 50.31	–54 03 00.0			–	–85	–85,–84	0.20	mg
G 327.935–0.123	15 54 33.09	–53 51 29.1			–	–98	–100,–76	2.1	
G 328.236–0.548	15 57 58.21	–53 59 25.4	–38	–39,–37	30	–38	–40,10	20	omcg
G 328.254–0.532	15 57 59.69	–53 58 00.7	–50	–53,–48	200	–50	–51,–48	155	omg
G 328.306+0.432	15 54 05.91	–53 11 37.4	–96	–97,–87	40	–93	–96,–87	141	c
G 328.808+0.633	15 55 48.23	–52 43 05.2	–46	–47,–44	10	–46	–48,–44	4.4	omcg
G 329.021–0.186	16 00 24.32	–53 12 16.9	–42	–43,–41	2.4	–44	–44,–43	0.34	g
G 329.029–0.199	16 00 30.22	–53 12 34.3	–38	–40,–37	1.6			<0.2	og
G 329.030–0.205	16 00 31.90	–53 12 48.7	–39	–54,–34	8	–46	–52,–35	6	om
G 329.031–0.198	16 00 30.34	–53 12 26.5	–39	–54,33	5	–52	–65,33	1.2	omg
G 329.066–0.307	16 01 09.89	–53 16 01.5	–48	–50,–47	1.4	–45	–46,–45	0.6	omg
G 329.183–0.313	16 01 46.90	–53 11 41.7	–51	–66,–36	24	–50	–60,–39	34	omg
G 329.342+0.130	16 00 38.87	–52 45 22.9	–112	–115,–95	1.1	–112	–114,–100	2.2	
G 329.404–0.459	16 03 31.81	–53 09 30.8	–113	–117,–106	3.1	–113	–116,–111	2.4	
G 329.405–0.459	16 03 32.15	–53 09 29.0	–78	–80,–60	15	–77	–79,–44	10	om
G 329.407–0.459	16 03 32.77	–53 09 25.0	–74	–76,–72	80			<0.2	mg
G 329.421–0.167	16 02 19.85	–52 55 41.8			<0.8	–77	–78,–75	2.4	
G 329.424–0.164	16 02 20.03	–52 55 25.9	–78	–83,–60	0.8			<0.2	g
G 329.426–0.161	16 02 19.71	–52 55 12.8	–73	–78,–71	8	–73	–74,–72	10	
G 329.457+0.503	15 59 36.93	–52 23 53.6			–	–66	–68,–65	4.3	
G 329.622+0.138	16 02 00.28	–52 33 57.7			–	–82	–110,–66	30	mg
G 330.070+1.064	16 00 15.56	–51 34 25.7			–	–50	–75,–45	11	mγ
G 330.879–0.367	16 10 20.04	–52 06 06.8	–64	–72,–28	90	–60	–72,–25	95	omc
G 330.954–0.182	16 09 52.65	–51 54 54.6	–80	–150,70	240	–91	–191,56	323	ocg
G 331.132–0.244	16 10 59.73	–51 50 22.5	–99	–102,–73	280	–99	–118,–55	47	omg
G 331.278–0.188	16 11 26.51	–51 41 55.8	–86	–104,–79	55	–90	–118,–64	42	omg
G 331.342–0.346	16 12 26.49	–51 46 14.9	–60	–62,–59	1.8	–62	–64,–60	11	omg
G 331.418+0.252	16 10 10.56	–51 16 52.2			–	–71	–71,–70	0.6	g
G 331.442–0.187	16 12 12.46	–51 35 09.3	–88	–93,–72	70	–88	–113,–80	212	omcg
G 331.512–0.103	16 12 10.01	–51 28 36.7	–89	–162,–33	700	–90	–159,–32	534	ocg
G 331.555–0.122	16 12 27.20	–51 27 42.6	–99	–170,–96	20	–99	–166,–86	9	
G 332.094–0.421	16 16 16.68	–51 18 26.2			–	–59	–59,–58	0.29	m
G 332.296–0.094	16 15 45.84	–50 55 52.7			–	–50	–71,–43	6	m
G 332.349–0.433	16 17 30.03	–51 08 16.6			–	–67	–68,–67	2.9	
G 332.352–0.117	16 16 07.10	–50 54 31.0	–45	–48,–41	2.0	–60	–61,–60	0.5	om
G 332.604–0.167	16 17 29.45	–50 46 11.7			–	–46	–48,–45	2.4	mg
G 332.725–0.621	16 20 02.91	–51 00 33.1	–42	–43,–41	0.6	–58	–59,–56	5	omg
G 332.826–0.549	16 20 11.17	–50 53 14.6	–56	–72,–30	45	–59	–71,–35	70	mc
G 332.964–0.679	16 21 23.03	–50 52 57.3			–	–52	–52,–50	2.9	mg
G 333.030–0.063	16 18 56.86	–50 23 53.6			–	–40	–153,–40	3.4	mc
G 333.055–0.436	16 20 42.47	–50 38 46.4			–	–47	–57,–48	0.39	
G 333.114–0.439	16 20 59.30	–50 36 21.9	–62	–63,–60	4.6	–62	–62,–53	2.0	
G 333.121–0.434	16 20 59.70	–50 35 50.8	–57	–59,12	38	–47	–91,–33	21	m
G 333.126–0.440	16 21 02.69	–50 35 54.1	–50	–70,–48	19	–52	–72,–47	12	m
G 333.128–0.440	16 21 03.18	–50 35 51.8			<0.2	–124	–125,–124	0.79	m
G 333.130–0.425	16 20 59.75	–50 35 05.1	–39	–67,–38	23	–64	–65,–31	1.9	
G 333.132–0.560	16 21 36.46	–50 40 45.4			–	–53	–67,–46	1.9	
G 333.219–0.062	16 19 47.40	–50 15 53.8			<0.3	–13	–14,84	0.5	g
G 333.234–0.060	16 19 50.85	–50 15 09.7	–88	–102,–83	140	–88	–102,82	117	og
G 333.315+0.106	16 19 28.75	–50 04 39.7	–48	–68,–41	2.2	–48	–60,–48	6	omg
G 333.387+0.032	16 20 07.52	–50 04 47.4	–61	–63,–60	0.4	–61	–61,–60	0.14	omg
G 333.467–0.164	16 21 20.20	–50 09 46.1	–44	–46,–40	3.5	–42	–47,–40	3.2	om

Table 6.1: – continued

Water maser (l, b) (degrees)	RA (J2000) (h m s)	Dec (J2000) (° ′ ″)	Vpeak (km s^{-1}) 2003	Vrange (km s^{-1}) 2003	Speak (Jy) 2003	Vpeak (km s^{-1}) 2004	Vrange (km s^{-1}) 2004	Speak (Jy) 2004	Assoc.
G 333.608–0.215	16 22 11.08	–50 05 56.3	–51	–76,–45	50	–49	–83,–41	24	o
G 333.646+0.058	16 21 09.12	–49 52 45.1			–	–89	–90,–84	3.3	m
G 333.682–0.436	16 23 29.67	–50 12 07.4			–	–3	–3,–2	0.24	mg
G 333.930–0.134	16 23 14.68	–49 48 48.8			–	–46	–50,–45	0.18	m
G 334.635–0.015	16 25 45.83	–49 13 37.0			–	–26	–29,–15	49	mg
G 334.935–0.098	16 27 24.22	–49 04 11.0			–	–17	–18,–14	1.0	mg
G 334.951–0.092	16 27 26.96	–49 03 14.7			–	–21	–25,–20	1.3	
G 335.059–0.428	16 29 23.20	–49 12 31.3			t	–38	–39,–37	1.7	
G 335.060–0.428	16 29 23.24	–49 12 28.0	–46	–50,–37	12	–37	–44,15	3.0	omg
G 335.070–0.423	16 29 24.72	–49 11 47.7	–88	–109,–84	1.0	–90	–105,–84	5	g
G 335.585–0.285	16 30 57.34	–48 43 39.4	–45	–50,–40	30	–42	–49,–32	25	omg
G 335.586–0.290	16 30 58.73	–48 43 51.2	–48	–61,–33	5	–56	–57,–42	20	omg
G 335.588–0.264	16 30 52.52	–48 42 39.5	–51	–56,–48	16			<0.2	g
G 335.727+0.191	16 29 27.52	–48 17 51.9			–	–51	–51,–42	13	m
G 335.787+0.177	16 29 46.18	–48 15 49.1	–55	–56,–48	3 .0	–49	–59,–45	10	
G 335.789+0.174	16 29 47.33	–48 15 50.8	–46	–51,–45	3.0			<0.2	omg
G 335.789+0.183	16 29 45.10	–48 15 30.4	–91	–112,–89	4.2			<0.2	
G 336.018–0.827	16 35 09.35	–48 46 47.7	–54	–59,–36	120	–54	–59,–36	82	omc
G 336.352–0.149	16 33 30.73	–48 04 27.6	–79	–81,–78	0.4	–79	–81,–78	0.43	
G 336.359–0.137	16 33 29.37	–48 03 41.5	–67	–67,–66	0.5			<0.2	omc
G 336.433–0.262	16 34 20.31	–48 05 30.5			–	–89	–90,–88	0.6	mg
G 336.496–0.258	16 34 34.52	–48 02 34.3			–	–25	–38,–14	8	
G 336.830–0.375	16 36 26.19	–47 52 29.5			–	–20	–45,–19	0.28	mg
G 336.864+0.005	16 34 54.50	–47 35 37.7	–78	–80,–64	3.0	–66	–79,–65	2.2	om
G 336.864–0.002	16 34 56.02	–47 35 55.3	–73	–76,–71	4.5	–73	–77,–71	1.5	
G 336.870–0.003	16 34 57.91	–47 35 42.7	–77	–78,–55	2.0	–77	–78,–71	3.7	
G 336.983–0.183	16 36 12.38	–47 37 59.1	–76	–77,–74	0.4	45	–78,45	0.18	o#mc
G 336.991–0.024	16 35 32.53	–47 31 12.4	–48	–61,–44	4	–49	–54,–44	1.0	c
G 336.994–0.027	16 35 34.01	–47 31 12.2	–121	–137,–80	160	–120	–177,–47	158	omg
G 336.995–0.024	16 35 33.53	–47 31 00.6			<0.2	–54	–54,–48	1.1	g
G 337.258–0.101	16 36 56.36	–47 22 27.5	–69	–71,–52	1.6	–69	–69,–68	0.33	omg
G 337.404–0.402	16 38 50.57	–47 28 00.8	–40	–53,–37	140	–40	–49,–35	137	omcg
G 337.612–0.060	16 38 09.46	–47 05 00.3	–52	–101,–47	38	–51	–99,–46	17	omg
G 337.687+0.137	16 37 35.60	–46 53 46.3			–	–74	–151,–73	0.6	mg
G 337.705–0.053	16 38 29.72	–47 00 35.7	–48	–147,5	54	–49	–159,–31	39	omcg
G 337.916–0.477	16 41 10.49	–47 08 02.9	–46	–80,–28	400	–33	–65,–27	321	o
G 337.920–0.456	16 41 06.14	–47 07 02.3	–40	–42,–39	50	–40	–69,–27	22	om
G 337.994+0.133	16 38 48.63	–46 40 15.7	–114	–117,–110	4.5	–113	–116,–111	4.5	
G 337.998+0.137	16 38 48.53	–46 39 56.4	–39	–50,–32	30	–38	–47,–30	27	omg
G 338.069+0.011	16 39 37.98	–46 41 44.9	–37	–40,–21	1.3	–28	–46,–22	3.9	g
G 338.075+0.012	16 39 38.88	–46 41 26.8	–50	–51,–50	0.5			<0.2	omc
G 338.075+0.010	16 39 39.78	–46 41 31.8	–132	–139,–21	1.2	–48	–51,–28	1.2	m
G 338.077+0.019	16 39 37.69	–46 41 05.6	–40	–41,–38	1.0	–40	–40,–39	1.3	g
G 338.281+0.542	16 38 09.16	–46 11 02.6	–61	–68,–59	12	–64	–67,–58	4.6	omg
G 338.427+0.051	16 40 50.25	–46 24 05.5			–	–30	–46,–29	0.48	
G 338.430+0.053	16 40 50.50	–46 23 53.0			–	–44	–51,–29	3.2	g
G 338.433+0.057	16 40 50.08	–46 23 33.8			–	–29	–30,–29	0.19	m
G 338.435+0.055	16 40 51.23	–46 23 34.5			–	–31	–31,–30	0.58	
G 338.436+0.057	16 40 51.05	–46 23 26.8			–	–35	–56,–34	0.30	
G 338.440+0.064	16 40 49.87	–46 22 59.5			–	–81	–81,–80	0.6	g
G 338.461–0.245	16 42 15.57	–46 34 18.6	–53	–119,–51	9	–52	–114,–49	8	omg
G 338.462–0.259	16 42 19.49	–46 34 48.3			<0.2	–54	–55,–53	0.35	
G 338.472+0.289	16 39 58.99	–46 12 36.2	–54	–62,–22	25	–29	–62,–25	10	omg
G 338.562+0.217	16 40 38.12	–46 11 24.8			–	–39	–40,–39	0.22	mg
G 338.567+0.110	16 41 07.16	–46 15 28.1			–	–76	–92,–74	3.2	m
G 338.682–0.084	16 42 24.12	–46 17 59.1	–6	–18,–5	2.2	–16	–18,–6	0.7	ocg
G 338.920+0.550	16 40 34.02	–45 42 07.9	–110	–125,–65	17	–68	–127,–64	5.3	mg
G 338.925+0.556	16 40 33.63	–45 41 37.9	–63	–85,–61	160	–62	–86,–6	116	om
G 338.924–0.060	16 43 13.25	–46 06 04.2			–	–64	–69,–63	2.3	
G 339.582–0.127	16 45 58.88	–45 38 47.4			–	–28	–32,–26	0.27	mg

Table 6.1: – continued

Water maser (l, b) (degrees)	RA (J2000) (h m s)	Dec (J2000) (° ′ ″)	Vpeak (km s^{-1}) 2003	Vrange (km s^{-1}) 2003	Speak (Jy) 2003	Vpeak (km s^{-1}) 2004	Vrange (km s^{-1}) 2004	Speak (Jy) 2004	Assoc.
G 339.584–0.128	16 45 59.63	–45 38 44.3			–	–40	–41,–26	1.8	g
G 339.585–0.126	16 45 59.18	–45 38 36.7			–	–41	–75,–39	0.40	g
G 339.586–0.128	16 45 59.92	–45 38 39.7			–	–106	–112,–105	0.5	g
G 339.609–0.115	16 46 01.57	–45 37 07.3			<0.2	–71	–82,–67	3.0	
G 339.622–0.121	16 46 06.03	–45 36 44.5	–34	–38,–32	90	–33	–36,–32	43	om
G 339.762+0.055	16 45 51.56	–45 23 31.0			–	–57	–58,–57	0.25	mg
G 339.884–1.259	16 52 04.71	–46 08 33.6	–32	–50,–28	50	–51	–52,–24	4.3	omγ
G 340.054–0.243	16 48 13.82	–45 21 43.9	–54	–58,–44	35			–	omg
G 340.785–0.096	16 50 14.84	–44 42 24.7	–120	–121,–111	1.0			<0.2	omg
G 341.218–0.212	16 52 17.92	–44 26 51.6	–43	–47,–38	120	–39	–49,–23	33	omg
G 341.276+0.062	16 51 19.50	–44 13 44.0	–77	–80,–58	5	–64	–83,–62	10	omg
G 342.484+0.183	16 55 02.39	–43 12 59.3			–	–43	–44,–36	0.6	mg
G 343.126–0.065	16 58 17.54	–42 52 15.8	–16	–17,–15	2.5	–21	–23,–20	8	
G 343.127–0.063	16 58 17.29	–42 52 06.6	–35	–45,–20	250	–30	–46,–16	208	o
G 344.226–0.576	17 04 09.36	–42 18 58.0			<0.2	–19	–19,–18	0.33	
G 344.228–0.569	17 04 07.85	–42 18 38.9	–24	–28,31	8	–25	–52,–9	1.4	omg
G 344.421+0.046	17 02 08.53	–41 46 56.4	–27	–32,–18	1.8	–26	–31,–24	0.9	
G 344.582–0.024	17 02 57.94	–41 41 54.1	–4	–20,5	250	–4	–52,6	127	omcg
G 345.004–0.224	17 05 11.12	–41 29 04.1	–23	–46,16	3.0	15	–89,15	3.7	om#cg
G 345.010+1.793	16 56 47.51	–40 14 23.9	–17	–19,10	2.0			<0.2	omcγ
G 345.010+1.802	16 56 45.41	–40 14 04.2	–28	–33,–26	7	–25	–31,–18	23	γ
G 345.012+1.797	16 56 47.01	–40 14 08.5	–12	–13,7	50	–12	–12,7	29	mγ
G 345.397–0.950	17 09 33.08	–41 36 20.4	–21	–22,–20	3.1	–21	–27,–20	6	
G 345.402–0.948	17 09 33.62	–41 36 02.9	–26	–32,–21	8	–23	–32,–21	2.9	
G 345.405–0.947	17 09 33.83	–41 35 50.8			<0.5	–28	–28,–23	0.5	
G 345.406–0.942	17 09 32.71	–41 35 37.6	–15	–19,–12	3.0	–18	–20,–17	1.9	
G 345.408–0.953	17 09 35.85	–41 35 56.5			<0.5	–15	–16,36	0.5	o#m#c
G 345.412–0.955	17 09 37.08	–41 35 48.9			<0.2	–55	–55,–54	1.6	
G 345.425–0.951	17 09 38.64	–41 35 03.3	–13	–15,–12	1.5	–13	–16,–13	1.1	m
G 345.438–0.074	17 05 56.75	–41 02 54.9	–11	–32,–9	40	–12	–37,–8	15	o
G 345.482+0.309	17 04 28.41	–40 46 52.1	–52	–80,–24	15	–55	–82,–51	1.8	
G 345.487+0.314	17 04 28.19	–40 46 28.6	–16	–24,2	6	–13	–39,–12	0.7	m
G 345.493+1.469	16 59 41.47	–40 03 46.2	5	3,6	6			<0.2	oγ
G 345.494+1.470	16 59 41.15	–40 03 39.9	1	–16,2	1.0	0	–18,–4	1.8	γ
G 345.495+1.473	16 59 40.78	–40 03 28.9	–60	–62,–16	4.0	–9	–10,–8	1.5	γ
G 345.505+0.348	17 04 23.02	–40 44 23.5	–3	–43,1	22	–4	–42,4	4.5	om
G 345.505+0.343	17 04 24.35	–40 44 32.1			<0.2	–68	–70,–67	0.8	
G 345.699–0.090	17 06 50.72	–40 50 58.9	–10	–87,102	200	–5	–92,141	216	og
G 346.480+0.132	17 08 22.67	–40 05 26.9	–10	–12,–8	1.2			<0.2	omg
G 346.522+0.085	17 08 42.35	–40 05 08.1			–	4	–2,14	2.9	m
G 346.529+0.106	17 08 38.12	–40 04 03.9			–	4	–1,5	1.6	
G 347.588+0.213	17 11 27.61	–39 09 08.1			–	–93	–94,–93	0.7	
G 347.623+0.148	17 11 50.09	–39 09 45.8	–118	–120,–117	0.5	–118	–122,–116	1.0	
G 347.628+0.149	17 11 50.85	–39 09 29.6	–125	–133,–122	0.5			<0.2	omg
G 347.632+0.210	17 11 36.30	–39 07 06.5			–	–88	–95,–24	6	mc
G 348.533–0.974	17 19 16.20	–39 04 30.6	–56	–59,–10	3.2	–31	–93,24	1.8	
G 348.534–0.983	17 19 18.64	–39 04 47.3	–21	–30,–11	2.2	–14	–109,–12	0.9	
G 348.551–0.979	17 19 20.61	–39 03 49.2	–30	–32,–15	1.4	–18	–18,–17	0.28	mg
G 348.726–1.038	17 20 06.42	–38 57 13.2	–11	–64,42	115	–10	–77,61	162	γ
G 348.885+0.096	17 15 50.25	–38 10 12.3	–81	–84,–77	8	–80	–87,–77	8	omg
G 348.892–0.180	17 17 00.26	–38 19 27.9	7	6,12	2.0			–	omg
G 349.052+0.002	17 16 43.25	–38 05 18.2	15	14,17	3.0			<0.2	
G 349.067–0.018	17 16 50.82	–38 05 13.8	5	3,7	1.6	13	–14,19	1.0	omg
G 349.074–0.015	17 16 51.23	–38 04 49.3	–27	–32,–20	1.6	–26	–32,–24	1.2	g
G 349.068+0.110	17 16 19.24	–38 00 48.3	–25	–32,–22	3.0	–21	–22,–20	1.4	
G 349.092+0.105	17 16 24.66	–37 59 45.4	–80	–84,–74	43	–80	–84,–72	154	omg
G 350.015+0.433	17 17 45.43	–37 03 12.9	–35	–50,–26	4.7			–	omg
G 350.098+0.099	17 19 21.82	–37 10 41.2	–44	–45,–42	1.8			<0.2	
G 350.098+0.080	17 19 26.67	–37 11 20.8	–66	–68,–65	6	–67	–69,–67	2.6	g
G 350.100+0.081	17 19 26.74	–37 11 09.8	–68	–69,–67	4.0	–68	–69,–63	5	

Table 6.1: – continued

Water maser (l, b) (degrees)	RA (J2000) (h m s)	Dec (J2000) (° ′ ″)	Vpeak (km s^{-1}) 2003	Vrange (km s^{-1}) 2003	Speak (Jy) 2003	Vpeak (km s^{-1}) 2004	Vrange (km s^{-1}) 2004	Speak (Jy) 2004	Assoc.
G 350.105+0.084	17 19 26.78	−37 10 51.5	−71	−102,−38	6	−71	−74,−29	14	m
G 350.110+0.087	17 19 26.96	−37 10 29.0	−72	−74,−71	8	−72	−73,−70	14	g
G 350.112+0.089	17 19 26.96	−37 10 19.9	−172	−175,−110	2.0	−128	−164,−106	2.9	
G 350.113+0.095	17 19 25.69	−37 10 04.8	−66	−70,−64	2.5	−64	−79,−63	1.4	og
G 350.274+0.120	17 19 47.07	−37 01 16.6			–	−63	−63,−61	2.9	
G 350.299+0.122	17 19 50.89	−37 00 00.6			–	−68	−68,−67	0.17	m
G 350.330+0.100	17 20 01.79	−36 59 14.3	−68	−69,−60	1.0	−62	−68,−48	1.9	o
G 350.341+0.140	17 19 53.60	−36 57 19.0			–	−105	−105,−58	3.2	g
G 350.686−0.491	17 23 28.71	−37 01 47.9	−23	−22,−24	0.6	−14	−14,−13	1.0	omg
G 350.690−0.490	17 23 29.19	−37 01 35.6			<0.6	−22	−24,−21	3.4	
G 351.160+0.696	17 19 57.50	−35 57 54.1	−3	−11.5,−0.5	9	−3	−10,2	18	omc
G 351.163+0.696	17 19 58.13	−35 57 48.9			t	−10	−13,−9	10	
G 351.240+0.668	17 20 17.98	−35 54 57.6			–	−24	−38,31	21	
G 351.243+0.671	17 20 17.76	−35 54 42.8			–	−77	−108,84	453	m
G 351.246+0.668	17 20 19.01	−35 54 38.2			–	21	19,22	1.3	c
G 351.417+0.646	17 20 53.29	−35 46 58.3	−10	−58,50	1400			–	om
G 351.582−0.353	17 25 25.35	−36 12 44.0	−89	−120,−87	1600			–	omg
G 351.775−0.536	17 26 42.50	−36 09 15.9	−2	−32,21	85			–	om
G 352.098+0.160	17 24 45.25	−35 29 48.8			–	−75	−75,−73	2.5	g
G 352.111+0.176	17 24 43.79	−35 28 37.7			–	−60	−61,−60	1.3	mg
G 352.133−0.944	17 29 22.46	−36 04 59.9			–	−11	−17,−6	27	mg
G 352.162+0.199	17 24 46.36	−35 25 19.9	−45	−46,−44	1	−45	−119,−43	0.28	og
G 352.517−0.155	17 27 11.34	−35 19 32.0	−49	−53,−46	12			–	om
G 352.525−0.158	17 27 13.44	−35 19 15.7	−51	−53,−49	3.6			–	mg
G 352.623−1.076	17 31 14.93	−35 44 47.5	2	0,2	28	2	−7,3	8	γ
G 352.630−1.067	17 31 13.94	−35 44 08.8	−2	−10,20	35	0	−13,18	700	omγ
G 353.273+0.641	17 26 01.57	−34 15 14.7			–	−49	−110,−5	366	m
G 353.408−0.350	17 30 23.38	−34 41 29.8			<0.2	−14	−15,−13	0.6	g
G 353.411−0.356	17 30 25.31	−34 41 35.0			<0.2	−20	−21,−17	6.4	
G 353.411−0.362	17 30 26.78	−34 41 46.6			<0.2	−7	−7,−5	1.8	c
G 353.413−0.367	17 30 28.47	−34 41 49.1	−17	−29,−8	2.0	−20	−26,−9	7	g
G 353.413−0.365	17 30 27.84	−34 41 44.6	−20	−24,−18	4.5	−19	−25,−18	2.2	
G 353.414−0.363	17 30 27.56	−34 41 38.9	−10	−11,−9	2	1	−22,7	1.7	
G 353.463+0.563	17 26 51.25	−34 08 25.3	−47	−52,−46	1			–	g
G 353.464+0.562	17 26 51.61	−34 08 24.1	−60	−61,−59	0.7			–	omg
G 354.594+0.469	17 30 14.47	−33 15 03.2	−22	−25,−20	9			<0.2	
G 354.615+0.472	17 30 17.22	−33 13 54.4	−38	−40,−12	1.6			<0.2	om
G 354.703+0.297	17 31 12.96	−33 15 17.6			<0.4	105	104,112	1.6	
G 354.712+0.293	17 31 15.38	−33 14 57.8	96	95,105	1.1			<0.2	g
G 354.722+0.302	17 31 14.87	−33 14 08.3			<0.2	99	96,101	0.38	
G 355.343+0.147	17 33 29.00	−32 48 00.1	17	9,35	34			–	om
G 355.345+0.149	17 33 28.83	−32 47 49.9	72	8,109	2.2			–	m
G 357.965−0.164	17 41 20.12	−30 45 15.9	−4	−5,−3	53	−19	−20,−19	0.9	mg
G 357.967−0.163	17 41 20.30	−30 45 07.0	0	−80,100	40	−65	−81,87	57	om
G 358.371−0.468	17 43 32.01	−30 34 11.4	10	−5,12	2.7	2	2,31	1.4	mg
G 358.386−0.483	17 43 37.72	−30 33 50.6	−1	−4,1	4.5	0	−3,1	3.6	omcg
G 359.137+0.032	17 43 25.61	−29 39 18.6	−1	−117,26	300			–	omg
G 359.419−0.104	17 44 38.27	−29 29 12.0			<0.2	−26	−59,2	1.0	
G 359.436−0.102	17 44 40.23	−29 28 12.2	−59	−61,−50	15	−59	−61,−54	9	mg
G 359.436−0.104	17 44 40.66	−29 28 16.1	−56	−57,−55	1.5	−47	−48,−47	0.37	om
G 359.441−0.111	17 44 42.87	−29 28 15.4	−65	−66,−64	1.8			<0.2	
G 359.442−0.106	17 44 42.00	−29 28 00.6	−53	−54,−52	9	−53	−56,−52	0.928	g
G 359.442−0.104	17 44 41.47	−29 27 58.8			t	−60	−62,−58	0.8	
G 359.443−0.104	17 44 41.82	−29 27 56.5			t	−49	−52,−48	0.6	g
G 359.615−0.243	17 45 39.12	−29 23 29.6	22	−16,73	7	64	−15,68	14	omg
G 359.969−0.457	17 47 20.08	−29 11 59.0	11	10,16	27			–	om
G 0.209−0.002	17 46 07.44	−28 45 32.1			–	39	18,42	2.2	c
G 0.212−0.002	17 46 07.86	−28 45 23.0			–	56	55,65	0.9	m
G 0.216−0.023	17 46 13.20	−28 45 49.8			–	−11	−16,8	1.7	g
G 0.308−0.177	17 47 02.38	−28 45 55.2			–	−26	−27,−26	1.8	g

Table 6.1: – continued

Water maser (l, b) (degrees)	RA (J2000) (h m s)	Dec (J2000) (° ′ ″)	Vpeak (km s^{-1}) 2003	Vrange (km s^{-1}) 2003	Speak (Jy) 2003	Vpeak (km s^{-1}) 2004	Vrange (km s^{-1}) 2004	Speak (Jy) 2004	Assoc.
G 0.316–0.201	17 47 09.29	–28 46 15.5			–	23	14,31	22	mg
G 0.376+0.040	17 46 21.29	–28 35 39.7	40	5,58	55			–	omg
G 0.497+0.188	17 46 03.96	–28 24 50.7	–8	–72,25	7	26	–50,34	2.5	omg
G 0.547–0.851	17 50 14.52	–28 54 28.8	20	–60,110	200			–	omg
G 0.655–0.045	17 47 20.88	–28 23 59.9	–52	–55,–50	4.0			–	
G 0.657–0.042	17 47 20.44	–28 23 46.4	62	60,64	70			–	og
G 0.665–0.032	17 47 19.07	–28 23 03.5	4	0,7	4.3			–	g
G 0.668–0.035	17 47 20.26	–28 23 02.6	59	50,90	408			–	og
G 0.677–0.028	17 47 19.64	–28 22 18.9	36	14,132	330			–	g
G 2.143+0.009	17 50 36.13	–27 05 46.4	37	35,70	0.6			–	omg
G 2.536+0.198	17 50 46.66	–26 39 44.9			–	25	–1,63	30	m
G 5.886–0.392	18 00 30.52	–24 03 58.2	11	–10,23	40			–	o$^{\#}$m$^{\#}$
G 5.897–0.445	18 00 43.90	–24 04 58.1			–	19	19,20	0.9	
G 5.901–0.430	18 00 40.95	–24 04 19.6			–	14	–40,30	3.9	m
G 5.913–0.388	18 00 33.12	–24 02 28.4	–50	–65,–47	9.2			–	g
G 6.049–1.447	18 04 53.19	–24 26 40.3	20	18,22	1.0			–	oγ
G 6.534–0.105	18 00 49.44	–23 21 40.2			–	22	6,23	0.5	g
G 6.611–0.082	18 00 54.15	–23 17 00.8			–	6	–34,11	7	mg
G 6.796–0.257	18 01 57.71	–23 12 32.5	14	10,20	10	1	–1,24	5	omg
G 8.139+0.226	18 03 00.83	–21 48 09.5			–	16	1,24	18	mg
G 8.670–0.356	18 06 19.17	–21 37 31.0	34	30,44	10	36	–9,43	3.4	omc
G 8.673–0.354	18 06 18.98	–21 37 17.9	–4	–23,–3	0.5	–8	–20,4	0.36	
G 9.620+0.194	18 06 14.97	–20 31 37.5	5	–30,50	25	6	–19,11	12	o
G 9.622+0.195	18 06 14.88	–20 31 31.0	21	0,22	1.4	22	0,23	1.3	om$^{\#}$
G 9.986–0.028	18 07 50.20	–20 18 55.9			–	49	44,60	4.0	mg
G 10.288–0.125	18 08 49.44	–20 05 57.4			–	9	9,11	0.5	m
G 10.307–0.270	18 09 24.29	–20 09 08.8			–	33	32,33	0.8	
G 10.323–0.160	18 09 01.57	–20 05 07.6			–	–3	–6,62	3.2	m
G 10.331–0.159	18 09 02.30	–20 04 40.2			–	11	7,22	1.0	
G 10.342–0.143	18 09 00.11	–20 03 35.8			–	8	–40,61	4.8	mg
G 10.445–0.018	18 08 45.01	–19 54 35.1	71	58,85	6	70	69,81	2.7	
G 10.473+0.027	18 08 38.30	–19 51 48.8	60	30,93	45	62	28,129	169	omcg
G 10.480+0.034	18 08 37.69	–19 51 12.4	64	63,65	12			<0.2	om
G 10.623–0.383	18 10 28.57	–19 55 49.4	2	–11,5	350			–	og
G 10.625–0.335	18 10 18.07	–19 54 20.5			–	–5	–6,–5	0.40	
G 10.959+0.022	18 09 39.38	–19 26 27.0			–	25	7,26	2.9	mcg
G 11.034+0.062	18 09 39.75	–19 21 21.1	18	16,19	0.6			–	om
G 11.498–1.486	18 16 22.32	–19 41 26.1			–	17	–3,21	112	mγ
G 11.903–0.142	18 12 11.41	–18 41 33.0	36	35,38	0.3			<0.2	om
G 12.203–0.107	18 12 40.25	–18 24 47.4	33	32,35	6	35	32,37	8	m
G 12.209–0.102	18 12 39.88	–18 24 17.1	21	–12,42	141	22	–15,50	51	mcg
G 12.216–0.119	18 12 44.55	–18 24 25.2	26	25,42	6	26	0,38	10	og
G 12.681–0.183	18 13 54.82	–18 01 47.0	61	55,63	1200	61	17,62	445	omg
G 12.884+0.502	18 11 47.92	–17 31 21.3	42	41,43	1.3	40	34,41	1.1	
G 12.889+0.489	18 11 51.54	–17 31 27.9	30	28,32	45	30	28,39	59	omg
G 12.901–0.242	18 14 34.50	–17 51 51.6	35	23,37	8	36	23,37	12	g
G 12.908–0.260	18 14 39.45	–17 52 01.4	37	21,39	0.8			<0.2	om
G 15.016–0.679	18 20 23.11	–16 12 38.8			t	19	14,21	11	
G 15.025–0.658	18 20 19.50	–16 11 31.9			t	25	14,31	4.2	
G 15.026–0.654	18 20 18.72	–16 11 23.3	27	27,31	29	28	26,31	16	
G 15.028–0.673	18 20 23.04	–16 11 48.4	19	17,28	197	20	14,31	67	
G 15.032–0.667	18 20 22.35	–16 11 27.2	45	44,46	1.8	40	–8,41	1.1	g
G 15.032–0.670	18 20 23.01	–16 11 30.1			t	26	14,28	12	
G 15.034–0.667	18 20 22.58	–16 11 18.4			t	17	17,21	3.8	
G 17.638+0.156	18 22 26.45	–13 30 12.4	27	15,29	230	27	17,35	245	om

the majority of sources, the spectra are taken from the 2004 data, except where sources were either not observed or not detected at this epoch. For these latter cases we show the 2003 spectra and distinguish them from the 2004 spectra with a '2003' in the top left hand corner of each spectrum. The 2003 spectra were obtained directly from the uv data with a phase shift to the source position, and amplitude correction for offset from the field centre. For eight sources we show a spectrum from each epoch to either highlight that a weak source is a genuine detection (333.387+0.032 and 336.983-0.183) or to give an indication of the level of variability seen over the 10 month time-scale (284.350–0.418, 321.148–0.529, 327.291–0.578, 345.004–0.224, 15.026–0.654 and 15.028–0.673). A velocity range of 200 km s^{-1} is shown for the majority of sources, but there are several instances where we either decreased this value to clearly show individual features in spectra that are complex (or include multiple nearby sources) or increased it in order to display extremely high velocity features. A decreased velocity range of 100 km s^{-1} is shown for the following sources; 301.136–0.225, 301.136–0.226a, 301.136–0.226b, 301.137–0.225, 335.060–0.428/335.059–0.428, 336.991–0.024, 336.995–0.024, 359.441–0.111, 359.442–0.106, 359.442–0.104, 359.443–0.104. An increased range of 300 km s^{-1} was used for 320.120–0.440, 330.954–0.182, 333.219–0.062, 333.234–0.060, 345.699–0.090, 357.965–0.164, 357.967–0.163, 0.547–0.851, 0.668–0.035, 0.665–0.032, 0.655–0.045, 0.657–0.042 and 0.677–0.028.

A number of the sources that we detect have been observed previously and have been presented in the literature (e.g. Johnston et al., 1972; Caswell et al., 1974; Kaufmann et al., 1976; Genzel & Downes, 1977; Batchelor et al., 1980; Braz & Scalise, 1982; Braz & Epchtein, 1983; Caswell et al., 1989; Hofner & Churchwell, 1996, and references therein) but the majority of these earlier observations (performed up to 20 years ago) were made with relatively poor positional accuracy. Due to the intrinsically variable nature of water masers, many sources exhibit levels of variability so extreme that they display no common spectral features at epochs separated by many years. This, combined with the tendency of water masers to form in clusters, and the previously poor positional information, mean that it is almost impossible to accurately match up sources from the literature with our present data. We have therefore limited our references (in Section 6.3.1) to previous detections of sources that were observed with high positional

precision (e.g. Forster & Caswell, 1989; Caswell & Phillips, 2008, Chapter 3), or where there was little doubt that the sources were the same.

The majority of OH maser targets were observed in both 2003 and 2004, whereas the methanol maser targets were observed in 2004 only. Where appropriate data were available for both epochs, reported positions are the average of the two since, in general, it provides the most accurate positions for the sources. For sources north of declination –20°, we have used a weighting of 2:1 for the declinations in favour of the 2004 data to account for the three times more elongated beam of the 2003 observations (a consequence of the different array configurations). Sources that were observed at both epochs allowed a direct comparison of the positions for each of the sources and therefore afford verification of the positional uncertainties.

Additional to direct comparison of 2003 with 2004 data, an overall assessment of data quality and reliability was made in several other ways. Forster & Caswell (1989) and Forster & Caswell (1999) used their VLA observations of a sample of more than 70 SFR targets with OH and water masers, to show that more than half were a simple association of water and OH masers coincident to within their combined relative errors (of typically 1 arcsec). Subsequent observation of the more southerly OH masers in that sample with the ATCA (Caswell, 1998) showed that the most southerly ones (observed by the VLA inevitably at low elevation) had significantly larger position uncertainties, and corrections to the positions resulted in an increased number of close OH/water maser associations. Thus we may expect the majority of our sample to show a water maser position coincident with OH, and thus the OH position is an indirect check on the accuracy of the newly derived water positions.

A further assessment was made using the 35 masers north of declination –47 degrees which are present in the Forster & Caswell (1989) target list. The Forster & Caswell (1989) absolute positions for the more southerly targets, although of variable quality for the OH masers (where ionospheric effects at low elevation can be significant), appear to remain excellent for the water masers. Thus we can directly compare our positions to those of Forster & Caswell (1989), to assess the errors in our current data. Furthermore, in some fields there is a strong ultracompact HII (UCHII) region that has been measured to subarcsecond accuracy,

such as in the 6 GHz observations of Caswell (1997) and C2001; where these are detectable in the current 22 GHz observations, they allow a further check on the positions, without the need for any assumptions concerning the true relative positions of the masers.

From these many comparisons, we are able to estimate our rms positional uncertainty as 2 arcsec. The target OH and methanol masers have rms position uncertainties of 0.4 arcsec (Caswell, 1998, 2009). An additional positional uncertainty in characterising any water maser site by a single position arises because a single site sometimes consists of many separate spots with angular separations as extensive as 4 arcsec (e.g. Reid et al., 1988), explicable by an outflow (e.g. Caswell & Phillips, 2008). We therefore regard our water maser sources to be associated with OH or methanol masers when they are separated by less than 3 arcsec, a threshold which captures most associations without diluting them with too many false, chance, coincidences; see also further discussion in Section 6.4.2. Where the water maser positions are derived from a single epoch, we relax this threshold to 4.5 arcsec. As the positions of the 22 GHz radio continuum have also been determined from a single epoch, a threshold of 4.5 arcsec is similarly adopted for continuum associations. Most of our proposed associations correspond to a much better accuracy (see Table 6.3) than our thresholds. There are, however, some more complex cases that have been judged on individual merit as discussed in detailed considerations summarized in Section 6.3.1. For example, the required precision of agreement was relaxed for sources believed to be nearby, at a distance of less than 2 kpc. Comparison of our 379 water maser positions with the positions of OH and methanol masers shows that 128 are coincident with both species, 33 are coincident with OH only and 70 are coincident with the location of methanol masers (see Section 6.4.3 for more extensive discussion). Surprisingly, 148 sources have no association with other maser species and we describe these as 'solitary'.

Details for the 379 sources that we detect are presented in Table 6.1 and, following the usual practice, the Galactic longitude and latitude of each source, listed in the first column, is used as an identifying source name for each water maser. These Galactic coordinates are derived from the more precise measurements of equatorial coordinates given in columns 2 and 3. The peak velocity and

velocity range (w.r.t. lsr), followed by the peak flux density, are given in columns 4, 5 and 6 for the 2003 epoch and in columns 7, 8 and 9 for the 2004 epoch. The presence of a '–' in either column 6 or 9 indicates that no observations were made for that source during the 2003 or 2004 observations respectively and a 't' in either column indicates that there is a comment in the text of Section 6.3.1 explaining the nature of the detection status at the indicated epoch. The presence of a number preceded by a '<' in either column 6 or 9 indicates that no emission above the quoted flux density was detected at that epoch. Column 10 gives a list of associations for each water maser source; here, the presence of an 'o' denotes the presence of an associated OH maser, 'm' the presence of an associated methanol maser, 'c' the presence of associated 22 GHz continuum emission (in our observations) and 'g' the presence of an associated GLIMPSE point source. A 'γ' in this column indicates that the source is outside the GLIMPSE survey region. A '#' following an 'o' indicates that the OH maser is strictly outside our association threshold but is associated with the methanol maser that falls within our threshold for a given source, meaning that either all three sources are coincident or the water maser is offset; similarly for the case where a '#' follows an 'm'. In some cases we have the situation that both the OH and the methanol masers are strictly located outside the association threshold but we regard them as associated through special circumstances, in which case we have used the '#' after both the 'o' and the 'm'. In the case of 301.136-0.226 a second water maser site lies within the association threshold for the same methanol and OH masers and the association is shown in parentheses.

OH masers that were searched and resulted in no water maser detection are listed in Table 6.2. The first column gives the name of the OH maser followed by its right ascension and declination. Column 4 gives the angular separation between the OH maser and the nearest methanol maser (Caswell, 2009) within 2.5 arcsec, and when a '–' is present, this signifies that there is no methanol maser within 2.5 arcsec of the OH maser.

An extensive list of the OH and methanol masers associated with our water maser sources, as well as water maser associations with 22 GHz continuum sources is given in Table 6.3. All OH and methanol masers as well as 22 GHz radio continuum that fall within 5 arcsec of the water masers are presented. Column 1

in Table 6.3 gives the water maser source name, and the name of the nearby OH and methanol masers are given in columns 2 and 4 respectively. The source names, based on the precise positions of individual species, inevitably differ slightly in a few cases due to different small position errors. The angular separations between the water masers and OH masers are given in column 3, and between water and methanol masers in column 5. Columns 6, 7 and 8 give the peak velocity of the water (2004 values are given unless not available, in which case the 2003 value is used) and the coincident OH and methanol maser sources. Column 9 gives the Galactic coordinates of 22 GHz continuum sources that we detect, followed by the angular separation between the continuum source and the water maser in column 10. The discussion of individual sources in Section 6.3.1 includes some comparisons between the positions of water maser sources and other masers, continuum and GLIMPSE sources.

A complete list of the continuum sources detected towards water maser sources in the 2004 observations is given in Table 6.4. Associations between the 29 water maser sources observed only during the 2003 observations and possibly associated 22 GHz continuum sources (see Section 6.4.6) have not been determined.

Table 6.2: *OH masers with no associated water maser emission. Listed in column 1 is the OH maser source name followed in columns 2 and 3 by the right ascension and declination. Column 4 shows the angular separation between the listed OH maser and a nearby methanol maser; a – in this column indicates that there is no known methanol maser sources within 2.5 arcsec.*

OH maser (l, b) degrees	RA (J2000) (h m s)	Dec (J2000) (° ′ ″)	Methanol maser sep. (arcsec)
G 232.621+0.996	07 32 09.82	−16 58 13.0	0.7
G 300.969+1.147	12 34 53.24	−61 39 40.3	0.5
G 305.200+0.019	13 11 16.90	−62 45 54.7	0.5
G 305.202+0.208	13 11 10.61	−62 34 37.8	1.3
G 306.322−0.334	13 21 23.00	−63 00 30.4	0.9
G 309.921+0.479	13 50 41.73	−61 35 09.8	0.9
G 313.705−0.190	14 22 34.72	−61 08 27.4	0.8
G 316.359−0.362	14 43 11.00	−60 17 15.3	2.5
G 321.030−0.485	15 15 51.67	−58 11 18.0	0.9
G 323.459−0.079	15 29 19.36	−56 31 21.4	1.4
G 328.307+0.430	15 54 06.48	−53 11 40.3	–
G 329.339+0.148	16 00 33.15	−52 44 39.8	0.2
G 331.542−0.066	16 12 09.05	−51 25 47.2	0.5
G 331.543−0.066	16 12 09.16	−51 25 45.3	0.2
G 331.556−0.121	16 12 27.19	−51 27 38.1	0.2
G 332.295+2.280	16 05 41.72	−49 11 30.5	0.2
G 332.824−0.548	16 20 10.23	−50 53 18.1	–
G 333.135−0.431	16 21 02.97	−50 35 10.1	2.4
G 335.556−0.307	16 30 56.00	−48 45 51.0	0.8
G 336.822+0.028	16 34 38.26	−47 36 33.0	0.8
G 336.941−0.156	16 35 55.22	−47 38 45.7	0.4
G 338.875−0.084	16 43 08.23	−46 09 12.8	0.2
G 339.053−0.315	16 44 49.16	−46 10 14.4	2.2
G 339.282+0.136	16 43 43.12	−45 42 08.4	0.4
G 339.682−1.207	16 51 06.21	−46 15 57.8	0.4
G 343.930+0.125	17 00 10.92	−42 07 18.7	0.6
G 344.419+0.044	17 02 08.67	−41 47 08.6	1.8
G 345.498+1.467	16 59 42.81	−40 03 36.2	0.4
G 347.870+0.014	17 13 08.80	−39 02 29.5	–
G 348.550−0.979	17 19 20.39	−39 03 51.8	0.3
G 348.579−0.920	17 19 10.56	−39 00 24.5	0.6
G 348.698−1.027	17 19 58.91	−38 58 14.1	–
G 348.703−1.043	17 20 03.96	−38 58 31.3	1.2
G 348.727−1.037	17 20 06.55	−38 57 08.2	0.9
G 350.011−1.342	17 25 06.50	−38 04 00.7	0.5
G 353.410−0.360	17 30 26.20	−34 41 45.5	0.3
G 354.724+0.300	17 31 15.52	−33 14 05.3	0.5
G 356.662−0.264	17 38 29.22	−31 54 40.6	2.0
G 3.910+0.001	17 54 38.77	−25 34 45.2	0.5
G 8.683−0.368	18 06 23.46	−21 37 10.2	0.4
G 12.025-0.031	18 12 01.88	−18 31 55.6	0.3
G 15.034−0.677	18 20 24.75	−16 11 34.9	0.6

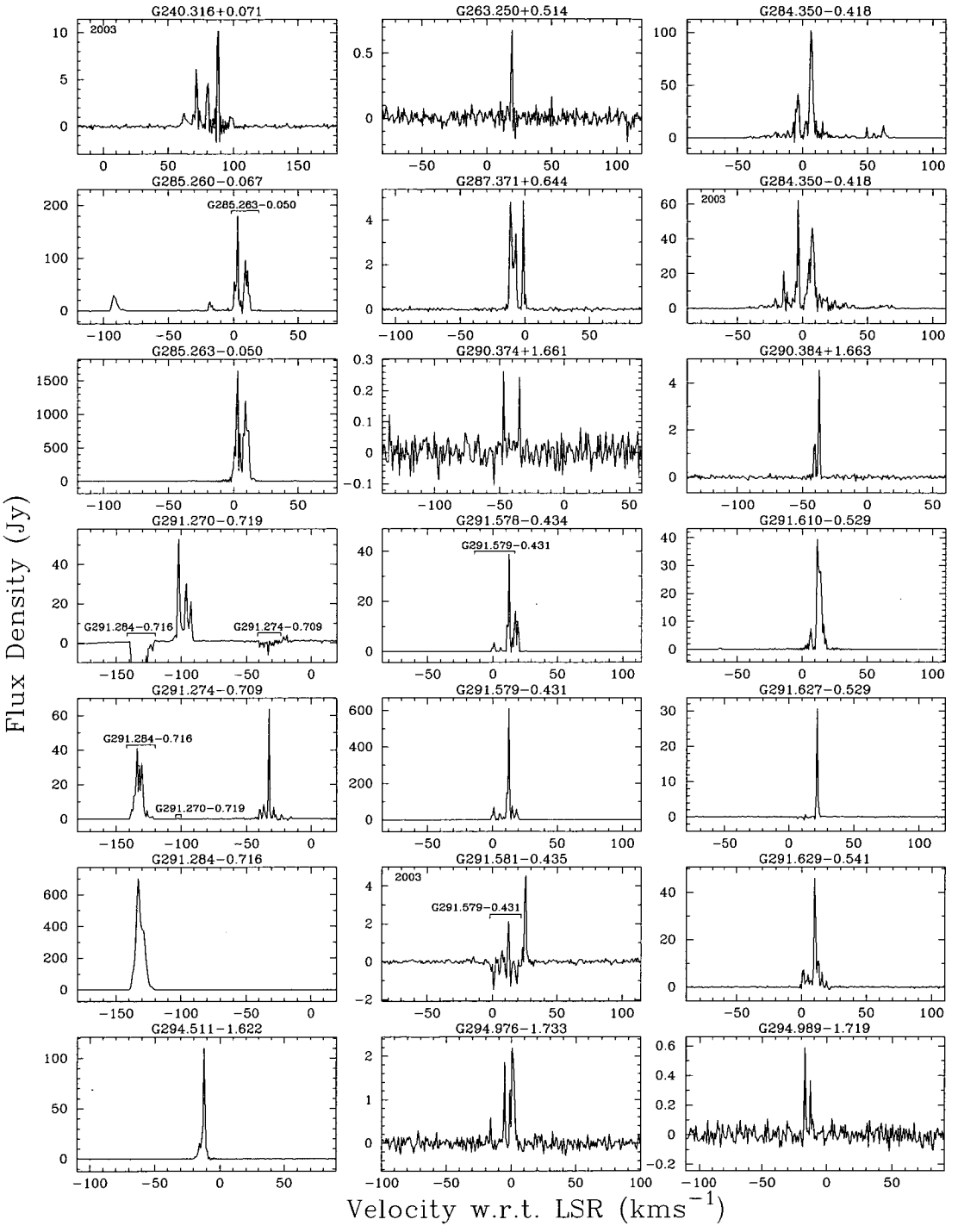

Figure 6.1: *Spectra of the 22 GHz water masers detected towards sites of OH and methanol masers.*

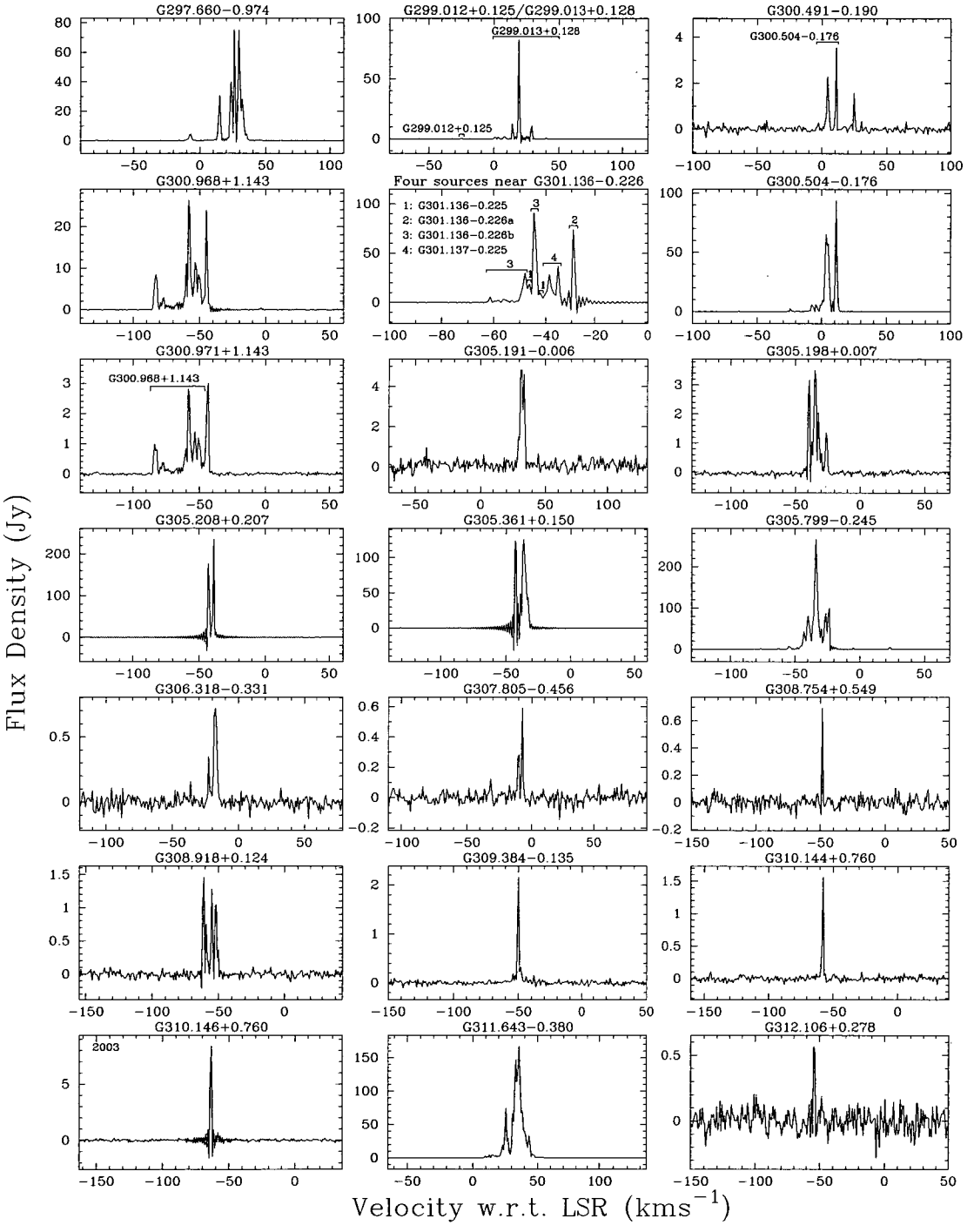

Figure 6.1: –continuued

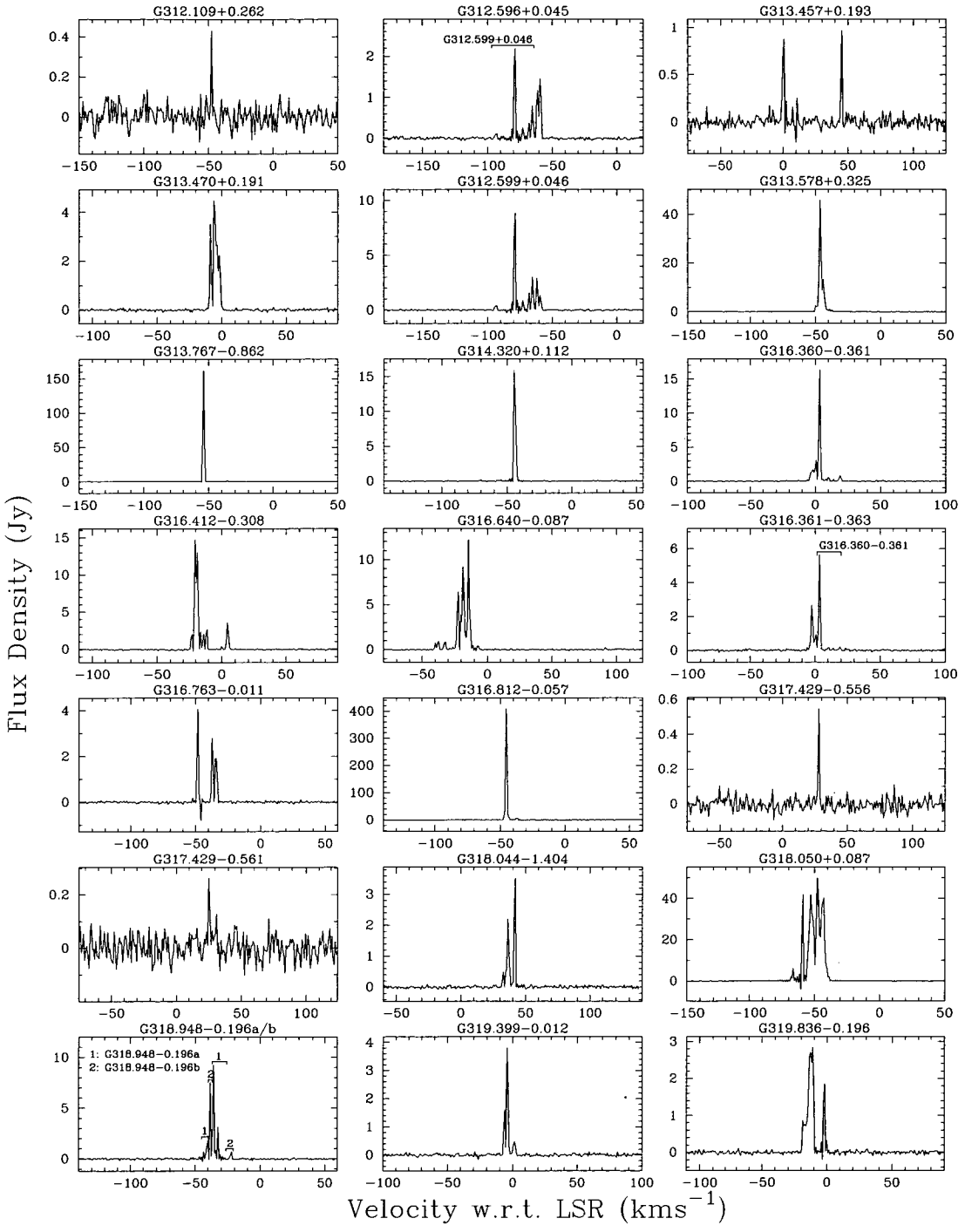

Figure 6.1: –continued

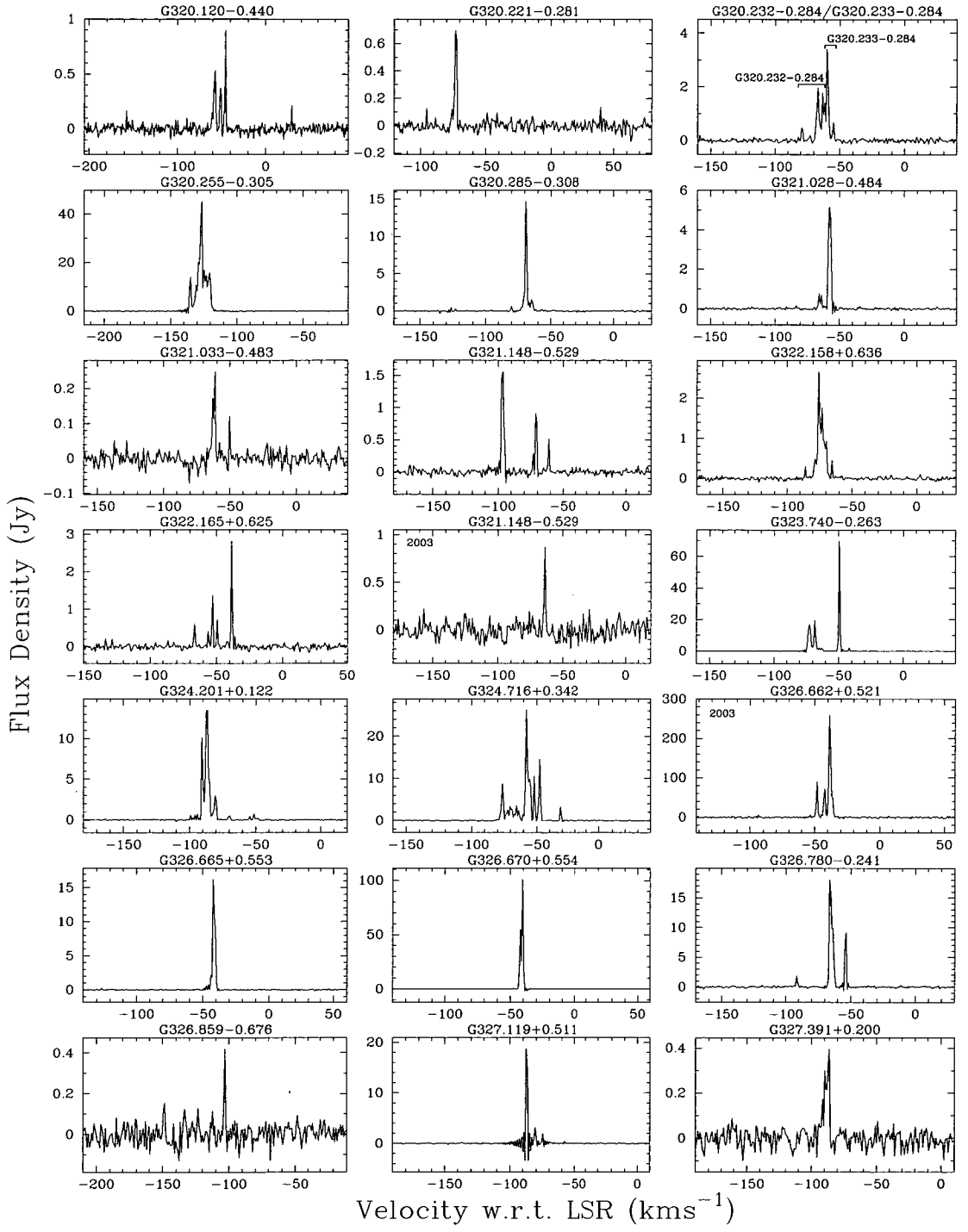

Figure 6.1: –continuued

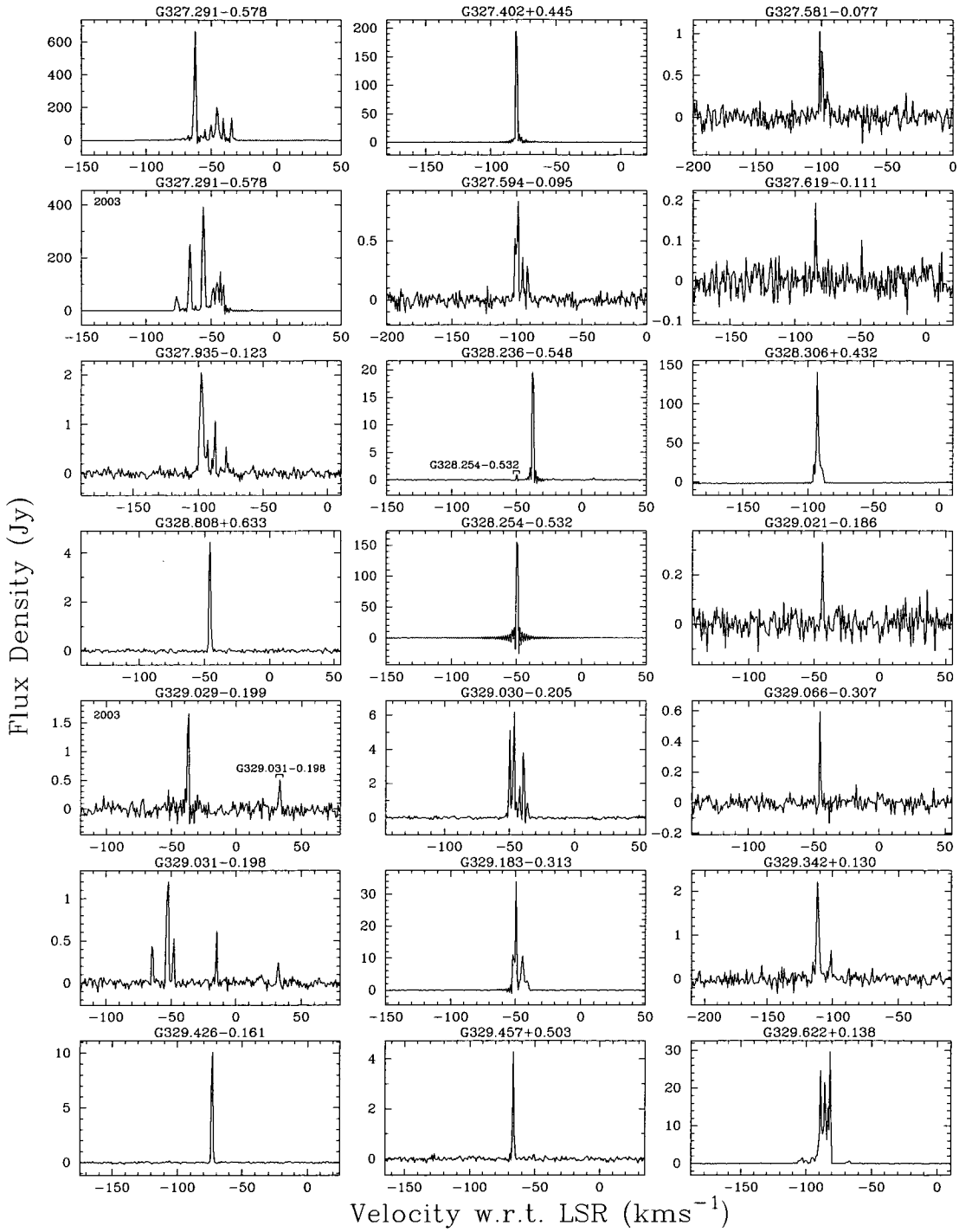

Figure 6.1: -continuued

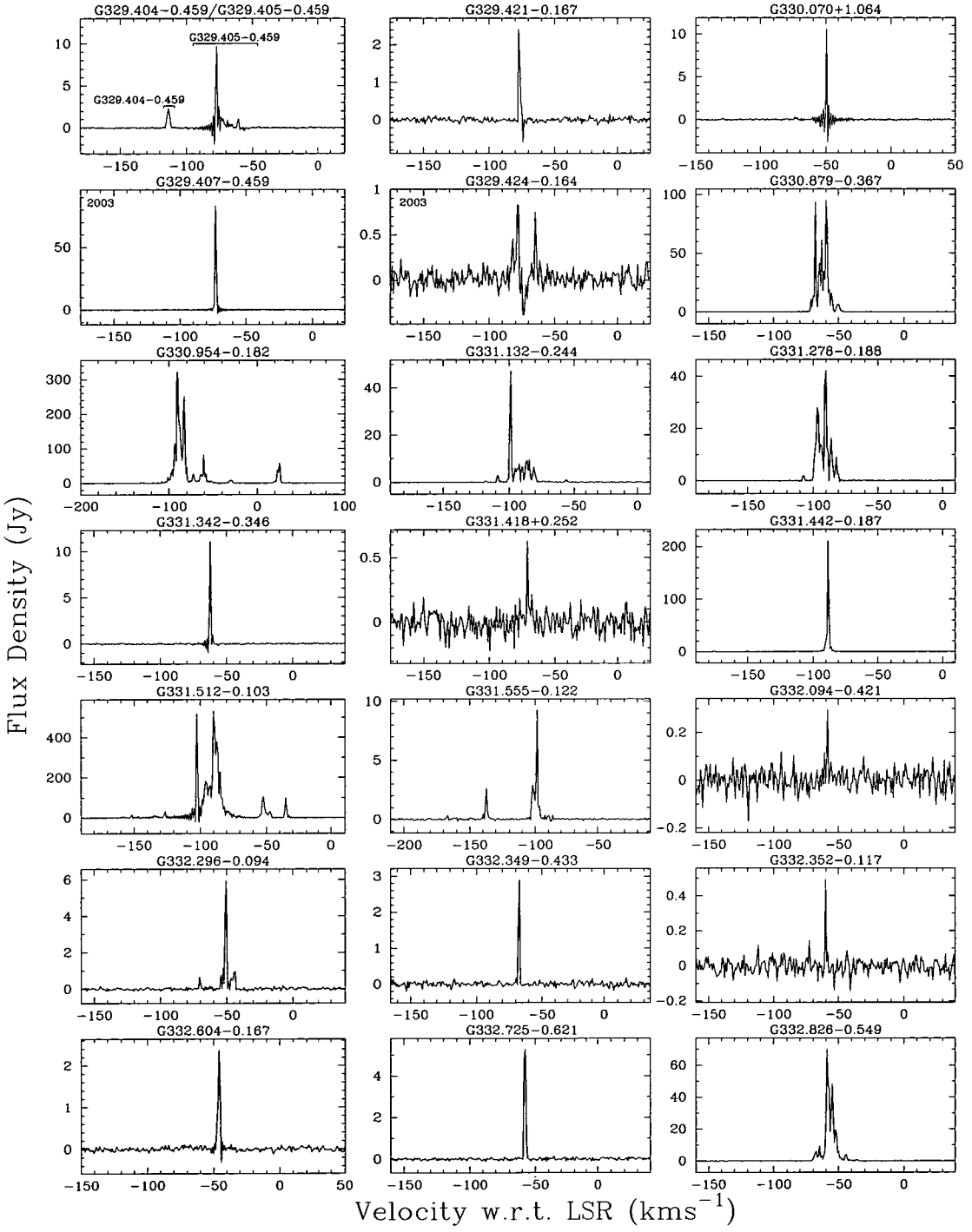

Figure 6.1: –continuued

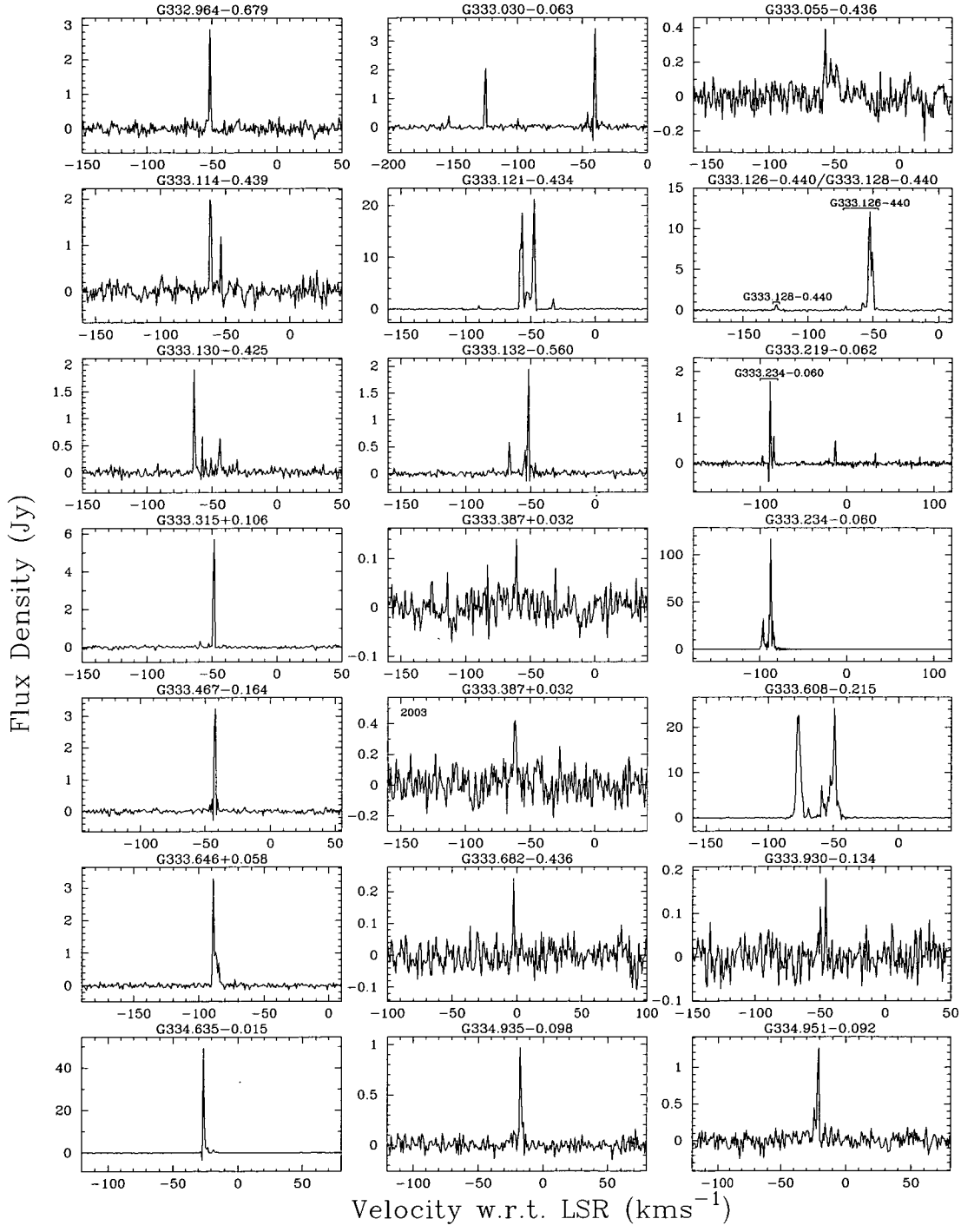

Figure 6.1: -continuued

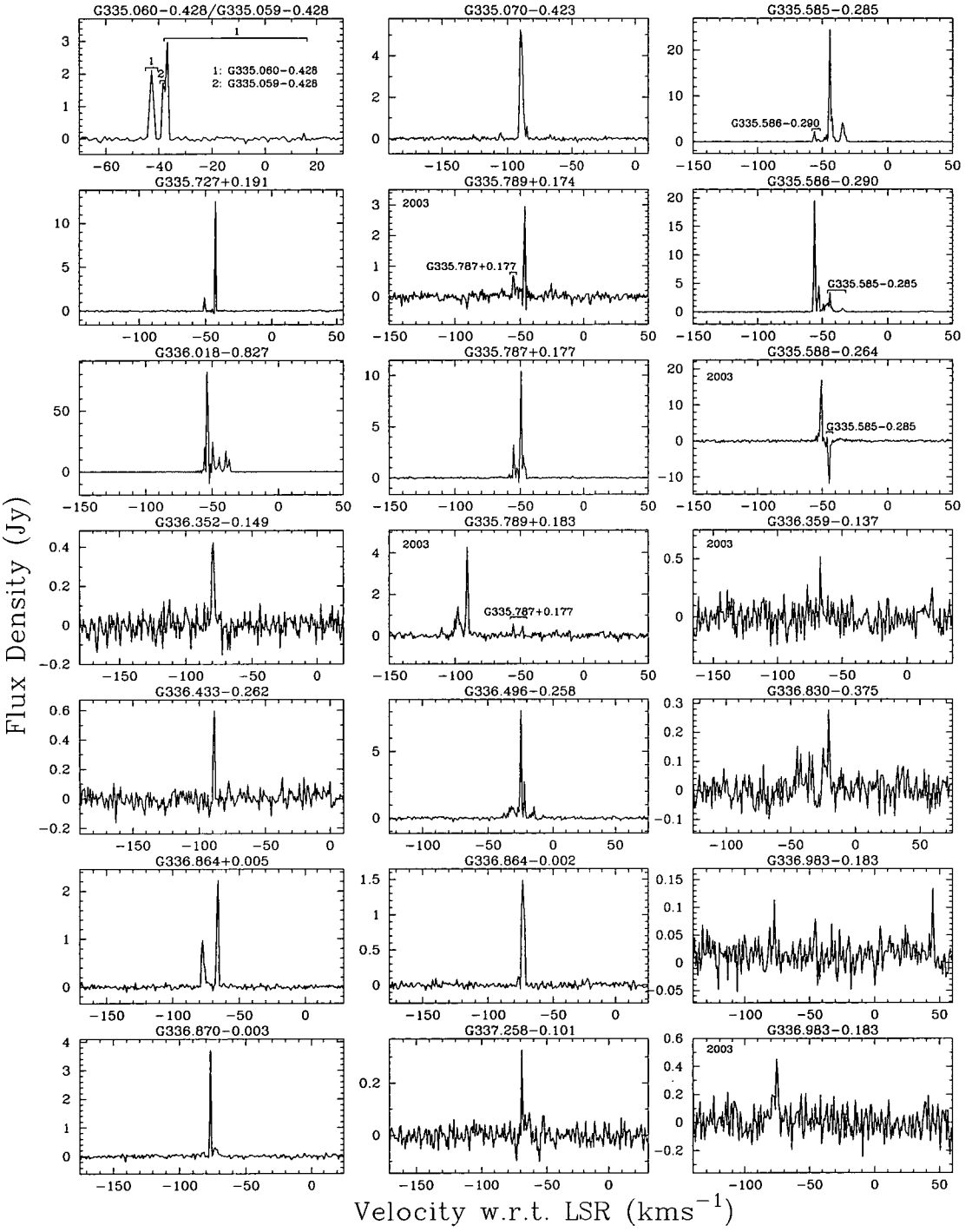

Figure 6.1: –continuued

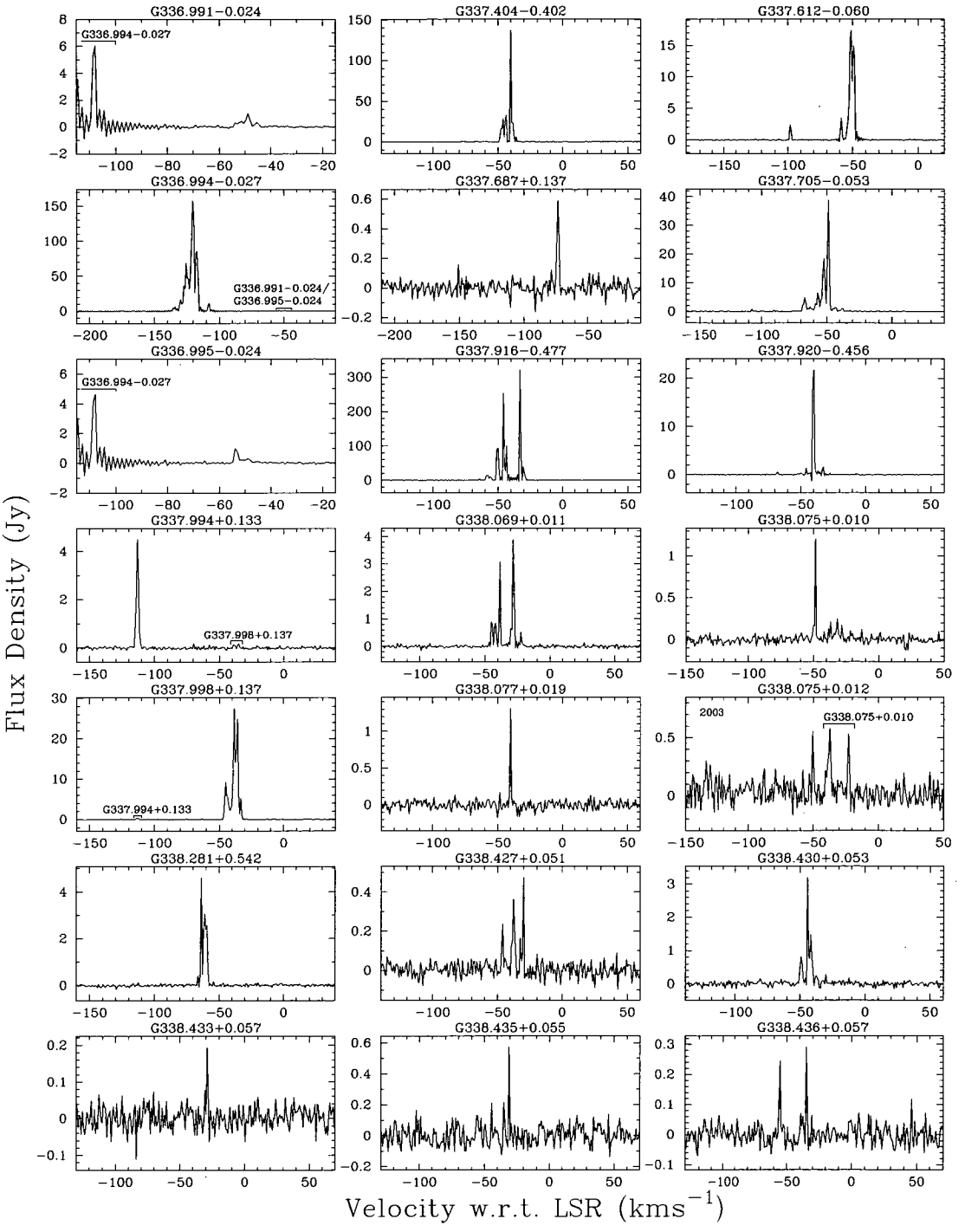

Figure 6.1: –continued

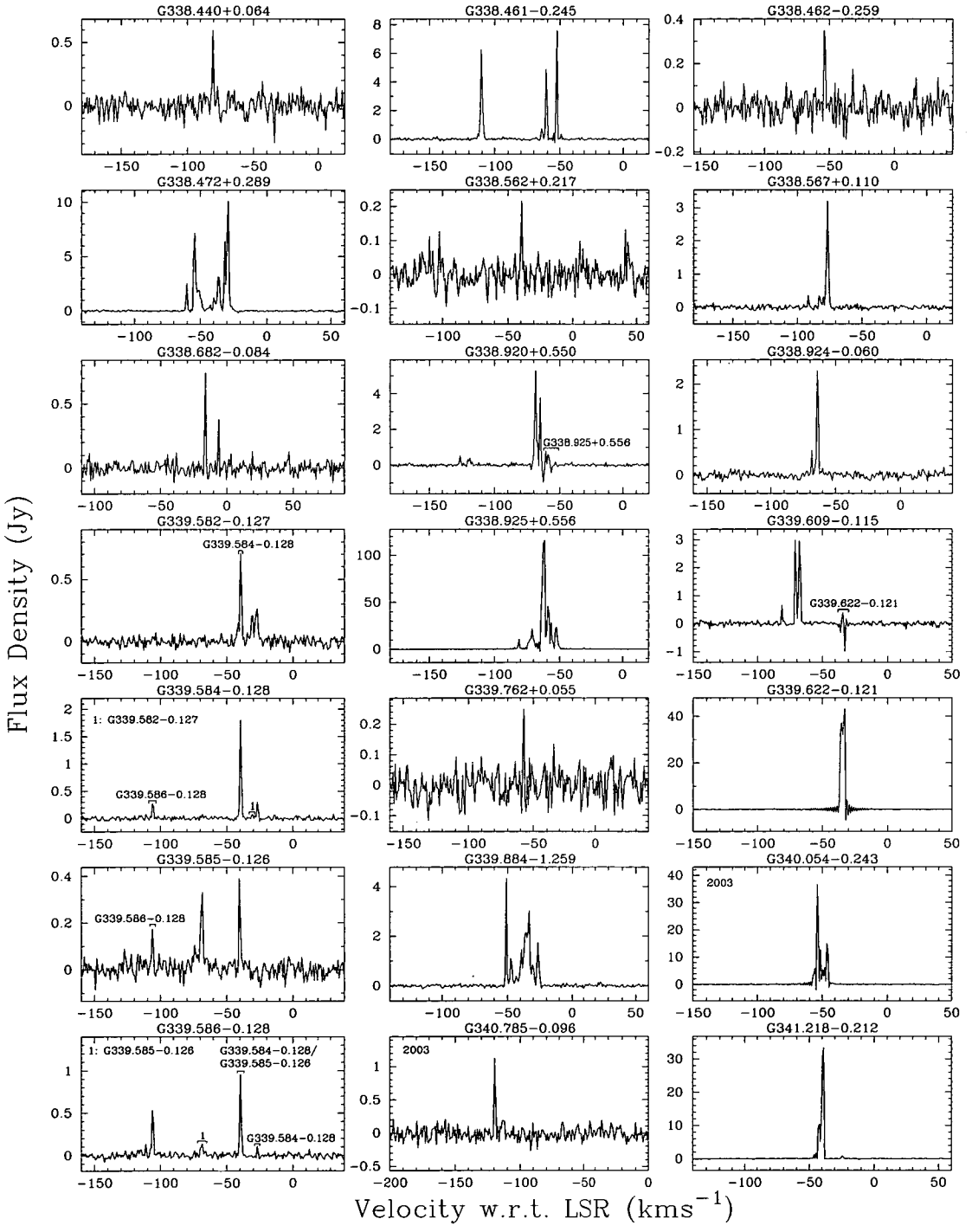

Figure 6.1: -continuued

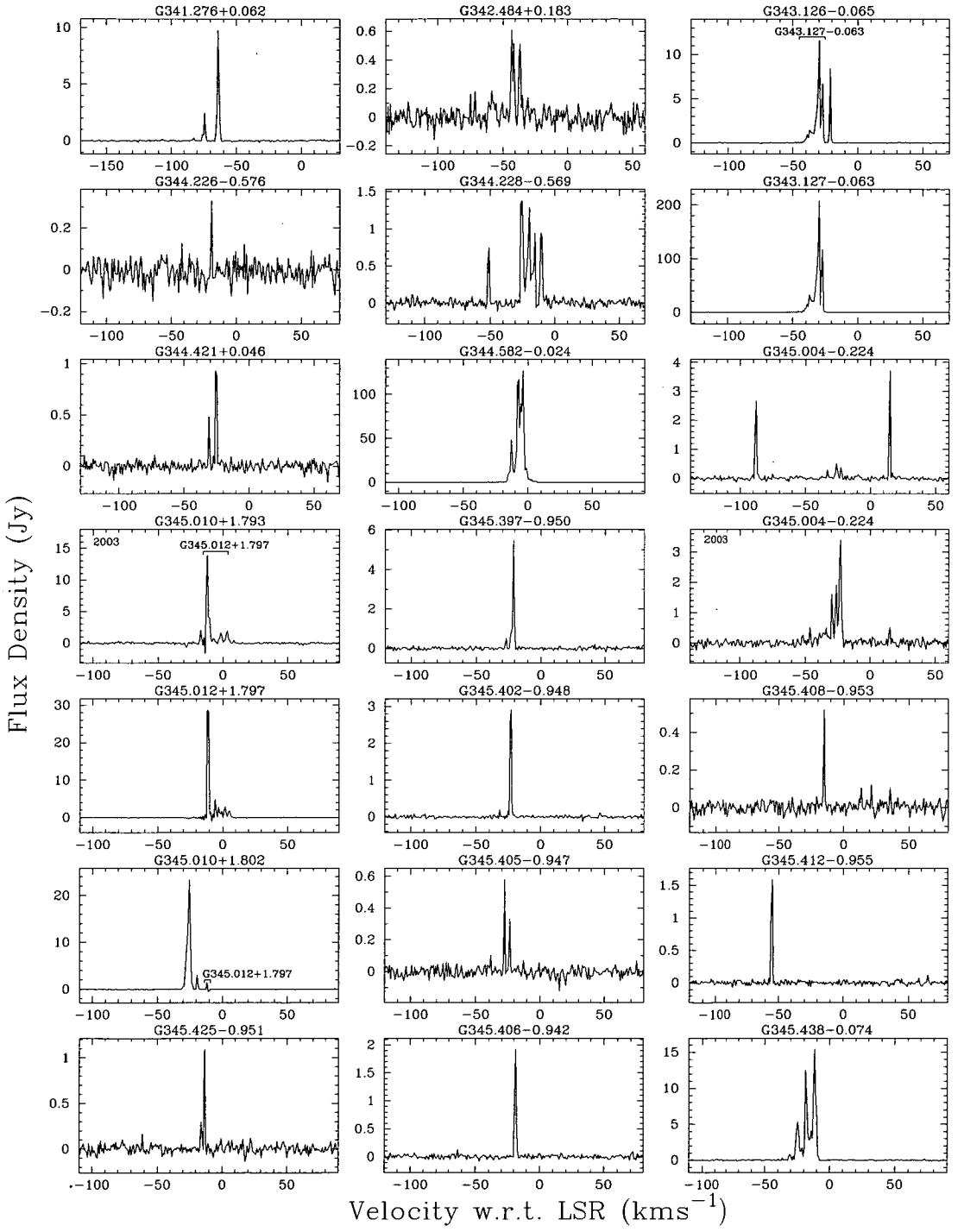

Figure 6.1: –continuued

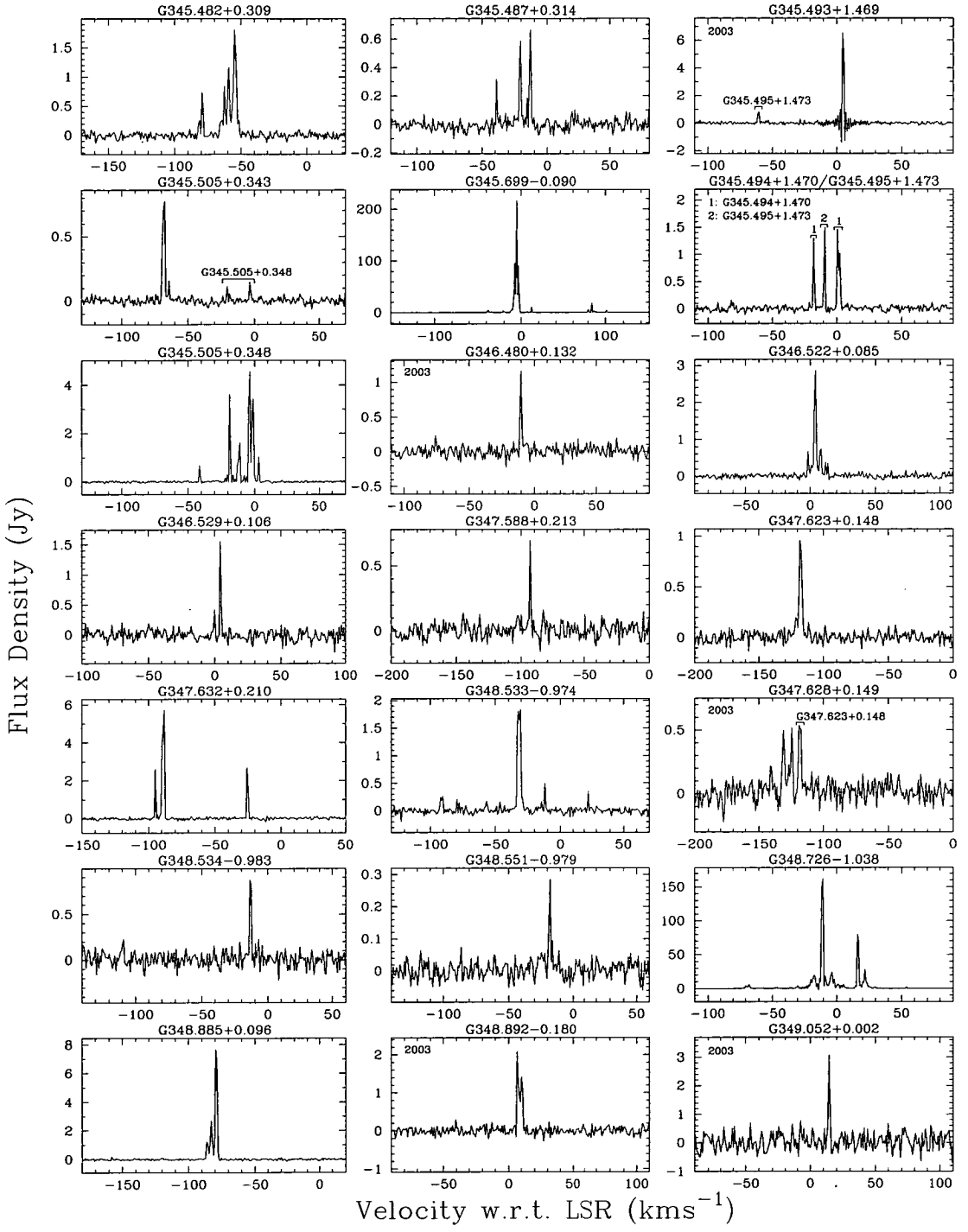

Figure 6.1: –continuued

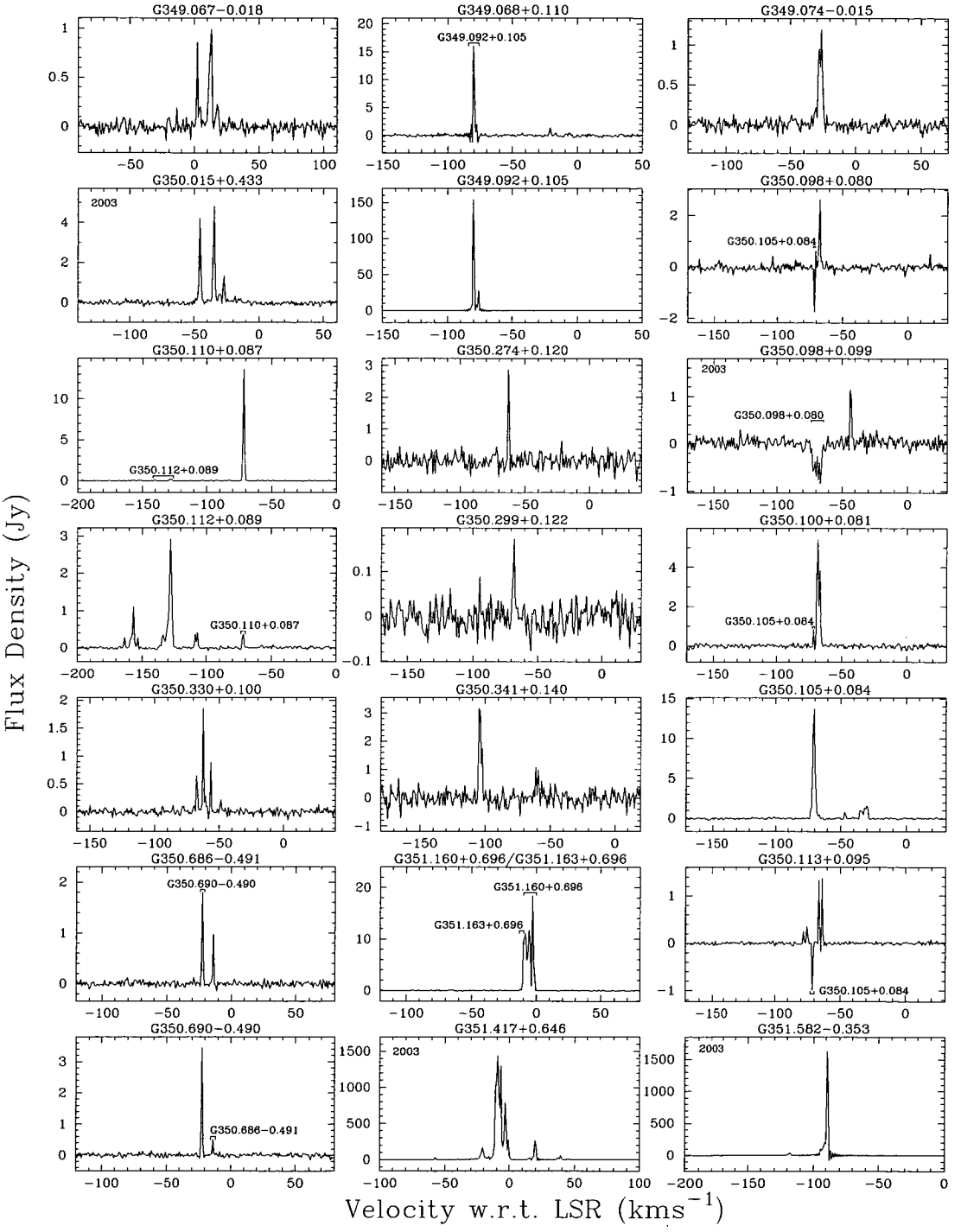

Figure 6.1: –continued

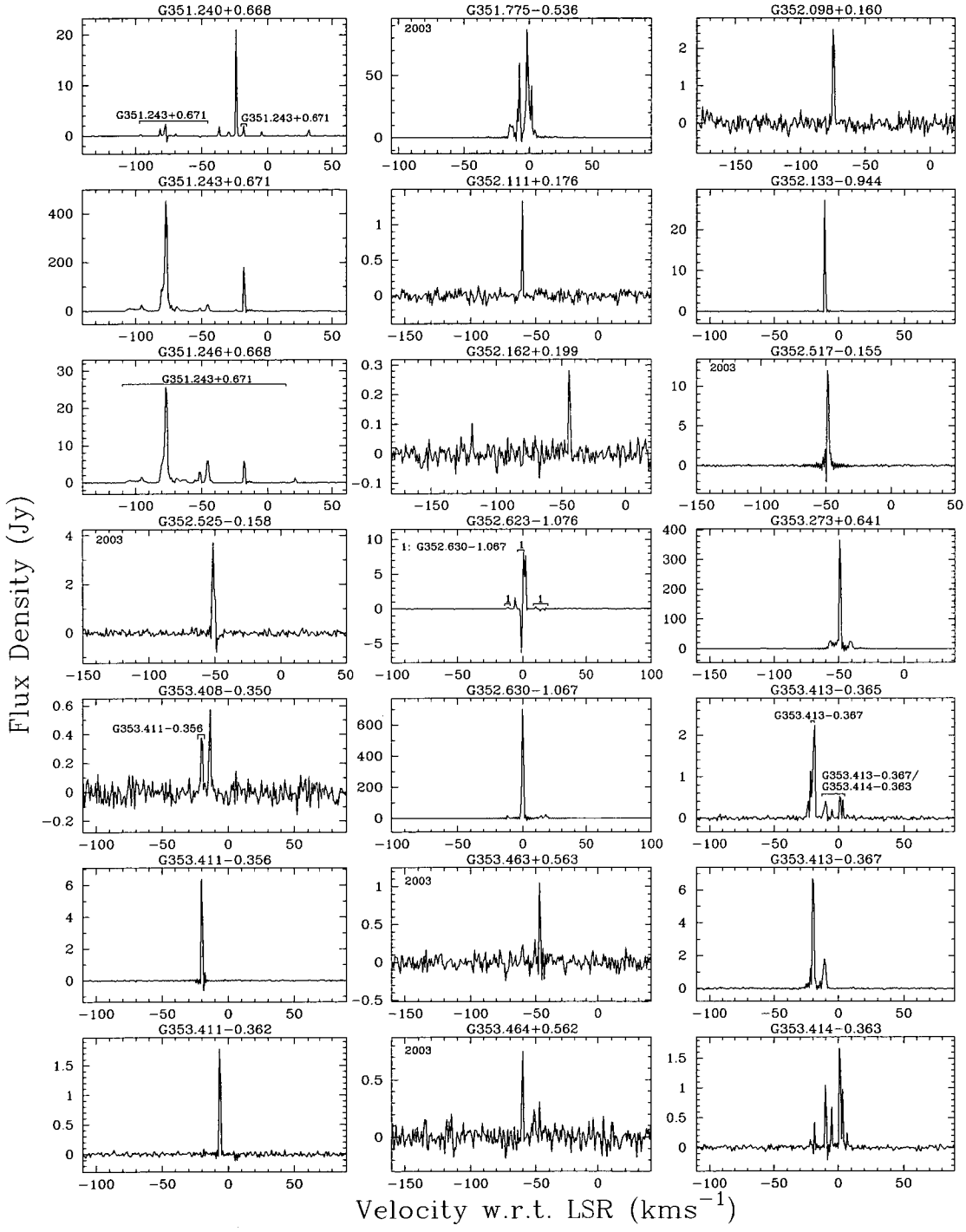

Figure 6.1: –continuued

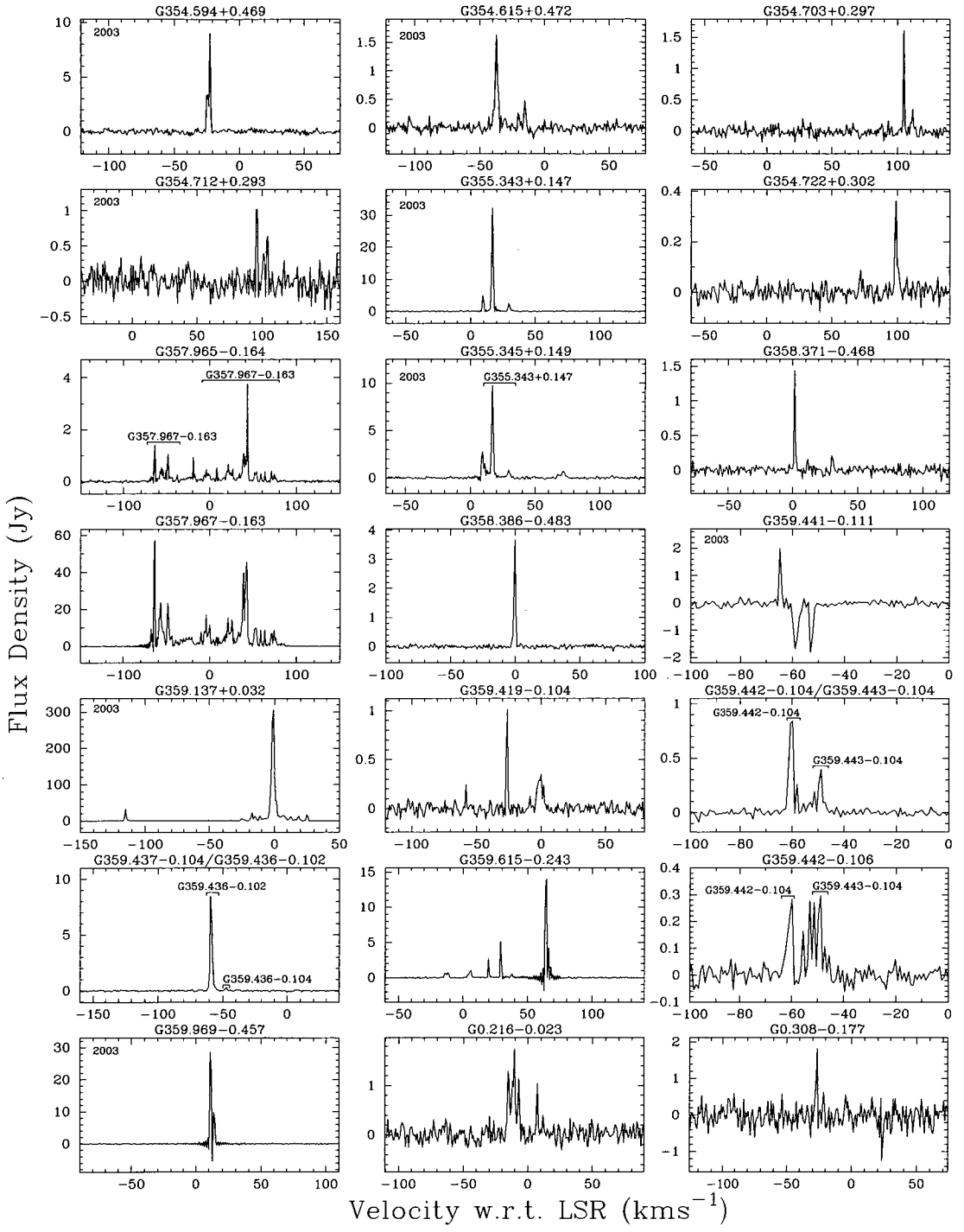

Figure 6.1: –continuued

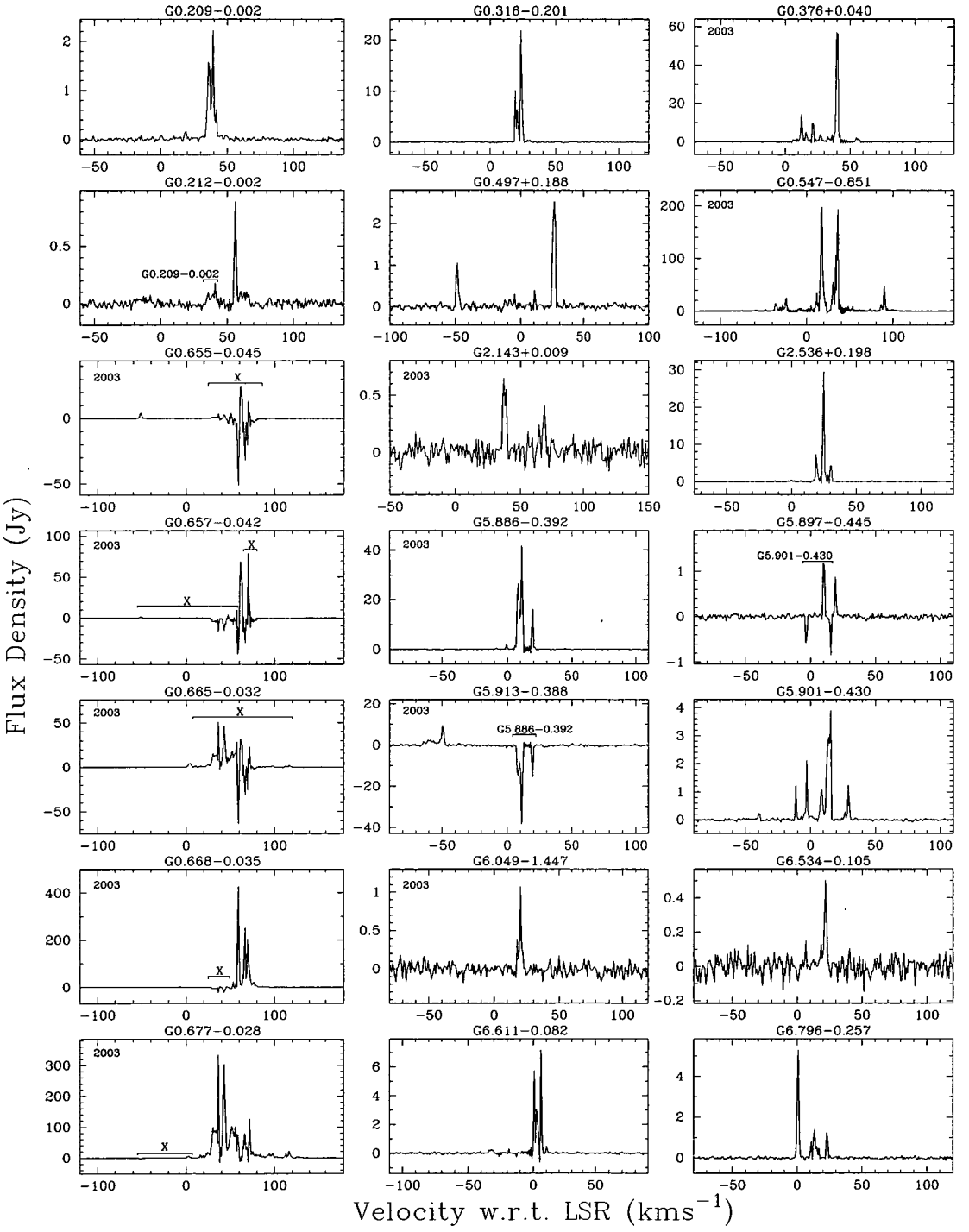

Figure 6.1: -continuued

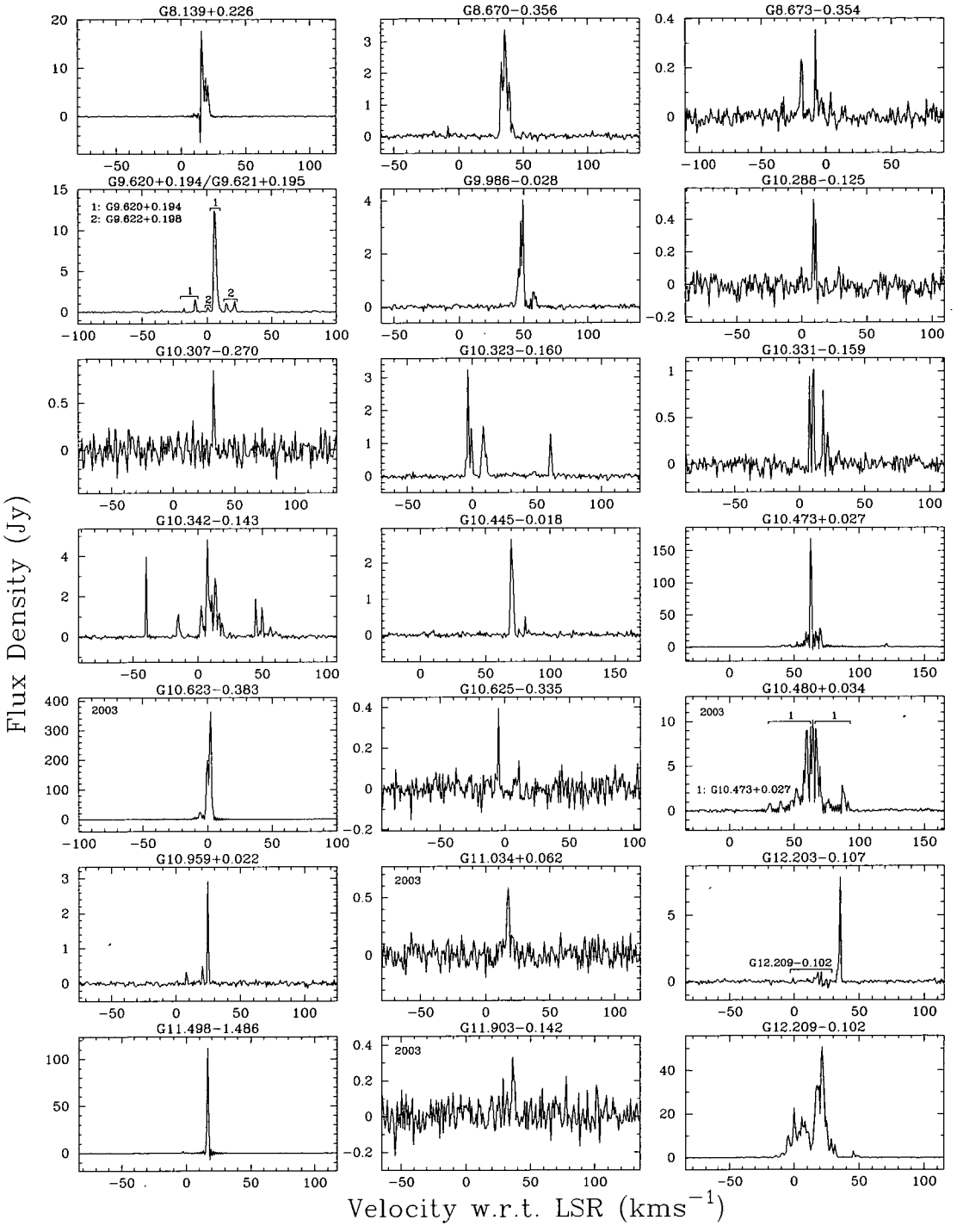

Figure 6.1: –continued

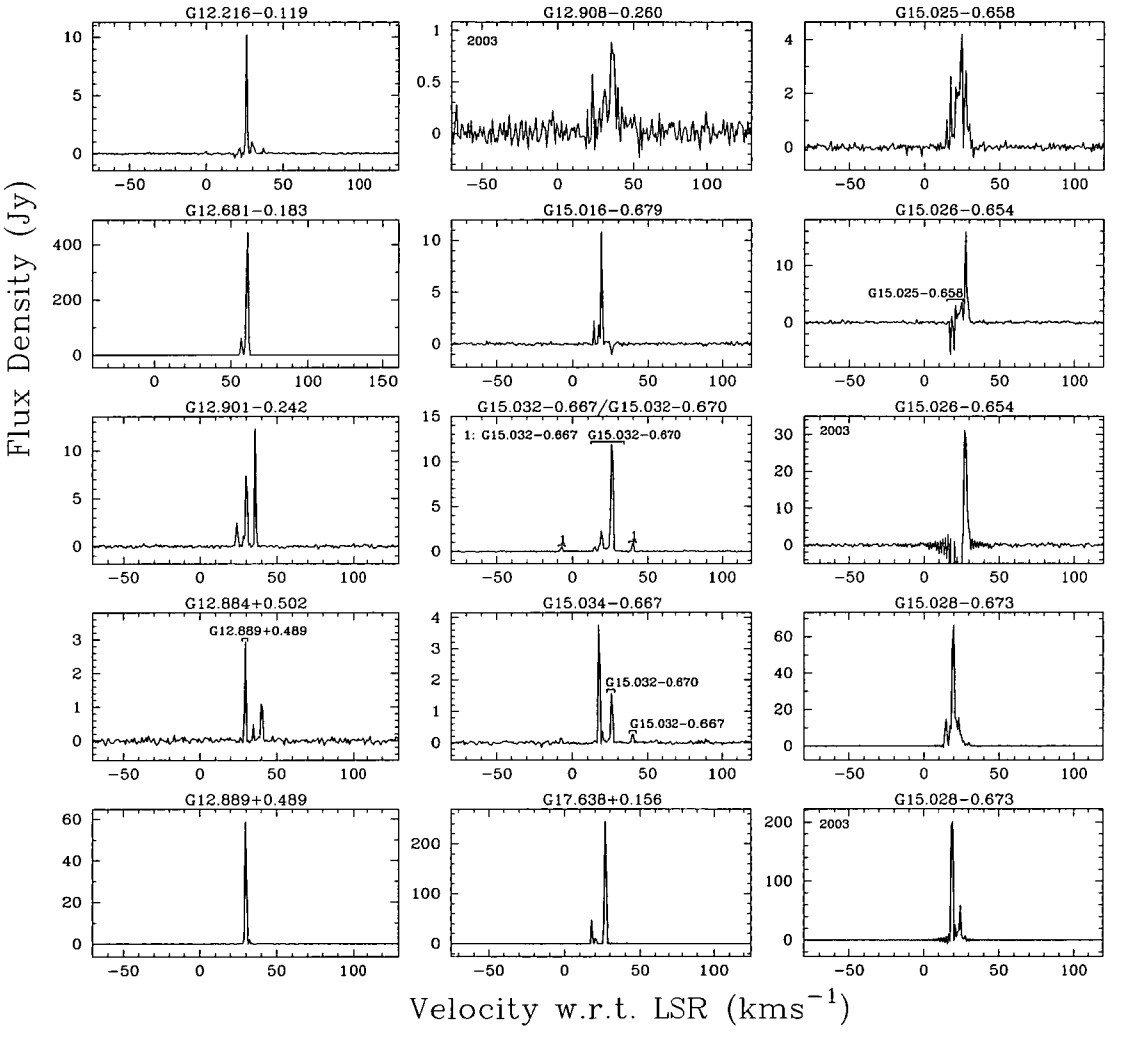

Figure 6.1: –continuued

Table 6.3: *Water maser sources with associated OH and methanol masers as well as 22 GHz continuum emission. Column 1 shows the water maser source name; column 2 gives the source name of the nearest OH maser within 5 arcsec (– if none) of the detected water maser; column 3 gives the angular separation between the water and the OH masers; column 4 gives the source name of the nearest methanol maser within 5 arcsec (– if none) of the detected water maser; column 5 gives the angular separation between the water maser and the methanol maser; columns 6, 7 and 8 give the water maser, OH maser and methanol maser peak velocities; column 9 gives detected UCHII regions with 5 arcsec of the detected water masers (– if none); and column 10 gives the angular separation between the UCHII region and the detected water maser.*

Water (l,b) (degrees)	OH (l,b) (degrees)	Sep. (arcsec)	Methanol (l,b) (degrees)	Sep. (arcsec)	Water Vpeak (km s^{-1})	OH Vpeak (km s^{-1})	Methanol Vpeak (km s^{-1})	Continuum (l,b) (degrees)	Sep. (arcsec)
G 240.316+0.071	G 240.316+0.071	0.7	–		89	63		–	
G 263.250+0.514	G 263.250+0.514	2.1	G 263.250+0.514	1.5	20	15.3	12.3	–	
G 284.350–0.418	G 284.351–0.418	1.1	–		7	6		–	
G 285.263–0.050	G 285.263–0.050	2.0	–		3	6		–	
G 287.371+0.644	G 287.371+0.644	1.6	G 287.371+0.644	1.5	–11	–4	–1.8	–	
G 290.374+1.661	G 290.374+1.661	1.6	G 290.374+1.661	1.0	–12	–23.3	–24.2	–	
G 291.270–0.719	–		G 291.270–0.719	2.5	–102		–26.5	–	
G 291.274–0.709	G 291.274–0.709	1.3	G 291.274–0.709	0.7	–32	–24.5	–29.6	–	
G 291.579–0.431	G 291.579–0.431	0.6	G 291.579–0.431	0.7	13	13	14.5	–	
G 291.581–0.435	–		G 291.582–0.435	3.8	26		10.5	–	
G 291.610–0.529	G 291.610–0.529	0.7	–		12	18		G 291.611–0.529	2.6
G 291.627–0.529	–		–					G 291.626–0.531	4.8
G 294.511–1.622	G 294.511–1.621	2.1	G 294.511–1.621	1.8	–12	–12.7	–12.3	–	
G 294.989–1.719	–		G 294.990–1.719	2.5	–17		–12.3	–	
G 297.660–0.974	G 297.660–0.973	2.0	–		26	27.6		–	
G 299.013+0.128	G 299.013+0.128	1.2	G 299.013+0.128	1.1	19	20.3	18.4	G 299.012+0.128	3.3
G 300.504–0.176	G 300.504–0.176	0.6	G 300.504–0.176	1.8	11	22.4	7.5	–	

Table 6.3: - continued

Water (l, b) (degrees)	OH (l, b) (degrees)	Sep. (arcsec)	Methanol (l, b) (degrees)	Sep. (arcsec)	Water Vpeak (km s^{-1})	OH Vpeak (km s^{-1})	Methanol Vpeak (km s^{-1})	Continuum (l, b) (degrees)	Sep. (arcsec)
G 301.136–0.226b	G 301.136–0.226	2.0	G 301.136–0.226	2.5	–44	–40.2	–39.8	G 301.136–0.226	1.0
G 301.137–0.225	G 301.136–0.226	2.0	G 301.136–0.226	2.0	–35	–40.2	–39.8	–	
G 305.208+0.207	G 305.208+0.206	3.0	G 305.208+0.206	2.7	–42	–38	–38.3	–	
G 305.361+0.150	G 305.362+0.150	2.1	G 305.362+0.150	2.0	–36	–39.5	–36.5	–	
G 305.799–0.245	G 305.799–0.245	3.0	G 305.799–0.245	2.5	–34	–36.7	–39.5	–	
G 307.805–0.456	G 307.805–0.456	1.5	–		–7	–14.5		–	
G 308.754+0.549	G 308.754+0.549	0.8	G 308.754+0.549	1.4	–48	–43.5	–51.0	–	
G 308.918+0.124	G 308.918+0.123	3.0	G 308.918+0.123	3.6	–61	–54	–54.7	–	
G 309.384–0.135	G 309.384–0.135	1.3	G 309.384–0.135	0.6	–50	–52	–49.6	–	
G 310.144+0.760	G 310.144+0.760	2.2	G 310.144+0.760	1.0	–63	–57	–55.6	–	
G 311.643–0.380	G 311.643–0.380	1.3	G 311.643–0.380	0.4	36	38	32.5	G 311.643–0.380	1.3
G 312.109+0.262	–		G 312.108+0.262	1.9	–48		–50.0	–	
G 312.596+0.045	–		G 312.597+0.045	1.6	–59		–60.0	–	
G 312.599+0.046	G 312.598+0.045	2.1	G 312.598+0.045	2.1	–79	–65.2	–67.9	–	
G 313.457+0.193	–		–					G 313.458+0.193	2.1
G 313.470+0.191	G 313.469+0.190	0.9	G 313.469+0.190	1.1	–15	–10	–9.4	–	
G 313.578+0.325	G 313.577+0.325	1.0	G 313.577+0.325	1.9	–47	–47	–47.9	–	
G 313.767–0.862	G 313.767–0.863	1.1	G 313.767–0.863	0.9	–54	–53.5	–54.6	–	
G 314.320+0.112	G 314.320+0.112	2.2	G 314.320+0.112	2.3	–45	–45	–43.7	–	
G 316.361–0.363	–		G 316.359–0.362	3.2	–3		3.5	–	
G 316.412–0.308	G 316.412–0.308	1.5	G 316.412–0.308	2.3	–20	–2	–5.7	G 316.412–0.308	0.7
G 316.640–0.087	G 316.640–0.087	0.7	G 316.640–0.087	0.9	–15	–22	–19.8	–	
G 316.763–0.011	G 316.763–0.012	1.0	–		–48	–40		–	
G 316.812–0.057	G 316.811–0.057	2.2	G 316.811–0.057	2.5	–46	–43.5	–46.3	–	
G 317.429–0.561	G 317.429–0.561	2.1	–		25	25.5		G 317.430–0.561	2.6
G 318.044–1.404	G 318.044–1.405	2.0	G 318.043–1.404	1.6	42	45	46.2	–	
G 318.050+0.087	G 318.050+0.087	0.6	G 318.050+0.087	0.4	–48	–53	–46.5	–	

Table 6.3: – continued

Water (l, b) (degrees)	OH (l, b) (degrees)	Sep. (arcsec)	Methanol (l, b) (degrees)	Sep. (arcsec)	Water Vpeak (km s^{-1})	OH Vpeak (km s^{-1})	Methanol Vpeak (km s^{-1})	Continuum (l, b) (degrees)	Sep. (arcsec)
G 318.948–0.196b	G 318.948–0.196	0.8	G 318.948–0.196	0.9	–38	–35.5	–34.7	–	
G 319.399–0.012	G 319.398–0.012	1.1	–		–5	–1		G 319.399–0.012	0.8
G 319.836–0.196	G 319.836–0.196	1.5	G 319.836–0.197	1.6	–11	–10.5	–9.1	–	
G 320.120–0.440	G 320.120–0.440	0.5	–		–46	–55.5		–	
G 320.232–0.284	G 320.232–0.284	0.4	G 320.231–0.284	0.6	–67	–64	–66.5	–	
G 320.233–0.284	–		–					G 320.234–0.283	3.5
G 321.033–0.483	–		G 321.033–0.483	0.5	–61		–61.6	–	
G 321.148–0.529	G 321.148–0.529	1.1	G 321.148–0.529	1.1	–97	–63	–66.1	–	
G 322.158+0.636	G 322.158+0.636	1.2	G 322.158+0.636	1.2	–76	–61	–63.3	–	
G 323.740–0.263	G 323.740–0.263	1.1	G 323.740–0.263	0.6	–50	–39	–51.1	–	
G 324.201+0.122	G 324.200+0.121	2.9	–		–87	–91.5		–	
G 324.716+0.342	G 324.716+0.342	1.7	G 324.716+0.342	1.5	–58	–50	–46	–	
G 326.662+0.521	–		G 326.662+0.521	2.0	–39		–38.6	–	
G 326.670+0.554	G 326.670+0.554	2.6	–		–40	–40.8		–	
G 326.780–0.241	G 326.780–0.241	0.9	–		–66	–65		–	
G 326.859–0.676	–		G 326.859–0.677	3.4	–103		–58.0	–	
G 327.119+0.511	G 327.120+0.511	2.3	G 327.120+0.511	1.8	–88	–80.5	–87.0	–	
G 327.291–0.578	G 327.291–0.578	1.2	G 327.291–0.578	0.8	–63	–50.5	–36.8	–	
G 327.391+0.200	–		G 327.392+0.199	1.5	–86		–84.6	–	
G 327.402+0.445	G 327.402+0.444	3.2	G 327.402+0.444	1.6	–81	–77	–82.6	G 327.402+0.445	0.6
G 327.619–0.111	–		G 327.618–0.111	0.9	–85		–97.6	–	
G 328.236–0.548	G 328.237–0.547	2.9	G 328.237–0.547	2.6	–38	–41	–44.5	G 328.236–0.547	2.1
G 328.254–0.532	G 328.254–0.532	1.5	G 328.254–0.532	0.8	–50	–37	–37.5	–	
G 328.306+0.432	–		–					G 328.307+0.431	3.3
G 328.808+0.633	G 328.809+0.633	2.9	G 328.808+0.633	2.4	–46	–43.5	–43.8	G 328.808+0.633	2.0
G 329.029–0.199	G 329.029–0.200	1.9	–		–38	–38.5		–	
G 329.030–0.205	G 329.029–0.205	1.5	G 329.029–0.205	1.3	–46	–38.5	–37.4	–	

Table 6.3: – continued

Water (l,b) (degrees)	OH (l,b) (degrees)	Sep. (arcsec)	Methanol (l,b) (degrees)	Sep. (arcsec)	Water Vpeak (km s^{-1})	OH Vpeak (km s^{-1})	Methanol Vpeak (km s^{-1})	Continuum (l,b) (degrees)	Sep. (arcsec)
G 329.031–0.198	G 329.031–0.198	1.3	G 329.031–0.198	0.8	–52	–45.5	–45.5	–	
G 329.066–0.307	G 329.066–0.308	1.5	G 329.066–0.308	1.2	–45	–43.5	–43.8	–	
G 329.183–0.313	G 329.183–0.314	2.3	G 329.183–0.314	1.9	–50	–53	–55.7	–	
G 329.405–0.459	G 329.405–0.459	2.0	G 329.405–0.459	1.5	–77	–69.5	–70.5	–	
G 329.407–0.459	–		G 329.407–0.459	2.1	–74		–66.7	–	
G 329.622+0.138	–		G 329.622+0.138	1.7	–82		–84.8	–	
G 330.070+1.064	–		G 330.070+1.064	1.2	–50		–38.8	–	
G 330.879–0.367	G 330.878–0.367a	0.9	G 330.878–0.367	2.6	–60	–61.8	–59.3	G 330.879–0.367	1.7
	G 330.878–0.367b	1.2	–			–65.6			
G 330.954–0.182	G 330.954–0.182	1.3	G 330.953–0.182	3.9	–91	–85.5	–87.6	G 330.954–0.182	1.6
G 331.132–0.244	G 331.132–0.244	0.2	G 331.132–0.244	0.3	–99	–88.5	–84.3	–	
G 331.278–0.188	G 331.278–0.188	0.9	G 331.278–0.188	1.1	–90	–89.5	–78.2	–	
G 331.342–0.346	G 331.342–0.346	1.4	G 331.342–0.346	1.6	–62	–67	–67.4	–	
G 331.442–0.187	G 331.442–0.186	0.5	G 331.442–0.187	0.9	–88	–83	–88.4	G 331.443–0.187	3.5
G 331.512–0.103	G 331.512–0.103	1.4	–		–90	–88.2		G 331.512–0.103	1.0
G 331.555–0.122	G 331.556–0.121	4.5	G 331.556–0.121	4.4	–99	–100	–103.4	–	
G 332.094–0.421	–		G 332.094–0.421	2.2	–59		–58.6	–	
G 332.296–0.094	–		G 332.295–0.094	4.4	–50		–47.0	–	
G 332.352–0.117	G 332.352–0.117	0.8	G 332.352–0.117	0.2	–60	–44	–41.8	–	
G 332.604–0.167	–		G 332.604–0.167	1.6	–46		–50.9	–	
G 332.725–0.621	G 332.726–0.621	1.4	G 332.726–0.621	1.0	–58	–48	–49.6	–	
G 332.826–0.549	–		G 332.826–0.549	3.0	–59		–61.7	G 332.826–0.549	1.1
G 332.964–0.679	–		G 332.963–0.679	1.6	–52		–45.8	–	
G 333.030–0.063	–		G 333.029–0.063	1.3	–40		–55.2	G 333.030–0.063	0.7
G 333.121–0.434	–		G 333.121–0.434	1.2	–47		–49.3	–	
G 333.126–0.440	–		G 333.126–0.440	1.0	–52		–43.9	–	
G 333.128–0.440	–		G 333.128–0.440	2.5	–124		–44.6	–	

Table 6.3: – continued

Water (l,b) (degrees)	OH (l,b) (degrees)	Sep. (arcsec)	Methanol (l,b) (degrees)	Sep. (arcsec)	Water Vpeak (km s^{-1})	OH Vpeak (km s^{-1})	Methanol Vpeak (km s^{-1})	Continuum (l,b) (degrees)	Sep. (arcsec)
G 333.234–0.060	G 333.234–0.060	0.6	–		–88	–84		–	
G 333.315+0.106	G 333.315+0.105	2.8	G 333.315+0.105	3.0	–48	–47	–45	–	
G 333.387+0.032	G 333.387+0.032	0.6	G 333.387+0.032	1.1	–61	–74	–73.9	–	
G 333.467–0.164	G 333.466–0.164	2.1	G 333.466–0.164	2.5	–42	–43.5	–42.5	G 333.466–0.163	4.7
G 333.608–0.215	G 333.608–0.215	0.2	–		–49	–51		–	
G 333.646+0.058	–		G 333.646+0.058	0.9	–89		–87.3	–	
G 333.682–0.436	–		G 333.683–0.437	1.6	–3		–5.3	–	
G 333.930–0.134	–		G 333.931–0.135	1.5	–46		–36.7	–	
G 334.635–0.015	–		G 334.635–0.015	1.0	–26		–30	–	
G 334.935–0.098	–		G 334.935–0.098	0.4	–17		–19.5	–	
G 335.060–0.428	G 335.060–0.427	1.5	G 335.060–0.427	1.3	–37	–36	–47.0	–	
G 335.585–0.285	G 335.585–0.285	0.5	G 335.585–0.285	0.7	–42	–48	–49.3	–	
G 335.586–0.290	G 335.585–0.289	1.1	G 335.585–0.289	0.8	–56	–53.5	–51.4	–	
			G 335.585–0.290	2.3			–47.3		
G 335.727+0.191	–		G 335.726+0.191	2.0	–51		–44.4	–	
G 335.789+0.174	G 335.789+0.174	0.5	G 335.789+0.174	0.9	–46	–51.5	–47.6	–	
G 336.018–0.827	G 336.018–0.827	0.6	G 336.018–0.827	0.9	–54	–41.5	–53.4	G 336.018–0.828	0.5
G 336.359–0.137	G 336.358–0.137	3.0	G 336.358–0.137	3.1	–67	–82	–73.6	G336.360–0.137	3.8
G 336.433–0.262	–		G 336.433–0.262	1.9	–89		–93.3	–	
G 336.830–0.375	–		G 336.830–0.375	1.6	–20		–22.7	–	
G 336.864+0.005	G 336.864+0.005	1.2	G 336.864+0.005	0.7	–66	–89	–76.1	–	
G 336.983–0.183	G 336.984–0.183	4.2	G 336.983–0.183	3.0	45	–80.5	–80.8	G 336.984–0.184	2.5
G 336.991–0.024	–		–					G 336.990–0.025	2.3
G 336.994–0.027	G 336.994–0.027	1.0	G 336.994–0.027	0.6	–120	–123	–125.8	–	
G 337.258–0.101	G 337.258–0.101	0.7	G 337.258–0.101	1.2	–69	–70	–69.3	–	
G 337.404–0.402	G 337.405–0.402	1.5	G 337.404–0.402	0.7	–40	–38	–39.7	G 337.404–0.403	2.0
G 337.612–0.060	G 337.613–0.060	0.6	G 337.613–0.060	0.9	–51	–42	–42	–	

Table 6.3: – continued

Water (l,b) (degrees)	OH (l,b) (degrees)	Sep. (arcsec)	Methanol (l,b) (degrees)	Sep. (arcsec)	Water Vpeak (km s^{-1})	OH Vpeak (km s^{-1})	Methanol Vpeak (km s^{-1})	Continuum (l,b) (degrees)	Sep. (arcsec)
G 337.687+0.137	–		G 337.686+0.137	2.3	–74		–74.9	–	
G 337.705–0.053	G 337.705–0.053	0.6	G 337.705–0.053	0.9	–49	–49	–54.6	G 337.706–0.054	1.1
G 337.916–0.477	G 337.916–0.477	0.6	–		–33	–51		–	
G 337.920–0.456	G 337.920–0.456	0.7	G 337.920–0.456	0.9	–40	–39.5	–38.8	–	
G 337.998+0.137	G 337.997+0.136	1.3	G 337.997+0.136	1.1	–38	–35.5	–32.3	–	
G 338.075+0.012	G 338.075+0.012	2.1	G 338.075+0.012	2.3	–50	–47	–53.0	G 338.075+0.012	2.9
G 338.075+0.010	–		G 338.075+0.009	1.3	–48		–38.2	–	
G 338.281+0.542	G 338.280+0.542	1.2	G 338.280+0.542	1.1	–64	–61	–56.8	–	
G 338.433+0.057	–		G 338.432+0.058	4.4	–29		–30.2	–	
G 338.461–0.245	G 338.461–0.245	0.4	G 338.461–0.245	0.8	–52	–56	–50.4	–	
G 338.472+0.289	G 338.472+0.289	1.2	G 338.472+0.289	1.1	–29	–32	–30.5	–	
G 338.562+0.217	–		G 338.561+0.218	2.0	–39		–40.8	–	
G 338.567+0.110	–		G 338.566+0.110	1.4	–76		–75	–	
G 338.682–0.084	G 338.681–0.084	1.4	–		–16	–22		G 338.681–0.085	1.5
G 338.920+0.550	–		G 338.920+0.550	0.8	–68		–61.4	–	
G 338.925+0.556	G 338.925+0.557	0.9	G 338.925+0.557	1.3	–62	–61	–62.3	–	
G 339.582–0.127	–		G 339.582–0.127	0.6	–28		–31.3	–	
G 339.622–0.121	G 339.622–0.121	0.8	G 339.622–0.121	1.3	–33	–37.3	–32.8	–	
G 339.762+0.055	–		G 339.762+0.054	1.6	–57		–51	–	
G 339.884–1.259	G 339.884–1.259b	0.7	G 339.884–1.259	0.8	–51	–36	–38.7	–	
	G 339.884–1.259a	1.2	–			–29			
G 340.054–0.243	G 340.054–0.244	1.4	G 340.054–0.244	0.8	–54	–53.6	–59.7	–	
G 340.785–0.096	G 340.785–0.096	2.2	G 340.785–0.096	1.6	–120	–102	–105.1	–	
G 341.218–0.212	G 341.218–0.212	1.2	G 341.218–0.212	1.0	–39	–37.3	–37.9	–	
G 341.276+0.062	G 341.276+0.062	0.9	G 341.276+0.062	1.1	–64	–73	–73.8	–	
G 342.484+0.183	–		G 342.484+0.183	1.1	–43		–41.8	–	
G 343.127–0.063	G 343.127–0.063	2.1	–		–30	–31.5		–	

Table 6.3: – continued

Water (l, b) (degrees)	OH (l, b) (degrees)	Sep. (arcsec)	Methanol (l, b) (degrees)	Sep. (arcsec)	Water Vpeak (km s^{-1})	OH Vpeak (km s^{-1})	Methanol Vpeak (km s^{-1})	Continuum (l, b) (degrees)	Sep. (arcsec)
G 344.228–0.569	G 344.227–0.569	1.4	G 344.227–0.569	1.0	–25	–30.5	–19.8	–	
G 344.421+0.046	–		G 344.421+0.045	3.4	–26		–71.5	–	
G 344.582–0.024	G 344.582–0.024	2.2	G 344.581–0.024	2.5	–4	–2.3	1.4	G 344.582–0.024	1.7
G 345.004–0.224	G 345.003–0.224	3.0	G 345.003–0.224	3.1			–26.2	G 345.004–0.225	3.6
			G 345.003–0.223	3.3	15	–27	–22.5		
G 345.010+1.793	G 345.010+1.793	1.5	G 345.010+1.792	2.1	–17	–22.5	–18	G 345.010+1.792	4.3
G 345.012+1.797	–		G 345.012+1.797	2.2	–12		–12.7	–	
G 345.408–0.953	G 345.407–0.952	4.6	G 345.407–0.952	4.9	–15	–17.6	–14.4	G 345.408–0.952	3.2
G 345.425–0.951	–		G 345.424–0.951	1.6	–13		–13.5	–	
G 345.438–0.074	G 345.437–0.074	1.9	–		–12	–24.3		–	
G 345.487+0.314	–		G 345.487+0.314	0.6	–13		–22.6	–	
G 345.493+1.469	G 345.494+1.469	3.3	–		5	–12.7		–	
G 345.505+0.348	G 345.504+0.348	1.8	G 345.505+0.348	2.2	–4	–19.5	–17.7	–	
G 345.699–0.090	G 345.698–0.090	1.2	–		–5	–6		–	
G 346.480+0.132	G 346.481+0.132	1.5	G 346.481+0.132	1.4	–10	–8	–5.5	–	
G 346.522+0.085	–		G 346.522+0.085	0.7	4		5.5	–	
G 347.628+0.149	G 347.628+0.148	2.0	G 347.628+0.149	0.9	–125	–94.3	–96.6	–	
G 347.632+0.210	–		G 347.631+0.211	2.9	–88		–91.9	G 347.632+0.210	0.9
G 348.551–0.979	G 348.550–0.979	3.7	G 348.550–0.979n	1.9	–18	–19.7	–20.0	–	
			G 348.550–0.979	3.4			–10		
G 348.726–1.038	–		G 348.727–1.037	4.4	–10		–7.6	–	
G 348.885+0.096	G 348.884+0.096	1.2	G 348.884+0.096	1.4	–80	–73.2	–76.2	–	
G 348.892–0.180	G 348.892–0.180	0.6	G 348.892–0.180	1.0	7	9.5	1.4	–	
G 349.067–0.018	G 349.067–0.017	1.1	G 349.067–0.017	1.1	13	15	6.9	–	
G 349.092+0.105	G 349.092+0.106	0.8	G 349.092+0.106	0.9	–80	–80	–80.4	–	
			G 349.092+0.105	2.0			–76.5		

Table 6.3: – continued

Water (l,b) (degrees)	OH (l,b) (degrees)	Sep. (arcsec)	Methanol (l,b) (degrees)	Sep. (arcsec)	Water Vpeak (km s^{-1})	OH Vpeak (km s^{-1})	Methanol Vpeak (km s^{-1})	Continuum (l,b) (degrees)	Sep. (arcsec)
G 350.015+0.433	G 350.015+0.433	0.1	G 350.015+0.433	1.0	–35	–33	–31.7	–	
G 350.113+0.095	G 350.113+0.095	1.3	–		–64	–71		–	
G 350.105+0.084	–		G 350.104+0.084	2.0	–71		–68.4	–	
			G 350.105+0.083	3.3			–74.0		
G 350.299+0.122	–		G 350.299+0.122	0.7	–68		–62.1	–	
G 350.330+0.100	G 350.329+0.100	2.5	–		–62	–64		G 350.331+0.099	3.9
G 350.686–0.491	G 350.686–0.491	0.4	G 350.686–0.491	1.3	–14	–14.5	–13.8	–	
G 351.160+0.696	G 351.160+0.697	2.5	G 351.160+0.697	1.3	–3	–8.5	–5.2	G 351.161+0.696	3.0
G 351.243+0.671	–		G 351.243+0.671	3.4	–77		2.5		
G 351.246+0.668	–		–					G 351.247+0.667	3.6
G 351.417+0.646	G 351.417+0.645	3.7	G 351.417+0.646	1.7	–10	–9.1	–11.2	–	
			G 351.417+0.645	3.1			–10.4		
G 351.582–0.353	G 351.581–0.353	1.6	G 351.581–0.353n	2.1	–89	–97.6	–91.1	–	
			G 351.581–0.353	3.4			–94.4		
G 351.775–0.536	G 351.775–0.536	1.8	G 351.775–0.536	1.9	–2	–2	1.3	–	
G 352.111+0.176	–		G 352.111+0.176	2.8	–60		–54.8	–	
G 352.133–0.944	–		G 352.133–0.944	2.8	–11		–16	–	
G 352.162+0.199	G 352.161+0.200	1.0	–		–45	–42.2		–	
G 352.517–0.155	G 352.517–0.155	0.2	G 352.517–0.155	0.3	–49	–50.6	–51.2	–	
G 352.525–0.158	–		G 352.525–0.158	0.3	–51		–53	–	
G 352.623–1.076	–		G 352.624–1.077	4.7	–6		5.8	–	
G 352.630–1.067	G 352.630–1.067	0.5	G 352.630–1.067	0.4	0	0	–2.8	–	
G 353.273+0.641	–		G 353.273+0.641	0.3	–49		–5.2	–	
G 353.411–0.362	–		–					G 353.411–0.362	1.7
G 353.464+0.562	G 353.464+0.562	0.9	G 353.464+0.562	1.9	–60	–45	–50.7	–	
G 354.615+0.472	G 354.615+0.472	1.9	G 354.615+0.472	1.8	–38	–15.4	–24.6	–	
G 355.343+0.147	G 355.344+0.147	2.0	G 355.344+0.147	1.7	17	19	20	–	
			G 355.343+0.148	2.7			5.7		

Table 6.3: – continued

Water (l, b) (degrees)	OH (l, b) (degrees)	Sep. (arcsec)	Methanol (l, b) (degrees)	Sep. (arcsec)	Water Vpeak (km s^{-1})	OH Vpeak (km s^{-1})	Methanol Vpeak (km s^{-1})	Continuum (l, b) (degrees)	Sep. (arcsec)
G 355.345+0.149	–		G 355.346+0.149	1.4	72		10	–	
G 357.965–0.164	–		G 357.965–0.164	1.5	–19		–8.8	–	
G 357.967–0.163	G 357.968–0.163	1.7	G 357.967–0.163	0.5	–65	–6.3	–3.2	–	
G 358.371–0.468	–		G 358.371–0.468	1.0	1		1	–	
G 358.386–0.483	G 358.387–0.482a	2.3	G 358.386–0.483	1.5	0	–6.3	–6.0	G 358.387–0.483	3.4
	G 358.387–0.482b	3.3	–			–7.8			
G 359.137+0.032	G 359.137+0.032	1.3	G 359.138+0.031	1.5	–1	–1	–3.9	–	
G 359.436–0.102	–		G 359.436–0.102	0.4	–59		–53.6	–	
G 359.436–0.104	G 359.436–0.103	1.9	G 359.436–0.104	0.7	–47	–52	–52	–	
G 359.615–0.243	G 359.615–0.243	0.8	G 359.615–0.243	0.6	64	22.5	22.5	–	
G 359.969–0.457	G 359.970–0.457	1.2	G 359.970–0.457	1.3	11	15.5	23.0	–	
G 0.209–0.002	–		–					G 0.209–0.002	2.4
G 0.212–0.002	–		G 0.212–0.001	3.7	56		49.2	–	
G 0.316–0.201	–		G 0.316–0.201	0.7	23		21	–	
			G 0.315–0.201	2.1			18		
G 0.376+0.040	G 0.376+0.040	1.3	G 0.376+0.040	1.6	40	36	37.1	–	
G 0.497+0.188	G 0.496+0.188	2.1	G 0.496+0.188	2.1	26	–5.5	0.8	–	
G 0.547–0.851	G 0.546–0.852	2.7	G 0.546–0.852	3.2	20	13.5	13.8	–	
G 0.657–0.042	G 0.658–0.042	0.4	G 0.657–0.041	4.8	62	52		–	
G 0.668–0.035	G 0.666–0.035	4.0	–		59	61		–	
G 2.143+0.009	G 2.143+0.009	0.8	G 2.143+0.009	0.1	37	59.8	62.7	–	
G 2.536+0.198	–		G 2.536+0.198	2.5	25		3.2	–	
G 5.886–0.392	G 5.885–0.392	6.3	G 5.885–0.392	5.5	11	13.9	6.7	–	
G 5.901–0.430	–		G 5.900–0.430	1.7	14		10	–	
G 6.049–1.447	G 6.048–1.447	2.0	–		20	11.2		–	
G 6.611–0.082	–		G 6.610–0.082	2.1	6		0.7	–	

Table 6.3: – continued

Water (l, b) (degrees)	OH (l, b) (degrees)	Sep. (arcsec)	Methanol (l, b) (degrees)	Sep. (arcsec)	Water Vpeak (km s^{-1})	OH Vpeak (km s^{-1})	Methanol Vpeak (km s^{-1})	Continuum (l, b) (degrees)	Sep. (arcsec)
G 6.796–0.257	G 6.795–0.257	2.1	G 6.795–0.257	2.4	1	16.1	26.6	–	
G 8.139+0.226	–		G 8.139+0.226	1.2	16		20.0	–	
G 8.670–0.356	G 8.669–0.356	2.9	G 8.669–0.356	2.7	36	39.2	39.3	G 8.670–0.356	1.1
G 9.620+0.194	G 9.620+0.194	1.6	–		6	22		–	
G 9.622+0.195	G 9.621+0.196	2.9	G 9.621+0.196	3.3	22	1.4	1.3	–	
G 9.986–0.028	–		G 9.986–0.028	1.3	49		47.1	–	
G 10.288–0.125	–		G 10.287–0.125	1.9	9		5	–	
G 10.323–0.160	–		G 10.323–0.160	1.5	–3		10	–	
G 10.342–0.143	–		G 10.342–0.142	1.8	8		14.8	–	
G 10.445–0.018	G 10.444–0.018	3.3	G 10.444–0.018	3.7	70	75.5	73.2	–	
G 10.473+0.027	G 10.473+0.027	0.9	G 10.473+0.027	1.9	62	51.5	75	G 10.473+0.027	1.8
G 10.480+0.034	G 10.480+0.033	4.5	G 10.480+0.033	4.5	64	66	65	–	
G 10.623–0.383	G 10.623–0.383	0.6	–		2	–2		–	
G 10.959+0.022	–		G 10.958+0.022	1.4	25		24.4	G 10.959+0.022	0.7
G 11.034+0.062	G 11.034+0.062	1.6	G 11.034+0.062	1.5	18	21.7	20.6	–	
G 11.498–1.486	–		G 11.497–1.485	2.9	17		6.7	–	
G 11.903–0.142	G 11.904–0.141	3.5	G 11.904–0.141	4.4	36	40.5	42.8	–	
G 12.203–0.107	–		G 12.203–0.107	0.2	35		20.5	–	
G 12.209–0.102	–		G 12.209–0.102	1.0	22		19.8	G 12.209–0.102	3.0
G 12.216–0.119	G 12.216–0.119	1.5	–		26	27.9		–	
G 12.681–0.183	G 12.680–0.183	1.0	G 12.681–0.182	1.1	61	64.5	57.6	–	
G 12.889+0.489	G 12.889+0.489	3.0	G 12.889+0.489	2.7	30	33	39.3	–	
G 12.908–0.260	G 12.908–0.260	1.2	G 12.909–0.260	1.8	37	38	39.9	–	
G 17.637+0.156	G 17.638+0.157	2.1	G 17.638+0.157	2.2	27	20	20.7	–	

6.3.1 Individual sources

Here we draw attention to information on the sources that can not be adequately conveyed in the tables and spectra. We discuss some entries in the Table 6.1 where close companions may be either discrete extra maser sites, or merely multiple features in an unusually extended site. Our interpretation of the likely systemic velocity, based on association with methanol or OH maser emission, is given in some cases where water shows high velocity features that dominate the spectrum. Extreme variability is sometimes evident from Table 6.1, and a few examples of this variability are demonstrated by spectra shown from both 2003 and 2004. The absence of an entry at one epoch is occasionally due to confusion from nearby features, as remarked in these notes. There are many instances where high velocity emission is present (as indicated in Table 6.1), but is rather weak and barely visible on the spectrum, so we draw attention to it here.

284.350–0.418. This water maser is coincident with main-line OH maser 284.351–0.418, with accompanying emission at 6035 MHz (Caswell, 1997), but clearly offset from nearby methanol maser 284.352–0.419 by 6 arcsec. Spectra from epoch 2003 as well as 2004 are shown as an example of the typical variability seen between our observing epochs.

285.260-0.067 and 285.263-0.059. The latter is a very strong water maser associated with an OH maser and having similar velocity of its strongest emission. In the case of OH masers this systemic velocity is a reliable indication of the systemic velocity. The first maser, offset by 1 arcmin, may be loosely associated, but it is difficult to recognise possible emission near the systemic velocity because of confusion with the stronger companion. Its spectrum varied markedly from 2003 to 2004, and highly blue-shifted emission dominates the 2004 spectrum.

290.374+1.661 and 290.384+1.663. The first of these sources is coincident with both OH and methanol maser emission. The positions measured in 2003 and 2004 are coincident, but detected features do not overlap in velocity ranges. There has been a substantial decrease in the peak flux density from 3.5 Jy to 0.26 Jy from the first to the second epoch.

Table 6.4: *22 GHz continuum sources detected towards water maser sources (i.e. continuum sources within 4.5 arcsec of detected water masers). See Tables 6.1 and 6.3 for details of the water maser sources that these continuum sources are associated with. Columns one through to 5 show: the name of the continuum source in Galactic coordinates, the source right ascension, declination, peak flux density (mJy/beam) and integrated flux density (mJy). We present two additional continuum sources that fall just outside our association threshold and we distinguish these sources with a '#' following the source name in column 1.*

Continuum (l, b) (degrees)	RA(2000) (h m s)	Dec(2000) (° ′ ″)	Ipeak (mJy/beam)	Total Flux Density (mJy)
G 291.611–0.529	11 15 02.62	–61 15 51.4	350	446
G 291.626–0.531#	11 15 09.66	–61 16 15.7	137	357
G 299.012+0.128	12 17 24.12	–62 29 05.6	25	38
G 301.136–0.226	12 35 34.96	–63 02 31.6	1017	1116
G 311.643–0.380	14 06 38.73	–61 58 21.4	174	181
G 313.458+0.193	14 19 35.04	–60 51 52.1	205	272
G 316.412–0.308	14 43 23.25	–60 12 59.5	160	167
G 317.430–0.561	14 51 38.03	–60 00 19.5	32	35
G 319.399–0.012	15 03 17.60	–58 36 11.2	230	298
G 320.234–0.283	15 09 52.63	–58 25 32.4	282	293
G 327.402+0.445	15 49 19.35	–53 45 13.3	86	94
G 328.236–0.547	15 57 58.15	–53 59 23.4	26	36
G 328.307+0.431	15 54 06.24	–53 11 38.8	3361	3647
G 328.808+0.633	15 55 48.33	–52 43 07.0	1208	1357
G 330.879–0.367	16 10 19.95	–52 06 05.3	324	476
G 330.954–0.182	16 09 52.51	–51 54 54.1	2954	3151
G 331.443–0.187	16 12 12.83	–51 35 10.2	40	44
G 331.512–0.103	16 12 10.10	–51 28 37.2	109	113
G 332.826–0.549	16 20 11.12	–50 53 13.7	2510	2670
G 333.030–0.063	16 18 56.94	–50 23 53.5	27	25
G 333.466–0.163#	16 21 19.71	–50 09 45.6	141	254
G 336.018–0.828	16 35 09.39	–48 46 47.6	85.1	80.8
G 336.360–0.137	16 33 29.64	–48 03 38.8	189	293
G 336.984–0.184	16 36 12.60	–47 37 57.8	51	56.8
G 336.990–0.025	16 35 32.48	–47 31 14.6	91	102
G 337.404–0.403	16 38 50.59	–47 28 02.8	117	121
G 337.706–0.054	16 38 29.83	–47 00 35.7	244	262
G 338.075+0.012	16 39 39.15	–46 41 26.2	818	1144
G 338.681–0.085	16 42 24.19	–46 18 00.4	74	74
G 344.582–0.024	17 02 58.03	–41 41 52.7	19	21
G 345.004–0.225	17 05 11.36	–41 29 06.5	353	355
G 345.010+1.792	16 56 47.85	–40 14 25.8	362	367
G 345.408–0.952	17 09 35.62	–41 35 54.6	493	608
G 347.632+0.210	17 11 36.22	–39 07 06.2	46	48
G 350.331+0.099	17 20 02.09	–36 59 12.8	55	65
G 351.161+0.696	17 19 57.65	–35 57 51.8	238	271
G 351.247+0.667	17 20 19.29	–35 54 39.4	1280	1567
G 353.411–0.362	17 30 26.66	–34 41 46.0	384	788
G 358.387–0.483	17 43 37.96	–30 33 49.2	109	113
G 0.209–0.002	17 46 07.57	–28 45 30.5	75	95
G 8.670–0.356	18 06 19.15	–21 37 32.1	677	689
G 10.473+0.027	18 08 38.41	–19 51 47.9	152	151
G 10.959+0.022	18 09 39.43	–19 26 27.0	150	153
G 12.209–0.102	18 12 39.85	–18 24 20.0	119	140

The second source 290.384+1.663, is offset from the OH and methanol target and appears to be solitary, with no associated OH or methanol maser emission.

291.270–0.719, 291.274–0.709 and 291.284–0.716. The 2003 data for these sources are presented in Caswell (2004a), along with extensive discussion on associated sources. Note that the OH target 291.274–0.709 was a supplementary addition to the list of Caswell (1998). The variability of the water masers between the two epochs is moderate, with minimal changes in the velocity ranges of the detected emission but many changes in the relative flux densities of individual features.

291.270–0.719 is associated with methanol maser emission and has weak emission near the systemic velocity but much stronger emission blue-shifted by almost 80 km s^{-1}. 291.274–0.709, shows emission only near the systemic velocity and is coincident with both OH and methanol maser emission. The strongest source, 291.284–0.716, is associated with neither OH or methanol maser emission and shows no detectable water maser emission at the systemic velocity but has strong blue-shifted emission. Caswell & Phillips (2008) regard this source and 291.270-0.719 as members of a distinct class of water masers that are dominated by blue-shifted outflows.

291.578–0.434, 291.579–0.431 and 291.581–0.435. The main strong source 291.579–0.431 is a persistent maser detected in both 2003 and 2004, and also 1981 (Caswell et al., 1989), with intensity varying by a factor of 4. The other sources, detected at a single epoch, are even more variable. All are associated with NGC 3603 (Caswell, 2004a).

291.610–0.529, 291.627–0.529 and 291.629–0.541. The three water masers of this cluster were all detected both in 2003 and 2004 and are associated with NGC 3603 (Caswell, 2004a). Only G291.610–0.529 is coincident with an OH maser and none of the sources is associated with any methanol maser emission.

297.660-0.974. The strongest water maser peaks, at 29 km s^{-1} in 2003 and 26 km s^{-1} in 2004, agree well with the associated OH maser peak at 27.6 km s^{-1}, the probable systemic velocity for the region. There is a weak high velocity water maser feature of 0.6 Jy at a velocity of −78 km s^{-1}, slightly more than 100 km s^{-1} from the systemic velocity.

299.012+0.125 and 299.013+0.128. 299.013+0.128, with strongest peak at +19 km s^{-1} in both 2003 and 2004, was first detected by Caswell et al. (1989) and is in good agreement with the position and velocity of methanol and OH masers. In 2004 we detected an additional weak source, 299.012+0.125, offset by ∼9 arcsec. We regard the latter as most likely a distinct source, probably in the same cluster but lacking emission at its systemic velocity.

300.968+1.143 and 300.971+1.143. 300.968+1.143 was first observed by Caswell et al. (1989), with high velocity emission extending to −85 km s^{-1}, remaining similar in our observations in both 2003 and 2004. This source is solitary, offset from the target OH maser by 18 arcsec. Observations in 2004 uncovered an additional source, 300.971+1.143, with a flux density of 3 Jy. As can be seen in Table 6.1, in 2003 we placed an upper limit on the flux density of this source of 3 Jy, quite crude because at this velocity there was confusion by strong emission from 300.968+1.143 at this epoch.

301.136–0.225, 301.136–0.226a, 301.136–0.226b and 301.137–0.225. Although we list four distinct water maser positions, they probably represent a single maser site, with the last three locations all within 3 arcsec of OH and methanol maser emission, Confusion between features in 2003 prevented separate position measurement of any but the strongest feature.

305.191–0.006 and 305.198+0.007. 305.198+0.007 is probably the same source as 305.20+0.01 in Caswell et al. (1989). Both of these water masers are offset from the target OH maser, 305.200+0.019 (with methanol maser, 305.199+0.005).

305.208+0.207 Two strong peaks have positions separated by about 1 arcsec, with the weaker peak slightly closer to the associated OH and methanol emission.

306.318–0.331. This is new solitary water maser source found offset from target OH and methanol maser positions by ∼15 arcsec.

308.754+0.549. The OH target is an addition to the Caswell (1998) list. Details of methanol, OH and water are given by Caswell (2004a).

308.918+0.124. The position of this water maser falls within our 3 arcsec association threshold of OH maser G 308.918+0.123 but lies 3.6 arcsec from methanol maser G 308.918+0.123. The OH and methanol masers are almost certainly coincident, with a measured separation of 0.6 arcsec, and we treat all three species as coincident.

309.921+0.479. Caswell et al. (1989) reported the detection of a 4.5-Jy water maser at –70 km s^{-1} towards this OH and methanol site. We detect no emission (< 0.3 Jy) in either 2003 or 2004.

310.144+0.760 and G 310.146+0.760. The first of this close pair of sources is located at the site of both OH and methanol maser emission and the second source is located at the site of an isolated 1720 MHz OH maser (Caswell, 2004c) and is strongly variable.

311.94–0.14. This is a methanol site from Caswell (2009) with position 14 07 49.72, -61 23 08.3 (uncertainty 0.4 arcsec) from which there was no water detection in 2003 (this position was not observed in 2004). However a water maser was reported by Caswell et al. (1989) with peak flux density 38 Jy from the position 14 07 49.9 -61 23 20, nominally offset from the methanol by 12 arcsec but with rms position uncertainty of about 10 arcsec and thus possibly coincident with the methanol. An OH maser is listed by Caswell (1998) at 14 07 48.7 -61 23 22, nominally offset from the methanol by 16 arcsec, but again, possibly coincident (to within the OH position uncertainty of more than 15 arcsec). Like the water

maser, the OH has varied, and later observations to attempt an improved position determination failed to detect it. We have omitted this source from the statistics since for our position coincidence threshold of 3 arcsec. it may be an OH site accompanied by water, by methanol, by both or by neither, depending on the precise positions yet to be determined.

312.106+0.278 and 312.109+0.262. The second source is located towards the targeted methanol maser and consists of a single feature, with velocity similar to the methanol. The first source is a slightly stronger single feature, offset from the second by nearly 1 arcmin, and clearly offset in velocity by 6 km s^{-1}.

312.596+0.045 and 312.599+0.046. These sources are a close pair, separated by ~10 arcsec. The second of these sources was also detected by Caswell et al. (1989) and is coincident with both OH and methanol masers. The first source, 312.596+0.045, is coincident with a methanol maser site.

313.457+0.193 and 313.470+0.191. These sources have an angular separation of ~45 arcsec. 313.470+0.191 was also detected in Caswell et al. (1989) and is associated with both OH and methanol masers, with peak water maser velocity comparable to the systemic velocity of the region as traced by the coincident methanol maser with mid-range velocity of –8 km s^{-1}. 313.457+0.193 has an emission peak near –1 km s^{-1} at both epochs, suggesting its systemic velocity (and distance) is similar to that of its companion. We regard the slightly stronger emission at 45 km s^{-1} seen only in 2004 as a strongly varying high velocity feature.

316.360–0.361 and 316.361–0.363. Near these water masers lie an isolated methanol site (316.381–0.379) and a 'methanol with OH' site (316.359–0.362). Water maser 316.360–0.361 is offset from the methanol in the latter pair by 3.2 arcsec, and slightly further from the OH. Thus the water maser is formally rejected as part of an intimate association, but this remains somewhat uncertain. The second water maser source is further offset from these sources than the first and is thus very clearly a distinct, isolated site.

318.044–1.404 The OH and methanol maser counterparts show that the systemic velocity is indeed near +45 km s^{-1} and indicate a distant location outside the solar circle. The large latitude offset from the Galactic plane is consistent with the Galactic warp known to be present in this outer region of the Galaxy.

318.948–0.196a and 318.948–0.196b. This pair of sources is essentially one extended source. Using the 2004 data, we were able to distinguish two main sites (with an angular separation of just over 2 arcsec) which conveniently reveals the association with nearby OH and methanol masers that otherwise would have fallen outside our 3 arcsec coincidence threshold.

320.221–0.281, 320.232-0.284, 320.233-0.284, 320.255–0.305 and 320.285–0.308. We suggest that all 5 sites are at similar distance in a cluster with systemic velocity near –65 km s^{-1}. 320.232-0.284 has associated methanol and OH maser emission and 320.233-0.284, offset by nearly 5 arcsec, seems to be a separate site. 320.255-0.305 shows strong emission only near –126 km s^{-1}, highly blue-shifted from our suggested systemic velocity near –65 km s^{-1}, and apparently in a small class of water masers where blue-shifted emission dominates (Caswell & Phillips 2008). Interestingly, like 291.284–0.716, 320.255–0.305 is not associated with either OH or methanol maser emission. Emission from this region was reported, with lower position precision, by Caswell et al. (1989).

321.028–0.484 and 321.033–0.483. Both water masers are offset from the target OH and methanol maser 321.030–0.485 by more than 7 arcsec; the second water maser is associated with methanol maser 321.033–0.483.

321.148–0.529 The spectrum of this maser is shown at both epochs as an example of extreme variability with no common features seen in spectra observed less than 1 year apart.

323.459-0.079. A water maser was discovered (but without a precise position) by Caswell et al. (1989) towards this OH and methanol site, but was below our detection threshold of 0.2 Jy in both 2003 and 2004.

324.716+0.342. This source was detected by Caswell et al. (1989) at a peak flux density of 138 Jy, coincident with both OH and methanol maser emission. The water maser shows marked variability with peaks of 10 and 26 Jy during 2003 and 2004 respectively.

326.662+0.521, 326.665+0.553 and 326.670+0.554. This group of three sources is spread over 2 arcmin. 326.670+0.554 coincides with an OH maser; the water maser peak flared in 2004 relative to 2003. This maser is probably the same as one reported, with peak of 780 Jy, but with poor position, by Batchelor et al. (1980). In 2004 no targeted observation was made of the first source and although recognised at the beam edge in another observation, it was confused by a strong flare from 326.670+0.554. Measurement for the second source (326.665+0.553) is reported only from the 2004 measurements since the 2003 observations were confused by 326.662+0.521, preventing a useful upper limit estimate.

326.780-0.241 This is a new water maser coincident with an OH maser listed by Caswell (1998) with approximate coordinates 326.77-0.26; subsequent (previously unpublished) ATCA measurements of the OH show it to be coincident with the water maser.

326.859-0.676. This weak new water maser coincides spatially with methanol maser 326.859–0.667 (offset by 3.4 arcsec), whose systemic velocity is –58.0 km s^{-1}. It seems likely to be an association in which only a heavily blue-shifted water maser feature, at –103 km s^{-1}, is seen.

327.291-0.578. This strong water maser with peak of several hundred Janskys is associated with OH and methanol masers. Spectra are shown for 2003 and 2004 revealing great variability of the water maser, and can be compared with a spectrum shown by Batchelor et al. (1980) when its peak was over 1000Jy.

327.402+0.445. In contrast to the previous source, this water maser has greatly increased intensity compared to measurements by Batchelor et al. (1980). The water maser is associated with a strong methanol maser. An OH maser is

close to the methanol. We therefore treat the OH as an association also, although its separation from the water is just outside our formal association criterion.

328.306+0.432. This water maser is associated with 22 GHz radio continuum but appears to be truly offset from the target OH maser 328.307+0.430 (which has no accompanying methanol) by more than 5 arcsec.

328.808+0.633. Detected towards OH maser site 328.809+0.633. Also associated are many transitions of methanol and OH, including; 6.7, 12.2, 19.9, 85.5 and 107 GHz methanol masers (Caswell 2009; Caswell et al. 1995; Ellingsen et al. 2004; Ellingsen et al. 2003; Val'tts et al. 1999) as well as 1720, 4765, 6030, 6035 MHz and 13.4 GHz transitions of OH (Dodson & Ellingsen 2002; Caswell 2003, 2004b, 2004c). This source is also associated with strong 22 GHz radio continuum.

329.021–0.186, 329.029–0.199, 329.030-0.205 and 329.031–0.198. This cluster of four sources is spread over about 1 arcmin. The first source is solitary (no OH or methanol), the second (which varied below the detection limit in 2004) has OH, and the third and fourth are associated with both OH and methanol. Ellingsen (2006) showed that these OH, methanol and previously known water masers are associated with a filamentary infrared dark cloud as well as Class I methanol masers.

329.342+0.130. This water maser is clearly offset by almost 1 arcmin from the target OH maser 329.339+0.148 and no other water emission was detectable in the field. The water maser velocity is similar to that of its OH neighbour and they presumably reside in the same star formation cluster, discussed in detail by Caswell (2001, 2004). Note that the OH target is an addition to the Caswell (1998) list.

329.404–0.459, 329.405–0.459 and 329.407–0.459. The second source is at an OH and methanol maser site, and its velocity is similar, presumably representative of the systemic velocity. The first source is offset only 3 arcsec from

the second site, whereas its velocity is close to that of the previously discussed, more distant, cluster around 329.339+0.148. None the less, we suggest it most likely represents high velocity emission related to 329.405–0.459. Water maser 329.407–0.459, associated with a methanol maser, has shown extreme variability with peak flux density of 80 Jy in 2003 but not detected above our detection limit of 0.2 Jy in 2004.

329.421–0.167, 329.424–0.164 and 329.426–0.161. The only other maser species nearby, both spatially and in velocity, is a 1720 MHz maser 329.426–0.158 (Caswell, 2004c). We conclude that all four masers lie in the same star forming cluster but are not closely associated.

330.879–0.367 The water maser has been known for many years (Batchelor et al. 1980) and our precise position confirms that it coincides with one of the strongest known OH masers, accompanied by very weak methanol emission (Caswell 2009).

330.954–0.182. The water maser has remained very strong for many years (see Batchelor et al. (1980)) and has prominent high velocity emission (a feature at -191 km s^{-1} has a peak flux density of 0.3 Jy but is too weak to be seen on the spectra displayed here). OH and methanol emission are present nearby but spread over several arcsec, and the most detailed maps (Caswell et al. 2010) show the water to be associated with OH emission only, with the methanol emission clearly offset to another site offset to the south-west by more than 3 arcsec. We measure the flux density at 22 GHz of an associated strong UCHII region as 3.2 Jy.

331.418+0.252. This 0.6-Jy water maser was detected almost 50 arcsec from the targeted methanol maser 331.425+0.264. The water maser emission is observed towards an UCHII region that we detect at 22 GHz.

331.512–0.103. Batchelor et al. (1980) observed this source with a peak flux density of 4300 Jy. Observations of this source in 2003 and 2004 showed a

decrease in the flux density to 700 Jy and 534 Jy in 2003 and 2004 respectively. The water maser is coincident with an OH maser (but no methanol) and an UCHII region that we detect. The strongest water emission is near the systemic velocity, and almost symmetric about this there are multiple high velocity features extending for 70 km s^{-1}.

332.826–0.549. This is a strong new water maser coinciding with methanol and a 6035 MHz OH maser but offset 7 arcsec from a 1665 MHz OH maser.

333.219–0.062 and G 333.234–0.060. 333.234–0.060 was detected in both 2003 and 2004 and has been previously observed by Batchelor et al. (1980). At all epochs the peak has been more than 100 Jy at a velocity near -88 km s^{-1}, which is the mid-range velocity of an associated OH maser, and the likely systemic velocity. In our 2004 water observations, an extreme high velocity feature was observed with a peak flux density of 0.3 Jy at +81 km s^{-1} , more than 160 km s^{-1} from the systemic velocity. 333.219–0.062 is offset from 333.234–0.060 by almost an arcmin and is solitary. This source was observed with a peak flux density of 0.5 Jy in 2004 and was not detected in 2003 above 0.3 Jy. In the absence of an association with OH or methanol, its systemic velocity is unknown.

333.387+0.032. This weak water maser is located at the site of both OH and methanol maser emission. It was detected with a peak flux density of 0.4 Jy in 2003 and had decreased to 0.14 Jy in 2004. Spectra from both epochs are presented in Fig. 6.1.

333.608–0.215. This was one of the earliest observed water masers, discovered by Johnston et al. (1972) and was later observed by Batchelor et al. (1980) in 1976 with a peak flux density of 100 Jy. Presented in Chapter 3 are observations of this sources carried out with the ATCA, deriving a precise position for the source that is within 0.4 arcsec of the independent position quoted in Table 6.1. Both the spectrum of 2006 and that found in the present observations of 2003 differ markedly from the 2004 spectrum shown here, revealing strong variability of high velocity emission. This source is associated with an OH maser and is offset

by 15 arcsec from a bright UCHII region which was erroneously reported by Breen et al. (2007) as having an integrated flux density of 631 mJy at 22 GHz. The present observations find that the UCHII region has an integrated flux density of more than 16 Jy at 22 GHz.

333.930–0.134. This very weak water maser was observed at the 2004 epoch only. While the peak of the detected emission is a mere 0.18 Jy, the source position is in remarkably good correspondence with the targeted methanol maser, the separation being less than 1.5 arcsec.

335.059–0.428, 335.060–0.427 and 335.070–0.423. The first two of these sources are separated by 3.3 arcsec and therefore may be essentially a single source spread over a few arcsec. The second source, 335.060–0.427, with measurements in both 2003 and 2004, shows best positional agreement with an associated OH and methanol maser site. 335.059–0.428 was not recognisable as a distinct source in the 2003 data owing to confusion from the stronger companion 335.060–0.427.

335.070–0.423 is offset from the previous two sources by 43 arcsec and is solitary.

335.585–0.285, 335.586–0.290 and 335.588–0.264. These three sources are spread over almost 80 arcsec. The first two sources were detected at both epochs and are both coincident with both methanol and OH masers. The third source, 335.588–0.264, was detected with a peak flux density of 16 Jy in 2003 but not detectable above 0.2 Jy in 2004. It is isolated from other maser species and is devoid of detectable 22 GHz radio continuum emission.

335.787+0.177, 335.789+0.174 and 335.789+0.183. 335.789+0.174 was detected by Batchelor et al. (1980) as a 25 Jy source towards an OH maser with the same Galactic coordinates. Our observations detect a water maser of 3 Jy in 2003 and detect no emission above 0.2 Jy in 2004. 335.787+0.177, detected in both 2003 and 2004, is a solitary maser and has no detectable radio continuum at 22 GHz. The third source, 335.789+0.183, is also isolated from other maser

species as well as 22 GHz radio continuum emission. It was detected with a peak flux density of 4.2 Jy at a velocity of –91 km s^{-1} in 2003 and was not detectable above 0.2 Jy in 2004. If this velocity represents the systemic velocity, then its distance is likely to differ greatly from its apparent companions. Alternatively, it may be a companion at similar distance but showing no significant emission near the systemic velocity, and only blue-shifted emission. Such high velocity features are notoriously variable.

336.864+0.005, 336.864–0.002 and 336.870–0.003. These three sources are located within 40 arcsec of each other and were all detected in both the 2003 and 2004 observations. The first source is associated with both OH and methanol maser emission and the other two sources are solitary.

336.983–0.183. Figure 6.1 shows both the 2003 and 2004 spectrum for this weak source. The only significant feature in 2003 is a peak at –76 km s^{-1}. In 2004, emission near this velocity is weaker, and a high velocity feature near +45 km s^{-1} is marginally stronger. The source is associated with a methanol maser as well as an UCHII region that we list in Table 6.4. The methanol maser is strong, with a well-measured position and velocity near –81 km s^{-1}. Nearby is a weak OH maser just outside our criterion for an association with the water position, but slightly closer to the methanol. Furthermore, the position of 6035 MHz OH emission (Caswell 2001) is acceptably within our coincidence criterion, so we add this as an OH maser association with both methanol and water.

336.991–0.024, 336.994–0.027 and 336.995–0.024. These three sources appear clustered within ~15 arcsec. 336.994–0.027 is the strongest of the three (160 Jy), detected in 2003, 2004 and by Batchelor et al. (1980), and is associated with both OH and methanol maser emission, with systemic velocity near –120 km s^{-1}. The 2 weaker water sites have quite different radial velocities, near –50 km s^{-1}, and might be at a distance quite different from the strongest one. 336.991–0.024 was detected in both 2003 and 2004, with a peak flux density of 4 and 1 Jy at the respective epochs, and is associated with an UCHII region that we detect. 336.995–0.024 was detected only in 2004 and had a peak flux density

of 1.1 Jy.

337.994+0.133 and 337.998+0.137. Batchelor et al. (1980) detected 337.998+0.137 with a peak flux density of 200 Jy and we detected a decreased flux density of 30 and 27 Jy in 2003 and 2004 respectively. This source is coincident with both OH and methanol maser emission. 337.994+0.133 is a solitary maser, offset from the previous source by 19 arcsec.

338.069+0.011, 338.075+0.012, 338.075+0.010 and 338.077+0.019 Water maser emission from 338.069+0.011 is the strongest in this cluster at both epochs and has no other maser counterpart. 338.075+0.012 detected only in 2003, and the weakest of the group, coincides with OH and methanol maser emission. 338.075+0.010 is associated with a methanol maser with systemic velocity near -38 km s^{-1} ; the water maser emission in 2003 was strongest at a highly blue-shifted velocity, but by 2004 this had faded below detectability, leaving only features closely straddling the systemic velocity. 338.077+0.019 was detected in both 2003 and 2004, the spectrum remaining unchanged; it has no apparent association with other masers.

338.920+0.550 and 338.925+0.556 The stronger site, 338.925+0.556 coincides with OH and methanol masers. The weaker site, 338.920+0.550, is associated with a methanol maser with systemic velocity near -60 km s^{-1}, similar to the other site, and the water spectrum in 2003 was dominated by highly blue-shifted emission.

343.126–0.065 and 343.127–0.063. These two sources are separated by 9.3 arcsec. The second source is strong and associated with an OH maser, but not methanol. The first source is much weaker but clearly distinct and is solitary.

345.004-0.224 In 2003 the only water emission was near the systemic velocity, as defined by the associated methanol and OH masers. In 2004, high velocity features dominated. Spectra from both epochs are shown to demonstrate this interesting variability.

345.010+1.793, 345.010+1.802 and 345.012+1.797 In this small cluster, the first water maser coincides with an OH and methanol site, the second has no other maser counterpart, and the third, the strongest, has a methanol counterpart.

345.397-0.950, 345.402-0.948, 345.405-0.947, 345.406-0.942, 345.408-0.953, 345.412-0.955 and 345,425-0.951 One of these sites, 345.425-0.951, is coincident with a methanol maser site. We also accept a coincidence between 345.408-0.953 and an OH and methanol maser site, despite an offset of 4.6 arcsec, formally just outside our our criterion for a single epoch water measurement; there is evidence (from comparison of features common to 2003 and 2004, and a feature common to 2004 and Forster & Caswell (1989)) that the 2004 observation of this field yields positions slightly too far south and at too large an RA, a correction that would improve the coincidence. The systemic velocity of the two associated, methanol sites is near -15 km s^{-1}. In view of the large offset of the cluster from the Galactic plane in Galactic latitude, all water sites are likely to be clustered at a similar distance, irrespective of the water maser velocity. Their separation from each other is sufficiently large to suggest that each site has its own exciting star, and thus it seems likely to be a remarkable physical cluster of high-mass stars. Radhakrishnan et al. (1972) suggest that the distance to the complex is half the distance to the Galactic Centre.

345.487+0.314. As seen in the notes tabulating associations, there is a coincident methanol maser and no nearby ground-state OH maser. There is, however, a 6035 MHz excited state OH maser offset just over 3 arcsec to the north (Caswell 2001).

345.493+1.469, 345.494+1.470 and 345.495+1.473 The first site coincides with an OH maser that has no accompanying methanol maser. Another nearby OH maser site shows no methanol or water emission. All four sites are likely to lie in a nearby cluster, as evident from the large Galactic latitude, and the systemic velocity probably lies between -15 and 0 km s^{-1} , based on the OH velocities.

347.623+0.148 and 347.628+0.149 The first water maser, detected in both 2003 and 2004, has no coincident maser of OH or methanol. The second water maser, at similar velocity, was detected only in 2003 and coincides with OH and methanol, with systemic velocity near -95 km s^{-1}.

348.533–0.974, 348.534–0.983 and 348.551–0.979 The third water site is close to the original OH target but is more precisely coincident with the methanol site 348.550-0.979n (Caswell 2009). The original 'OH with methanol' target, 348.550-0.979, is regarded by Caswell (2009) as a nearby but distinct site and, on this interpretation, it is a site without detected water maser emission. The water masers 348.533–0.974 and 348.534–0.983 are new, chance, detections in the vicinity.

348.726–1.038 This water maser is offset from the target OH (with methanol) by more than 4 arcsec and is not formally an association. However, the large spread over several arcsec in the positions of individual water maser spots reveals a larger than usual maser site and the possibility of an association will require further investigation.

350.105+0.084 350.112+0.089 and 350.113+0.095 The first of these is associated with a methanol site, and the second with an OH site. In a cluster of 6 water maser sites showing peak emission at velocities between –72 and –44 km s^{-1}, they are the only 2 accompanied by maser emission of another species. Spatially in this same cluster, the water maser 350.112+0.089 displays a quite different velocity range, from -175 to -106 km s^{-1} suggesting that it might be at a quite different location, perhaps in the near side of the 3-kpc arm, whose characteristic velocity at this longitude extends to approximately -110 km s^{-1} (Green et al. 2009); see also the note for 351.582–0.353.

350.299+0.122. This is the weakest single epoch water maser that we list, with a peak flux density of 0.17 Jy. The position of the water maser is only 0.7 arcsec from the targeted methanol maser and its emission peak velocity of –68 km s^{-1} is within 6 km s^{-1} of the associated methanol maser peak emission.

Furthermore, there are no nearby water maser sources that could confuse the region and be detected as a sidelobe here; there is therefore little doubt that this is a genuine weak water maser.

351.240+0.668, 351.243+0.671 and 351.246+0.668 The first 2 sites were listed by Caswell & Phillips (2008), with special discussion of a blue-shifted outflow that dominates the emission from 351.243+0.671, and remarks that the water maser spots in the outflow are distributed over several arcsec. All three sites appear to be distinct, with large separations of more than 15 arcsec, yet close enough to suggest that they all lie in the same star-forming cluster, with systemic velocity +2.5 km s^{-1} as defined by the methanol maser counterpart to 351.243+0.671 (Caswell & Phillips 2008), and all lying in the large NGC 6334 complex, at a commonly accepted distance of 1.7 kpc

351.417+0.645 This maser coincides with an HII region NGC 6334F, a very strong methanol maser, and an OH maser (Caswell 1997) and its water maser emission was mapped by Forster & Caswell (1999), showing a scatter of spot positions over several arcsec, including an apparent jet-like feature.

351.582–0.353 This strong water maser is coincident with an OH and methanol maser site which is located in the near side of the expanding 3-kpc arm (Green et al. 2009; Caswell et al. 2010).

352.623-1.076 and 352.630-1.067 The second water maser coincides with an OH and methanol site. It flared from a peak of 35 Jy in 2003 to 700 Jy in 2004. It appears to be the same maser that was first reported by Sakellis et al. (1984) with peak flux density 346 Jy. The first source is solitary with no other maser counterpart and offset by more than 40 arcsec.

353.273+0.641 This site is the prime example of a class of water maser dominated by a blue-shifted outflow (Caswell & Phillips 2008); its systemic velocity is estimated from a coincident methanol maser.

353.408–0.350 to 353.414–0.363 inclusive This is a cluster of 6 solitary water maser sites. The target OH and methanol maser site 353.410–0.360 (Caswell 1997) lies in this cluster but none of the water maser sites coincide with it.

354,703+0.297, 354.712+0.293 and 354,722+0.302 The velocity of all three solitary water sites is near +100 km s^{-1}, similar to that of the nearby OH with methanol site 354.724+0.300. The velocity of the latter has been interpreted as evidence of a location in the the Galactic bar (Caswell 1997), which we suggest is an appropriate interpretation for all 4 sites.

357.965–0164 and 357.967–0.163 The two water sites are separated by 9 arcsec. The first site has a weak methanol counterpart but no OH; the second has stronger methanol and also OH. The methanol and OH emission is confined to a small range between –9 and +3 km s^{-1} , and thus the systemic velocity for both sites probably lies in this range. Water emission at the first site was strong in 2003 but weak in 2004, and confined to within about 15 km s^{-1} of the systemic velocity. Water emission at the second site is seen not only near the systemic velocity but also at many blue-shifted and red-shifted high velocities; in 2004 the high velocity features were stronger than emission near the systemic velocity.

359.436–0.102 to 359.443–0.104 inclusive The six water maser sites in this cluster all have similar velocities. Confusion prevented a useful upper limit estimate for emission from 2 of them not detected in 2003. One site has an OH with methanol counterpart and another, a methanol counterpart. The methanol sites appear to be located in the near side of the 3 kpc arm (Green et al 2009) and this interpretation can be applied to all six water sites in the cluster.

0.655–0.045 to 0.677–0.028 These five sites lie within the Sgr B2 complex and are clearly distinguishable with our spatial resolution. Two of them have associated OH maser emission but none have associated methanol masers.

5.886–0.392 This site has OH and water masers spread over more than 5 arcsec, associated with a compact HII region that is likely to be approaching the

end of its masing phase (Caswell 2001) and with various distance estimates, of which 2 kpc is currently favoured (Stark et al. 2007). It was observed by Forster & Caswell (1989; 1999) and our 2003 water maser observations were made to assess the changes over a decade. We cite the position of the strongest feature during our observations and note that there are many components at offset positions. Our water reference position and the OH reference position from Caswell (1998) are 6 arcsec apart but we list it as an association with OH on the basis of the intermingled features mapped by Forster & Caswell (1999).

9.620+0.194 and 9.622+0.196 These coincide respectively with an OH maser site with no reported methanol, and the strongest known methanol site which also has a coincident OH maser. A third methanol maser site in this cluster, 9.619+0.193, shows no detectable water maser emission.

10.473+0.027 and 10.480+0.034 The first source was detected in both 2003 and 2004, and the spectrum shown is from 2004 when a strong flare occurred. The spectrum shown for 10.480+0.034 is from 2003 when 10.473+0.027 was not flaring, and confusion from 10.473+0.027 was much less.

10.623–0.383. Note a small correction to the Caswell (1998) OH position, for which the RA should be $18^h10^m28.67^s$ (not 28.61). Our water measurement in 2003 is in good agreement with the revised OH position and the measurement of Forster & Caswell (1989).

11.903-0.141. We detect a weak water maser at this site which is probably the same source that was first reported by Caswell et al. (1983) with peak flux density 7.9 Jy (but with position uncertainty exceeding 10 arcsec). Note a small transcription error in the target OH position from Forster & Caswell (1989), Forster & Caswell (1999) and Caswell (1998), for which the RA should be $18^h12^m11.46^s$ (not 11.56). Our water maser position is in satisfactory agreement with the corrected OH position. The corrected OH position also agrees better with the 6035 MHz maser position (Caswell, 1997), and with its associated UCHII region (Caswell, 1997) for which improved measurements by Forster & Caswell

(2000) at 8.7 GHz give a flux density of 33.9 mJy.

15.016–0.679 to 15.034-0.667 inclusive These all reside in the well-known nearby star-forming complex M17. All seven masers were recognisable and spatially distinct in the 2004 observations but only 3 were distinct in the 2003 observations, partly due to the stronger confusing emission from 15.028–0.673 at the earlier epoch. Spectra for the two strongest sources from the 2003 epoch are shown in Fig. 6.1 and are in addition to the 2004 spectra.

6.4 Discussion

6.4.1 Water maser variability

Water masers have been noted on many occasions for their often extreme variability over relatively short timescales, and some studies have extended over several decades (e.g. Felli et al., 2007). As our data are confined to only two epochs, and limited to coarse spectral resolution, we do not attempt a detailed study of the variability of our sources. However, we are able to highlight some interesting examples of variability, and the large size of our sample allows us to derive several interesting statistics.

For the 207 sources observed and detected at both epochs, we see variability ranging from sources showing no measurable variability to occasional extreme levels, and many intensities varying by factors of more than two. High velocity features can be particularly variable, with many spectral features of sources not being common to both epochs.

As noted in Section 6.3, Fig. 6.1 includes the spectra of eight sources from both epochs (284.350–0.418, 321.148–0.529, 327.291–0.578, 333.387+0.032, 336.983–0.183, 345.004–0.224, 15.026–0.654 and 15.028–0.673). They illustrate changes seen over the 10-month time scale and highlight the fact that, for four of the examples, the feature with the strongest peak at the two epochs is at a different velocity.

A qualitative impression from the full set of spectra at both epochs (including our unpublished material for the 2003 epoch) is that the spectra of many sources

show little resemblance at the two epochs. Quantitatively, we use the data of Table 6.1 to derive the plot of Fig. 6.2 which compares the velocity of the water maser peak emission in 2003 and 2004. An interesting statistic for the sources measured at two epochs shows that the strongest peak is at a significantly different velocity (offset more than 2 km s^{-1}) for 38 per cent (78 of 207) of the sites. However, from Fig. 6.2 we see that a much smaller fraction of velocity differences exceed 10 km s^{-1}. These large velocity differences generally represent the truly high velocity features which, in a few sources, can dominate the spectrum at some epochs since they have highly variable intensities. For example, the source 357.967-0.163 has the 2003 peak intensity at 0 km s^{-1} (near systemic) but the 2004 peak at -65 km s^{-1} (a high velocity feature); and the source 336.983-0.183 has the 2003 peak intensity at -76 km s^{-1} (near systemic) but the 2004 peak at +45 km s^{-1} (a high velocity feature).

We have observations available in both 2003 and 2004 for 253 water masers; 46 of them (17 per cent) were detected at only one epoch. Only 16 (one-third) of these sources that varied below our detection limit at one of the epochs were stronger than 2 Jy when detectable, with the strongest source being 80 Jy. Half of the sources detected only at one epoch show a single feature and the majority of the others exhibited 3 or fewer features. In comparison, the vast majority of water maser sources that are associated with OH or methanol masers exhibit five or more spectral features. We have investigated the associations with other maser species for these 46 sources to search for other possible properties in common. Of the 46 sources, 12 are associated with both OH and methanol masers, 2 are associated with OH masers only, 3 are associated with methanol masers only and 28 are solitary (no association with another maser species). A chi-squared test was carried out on the percentage of sources in each of these groups compared to what would be expected if these sources were distributed in the same way as our entire sample. We find that a statistically significant higher percentage of the sources detected at only one epoch are solitary (p-value 0.02), compared to the distribution of associations in our full sample. The numbers of sources that varied below the detection limit at one epoch and are associated with combinations of OH and/or methanol masers are as expected from the distribution of the entire sample.

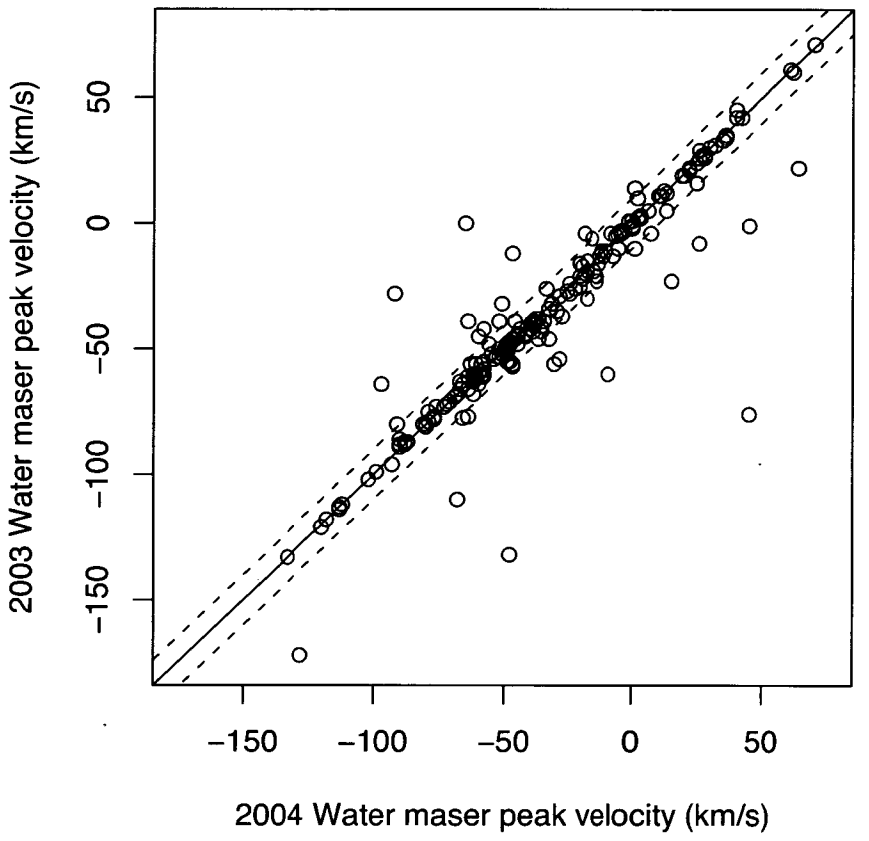

Figure 6.2: *2004 peak water maser velocity versus 2003 peak water maser velocity. Overlaid is a solid line with a slope of 1 and two dashed lines showing a deviation of 10 km s^{-1} either side of the solid line.*

Claussen et al. (1996) suggested that water masers associated with low mass stars were in general both weaker and more variable than those associated with high-mass stars. As we find that the sources only detectable at one epoch are biased towards solitary sources and are in general relatively weak, it is possible that a number of these water masers are in fact associated with lower mass stars perhaps residing in the same stellar clusters as the high-mass star formation regions towards which the observations were targeted (see also end of Section 6.4.6 and Section 6.4.7).

The potential of water masers for mapping the distribution of massive SFRs throughout the Galaxy has been demonstrated for a few sources by astrometry sufficiently precise to achieve parallax measurements and precise distances (e.g. Sato et al. 2008). Water masers appear to provide the largest population to make these investigations, but with several caveats. Firstly, a site must have individual maser spots persisting for more than a year. Despite the extreme variability shown by all spots at some sites, and some spots at most sites, our data reassuringly demonstrate that there still remain an enormous number of suitable sites. A second reservation concerns the ability to associate a systemic velocity with the precise distance, enabling mapping of the Galactic velocity field. As we shall see in Sections 6.4.3 and 6.4.4, the estimate of the systemic velocity for an isolated water maser is uncertain, but an excellent estimate can be obtained from the OH or methanol masers accompanying many water masers. Note that the spatial correspondence between maser species is usually sufficient to yield very high confidence associations, whereas associations with more diffusely distributed thermal emission in molecular clouds are less reliable. So, associated OH or methanol masers are the key to establishing the systemic velocity of a water maser. We note that for sites with OH but no methanol, parallax determinations are beyond present capabilities except through the use of associated water masers. And even for some methanol sites, it may turn out that an associated water maser provides the best parallax measurement. Thus the important role of water masers in these Galactic studies is assured.

6.4.2 Spatial distributions of maser spots

The VLA study of water masers by Forster & Caswell (1989) and Forster & Caswell (1999) examined the distributions of maser spots, both in velocity and spatially, for the masers that were quite strong and/or displayed many spectral features. It was shown that, where many maser spots were present, they lay either within a diameter rarely exceeding 30 mpc, or in a few clusters of this size separated by distances at least several times larger. The quite large beamsize used in the present observations precludes detailed study of the spot distributions, but allows recognition of clusters with several distinct members, of which there are many. We do however, find a substantial number of water maser sources that show distinguishable angular separations between clusters of maser spots emitting near the systemic velocity, and those emitting at high velocities. The separations are generally of the order of 2 or 3 arcsec, and are plausibly attributed to associated outflowing material. Occasionally, separations between systemic and high velocity components exceed 4 arcsec, and even in these cases it seems credible that these are associated outflows.

6.4.3 Detection statistics and relationship to ground-state OH and methanol masers

The position measurements and new detections of water masers reported in Table 6.1 mostly arose from a search at all the positions of southern SFR maser sites with ground-state OH main-line (1665 and 1667 MHz) masers that had not previously been searched. The target list corresponded to table 1 of Caswell (1998), plus a few modifications which we briefly summarise here. Small position corrections were needed for 10.623-0.383 and 11.904-0.141; and an improved (previously unpublished) position has been determined for 326.780-0.241, listed by Caswell (1998) at the approximate position 326.77-0.26. The list was augmented by 291.274–0.709, 308.754+0.549 and 329.339+0.148 (see notes for these sources in Section 6.3.1 and Caswell (2001)). The OH source 311.94+0.14 still has no precise position measurement and, although searched for water, has been omitted from the statistics, as discussed under the note on 311.947+0.142.

Because the observations were targeted toward OH masers detected in a blind search, the detection statistics can be meaningfully computed. The new search has established sensitive upper limits for water masers toward 42 main-line OH maser sources, and a net detection rate for water masers towards OH masers of 79 per cent. Additional observations were made towards a selection of 104 methanol masers with no reported OH counterpart (chiefly from Caswell, 2009).

As noted in Section 6.3, of the 379 detected water maser sources, 128 are associated with both OH and methanol masers, 33 are associated with OH masers only, 70 are associated with methanol masers only and 148 are solitary (i.e. not associated with either OH or methanol maser emission). The water maser detection rate towards sources exhibiting both OH and methanol maser emission is 77 per cent (128 of 166). In contrast, the water maser detection rate towards OH maser sites (with no methanol) is 89 per cent (33 of 37). In order to determine if water masers were preferentially detected towards OH masers without associated methanol masers we carried out a chi-squared test. The resultant p-value of 0.6 means that the higher detection rate of water masers towards OH maser sources without associated methanol is not statistically significant.

Because the sample of methanol masers targeted in 2004 was not homogeneous, it is difficult to draw strong conclusions concerning methanol/water associations from the detection statistics. However, the fact that we find 70 associations of water towards methanol masers without OH (from a total sample of 104), and 33 associations of water towards OH masers with no methanol (from a total sample of 37), along with a detection rate of 77 per cent towards sources exhibiting both OH and methanol masers, indicates that the overlap between the lifetimes of water, OH and methanol masers is large. A possible interpretation is that during the evolution of the star the methanol masers are not only the first maser species to appear but also the first species to turn off whereas the OH and water both persist for longer.

Table 6.5 presents both the average and median flux densities of the water masers that we detect, broken up into categories according to their association with OH and methanol masers as well as 22 GHz radio continuum. Where a source was detected in both 2003 and 2004 we have used the two recorded values of flux density as separate entries. In column 1 the types of association are listed.

Table 6.5: *The average and median water maser flux densities for the water maser sources we detect.*

Water classification	Average flux density (Jy)	Median flux density (Jy)
all sources	57.1	5
with OH	96.1	15
with methanol	68.3	9
with continuum	74.9	18
only OH	138.2	25
only methanol	26.1	3.5
solitary	18.9	2.8

Here 'all sources' incorporates all water maser peak flux densities detected at either epoch; 'with' OH, methanol or continuum refers to water masers that are associated with the afore-mentioned source but not limited to associations with only these sources; 'only' OH or methanol incorporates only those water maser sources exclusively associated with either OH or methanol masers, but places no restrictions on their association with 22 GHz radio continuum; and 'solitary' refers to water sources that are not associated with either OH or methanol masers. We find that there is trend of increasing water maser flux density from solitary sources to sources associated with methanol masers to sources associated with OH masers and 22 GHz radio continuum. This may indicate that the water masers increase in flux density as the sources evolve, similarly to that found in Chapter 4 for 6.7 GHz methanol masers. We note, however, that the average and median flux density of the solitary water masers is likely to be at least partly due to some of these sources being associated with low-mass stars.

The recent completion of the Southern Hemisphere component of the Methanol Multibeam (MMB) survey (Green et al. 2009; Caswell et al. 2010) for 6.7 GHz methanol masers will soon provide an even more extensive catalogue of SFRs than the OH catalogue of Caswell (1998) to search for associated water maser

emission. The MMB survey is the most sensitive survey yet undertaken for young high-mass stars in the Galaxy and is complete within 2 degrees of the Galactic plane. Water maser observations towards this unbiased catalogue of methanol masers will enable meaningful detection statistics for methanol and water maser associations to be derived and allow comparison with our statistics derived from the comparison of OH and water maser associations. Due to this, coupled with the fact that our methanol targeted sample is not homogeneous, we do not attempt to draw further conclusions from this methanol sample. We anticipate that comparisons between the sources detected in the MMB survey and infrared data, in conjunction with follow-up observations for 22 GHz water masers, 12.2 GHz methanol masers and other non-masing molecular species will uncover unique insights into the differing physical conditions responsible for the presence/absence of the different methanol maser transitions.

Beuther et al. (2002) conducted a high resolution study of the water and methanol masers in 29 high-mass star formation regions and found that 10 methanol masers coincide spatially with water masers to within their uncertainty of about 1.5 arcsec. They remarked that no spatial correlations exists between the two maser species, which is clearly not an inference from their results and refers presumably to the common expectation that detailed correlations of maser spots is unlikely.

Our finding is that occurrence of a water maser at nearly 80 per cent of the OH maser targets is comparable to the occurrence of methanol at OH targets. This might seem surprising in view of the difference in favoured pumping schemes, where both OH and methanol depend on far IR radiation, whereas the favoured pumping scheme for water masers is collisional (Elitzur, Hollenbach & McKee 1989). However, it is consistent with the expectation that in most locations where methanol and OH masers occur there are coincident, or nearby, shocked regions with high densities suitable for the excitation of water masers. Pursuing this further, the apparently larger number of water masers than other maser species is consistent with the extremely common occurrence of such shocked regions, not only in the envelope of a high-mass star, but also in outflows and in lower mass stars with less IR flux.

Interestingly, pumping of the formaldehyde masers (which are uncommon, but

also trace SFRs) is unclear, since the Boland & de Jong (1981) radiative pump seems deficient and may need shocks and collisions, according to Hoffman et al. (2003).

6.4.4 Velocity distributions of maser features

The velocity distributions for the water masers have intrinsic interest but are most fruitfully studied in comparison with OH and methanol counterparts where available. The velocity range of water maser emission at many sites is larger than for OH or methanol, with the velocity range of water masers measured in 2003 having an average of 27 km s^{-1} and a median of 15 km s^{-1} and those measured in 2004 showing an average velocity range of 30 km s^{-1} and a median of 15 km s^{-1}. In contrast, methanol masers rarely show emission that exceeds a velocity range of 16 km s^{-1} (Caswell, 2009), and Caswell (1998) found the median velocity range of 100 OH masers with flux densities greater than 2.7 Jy to be 9 km s^{-1}.

Sometimes the water emission is remarkably symmetric about the systemic velocity but, more often, is asymmetric. The strongest water maser emission is generally confined to the velocity ranges of the associated OH and methanol masers. The velocity of methanol maser emission is regarded as a reliable indication of the systemic velocity for the regions that these masers are tracing (e.g. Caswell, 2009; Pandian et al., 2009), allowing kinematic distances for the sources to be computed. OH masers are slightly less reliable tracers of systemic velocities because small changes to the apparent radial velocity are caused by the Zeeman effect. Water masers however, are generally regarded as unreliable tracers of systemic velocities, as they commonly trace high velocity outflows and have large velocity ranges.

We first compare the peak velocities of methanol and OH masers in Fig. 6.3, (using the population of 165 sources studied in this paper, including sources both with and without associated water maser emission). This clearly demonstrates the close similarity in the velocity of their peaks. The average difference between the peak velocities of the OH and methanol masers is 3.4 km s^{-1}, with a median difference of 2.2 km s^{-1}.

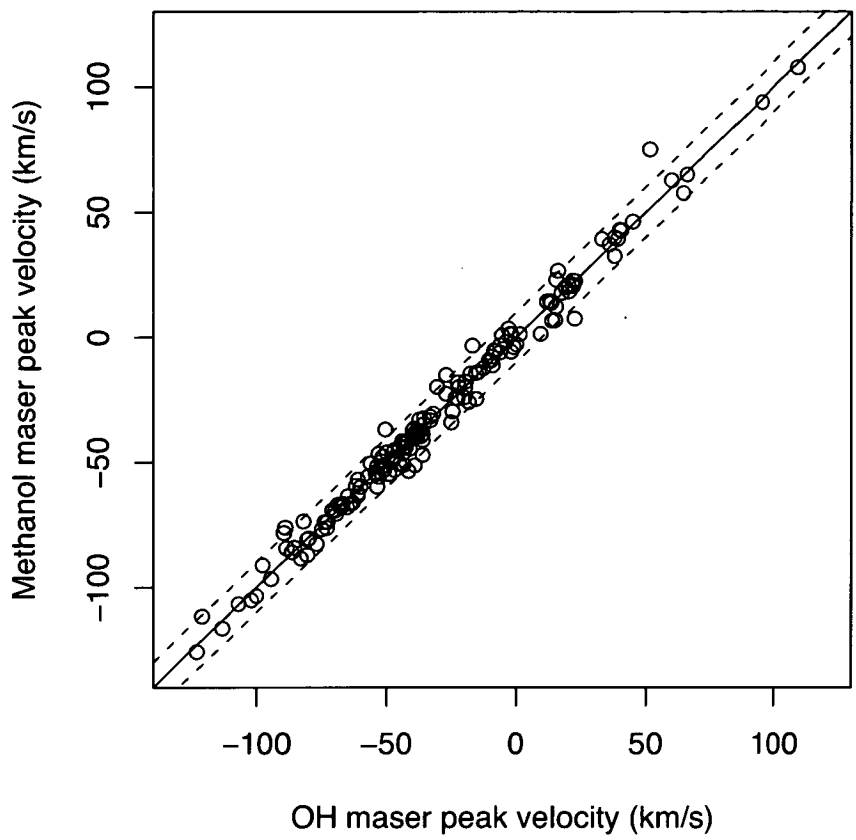

Figure 6.3: *OH maser peak velocity versus methanol maser peak velocity. Overlaid is a solid line with a slope of 1 and two dashed lines showing a deviation of 10 km* s^{-1} *either side of the solid line.*

We now compare the velocity of the peak emission of our large sample of water masers with the peak of associated OH and methanol masers (Figs 6.4 and 6.5, respectively). The 2004 peak velocities were used where possible and 2003 peak velocities were used otherwise. In the case of 160 OH-water maser associations, we find that the average difference in the peak velocities is 7.8 km s^{-1} and the median difference is 4 km s^{-1}. In the case of 197 methanol-water maser associations we find that the average difference in the peak velocities is 8.8 km s^{-1} and the median difference is 4.2 km s^{-1}. Thus for the majority of sources there is quite good correspondence between the velocity of the peaks of water masers and those of the associated OH or methanol maser peak emission, but there are some striking outliers.

Comparison of Fig. 6.3 with Figs 6.4 and 6.5 highlights the closer correspondence between the peak velocities of the OH and methanol masers than either of these species compared to the associated water maser peak velocity. 93 percent of the OH and methanol maser peak velocities are in agreement to within 10 km s^{-1}, whereas for the water-methanol and water-OH peak velocities this number falls to 78 and 79 per cent.

We now look in more detail at the outlying sources in Figs 6.4 and 6.5. The isolated source at the lower right of the plots is 336.983–0.183 and, as remarked in the note of Section 6.3.1, the high-velocity water feature is accompanied by emission at the systemic velocity (methanol and OH peak velocity) which is of comparable intensity (or stronger at the 2003 epoch). Disregarding this source, Fig. 6.4 shows only a small number of dominant high-velocity features (offset more that 30 km s^{-1}) with no preference for red or blue shifts. In Fig. 6.5, we distinguish the sources with only methanol from those with OH as well as methanol. We note that there is a striking group of six highly blue-shifted features of which five have no OH emission. These are some of the distinct population of dominant blue-shifted outflows discussed by Caswell & Phillips (2008).

6.4.5 Clustering of maser sites and association with other masers of OH

In addition to the water maser sources that we find to be intimately associated with the OH and methanol masers that were targeted, we frequently detect water masers separated from the target OH and methanol masers by ~10 arcsec or more. Furthermore, we find the occurrence of multiple water maser sites within the HPBW of the ATCA primary beam to be common, with the number of sources often exceeding two and reaching as high as seven. Fig. 6.6 shows a histogram of the number of water masers in the targeted ATCA fields that are solitary (i.e. in addition to the water masers detected at the targets of OH and methanol). There are 90 cases where there is one or more solitary maser within the HPBW of a target OH or methanol maser. This means that observations targeted towards OH and methanol masers have a 29 per cent chance of detecting at least one unrelated water maser within ~2 arcmin of the target source.

Clusters comprising combinations of water, OH and methanol masers spread over ~20 arsec are common. Comparative studies of sites within these clusters, where we can infer that near-contemporaneous formation of several high-mass stars has occurred, hold promise for unravelling the preferred environments and stellar evolutionary stages for different maser species; future studies of water masers and associated IR sources will play a major role in this investigation.

Six sites of 1720 MHz maser emission, believed to be of the SFR variety but with no other maser species, were listed by Caswell (2004c), and these have also been searched for water masers. A new water maser was detected towards one of them, 310.146+0.760, as well as towards its cluster companion the OH 1665 MHz and methanol maser 310.144+0.760, offset nearly 10 arcsec. The 1720 MHz maser 329.426-0.158 was previously the only maser detected in a putative SFR (with an HII region nearby both spatially and in velocity). Although no water was found at the 1720 MHz site, two new water maser sites were discovered, with offsets of only 20 arcsec, and therefore credibly within this SFR and therefore now increasing its known maser population to a cluster of three masers.

Two sites that currently are known as masers only at the 6035 MHz excited-state of OH were also searched for water. No water detection was made towards

either 311.596-0.398 or 345.487+0.314.

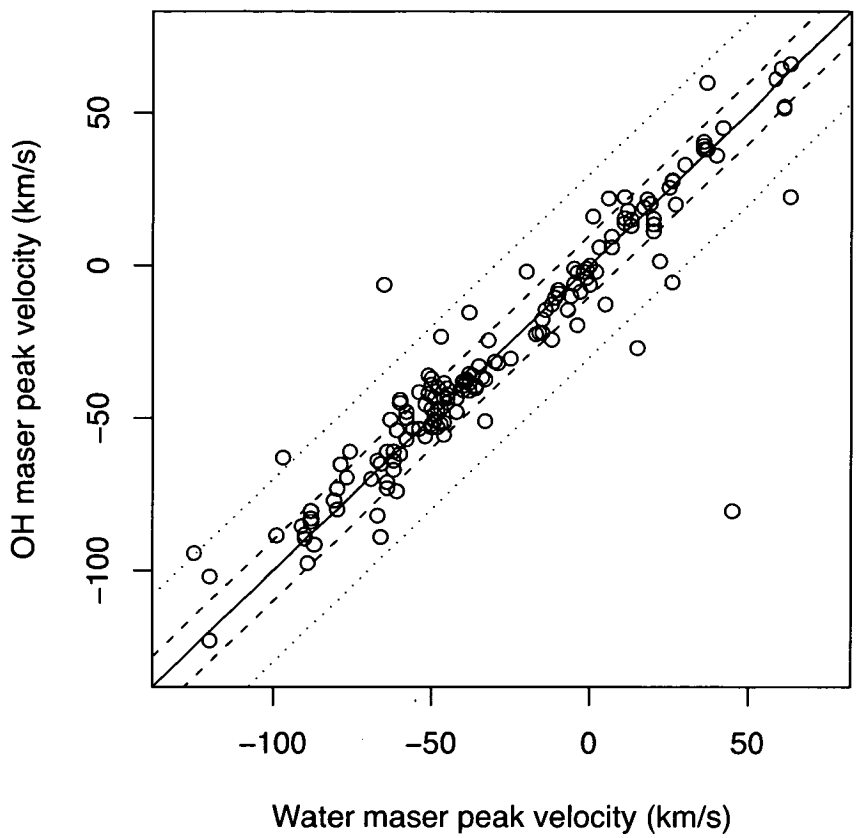

Figure 6.4: *Water maser peak velocity versus OH maser peak velocity. Overlaid is a solid line with a slope of 1 and two dashed lines showing a deviation of 10 km* s^{-1} *either side of the solid line. An additional pair of lines (dotted) shows a deviation of 30 km* s^{-1}.

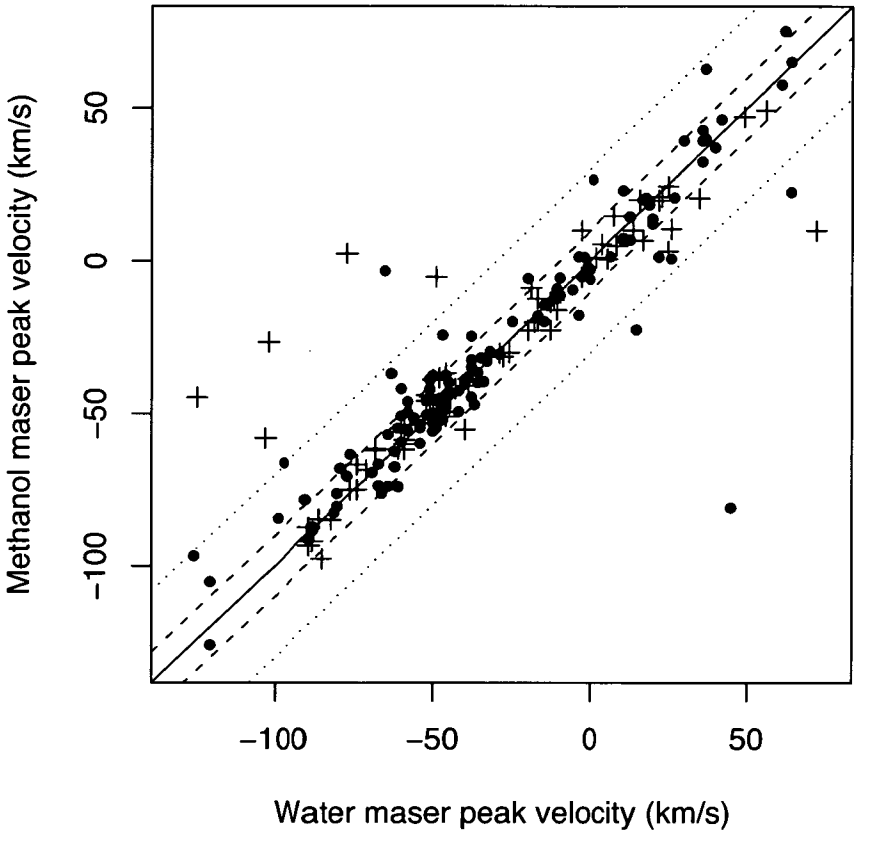

Figure 6.5: *Water maser peak velocity versus methanol maser peak velocity. Overlaid is a solid line with a slope of 1 and two dashed lines showing a deviation of 10 km* s^{-1} *either side of the solid line. An additional pair of lines (dotted) shows a deviation of 30 km* s^{-1} *. We distinguish sources with only methanol (cross) from those with OH as well as methanol (dot).*

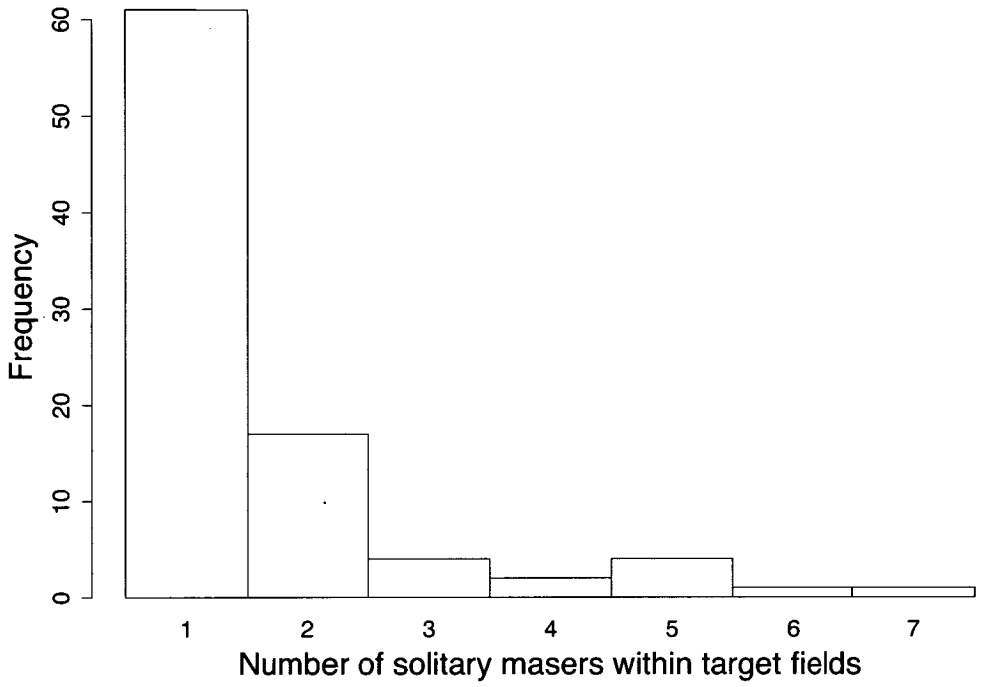

Figure 6.6: *Histogram of the number of solitary water masers detected in single ATCA fields.*

6.4.6 Association with continuum UCHII regions

The present observations, although focused on spectral line emission, also allowed a search at each maser site for an associated UCHII region, to a limit of $\sim$ 30 mJy if the region is not too confused. Although this is two orders of magnitude less sensitive than can be achieved with a targeted wide bandwidth survey (Forster & Caswell 2000), it is at higher frequency, and provides in many cases a useful first estimate.

The sensitivity to radio continuum is not uniform for all sources, and is especially poor for observations with maser emission over an extensive velocity range, leaving little of the bandpass free from line emission. Due to this, and our short integration times we are sensitive only to relatively strong UCHII regions.

We have not used the continuum data collected at the 2003 epoch since the *uv*-coverage (with an EW array) was significantly poorer than achieved with the

Table 6.6: *Comparison between water maser associations and the presence of associated 22 GHz radio continuum. Column 1 describes the water maser associations, column 2 shows the number of water maser sources observed in 2004 that fall under the given association. Column 3 gives the number of sources within each category that are associated with 22 GHz radio continuum and column 4 shows this number as a percentage of the water maser sources in each category.*

Water association	# of sources total (2004)	# of sources with cont	% with cont
OH & methanol	112	24	21.4
OH	28	6	21.4
methanol	67	5	7.5
solitary	143	7	4.8

H168 array in 2004. The 29 water maser sources observed only during the 2003 observations have therefore been removed from the subsequent statistics. Table 6.6 presents the number of water maser sources observed in 2004, broken up into the categories of solitary, associated with an OH maser, associated with both OH and methanol masers, and associated with a methanol maser (numbers shown in column 2). Column 3 shows the number of water maser sources in each category that are also associated with 22 GHz radio continuum from UCHII regions that we detect, while column 4 shows the percentage of sources with detectable 22 GHz radio continuum in each category. We find associations with UCHII regions, indicative of an embedded massive early type star, for 42 of the water maser sources that we detect.

Due to the targeted nature of this search, with the OH sample being complete but the methanol sample incomplete, percentages are presented in Table 6.6 to reveal more clearly the correlations. The percentages of water maser sources with associated UCHII region in Table 6.6 show that UCHII regions are preferentially detected toward water maser sources with associated OH masers.

We find that our overall detection rate for UCHII regions towards water maser

sources with associated OH masers (with or without associated methanol) is 21.4 per cent while our detection rate towards water maser sources without associated OH masers (solitary or with methanol) is 5.0 per cent. Forster & Caswell (2000) conducted a sensitive search at 8.7 GHz for UCHII regions towards OH and water masers which showed that 52 per cent of the OH masers they targeted had an associated UCHII region. While our observations are almost two orders of magnitude less sensitive than was achieved by Forster & Caswell (2000), they are at a higher frequency allowing us to potentially detect emission from hyper-compact (HC) H II regions which are typically optically thick at centimetre wavelengths. Comparison with the detection rate of Forster & Caswell (2000) suggests that a more sensitive search at 8.7 GHz for UCHII regions towards our OH maser associated water maser sources would more than double our detections from 30 sources to ~71.

Our results support arguments (Caswell (2001); Beuther et al. (2002); Chapter 4) that methanol maser emission is often seen prior to any OH maser emission, but is sensitive to the onset of emission from UCHII regions, and less able to survive the later stages of the evolution of the UCHII region. Carrying on these arguments to include water masers we find that the water masers are also present at the early stages of formation, like the methanol masers, prior to the onset of OH maser emission. These statistics for solitary water sites naively suggest that these water masers precede the onset of strong UCHII regions. However, as mentioned in Section 6.4.1, it is possible that a significant population of the solitary water masers are associated with low mass stars and this provides an alternative explanation.

6.4.7 Comparison with GLIMPSE objects

Association with GLIMPSE point sources

We have compared the positions of the 379 water maser sources with the positions of sources in the GLIMPSE point source catalogue. We find that 343 of our water maser sources are within the Galactic longitude and latitude ranges observed by GLIMPSE and that 165 of these are within 3 arcsec of a GLIMPSE point source (48 per cent). This number increases to 211 if sources from the GLIMPSE archive

are included (62 per cent). The fraction of the water maser sources associated with point sources contained in either the GLIMPSE point source catalogue or the supplementary archive catalogue, is similar to that found by Ellingsen (2006) when comparing the positions of 56 methanol masers with GLIMPSE sources (68 percent).

We have further investigated the associations between water maser and GLIMPSE sources by comparing the GLIMPSE source association rates of water masers in their association categories (i.e. associated with both OH and methanol masers, associated with OH masers, associated with methanol masers etc.). Association rates are as follows:

- 76 of the 165 GLIMPSE detections have both OH and methanol (i.e. 46% of the GLIMPSE sources are associated with OH, methanol and water and 60% of the OH methanol and water sources have an associated GLIMPSE source).
- 91 of 165 GLIMPSE detections have OH detections (i.e. 55% of the GLIMPSE sources have an associated OH maser and 57% of OH maser sources have an associated GLIMPSE source).
- 109 of 165 GLIMPSE detections have methanol detections (i.e. 66% of the GLIMPSE sources have an associated methanol maser and 56% of methanol maser sources have an associated GLIMPSE source).
- 18 of 165 GLIMPSE detections have associated radio continuum (i.e. 11% of the GLIMPSE sources have an associated UCHII region and 43% of UCHII regions have an associated GLIMPSE source).
- 41 of 165 GLIMPSE detections only have an associated water maser (i.e. 25% of the GLIMPSE sources are only associated with a water maser and 29% of the water only sources have an associated GLIMPSE source).

The GLIMPSE point source association rates are similar in all categories except for solitary water masers and water masers associated with radio continuum where the association rates are significantly lower. In the case of the radio continuum, it is likely that a large number of sources exhibiting strong radio continuum

would no longer be point sources at mid-infrared frequencies (because sources exhibiting strong radio continuum are likely to be more evolved) and this would therefore account for the lower association rate. The lower association rate between GLIMPSE point sources and solitary water masers could be explained by a tendency for these water sources to be associated with more extended objects, or, alternatively, that the solitary water masers are commonly associated with lower luminosity sources.

Figure 6.7 shows a plot of the [3.6]–[4.5] μm versus [5.8]–[8.0] μm colours of the GLIMPSE point sources associated with the water masers. Flux density measurements for all four of the IRAC bands had to be available for the inclusion in this plot thus limiting the plotted sample to 14 solitary water masers (i.e. with no methanol or OH maser counterpart) and 58 water masers with either a methanol or an OH counterpart. We find, similarly to previous comparisons (e.g. Ellingsen, 2006, Chapter 4), that the GLIMPSE sources associated with the masers are located above the majority of the comparison sources in the colour-colour plot. This figure also reveals an apparent difference in the ranges of the [3.6]–[4.5] μm colours for solitary water masers compared with water masers that are associated with methanol, OH or continuum (or a combination of these).

We have carried out a t-test (testing the hypothesis that there is no difference between the means) on both the [3.6]–[4.5] and [5.8]–[8.0] μm colours of those GLIMPSE sources associated with solitary water masers compared to those associated with water masers as well as OH, methanol or radio continuum. In the case of the [5.8]–[8.0] μm colours we find that there is no statistically significant difference between the values associated with the two groups of water maser sources. For the [3.6]–[4.5] μm colours we find that there is a statistically significant difference (p-value 0.007) between the GLIMPSE sources associated with solitary water masers and those water masers with associated methanol, OH or radio continuum sources.

As can be seen in Fig. 6.7, the [3.6]–[4.5] μm colour tends towards smaller values in the case of the solitary water masers. Since there is no difference in the [5.8]–[8.0] μm colours between the two groups of sources this means the solitary water maser associated GLIMPSE sources have a much less steep spectrum at wavelengths < 5 μm than at wavelengths greater than this. This indicates that

these sources may be colder in general. Another explanation may be that the GLIMPSE sources associated with the solitary water masers have a relative excess of 4.5 μm flux density, similar to extended green objects (EGOs) (Cyganowski et al., 2008).

In Section 6.4.1 we suggested that some fraction of the solitary water masers are likely to be associated with low-mass stars rather than the high-mass star formation regions where these observations were targeted. According to Cyganowski et al. (2008), GLIMPSE is too shallow to detect emission from outflows associated with low-mass stars (except perhaps for the closest low-mass star formation regions). Furthermore, if GLIMPSE detected infrared emission associated with low-mass stars it certainly would not detect it as a point source because the space density would be much too high. We therefore conclude that none of the sources included in Fig. 6.7 are associated with low-mass stars and therefore can not be responsible for the difference. However, it is possible that the lower association rate for solitary water maser sources with GLIMPSE point sources is partially because some fraction of the solitary water maser sources are associated with low-mass stars.

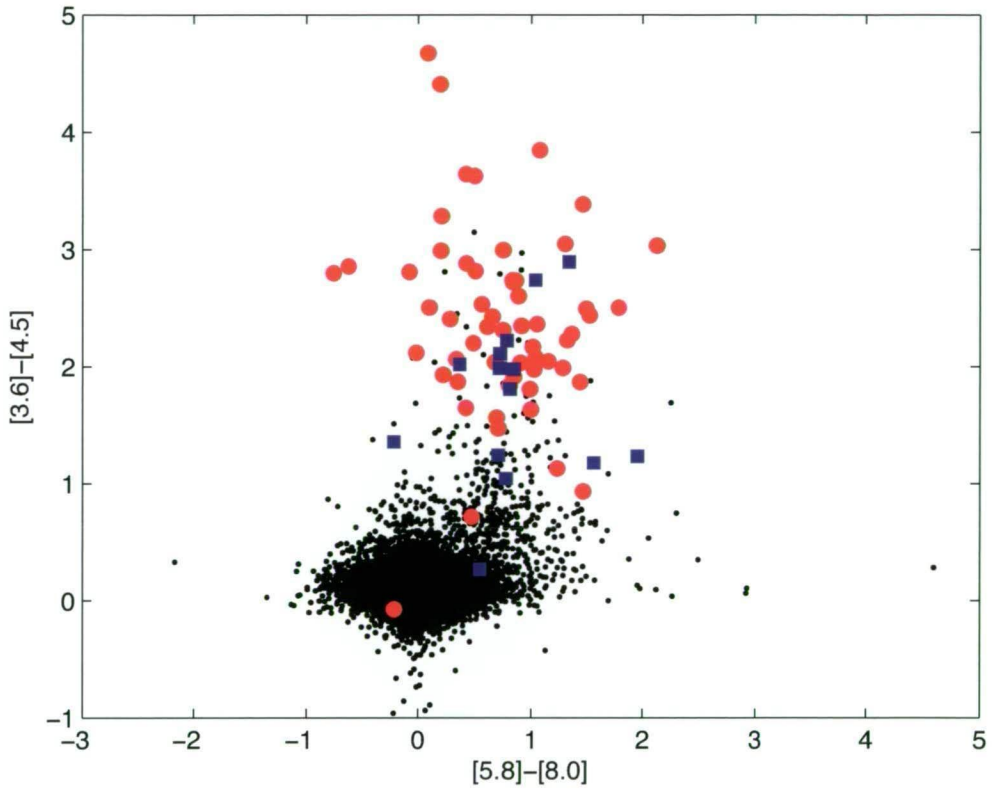

Figure 6.7: *Colour-colour plot of GLIMPSE point source data. Water maser sources with associated OH and/or methanol maser emission are represented by red circles and solitary water maser sources are represented by the blue squares. The black dots represent all of the GLIMPSE point sources within 30 arcmin of* l = *326.5 degrees,* b = *0.0 degrees.*

Table 6.7: *Comparison between water maser associations in our full sample with water maser associations for sources associated with EGOs. Column 1 describes the water maser associations, column 2 shows the percentage of water maser sources in each category (from the full sample) and column 3 gives the percentage of sources in each category that are also associated with an EGO (Cyganowski et al., 2008).*

Water association	% of full sample	% of sources with EGOs
OH & methanol	33.8	55.6
OH	8.7	7.9
methanol	18.5	20.6
solitary	39.0	15.9
Total	100	100

Association with extended green objects (EGOs)

We have compared the locations of the EGOs presented in Cyganowski et al. (2008) with our 379 water masers. In order to avoid large numbers of chance associations between EGOs and water masers, we consider an EGO to be associated with a nearby water maser when the angular separation is less than 10 arcsec. Cyganowski et al. (2008) compared the locations of 6.7GHz methanol masers with the images of their EGOs and show that this separation captures most of the associations while minimizing the chance coincidences that would result from a larger threshold. We find that 63 of the water masers are coincident with an EGO identified by Cyganowski et al. (2008).

Table 6.7 shows in the second column the percentage of the full sample of 379 water masers that fall within the four categories: associated with both OH and methanol masers, associated with only OH masers, associated with only methanol masers, and solitary; and in the third column, the number of water sources in each category that are also associated with EGOs as a percentage of the total number EGO-associated sources. This table shows that those water maser sources coincident with EGOs and associated with only methanol or OH masers

are distributed in similar fashion to our complete sample of water masers, with little difference between the percentage of water sources presented in columns two and three. However, in the case of the solitary water sources, the association rate with EGOs is much lower than would be expected (similar to solitary water masers associated with GLIMPSE point sources). The absence of EGO associations with a large number of the water maser only sources may suggest that solitary water masers are associated with lower luminosity sources. Alternatively, considering that the water maser only sources tend to be associated with GLIMPSE point sources with dominant 4.5 μm emission, a characteristic shared by EGOs, the water maser only sources may represent a class of younger sources, the majority of which have not yet produced an extended outflow. Perhaps this indicates that these solitary water masers are associated with outflow related sources: compact green objects, pre-cursors to EGOs.

We find that there is a higher association rate with EGOs for those water maser sources accompanied by both methanol and OH masers. This indicates that EGOs persist into the stage of star formation that is evolved enough to have produced an OH maser but not so evolved that the production of an associated strong UCHII region has caused the methanol maser emission to cease. Eighty-nine of the water maser sources we detect that are associated with both OH and methanol masers are within the regions covered by GLIMPSE and have been inspected for the presence of EGOs (Cyganowski et al., 2008). We find that 35 of these 89 sources are associated with an EGO, a rate of 39 per cent. This lends further credence to the idea the EGOs are not exclusively tracing the earliest stages of massive star formation but persist well into the stage where OH masers are present. Furthermore, as there is a large number of these objects, they must have a significant lifetime.

6.5 Summary

From a large sample of water masers measured with precise positions at two epochs, we conclude that spectra are highly variable but positions are generally persistent. Of 207 sources that were observed on both epochs, 17 % were only detectable on one occasion.

The occurrence of a water maser at nearly 80 per cent of the OH maser targets is comparable to that of methanol at OH sites. This is despite the difference in favoured pumping schemes, where both OH and methanol depend on far IR radiation, whereas the favoured pumping scheme for water masers is collisional.

Our study of water masers at methanol maser sites is preliminary, but the common presence of water at methanol sites is confirmed. We argue that there is indeed an important role for water masers in mapping the Galaxy and its velocity field. We find that there is generally, a quite good correspondence between the water maser peak velocity and that of associated methanol and OH masers. The present contribution of a large number of water masers with accurate positions in the southern Galaxy has been an important step in advancing such a project, and reveals the value of conducting even larger future surveys with complete Galactic plane coverage.

By comparing the peak flux density of water maser sources broken into their association categories, we find evidence that suggests that the water masers increase in flux density as they evolve. Comparison of the GLIMPSE point sources associated with each of these association categories shows that the GLIMPSE point sources that are associated with the solitary water masers have different properties. We suggest that these sources are either colder, or have a relative excess in 4.5 μm flux (similar to the characteristics of EGOs). Further to this, we find a lower association rate between the solitary water masers and EGOs, suggesting that these sources are too young to have an extended outflow.

The water masers presented in this chapter, when combined with the other large sample of water maser sources presented in Chapter 5, constitute a very large sample of sources with accurately determined positions. These sources will be very useful in future studies of water masers.

7

12.2 GHz methanol masers towards MMB 6.7 GHz detections: sources south of declination −20 degrees

7.1 Introduction

12.2 GHz methanol maser emission is unlikely to exist at locations where 6.7 GHz methanol masers are undetectable, and therefore a complete sample of 12.2 GHz methanol masers can be gained by targeting 6.7 GHz methanol masers detected in a non-biased manner (see Section 2.2 for detailed information on individual maser species). In this chapter, I present the 12.2 GHz follow up observations towards 6.7 GHz methanol masers detected in the methanol multibeam (MMB) survey (see Green et al. (2009) for a description of the survey and also Section 7.2 for a summary), the most extensive search for these sources completed to date. The completion of the Parkes MMB survey presented a unique opportunity to undertake the definitive search for 12.2 GHz methanol masers and comparison between the properties of the two transitions. We have now completed 12.2 GHz observations towards all sources detected in the MMB survey with declinations south of −20 degrees, using the Parkes 64m radio telescope during 2008 June and December. For two sources, additional observations were carried out in 2010 March.

Carrying out follow up observations in a timely manner is important for maser

sources as they are commonly variable, sometimes at extreme levels. In order to combat this, these follow up observations were carried out prior to the publication of the 6.7 GHz MMB detections, as near as possible to the final 'MX' spectra obtained for the 6.7 GHz methanol masers detected in the MMB survey. The majority of the final 6.7 GHz methanol maser spectra were obtained in 2008 March and August and 2009 March. Obtaining near-single-epoch observations of the two methanol maser transitions, particularly given the unbiased nature of the targets, provides an extremely valuable data set of a very large sample of sources, much larger than any previous studies. Furthermore, splitting the follow up observations into multiple epochs allowed for the confirmation of marginal detections from the first epoch, and also allows for an investigation on the level and timescale of variability in the detected sources.

Commonly, comparison of different maser transition requires interferometric observations for the respective transitions. For example, in the case of the water masers presented in Chapter 6 we found that there was a 29 % chance of detecting an unrelated water maser within a 2 arcmin beam when targeting either OH or methanol masers. The use of a single dish for follow up observations at the 22 GHz transition of water is therefore not sufficient due to the enormous scope for chance detections to be wrongly regarded as at the sites of the maser targets. However, in the case of 12.2 and 6.7 GHz methanol masers, previous interferometric observations of the two methanol transitions have shown that analysis of the spectra of the respective transitions can be used as an indicator of whether or not the two transitions are co-spatial. This is fortunate considering that neither the ATCA or VLA operates at the frequency of the 12.2 GHz methanol maser. This allows us to regard interferometric observations as a luxury, rather than a necessity in confidently assessing whether or not the 6.7 and 12.2 GHz sources are co-spatial. Furthermore, as ATCA positions for the 6.7 GHz methanol masers are available, any potential confusion that may be introduced where more than one 6.7 GHz methanol maser falls within the primary beam of Parkes at 12.2 GHz, can easily be identified. Like other species of masers, methanol masers commonly consist of multiple spots that are typically contained within an arcsecond (Caswell et al., 2010). However, unlike water masers, methanol masers infrequently form in clusters of several distinct sites (spread over an arcminute or more), meaning

that regions where there are more than one methanol maser within the primary beam of Parkes are relatively few.

Comparison between the locations of the detected 12.2 GHz sources, with GLIMPSE data and the characteristics of the target 6.7 GHz methanol masers allows for an investigation of the relative evolutionary stage of massive star formation that is traced by 6.7 GHz methanol masers with, and those without, associated 12.2 GHz methanol masers. Additionally, insight into the physical conditions that are responsible for the presence or absence of 12.2 GHz methanol masers can be achieved from such a large sample. The work presented in this chapter builds on some of the results presented in Chapter 4 and, in fact, 12.2 GHz observations towards 55 of the 6.7 GHz maser sources presented in this chapter are also presented in Chapter 4 and in many cases use the same observations. The overlap of sources is relatively small since the sample in this chapter is restricted to a southern sample, whereas the sample presented in Chapter 4 target a number of sources north of declination –20 degrees.

Ideally we would like to be able to use observations of masers to probe the physical conditions in star formation regions on AU-scales. Unfortunately the non-linear behaviour and complexity of the pumping models makes this a very challenging task. Pumping models of methanol masers (e.g. Cragg et al., 2005) predict that the 6.7 and 12.2 GHz transitions are inverted over very similar ranges of parameter space. The absence of 12 GHz masers associated with a large fraction of 6.7 GHz sources implies that the physical conditions are commonly close to the point where the 12 GHz masers switch on/off. We use the large, near simultaneous observations of hundreds of 6.7 and 12.2 GHz methanol masers collected from the MMB survey and this project to make a detailed investigation of the range and distribution of the intensity ratio for these two transitions. Combining this with our evolutionary studies, unique insight into the changes in physical conditions responsible for the presence/absence of the different methanol maser transitions are gained.

7.2 The Methanol Multibeam (MMB) Survey

A purpose built seven beam methanol multibeam receiver has been used to survey the Galaxy for emission from the 6.7 GHz methanol maser transition, pinpointing the locations of newly forming high mass stars. The receiver was jointly constructed by the ATNF and the Jodrell Bank Observatory and was commissioned at Parkes in January 2006. The MMB survey constitutes the most sensitive large scale search for the strong widespread emission exhibited from the 6.7 GHz methanol maser transition. In addition to this, excited OH masers at 6 GHz have been concurrently searched for and, although neither as strong or widespread, a number of detections have been made. Furthermore, follow up interferometric observations have allowed continuum information to be gathered. The results of these observations will be compared with our observations in the future, but are not part of the current investigation.

The complete Methanol Multibeam (MMB) Survey will cover the full Galactic plane, $0° < l < 360°$ and $b = \pm 2°$. Observations of the large portion of the Galactic plane visible to the Parkes radio telescope have now been completed. Detections made in this manner, have to be complemented by follow up observations using an interferometer in order to achieve the needed positional accuracy for the sources, allowing comparison with data from other wavelengths. For the majority of the southern hemisphere detections, these have been carried out with the ATCA but for some more northern sources either MERLIN or the EVLA have been used. Once accurate positions were determined, a 'final' sensitive spectrum for each source was gained through additional Parkes observations in 'MX' mode (each beam of the receiver is cycled through the onsource position, while observations using the beams that are not onsource are combined to form sensitive reference observations). Further details about the MMB survey strategy are presented in Green et al. (2009). A few important characteristics are as follows: the rms noise of the survey observations (at 6.7 GHz) was typically 0.17 Jy; the positional uncertainties gained from the interferometric observations are ~0.4 arcsec; and the rms noise levels of the 'MX' spectra are typically 0.07 Jy and have a spectral resolution of 0.11 km s^{-1}.

The search for 6.7 GHz methanol masers is now producing its first survey

results, with the first paper focusing on the Galactic Centre region (Caswell et al., 2010). Further publications are imminent, with the second paper being accepted for publication in 2010 July (Green et al., 2010).

7.3 Observations and data reduction

7.3.1 12.2 GHz observations and data reduction

The southern hemisphere component of the MMB survey has detected nearly 1000 6.7 GHz methanol masers, the majority of which have now been followed up with the ATCA, MERLIN or VLA in order to determine accurate positions for the sources. 12.2 GHz follow up observations towards 593 6.7 GHz methanol masers detected in the MMB survey were carried out with the Parkes radio telescope during 2008 June and December. The sources searched correspond to all of the MMB detections that lie south of declination −20 degrees. This declination cutoff was imposed for several reasons, foremost of which was that at the time of the observations, the more northern sources detected in the MMB survey had not yet been followed up with the ATCA, MERLIN or the VLA and therefore many had no accurately determined positions. Given the smaller Parkes beam and weaker sources expected at 12.2 GHz, follow up observations towards positions with potential errors sometimes comparable to half of the HPBW (potentially placing the sources at the half power point) were deemed unwise until accurate positions were known. An exception was G 10.35–0.13 where the accurate position was obtained after the observation at 12.2 GHz. Due to this the position extracted from the survey cube was used, which was later found to be offset 24 arcsec from the preferred position.

Observations were carried out in an identical setup to those presented in Chapter 4 and here we only give a brief description. The observations were made with the Ku-band receiver which detected two orthogonal linear polarizations and had typical system temperatures of 205 and 225 Jy for the respective polarizations throughout the observations in 2008 June and slightly higher at 220 and 240 Jy in 2008 December. Flux density calibration is with respect to PKS B1934-638. The Parkes multibeam correlator was configured to record 8192 channels over 16 MHz

for each of the recorded linearly polarized signals. This configuration yielded a usable velocity coverage of $\sim$290 km s^{-1} and a spectral resolution of 0.08 km s^{-1}, after Hanning smoothing. The Parkes radio telescope has rms pointing errors of $\sim$10 arcsec and at 12.2 GHz the telescope has a half power beam width of 1.9 arcmin. For two sources (G 351.611+0.172 and G 10.35–0.13), no usable data was obtained in either the 2008 June or December observations. Instead, the data presented in Table 7.1 and in Fig. 7.1 were taken in 2010 March.

The observation strategy was crafted such that the majority of 6.7 GHz methanol masers had 10 minutes of integration time at 12.2 GHz over the two epochs, yielding rms noise limits of $\sim$0.11 Jy. Sources observed for 5 minutes in 2008 June, achieving no detection, were observed for another 5 minutes in December. However not all sources that were observed for 10 minutes in 2008 June achieving no detection were repeated in December. Likewise, confident detections were not routinely repeated, regardless of their integration times.

Sources were observed with a fixed frequency of 12178 MHz which alleviated the requirement for a unique reference spectrum to be obtained for each of the sources, making efficient use of our allocation of time on the Parkes radio telescope by effectively cutting our required observing time by half. Instead, all spectra collected were combined to form a much more sensitive reference bandpass made up of the median value of each of the channels. Since the target sources were spread over a large Galactic longitude range, sources were detected at different frequencies within the bandpass and this combined with the narrow nature of the sources means that this technique works very well, even in the case where a high number of strong detections are expected. Employing this method also results in lower noise in the quotient spectrum since the reference spectrum does not add significantly to the noise.

Data were reduced using ASAP in an identical manner as for the sources presented in Chapter 4. After reduction, the characteristics of each of the detected lines were extracted and are present in Table 7.1. Marginal detections were considered along with their associated 6.7 GHz spectrum, and were assessed on an individual case basis. Sources that were observed at both epochs were first reduced individually and searched for detections and then the data were averaged and searched once more in order to pick up any stable but weak emission. Only

three sources were identified in this manner (out of 208 sources that were observed at both epochs with no detection at either epoch).

7.3.2 6.7 GHz maser targets

Since, at the time of writing, few of the MMB data for the 6.7 GHz sources within the portion of the Galaxy chosen for this project have been published, the spectra from the final Parkes observations ('MX' observations at the accurately determined positions) for each of these sources were obtained in advance of their publication. Spectra for each of the 6.7 GHz methanol masers detected in the MMB survey (with declinations south of –20 degrees declination) were inspected and peak flux densities, velocity range and peak as well as the integrated flux density were extracted. These values were determined independently of those presented in Caswell et al. (2010); Green et al. (2010), however large discrepancies between values are not expected. For some sources in regions of confusion, ATCA data had to be inspected to to determine which spectral features were associated with which position. Values for some sources had to be extracted from the Parkes survey cubes as the follow up Parkes observation was not available and these are marked in Table 7.1 with a 'c' in column 7.

7.4 Results

Observations conducted with the Parkes radio telescope over two epochs resulted in the detection of 250 12.2 GHz methanol masers towards 580 6.7 GHz methanol masers detected in the MMB survey, a detection rate of 43 %. A number of the 12.2 GHz sources that we detect have been observed previously and references to these observations are shown in Table 7.1. A search of the literature indicates that 148 of the 250 12.2 GHz methanol masers that we detect are new discoveries. The observations targeted a total of 593 sources south of our declination cutoff of –20 degrees but 13 sources have been removed from the detection statistics for the following reasons: G 320.263–0.534 because as of 2010 April the exact nature of this detection at 6.7 GHz was unclear (follow up observations appeared not to show any unique spectral features at this site); G 338.925+0.634

because features could not be separated from nearby source G 338.926+0.634 and so we regard the two sources as one; G 353.410–0.360 because it was not detected in any of the 6.7 GHz follow up observations or in our 12.2 GHz observations; and G 0.645–0.042, G 0.647–0.055, G 0.651–0.049, G 0.657–0.041, G 0.665–0.036, G 0.666–0.029, G 0.667–0.034, G 0.672–0.031, G 0.673–0.029 and G 0.677–0.025 because they are unable to be separated by our single dish observations. An additional source, G 338.925+0.557, has been excluded from all analysis subsequent to the detection statistics because at the time of the 12.2 GHz observations there was no final Parkes observation of the 6.7 GHz emission for this source and the survey cube spectrum could not be accessed.

Table 7.1 presents the characteristics of both the 6.7 GHz and 12.2 GHz sources, including 5-σ detection limits for 12.2 GHz non-detections. Given the luxury of knowing the velocity of the 6.7 GHz maser emission, we have been able to readily and reliably identify sources that are much weaker than the 5-σ detection limits. A number of weak sources can confidently been regarded as genuine at 3- to 4-σ levels. The details presented in Table 7.1 follow the usual practice in column 1 where the Galactic longitude and latitude is used as a source name for each source (references to previous 12.2 GHz observations are noted as superscripts after source names); columns 2 and 3 give the equatorial coordinates for each of the sources and have been derived from interferometric observations of the 6.7 GHz methanol masers detected in the MMB survey; column 4 gives the peak flux density (Jy) of the 6.7 GHz sources, derived from follow up MX observations at the accurate 6.7 GHz position (unless otherwise noted); columns 5 and 6 give the peak velocity and velocity ranges (km s^{-1}) of the 6.7 GHz emission respectively (also derived from Parkes MX observations); column 7 gives the integrated flux density of the 6.7 GHz sources (Jy km s^{-1}); columns 8 to 11 give 12.2 GHz data from the 2008 June epoch, and give the peak flux density (Jy) or 5-σ detection limit, velocity of the 12.2 GHz peak (km s^{-1}), velocity range (km s^{-1}) and integrated flux density (Jy km s^{-1}), respectively; columns 12 to 15 give the 2008 December information and present the information as for the 2008 June data in columns 8 to 11.

Spectra for each of the 12.2 GHz detections are presented in Fig. 7.1. The epoch of the observation, either 2008 June or 2008 December, is annotated in

the top left hand corner of each of the spectra. For one detection no observations were carried out during either 2008 June or December so this source was observed 2010 March in further observations and is accordingly marked. For some weak sources where observations were carried out during both 2008 June and December, the average of the two spectra is presented in Fig. 7.1 and are annotated with a '2008 Jun,Dec' in the top left hand corner of the spectrum. Spectra are presented in order of increasing Galactic longitude unless there is a need for nearby sources to be vertically aligned. The velocity range of the majority of spectra is 30 km s^{-1}, centred on the velocity of the 6.7 GHz methanol maser peak emission. This method was chosen to give an immediate feeling for the basic structure of the two methanol maser transitions, in a number of cases showing that lone features detected at 12.2 GHz are associated with the 6.7 GHz peak emission. A velocity range of 30 km s^{-1} allows the full velocity range of the 6.7 GHz methanol maser emission to be shown in the majority of cases. For some sources, the center velocity of the spectra had to be changed from the 6.7 GHz peak velocity in order to contain the full extent of the 6.7 GHz emission, this was especially common for sources that were complicated by emission from nearby sources and therefore had to be aligned. Sources not centred on the velocity of the 6.7 GHz peak are; G 305.199+0.005, G 305.200+0.019, G 305.202+0.208, G 305.208+0.206, G 335.060–0.427, G 337.613–0.060, G 340.785–0.096, G 350.340+0.141, G 351.417+0.645, G 351.417+0.646, G 351.445+0.660, G 352.083+0.167, G 352.111+0.176, G 0.647–0.055, G 0.657–0.041, G 0.667–0.034, G 2.536+0.198, G 8.683–0.368, G 9.619+0.193, G 10.323–0.160 and G 10.342–0.142.

Table 7.1: *Characteristics of the 6.7 GHz methanol maser targets as well as the 12.2 GHz methanol maser emission that we detect. Column 1 gives the Galactic longitude and latitude of each source and is used as an identifier (references for previously detected 12.2 GHz sources follow the source name and are as follows; 1: Breen et al. (2010a) (Chapter 4); 2: Caswell et al. (1995b); 3: Gaylard, MacLeod & van der Walt (1994); 4: Koo et al. (1988); 5: Catarzi, Moscadelli & Panella (1993); 6: Kemball, Gaylard & Nicolson (1988), 7: Batrla et al. (1987); 8: Caswell et al. (1993); 9: Norris et al. (1987); 10: MacLeod, Gaylard & Kemball (1993); and are presented as superscripts after the source name (and are followed by a '*' if we fail to detect any emission)); columns 2 and 3 give the equatorial coordinates for each of the sources and have been derived from interferometric observations of the 6.7 GHz methanol masers detected in the MMB survey; column 4 gives the peak flux density (Jy) of the 6.7 GHz sources, derived from follow up MX observations at the accurate 6.7 GHz position (unless otherwise noted); columns 5 and 6 give the peak velocity and velocity ranges (km s^{-1}) of the 6.7 GHz emission respectively (also derived from Parkes MX observations); column 7 gives the integrated flux density of the 6.7 GHz sources (Jy km s^{-1}); columns 8 to 11 give 12.2 GHz data from the 2008 June epoch, and give the peak flux density (Jy) or 5-σ detection limit, velocity of the 12.2 GHz peak (km s^{-1}), velocity range (km s^{-1}) and integrated flux density (Jy km s^{-1}), respectively; columns 12 to 15 give the 2008 December information and present the information as for the 2008 June data in columns 8 to 11. The presence of a 't' in any of the columns indicates that the characteristics associated with a source are discussed in Section 7.5. A 'c' in column 7 (6.7 GHz integrated flux density) indicates that the 6.7 GHz source statistics were derived from the MMB data cube, rather than follow up MX observations which means that while the flux density and velocity ranges are a good estimate they are not as reliable as that of other sources and secondly that no integrated flux density could be computed. The presence of a '–' in any of the columns showing source flux density indicates that no observation was made at the given epoch. The presence of 'conf' in the columns showing the integrated flux density indicates that a value for this characteristic could not be extracted do to confusion from nearby sources. For five sources, a second line is used to present observations completed during 2010 March or to list characteristics of sources identified in the average spectrum of the two 2008 observations.*

Methanol maser	RA	Dec					2008 June				2008 December			
(l, b) (degrees)	(J2000) (h m s)	(J2000) ($^\circ$ ′ ″)	$S_{6.7}$ (Jy)	$Vp_{6.7}$	$Vr_{6.7}$	$I_{6.7}$ (Jy)	$S_{12.2}$	$Vp_{12.2}$	$Vr_{12.2}$	$I_{12.2}$	$S_{12.2}$	$Vp_{12.2}$	$Vr_{12.2}$	$I_{12.2}$
G 254.880+0.451	08 22 25.25	−36 15 00.1	1.6	30.2	30,30.5	0.5	<0.75		−210,130		<1.35		−205,135	
G 259.939−0.041	08 35 31.07	−40 38 23.9	1.4	−1	−1.2,−0.9	0.3	<0.50		−210,130		–			
G 263.250+0.514	08 48 47.84	−42 54 28.3	67.3	12.3	11.7,16.9	60.2	0.4	12.4	12.3,12.5	0.1	0.7	12.5	12.2,12.5	0.2

Table 7.1: – continued

Methanol maser	RA	Dec					2008 June				2008 December			
(l, b) (degrees)	(J2000) (h m s)	(J2000) (^{o} ′ ″)	$S_{6.7}$ (Jy)	$Vp_{6.7}$	$Vr_{6.7}$	$I_{6.7}$ (Jy)	$S_{12.2}$	$Vp_{12.2}$	$Vr_{12.2}$	$I_{12.2}$	$S_{12.2}$	$Vp_{12.2}$	$Vr_{12.2}$	$I_{12.2}$
G 264.140+2.018	08 58 11.66	−42 37 30.6	7.6	8.3	7.9,8.7	2.2	–				<0.60		−205,135	
G 264.289+1.469	08 56 26.80	−43 05 42.1	0.5	8.7	8.5,8.8	0.2	0.3	8.7	8.6,8.8	0	<0.80		−205,135	
G 269.153−1.128	09 03 33.46	−48 28 02.6	4.1	16	8.8,16.3	1.9	<0.75		−210,130		–			
G 269.456−1.467[1]	09 03 14.78	−48 55 11.2	5.2	56.1	53.7,56.5	2.2	1.4	56	55.8,56.4	0.4	–			
G 269.658−1.270	09 04 57.72	−48 56 18.4	5.4	16.3	14.2,16.8	3.1	<0.50		−210,130		<0.75		−205,135	
G 270.255+0.835	09 16 41.51	−47 56 12.1	0.4	4	3,5.2	0.3	<0.75		−210,130		–			
G 281.710−1.104	10 05 05.63	−56 57 24.7	0.3	1.2	1,1.2	0.1	<0.55		−210,130		<0.55		−205,135	
G 284.352−0.419[2*]	10 24 10.89	−57 52 38.8	2.5	4	2.7,4.5	1.1	<0.75		−210,130		<0.55		−205,135	
G 284.694−0.361	10 26 36.29	−58 00 34.3	3.3	13.4	12.1,13.7	1.8	<0.55		−210,130		<0.75		−205,135	
G 285.337−0.002	10 32 09.62	−58 02 04.6	11.8	0.8	−8.2,2.5	10.6	1.4	0.6	0.4,1.1	0.5	–			
G 286.383−1.834	10 31 55.12	−60 08 38.6	15.5	9.6	8.3,10.1	7.7	4.3	9.6	9.2,9.9	1.7	–			
G 287.371+0.644[1,3]	10 48 04.44	−58 27 01.0	104.2	−1.8	−2.7,−0.3	69.2	49.1	−2	−2.6,−0.9	20.2	52.2	−2.0	−2.6,−0.9	21.5
G 290.374+1.661	11 12 18.10	−58 46 21.5	2.1	−24.1	−26.4,−23	1.1	<0.80		−205,135		<0.55		−200,140	
G 290.411−2.915[1]	10 57 33.89	−62 59 03.5	4.6	−16	−16.9,−14.6	2.2	1.6	−16.1	−16.6,−15.9	0.4	–			
G 291.274−0.709[1,2,8,9]	11 11 53.35	−61 18 23.7	65.3	−30.5	−31,−28	89.4	3	−29.1	−30.1,−28.7	2.3	–			
G 291.270−0.719	11 11 49.44	−61 18 51.9	7.4	−31.1	−34.4,−25.8	2.5	<0.75		−205,135		<0.90		−200,140	
G 291.579−0.431	11 15 05.76	−61 09 40.8	1	15.3	11.7,19.3	1.2	<0.60		−200,140		<0.55		−200,140	
G 291.582−0.435	11 15 06.61	−61 09 58.3	2.9	10.4	9.3,10.7	1.7	<0.55		−200,140		–			
G 291.642−0.546	11 15 14.32	−61 17 26.7	0.2	12.1	12.1,12.2	0.02	<0.60		−180,160		<0.85		−200,140	
G 291.879−0.810	11 16 17.35	−61 37 20.7	1.2	33.6	30.5,34	0.7	<0.55		−180,160		<0.75		−200,140	
G 292.074−1.131	11 16 51.24	−61 59 32.6	0.8	−19	−19.1,−18.9	0.2	<0.55		−180,160		<0.75		−200,140	
G 292.468+0.168	11 23 42.17	−60 54 33.5	4.3	10.4	8.3,11.5	4.5	<0.50		−180,160		<0.75		−200,140	
G 293.723−1.742	11 28 32.97	−63 07 18.6	0.6	24.4	23.2,25.5	0.2	0.6	24.3	24.1,24.4	0.1	<0.80		−200,140	
G 293.827−0.746	11 32 05.56	−62 12 25.3	2.5	36.9	35,39.2	2.9	<0.55		−200,140		–			
G 293.942−0.874[1]	11 32 42.09	−62 21 47.5	4.3	41.1	37.4,41.3	1.3	2.2	41	40.7,41.3	0.6	–			
G 294.337−1.706	11 33 49.91	−63 16 32.5	0.1	−10.6	−11.9,−9.1	0.1	<0.50		−180,160		<0.75		−200,140	
G 294.511−1.621	11 35 32.25	−63 14 43.2	7.1	−11.9	−13.3,−5.4	15.1	<0.55		−200,140		–			
G 294.977−1.734	11 39 13.94	−63 29 04.6	1.99	−5.28	−6.69,−4.76	c	<0.50		−180,160		<0.75		−200,140	
G 294.990−1.719	11 39 22.88	−63 28 26.4	10.7	−12.2	−12.6,−11.8	4.3	<0.55		−200,140		–			
G 296.893−1.305	11 56 50.07	−63 32 05.5	1.2	22.2	21,22.9	1.4	<0.55		−180,160		–			
G 297.406−0.622	12 02 30.42	−62 58 03.8	1.4	27.8	27.6,28.1	0.5	<0.55		−180,160		<0.75		−200,140	
G 298.177−0.795	12 08 57.56	−63 16 25.8	2.6	23.5	22.9,27.8	3.3	<0.55		−175,165		<0.75		−200,140	
G 298.213−0.343	12 09 55.18	−62 50 01.1	2.4	33.4	32.7,38	2.3	<0.55		−175,165		<0.80		−200,140	
G 298.262+0.739	12 11 47.65	−61 46 20.9	14.6	−30.1	−30.9,−29.1	9.3	<0.55		−200,140		–			
G 298.632−0.362	12 13 31.63	−62 55 01.0	1.3	37.3	37,45.2	1	0.3	37.3	36.9,37.3	0.1	<0.85		−200,140	
G 298.723−0.086	12 14 39.50	−62 39 25.9	1.1	23.5	13.8,24.6	0.5	<0.50		−175,165		<0.75		−200,140	
G 299.013+0.128	12 17 24.60	−62 29 03.7	8.2	18.4	18.1,19.1	3.3	<0.55		−200,140		<0.75		−200,140	
G 299.772−0.005	12 23 48.97	−62 42 25.3	15.6	−6.8	−9.6,−0.2	12.7	0.4	−7	−7.3,−7	0.1	<0.55		−200,140	
G 300.504−0.176	12 30 03.58	−62 56 48.7	4.1	7.4	2.9,10.1	4.4	<0.55		−200,140		–			
G 300.969+1.148[2]	12 34 53.29	−61 39 40.0	4.7	−37.1	−39.4,−35.4	5.5	0.5	−36.8	−37,−36.8	0.1	–			
G 301.136−0.226	12 35 35.14	−63 02 32.6	1.7	−39.7	−40.2,−37.8	1.5	<0.55		−175,165		–			

Table 7.1: – continued

Methanol maser	RA	Dec					2008 June				2008 December			
(l, b) (degrees)	(J2000) (h m s)	(J2000) (° ′ ″)	$S_{6.7}$ (Jy)	$Vp_{6.7}$	$Vr_{6.7}$	$I_{6.7}$ (Jy)	$S_{12.2}$	$Vp_{12.2}$	$Vr_{12.2}$	$I_{12.2}$	$S_{12.2}$	$Vp_{12.2}$	$Vr_{12.2}$	$I_{12.2}$
G 302.032–0.061	12 43 31.92	−62 55 06.7	10.7	−35.5	−42.6,−33.8	14	<0.55		−200,140		–			
G 302.034+0.625	12 43 43.44	−62 13 58.5	1.3	−39.1	−46.9,−38.9	1.3	–				<0.55		−200,140	
G 302.455–0.741	12 47 08.65	−63 36 30.2	1.2	32.6	32.4,38	1.1	–				<0.55		−200,140	
G 303.507–0.721	12 56 36.66	−63 35 14.5	2.1	14.2	10.7,17.7	1.2	–				<0.55		−200,140	
G 303.846–0.363	12 59 33.37	−63 13 14.7	7.4	24.8	22.5,32.9	8.6	2	24.8	24.6,26.9	0.6	–			
G 303.869+0.194	12 59 35.84	−62 39 47.6	0.9	−36.9	−37.1,−36.2	0.6	<0.50		−175,165		<0.75		−200,140	
G 304.367–0.336	13 04 09.82	−63 10 20.2	0.9	32.7	31.9,40.5	0.5	<0.75		−175,165		<0.75		−200,140	
G 304.887+0.635	13 08 11.95	−62 10 21.9	1	−35.1	−35.7,−34.9	0.3	<0.80		−175,165		<0.75		−200,140	
G 305.200+0.019[1,2]	13 11 16.93	−62 45 55.1	44.9	−33.1	−37.6,−30.3	45	10.5	−31.9	−33.2,−31.6	8.8	–			
G 305.199+0.005[1]	13 11 17.20	−62 46 46.0	6	−42.7	−44.3,−38	7.8	0.6	−42.7	−42.8,−42.6	0.1	–			
G 305.202+0.208[1,2,8,9,10]	13 11 10.49	−62 34 38.8	90.5	−44	−46.1,−43	40.7	3.5	−43.9	−45,−43.6	1.8	1	−43.9	−45.2,−43.7	0.6
G 305.208+0.206[1,2,8,9,10]	13 11 13.71	−62 34 41.4	457.4	−38.3	−43,−33.4	374.9	1.8	−36.5	−40.4,−35.9	1.7	2	−36.5	−40.4,−35.9	1.9
G 305.248+0.245	13 11 32.47	−62 32 09.1	7.1	−32.2	−35.2,−28.2	7.3	<0.55		−200,140		–			
G 305.362+0.150	13 12 35.86	−62 37 17.9	5	−36.4	−37.2,−34.8	3.5	<0.55		−200,140		–			
G 305.366+0.184[1,2]	13 12 36.74	−62 35 14.7	3.2	−33.8	−47.2,−30	3	3.3	−34.3	−34.8,−33.6	1.6	–			
G 305.475–0.096	13 13 45.75	−62 51 28.3	2.9	−35.4	−53.9,−27	5.6	<0.80		−175,165		<0.80		−200,140	
G 305.563+0.013[1]	13 14 26.90	−62 44 29.4	4.9	−37.3	−41.4,−32.3	6.7	1.5	−37.2	−37.4,−32.5	1.3	–			
G 305.573–0.342	13 14 49.12	−63 05 38.4	1	−51	−54.6,−50.5	0.7	–				<0.55		−200,140	
G 305.615–0.344	13 15 11.31	−63 05 29.8	3.6	−34.9	−35.5,−26.6	7.2	<0.75		−175,165		<0.55		−200,140	
G 305.634+1.645	13 13 49.43	−61 06 32.4	7.2	−54.8	−57.5,−54.4	4.8	<0.75		−175,165		<0.75		−200,140	
G 305.646+1.589	13 13 58.05	−61 09 51.7	3.9	−58.1	−59.6,−54.7	4	<0.75		−175,165		<0.75		−200,140	
G 305.799–0.245	13 16 43.23	−62 58 32.9	0.5	−36.4	−39.8,−27.1	0.5	<0.55		−200,140		–			
G 305.822–0.115	13 16 48.71	−62 50 38.1	2.7	−42.1	−46.5,−38.6	1.9	<0.75		−175,165		<0.75		−200,140	
G 305.887+0.017	13 17 15.53	−62 42 23.0	9.5	−34.1	−34.7,−29.5	4.5	<0.80		−175,165		<0.75		−200,140	
G 305.940–0.164	13 17 53.05	−62 52 50.5	0.8	−51	−51.1,−50.8	0.3	0.7	−51	−51.1,−50.9	0.1	<0.75		−200,140	
G 306.322–0.334	13 21 23.01	−63 00 29.5	0.6	−24.6	−24.6,−22.4	0.4	<0.50		−200,140		–			
G 307.133–0.477	13 28 38.29	−63 02 40.4	2.4	−38.7	−39.7,−33.7	3.5	<0.75		−175,165		<0.75		−200,140	
G 308.056–0.396	13 36 32.16	−62 49 05.6	1.5	−11.8	−12,−7.3	0.6	<0.75		−175,165		<0.75		−200,140	
G 308.651–0.507	13 41 50.19	−62 49 05.2	5.7	3.1	1.6,3.4	4.4	1	3	2.7,3.2	0.4	–			
G 308.686+0.530	13 40 25.33	−61 47 37.6	1.8	−52.9	−57.7,−44.1	1.4	<0.75		−175,165		<0.75		−200,140	
G 308.715–0.216	13 41 53.59	−62 31 11.7	1	−12.6	−16.6,−9.7	1.5	<0.55		−175,165		<0.75		−200,140	
G 308.754+0.549	13 40 57.60	−61 45 43.4	11.9	−45.3	−51.4,−38.5	18.9	0.5	−51.2	−51.2,−43.4	0.1	<0.80		−200,140	
G 308.918+0.123[2,8,9]	13 43 01.85	−62 08 52.2	41.7	−54.7	−55.7,−52.4	43.9	–				8.2	−53.3	−54.7,−53	4.6
G 309.384–0.135	13 47 23.98	−62 18 12.0	1.4	−49.7	−50.3,−49.5	0.6	<0.50		−175,165		<0.75		−200,140	
G 309.901+0.231	13 51 01.05	−61 49 56.0	21	−54.6	−56.6,−52	16.6	–				5.6	−54.6	−55.6,−53.9	2.1
G 309.921+0.479[1,2,8,9]	13 50 41.78	−61 35 10.2	884.7	−59.7	−64.1,−53.8	1038.1	178.9	−59.8	−61.3,−57.7	108.3	–			
G 310.144+0.760[3]	13 51 58.43	−61 15 41.3	78.2	−55.8	−58.8,−53.9	99.2	49.9	−55.7	−57.8,−54.6	47.3	–			
G 310.180–0.122	13 54 01.78	−62 06 34.6	1.1	3.2	3,3.9	0.7	<0.50		−170,170		<0.75		−200,140	
G 311.230–0.032	14 02 27.47	−61 45 14.4	2.3	24.8	22.8,26.6	1.9	<0.75		−170,170		<0.75		−200,140	
G 311.551–0.055	14 05 07.06	−61 41 15.9	1	−56.2	−57.8,−56.1	0.4	<0.80		−170,170		<0.75		−200,140	
G 311.628+0.266	14 04 59.20	−61 21 29.4	4.3	−57.6	−61.3,−55.2	5	0.6	−57.5	−57.6,−57.4	0.2	0.9	−57.5	−57.9,−57.3	0.2
G 311.643–0.380	14 06 38.77	−61 58 23.1	10.3	32.6	31.5,36.1	8.8	<0.80		−170,170		<0.75		−200,140	

Table 7.1: – continued

Methanol maser (l, b) (degrees)	RA (J2000) (h m s)	Dec (J2000) (° ′ ″)	$S_{6.7}$ (Jy)	$Vp_{6.7}$	$Vr_{6.7}$	$I_{6.7}$ (Jy)	2008 June $S_{12.2}$	2008 June $Vp_{12.2}$	2008 June $Vr_{12.2}$	2008 June $I_{12.2}$	2008 December $S_{12.2}$	2008 December $Vp_{12.2}$	2008 December $Vr_{12.2}$	2008 December $I_{12.2}$
G 311.729–0.735	14 08 13.97	–62 17 16.5	0.5	31.1	25.7,31.2	0.3	<0.75		–170,170		<0.75		–200,140	
G 311.947+0.142	14 07 49.72	–61 23 08.3	0.3	–43.9	–47.2,–43.7	0.1	<0.75		–170,170		<0.75		–200,140	
G 312.071+0.082	14 08 58.20	–61 24 23.8	67.9	–34.8	–35.3,–29.9	75.8	12	–34.8	–35.2,–32.4	10.1	–			
G 312.108+0.262	14 08 49.31	–61 13 25.1	19.7	–49.9	–54.1,–48.4	16.2	<0.75		–170,170		<0.75		–200,140	
G 312.307+0.661	14 09 24.95	–60 47 00.5	4.1	–12.3	–12.7,–11.9	1.5	<0.75		–170,170		<0.75		–200,140	
G 312.501–0.084	14 12 48.95	–61 26 03.2	1.2	21.8	21.5,24.7	0.5	<0.75		–170,170		<0.75		–200,140	
G 312.598+0.045	14 13 15.03	–61 16 53.6	23.1	–67.8	–68.2,–64.1	8.3	<0.75		–170,170		<0.75		–200,140	
G 312.597+0.045	14 13 14.35	–61 16 57.7	0.9	–59.6	–59.9,–59.3	0.4	<0.75		–170,170		<0.75		–200,140	
G 312.702–0.087	14 14 25.12	–61 22 29.0	0.8	–59.3	–59.3,–55.5	0.9	<0.80		–170,170		<0.75		–200,140	
G 312.698+0.126	14 13 49.85	–61 10 24.1	1.6	29.5	28.1,35.4	1.1	<0.75		–170,170		<0.75		–200,140	
G 313.469+0.190[2]	14 19 40.94	–60 51 47.3	29.9	–9.3	–15.5,–5.1	36.1	–				4.9	–9.3	–12.4,–8	4.3
G 313.577+0.325[3]	14 20 08.58	–60 42 00.8	100.5	–47.8	–53.3,–46	56.4	<0.75		–170,170		0.7	–47.8	–47.9,–47.6	0.2
G 313.705–0.190	14 22 34.74	–61 08 26.8	1.7	–41.4	–46.8,–41.3	0.8	<0.80		–170,170		<0.75		–200,140	
G 313.767–0.863	14 25 01.73	–61 44 58.1	13.6	–44.8	–45.3,–40.5	26.9	<0.80		–170,170		<0.75		–200,140	
G 313.774–0.863	14 25 04.80	–61 44 50.3	13	–56.4	–57.3,–52.6	13.8	<0.75		–170,170		<0.75		–200,140	
G 313.994–0.084	14 24 30.78	–60 56 28.3	15	–4.9	–9.2,–2.5	14.5	1.6	–4.8	–8.1,–4.4	1	–			
G 314.221+0.273	14 25 12.89	–60 31 38.4	2.8	–61.6	–61.8,–60.6	1	<0.70		–170,170		<0.75		–200,140	
G 314.320+0.112	14 26 26.20	–60 38 31.3	36.9	–43.4	–58.5,–42.7	28.4	<0.75		–170,170		<0.75		–200,140	
G 315.803–0.575	14 39 46.46	–60 42 39.6	8.9	8.2	7.9,8.5	3	<0.70		–170,170		<0.75		–200,140	
G 316.359–0.362[2,3]	14 43 11.20	–60 17 13.3	98.4	3.4	1.1,8.4	77.2	–				9.9	3.3	1.3,7.3	6.8
G 316.381–0.379[2]	14 43 24.21	–60 17 37.4	18.1	–0.7	–5.9,1	34	1.7	–0.6	–4.8,0.7	2.2	–			
G 316.412–0.308	14 43 23.34	–60 13 00.9	11	–5.7	–6.4,–1.9	10	<0.75		–170,170		<0.80		–200,140	
G 316.484–0.310	14 43 55.37	–60 11 18.8	0.7	–11.5	–15.6,–11.5	0.3	<0.75		–170,170		<0.75		–200,140	
G 316.640–0.087[2,3,8,9]	14 44 18.45	–59 55 11.5	96.3	–20.4	–25.1,–15.7	177.6	–				19.2	–20	–22.6,–16.5	34.8
G 316.811–0.057[2]	14 45 26.43	–59 49 16.3	50.7	–45.7	–48.5,–37.2	54.1	–				18.1	–46.5	–47.5,–45.8	13.4
G 317.029+0.361	14 45 35.54	–59 20 58.6	0.9	–47.9	–51.1,–46.6	0.5	<0.75		–170,170		<0.75		–200,140	
G 317.061+0.256	14 46 10.31	–59 25 50.5	0.7	–43.8	–44,–43.5	0.2	<0.70		–170,170		<0.75		–200,140	
G 317.466–0.402	14 51 19.69	–59 50 50.7	50.9	–37.7	–50.9,–35.2	92.5	–				5.6	–37.6	–41.5,–35.6	8.5
G 317.701+0.110	14 51 11.69	–59 17 02.1	23.1	–42.2	–47.2,–40	25.8	<0.70		–170,170		<0.75		–200,140	
G 318.050+0.087[2,3]	14 53 42.67	–59 08 52.4	11.4	–51.7	–56.5,–46.1	5.5	–				2.3	–51.7	–52,–51.4	0.8
G 318.044–1.404	14 59 08.61	–60 28 25.5	6.1	46.3	44.6,46.6	3	<0.75		–170,170		<0.75		–200,140	
G 318.472–0.214	14 57 42.86	–59 13 15.9	1.1	–19.1	–20.3,–18.6	0.8	<0.75		–170,170		<0.75		–200,140	
G 318.948–0.196[1,2,6,8]	15 00 55.40	–58 58 52.1	569.2	–34.6	–38.9,–30.8	525.7	139.4	–34.5	–35.6,–32.1	91	–			
G 319.163–0.421	15 03 13.74	–59 04 30.5	7	–21.1	–22.5,–12.5	7.1	–				6.9	–22.1	–22.5,–20.9	4.7
G 319.836–0.197	15 06 54.65	–58 33 00.0	0.2	–9.3	–13.3,–9.1	0.1	<0.75		–190,150		<0.75		–200,140	
G 320.123–0.504	15 10 00.17	–58 40 18.0	3.6	–10.1	–11.3,–9.4	2.8	<0.75		–190,150		<0.75		–200,140	
G 320.231–0.284	15 09 51.94	–58 25 38.5	53.7	–62.3	–71,–57.9	67.1	0.5	–66.4	–66.5,–66.3	0.1	0.3	–63.2	–63.4,–63.2	0.1
G 320.244–0.562	15 11 01.61	–58 39 37.7	1.5	–49.6	–50,–49	1.2	0.6	–49.8	–49.9,–49.1	0.2	<0.55		–200,140	
G 320.263–0.534	15 11 03.03	–58 37 37.5	0.8	–49.6	–50,–49	0.5	<0.75		–190,150		<0.75		–200,140	
G 320.285–0.308	15 10 19.00	–58 25 16.7	0.8	–69	–69,–61.9	0.5	<0.75		–190,150		<0.75		–200,140	
G 320.427+0.103	15 09 39.90	–57 59 41.6	2.6	–13.5	–13.6,–13	1.2	<0.75		–190,150		<0.75		–200,140	

Table 7.1: – continued

Methanol maser	RA	Dec					2008 June				2008 December			
(l, b) (degrees)	(J2000) (h m s)	(J2000) (^{o} ′ ″)	$S_{6.7}$ (Jy)	$Vp_{6.7}$	$Vr_{6.7}$	$I_{6.7}$ (Jy)	$S_{12.2}$	$Vp_{12.2}$	$Vr_{12.2}$	$I_{12.2}$	$S_{12.2}$	$Vp_{12.2}$	$Vr_{12.2}$	$I_{12.2}$
G 320.424+0.089	15 09 41.56	−58 00 29.2	1.9	−8	−9.3,−4.4	2.4	<0.70		−190,150		<0.75		−200,140	
G 320.625+0.098	15 10 58.12	−57 53 53.4	0.5	−7.6	−8.1,−7.1	0.3	<0.75		−190,150		<0.80		−200,140	
G 320.780+0.248	15 11 23.48	−57 41 25.1	34.9	−5.1	−10.3,−3.5	48.7	–				12.1	−5.2	−6.1,−4.2	13
G 321.033−0.483	15 15 52.63	−58 11 07.7	82.2	−61.2	−69,−54	conf	<0.80		−190,150		<0.80		−200,140	
G 321.030−0.485[3]	15 15 51.79	−58 11 18.0	19.9	−66.5	−68,−56	conf	16.1	−66.6	−67.2,−65.4	9	–			
G 321.148−0.529[2]	15 16 48.39	−58 09 50.2	9.1	−66.1	−67.4,−61.1	4.6	1.4	−66.1	−66.3,−65.8	0.4	–			
G 321.704+1.168	15 13 44.72	−56 25 34.4	2.09	−44.27	−46.2,−43.22	c	<0.70		−190,150		<0.80		−200,140	
G 322.158+0.636[2,8,10]	15 18 34.64	−56 38 25.3	323.8	−63.3	−66.4,−50.6	627.8	–				13.4	−63.4	−64.1,−52.9	14.6
G 322.705−0.331	15 25 47.52	−57 09 15.5	2.4	−21.6	−23.5,−21.1	1	<0.75		−165,175		<0.80		−200,140	
G 323.459−0.079[2,6,8]	15 29 19.33	−56 31 22.8	17.8	−66.9	−68.3,−65.9	11.6	–				11.4	−66.7	−67.4,−66.5	3.8
G 323.740−0.263[1,2,6,8,9]	15 31 45.45	−56 30 50.1	3161.9	−51.1	−59.7,−40.3	5121.3	396.5	−48.7	−52.4,−48.1	684	–			
G 323.766−1.370	15 36 37.69	−57 24 01.6	2.5	46.6	46.5,51.2	0.9	<0.75		−165,175		<0.75		−200,140	
G 323.793−0.397	15 32 38.09	−56 35 36.5	2.4	−22.6	−25.5,−22.4	0.8	<0.75		−165,175		<0.75		−200,140	
G 323.799+0.017	15 30 57.12	−56 15 01.5	6.7	−56.1	−59.8,−55.8	3.1	<0.75		−165,175		<0.55		−200,140	
G 324.716+0.342	15 34 57.47	−55 27 23.6	10.3	−45.9	−50.3,−45.1	4.6	<0.70		−165,175		<0.80		−200,140	
G 324.789−0.378	15 38 22.85	−55 59 47.0	1.2	11.8	11.7,12.1	0.4	<0.70		−165,175		<0.75		−200,140	
G 324.915+0.158	15 36 51.17	−55 29 22.9	9.6	−4.9	−5.8,−0.6	24.9	1.2	−3.7	−5,−1.5	1.5	–			
G 324.923−0.568	15 39 57.64	−56 04 08.3	3.2	−78.1	−79.6,−77.7	2.2	1	−78.2	−79.7,−78.1	0.3	–			
G 325.659−0.022	15 41 48.70	−55 11 27.0	0.6	29.4	29.3,29.7	0.2	<0.75		−165,175		<0.75		−200,140	
G 326.323−0.393	15 47 04.58	−55 04 50.4	3.2	−69.3	−77.1,−67.6	2.7	<0.75		−165,175		<0.75		−200,140	
G 326.448−0.748	15 49 18.63	−55 16 51.6	4.5	−68.5	−73.5,−57.5	12.1	1.2	−60.9	−71,−57.7	0.8	–			
G 326.475+0.703	15 43 16.64	−54 07 14.6	128.8	−38.5	−50.6,−36.7	135.1	–				17.2	−38.5	−49.5,−37.6	9.1
G 326.476+0.695	15 43 18.90	−54 07 35.5	3.3	−43.5	−43.8,−43.1	1.3	–				<0.80		−200,140	
G 326.608+0.799	15 43 35.99	−53 57 47.3	1.3	−44.9	−45.1,−44.3	0.5	<0.75		−165,175		<0.80		−200,140	
G 326.641+0.611	15 44 33.33	−54 05 31.5	30.8	−42.5	−45.3,−34.9	25.4	0.7	−39.9	−40.1,−39.5	0.3	–			
G 326.662+0.520	15 45 02.95	−54 09 03.1	15.9	−38.6	−42.7,−38.3	20.6	<0.75		−165,175		<0.80		−200,140	
G 326.859−0.677	15 51 14.19	−54 58 04.8	15.3	−58.1	−62.4,−57.1	11.7	2.1	−58	−58.3,−57.9	0.7	–			
G 326.986−0.031	15 49 07.67	−54 23 04.5	2.3	−60.7	−60.8,−56.6	1.4	<0.70		−165,175		<0.75		−200,140	
G 327.120+0.511[2]	15 47 32.73	−53 52 38.4	54.8	−87.1	−92.4,−82.9	48.2	–				2.9	−89.6	−90.1,−89.2	1.2
G 327.282−0.469	15 52 36.03	−54 32 24.0	5.4	0.1	−1.3,1.8	4.5	1.1	0.2	−0.3,0.3	0.6	1.5	−0.1	−0.2,0.2	0.5
G 327.291−0.578[2*]	15 53 07.65	−54 37 06.1	2.5	−37	−45.4,−36.8	2.4	–				<0.80		−200,140	
G 327.402+0.445[2,8]	15 49 19.50	−53 45 13.9	81.2	−82.6	−84.4,−69.9	134.6	–				54.6	−82.7	−84.1,−75.2	34.5
G 327.392+0.199	15 50 18.48	−53 57 06.3	8.4	−84.1	−86.1,−79.5	10.4	0.7	−83.2	−84.6,−81.9	0.5	0.8	−83.3	−83.5,−81.9	0.7
G 327.395+0.197	15 50 20.06	−53 57 07.5	9.2	−88.9	−89.7,−88.3	3.5	<0.80		−165,175		<0.80		−200,140	
G 327.566−0.850	15 55 47.61	−54 39 11.4	11.7	−28.8	−30.4,−21.6	9.7	<0.75		−165,175		<0.80		−200,140	
G 327.590−0.094	15 52 36.82	−54 03 18.7	4	−86.3	−86.6,−85.7	1.7	<0.70		−165,175		<0.80		−200,140	
G 327.618−0.111	15 52 50.22	−54 03 00.8	2.1	−98.1	−98.8,−94.3	1.9	<0.70		−165,175		<0.80		−200,140	
G 327.710−0.394	15 54 32.98	−54 12 36.4	4.2	−77.6	−78.6,−72.2	3.2	<0.70		−165,175		<0.80		−200,140	
G 327.808−0.634	15 56 06.91	−54 19 54.4	2.7	−42.3	−42.6,−41.9	1.2	<0.70		−165,175		<0.80		−200,140	
G 327.863+0.098	15 53 13.44	−53 44 01.8	1.6	−46.2	−47.4,−45.9	0.9	<0.70		−165,175		<0.80		−200,140	
G 327.945−0.115	15 54 33.91	−53 50 44.3	7.8	−51.6	−52,−50.8	3.6	3.3	−51.7	−51.9,−51.2	1.3	–			
G 328.140−0.432	15 56 57.75	−53 57 48.7	15.7	−39.6	−40.2,−36.3	19.8	<0.75		−165,175		<0.75		−200,140	

Table 7.1: – continued

Methanol maser (l, b) (degrees)	RA (J2000) (h m s)	Dec (J2000) (° ′ ″)	$S_{6.7}$ (Jy)	$Vp_{6.7}$	$Vr_{6.7}$	$I_{6.7}$ (Jy)	2008 June $S_{12.2}$	2008 June $Vp_{12.2}$	2008 June $Vr_{12.2}$	2008 June $I_{12.2}$	2008 December $S_{12.2}$	2008 December $Vp_{12.2}$	2008 December $Vr_{12.2}$	2008 December $I_{12.2}$
G 328.164+0.587	15 52 42.37	−53 09 50.5	1.6	−91.9	−92.1,−91.3	0.5	<0.75		−165,175		<0.80		−200,140	
G 328.237−0.547[2,8,9]	15 57 58.28	−53 59 22.7	1340	−44.7	−46.2,−31.7	808.4	–				25.6	−44.7	−45.2,−44.1	9.8
G 328.254−0.532[2,8,9]	15 57 59.75	−53 58 00.4	361	−37.4	−50.4,−35.5	236	–				6.4	−36.8	−37.7,−36.4	2.8
G 328.385+0.131	15 55 47.33	−53 22 30.8	1.6	28.9	28.7,29.2	0.6	<0.75		−165,175		<0.80		−200,140	
G 328.808+0.633[2,8,9]	15 55 48.45	−52 43 06.6	295.7	−43.8	−47,−42	conf	21.5	−46.4	−46.9,−43.3	10.3	–			
G 328.809+0.633[2,8,9]	15 55 48.70	−52 43 05.5	346.1	−44.2	−45,−43	conf	5.4	−43.5	−44.6,−43.3	1.9	–			
G 328.819+1.704	15 51 24.42	−51 53 05.4	1.5	−86.3	−88.7,−71.2	1.4	<0.75		−165,175		<0.80		−200,140	
G 328.942+0.565	15 56 46.17	−52 41 04.8	2.1	−90.9	−98.9,−87.7	2.8	0.5	−98.8	−98.9,−89	0.1	0.7	−98.8	−98.9,−90.4	0.2
G 329.029−0.205[2,8,9]	16 00 31.80	−53 12 49.6	113.4	−36.9	−42,−33.5	210.3	15.5	−37.3	−40.3,−36.8	7.8	–			
G 329.031−0.198	16 00 30.32	−53 12 27.3	32	−46	−48.1,−42	35.5	<0.75		−165,175		–			
G 329.066−0.308	16 01 09.93	−53 16 02.6	14.4	−43.9	−48.6,−40.2	18.4	0.6	−43.5	−43.8,−43.5	0.2	0.9	−43.5	−43.7,−43.4	0.2
G 329.183−0.314[2]	16 01 47.01	−53 11 43.3	5.1	−55.6	−59.9,−50.2	8.7	1.3	−58.2	−59.3,−58.1	0.3	–			
G 329.272+0.115	16 00 21.77	−52 48 48.1	1.3	−72	−72.1,−71.9	0.3	<0.70		−165,175		<0.80		−200,140	
G 329.341−0.644	16 04 01.70	−53 20 21.1	3	−81.3	−81.6,−81.1	1	<0.70		−165,175		<0.80		−200,140	
G 329.339+0.148	16 00 33.13	−52 44 39.8	23.8	−106.4	−107.5,−105.5	13.2	3.2	−106.3	−107.3,−106	1.3	–			
G 329.407−0.459[2,10]	16 03 32.65	−53 09 26.9	95.7	−66.7	−68,−66	conf	0.5	−68.3	−68.3,−65.9	0.2	0.4	−68.3	−68.3,−68	0.1
G 329.405−0.459[2,10]	16 03 32.16	−53 09 30.5	50.9	−70.4	−73.3,−63.2	conf	0.7	−71.6	−71.7,−63.6	0.3	0.7	−71.7	−71.8,−70.1	0.2
G 329.469+0.503	15 59 40.71	−52 23 27.3	18.2	−72	−73.7,−58.8	24.7	<0.70		−165,175		<0.80		−200,140	
G 329.526+0.216	16 01 11.70	−52 34 14.5	1.8	−92.8	−93.2,−92.5	0.7	<0.75		−165,175		<0.80		−200,140	
G 329.556+0.181	16 01 29.44	−52 34 39.9	1.5	−106.5	−109.1,−92.6	1.8	<0.75		−165,175		<0.80		−200,140	
G 329.610+0.114[3]	16 02 03.14	−52 35 33.5	44.3	−60.1	−68.9,−58.6	31.7	–				19.5	−60.2	−61.4,−59.5	10.8
G 329.622+0.138	16 02 00.30	−52 33 59.4	2	−85	−85.7,−83.1	1	0.5	−84.9	−85,−84.7	0.1	<0.80		−200,140	
G 329.719+1.164	15 58 07.09	−51 43 32.6	7.7	−75.9	−82.5,−72.8	9.4	–				1.9	−75.6	−75.9,−75.5	0.6
G 330.070+1.064	16 00 15.43	−51 34 25.6	8.7	−41.8	−55.5,−35.3	8.8	–				3.5	−42.1	−42.5,−41.8	1.5
G 330.226+0.290	16 04 18.94	−52 03 12.8	1.1	−90.5	−92.2,−74.5	1.5	1.4	−92.2	−92.4,−90.3	0.3	<0.75		−200,140	
G 330.283+0.493	16 03 43.06	−51 51 48.3	4.4	−88.8	−90,−87.5	5.2	1.6	−88.1	−89.1,−87.9	1.1	–			
G 330.878−0.367	16 10 19.80	−52 06 07.9	0.8	−59.2	−59.4,−57.8	0.4	<0.75		−165,175		<0.80		−200,140	
G 330.875−0.383	16 10 23.09	−52 06 58.7	0.3	−69.7	−69.7,−69.5	0.04	<0.75		−165,175		<0.80		−200,140	
G 330.953−0.182	16 09 52.36	−51 54 57.5	6.8	−87.5	−90.1,−87.1	4.4	<0.50		−185,155		–			
G 330.998+0.093	16 08 53.08	−51 40 59.2	0.7	−28.6	−29.4,−28.4	0.4	<0.75		−165,175		<0.80		−200,140	
G 331.059+0.375	16 07 56.84	−51 25 59.8	2.9	−82.5	−82.9,−69.7	4.1	<0.70		−165,175		<0.80		−200,140	
G 331.120−0.118	16 10 23.04	−51 45 20.6	2.5	−93.1	−94.5,−91.2	2.2	0.5	−93.5	−93.6,−92.9	0.2	0.7	−93.6	−93.7,−92.7	0.5
G 331.132−0.244	16 10 59.77	−51 50 22.4	20.4	−84.3	−92.1,−81	29	<0.75*		−165,175		<0.60*		−200,140	
	*Av Jun & Dec						0.3	−84.6	−84.9,−84.6	0.1				
G 331.134+0.156	16 09 15.17	−51 32 38.7	1.7	−72.1	−83.5,−72	1.1	<0.75		−165,175		<0.80		−200,140	
G 331.278−0.188[1,2,8,9]	16 11 26.59	−51 41 56.7	89	−78.1	−87.7,−76.9	221	75.9	−78.8	−83.2,−77.8	56.3	–			
G 331.342−0.346	16 12 26.45	−51 46 16.4	85.6	−65.1	−76.4,−60.7	126.7	<0.75*		−160,180		<0.60*		−200,140	
	*Av Jun & Dec						0.4	−71.0	−71.8,−71.0	0.2				
G 331.425+0.264	16 10 09.36	−51 16 04.5	16.3	−88.8	−91.5,−77.3	15.6	–				6.7	−88.6	−90.5,−78.5	4.8
G 331.442−0.187[3]	16 12 12.49	−51 35 10.1	61.2	−87.8	−93.3,−83.9	135.5	–				6.4	−87.7	−92.9,−84.5	4.7
G 331.437−0.304	16 12 42.00	−51 40 30.9	5.9	−89.8	−90.7,−85.3	5.7	<0.75		−160,180		0.5	−89.9	−90,−89.5	0.1

Table 7.1: – continued

Methanol maser	RA	Dec					2008 June				2008 December			
(l, b) (degrees)	(J2000) (h m s)	(J2000) (° ′ ″)	$S_{6.7}$ (Jy)	$Vp_{6.7}$	$Vr_{6.7}$	$I_{6.7}$ (Jy)	$S_{12.2}$	$Vp_{12.2}$	$Vr_{12.2}$	$I_{12.2}$	$S_{12.2}$	$Vp_{12.2}$	$Vr_{12.2}$	$I_{12.2}$
G 331.542−0.066	16 12 09.02	−51 25 47.6	6.9	−86	−90.2,−85.2	3.5	<0.75		−160,180		<0.60		−200,140	
G 331.543−0.066	16 12 09.14	−51 25 45.3	15.3	−84	−85,−79.9	13.9	<0.75		−160,180		<0.60		−200,140	
G 331.556−0.121[2]	16 12 27.21	−51 27 38.2	52.1	−97.1	−105.1,−93.8	64.4	–				8.9	−104.4	−105,−96.7	8.5
G 331.710+0.603	16 10 01.77	−50 49 32.3	17.8	−73.3	−75.6,−69.7	16.8	<0.75		−160,180		<0.80		−200,140	
G 331.900−1.186	16 18 49.13	−51 59 28.2	2.4	−46.3	−59.2,−45.7	2.9	<0.75*		−160,180		<0.55*		−200,140	
	*Av Jun & Dec						0.4	−46.8	−59.1,−46.8	0.1				
G 332.094−0.421	16 16 16.45	−51 18 25.7	12.5	−58.5	−62,−58	13.8	1.2	−58.5	−60.4,−58.5	0.3	–			
G 332.295−0.094	16 15 45.40	−50 55 53.7	8	−42.6	−59.2,−42	14.3	3.1	−43.4	−45.1,−42.2	1.7	–			
G 332.295+2.280[3]	16 05 41.72	−49 11 30.3	152.5	−24	−27,−20.6	116.8	64	−24	−24.7,−22.1	31.4	–			
G 332.351−0.436	16 17 31.51	−51 08 22.0	8.5	−52.8	−54.2,−43.2	6.7	<0.70		−160,180		<0.80		−200,140	
G 332.352−0.117	16 16 07.11	−50 54 31.2	6.3	−44.6	−56,−41.4	6.3	<0.75		−160,180		<0.60		−200,140	
G 332.364+0.607	16 13 01.46	−50 22 36.9	0.4	−48.5	−48.6,−48.2	0.2	<0.70		−160,180		<0.80		−200,140	
G 332.560−0.148	16 17 12.12	−50 47 12.6	1.5	−54.8	−56.3,−54.4	1.5	<0.70		−160,180		<0.80		−200,140	
G 332.583+0.147	16 16 00.86	−50 33 31.6	4.7	−39.9	−40.7,−38.8	3.8	<0.70		−160,180		<0.80		−200,140	
G 332.604−0.168	16 17 29.33	−50 46 13.0	0.4	−49.8	−56.3,−41.9	0.6	<0.70		−160,180		<0.55		−200,140	
G 332.653−0.621	16 19 43.48	−51 03 36.4	5.7	−50.6	−51.1,−44.5	5	<0.50		−160,180		<0.80		−200,140	
G 332.701−0.588	16 19 47.43	−51 00 09.4	0.4	−62.8	−62.8,−62.7	0.1	<0.70		−160,180		–			
G 332.726−0.621[1]	16 20 02.95	−51 00 32.0	5.1	−47.4	−56.7,−43.7	7.3	0.5	−47.4	−47.5,−47.3	0.1	–			
G 332.813−0.701	16 20 48.12	−51 00 15.6	7	−53.2	−58.9,−50.4	7.3	0.4	−58.2	−58.7,−58	0.2	0.4	−58.6	−58.9,−58.4	0.1
G 332.826−0.549	16 20 10.85	−50 53 14.2	2	−61.8	−62.1,−54.1	3.3	<0.75		−160,180		–			
G 332.854+0.817	16 14 20.45	−49 53 13.0	1.1	−49	−49.2,−45	0.6	<0.70		−160,180		–			
G 332.960+0.135	16 17 46.02	−50 18 18.0	1.9	−54.2	−54.7,−54	−54.2	<0.70		−160,180		<0.55		−200,140	
G 332.963−0.679	16 21 22.92	−50 51 58.5	26	−45.9	−49.8,−38	28.1	<0.70		−160,180		–			
G 332.942−0.686	16 21 19.00	−50 54 10.2	7.9	−52	−55.7,−51.1	9.1	<0.70		−160,180		–			
G 332.975+0.773	16 15 04.51	−49 50 09.3	1.4	−50.9	−55.4,−50.7	0.6	<0.70		−160,180		–			
G 332.987−0.487	16 20 37.80	−50 43 49.7	8.3	−55.7	−67.5,−51.2	8.6	<0.75		−160,180		–			
G 333.029−0.063	16 18 56.73	−50 23 54.3	1.2	−40.1	−40.6,−39.5	0.8	<0.70		−160,180		–			
G 333.029−0.015	16 18 44.17	−50 21 50.6	5.4	−54.1	−62.4,−52.6	7.5	0.9	−53.8	−61,−53.7	0.6	–			
G 333.068−0.447[2]	16 20 48.97	−50 38 40.4	18.5	−54.4	−56.4,−53.5	9.3	<0.75		−160,180		0.4	−54.4	−54.6,−54.4	0.1
G 333.109−0.500	16 21 14.19	−50 39 13.1	1.5	−60.8	−61.1,−52.5	0.6	<0.70		−160,180		–			
G 333.128−0.560	16 21 35.38	−50 40 56.5	8.7	−52.7	−60.9,−52	13.8	<0.75		−160,180		–			
G 333.130−0.560	16 21 35.73	−50 40 51.0	23.7	−56.7	−64.4,−56.3	14.6	<0.70		−160,180		–			
G 333.121−0.434	16 20 59.71	−50 35 52.1	17.5	−48.5	−56.4,−47.8	19.2	<0.80		−160,180		–			
G 333.126−0.440	16 21 02.61	−50 35 54.8	8.2	−43.9	−44.5,−42.4	4	<0.80		−160,180		–			
G 333.128−0.440	16 21 03.30	−50 35 49.5	1.4	−44	−47.8,−45.4	1.3	<0.80		−160,180		<0.65		−200,140	
G 333.163−0.101[2]	16 19 42.67	−50 19 53.2	9.8	−95.1	−95.8,−90	5.4	–				5.5	−95.2	−95.5,−94.8	2.1
G 333.184−0.091	16 19 45.62	−50 18 35.0	7.4	−81.9	−91.4,−81	7	0.5	−81.7	−81.9,−81.4	0.2	0.7	−81.7	−82,−81.4	0.2
G 333.234−0.060	16 19 50.89	−50 15 10.7	1.3	−91.8	−92.5,−79.6	2.5	<0.75		−160,180		–			
G 333.315+0.105	16 19 29.01	−50 04 41.3	17.9	−41.3	−51.4,−36.9	41.2	<0.70		−160,180		–			
G 333.387+0.032	16 20 07.59	−50 04 47.2	3.5	−73.8	−74.2,−60.2	3.9	<0.70		−160,180		–			
G 333.466−0.164	16 21 20.18	−50 09 48.6	30.1	−42.2	−50.9,−37.1	35.2	<0.75		−160,180		–			
G 333.562−0.025	16 21 08.80	−49 59 48.0	33.4	−35.3	−43.9,−33.1	55.8	–				14.7	−34.9	−44.1,−34.1	14.2

Table 7.1: – continued

Methanol maser (l, b) (degrees)	RA (J2000) (h m s)	Dec (J2000) (° ′ ″)	$S_{6.7}$ (Jy)	$Vp_{6.7}$	$Vr_{6.7}$	$I_{6.7}$ (Jy)	2008 June $S_{12.2}$	2008 June $Vp_{12.2}$	2008 June $Vr_{12.2}$	2008 June $I_{12.2}$	2008 December $S_{12.2}$	2008 December $Vp_{12.2}$	2008 December $Vr_{12.2}$	2008 December $I_{12.2}$
G 333.646+0.058	16 21 09.14	−49 52 45.9	8.4	−87.3	−89,−80.8	10.2	0.6	−87.5	−87.7,−87.5	0.1	<0.75		−200,140	
G 333.683−0.437	16 23 29.78	−50 12 08.6	25.2	−5.6	−7.7,−0.4	20.5	–				8.4	−5.5	−7.6,−4.6	4.8
G 333.761−0.226	16 22 54.27	−49 59 54.5	3.4	−55.2	−56.5,−51.3	2.4	<0.70		−160,180		–			
G 333.851+0.527	16 20 00.92	−49 24 06.9	0.8	−40.3	−49.7,−40.1	0.4	<0.70		−160,180		–			
G 333.900−0.099	16 22 57.39	−49 48 35.1	0.7	−59.4	−59.6,−56.6	0.7	<0.75		−160,180		–			
G 333.931−0.135	16 23 14.83	−49 48 48.9	15	−36.9	−37.3,−36.3	6.1	<0.75		−160,180		–			
G 334.138−0.023	16 23 39.56	−49 35 15.2	2.9	−31.1	−34.3,−30.5	3	1	−31.2	−31.3,−31.1	0.2	–			
G 334.307−0.079	16 24 38.12	−49 30 24.5	2	−36.7	−37.8,−33	1.8	1.2	−36.5	−36.9,−36.2	0.5	–			
G 334.635−0.015	16 25 45.73	−49 13 37.4	28.5	−30.1	−32,−27	28.4	1.7	−30.2	−30.6,−29.8	0.8	–			
G 334.933−0.307	16 28 18.81	−49 12 57.6	3.3	−102.8	−111.2,−100.8	3.5	2.8	−102.8	−103.7,−101.8	2.1	–			
G 334.935−0.098	16 27 24.25	−49 04 11.3	4.6	−21	−22.4,−16.8	4.9	0.7	−17.9	−18.9,−17.2	0.5	–			
G 335.060−0.427	16 29 23.13	−49 12 27.1	42.2	−46.9	−47.7,−25.8	48.2	–				18.5	−47	−47.3,−46.4	5.7
G 335.426−0.240	16 30 05.58	−48 48 44.8	66.5	−50.5	−53.5,−39.7	21.7	–				17.6	−50.7	−53.3,−50.3	8
G 335.556−0.307[2]	16 30 55.96	−48 45 50.0	22.3	−116.3	−119.7,−110.6	35.2	–				5.3	−114.7	−116.7,−114.4	1.8
G 335.585−0.285	16 30 57.28	−48 43 39.7	34.8	−48.6	−50.5,−43.5	47.1	<0.80		−160,180		<0.65		−200,140	
G 335.585−0.290	16 30 58.79	−48 43 53.1	51.5	−51.3	−56.5,−49.8	39.4	1.1	−53.5	−54.3,−52.8	0.6	1.1	−53.3	−54.4,−53.2	0.5
G 335.726+0.191[2]	16 29 27.37	−48 17 53.2	49.2	−44.4	−54.9,−43.3	38.6	–				8	−44.5	−44.8,−43.5	5.8
G 335.789+0.174[2,8,9]	16 29 47.33	−48 15 51.7	166.3	−47.5	−56.5,−44.2	377.7	–				162.3	−46.2	−51,−45.4	145.8
G 335.824−0.177	16 31 28.33	−48 28 49.2	0.9	−26.1	−26.2,−26	0.2	–				<0.55		−200,140	
G 336.018−0.827[3]	16 35 09.30	−48 46 46.8	87.2	−53.2	−54.6,−39.1	180.9	7.7	−40.2	−53.4,−39.5	6.5	–			
G 336.358−0.137[2]	16 33 29.17	−48 03 43.9	12.7	−73.5	−81.2,−70.9	20.8	–				2.6	−74.7	−79.7,−73.5	1.5
G 336.409−0.257	16 34 13.20	−48 06 20.9	6.1	−85.9	−86.1,−83.9	5.3	–				<0.60		−200,140	
G 336.433−0.262[2,8]	16 34 20.22	−48 05 32.2	24.3	−93	−95.8,−86.1	41.9	–				14.5	−93.1	−93.6,−87.1	9.6
G 336.464−0.157	16 34 00.01	−47 59 53.2	0.7	−85.8	−86.3,−77.9	0.6	–				<0.55		−200,140	
G 336.496−0.271	16 34 38.02	−48 03 03.9	17	−24.1	−27.1,−19.1	20.5	7.6	−24	−24.9,−21.3	5.7	–			
G 336.526−0.156	16 34 15.00	−47 57 07.4	0.7	−94.9	−95.1,−88.2	0.3	–				<0.55		−200,140	
G 336.703−0.099	16 34 42.76	−47 46 57.6	3.2	−35.6	−37.3,−35.3	0.8	<0.75		−160,180		–			
G 336.809+0.119	16 34 11.11	−47 33 35.3	5.5	−84.4	−85.9,−78.4	10.6	<0.75		−160,180		–			
G 336.822+0.028[2]	16 34 38.28	−47 36 32.2	28.2	−76.8	−79.9,−74.2	21.5	–				4.8	−76.7	−77.3,−76.5	1.3
G 336.825+0.139	16 34 09.82	−47 31 52.9	3.4	−88.4	−89.5,−86.8	4.5	1.4	−88.4	−89.1,−87.3	0.7	–			
G 336.830−0.375	16 36 26.19	−47 52 31.1	19.6	−22.8	−27.3,−17.4	38.5	<0.75		−160,180		<0.8		−200,140	
G 336.864+0.005[2]	16 34 54.44	−47 35 37.3	58.7	−76.1	−81.7,−67.6	46.1	<0.75		−160,180		0.5	−75.3	−75.4,−74.8	0.1
G 336.916−0.024	16 35 14.27	−47 34 30.1	4.1	−127.4	−127.9,−114.2	2.4	2.6	−127.2	−127.5,−115.0	1.2	–			
G 336.941−0.156	16 35 55.19	−47 38 45.4	23.4	−67.2	−79.4,−62.3	48.2	–				10.8	−66.6	−76.7,−64.5	12.3
G 336.957−0.225	16 36 16.99	−47 40 48.6	1.6	−68	−85.4,−63.9	2.9	1	−68	−68.2,−67.4	0.5	–			
G 336.958−0.977	16 39 37.55	−48 10 58.4	0.8	−49.3	−50.5,−47.8	0.5	<0.75		−160,180		–			
G 336.983−0.183	16 36 12.41	−47 37 58.2	12.5	−80.7	−89.4,−78.5	16.5	–				2.5	−79.8	−85.7,−75.2	2.7
G 336.994−0.027	16 35 33.98	−47 31 11.7	25.8	−125.8	−126.8,−115.3	20	<0.70		−160,180		–			
G 337.052−0.226	16 36 40.12	−47 36 38.2	13.9	−77.6	−78.4,−74.9	15.7	–				0.4	−76.7	−77,−76.4	0.1
G 337.097−0.929	16 39 57.77	−48 02 49.1	6.8	−40.4	−42.5,−37.4	5	1.4	−40.6	−40.9,−40.2	0.6	–			
G 337.132−0.068	16 36 17.67	−47 26 41.0	2	−60.6	−62.3,−59.5	1.8	<0.70		−160,180		0.7	−59.7	−60.2,−59.6	0.2

Table 7.1: – continued

Methanol maser	RA	Dec					2008 June				2008 December			
(l, b)	(J2000)	(J2000)	$S_{6.7}$	$Vp_{6.7}$	$Vr_{6.7}$	$I_{6.7}$	$S_{12.2}$	$Vp_{12.2}$	$Vr_{12.2}$	$I_{12.2}$	$S_{12.2}$	$Vp_{12.2}$	$Vr_{12.2}$	$I_{12.2}$
(degrees)	(h m s)	(° ′ ″)	(Jy)			(Jy)								
G 337.153−0.395	16 37 48.86	−47 38 56.5	17.4	−49.4	−50.9,−47.8	15.3	–				1.2	−48.3	−50,−48.2	0.4
G 337.176−0.032	16 36 18.84	−47 23 19.8	4.5	−64.8	−74.8,−62.9	7	0.5	−64.8	−65.1,−64.7	0.2	0.5	−64.7	−65.3,−64.7	0.2
G 337.202−0.094	16 36 41.22	−47 24 40.2	1.4	−67.6	−83.2,−65.9	3.6	<0.80		−160,180		–			
G 337.201+0.114	16 35 46.56	−47 16 16.7	7.2	−57.5	−64.5,−51.9	23.1	–				4.4	−54.6	−57.7,−53.3	4
G 337.258−0.101	16 36 56.32	−47 22 26.4	7.7	−69.3	−73.7,−63.6	16.9	<0.70		−160,180		–			
G 337.263−0.070	16 36 49.36	−47 20 58.7	1.1	−39.4	−41.3,−39.1	0.9	–				<0.60		−200,140	
G 337.300−0.874	16 40 31.34	−47 51 32.1	2.2	−87.4	−97.5,−87.4	4.3	<0.70		−160,180		–			
G 337.404−0.402[2]	16 38 50.51	−47 28 00.3	77.4	−39.6	−43.3,−36.5	75.8	–				4.2	−39.4	−42.5,−38.5	2.1
G 337.388−0.210	16 37 56.01	−47 21 01.2	22.8	−56.2	−67,−52	43.3	–				2.9	−55.5	−66,−54.9	4.8
G 337.517−0.348	16 39 03.09	−47 20 48.7	0.7	9.4	9.2,9.8	0.3	–				<0.55		−200,140	
G 337.613−0.060[2,8,9]	16 38 09.54	−47 04 59.9	21	−41.6	−53.6,−38	47.5	–				5.7	−42.2	−53.6,−40.5	7.9
G 337.632−0.079[2]	16 38 19.13	−47 04 53.5	14.5	−56.9	−63.2,−54	19.1	<0.75		−160,180		0.5	−55.5	−56.8,−54.6	0.2
G 337.686+0.137	16 37 35.42	−46 53 47.6	0.7	−75.1	−75.4,−73.8	0.5	<0.75		−160,180		<0.80		−200,140	
G 337.705−0.053[2,8,9]	16 38 29.63	−47 00 35.5	170.2	−54.6	−58.1,−43.2	246.2	–				94.1	−54.6	−55.6,−50.8	37.2
G 337.710+0.089	16 37 53.41	−46 54 40.8	3.3	−72.6	−78.7,−72.4	1.5	<0.75		−160,180		<0.75		−200,140	
G 337.720+0.065	16 38 02.21	−46 55 13.6	0.7	−63.9	−69.9,−63.8	0.4	<0.75		−160,180		<0.75		−200,140	
G 337.844−0.375	16 40 26.67	−47 07 13.4	5.8	−38.6	−42.2,−37.3	3.4	0.9	−38.6	−39.1,−38.1	0.3	–			
G 337.920−0.456[2]	16 41 06.05	−47 07 02.1	32.3	−37.8	−40.7,−35.8	27.1	–				0.6	−37.8	−37.9,−37.7	0.2
G 337.966−0.169	16 40 01.09	−46 53 34.5	9.3	−59.4	−67,−54.2	16.3	<0.75		−160,180		0.6	−59	−59.2,−58.9	0.2
G 337.997+0.136	16 38 48.50	−46 39 57.5	6	−32.3	−35,−31.2	2.6	<0.75		−160,180		<0.80		−200,140	
G 338.075+0.012[2,8]	16 39 39.04	−46 41 28.0	13.9	−44	−53.9,−42.8	18.9	5.9	−53.1	−53.6,−52.6	3	7.5	−53.1	−54,−52.5	4
G 338.075+0.009	16 39 39.80	−46 41 33.4	4.4	−39.1	−41.9,−35.6	10.3	–				<0.80		−200,140	
G 338.069+0.011	16 39 37.95	−46 41 45.3	2.6	−39.9	−40.3,−39.7	1.3	<0.80		−160,180		<0.80		−200,140	
G 338.140+0.178	16 39 10.92	−46 31 55.2	7.2	−34.5	−42.6,−33.7	4.7	<0.70		−160,180		<0.80		−200,140	
G 338.160−0.064	16 40 18.70	−46 40 37.8	2.5	−66.2	−68.4,−62.2	4.4	0.8	−66.1	−66.5,−65.9	0.2	0.6	−66.2	−66.3,−65.9	0.2
G 338.287+0.120	16 40 00.13	−46 27 37.1	26.1	−39.9	−43.8,−35.7	13.9	<0.75		−160,180		<0.55		−200,140	
G 338.280+0.542	16 38 09.08	−46 11 03.1	5.4	−56.7	−62.2,−56.5	3	<0.75		−160,180		<0.55		−200,140	
G 338.325−0.409	16 42 27.53	−46 46 54.3	2.8	−25.7	−34.2,−25	1.9	<0.75		−160,180		<0.80		−200,140	
G 338.392−0.403	16 42 41.27	−46 43 39.0	5.3	−33.5	−34,−32.6	2.2	<0.70		−160,180		<0.80		−200,140	
G 338.396−0.007	16 40 58.41	−46 27 47.8	2.7	−48.9	−54.2,−44.5	2.5	<0.75		−160,180		<0.75		−200,140	
G 338.388+0.162	16 40 12.37	−46 21 25.6	3.6	−29.8	−37.1,−26.2	8.9	1.8	−30.1	−30.2,−29.3	1.1	–			
G 338.432+0.058	16 40 49.79	−46 23 37.0	30.4	−30.2	−33.5,−22.5	20.1	<0.75		−160,180		<0.80		−200,140	
G 338.461−0.245[2,8]	16 42 15.50	−46 34 18.4	69.3	−51.7	−63.3,−48.7	144.8	–				9.4	−52.2	−52.6,−51.2	5.9
G 338.472+0.289	16 39 58.91	−46 12 35.4	0.9	−29.4	−34.8,−29.2	0.7	–				<0.55		−200,140	
G 338.497+0.207	16 40 25.89	−46 14 43.5	3.3	−28.1	−30.7,−27.9	2.2	–				<0.55		−200,140	
G 338.566+0.110	16 41 07.03	−46 15 28.3	2.7	−74.7	−78.5,−74.2	2	–				<0.55		−200,140	
G 338.561+0.218	16 40 37.96	−46 11 25.8	38.3	−39.1	−43.8,−29.6	87	–				25.6	−40.2	−41.4,−37.7	33.8
G 338.875−0.084[2]	16 43 08.25	−46 09 12.8	19.5	−41.3	−42.2,−35.1	13.1	–				1	−41.4	−41.5,−40.4	0.5
G 338.850+0.409	16 40 54.29	−45 50 52.0	1.6	−55.7	−59.6,−54.4	1.4	–				<0.55		−200,140	
G 338.902+0.394	16 41 10.06	−45 49 05.4	1.7	−26	−35.4,−19.1	3.4	–				1	−26	−26.5,−25.7	0.6
G 338.920+0.550	16 40 34.01	−45 42 07.1	76.5	−61.3	−67.8,−58.3	68.4	–				0.6	−66.8	−66.9,−66.7	0.1
G 338.925+0.634	16 40 13.56	−45 38 33.2	t				–				t			

Table 7.1: – continued

Methanol maser	RA	Dec					2008 June				2008 December			
(l, b)	(J2000)	(J2000)	$S_{6.7}$	$Vp_{6.7}$	$Vr_{6.7}$	$I_{6.7}$	$S_{12.2}$	$Vp_{12.2}$	$Vr_{12.2}$	$I_{12.2}$	$S_{12.2}$	$Vp_{12.2}$	$Vr_{12.2}$	$I_{12.2}$
(degrees)	(h m s)	(° ′ ″)	(Jy)			(Jy)								
G 338.926+0.634	16 40 13.95	−45 38 29.7	65.3	−60.8	−68.5,−52.1	102.2	–				33.2	−60.6	−61.9,−52.8	21.9
G 338.925+0.557	16 40 33.53	−45 41 37.1	t				–				<0.75		−200,140	
G 338.935−0.062[2]	16 43 16.01	−46 05 40.2	29.3	−41.9	−43.1,−41.2	13.6	–				10	−42.2	−43.1,−41.4	3.1
G 339.053−0.315	16 44 48.99	−46 10 13.0	129.1	−111.6	−124.3,−110.1	117.3	–				47.5	−111.8	−124,−110.2	39.8
G 339.064+0.152	16 42 49.56	−45 51 23.8	3.6	−87.5	−90.5,−82.3	8.2	–				0.5	−85.8	−87.6,−85.7	0.5
G 339.204−0.018	16 44 05.68	−45 51 43.3	2	−14.3	−16.7,−11.6	4.2	–				<0.55	−200	140,	
G 339.282+0.136	16 43 43.11	−45 42 08.0	5.7	−70	−71.7,−68.4	7.1	–				1.3	−70.9	−71.1,−69.9	0.7
G 339.294+0.139	16 43 44.95	−45 41 28.0	7	−74.6	−75.9,−66.2	7.6	–				<0.60		−200,140	
G 339.477+0.043	16 44 50.98	−45 36 56.1	2.7	−9.5	−20.5,−5.8	2.5	–				<0.55		−200,140	
G 339.476+0.185	16 44 13.79	−45 31 24.8	7.2	−87.6	−98.1,−86.5	5.7	–				0.5	−98.1	−98.1,−87.4	0.1
G 339.582−0.127	16 45 58.82	−45 38 47.2	13	−30.4	−31.6,−29.6	11	–				1.6	−30.5	−30.7,−30.2	0.4
G 339.622−0.121[2,8]	16 46 05.99	−45 36 43.3	86.4	−32.9	−39.3,−31.6	141.4	–				3.4	−32.8	−39.1,−31.7	2.3
G 339.681−1.208	16 51 06.21	−46 16 02.8	70.1	−21.4	−41.9,−20.7	69.2	–				<0.55		−200,140	
G 339.762+0.054	16 45 51.56	−45 23 32.6	8	−51	−54,−49.5	9.1	–				2.6	−50.4	−51.7,−49.5	1.7
G 339.884−1.259[2,8,9]	16 52 04.67	−46 08 34.1	1510.3	−38.7	−45,−27.5	2568.2	–				846.5	−38.7	−39.4,−32.4	749.8
G 339.909+0.240	16 45 36.17	−45 09 36.5	0.5	−12.1	−12.5,−11.9	0.3	–				<0.55		−200,140	
G 339.949−0.539	16 49 07.98	−45 37 58.3	70.8	−97.8	−107.9,−89.5	195.3	–				12	−97.6	−100.4,−94	10.6
G 339.980−0.538	16 49 14.73	−45 36 31.6	7	−89.2	−89.4,−89	2.1	–				<0.55		−200,140	
G 339.986−0.425	16 48 46.31	−45 31 51.3	87.9	−89.4	−91.8,−86.2	109.4	–				63.8	−89.4	−89.9,−87.1	54
G 340.034−1.110	16 51 58.07	−45 55 56.5	6.8	−27.5	−28.8,−24.3	3.4	–				<0.55		−200,140	
G 340.054−0.244[2]	16 48 13.89	−45 21 43.3	47.6	−59.4	−62.6,−58.5	38.7	–				8.3	−59.8	−60.1,−59.3	2.8
G 340.118−0.021	16 47 30.00	−45 10 12.1	1.2	−123.3	−123.8,−118.1	0.8	–				0.5	−123.8	−124,−123.5	0.2
G 340.182−0.047	16 47 50.79	−45 08 15.9	3.1	−131.1	−132.1,−117.6	3	–				<0.55		−200,140	
G 340.249−0.372	16 49 30.08	−45 17 44.4	0.7	−51.2	−51.5,−51.2	0.2	–				<0.60		−200,140	
G 340.249−0.046	16 48 05.18	−45 05 08.4	11.9	−126.3	−135.3,−119.9	18.9	–				<0.60		−200,140	
G 340.518−0.152	16 49 31.36	−44 56 54.6	7.3	−48.2	−50.2,−43.6	6.4	–				2	−48.3	−50,−48.1	1.1
G 340.543−0.162	16 49 39.53	−44 56 07.9	1	−51.6	−52.1,−51.4	0.5	–				<0.55		−200,140	
G 340.655−0.235	16 50 22.89	−44 53 48.1	1.2	−21.6	−21.7,−21.4	0.3	<0.75		−160,180		<0.80		−200,140	
G 340.785−0.096[2,8,9]	16 50 14.84	−44 42 26.3	157.6	−108.1	−111.7,−84.7	268.5	–				42.3	−105.3	−109,−89	40.7
G 340.970−1.022	16 54 57.32	−45 09 05.2	10.1	−31.4	−33.9,−19.7	9.1	<0.70		−155,185		<0.80		−200,140	
G 341.124−0.361	16 52 36.76	−44 36 52.7	1.6	−37.2	−43.7,−36.1	1.3	<0.70		−155,185		<0.75		−200,140	
G 341.218−0.212[2,8,9]	16 52 17.84	−44 26 52.1	191.6	−37.9	−50.4,−35.1	336.3	–				1.2	−38.7	−48,−37.1	1.2
G 341.238−0.270[2]	16 52 37.41	−44 28 07.7	4.3	−51.3	−52.3,−49.3	7.2	1.1	−51.2	−52,−49.5	0.8	–			
G 341.276+0.062	16 51 19.41	−44 13 44.5	7.7	−70.6	−77.3,−70	9.3	0.8	−73.5	−73.8,−70.4	0.6	–			
G 341.367+0.336	16 50 28.22	−43 59 02.2	1	−80.5	−81,−79.8	0.4	<0.75		−155,185		<0.75		−200,140	
G 341.990−0.103	16 54 32.89	−43 46 51.4	1.3	−37	−41.8,−36.8	0.5	<0.70		−155,185		<0.80		−200,140	
G 341.973+0.233	16 53 02.98	−43 34 54.7	1.4	−11.9	−12.4,−11.2	1	<0.70		−155,185		<0.55		−200,140	
G 342.251+0.308	16 53 41.86	−43 19 09.8	1.9	−122.7	−123.8,−120.4	2.3	<0.70		−155,185		<0.70		−200,140	
G 342.338+0.305	16 54 00.71	−43 15 12.3	0.9	−112.1	−112.5,−108.8	1.4	<0.70		−155,185		0.8	−112.2	−112.2,−112.1	0.1
G 342.368+0.140	16 54 49.15	−43 20 03.6	3.5	−7.2	−15.4,1	9.1	<0.70		−155,185		–			

Table 7.1: – continued

Methanol maser	RA	Dec					2008 June				2008 December			
(l, b) (degrees)	(J2000) (h m s)	(J2000) (^{o} $'$ $''$)	$S_{6.7}$ (Jy)	$Vp_{6.7}$	$Vr_{6.7}$	$I_{6.7}$ (Jy)	$S_{12.2}$	$Vp_{12.2}$	$Vr_{12.2}$	$I_{12.2}$	$S_{12.2}$	$Vp_{12.2}$	$Vr_{12.2}$	$I_{12.2}$
G 342.446−0.072	16 55 59.94	−43 24 22.5	2.1	−20.2	−32.2,−14.3	3	0.5	−20.1	−20.2,−19.4	0.1	–			
G 342.484+0.183	16 55 02.30	−43 12 59.8	81.2	−42.2	−44.3,−38.4	82.8	–				8.1	−42.2	−43,−41	5.7
G 342.954−0.019	16 57 30.66	−42 58 34.8	2	−3.1	−13.2,−2.1	4.5	<0.75		−155,185		–			
G 343.354−0.067	16 59 04.24	−42 41 34.6	17.9	−117.7	−133.1,−116.6	12.9	0.6	−127.7	−127.8,−127.6	0.1	0.5	−116.8	−116.9,116.8	0.1
G 343.502−0.472	17 01 18.40	−42 49 36.8	13.2	−39	−43,−31.8	9.3	0.4	−42.5	−42.6,−41.9	0.2	–			
G 343.756−0.163	17 00 49.89	−42 26 08.2	5.1	−30.8	−32.4,−23	4.2	<0.50		−155,185		–			
G 343.929+0.125[2]	17 00 10.91	−42 07 19.3	9	14.5	7.7,18.8	15.6	2.4	13.7	13.4,14.5	1.2	–			
G 344.227−0.569[2,10]	17 04 07.78	−42 18 39.5	90.2	−19.7	−32.1,−10.6	128.1	2.4	−19.7	−30.8,−18.7	3.1	–			
G 344.421+0.045[2]	17 02 08.77	−41 46 58.5	17.2	−71.4	−72.3,−70.6	11.4	0.8	−71.5	−71.8,−71.2	0.3	–			
G 344.419+0.044	17 02 08.62	−41 47 10.3	2.3	−64.9	−65,−63	1.5	<0.75		−155,185		<1.45		−200,140	
G 344.581−0.024	17 02 57.71	−41 41 53.8	3.5	1.5	−4.5,5.8	2.8	<0.70		−155,185		–			
G 345.003−0.223[8,9]	17 05 10.89	−41 29 06.2	235.6	−23.1	−24.9,−20.2	227.5	1	−22.2	−23.1,−21.7	0.8	–			
G 345.003−0.224[8,9]	17 05 11.23	−41 29 06.9	83.7	−26.1	−32.7,−25	119.7	0.9	−28.5	−30.3,−28.3	0.4	–			
G 345.010+1.792[2,8,9]	16 56 47.58	−40 14 25.8	268.5	−21	−23.5,−16	513.5	296.5	−21.8	−23.5,−16.8	305.3	–			
G 345.012+1.797[2,8,9]	16 56 46.82	−40 14 08.9	32.4	−12	−16,−10.1	52.9	12.2	−10.8	−13.1,−10.4	12.5	–			
G 345.131−0.174	17 05 23.24	−41 21 10.9	3.1	−28.9	−34,−28.6	2.1	<0.70		−155,185		–			
G 345.198−0.030	17 04 59.49	−41 12 45.7	2.5	−0.5	−3.8,0.8	2.8	1.2	−0.5	−1.5,−0.2	0.7	–			
G 345.205+0.317	17 03 32.87	−40 59 46.6	0.8	−63.5	−64,−60.4	0.6	<0.75		−155,185		–			
G 345.407−0.952	17 09 35.42	−41 35 57.1	2	−14.2	−15,−14	1.5	<0.80		−155,185		–			
G 345.424−0.951	17 09 38.56	−41 35 04.6	1.8	−13.1	−21.1,−6.9	2.5	<0.75		−155,185		–			
G 345.441+0.205	17 04 46.87	−40 52 38.0	2.3	0.9	−12.3,1.3	4.4	<0.75		−155,185		–			
G 345.487+0.314	17 04 28.24	−40 46 28.7	2.8	−22	−23,−21.5	2.6	<0.75		−155,185		–			
G 345.505+0.348[2,10]	17 04 22.91	−40 44 21.7	299.6	−17.8	−24.2,−10	733	8.4	−17.7	−18.5,−15.5	5.1	–			
G 345.498+1.467	16 59 42.84	−40 03 36.1	1.2	−14.2	−14.4,−13.5	0.7	<0.75		−155,185		–			
G 345.576−0.225	17 07 01.50	−41 01 43.4	0.6	−126.9	−126.9,−126.6	0.2	<0.80		−155,185		–			
G 345.807−0.044	17 06 59.85	−40 44 08.2	1	−1.6	−2.6,−1.2	0.9	<0.75		−155,185		0.3	−1.5	−2.1,−1.3	0.1
G 345.824+0.044	17 06 40.70	−40 40 09.9	3.2	−10.3	−11.8,−8.9	1.7	<0.70		−155,185		–			
G 345.949−0.268	17 08 23.64	−40 45 21.5	1.5	−22	−22.3,−21.7	0.6	<0.75		−155,185		<0.80		−200,140	
G 345.985−0.020	17 07 27.58	−40 34 43.6	5.7	−83.2	−84.3,−81.8	4.4	<0.70		−155,185		<0.80		−200,140	
G 346.036+0.048	17 07 20.02	−40 29 49.0	9	−6.4	−14.5,−4.3	8.5	<0.75		−155,185		<0.55		−200,140	
G 346.231+0.119	17 07 39.09	−40 17 53.2	1.5	−95	−96.6,−92.5	1.6	–				<0.55		−200,140	
G 346.480+0.221	17 08 00.11	−40 02 15.9	30.2	−18.9	−20.5,−13.7	21.9	8.7	−19	−19.7,−13.7	6.6	–			
G 346.481+0.132	17 08 22.72	−40 05 25.6	2.1	−5.5	−11.6,−4.3	2.7	<0.75		−155,185		<0.75		−200,140	
G 346.517+0.117	17 08 33.20	−40 04 14.3	0.8	−11	−11.2,−1.7	0.9	<0.70		−155,185		<0.75		−200,140	
G 346.522+0.085	17 08 42.29	−40 05 07.8	1.9	5.7	5.6,6.1	0.6	<0.70		−155,185		<0.55		−200,140	
G 347.230+0.016	17 11 11.18	−39 33 27.2	0.9	−68.9	−69.1,−68.7	0.3	<0.70		−155,185		<0.80		−200,140	
G 347.583+0.213[2]	17 11 26.72	−39 09 22.5	3.2	−102.3	−103.5,−94.4	6.3	0.8	−102.7	−102.8,−101.7	0.5	–			
G 347.628+0.149	17 11 50.92	−39 09 29.2	19.2	−96.5	−97.8,−91.7	6.9	<0.75		−155,185		<0.80		−200,140	
G 347.631+0.211	17 11 36.05	−39 07 07.0	5.8	−91.9	−93.4,−89.3	5.4	<0.70		−155,185		<0.75		−200,140	
G 347.817+0.018	17 12 58.05	−39 04 56.1	2.5	−24.1	−26.4,−23	4.3	<0.75		−155,185		<0.75		−200,140	
G 347.863+0.019[2]	17 13 06.23	−39 02 40.0	6.4	−34.7	−37.6,−28.1	8.7	1.6	−35.3	−36.5,−23.6	1.3	–			
G 347.902+0.052[2]	17 13 05.11	−38 59 35.5	5.4	−27.4	−30.8,−26.6	6.4	1.3	−27.3	−27.8,−27	0.7	–			

Table 7.1: – continued

Methanol maser (l, b) (degrees)	RA (J2000) (h m s)	Dec (J2000) (° ′ ″)	$S_{6.7}$ (Jy)	$Vp_{6.7}$	$Vr_{6.7}$	$I_{6.7}$ (Jy)	2008 June $S_{12.2}$	2008 June $Vp_{12.2}$	2008 June $Vr_{12.2}$	2008 June $I_{12.2}$	2008 December $S_{12.2}$	2008 December $Vp_{12.2}$	2008 December $Vr_{12.2}$	2008 December $I_{12.2}$
G 348.027+0.106	17 13 14.12	−38 51 38.8	3.1	−121.2	−122.4,−114.6	4.5	<0.70		−155,185		<0.80		−200,140	
G 348.195+0.768	17 11 00.20	−38 20 05.5	4.5	−0.8	−2.1,−0.5	1.9	0.5	−0.8	−0.9,−0.8	0.1	0.4	−0.9	−1,−0.8	0.1
G 348.550−0.979[2,8]	17 19 20.41	−39 03 51.6	35.9	−10	−19,−7	81	8.9	−10.1	−10.9,−9.4	3.7	–			
G 348.550−0.979n[2,8]	17 19 20.45	−39 03 49.4	21.3	−20	−23,−14	48.6	1	−22.1	−22.2,−21.8	0.3	–			
G 348.579−0.920	17 19 10.61	−39 00 24.2	0.7	−14.1	−15,−13.4	0.3	<0.75				<0.80		−200,140	
G 348.617−1.162	17 20 18.65	−39 06 50.8	47.6	−11.4	−21.4,−7.4	77.1	–				27.6	−11.5	−21.3,−9.9	39.2
G 348.654+0.244	17 14 32.37	−38 16 16.8	0.8	16.9	16.5,17.1	0.3	–				<0.55		−200,140	
G 348.723−0.078	17 16 04.77	−38 24 08.8	2.6	11.5	8.9,12	3.5	–				0.9	11.6	9.7,11.7	0.9
G 348.703−1.043[2,8]	17 20 04.06	−38 58 30.9	65	−3.5	−17.5,−2.6	212.9	–				34.5	−3.5	−16.3,−2.9	26
G 348.727−1.037[2,8]	17 20 06.54	−38 57 09.1	82.6	−7.4	−12.1,−6	149.3	–				13.3	−7.4	−9.1,−6.6	8.9
G 348.884+0.096	17 15 50.13	−38 10 12.4	12.2	−74.5	−77.1,−73.7	17.3	–				3.3	−74.4	−76.6,−74.1	2.7
G 348.892−0.180	17 17 00.23	−38 19 28.9	2.7	1.5	1.3,1.7	0.8	–				<0.55		−200,140	
G 349.067−0.017[2*]	17 16 50.74	−38 05 14.3	2.3	11.6	4.6,15.8	5.5	–				<0.55		−200,140	
G 349.092+0.105	17 16 24.74	−37 59 47.2	33.3	−76.5	−77.9,−73.4	22.3	–				<0.60		−200,140	
G 349.092+0.106	17 16 24.59	−37 59 45.8	11.2	−81.4	−82.2,−78.1	12.5	–				0.5	−80.4	−81.6,−80.2	0.2
G 349.151+0.021	17 16 55.88	−37 59 47.9	3.4	14.5	11.5,24.8	1.6	–				<0.60		−200,140	
G 349.579−0.679	17 21 05.44	−38 02 54.7	1.9	−24.9	−25.7,−24	1.8	–				<0.55		−200,140	
G 349.799+0.108	17 18 27.74	−37 25 03.5	3	−64.7	−65.2,−57.3	7.8	–				1.3	−59.5	−59.7,−59.1	0.6
G 349.884+0.231	17 18 12.37	−37 16 40.0	7	16.2	13.5,17.3	7.6	–				<0.55		−200,140	
G 350.011−1.342	17 25 06.54	−38 04 00.7	2.4	−25.8	−26.1,−25.3	0.9	–				<0.60		−200,140	
G 350.015+0.433	17 17 45.45	−37 03 11.9	7.2	−30.3	−36.3,−28.7	7.8	–				<0.55		−200,140	
G 350.104+0.084	17 19 26.68	−37 10 53.1	12.3	−68	−68.9,−67.6	6	–				<0.75		−200,140	
G 350.105+0.083[2]	17 19 27.01	−37 10 53.3	13.7	−74	−79.3,−60.3	57.6	–				1.4	−74.1	−74.8,−66.9	1.1
G 350.116+0.084	17 19 28.83	−37 10 18.8	13.3	−68	−68.9,−67	7.8	–				<0.60		−200,140	
G 350.116+0.220	17 18 55.11	−37 05 38.1	2.8	4.2	3.5,7.4	1.2	–				<0.60		−200,140	
G 350.189+0.003	17 20 01.41	−37 09 30.7	1.1	−62.5	−64.4,−62.2	0.4	–				<0.60		−200,140	
G 350.299+0.122	17 19 50.87	−36 59 59.9	31.3	−62.1	−69.1,−60.2	38.8	–				0.6	−63.6	−63.7,−63.5	0.1
G 350.340+0.141	17 19 53.43	−36 57 18.8	2.3	−58.3	−59.4,−57.1	1.2	–				0.6	−58.5	−58.5,−58.4	0.1
G 350.344+0.116	17 20 00.03	−36 58 00.1	21.2	−65.4	−66.1,−55.5	21.4	–				7.2	−65.4	−65.7,−64.9	3
G 350.356−0.068	17 20 47.55	−37 03 42.0	1.4	−67.6	−69.3,−66.2	1.2	–				<0.60		−200,140	
G 350.470+0.029	17 20 43.24	−36 54 46.6	1.4	−6.3	−11.8,−5.9	1.1	–				0.7	−6.2	−6.4,−6.1	0.1
G 350.520−0.350	17 22 25.32	−37 05 13.4	1.7	−24.6	−24.8,−13.8	0.9	–				<0.55		−200,140	
G 350.686−0.491[3]	17 23 28.63	−37 01 48.8	17.8	−13.7	−14.9,−13.6	10.6	–				12.7	−13.8	−15.1,−13.7	4
G 350.776+0.138	17 21 08.58	−36 35 58.8	0.6	38.7	33.5,42.5	0.5	–				<0.60		−200,140	
G 351.161+0.697	17 19 57.50	−35 57 52.8	17	−5.2	−12.2,−2.2	12	–				<0.75		−200,140	
G 351.242+0.670	17 20 17.84	−35 54 46.0	0.8	2.4	2.3,2.7	0.2	–				<0.80		−200,140	
G 351.251+0.652	17 20 23.87	−35 54 57.0	1	−7.1	−10.6,−7	0.4	–				<0.65		−200,140	
G 351.382−0.181	17 24 09.58	−36 16 49.3	19.7	−59.7	−68.4,−58.7	10.3	–				2	−59.7	−60.5,−59.4	0.7
G 351.417+0.645[2,7,8]	17 20 53.37	−35 47 01.2	3423.3	−10.4	−12.1,−6.1	2932.5	–				976.5	−10.4	−12.0,0.4	866.3
G 351.417+0.646[2,7,8]	17 20 53.18	−35 46 59.3	t	−11.2	−12,−7		–				692.5	−11.2	t	t
G 351.445+0.660[2,7,8]	17 20 54.61	−35 45 08.6	t	−9.2	−14,1		–				36.8	−9.3	−9.6,−0.2	19.2

Table 7.1: – continued

Methanol maser	RA	Dec					2008 June				2008 December			
(l, b) (degrees)	(J2000) (h m s)	(J2000) (° ′ ″)	$S_{6.7}$ (Jy)	$Vp_{6.7}$	$Vr_{6.7}$	$I_{6.7}$ (Jy)	$S_{12.2}$	$Vp_{12.2}$	$Vr_{12.2}$	$I_{12.2}$	$S_{12.2}$	$Vp_{12.2}$	$Vr_{12.2}$	$I_{12.2}$
G 351.581−0.353[pest*]	17 25 25.12	−36 12 46.1	47.5	−94.2	−100.4,−87	49.6	<0.75		−150,190		<0.80		−200,140	
G 351.611+0.172	17 23 21.25	−35 53 32.4	4	−43.6	−46.1,−31.8	11.6	–				–			
	2010 Mar						2	−37.3	−43.7,−35.7	2.0				
G 351.688+0.171	17 23 34.52	−35 49 46.3	41.5	−36.1	−47.6,−35.3	55.8	–				21	−36.2	−44.5,−35.3	14.3
G 351.775−0.536[2,10]	17 26 42.57	−36 09 17.6	231.4	1.3	−3.6,2.6	206.5	–				12.4	1.8	0.8,2.3	4.7
G 352.083+0.167	17 24 41.22	−35 30 18.6	6.8	−66.1	−67,−63.8	4.1	2.8	−66.2	−66.5,−65.7	1.1	–			
G 352.111+0.176	17 24 43.56	−35 28 38.4	7.5	−54.8	−60.9,−49.4	11.1	3.1	−54.1	−55,−53	2.8	–			
G 352.133−0.944	17 29 22.23	−36 05 00.2	16.3	−7.7	−18.5,−5.3	29.9	<0.75		−150,190		<0.80		−200,140	
G 352.517−0.155	17 27 11.34	−35 19 32.4	9.7	−51.2	−52.3,−48.4	11.3	<0.70		−150,190		<0.80		−200,140	
G 352.525−0.158	17 27 13.42	−35 19 15.5	0.6	−53	−55.4,−52.5	0.4	<0.75		−150,190		<0.80		−200,140	
G 352.584−0.185	17 27 29.58	−35 17 14.6	6.4	−85.7	−94.7,−78.4	5.3	<0.75		−150,190		<0.80		−200,140	
G 352.604−0.225	17 27 42.73	−35 17 34.2	3.3	−81.7	−84.9,−79.4	2.9	<0.75		−150,190		<0.80		−200,140	
G 352.624−1.077	17 31 15.31	−35 44 47.7	18.7	−5.9	−1.9,−6.9	15.1	<0.75		−150,190		<0.80		−200,140	
G 352.630−1.067	17 31 13.91	−35 44 08.7	184	−2.9	−7.5,−2.1	101.3	<0.75		−150,190		<0.80		−200,140	
G 352.855−0.201	17 28 17.59	−35 04 12.9	1.3	−51.3	−53.5,−50	1.4	<0.75		−150,190		<0.80		−200,140	
G 353.216−0.249	17 29 27.80	−34 47 47.3	0.6	−10.7	−23.1,−10.4	0.5	<0.75		−150,190		<0.80		−200,140	
G 353.273+0.641	17 26 01.58	−34 15 15.4	8.3	−4.4	−6.4,−2.8	7.8	<0.75		−150,190		<0.80		−200,140	
G 353.363−0.166	17 29 31.40	−34 37 40.3	2.8	−79	−80.7,−77.2	0.9	<0.70		−150,190		<0.80		−200,140	
G 353.370−0.091	17 29 14.27	−34 34 50.2	1.4	−44.7	−61.9,−41.3	2.4	<0.75		−150,190		0.6	−44.6	−44.7,−44.4	0.2
G 353.378+0.438	17 27 07.59	−34 16 50.5	1	−15.7	−16.2,−14.4	1.2	<0.75		−150,190		<0.55		−200,140	
G 353.410−0.360[2,8,9]	17 30 26.18	−34 41 45.6	t				–				<0.80		−200,140	
G 353.429−0.090	17 29 23.48	−34 31 50.3	13.4	−61.8	−65.6,−45.5	16.4	<0.75		−150,190		<0.80		−200,140	
G 353.464+0.562	17 26 51.53	−34 08 25.7	11.9	−50.3	−52.3,−49.6	9.6	<0.70		−150,190		<0.75		−200,140	
G 353.537−0.091	17 29 41.25	−34 26 28.4	2.5	−56.6	−58.3,−54	2.7	0.6	−56.6	−56.9,−55.1	0.2	0.8	−56.7	−56.9,−56.5	0.2
G 354.206−0.038	17 31 15.01	−33 51 15.1	1.1	−37.1	−37.2,−35.5	0.4	<0.75		−150,190		<0.80		−200,140	
G 354.308−0.110	17 31 48.56	−33 48 29.1	3.4	18.8	11.2,19.1	5.3	<0.75		−150,190		<0.55		−200,140	
G 354.496+0.083	17 31 31.77	−33 32 44.0	8.4	27	17.6,27.3	6.3	2.1	27	25.6,27.3	1.1	–			
G 354.615+0.472[2,8,9]	17 30 17.13	−33 13 55.1	166.8	−24.4	−27,−13.1	277.5	–				33.4	−16.5	−24.8,−15.5	16.2
G 354.701+0.299	17 31 12.06	−33 15 16.7	1.3	102.8	98.1,102.9	1	<0.75		−150,190		<0.80		−200,140	
G 354.724+0.300	17 31 15.55	−33 14 05.7	12.6	93.9	91.3,94.4	13	3.3	93.9	92.3,94.1	1.7	–			
G 355.184−0.419	17 35 20.49	−33 14 28.6	1.35	−1.42	−1.77,0.34	c	–				<0.70		−200,140	
G 355.343+0.148	17 33 28.84	−32 48 00.2	1.4	6	5,6.5	0.9	–				<0.55		−200,140	
G 355.344+0.147	17 33 29.06	−32 47 58.9	10.2	20	18.7,20.5	6.1	–				<0.60		−200,140	
G 355.346+0.149	17 33 28.91	−32 47 49.5	7.4	10.5	8.2,12.2	5.6	–				<0.60		−200,140	
G 355.538−0.105	17 34 59.60	−32 46 22.7	1.3	3.8	−3,4.7	2.4	–				<0.60		−200,140	
G 355.545−0.103	17 35 00.28	−32 45 58.1	1.2	−28.2	−30,−27.9	1	–				<0.80		−200,140	
G 355.642+0.398	17 33 15.40	−32 24 46.8	1.4	−7.9	−8.3,−7.6	0.8	–				<0.55		−200,140	
G 355.666+0.374	17 33 24.92	−32 24 21.1	2.5	−3.3	−4.2,0.6	2.1	<0.70		−150,190		<0.80		−200,140	
G 356.054−0.095	17 36 16.55	−32 20 02.7	0.5	16.7	16.5,17	0.2	<0.70		−150,190		<0.80		−200,140	
G 356.662−0.263	17 38 29.16	−31 54 38.8	8.4	−53.8	−56.4,−43.8	11.1	<0.75		−150,190		<0.55		−200,140	
G 357.558−0.321	17 40 57.19	−31 10 59.3	2.7	−3.9	−5,−0.5	1.5	<0.75		−150,190		<0.80		−200,140	
G 357.559−0.321	17 40 57.33	−31 10 56.9	2	16.2	15.6,17.8	1.9	0.9	16.1	15.9,16.2	0.2	0.7	16	15.9,16.2	0.2

Table 7.1: – continued

Methanol maser	RA	Dec					2008 June				2008 December			
(l, b) (degrees)	(J2000) (h m s)	(J2000) (° ′ ″)	$S_{6.7}$ (Jy)	$Vp_{6.7}$	$Vr_{6.7}$	$I_{6.7}$ (Jy)	$S_{12.2}$	$Vp_{12.2}$	$Vr_{12.2}$	$I_{12.2}$	$S_{12.2}$	$Vp_{12.2}$	$Vr_{12.2}$	$I_{12.2}$
G 357.922–0.337	17 41 54.94	–30 52 55.1	1	–4.6	–6,–4.4	0.8	<0.75		–150,190		–			
G 357.924–0.337	17 41 55.17	–30 52 50.2	2.3	–2.1	–4.3,2.9	1.7	0.7	–2.4	–2.6,–1.7	0.3	–			
G 357.965–0.164	17 41 20.14	–30 45 14.4	2.8	–8.6	–8.9,4.6	3.7	<0.75		–150,190		<0.80		–200,140	
G 357.967–0.163	17 41 20.26	–30 45 06.9	47.5	–3.1	–5.9,0.4	103.7	0.9	–2.9	–3.6,–2.5	0.2	1	–3	–8.8,–2.8	0.4
G 358.263–2.061	17 49 37.63	–31 29 18.0	19	5	1,6.2	17.1	0.5	1.9	1.5,1.9	0.1	0.5	1.7	1.5,1.7	0.1
G 358.371–0.468	17 43 31.95	–30 34 11.0	44	1.3	–0.9,13.2	30.8	1.9	1.4	1,1.6	0.7	8.1	1.3	0.8,2	3.2
G 358.386–0.483	17 43 37.83	–30 33 51.5	7	–6	–6.2,–5.8	1.9	<0.85		–150,190		<0.90		–200,140	
G 358.460–0.391	17 43 26.76	–30 27 11.3	0.9	3.3	–0.5,3.5	0.5	<0.70		–150,190		<0.80		–200,140	
G 358.460–0.393	17 43 27.24	–30 27 14.6	11.2	–7.3	–8.4,5.6	9.7	<0.70		–150,190		–			
G 358.721–0.126	17 43 02.31	–30 05 29.9	3	10.6	9.3,14.9	4.2	0.7	10.5	10.5,10.6	0.1	–			
G 358.809–0.085	17 43 05.40	–29 59 45.8	6.9	–56.2	–59.1,–51.2	6.6	0.3	–56.2	–56.2,–56.1	0.03	0.3	–56.2	–56.3,–56.1	0.1
G 358.841–0.737	17 45 44.29	–30 18 33.6	10.9	–20.6	–29.3,–17.6	6.7	3.2	–20.7	–21.3,–20.4	1.4	–			
G 358.906+0.106	17 42 34.57	–29 48 46.8	1.9	–17.9	–20.3,–17.2	1.7	<0.70		–150,190		0.7	–17.3	–18.2,–17.2	0.1
G 358.931–0.030	17 43 10.02	–29 51 45.8	5.9	–15.9	–22.2,–14.7	9	<0.75		–150,190		<0.80		–200,140	
G 358.980+0.084	17 42 50.44	–29 45 40.4	1.13	6.22	5.49,7.01	c	<0.75		–150,190		<0.75		–200,140	
G 359.138+0.031	17 43 25.69	–29 39 17.4	16.5	–3.9	–5,0.5	13.6	<0.75		–150,190		<0.80		–200,140	
G 359.436–0.104	17 44 40.60	–29 28 16.0	13.7	–52.3	–57.5,–50.5	17.8	<0.75		–150,190		0.5	–56.5	–56.5,–56.3	0.1
G 359.436–0.102	17 44 40.21	–29 28 12.5	73.5	–46.8	–53,–45.5	49.8	<0.75		–150,190		<0.80			
G 359.615–0.243[2,8]	17 45 39.09	–29 23 30.0	38.6	19.3	18.1,25.1	56	–				5.7	19.3	19.1,24.5	6.4
G 359.938+0.170	17 44 48.55	–28 53 59.4	2.3	–0.5	–0.8,–0.3	0.7	<0.70		–150,190		<0.80		–200,140	
G 359.970–0.457	17 47 20.17	–29 11 59.4	2.4	23.1	22.8,23.2	0.7	<0.75		–150,190		<0.80		–200,140	
G 0.092–0.663	17 48 25.90	–29 12 05.9	18.9	23.8	9.8,25.4	33.7	–				6.3	23.5	21,23.9	3.9
G 0.167–0.446	17 47 45.46	–29 01 29.3	1.3	13.8	11.9,16.5	0.6	<0.70		–150,190		<1.25		–200,140	
G 0.212–0.001[1]	17 46 07.63	–28 45 20.9	3.3	49.5	42.1,50.3	4.8	0.8	49.4	48.9,49.6	0.5	–			
G 0.315–0.201[1,3]	17 47 09.13	–28 46 15.7	67.9	19.4	14.6,28	70.6	2.4	18.2	17.7,20	1.9	–			
G 0.316–0.201	17 47 09.33	–28 46 16.0	0.6	21	20.8,22.7	0.4	<0.55		–150,190		–			
G 0.376+0.040	17 46 21.41	–28 35 40.0	0.6	37.1	37,37.3	0.2	<0.75		–150,190		<0.80		–200,140	
G 0.409–0.504	17 48 33.48	–28 50 52.5	2.6	25.4	22.5,26.6	1.9	<0.75		–150,190		<0.80		–200,140	
G 0.475–0.010	17 46 47.07	–28 32 06.9	3.1	28.8	25.8,33.2	4.8	<0.75		–150,190		<0.80		–200,140	
G 0.496+0.188 [1,3]	17 46 03.96	–28 24 52.8	24.5	0.9	–12.4,2.1	50.7	17.7	1	–9.7,1.5	15.8	–			
G 0.546–0.852[1,2,4,8]	17 50 14.53	–28 54 31.2	61.9	11.8	8,20.3	200.7	3.9	18.4	13.7,19.2	2.5	–			
G 0.645–0.042	17 47 18.65	–28 24 25.0	54.4	49.5	46,53		t				–			
G 0.647–0.055	17 47 22.04	–28 24 42.6	2		49,52		t				–			
G 0.651–0.049[2,8]	17 47 21.12	–28 24 18.2	21.5	48.3	46,49		t				–			
G 0.657–0.041	17 47 20.05	–28 23 46.5	1.8		48,56		t				–			
G 0.665–0.036[7]	17 47 20.04	–28 23 12.8	2.6	60.4	58,62		t				–			
G 0.666–0.029	17 47 18.64	–28 22 54.6	34.4	70.5	68,73		t				–			
G 0.667–0.034	17 47 19.87	–28 23 01.3	0.4		49,56		t				–			
G 0.672–0.031	17 47 20.04	–28 22 41.3	7.3	58.2	55,59		t				–			
G 0.673–0.029	17 47 19.54	–28 22 32.6	0.4		65.5,66.5		t				–			
G 0.677–0.025	17 47 19.28	–28 22 14.8	4.9	73.3	70,77		t				–			

Table 7.1: – continued

Methanol maser	RA	Dec					2008 June				2008 December			
(l, b) (degrees)	(J2000) (h m s)	(J2000) (° ′ ″)	$S_{6.7}$ (Jy)	$Vp_{6.7}$	$Vr_{6.7}$	$I_{6.7}$ (Jy)	$S_{12.2}$	$Vp_{12.2}$	$Vr_{12.2}$	$I_{12.2}$	$S_{12.2}$	$Vp_{12.2}$	$Vr_{12.2}$	$I_{12.2}$
G 0.695−0.038	17 47 24.74	−28 21 43.6	32.3	68.6	64,75		<0.60		−150,190		–			
G 0.836+0.184	17 46 52.86	−28 07 34.8	6.6	3.5	−2.2,4.1	3.7	<0.50		−150,190		0.6	3.5	−2.2,3.6	0.1
G 1.008−0.237	17 48 55.29	−28 11 47.9	13.6	1.6	1,7.4	10.1	<0.75		−150,190		<0.80		−200,140	
G 1.147−0.124	17 48 48.53	−28 01 11.2	3	−15.3	−20.7,−14.7	4	<0.50		−150,190		0.5	−19.4	−19.5,−19.4	0.1
G 1.329+0.150	17 48 10.31	−27 43 20.7	2.1	−12.2	−12.3,−11.9	0.6	<0.70		−150,190		<0.80		−200,140	
G 1.719−0.088	17 49 59.84	−27 30 36.9	7.8	−8.1	−8.4,−2.3	6.7	0.8	−8	−8.1,−7.8	0.2	–			
G 2.143+0.009	17 50 36.14	−27 05 46.5	7.1	62.6	53.4,64.7	18.3	<0.70		−150,190		<0.80		−200,140	
G 2.521−0.220	17 52 21.17	−26 53 21.1	1	−6.1	−7.2,4.4	0.8	<0.70		−150,190		<0.75		−200,140	
G 2.536+0.198 [1]	17 50 46.48	−26 39 44.9	29.4	3.1	2.2,20.3	52.8	3.7	6.9	3.3,7.2	2.6	–			
G 2.591−0.029	17 51 46.69	−26 43 51.2	1.8	−8.3	−9,−4	2.1	<0.70		−150,190		<0.80		−200,140	
G 2.615+0.134	17 51 12.30	−26 37 37.2	1.2	94.1	93.7,103.7	1.9	0.6	94.2	94.1,94.3	0.1	<0.55		−200,140	
G 2.703+0.040	17 51 45.98	−26 35 56.7	9	93.5	92.2,97.8	16.2	2.6	93.6	92.9,94.8	1.3	–			
G 3.253+0.018	17 53 05.96	−26 08 13.0	3.5	2.2	−1,2.9	5.3	0.9	2.4	−0.3,2.6	0.6	–			
G 3.312−0.399	17 54 50.11	−26 17 51.5	1.2	0.4	0.2,9	0.8	<0.70		−150,190		<0.75		−200,140	
G 3.442−0.348	17 54 56.11	−26 09 35.6	1.1	−35.2	−35.3,−35	0.3	<0.70		−150,190		<0.75		−200,140	
G 3.502−0.200	17 54 30.06	−26 01 59.4	1.6	43.9	43.6,45.3	0.9	<0.70		−150,190		0.4	43.8	43.6,43.9	0.1
G 3.910+0.001	17 54 38.75	−25 34 44.8	5	17.8	16.9,24	4.1	<0.70		−145,195		<0.75		−200,140	
G 4.393+0.079	17 55 25.77	−25 07 23.6	6.7	1.9	0.2,9.2	11.4	2.1	1.9	0.5,2.2	1.6	–			
G 4.434+0.129	17 55 19.74	−25 03 44.8	3.3	−1	−1.3,13.8	2.2	<0.70		−145,195		<0.75		−200,140	
G 4.569−0.079	17 56 25.30	−25 03 03.7	0.4	9.5	9.2,9.6	0.1	<0.70		−145,195		<0.75		−200,140	
G 4.586+0.028	17 56 03.23	−24 58 55.9	1.2	26.1	14.2,26.9	1.4	<0.75		−145,195		<0.75		−200,140	
G 4.676+0.276	17 55 18.34	−24 46 45.3	2.1	4.5	−5.1,5.5	3.4	<0.75		−145,195		<0.80		−200,140	
G 4.866−0.171	17 57 25.96	−24 50 24.4	0.4	5.3	5.2,5.5	0.1	–				<0.55		−200,140	
G 5.618−0.082	17 58 44.78	−24 08 40.1	3.4	−27.1	−27.5,−18.3	4.7	<0.75		−145,190		<0.55		−200,140	
G 5.630−0.294	17 59 34.60	−24 14 23.7	1.3	10.5	9.4,21.6	3	0.8	10.6	9.6,11	0.7	–			
G 5.657+0.416	17 56 56.53	−23 51 42.0	1.7	20	13,25.1	2.8	<0.70		−145,195		<0.75		−200,140	
G 5.677−0.027	17 58 39.98	−24 03 57.2	0.8	−11.7	−12.5,−11.4	0.4	<0.70		−145,195		<0.75		−200,140	
G 5.885−0.393	18 00 30.65	−24 04 03.4	0.48	6	6.7,7.5	1	<0.75		−145,195		<0.80		−200,140	
G 5.900−0.430	18 00 40.87	−24 04 20.6	6.2	10	0.7,10.6	6.1	<0.75		−145,195		<0.55		−200,140	
G 6.189−0.358	18 01 02.16	−23 47 10.8	228.6	−30.1	−37.7,−27.8	193	5.5	−30.6	−34.4,−30.1	2.4	–			
G 6.368−0.052	18 00 15.82	−23 28 43.8	1.5	144.1	135.8,147.7	2.7	<0.70		−145,195		<0.75		−200,140	
G 6.539−0.108	18 00 50.86	−23 21 29.8	0.6	13.1	5.9,14.9	0.7	<0.70		−145,195		<0.75		−200,140	
G 6.588−0.192	18 01 16.09	−23 21 27.3	8	5.1	3.1,7.2	9.6	2.9	4.9	4.3,5.9	2.7	–			
G 6.610−0.082 [1]	18 00 54.03	−23 17 03.1	23.4	0.8	0.4,10.8	14.8	10.7	0.8	0.4,1.3	4.7	–			
G 6.795−0.257 [3]	18 01 57.75	−23 12 34.9	91.1	16.3	12.2,31.4	268.1	18	15.6	14.9,27.4	16.3	–			
G 6.881+0.093	18 00 49.38	−22 57 42.6	3.1	−2.2	−3.6,−2	1.6	<0.70		−145,195		<0.75		−200,140	
G 7.166+0.131	18 01 17.48	−22 41 44.0	2.6	85.7	74.4,90.2	4.1	<0.70		−145,195		<0.80		−200,140	
G 7.601−0.139	18 03 14.43	−22 27 00.9	8.7	154.6	151.3,156.3	8.4	<0.75		−145,195		<1.25		−200,140	
G 7.632−0.109	18 03 11.63	−22 24 32.4	6.5	157	146.7,158.5	8.7	2.7	156.9	149.4,158.4	1.7	–			
G 8.139+0.226	18 03 00.75	−21 48 09.9	11.4	19.9	19,21	7.6	<0.55		−145,195		<0.80		−200,140	
G 8.317−0.096	18 04 36.02	−21 48 19.6	4.5	47	44.8,50.5	5.6	1.1	47.6	46.7,48.5	1.1	–			
G 8.669−0.356 [1]	18 06 18.99	−21 37 32.2	10	39.2	36,39.9	6.5	0.4	39.3	39.3,39.4	0.05	<1.15		−200,140	

Table 7.1: – continued

Methanol maser	RA	Dec					2008 June				2008 December			
(l, b) (degrees)	(J2000) (h m s)	(J2000) (° ′ ″)	$S_{6.7}$ (Jy)	$Vp_{6.7}$	$Vr_{6.7}$	$I_{6.7}$ (Jy)	$S_{12.2}$	$Vp_{12.2}$	$Vr_{12.2}$	$I_{12.2}$	$S_{12.2}$	$Vp_{12.2}$	$Vr_{12.2}$	$I_{12.2}$
G 8.683–0.368[1,2,4,8]	18 06 23.49	–21 37 10.2	108.8	43.1	40.2,45.6	101	8.1	44.1	40.9,45.4	10.4	–			
G 8.832–0.028	18 05 25.67	–21 19 25.1	159.1	–3.8	–6.2,5.6	357.7	37	–5.2	–5.6,4.3	54.9	–			
G 8.872–0.493	18 07 15.34	–21 30 53.7	33.9	23.3	22.8,26.8	30.5	<0.70		–140,200		<0.75		–200,140	
G 9.215–0.202	18 06 52.84	–21 04 27.5	12	45.5	36.7,49.8	13.6	0.6	46.7	41.3,46.8	0.2	<0.80		–200,140	
G 9.621+0.196 [1,2,4,5,8,9]	18 06 14.67	–20 31 32.4	5240	1.3	–3.2,8.9	2211	401	1.4	–3,5.8	202.8	–			
G 9.619+0.193 [1]	18 06 14.92	–20 31 44.3	76.3	5.3	5.1,6.7	35.9	0.4	5.8	5.7,5.9	0.1	–			
G 9.986–0.028[1]	18 07 50.12	–20 18 56.5	67.6	42.2	40.6,51.4	85.2	1	47	44.2,47.2	0.5	–			
G 10.205–0.345	18 09 28.43	–20 16 42.5	2	6.6	6.3,10.4	1.1	–				<0.60		–200,140	
G 10.287–0.125	18 08 49.36	–20 05 59.0	8.1	8	1.7,8.5	11.4	<0.50		–140,200		<0.80		–200,140	
G 10.299–0.146	18 08 55.54	–20 05 57.5	0.9	19.9	19.3,20.3	0.7	<0.55		–140,200		<0.80		–200,140	
G 10.320–0.259	18 09 23.30	–20 08 06.9	9.5	39	25.6,39.9	12.8	3.9	36.3	35.9,39.2	1.9	–			
G 10.323–0.160[1]	18 09 01.46	–20 05 07.8	90	11.5	2.4,17.8	147.7	2.3	10.2	7.4,12.4	1.4	5.6	10.2	7.1,12.9	5.1
G 10.342–0.142	18 08 59.99	–20 03 35.4	15.1	15.4	7,17	22.4	–				5.2	7.5	7.1,8.6	2.7
G 10.35–0.13	18 08 58.87	–20 02 54.8	0.8	50	49.6,50.9	0.3	–							
	2010 Mar						<0.80		–160,180					

7.5 Individual sources

Here we draw attention to specific sources for which the information in Table 7.1 or Fig. 7.1 does not adequately describe them. Complex situations where more than one 12.2 GHz methanol maser is located within close proximity are discussed, particularly where there is no clear separation in velocity between sources. Variable sources (particularly those 12.2 GHz sources that have varied by more than 20 % between 2008 June and December), sources with interesting histories and associations with other maser species are also highlighted. Instances where the flux density of the 12.2 GHz methanol emission surpasses that of the 6.7 GHz counterpart are of particular interest and are noted below.

G 263.250+0.514. This new weak 12.2 GHz methanol maser is associated with the strongest 6.7 GHz methanol maser feature and almost doubled in strength between 2008 June (0.4 Jy) and December (0.7 Jy). This source also exhibits OH and water masers (Chapter 6; Caswell (1998)).

G 264.289+1.469. Associated with a weak 6.7 GHz methanol maser (0.5 Jy) this is a surprising new detection at 12.2 GHz. While the 12.2 GHz emission peaks at a mere 0.3 Jy (2008 June), the velocity of the emission matches that of the 6.7 GHz counterpart, leaving little doubt that it is real. Observations in 2008 December failed to detect any emission above a 5-σ detection limit of 0.8 Jy.

G 293.723–1.742. In 2008 June a 12.2 GHz methanol maser was detected towards this 6.7 GHz maser with a peak flux density the same as that of the 6.7 GHz maser at 0.6 Jy. In 2008 December no 12.2 GHz emission was detected above a 5-σ detection limit of 0.8 Jy.

G 298.632–0.362. Observations in 2008 June revealed a weak 12.2 GHz maser detected at 0.3 Jy (just shy of 3-σ) towards a 1.3 Jy 6.7 GHz source. However, given the matching velocities of the two methanol transitions, there is little doubt that the detection is authentic. Observations in 2008 December with a shorter integration time than the 2008 June observations failed to detect any

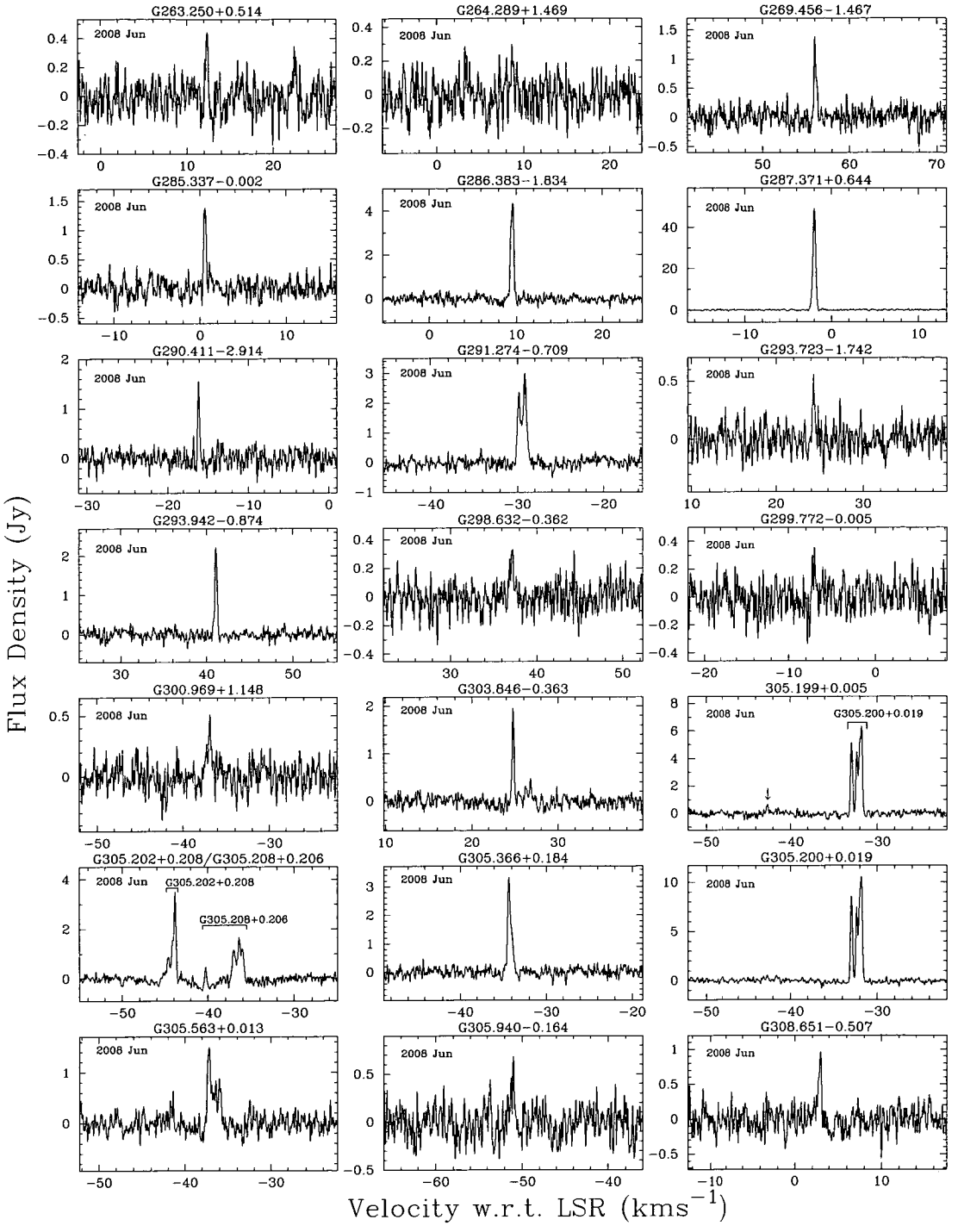

Figure 7.1: *Spectra of the 12.2 GHz methanol masers detected towards 6.7 GHz MMB sources.*

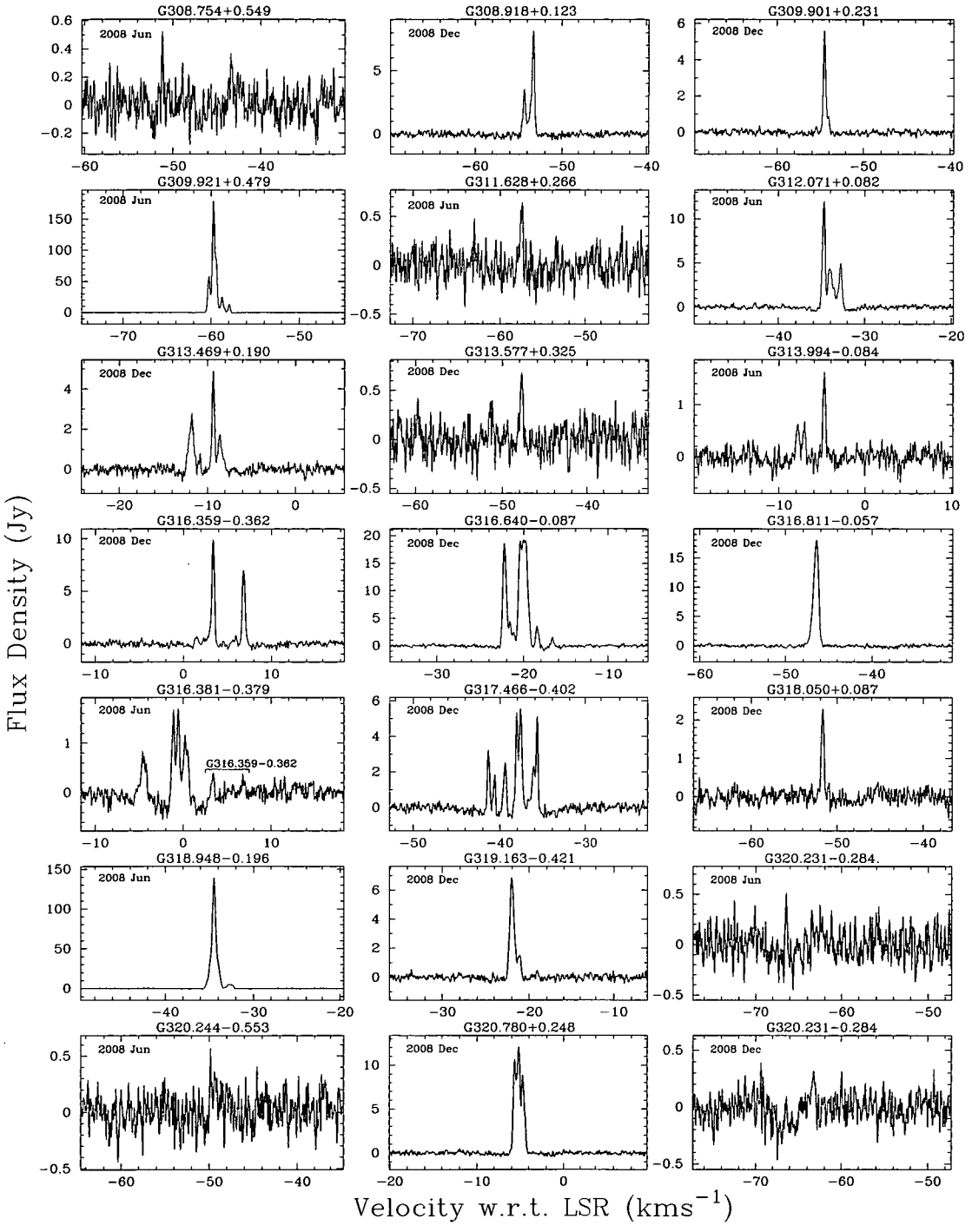

Figure 7.1: -continuued

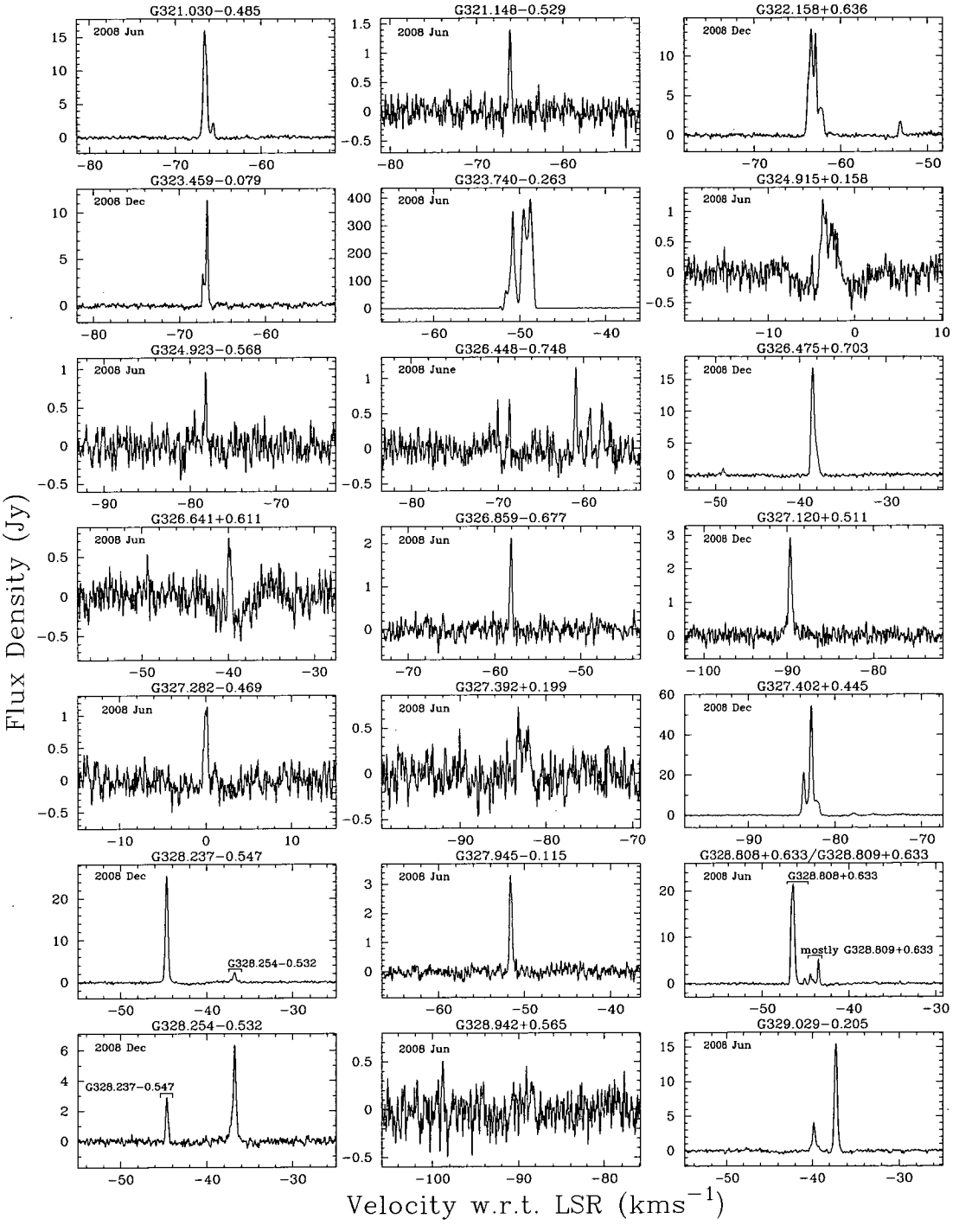

Figure 7.1: –continuued

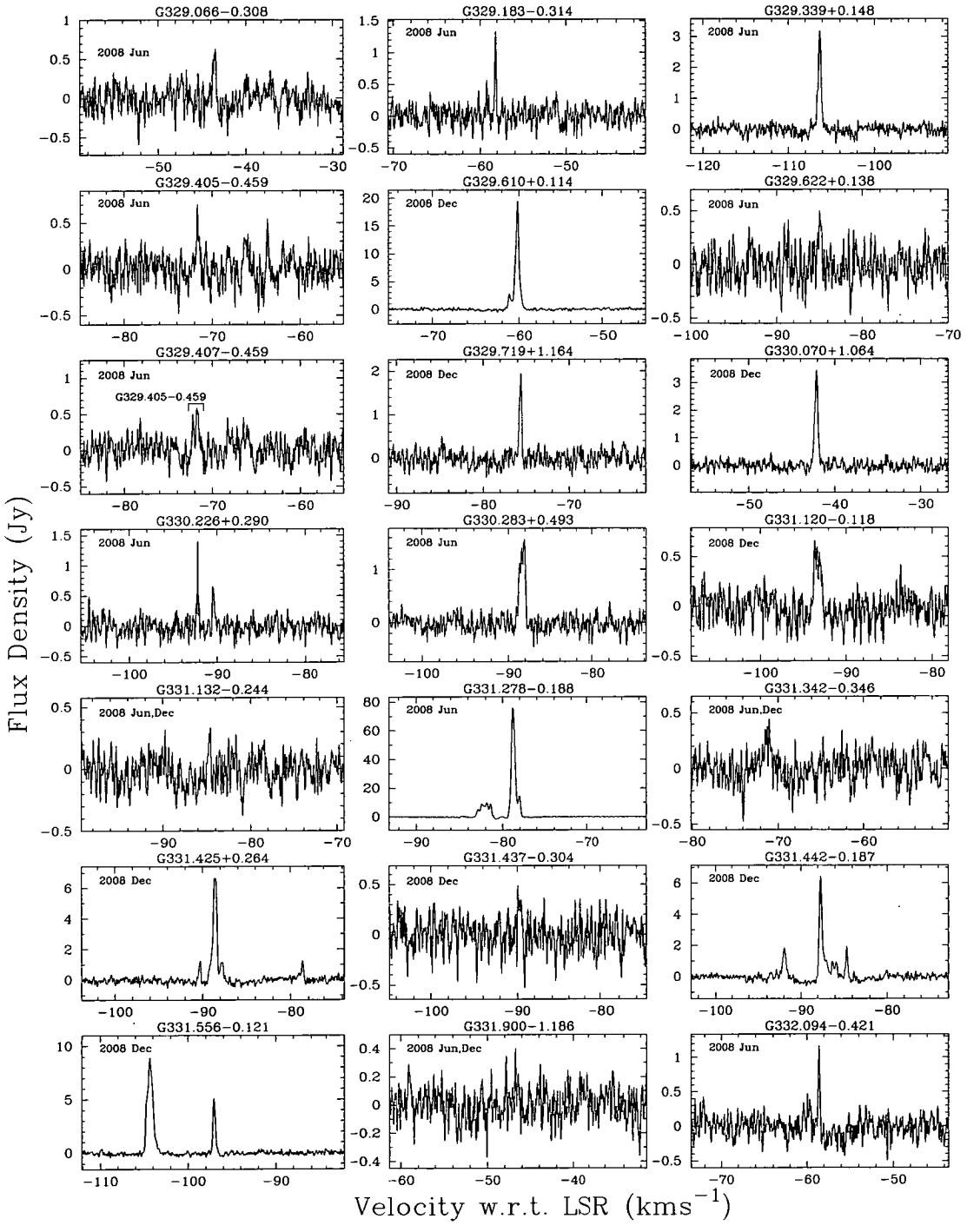

Figure 7.1: –continuued

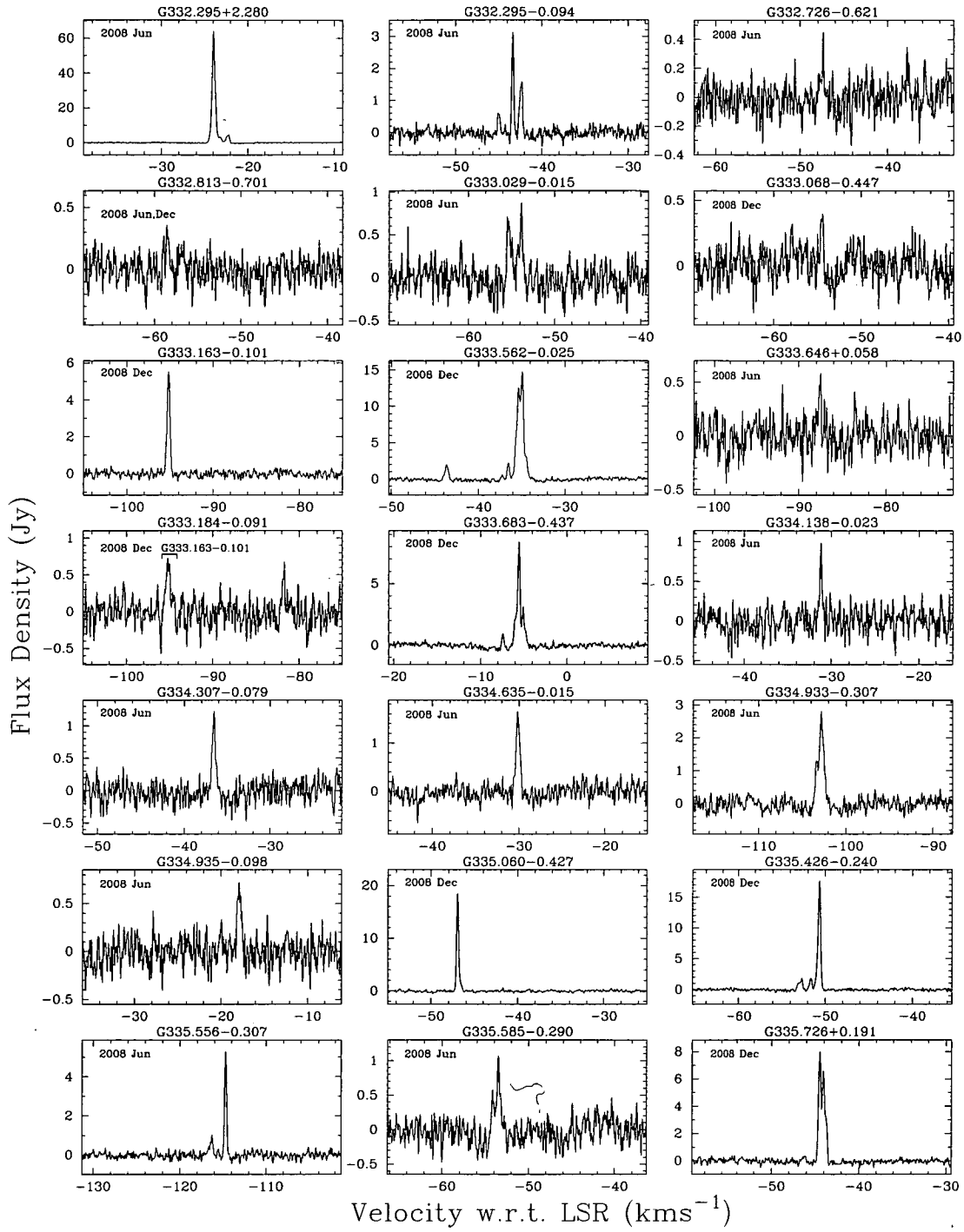

Figure 7.1: –continuued

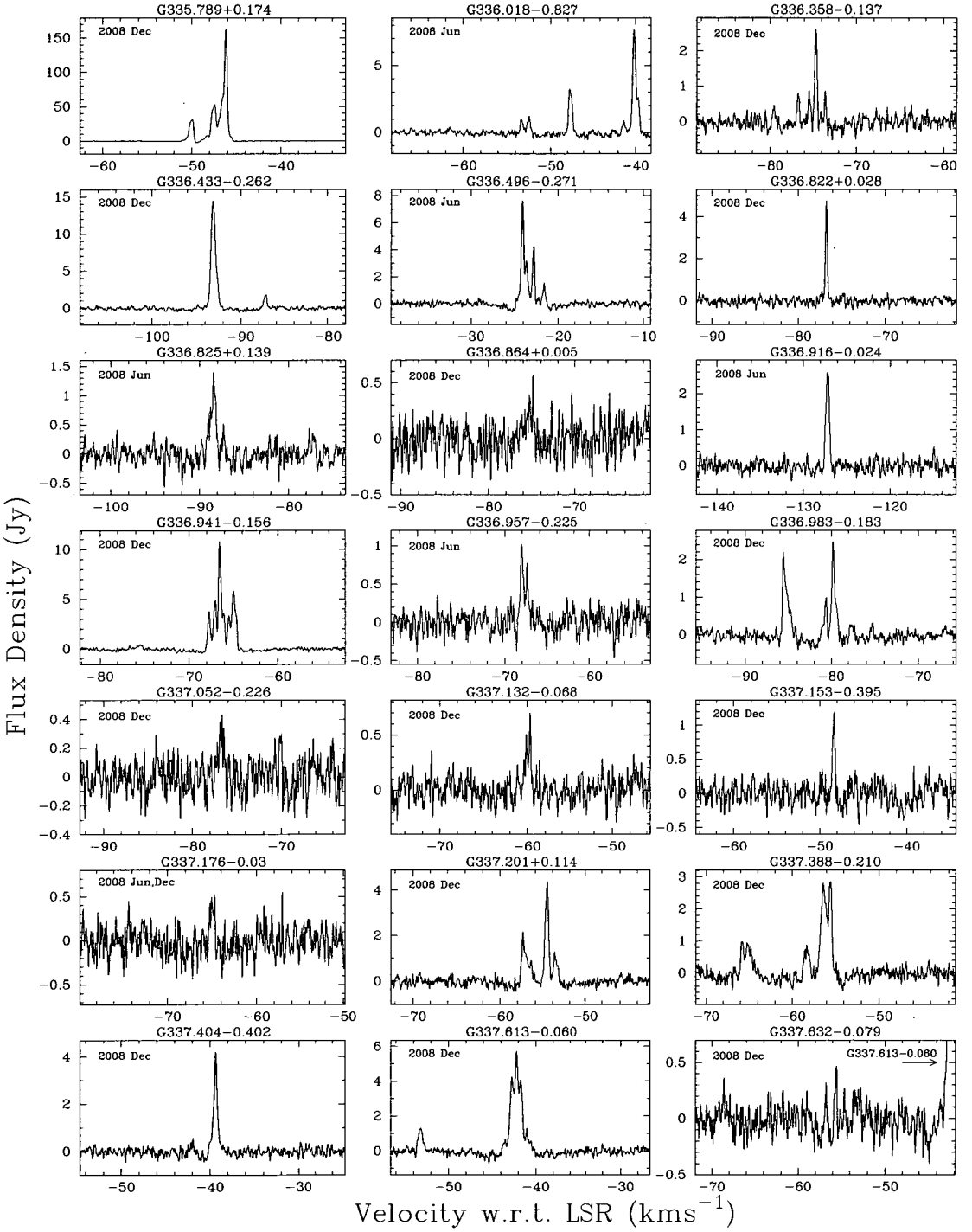

Figure 7.1: –continuued

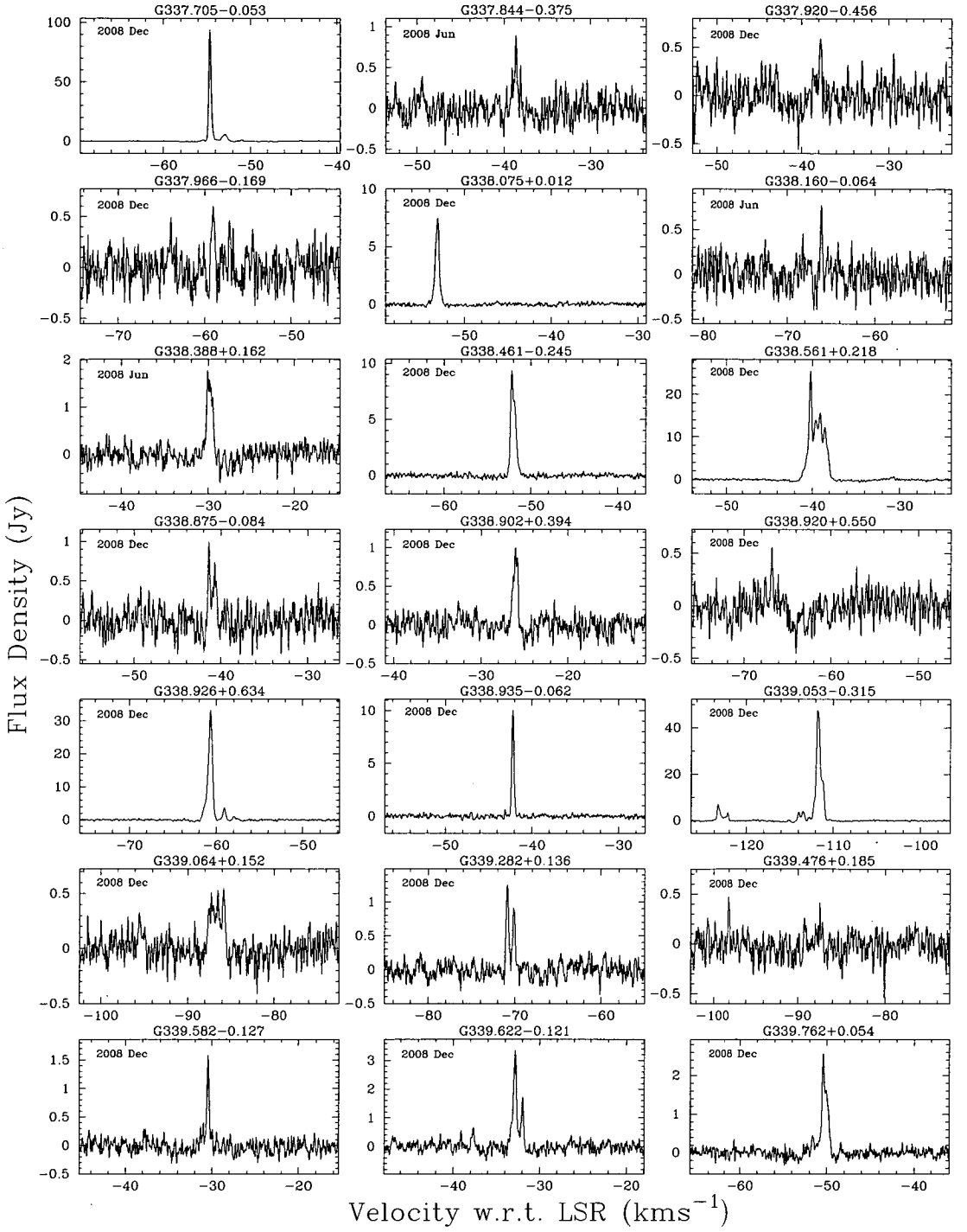

Figure 7.1: –continued

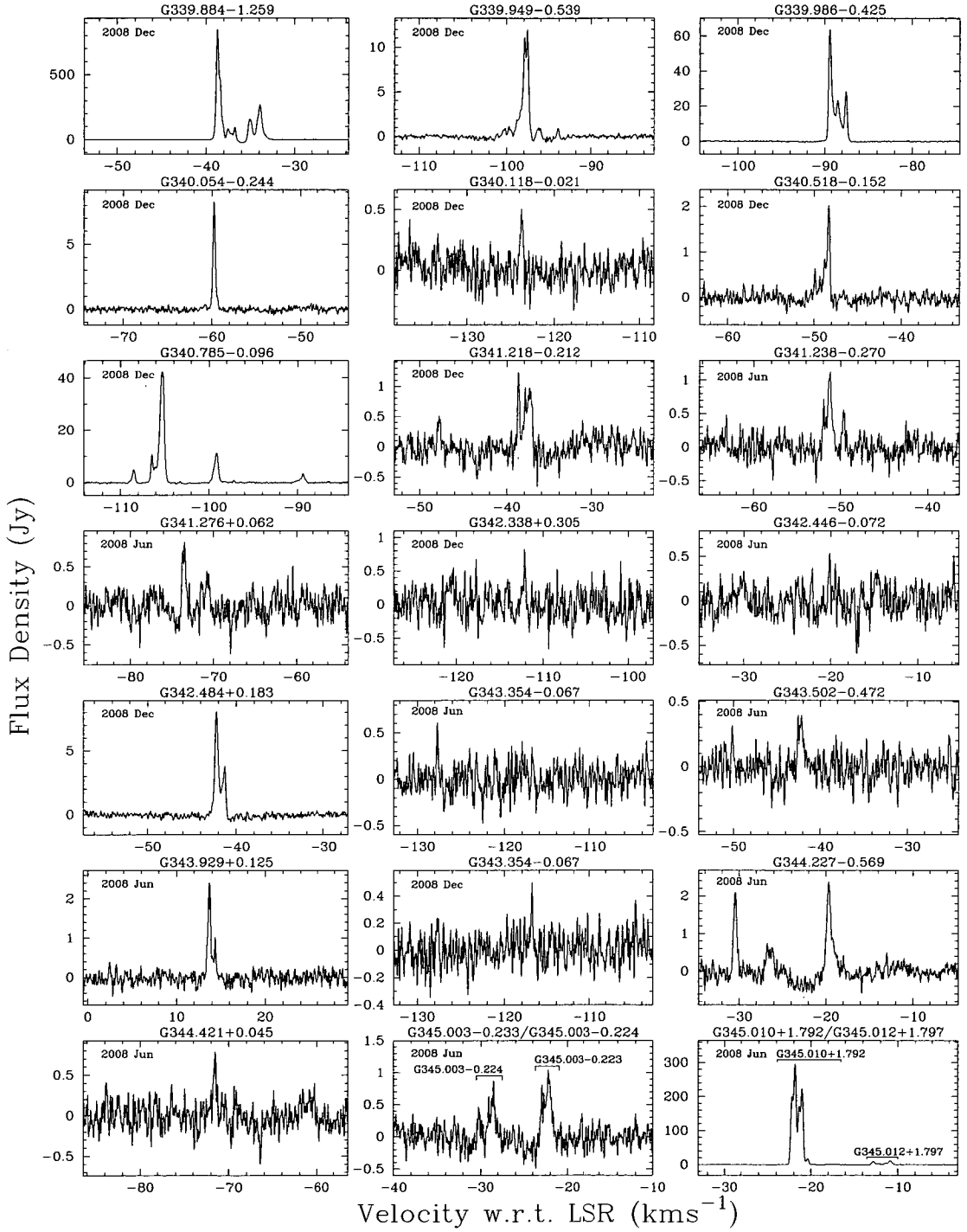

Figure 7.1: -continuued

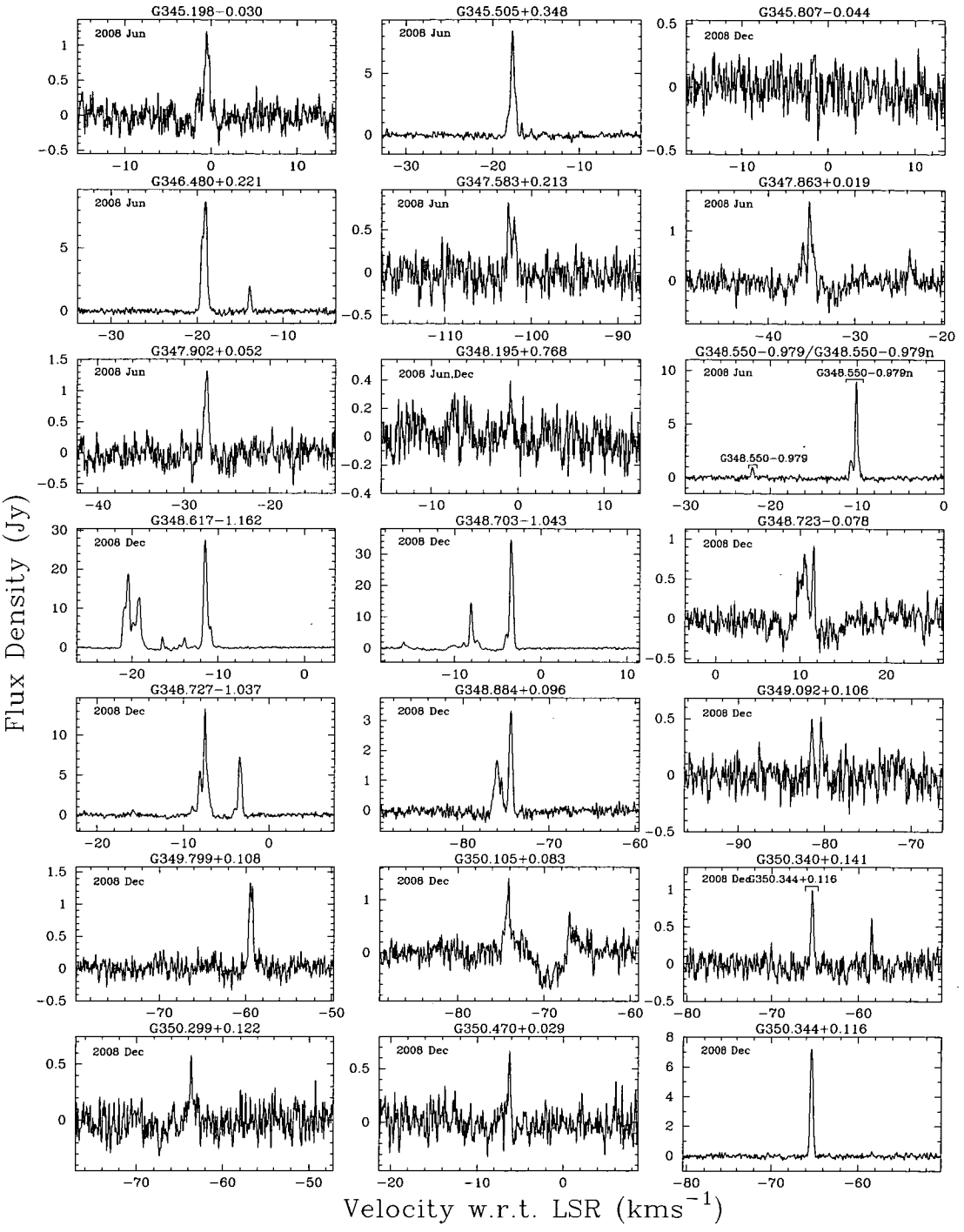

Figure 7.1: –continued

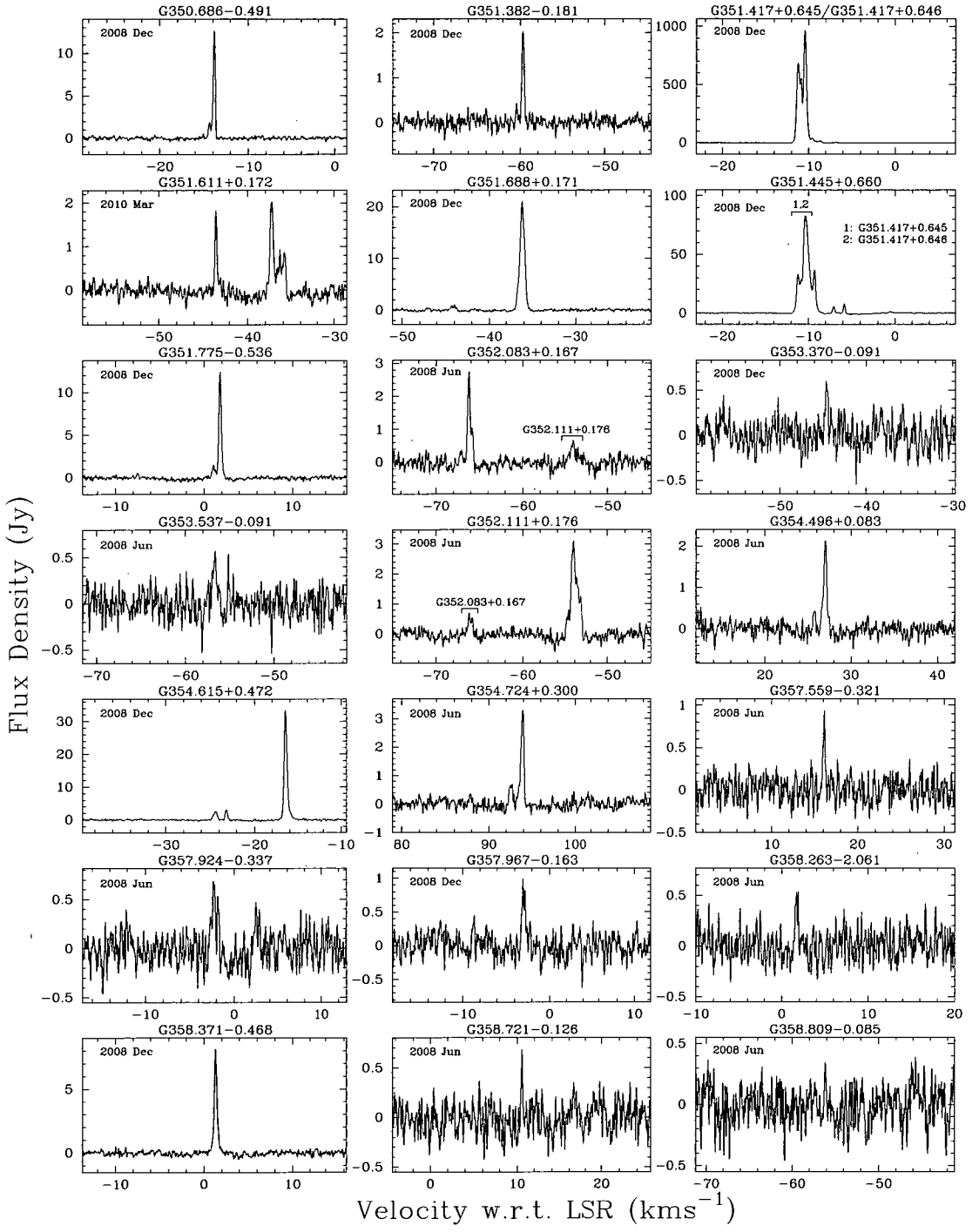

Figure 7.1: –continuued

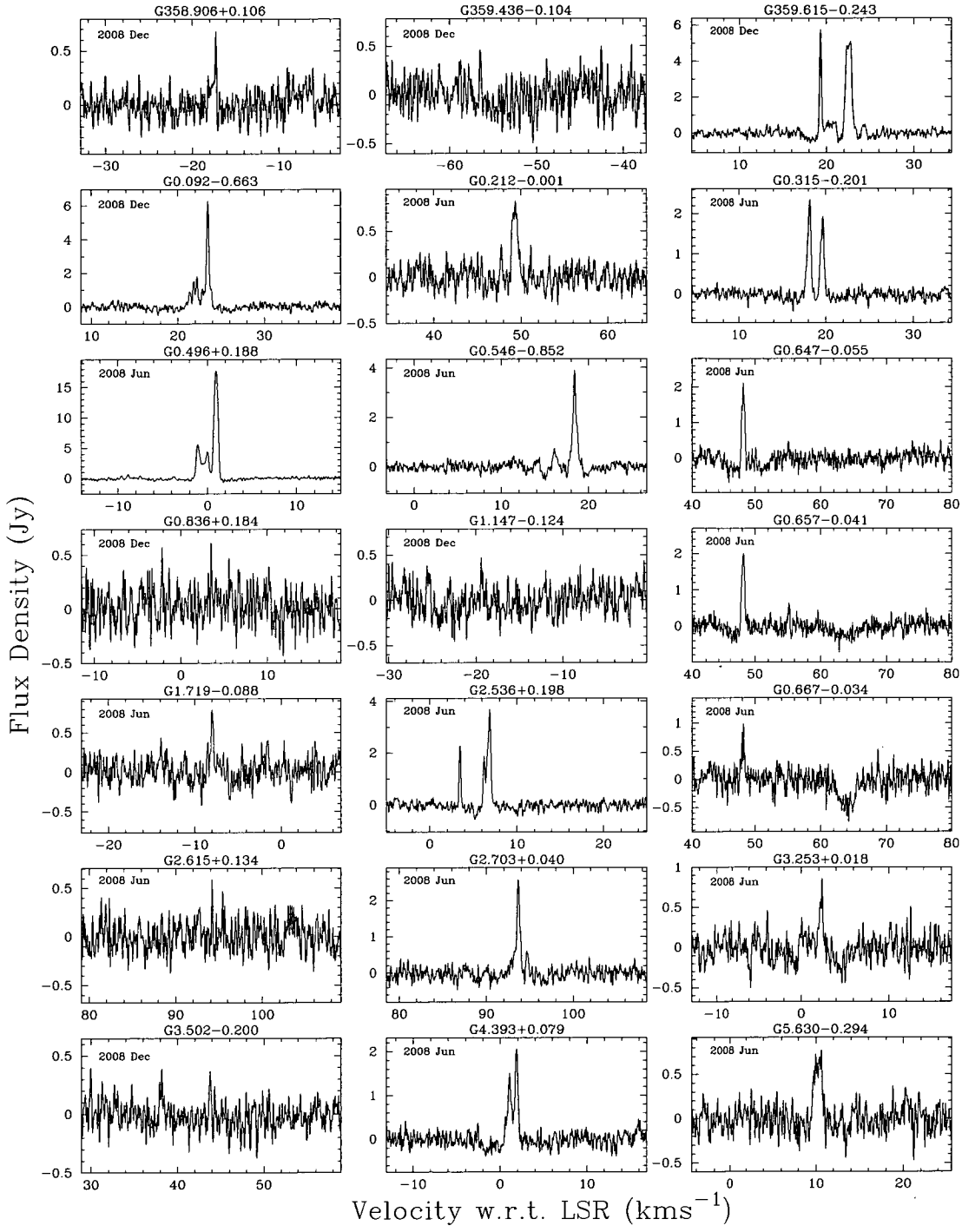

Figure 7.1: –continuued

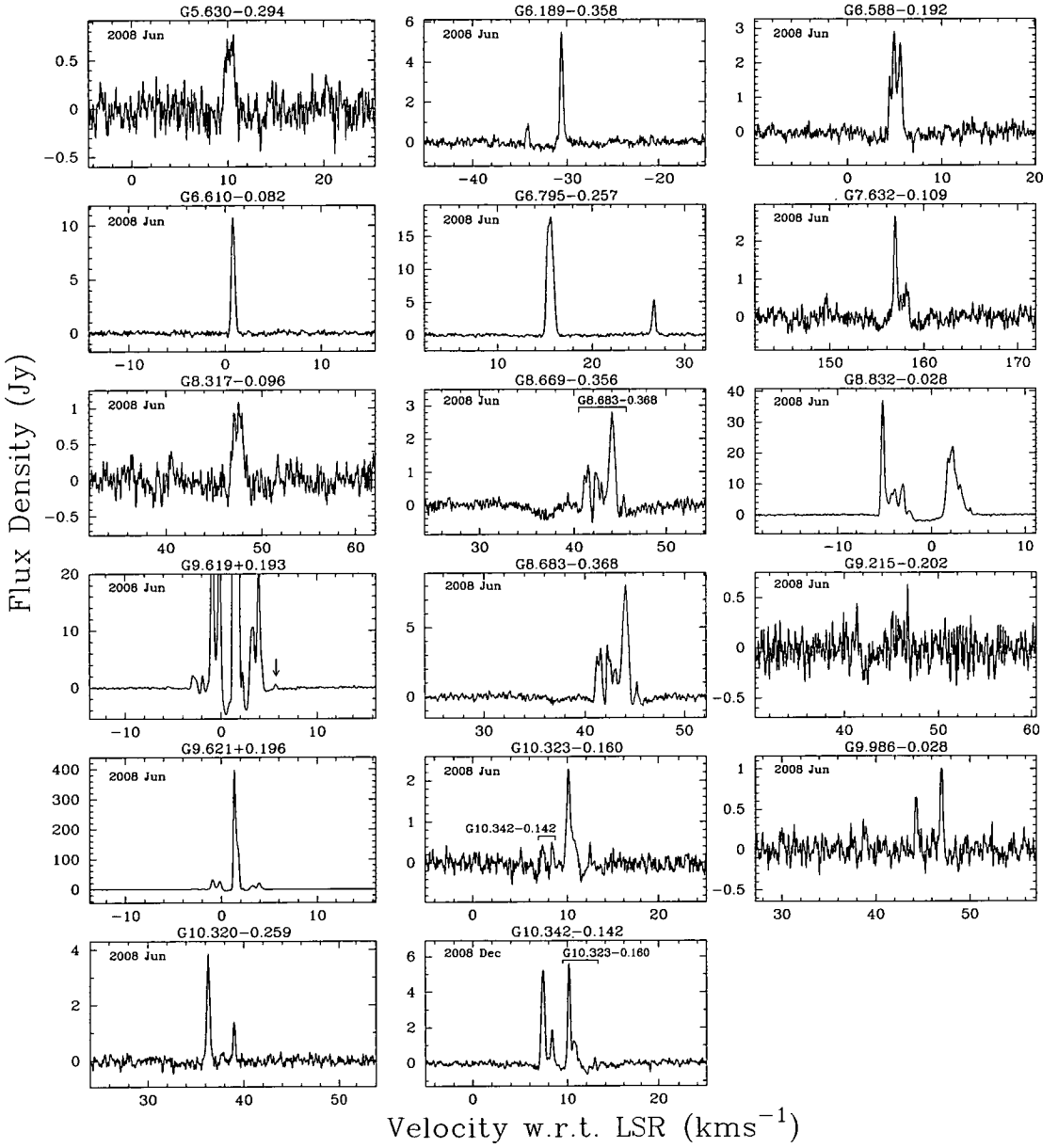

Figure 7.1: –continuued

emission above a 5-σ detection limit of 0.85 Jy.

G 299.772–0.005. While this source is only detected at a 3.6-σ level, it is clearly visible at the velocity of the 6.7 GHz source peak. No convincing emission was detected in 2008 Dec.

G 305.202+0.208 and G 305.208+0.206. These nearby sources were observed during both 2008 June and December. G 305.208+0.206 showed little variation between the two epochs, while G 305.202+0.208 halved in flux density between the observations in June and those in December (from 3.5 to 1.8 Jy). G 305.208+0.206 is associated with both OH and water masers (Caswell (1998);Chapter 6).

G 305.366+0.184. This 12.2 GHz source is associated with a 6.7 GHz secondary feature and shows stronger emission at 12.2 than 6.7 GHz (see Fig. 7.8). The 6.7 GHz observations were carried out on 2008 March 13, just over three months prior to the 12.2 GHz observations. While it is possible that variability between the epochs can account for this unusual circumstance, this source is worthy of concurrent follow up observation at both frequencies.

G 305.940–0.164. This weak 6.7 GHz methanol maser (0.8 Jy) showed 12.2 GHz emission (0.7 Jy) of comparable strength in 2008 June but no hint of a detection in 2008 December.

G 308.754+0.549. This 6.7 GHz methanol maser exhibited 12.2 GHz methanol maser emission at the velocities of two of its secondary features in 2008 June, but no believable emission in 2008 December. This source is associated with both OH and water masers (Caswell (1998);Chapter 6).

G 308.918+0.123. 12.2 GHz observations towards this source were carried out during 2008 December and showed stronger emission than was present at 6.7 GHz in 2009 March 12, almost three months later. Like G 305.366+0.184, this source needs further observations at both frequencies to determine if this

is due to variability. This source exhibits both OH and water maser emission (Caswell (1998);Chapter 6).

G 311.628+0.266. This source was observed at 12.2 GHz during both 2008 June and December and showed a moderate level of variability, increasing in flux density from 0.6 to 0.9 Jy.

G 317.466–0.402. The 12.2 GHz emission (observed 2008 December) associated with this source is stronger than its 6.7 GHz counterpart (observed 2008 Aug 19) for two features between –36.5 and –35.6 km s^{-1}.

G 319.163–0.42. The peak of the 12.2 GHz emission associated with this source is associated with a secondary feature in the 6.7 GHz spectrum and is stronger. The 6.6 GHz observations were carried out during 2008 Aug 20, four months prior to the 12.2 GHz follow up observations.

G 320.231–0.284. Spectra of the 12.2 GHz emission from both 2008 June and December are shown in Fig. 7.1, allowing the variability between the two epochs to be seen. Weak emission was detected at both epochs from different features, showing variability of at least a factor of two. Both OH and water masers are also coincident with this methanol maser site (Caswell (1998);Chapter 6).

G 320.224–0.562. 12.2 GHz emission was detected towards this relatively weak 6.7 GHz source (1.5 Jy) in 2008 June but no hint of emission was visible in 2008 December (5-σ detection limit of 0.55 Jy).

G 320.263–0.534. This 6.7 GHz methanol maser was listed in the MMB catalogue as of 2010 May, however, inspection of the spectra associated with this source together with nearby masers failed to show any features uniquely associated with this position. Due to this, along with the non-detection at 12.2 GHz, we have excluded this source from our detection statistics.

G 326.641+0.661. The 12.2 GHz emission detected towards this source in 2008 June consisted of a single spectral feature at a velocity of –39.9 km s^{-1}

with a peak flux density of 0.7 Jy. Observations of the target 6.7 GHz methanol maser during 2008 March 18 showed no emission at this velocity. This source is definitely in need of more observations. A spectrum showing both transitions is presented in Fig. 7.9.

G 327.282–0.469. The 12.2 GHz emission associated with this source increased in flux density by over one-third between June and December of 2008 (from 1.1 to 1.5 Jy).

G 328.808+0.633 and G 328.809+0.633. This close pair of sources are separated by less than 2 arcsec, making the emission very difficult to separate. While emission at 12.2 GHz between –46.9 and –44.6 km s^{-1} can be uniquely attributed to G 328.808+0.633, some component of the emission between –44.6 and –43.4 km s^{-1} is likely to be present at both positions with perhaps the strongest contribution from G 328.809+0.633. This site exhibits a wealth of maser sources, including OH and water (Caswell (1998);Chapter 6), but also many additional methanol and excited OH transitions (see comment in Chapter 6).

G 329.622+0.138. This 2 Jy 6.7 GHz methanol maser exhibited a 12.2 GHz counterpart in 2008 June of 0.5 Jy but no hint of emission was detected in 2008 Dec. This source is coincident with a water maser (Chapter 6).

G 330.226+0.290. 12.2 GHz emission was detected towards this source in 2008 June, with a peak flux density of 1.4 Jy at a velocity of –92.2 km s^{-1} . At this velocity only very weak (~0.2 Jy) 6.7 GHz emission was present in 2008 Aug 21. 12.2 GHz emission was also detected at the 6.7 GHz peak velocity (~0.7 Jy). No believable 12.2 GHz emission was detected towards this source in 2008 December (5-σ detection limit of 0.75 Jy).

G 331.132–0.244. No emission at 12.2 GHz was detected at either epoch of observations in 2008, but, weak emission is present in the average of the two epochs. The 12.2 GHz emission peaks at the velocity of a secondary feature in the 6.7 GHz spectrum at 0.3 Jy. Both water maser and OH maser emission have been

detected at this site (Caswell (1998); Chapter 6). The methanol maser emission at 6.7 GHz shows strong evidence for periodicity (Goedhart, Gaylard & van der Walt, 2004).

G 331.278–0.188. 12.2 GHz emission detected towards this source peaks at a velocity of –78.8 km s^{-1} coincident with a 6.7 GHz secondary feature. At this velocity the 12.2 GHz emission is stronger than the 6.7 GHz emission (76 Jy compared with 46 Jy). The 12.2 GHz observations were carried out 2 months prior to the 6.7 GHz observation. A spectrum comparing the two transitions is shown in Fig. 7.8. This methanol maser site is also associated with OH and water maser emission (Caswell (1998); Chapter 6).

G 331.342–0.346. 12.2 GHz observations were made towards this source in both 2008 June and December but emission could only be identified in the average of the two epochs. No 12.2 GHz emission is detected towards the strong 6.7 GHz features (up to 86 Jy) but only at a weak feature present at ∼–71.3 km s^{-1} which is 0.8 Jy at 6.7 GHz and 0.4 Jy at 12.2 GHz. Emission from both OH and water masers are also present at this methanol maser site (Caswell (1998); Chapter 6).

G 331.437–0.304. No hint of emission at 12.2 GHz was detected towards this source in 2008 June (5-σ detection limit of 0.75 Jy) however, in 2008 December a 0.5 Jy source was detected at the velocity of the 6.7 GHz peak.

G 331.900–1.186. Like G 331.132–0.244 and G 331.342–0.346, 12.2 GHz emission towards this source is only apparent in the average of the two epochs of observations. While the peak of the 12.2 GHz spectrum is very narrow at –46.8 km s^{-1}, it lines up with the peak of the 6.7 GHz peak emission. Perhaps even more believable, even though it is weaker (0.3 Jy), is the broader feature at –59.1 km s^{-1} which shows identical emission at both transitions.

G 332.813–0.701. This weak 12.2 GHz source was detected in both 2008 June and December but the average of the two is presented in Fig. 7.1 to maximize the signal-to-noise.

G 333.068–0.447. 12.2 GHz emission was detected at a peak flux density of 0.4 Jy in 2008 December at the velocity of the 6.7 GHz peak, but no emission was detected at 12.2 GHz in 2008 June (5-σ detection limit of 0.75 Jy).

G 333.646+0.058. Emission at 12.2 GHz (0.6 Jy) was detected towards this source in 2008 June at the velocity of the 6.7 GHz peak. Observations in 2008 December showed no emission (5-σ detection limit of 0.75 Jy). Emission from the 22 GHz transition is also found towards this site (Chapter 6).

G 335.426–0.240. This source exhibits multiple 12.2 GHz features with the features between –53.4 and –52.4 km s^{-1} showing stronger emission at 12.2 GHz (1.9 Jy) than 6.7 GHz (~0.2 Jy) emission. The 6.7 GHz observations were carried out 4 months prior to the 12.2 GHz follow up observations.

G 335.556–0.307. This source exhibits 12.2 GHz emission at the velocity of the 6.7 GHz peak as well as towards a secondary feature at –114.7 km s^{-1} . At this velocity the 12.2 GHz emission has a peak flux density of 5.3 Jy compared to the 6.7 GHz feature of 4.4 Jy. The 6.7 GHz observations were carried out 4 months prior to the 12.2 GHz follow up observations.

G 335.789+0.174. The peak of the 12.2 GHz emission detected towards this source is at the velocity of a secondary feature in the 6.7 GHz spectrum and is marginally stronger at 12.2 GHz (162 Jy) than it is at 6.7 GHz (145 Jy). In Chapter 6 we detect a somewhat variable water maser at this location, with a 3 Jy detection during observations conducted in 2003, but no detectable emission above 0.2 Jy in 2004. Caswell (1998) detected an OH maser at this location.

G 336.864+0.005. 12.2 GHz emission (0.5 Jy) was detected towards this relatively strong 6.7 GHz source (59 Jy) in 2008 December. However, observations in 2008 June failed to detect emission here (5-σ detection limit of 0.75 Jy). Observations conducted in Chapter 6 revealed a water maser at this site and Caswell (1998) detect an OH maser at this location.

G 336.957–0.225. The 12.2 GHz emission detected here consists of two main features, the first is at the velocity of the 6.7 GHz maser and is also the stronger 12.2 GHz feature. The second has a velocity of –67.4 km s^{-1} and is stronger at 12.2 GHz (0.8 Jy) than at 6.7 GHz (0.4 Jy). These 12.2 GHz observations were carried out 4 months after the 6.7 GHz observations.

G 337.132–0.068. The peak of the 12.2 GHz emission detected towards this source in 2008 December is 0.7 Jy at –59.7 km s^{-1}compared with a mere 0.3 Jy at 6.7 GHz for this feature. Observations of the two transitions were separated by 4 months. No 12.2 GHz emission was detected towards this source in 2008 June (5-σ detection limit of 0.7 Jy).

G 337.176-0.032. This source was detected with a peak flux density of 0.5 Jy in both 2008 June and December, however, in Fig. 7.1 the average of the two epochs is shown to maximise the signal-to-noise.

G 337.632–0.079. The peak of the 12.2 GHz emission associated with this source is at the velocity of a secondary feature in the 6.7 GHz spectrum, but also shows weak emission at the velocity of the 6.7 GHz peak. 12.2 GHz emission towards this source was detected with a peak flux density of 0.5 Jy in 2008 December but no emission was detected in 2008 June (5-σ detection limit of 0.75 Jy).

G 337.966–0.169. This source was only detectable during 2008 December (0.6 Jy) with no hint being present in 2008 June (5-σ detection limit of 0.75 Jy).

G 338.075+0.012. There is no 12.2 GHz emission associated with the 6.7 GHz emission peak at -44 km s^{-1} (14 Jy) but relatively strong 12.2 GHz emission is detected towards a 6.7 GHz secondary feature at –53.1 km s^{-1} (8.3 Jy). The flux density of the 12.2 GHz emission rose by ~27% between 2008 June and December, from a flux density of 5.9 to 7.5 Jy. In Chapter 6 we detect a weak water maser (0.5 Jy) towards this source (in 2003 but in 2004 the source was not detected) and Caswell (1998) detect an OH maser at this position.

G 338.561+0.218. This source exhibits numerous spectral features at both methanol transitions. The peak of the 12.2 GHz emission observed in 2008 December is at a velocity of -40.2 km s^{-1} and flux density of 26 Jy while the 6.7 GHz emission at this velocity had a flux density of ~15 Jy when measured in 2008 Aug 23. A very weak (0.22 Jy) water maser was detected at this location and is presented in Chapter 6).

G 338.925+0.634 and G 338.926+0.634. This pair of sources is separated by less than 7 arcsec and as such require interferometric data to separate them. While the 6.7 GHz emission has been observed with the ATCA in order to derive accurate positions, which features are associated with which location have not yet been determined from these data. For these reasons these sources are considered the same site for the purposes of this analysis. There is reasonably strong (33 Jy) 12.2 GHz emission detected towards these sources.

G 338.925+0.557. As of 2010 April this source did not have a Parkes 6.7 GHz MX observation. Due to this the details in columns 4 to 7 in Table 7.1 are missing and as a result this source has been excluded from the analysis. No 12.2 GHz emission was detected towards this source in 2008 Dec. However, water maser observations presented in Chapter 6 show that a strong (100+ Jy) water maser resides at this location, along with an OH maser Caswell (1998).

G 338.476+0.185. The peak of the 12.2 GHz emission detected here is associated with the weakest 6.7 GHz emission located at a velocity of -98.1 km s^{-1}. Observations in 2008 December showed 12.2 GHz emission of 0.5 Jy at this velocity, whereas 6.7 GHz observations on 2008 Aug 23 showed a 0.3 Jy feature.

G 342.338+0.305. The peak of this 12.2 GHz maser lines up perfectly in velocity with its 6.7 GHz counterpart. Although the 12.2 GHz emission is detected with a peak flux density of 0.8 Jy, this spectrum suffers from unusually high noise but given the agreement in velocity is certainly authentic. The 6.7 GHz emission at this velocity has a comparable strength, peaking at 0.9 Jy.

G 342.446–0.072. The peak of this 12.2 GHz source at a velocity of –20.1 km s^{-1} is barely visible above the noise in the spectrum (3.3-σ detection). Without the perfect correspondence with the velocity of the 6.7 GHz this source would not have been recognised.

G 343.354–0.067. 12.2 GHz spectra from both the 2008 June and December observations are presented in Fig. 7.1 to show the variability between the two epochs. Each epoch shows a single feature source, with distinctly different velocities although both corresponding to the velocity of 6.7 GHz methanol maser spectral features.

G 345.010+1.792. The peak of the 12.2 GHz emission associated with G 345.010+1.792 has a flux density that surpasses its 6.7 GHz counterpart. The peak of the 12.2 GHz emission is at –21.8 km s^{-1} and is 297 Jy and at this velocity the 6.7 GHz emission is half as strong. The 12.2 GHz observations were carried out in 2008 June and the 6.7 GHz observations were conducted in 2008 Aug. Spectra of both transitions are shown in Fig. 7.8. This unique source shows a multitude of other class II methanol maser transitions, yielding detections in at almost all of the transitions that have been searched for (Ellingsen et al., 2004, and references therein). This site additionally harbors strong radio continuum and a weak, variable water maser (Chapter 6), as well as an OH maser (Caswell, 1998).

G 345.807–0.044. 12.2 GHz emission was detected towards this source in 2008 December with a peak flux density of 0.3 Jy at the velocity of the 6.7 GHz emission which has a peak flux density of 1 Jy. The emission at 12.2 GHz is sufficiently broad that it is believable and combined with the matching velocity of the 6.7 GHz emission suggests this to be a real source.

G 347.863+0.019. 6.7 GHz observations in 2008 Aug of this source revealed emission between –37.6 and –28.1 km s^{-1}, peaking at 6.4 Jy at a velocity of –34.7 km s^{-1}. 12.2 GHz follow up observations during 2008 June (2 months prior to the 6.7 GHz observations) revealed similar but weaker emission associ-

ated with the strong 6.7 GHz features, as well as an additional feature at –23.7 km s^{-1} (0.7 Jy), outside the velocity range of the 6.7 GHz emission. The nearby source G 347.813+0.018 has 6.7 GHz emission over a velocity range covering this additional feature, but no feature at this velocity. Furthermore, no 12.2 GHz emission was detected toward G 347.813+0.018. G 347.863+0.019 is therefore another candidate that needs further observations to see if the 12.2 GHz emission truly dominates at this velocity.

G 348.195+0.768. Weak 12.2 GHz emission was detected towards this 6.7 GHz source during both epochs of observations at the velocity of the 6.7 GHz peak emission. However, given the limited signal-to-noise, Fig. 7.1 shows the average spectrum from the two epochs.

G 349.799+0.108. A comparison between the 6.7 and 12.2 GHz emission detected towards this source is shown in Fig. 7.8 and reveals strong emission at both transitions. The feature between –20 and –21.5 km s^{-1} is twice as strong at 12.2 GHz as it is at the usually stronger 6.7 GHz transition (19 Jy compared with 10 Jy).

G 351.417+0.645, G 351.417+0.646 and G 351.445+0.660. G 351.417+0.645 and G 351.417+0.646 are 6.7 GHz sources are separated by ~2 arcsec. Because they are so close, strong and have overlapping velocity ranges, they are very difficult to separate using single dish data. Due to this, Table 7.1 presents 6.7 GHz velocity ranges as published in Caswell (2009) from ATCA observations. There is undoubtedly 12.2 GHz emission associated with both of these 6.7 GHz sources and due to this we have regarded this close pair as one source in our analysis. Norris et al. (1993) present VLBI maps of the methanol masers associated with this region and show that the two sources are quite heavily blended together.

Located nearby G 351.417+0.645 and G 351.417+0.646 lies a very strong water maser (1400 Jy) as well as an OH maser (Chapter 6; Caswell (1998)).

G 351.445+0.660 is also confused by G 351.417+0.645 and G 351.417+0.646 at 6.6 GHz so the velocity range from Caswell (2009) is also used here. At 12.2 GHz this source is much less confused and is able to be clearly separated from the

emission associated with G 351.417+0.645 and G 351.417+0.646.

G 351.611+0.172. No 12.2 GHz observations were carried out towards this 6.7 GHz source in 2008. Further observations conducted in 2010 March detected a 2 Jy 12.2 GHz source. It is possible that there is some contribution to the feature between –35 and –37 km s^{-1} from nearby source G 351.688+0.171, but since there are no concurrent observations of the two sources it is difficult to confirm this.

G 353.370–0.091. During 2008 December a relatively weak 0.6 Jy source was detected at the velocity of the 6.7 GHz peak emission. Observations in 2008 June failed to detect any emission towards this source (5-σ detection limit of 0.75 Jy).

G 357.965–0.164 and G 357.967–0.163. 12.2 GHz emission is detected at the velocity of the peak 6.7 GHz feature towards G 357.967–0.163 in both 2008 June and December. Observations of nearby source G 357.965–0.164 in 2008 June revealed no 12.2 GHz emission, while no observations were conducted at this position in 2008 December there is a marginal peak at –8.8 km s^{-1} present in the 2008 December observations of G 357.967–0.163 which is outside the velocity range of the 6.7 GHz emission towards this source, but close to the peak velocity of the 6.7 GHz emission associated with G 357.965–0.164. Further observations of G 357.965–0.164 are needed to determine if there is weak, variable 12.2 GHz emission associated with this 6.7 GHz methanol maser.

Both G 357.965–0.164 and G 357.967–0.163 are coincident with water masers (Chapter 6), the first of which showed extreme variation over a ~10 month period reducing in flux density from 53 to 0.9 Jy. G 357.967–0.163 shows a total velocity range of 181 km s^{-1} over the two epochs and moderate levels of variability. This source also has an OH maser counterpart (Caswell, 1998).

G 358.371–0.468. 12.2 GHz observations in 2008 June were carried out towards a position offset from the accurate 6.7 GHz position by more than 1.2 arcmin, accounting for the change in flux density between epochs from 1.9 Jy

in June to 8.1 Jy in December where observations were targeted towards the accurate position. Also coincident with this methanol maser site is a water maser (Chapter 6).

G 358.809–0.085. Very weak 12.2 GHz emission was detected towards this source in both 2008 June and December. While the emission was only detected at 0.3 Jy at both epochs, its velocity matches that of the 6.7 GHz emission peak. Unfortunately, the noise in the 2008 December spectrum is quite high which makes the average of the two epochs no better than the more sensitive observations conducted in 2008 June.

G 358.906+0.106 and G 359.436–0.104. 12.2 GHz observations of G 358.906+0.106 were conducted in both 2008 June and December. Observations in June revealed no 12.2 GHz emission (5-σ detection limit of 0.70 Jy), however, observations in 2008 December discovered a 12.2 GHz source associated with a secondary 6.7 GHz feature (of almost the same strength as the peak feature) with a peak flux density of 0.7 Jy.

A very similar situation is observed for G 359.436–0.104. Weak emission of 0.5 Jy was detected in 2008 December but not 2008 June towards a weak secondary feature present in the 6.7 GHz spectrum.

G 0.645–0.042, G 0.647–0.055, G 0.651–0.049, G 0.657–0.041, G 0.665–0.036, G 0.666–0.029, G 0.667–0.034, G 0.672–0.031, G 0.673–0.029 and G 0.677–0.025. These 10 6.7 GHz methanol masers are clustered near Sgr B2 and are contained within a 3 arcmin region. These sources were presented in Caswell et al. (2010), however, positions and velocity ranges were taken from Houghton & Whiteoak (1995) who conducted high sensitivity ATCA observations towards this region. Due to the complex nature of these sources we have excluded them from our analysis. 12.2 GHz observations towards these sources reveal at least three distinct sites of emission, however, the exact origin of the emission cannot be determined from our single dish observations at this frequency. We have included spectra at the positions of G 0.647–0.055, G 0.657–0.041 and G 0.667–0.034 in Fig. 7.1 with an extended velocity range of 40 km s^{-1} so as to include the full velocity range

of all the 6.7 GHz sources. These three positions include all of the 12.2 GHz emission seen at any of the 10 positions, and show the strongest emission.

G 0.836+0.184. 12.2 GHz observations carried out in 2008 December showed weak (0.6 Jy), narrow emission whose peak not only lines up with the 6.7 GHz peak but so does the secondary feature at –2.2 km s^{-1}. The correspondence in velocity lends support that this source is a genuine detection which is needed since the signal-to-noise in the spectrum is not entirely convincing otherwise. No 12.2 GHz emission was detected at this position in 2008 June.

G 1.147–0.124. Like G 0.836+0.184, this source would never have been identified at 12.2 GHz without the added evidence provided by its spectrum at 6.7 GHz. This source shows no 12.2 GHz emission at the velocity of the 6.7 GHz peak emission during either 2008 June or December. However in 2008 December a weak but broad feature at –19.4 km s^{-1} was identified due to its correspondence with a secondary feature in the 6.7 GHz spectrum.

G 2.615+0.134. 12.2 GHz observations carried out in 2008 June discovered a weak maser (0.6 Jy) associated with the peak of the relatively weak 6.7 GHz source (1.2 Jy). Subsequent 12.2 GHz observations conducted in 2008 December failed to detect any hint of emission.

G 3.502–0.200. A weak but convincing 12.2 GHz source consisting of two features was detected towards this 6.7 GHz source in 2008 December with a peak flux density of 0.4 Jy. Observations in 2008 June showed no discernible emission at 12.2 GHz.

G 8.669–0.356. Observations at 12.2 GHz in 2008 June revealed a weak 0.4 Jy source at the velocity of the 10 Jy peak of the targeted 6.7 GHz maser. Further observations completed in 2008 December were of uncharacteristically poor sensitivity, with a 5-σ detection limit of 1.15 Jy, and it is therefore not surprising that no emission was detected at this epoch. Also located at this site are a water maser, 22 GHz radio continuum (Chapter 6) and an OH maser Caswell (1998).

G 10.323–0.160 and G 10.342–0.142. 12.2 GHz observations towards this pair of sources were conducted in 2008 June towards G 10.323–0.160 and 2008 December towards G 10.342–0.142. These two sources are separated by about 1.5 arcmin, however, emission from G 10.323–0.160 appears much stronger in 2008 December towards the offset position of nearby source G 10.342–0.142 implying an increase in flux density of at least a factor of 3 between the epochs. Both of these methanol maser sites are coincident with water masers (Chapter 6).

G 10.35–0.13. At the time of the 12.2 GHz observations, no accurate position for this 6.7 GHz MMB source had been derived. Due to this the best estimate of the source's position has been extracted from the survey cube. Subsequent ATCA observations have shown that the source is located 24 arcsec from the observed position.

7.6 Discussion

7.6.1 Detection statistics

Our detection rate of 43 % is significantly lower than previous searches of comparable sensitivity. For example, the detection rate of Caswell et al. (1995b) was 55 % in a search with a comparable detection limit and in Chapter 4 we find that 60 % of the 6.7 GHz methanol masers that were searched had 12.2 GHz counterparts. In order to determine the reasons for this apparent detection rate discrepancy, we must first examine the nature of the target sources used in previous searches. Caswell et al. (1995b) conducted their search towards 6.7 GHz methanol masers that had been detected towards OH maser targets, while in Chapter 4 we targeted 6.7 GHz methanol masers that had been detected towards *IRAS* selected regions (Walsh et al., 1997, 1998). Błaszkiewicz & Kus (2004) searched 261 6.7 GHz methanol masers and achieved a detection rate of 19 % in a survey of much lower sensitivity (accounting for the lower detection rate) which was also primarily directed towards 6.7 GHz methanol masers detected towards *IRAS* selected targets. Similarly Gaylard, MacLeod & van der Walt (1994) carried out a sensitivity limited search for 12.2 GHz methanol masers towards in-

frared selected 6.7 GHz targets, achieving a detection rate of 27 %. Given the high sensitivity and large scale of our observations, we can only directly compare our results with those of Caswell et al. (1995b) and those presented in Chapter 4; however, we are able to make some comparison with less sensitive searches by taking detection limits into account. For example, Gaylard, MacLeod & van der Walt (1994) had a sensitivity limit of ~10 Jy, if our detection limit was at this level our detection rate would be slightly lower than 10 % compared to their detection rate of 27 %. If our detection limit had been 4 Jy, like that of the search by Błaszkiewicz & Kus (2004), our detection rate would have dropped to 16 % compared to their detection rate of 19 %. It is therefore evident that even by taking detection limits of other surveys into account, our detection rate is lower than that of previous searches.

The marked drop in detection rate from our search compared to similar searches can most easily be accounted for by the absence of 6.7 GHz methanol maser target biases that were present in many previous searches. Our 6.7 GHz MMB targets were detected in a sensitive and unbiased manner. In contrast, all of the previous searches were subject to different levels of evolutionary biases, since both infrared colour and OH targeted searches would miss the vast majority of very young methanol masers. Add to this the fact that 12.2 GHz methanol masers are expected to be present at a time somewhat later than the onset of the 6.7 GHz emission (Chapter 4), it is not only not surprising, but expected, that our detection rate would be lower than such searches. Błaszkiewicz & Kus (2004) suggested that 12.2 GHz detection rates depended mainly on sensitivity; however, our search shows that the role of biases is perhaps an equally important factor.

7.6.2 Galactic distribution of methanol masers

Pestalozzi et al. (2005) compiled a catalogue of the 6.7 GHz methanol masers that were known prior to 2004. A total of 519 6.7 GHz sources were listed throughout the Galaxy and were detected in both targeted and blind searches (not all of which had been searched for 12.2 GHz counterparts). The distribution of the 6.7 GHz sources was found by the authors to be non-random throughout the

Galactic plane with a particularly high concentration between 20 and 50 degrees longitude, a region that falls outside the longitude range of sources within this Chapter. Pestalozzi et al. (2005) also found that the distribution of sources across the Galactic plane had a FWHM of 0.5° and commented that this could be attributed to the fact that blind searches had been targeted close to the Galactic plane.

The Galactic distribution of the 6.7 GHz methanol masers detected in the MMB survey is beyond the scope of this study and we only include preliminary findings which allow us to comment on the distribution of the associated 12.2 GHz sources. Our sample of 593 6.7 GHz methanol masers is slightly larger than that of Pestalozzi et al. (2005) and has the advantage that all sources were detected in an unbiased manner, although restricted to a portion of the southern Galactic plane. Fig. 7.2 presents histograms of the frequency of 6.7 GHz methanol masers in ranges of longitude (the incomplete bins, i.e. G 20 - G 10 and G 260 - G 250 have not been included) and latitude. Interestingly, we find that the distribution in longitude is very similar to that of Pestalozzi et al. (2005) with a peak of sources in the G 330 - G 340° longitude range, and a distinct lack of sources between G 250 - G 290°. In general, the number of sources in each Galactic longitude range has doubled from the restricted sample of Pestalozzi et al. (2005) with slightly higher increases in the G 350 - G 0° and G 260 - G 270° longitude ranges. We find that most of the sources are closely confined to the Galactic plane and, like Pestalozzi et al. (2005), find that a large proportion of sources are located within 0.25° of the Galactic Plane, meaning their concerns that this was in part a result of an observational bias were unnecessary.

Fig 7.3 shows the distribution of the 6.7 GHz methanol masers within the Galactic Plane and also the distribution of line-of-sight velocities versus Galactic longitude. In this figure, the 6.7 GHz sources with associated 12.2 GHz methanol masers have been distinguished from those without by the use of different symbols. The distribution of the 6.7 GHz methanol masers with and without 12.2 GHz counterparts appears to be approximately randomly distributed, with perhaps a curious cluster of sources with 12.2 GHz counterparts in the longitude range G 330 - G 340°.

A comparison of the detection rate of 12.2 GHz methanol masers split into 5° longitude bins shows that the detection rate is somewhat dependent on Galactic longitude range. Fig. 7.4 shows firstly the number of 6.7 GHz sources in the longitude range G 10 to G 290° broken up into 5° bins, and secondly the 12.2 GHz detection rates in each of these portions of the Galaxy. Sources outside this longitude range were omitted from this investigation as each 5° bin outside this range contained fewer than 5 sources, making the statistics meaningless. In this plot showing the detection rates, the diagonally shaded bars show the detection rates that would be needed to be, statistically, significantly different (both the upper and the lower) from the mean detection rate. The different levels in each longitude range are a result of the differing sample sizes in each region. For two regions (G 300 - G 305° and G 295 - G 300°) the detection rate would have to be zero to be significantly lower than the mean. For the G 335 - G 340° range, the detection rate is statistically significantly different than the mean detection rate (p-value=0.04 from a chi-squared test), showing a relative overabundance of 12.2 GHz sources. This may indicate that a burst of high-mass star formation occurred in this region at a time which now causes an abnormally high fraction of sources to be at the evolutionary stage where we see both methanol maser transitions.

The apparent relative under-abundance of 12.2 GHz detections at longitudes between G 270 - G 305 was further investigated and compared to a region of the same size, G 315 - G 350. The detection rate in the first region is 25 % and in the second the detection rate almost doubles to a rate of 47.9 %. The number of detections in both of these regions are not statistically significantly different from that expected from the mean detection rate. However, the detection rates in these regions are statistically different from one another (tested by calculating the expected number of detections in G 270 - G 305 using the detection rate of the G 315 - G 350 region and carrying out a chi-sqared test). In the G 270 - G 305 region, there is also a distinctly lower 6.7 GHz methanol maser density than other parts of the Galaxy. In the Large Magellanic Cloud, the heavy metal and complex molecule abundances are a likely explanation for the lack of many 6.7 GHz methanol masers, apparently underabundant by a factor of $\sim$45 compared to our Galaxy (Green et al., 2008). It is therefore possible that the underabundance of

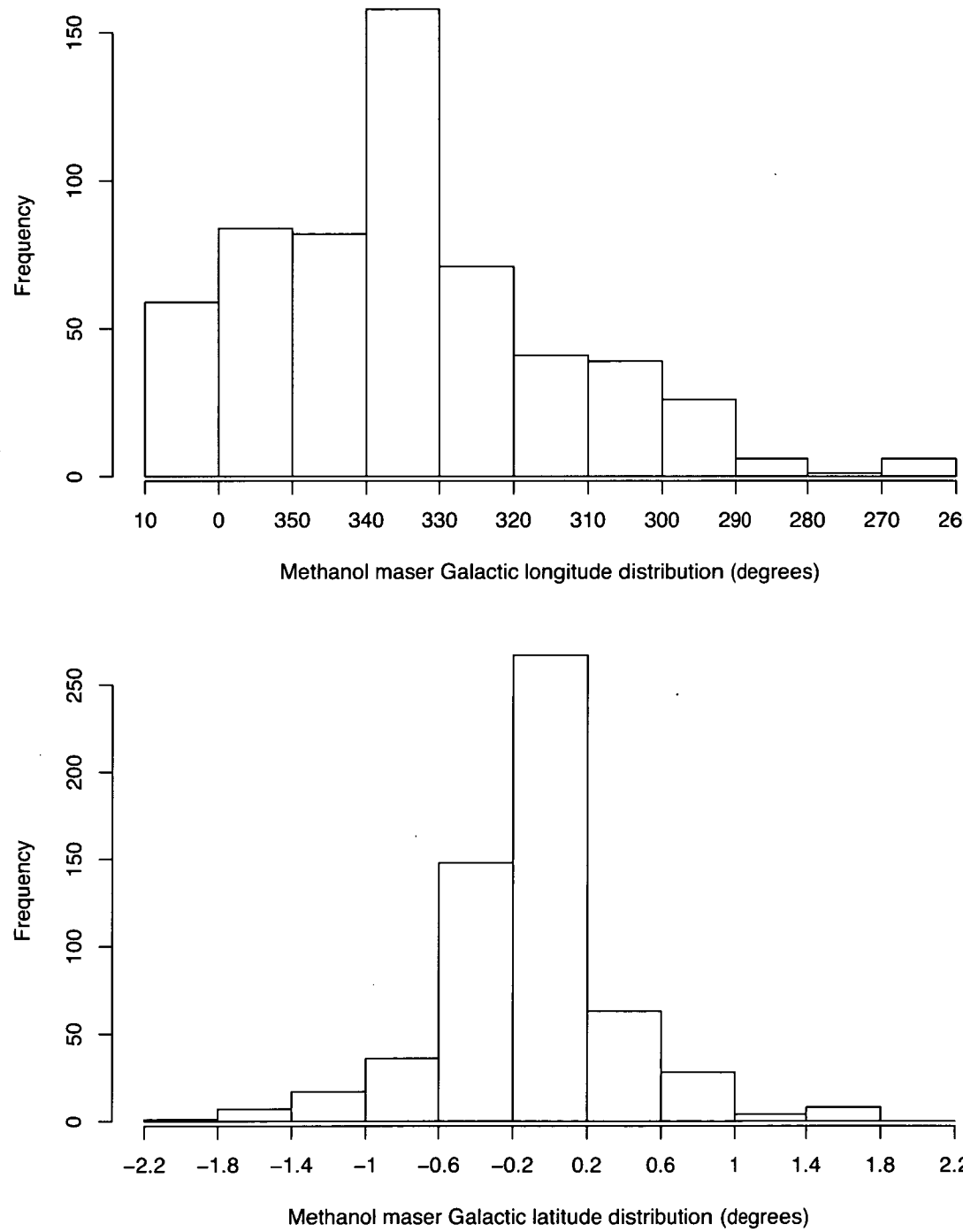

Figure 7.2: *Histograms of the number of 6.7 GHz methanol masers versus Galactic longitude (top) and latitude (bottom). Longitude ranges of G 10 to G 20 degrees and G 250 to G 260 degrees are not complete and so have been excluded.*

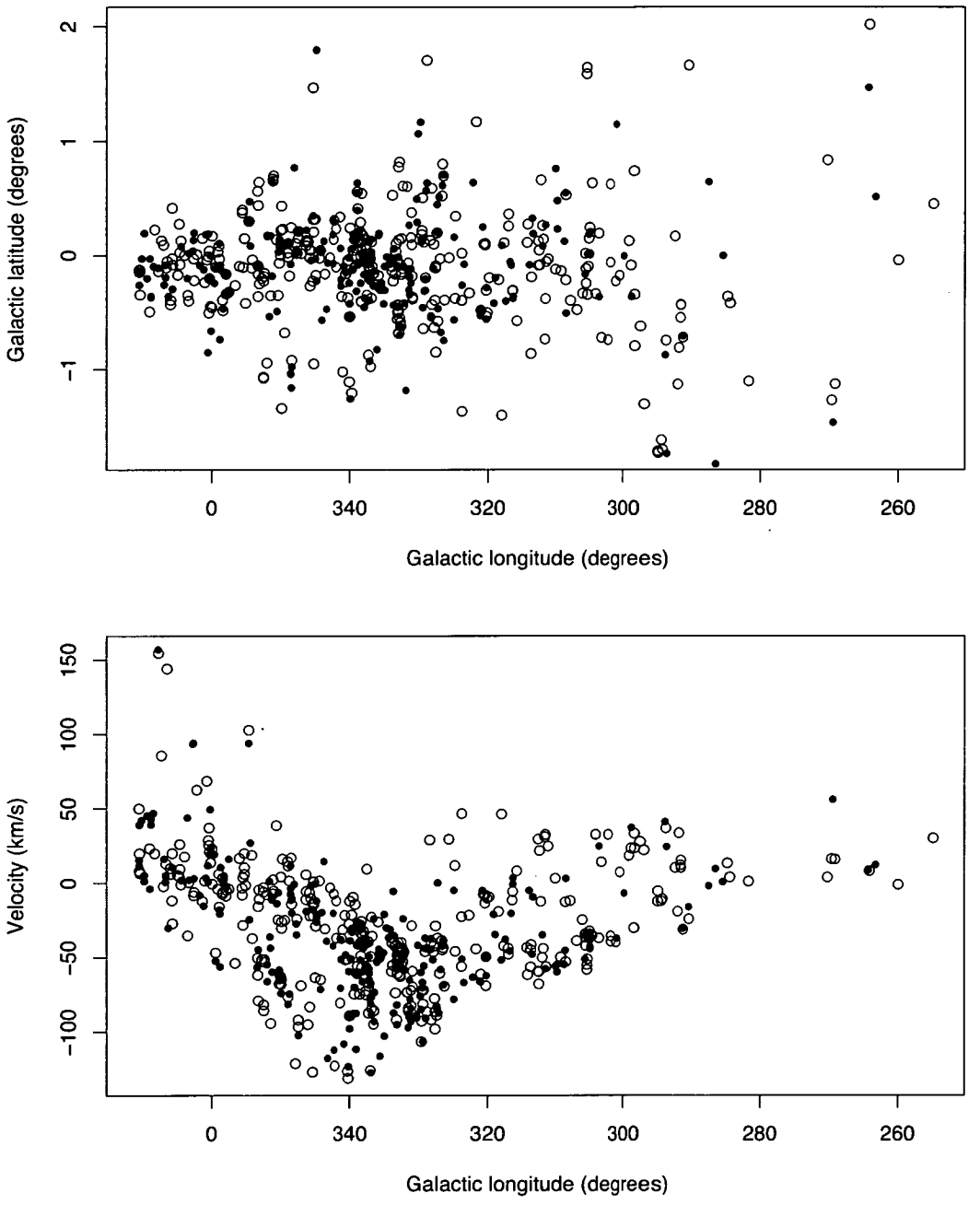

Figure 7.3: *Distribution of methanol masers in the southern portion of the Galactic plane (top) and distribution of peak 6.7 GHz methanol maser velocity versus Galactic longitude (bottom). Here open circles correspond to 6.7 GHz methanol masers with no detectable 12.2 GHz counterpart and dots mark the locations of 6.7 GHz methanol masers where we have detected emission at 12.2 GHz.*

6.7 GHz methanol masers in the G 315 - G 350 region could be attributed to low metallicity, which if it is the cause, has an effect on the 12.2 GHz association rate. Ellingsen et al. (2010) carried out a search for 12.2 GHz methanol maser emission towards the four known 6.7 GHz methanol masers in the LMC, detecting one source. Comparison of the 12.2 GHz detection rate in the LMC compared to that in the Galactic plane is difficult since the sample size in the LMC is so small and observations of two orders of magnitude greater sensitivity would be required to confidently determine if the sources in the LMC were under-luminous at 12.2 GHz compared to the Galactic sources (Ellingsen et al., 2010).

Fig. 7.5 shows all of the 6.7 GHz methanol masers detected in the MMB survey south of declination –20 degrees overlaid on spiral arm loci. The figure shows the velocity of the sources and the spiral arms plotted against Galactic longitude and therefore enables sources to be identified in relation to their associated spiral arm. The velocity assignment of the spiral arm loci have been made using the Brand & Blitz (1993) rotation curve rather than the updated prescription of Reid et al. (2009), since the shapes of the curves are based on old LSR and kinematics. The generally poor correspondence between the locations of the methanol maser sources and the spiral arms is partly attributed to the arms being inadequately described by the current models and partly that the plot of their positions does not allow for their finite width. For some sources, alternative explanations are viable, such as the seven sources with velocities which surpass that of the far 3 kpc arm, which have been attributed to probable association with the Galactic bar (Caswell et al. 2010; Green et al. 2010).

Fig. 7.6 shows a 'zoomed in' version of Fig. 7.5 with a restricted velocity and longitude range. Upon studying Figs 7.3, 7.5 and 7.6 an apparent tendency for the sources showing emission at both transitions of methanol to be clustered becomes evident, and likewise for the sources exhibiting only 6.7 GHz emission. A preliminary investigation has been conducted to determine if this is the case. For all sources harboring 12.2 GHz emission, the nearest neighbour (in angular separation only) has been examined to see if there is a higher proportion of sources with 12.2 GHz emission near other 12.2 GHz sources than would be expected if they were randomly distributed. Using this method we find that approximately 50 % of 12.2 GHz sources have another source with 12.2 GHz

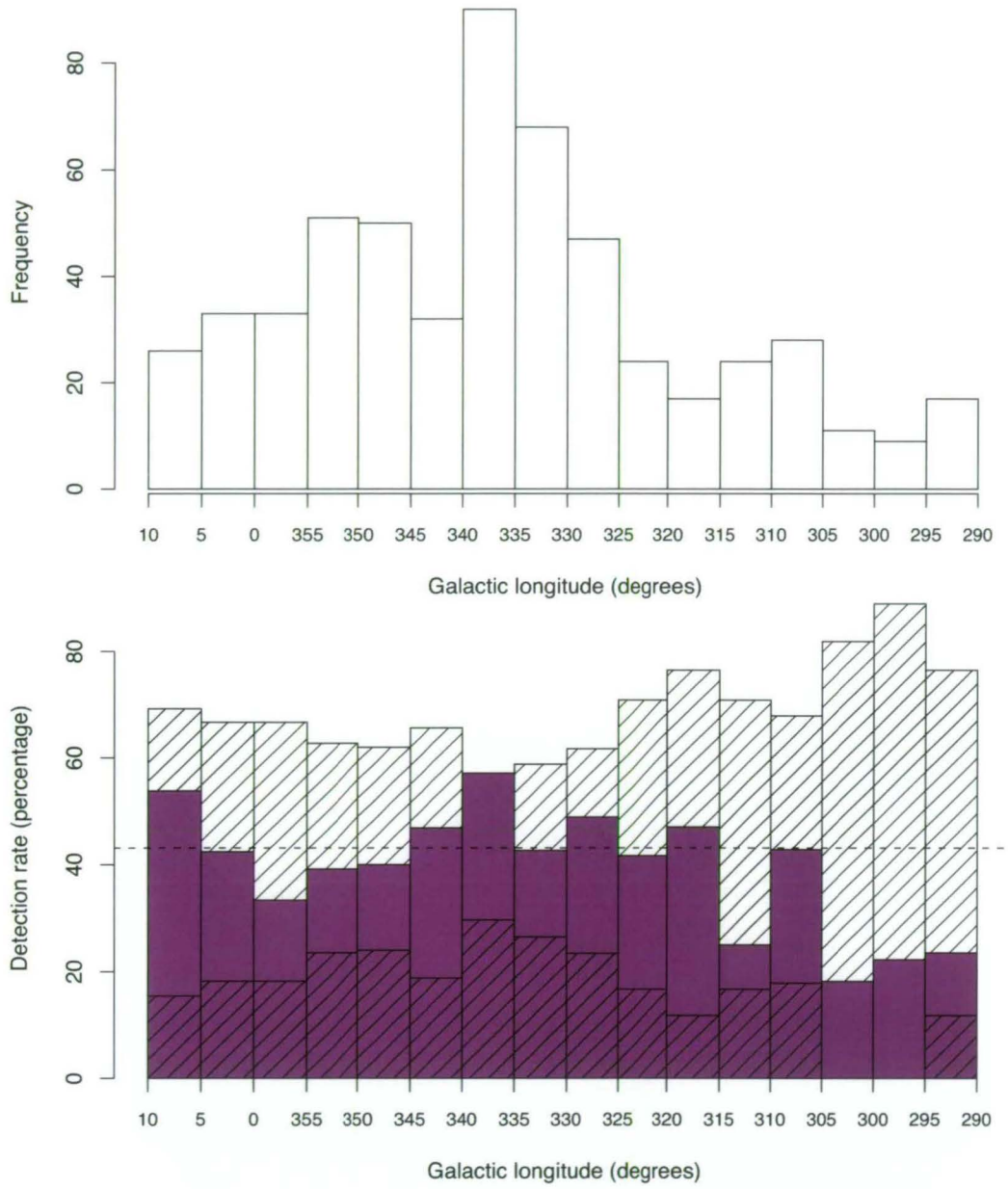

Figure 7.4: *Histogram of the number of 6.7 GHz sources in 5° Galactic longitude ranges (top) and plot of the 12.2 GHz detection rates in each of these longitude ranges (bottom). In the bottom plot, the purple bars correspond to the actual detection rates in each longitude range, the dashed horizontal line represents the average detection rate of 12.2 GHz sources and the diagonally shaded bars represent the detection rates that are statistically significantly different from the mean detection rate (p-value=0.05).*

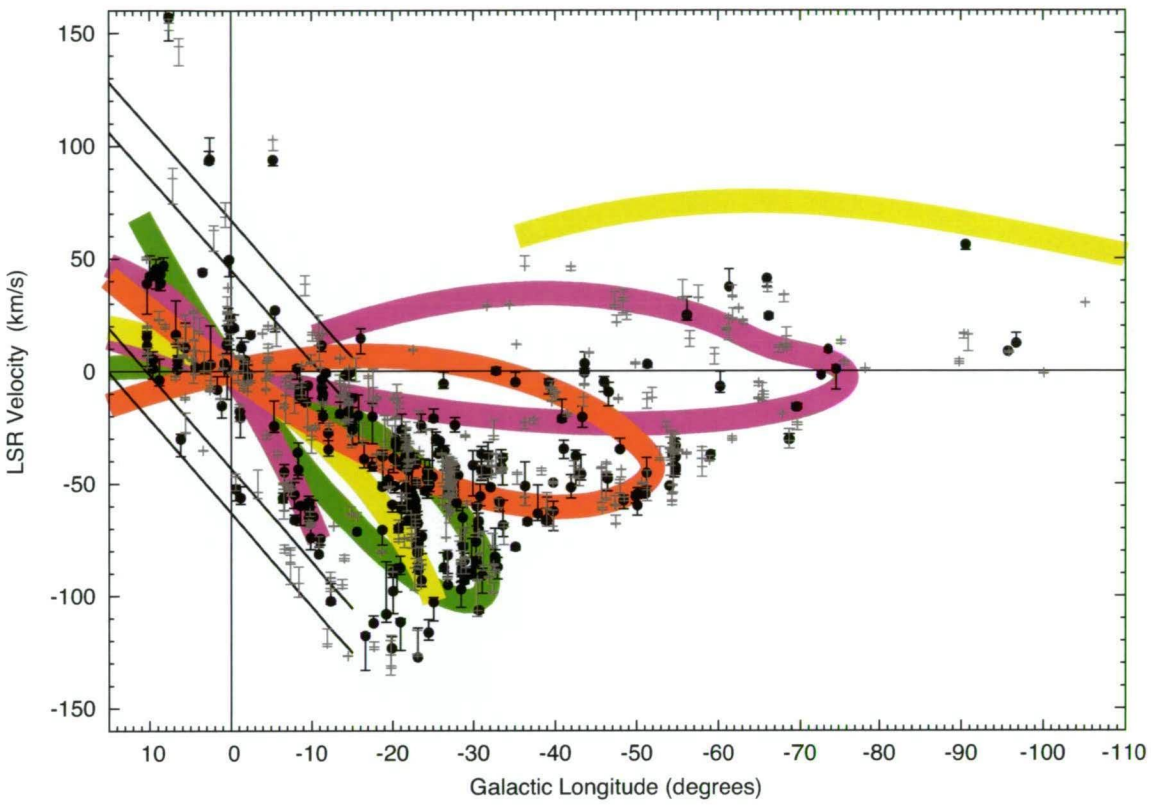

Figure 7.5: *Longitude versus velocity 'crayon' plot (adapted from Green et al. (2010) and produced by Dr James Green) showing all 6.7 GHz MMB masers detected south of declination –20°. Sources which also show emission at 12.2 GHz are represented by black circles and sources with no detectable 12.2 GHz emission are represented by grey crosses. Error bars in both cases show the velocity spread of the 6.7 GHz sources. The coloured loci are the spiral arms (yellow = Perseus; purple = Carina-Sagittarius; orange = Crux-Scutum; green = Norma) and are based on the logarithmic spirals of Georgelin & Georgelin (1976) with the updates from Taylor & Cordes (1993). The velocities of the spiral arms have been assigned using the Brand & Blitz (1993) rotation curve. The two parallel sets of black lines shows the region that was identified in CO emission and attributed to the 3 kpc arms (Dame & Thaddeus 2008).*

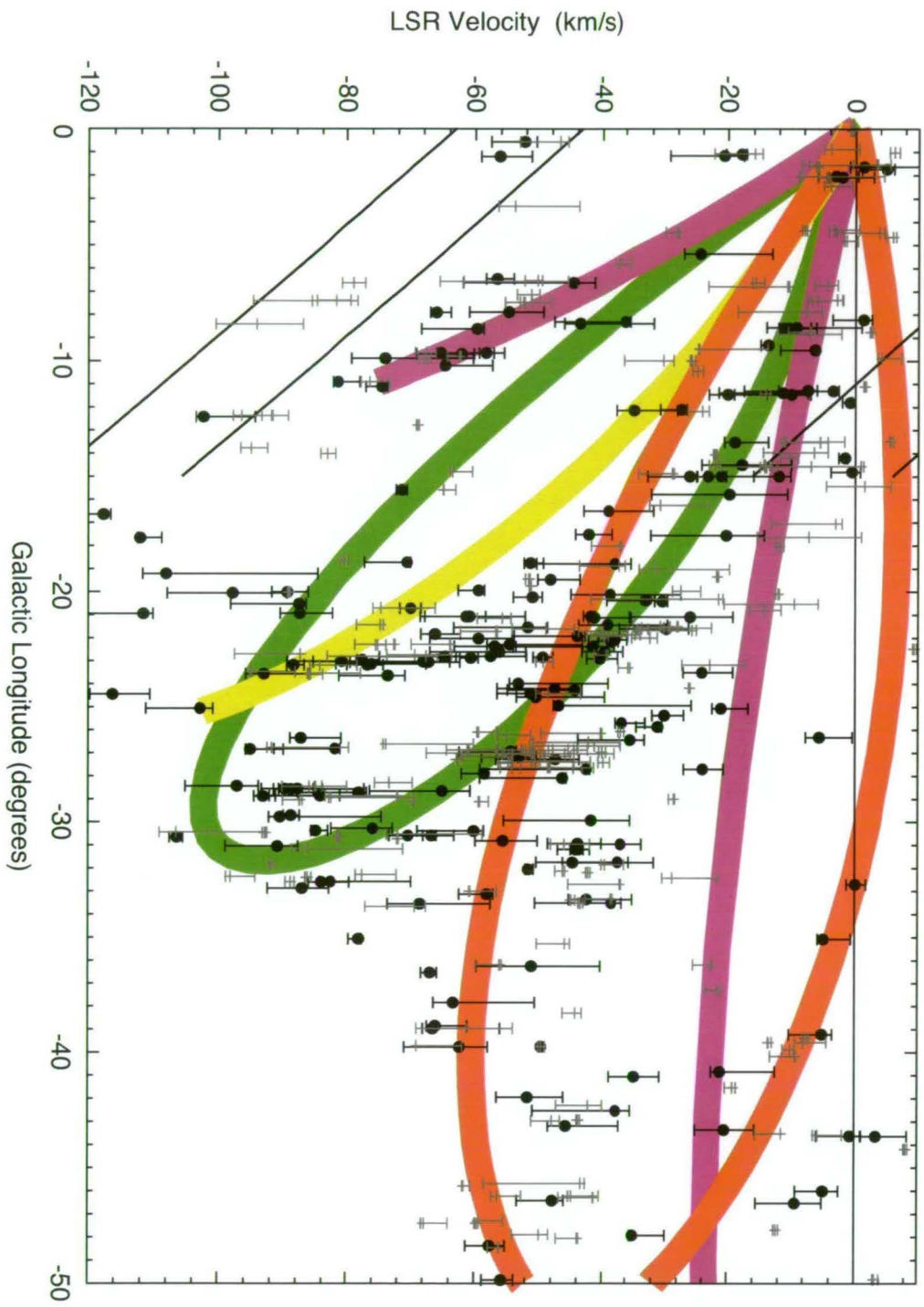

Figure 7.6: *This figure is a 'zoomed in' version of Fig 7.5, showing a restricted velocity and longitude range which allows this highly populated region to be more clearly seen.*

emission as its nearest neighbour compared to the expected proportion (based on detection statistics) of 43 %. The difference between these values is not quite statistically significant, but does warrant further, more sophisticated analysis.

The apparent clustering of 12.2 GHz detections was further tested by investigating the closest neighbour of each of the 12.2 GHz methanol masers on the longitude-velocity plot (Fig. 7.3). This was done by determining the linear separation between each of the 12.2 GHz methanol sources and all other sources on the plot. The difference in longitude between source was multiplied by two, making the ranges on each of the axes approximately equivalent. We find that for 51 % of 12.2 GHz methanol sources, the nearest source also exhibits 12.2 GHz emission. In this case, the number of 12.2 GHz with another 12.2 GHz source as a nearest neighbour (on the longitude-velocity plot) is statistically significantly higher that what would be expected from the 12.2 GHz detection rate (p-value of 0.05). While a lot of assumptions and approximations have gone into this analysis, if anything, these assumptions would cause a marked reduction in the chance of achieving a statistically significant result, even if sites exhibiting 12.2 GHz emission do tend to be clustered together. This supports the assertion presented earlier in this section, that the non-uniform detection statistics across the Galactic plane, imply that localised bursts of high-mass star formation has resulted in nearby sources to be at a similar evolutionary stage of star formation.

7.6.3 Comparison of flux densities and velocity ranges

Similar to previous searches, we find that 12.2 GHz methanol masers are, in general, weaker than their 6.7 GHz counterparts. The average peak flux density of our 6.7 GHz maser targets is 48.4 Jy with a median of 5.1 Jy compared with our detected 12.2 GHz methanol masers which have an average peak flux density of 23.0 Jy and a median of 2.0 Jy. Our detections at 12.2 GHz are primarily at the stronger 6.7 GHz sites, with the average 6.7 GHz peak flux density of sources with 12.2 GHz counterparts being 105.9 Jy, with a median of 15.4 Jy. In comparison, the average 6.7 GHz peak flux density for sources with no detectable 12.2 GHz counterpart is 6.8 Jy, with a median flux density of 2.5 Jy. The average peak to peak ratio of 6.7 GHz to 12.2 GHz methanol masers (for detected sources) is

17.7:1 and the median ratio is 4.3:1.

We find that there are very few weak 12.2 GHz sources with stable peak flux densities. 236 6.7 GHz methanol masers were searched at both epochs and 28 of these resulted in a detection at only one of these, while the remaining 208 sources showed no identifiable emission at either epoch. When the data for these sources were averaged over the two epochs, only three additional sources were identified. This shows that multiple epoch searches have a much higher merit than one-time searches, even of a higher sensitivity.

Comparison of integrated flux densities shows an even greater difference in 6.7 and 12.2 GHz methanol maser strength; the average 6.7 to 12.2 GHz integrated flux density is 41.1:1 with a median ratio of 10.1:1. The greater ratio of integrated flux densities is likely a result of the much simpler spectra often seen at 12.2 GHz, with relatively fewer features at 12.2 GHz compared to the 6.7 GHz sources.

Approximately 80 % of the 12.2 GHz peak velocities correspond to the peak velocity of the associated 6.7 GHz methanol maser. In all but one case (discussed in Section 7.6.3), the peak velocity of the remaining 20 % of 12.2 GHz sources corresponds to the velocity of a secondary feature of the 6.7 GHz maser spectrum. In some cases the weakest feature in the 6.7 GHz maser spectrum is the feature with an associated 12.2 GHz feature.

We find that the average velocity range of the target 6.7 GHz methanol masers is 6.9 km s^{-1}, with a median range of 5.7 km s^{-1}. There are only 8 instances where the 6.7 GHz velocity range surpasses 20 km s^{-1}, and in fact, this number only increases to 41 for velocity ranges greater than 15 km s^{-1}. The detected 12.2 GHz methanol maser sources have less extensive velocity ranges, with only 22 sources exceeding a range of 10 km s^{-1}. The average velocity range of the 12.2 GHz detections is 3.2 km s^{-1}, and the median range is 1.7 km s^{-1}. Interestingly, there are very few instances (14 of 250) where a 12.2 GHz methanol counterpart is detected toward a 6.7 GHz methanol maser with a velocity range less than 2 km s^{-1}, even though 112 6.7 GHz methanol masers fail to surpass this velocity range threshold. Therefore, we find a much lower 12.2 GHz detection rate (12.5 %) towards 6.7 GHz methanol masers with narrow velocity ranges (not greater than 2 km s^{-1}).

The relatively lower integrated flux densities and velocity ranges of the 12.2 GHz

methanol masers may indicate that sensitivity limitations have prevented us from detecting 12.2 GHz emission towards the often weaker 6.7 GHz methanol maser features that are present towards the minimum and/or maximum velocities of the emission. However, given that the integrated flux densities ratios of the two transitions are vastly different from the peak to peak ratio, this suggests that even in the cases where we detect both methanol transitions there is a larger gas volume conducive to the 6.7 GHz transition than the 12.2 GHz transition.

6.7 and 12.2 GHz methanol maser peak velocities

Fig. 7.7 presents histograms that show the velocity of the 6.7 and 12.2 GHz methanol maser peak with respect to the velocity range of the 6.7 GHz methanol maser. Sources with 6.7 GHz methanol maser velocity ranges of less than 2 km s^{-1} have been excluded from this plot to ensure that the analysis is not dominated by single-feature sources. Percentages of the velocity ranges are calculated from the minimum velocity of the 6.7 GHz maser emission. These histograms show that there are slightly more sources whose peaks lie close to either edge of the velocity range than in the center, for both the 6.7 and 12.2 GHz sources. It is not surprising that the 12.2 GHz sources follow a similar trend to the 6.7 GHz maser sources in this case, since 80 % of the 12.2 GHz maser peaks are shared with their associated 6.7 GHz emission.

The statistical significance in the different number of sources in each of the percentage of velocity range bins has been investigated by comparing the actual number to the number expected (which was taken to be even across the bins, i.e. total number of sources divided by the number of bins) in a chi-squared test. We find that more 6.7 GHz methanol maser peaks lie close to the minimum velocity range for the two bins between 0 and 20 % than the expected number (43) at an almost statistically significant level (p-value of 0.07). For the 12.2 GHz peaks (on the 0 to 10 % bin), we find that the number expected (23) almost achieves statistical significance from the number observed (14), with a p-value of 0.06. While the number of 12.2 GHz methanol maser peaks that fall within 10 to 20 % of the velocity range (measured from the minimum velocity) of the 6.7 GHz methanol maser is statistically significantly higher than the expected number (p-value 0.01). All other bins in either of the histograms shown in Fig. 7.7 have

p-values between 0.12 and 0.87. Intriguingly the two bins in each histogram that either achieve statistical significance, or close to it, all fall close to the minimum velocity range.

The elevated proportion of 6.7 GHz sources showing their peak emission within 20 % of the velocity range minimum value is consistent with the physical conditions present in the star formation regions. If the median velocity range of the 6.7 GHz methanol maser velocity range is considered indicative of the systemic velocity of the source, then the emission associated with the minimum velocity range corresponds to blue-shifted emission, i.e. emission that is coming towards us. This places the maser spots responsible for these blue-shifted features in front of the exciting source.

6.7 GHz sources with stronger 12.2 GHz features

An investigation of the peak flux densities of the 6.7 and 12.2 GHz methanol masers has shown that there is only one instance where the peak flux density of the 12.2 GHz surpasses that of the 6.7 GHz peak (G 345.010+1.792) and this is shown in Fig. 7.8. In addition to this, G 326.641+0.611 exhibits at least one feature that has no apparent 6.7 GHz counterpart (Fig. 7.9). A further 15 sources exhibit at least one feature that is stronger at 12.2 GHz than at 6.7 GHz and comparison spectra showing both transitions are presented in Fig. 7.8 along with G 345.010+1.792. Some number of these will be a result of variability between the 6.7 and 12.2 GHz observations which was commonly of the order of 3-4 months. All of these sources deserve further investigation, including near simultaneous observations of the two transitions.

If we include G 326.641+0.611, the average luminosity of the 6.7 GHz methanol masers displaying at least one stronger 12.2 GHz feature is similar to the average 6.7 GHz maser luminosity of the full sample of sources exhibiting 12.2 GHz counterparts (1022 compared with 985 Jy km s^{-1} kpc^2). Of these, 8 have no EGO or OH (+2 have no EGO and no OH obs), 2 have OH but no EGO, 1 has OH and an EGO, and 2 have no OH but an EGO. Given the relatively small number of sources, it is difficult to meaningfully interpret this information to say anything about the probable relative age of the sources.

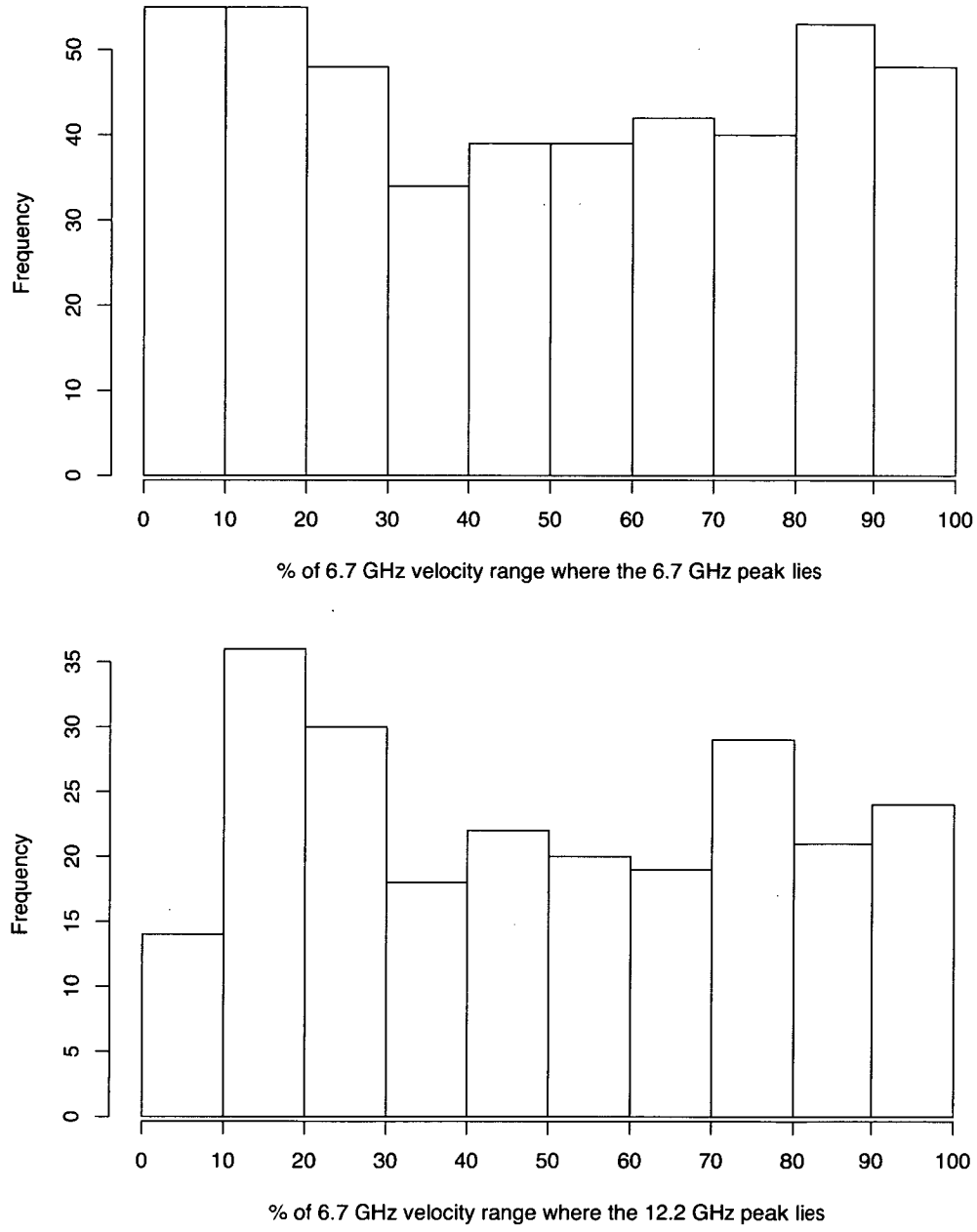

Figure 7.7: *Percentage of the 6.7 GHz methanol maser velocity range that the 6.7 GHz peak lies (top), and the 12.2 GHz lies (bottom). Only sources with 6.7 GHz methanol maser velocity ranges of more than 2 km* s^{-1} *are plotted.*

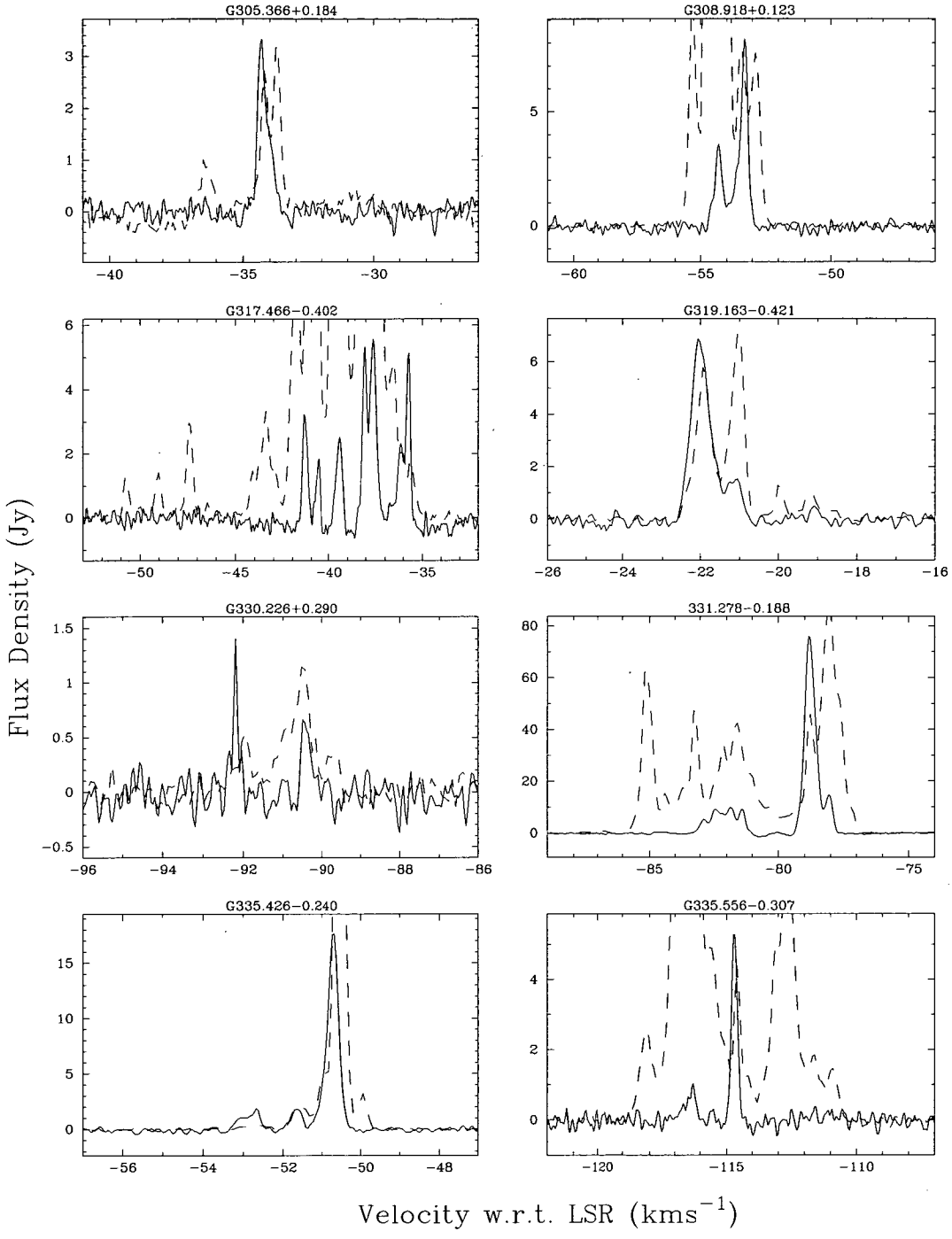

Figure 7.8: *Comparison between the 12.2 GHz emission (solid lines) and 6.7 GHz emission (dashed lines) for sources showing stronger emission at 12.2 GHz for at least one spectral feature.*

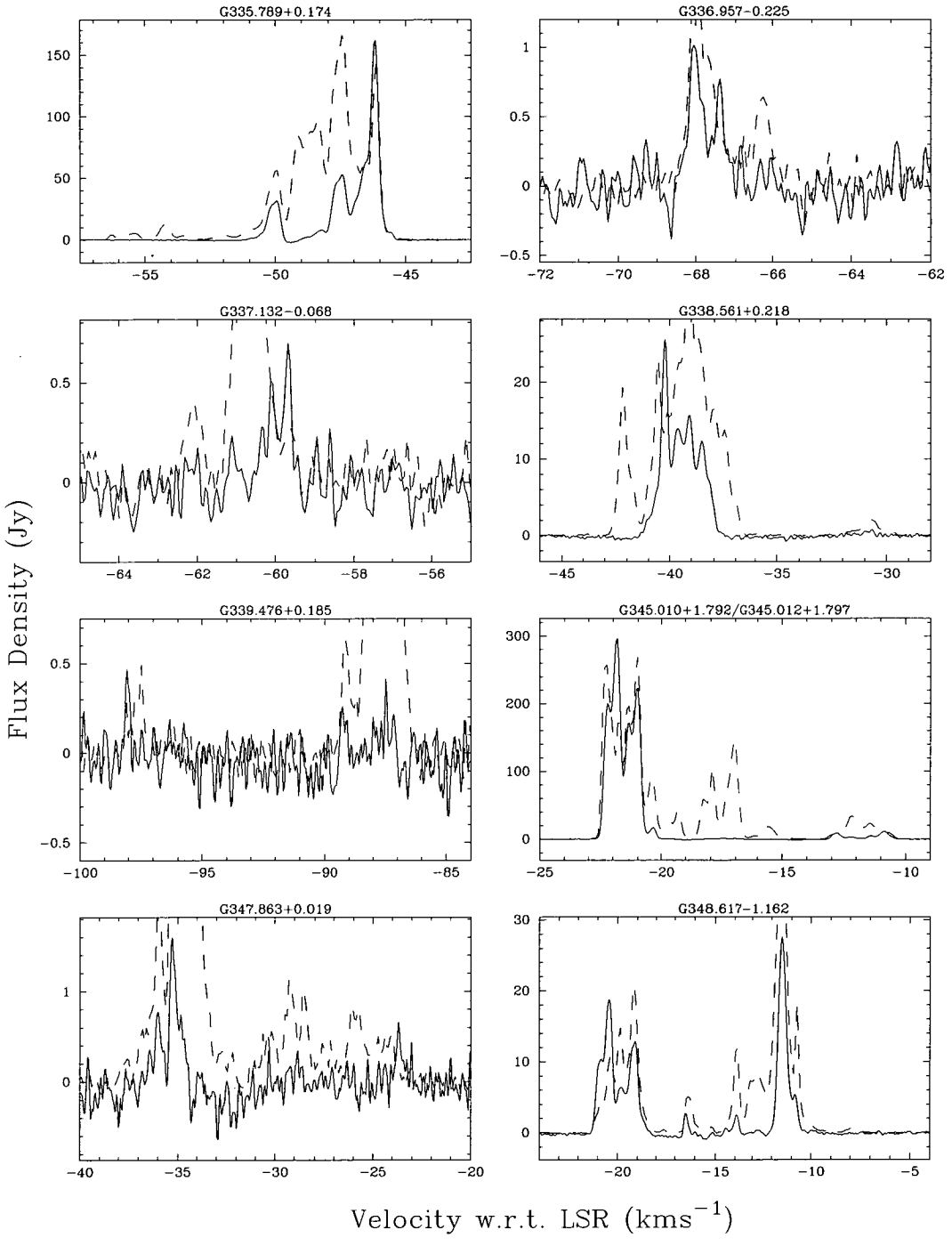

Figure 7.8: –continuued

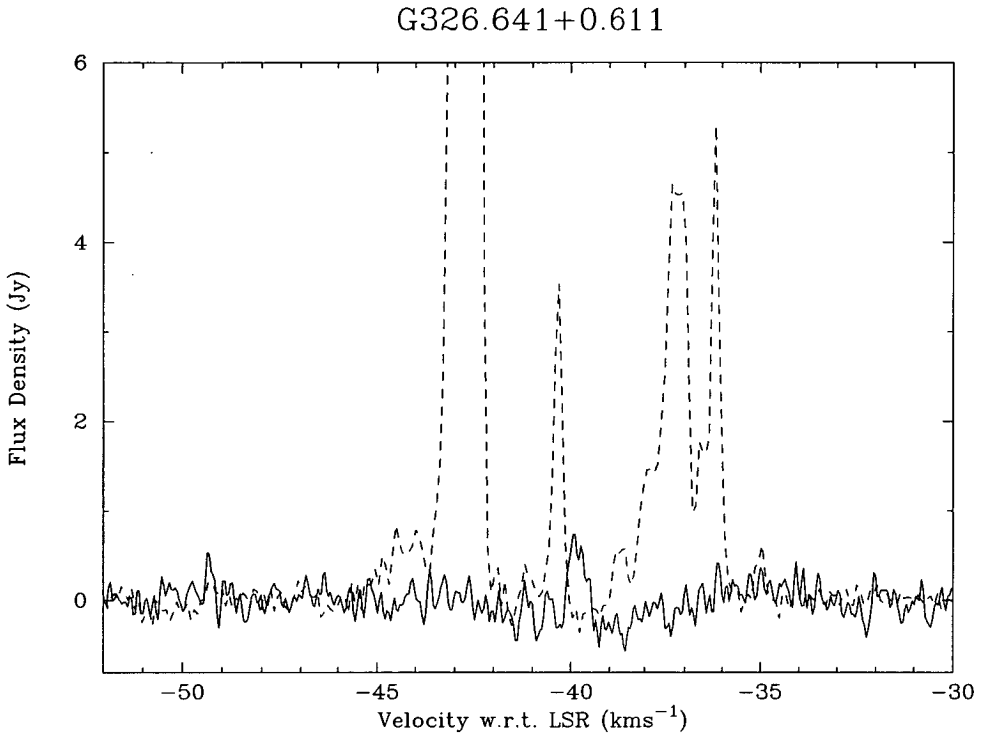

Figure 7.9: *Comparison between the 12.2 GHz emission (solid line) and 6.7 GHz emission (dashed line) for G326.641+0.611.*

7.6.4 Variability

Caswell et al. (1995b) showed from a large sample of 12.2 GHz methanol masers that some of these sources varied on time scales of three months by factors greater than 10 %, but rarely at the extreme levels that are seen in some water masers. The authors found that variations seen over a 3 month period were similar to the variations over 4 years (from comparing their data with Caswell et al. (1993)), suggesting that the sources go through quasi-periodic fluctuations. Long term monitoring of some 12.2 GHz methanol masers have shown remarkable periodicity in intensity fluctuations (e.g. Goedhart et al., 2005b, 2009). Goedhart et al. (2005a) conducted Very Long Baseline Array (VLBA) observations of G 9.62+0.02 and concluded that the periodic flares observed in this source could not have been caused by disruptions to the masing region, but more likely by periodic changes to the pump photon levels.

We carried out our 12.2 GHz observations over two epochs separated by 6 months, observing a large fraction of sources at both epochs. Repeat observations of sources were preferentially targeted towards those 6.7 GHz sources for which no 12.2 GHz methanol maser was observed in the first series of observations, or those with weak 12.2 GHz detections which needed confirmation. Due to the incomplete nature of the sample of sources studied at both epochs, an extensive study of variability cannot be completed. However, sources with two epochs of data have been used to investigate of the completeness of our search, and have allowed a preliminary assessment of 12.2 GHz source variability to be completed.

Towards 56 of the target 6.7 GHz methanol masers that were observed during both epochs, a 12.2 GHz source was detected at either one or both of the observations epochs. 28 of these 56 sources could only be identified at one epoch, the strongest of which was 1.4 Jy when detected. The average flux density of these once-detected-sources was $\sim$0.6 Jy on the epoch that they were detected, which is comparable to the 5-σ detection limits of our observations. However, as remarked in Section 7.4, many detections were confidently identified at the 3-σ level, since the velocities of the target 6.7 GHz methanol masers are known. In addition to this, averaging the observations of the source over the two epochs resulted in a decreased signal-to-noise in the detection of a number of sources.

These facts show that while the flux density of these sources is close to our detection limits (and in many cases less), these 28 weak sources do exhibit real variations in peak flux density of close to 50 % over the 6 month period. This suggests that the majority of these weak sources are more variable on average than the total 12.2 GHz methanol maser population. The luminosities of 6.7 and 12.2 GHz methanol masers are discussed in Section 7.6.6 and comparing the luminosities of the 6.7 GHz methanol masers with associated 12.2 GHz methanol masers that were detectable on only one of the two epochs has shown that the 6.7 GHz luminosity of these sources is weaker than the average of the full sample (208 compared with 985 Jy km s^{-1} kpc^2).

Given that half of the 56 weak 12.2 GHz sources that we detected were detectable at only one epoch, it is likely that a significant number of additional 12.2 GHz methanol masers would be detected if a second epoch of all single epoch non-detections were repeated, which potentially limits the completeness of our search. Of the 580 6.7 GHz methanol masers searched for 12.2 GHz methanol maser emission, 250 yielded detections. Of the remaining 330 6.7 GHz sources (with no detectable 12.2 GHz counterpart), 208 were observed at both epochs. Considering this, along with the 28 sources only detectable at one epoch, shows that 12 % of the sources that were observed at both, but not detectable at one epoch were detectable at the other (and the remaining 88 % resulted in no detection at either epoch). Since 122 6.7 GHz sources were observed at 12.2 GHz at only one epoch, resulting in no detection, we would expect to detect $\sim$15 additional 12.2 GHz sources (12 % of 122) if a second epoch of observations were carried out towards these 122 6.7 GHz sources. Additional observations of the 12.2 GHz non-detections that have only been searched at one epoch along with a sample of sources with no 12.2 GHz emission detected at two epochs will be carried out with the Parkes radio telescope in the future. These further observations will allow us to more confidently determine the completeness of the search and also investigate the time-scale of variability exhibited by these weak sources. When these observations have been completed, the search completeness can be tested by aligning all of the 12.2 GHz spectra, where no detection was identified, at the peak velocity of the 6.7 GHz maser and averaging the data for these sources ('stacking').

Our observations included many sources that had been previously observed at 12.2 GHz and analysis of the flux density of sources from our observations, with those made more than 10 years ago (e.g. Caswell et al., 1995b; Błaszkiewicz & Kus, 2004) will form part of a subsequent investigation, but, we note some sources which have shown marked variations since their previous publications. In particular, G 353.410–0.360 has exhibited extreme variations at 12.2 GHz between our observations and those completed by Caswell et al. (1995b) in their observations in 1992. This source was observed with a peak flux density of 19.5 Jy by Caswell et al. (1995a) and we detect no emission above 0.8 Jy in 2008 December. Interestingly, this source was also not detected at 6.7 GHz (above 0.5 Jy) during MMB observations on 2008 March 16 when it previously been observed at over 100 Jy (Caswell et al., 2010). Three other sources with previous 12.2 GHz detections (Caswell et al., 1995b) (G 284.352–0.419, G 327.291–0.578 and G 349.067–0.017) were not detected during these observations but were all reported to have peak flux densities of less than 1 Jy at the time of their detection. If we consider the completeness of our observations, the non-detections of these three sources is consistent with this.

Of the 28 sources that were observed and detected at both epochs, the average variation in peak flux density was 20 % (after accounting for a 10 % calibration uncertainty). Only 8 of these sources had flux densities greater than 1 Jy (as a result of the observational bias previously mentioned) at either epoch, so this statistic should not be considered as representative of the total 12.2 GHz source population. The sources showing the greatest variability between the June and December observations were G 305.202+0.208 and G 10.323–0.160 which decreased from 3.5 Jy to 1 Jy and increased from 2.3 Jy to 5.6 Jy, respectively. For G 10.323–0.160, this variation is a lower limit since the December measurement of 5.6 Jy was made at a position offset by ~1.5 arcmin (since no observation was made for this source in 2008 December, however, observations at this epoch did target nearby source G 10.342–0.142). Ten of the 28 sources showed no variation over the two epochs. A 2008 June peak flux density versus 2008 December peak flux density plot was produced and inspected but revealed no additional trends.

12.2 GHz spectra of both epochs for eight sources are shown in Fig. 7.10. For half of these sources, variability at a level significantly greater than the errors

introduced by calibration uncertainties and noise is seen. The remaining four sources show relatively weak emission at both epochs and so their flux densities may be influenced by noise. However, since we find many instances where weak sources are only detectable at one epoch (and are therefore variable) it is possible that some of the change in flux density between epochs is real for these sources.

7.6.5 Association with OH masers

The locations of the target 6.7 GHz methanol masers have been compared with OH masers detected by Caswell (1998) and their occurrence has been compared with the 12.2 GHz methanol maser detections. Caswell (1998) conducted a complete search of a portion of the Galactic plane (312° <l< 356°, $b = \pm 0.5°$) along with a range of targeted observations for OH masers, allowing us to not only identify methanol masers with associated OH masers but also, for a large number of sources, those without. 393 of our 6.7 GHz maser target sample correspond to locations searched for OH masers by Caswell (1998) and 144 of these are located within 1.5 arcsec of an OH maser. Using 1.5 arcsec as an association threshold takes into account the positional uncertainties for both sets of observations and therefore allows the majority of methanol-OH associations to be identified while minimizing the number of chance associations. Some OH and methanol maser sources separated by slightly more than this threshold were assessed individually and in some circumstances this threshold was relaxed for special cases.

The occurrence of the detected 12.2 GHz methanol masers was compared to the presence of OH masers in order to determine if the 12.2 GHz methanol masers are preferentially detected towards 6.7 GHz methanol masers with associated OH masers. This was seen in analysis by both Lewis (2008) and Chapter 4, in searches that were potentially biased towards more evolved 6.7 GHz sources, increasing the possibility that this finding was influenced by this bias since OH masers are expected to be associated with a later stage of evolution in star formation regions (e.g. Forster and Caswell 1989). We find, from our 12.2 GHz search towards our unbiased sample of 6.7 GHz methanol masers, that of the 393 6.7 GHz methanol masers with available OH data, 144 have associated OH masers and that 86 of these also have detections at the 12.2 GHz transition of methanol. This means

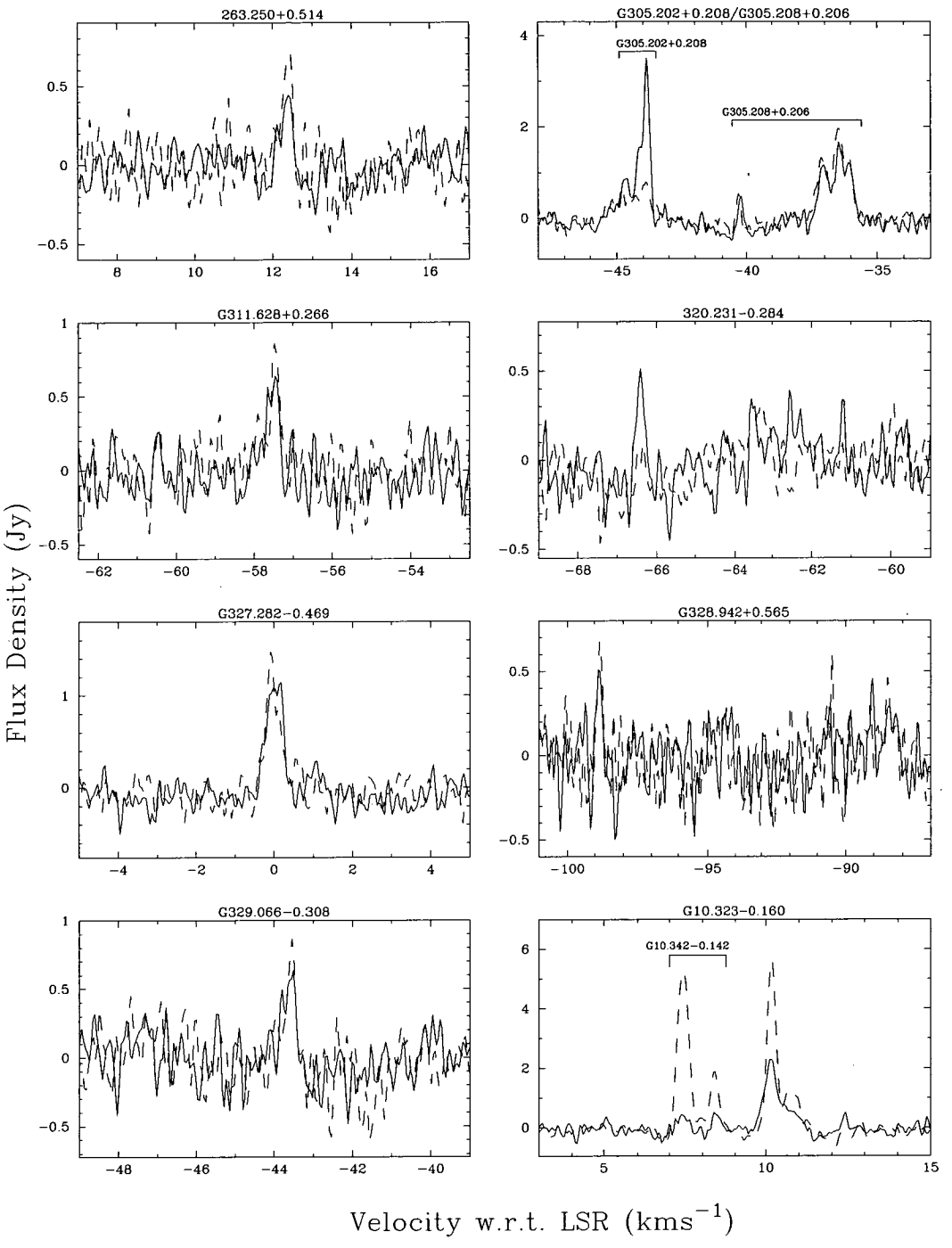

Figure 7.10: *Comparison between the 12.2 GHz emission detected in 2008 June (solid line) and 2008 December (dashed line) for eight of the most variable detected sources.*

that a search for 12.2 GHz towards 6.7 GHz methanol masers with OH masers would result in a detection rate of 60 %. For the 249 6.7 GHz methanol maser sources with no associated OH maser, 99 have associated 12.2 GHz emission and therefore a search toward these 6.7 GHz sources would yield a detection rate of 40 %. An alternative statistic is that 46.5 % of the 185 6.7 GHz methanol masers with 12.2 GHz counterparts (that fall within the regions completely searched for OH maser emission) have an OH maser counterpart. In comparison, the rate of OH maser association with the 28 weak 12.2 GHz methanol masers detected at only one epoch, mentioned in Section 7.6.4, is much lower with only one association out of 12 sources that fall within the region completely searched by Caswell (1998). This finding is consistent with these weak variable sources representing perhaps the youngest 12.2 GHz sources.

In the regions covered by complete searches for both 6.7 GHz methanol masers and OH masers (Caswell, 1998), the number of methanol masers detections outnumber OH detections by more than two to one. Many estimates suggest that the association rate for methanol masers towards OH masers may surpass 80 % (Caswell, 2009). However it is clear that the association rate for OH masers towards methanol masers is much lower, and in fact, is probably less than 40 %. These number statistics imply that the lifetime of methanol masers is much greater than that of the OH maser sources, but also shows that while the detection rate of 12.2 GHz methanol masers is greater at sites of OH masers, a search exclusively towards these sites would only uncover a small fraction of the total population, since so many methanol masers are devoid of OH counterparts. The elevated 12.2 GHz detection rate towards sources associated with OH masers also lends support to the idea that the 12.2 GHz sources are present towards the later stages of the period of evolution where 6.7 GHz masers are seen.

7.6.6 Source luminosities

Comparison between the luminosities of the two methanol maser transitions, with the other characteristics of each of the regions, has the potential to reveal much more insightful results than previous comparisons of only flux densities. In Chapter 4 we found that there was a relationship between increasing 6.7 GHz methanol

maser peak luminosity and evolution, with the more luminous 6.7 GHz methanol masers being associated with a generally later evolutionary stage of high-mass star formation (see Chapter 4). Unfortunately these findings were based on the peak flux densities of the 6.7 GHz sources extracted from the literature rather than the more appropriate integrated flux density (and in many cases the observations of the two transitions were separated by 10+ years). Since we have integrated flux densities for both of the methanol maser transitions available for our large sample of sources, here we repeat some of the analysis presented in Chapter 4.

Distances

The calculated luminosity of the methanol masers are clearly highly dependent on distance measurements used. We have calculated the kinematic distances using the 6.7 GHz methanol maser peak velocities for our sample using both the revised prescription offered by Reid et al. (2009) (which uses a flat rotation curve and updated solar parameters) as well as that of more traditional model of Brand & Blitz (1993). Pandian et al. (2009) shows that the agreement between the peak methanol maser velocity and molecular line data is within a few km s^{-1} for most 6.7 GHz sources and are therefore adequate for the computation of kinematic distances.

Table 7.3 presents the near and far distances calculated using the two different methods, which are in a number of cases are similar. But in general the near distances calculated using Reid et al. (2009) are slightly smaller than those calculated using Brand & Blitz (1993). Reid et al. (2009) commented that previous kinematic distances of sources for which they have parallax measurements were sometimes up to 2 times larger than the measurements derived from parallax measurements. There are a few instances where the derived kinematic distances are not sensible (e.g. for sources G 350.776+0.138, G 356.054–0.095, G 5.618–0.082) and in these cases neither the model of Brand & Blitz (1993) or the prescription of Reid et al. (2009) are able to give an acceptable distance, indicating that either these sources have anomalous velocities or they lie in poorly constrained regions of the Galaxy (especially when R $<$ 3.5 kpc, where extreme departures from circular rotation are known to be present (Caswell et al., 2010)).

Histograms of the 6.7 GHz integrated luminosities (Jy km s^{-1} kpc^2) calculated using each of the four derived distances shown in Table 7.3 are presented in Figs 7.11 and 7.12. Fig. 7.11 shows the luminosities calculated using the near (purple) and far (black outline) distances using Reid et al. (2009) (top) and Brand & Blitz (1993) (bottom). These histograms show that more of the luminosities calculated with near distances fall on the left hand side of the peak (which lies between 2 - 2.5 log Jy km s^{-1} kpc^2 in each case), with a much sharper fall off in numbers on the right hand side of the peak. In comparison, the far distance luminosities show a much more Gaussian-like profile. Overall, inspection of the histograms presented in Fig. 7.11 shows apparently little difference in the distribution of luminosities calculated using the models of Reid et al. (2009) and Brand & Blitz (1993).

Fig. 7.12 shows a comparison of luminosities calculated using the near distances from both models (top) and likewise for the far (bottom). These plots show that there are few significant differences between the luminosities calculated using the respective models, showing that the choice of model is much less important than the decision between near and far distances.

Comparison between 6.7 and 12.2 GHz luminosities

We have adopted the distances calculated using the prescription of Reid et al. (2009) since this method appears to achieve better correspondence with their parallax measurements and, in any case, as shown in Figs 7.11 and 7.12, the distributions of the calculated 6.7 GHz luminosities vary little from those calculated using the more traditional model of Brand & Blitz (1993). For the reasons argued in Chapter 4, Section 4.3.2 we have used the near distances in all analysis. Adopting either the near or the far distance for all sources will introduce large errors into analysis of maser luminosities, however, in the absence of parallax measurements or analysis of HI self absorption data, an assumption had to be made.

Preliminary analysis of HI self absorption towards the MMB sources has found that there is almost an even split between near and far distance assignments (James Green, private communication). Since the MMB survey is sensitive to the majority of sources throughout the Galaxy this split in assignments is expected.

Table 7.3: *Calculated methanol maser distances.*

Methanol maser (l, b) (degrees)	Reid09 near (kpc)	Error + (kpc)	Error − (kpc)	Reid09 far (kpc)	Error + (kpc)	Error − (kpc)	BB1993 near (kpc)	BB1993 far (kpc)
G 254.880+0.451	2.65	0.62	-0.64	2.65	0.62	-0.64	3.7	8.1
G 259.939-0.041	0	0	0	0	0	0	0.5	3.3
G 263.250+0.514	1.38	0.86	-1.26	1.38	0.86	-1.26	2.6	4.5
G 264.140+2.018	0.82	1.04	-0.82	0.82	1.04	-0.82	2.2	3.8
G 264.289+1.469	0.9	1.02	-0.9	0.9	1.02	-0.9	2.3	3.9
G 269.153-1.128	2.53	0.82	-1.08	2.53	0.82	-1.08	3.8	3.9
G 269.456-1.467	6.53	0.65	-0.64	6.53	0.65	-0.64	8	8.1
G 269.658-1.270	2.64	0.81	-1.06	2.64	0.81	-1.06	3.9	3.9
G 270.255+0.835	0.04	2.08	-0.04	0.04	2.08	-0.04	2.2	2.4
G 281.710-1.104	0.84	3.09	-0.84	2.57	1.36	-1.36	0.7	4.3
G 284.352-0.419	0.13	4.83	-0.13	4.04	0.92	-0.92	1	5.3
G 284.694-0.361	5.3	0.71	-0.83	5.3	0.71	-0.83	2	6.4
G 285.337-0.002	0.63	4.2	-0.63	3.81	1.01	-1.01	0.5	5.1
G 286.383-1.834	5.31	0.73	-5.02	5.31	0.73	-0.87	1.5	6.4
G 287.371+0.644	0.96	4.1	-0.96	4.05	1.01	-1.01	0.2	5.3
G 290.374+1.661	2.92	1.95	-1.95	2.92	1.95	-1.95	2.9	2.9
G 290.411-2.915	2.93	1.95	-1.95	2.93	1.95	-1.95	2.3	3.7
G 291.274-0.709	3.05	1.94	-1.94	3.05	1.94	-1.94	3	3
G 291.270-0.719	3.05	1.94	-1.94	3.05	1.94	-1.94	3	3
G 291.579-0.431	7.19	0.61	-0.65	7.19	0.61	-0.65	1.9	8.2
G 291.582-0.435	6.74	0.64	-6.61	6.74	0.64	-0.69	1.4	7.7
G 291.642-0.546	6.91	0.63	-0.67	6.91	0.63	-0.67	1.6	7.9
G 291.879-0.810	8.84	0.6	-0.59	8.84	0.6	-0.59	3.6	10
G 292.074-1.131	3.16	1.93	-1.93	3.16	1.93	-1.93	2.9	3.5
G 292.468+0.168	6.97	0.62	-6.84	6.97	0.62	-0.67	1.4	8
G 293.723-1.742	8.49	0.59	-0.59	8.49	0.59	-0.59	2.6	9.6
G 293.827-0.746	9.56	0.6	-0.59	9.56	0.6	-0.59	3.8	10.8
G 293.942-0.874	9.95	0.61	-0.59	9.95	0.61	-0.59	4.3	11.2
G 294.337-1.706	1.71	0.88	-0.88	5.22	0.88	-0.88	0.9	6.2
G 294.511-1.621	1.89	0.93	-0.93	5.08	0.93	-0.93	1	6.1
G 294.977-1.734	0.98	0.72	-0.72	6.11	0.72	-0.72	0.2	7
G 294.990-1.719	1.87	0.9	-0.9	5.23	0.9	-0.9	1	6.2
G 296.893-1.305	9.07	0.57	-0.57	9.07	0.57	-0.57	2.3	10.1
G 297.406-0.622	9.65	0.58	-0.57	9.65	0.58	-0.57	2.8	10.7
G 298.177-0.795	9.48	0.57	-0.56	9.48	0.57	-0.56	2.4	10.5
G 298.213-0.343	10.3	0.59	-0.57	10.3	0.59	-0.57	3.3	11.5
G 298.262+0.739	3.98	1.83	-1.83	3.98	1.83	-1.83	4	4
G 298.632-0.362	10.72	0.6	-0.58	10.72	0.6	-0.58	3.7	11.9
G 298.723-0.086	9.61	0.57	-0.56	9.61	0.57	-0.56	2.4	10.6
G 299.013+0.128	9.28	0.56	-0.56	9.28	0.56	-0.56	1.9	10.3
G 299.772-0.005	0.95	0.67	-0.61	7.39	0.61	-0.67	0.4	8.2
G 300.504-0.176	8.77	0.55	-8.44	8.77	0.55	-0.56	0.9	9.6
G 300.969+1.148	4.32	1.78	-1.78	4.32	1.78	-1.78	4.4	4.4
G 301.136-0.226	4.34	1.78	-1.78	4.34	1.78	-1.78	4.3	4.3
G 302.032-0.061	4.46	1.76	-1.76	4.46	1.76	-1.76	4.1	5
G 302.034+0.625	4.46	1.76	-1.76	4.46	1.76	-1.76	4.5	4.5
G 302.455-0.741	11.23	0.58	-0.56	11.23	0.58	-0.56	3.2	12.4
G 303.507-0.721	10.03	0.54	-0.53	10.03	0.54	-0.53	1.5	10.9
G 303.846-0.363	10.93	0.56	-0.54	10.93	0.56	-0.54	2.4	12
G 303.869+0.194	4.68	1.73	-1.73	4.68	1.73	-1.73	3.6	5.9
G 304.367-0.336	11.69	0.59	-0.56	11.69	0.59	-0.56	3.2	12.8
G 304.887+0.635	3.59	0.91	-0.91	6.02	0.91	-0.91	3.1	6.7
G 305.200+0.019	3.22	0.78	-0.78	6.47	0.78	-0.78	2.8	7.1

Table 7.3: – continued

Methanol maser (l, b) (degrees)	Reid09 near (kpc)	Error + (kpc)	Error − (kpc)	Reid09 far (kpc)	Error + (kpc)	Error − (kpc)	BB1993 near (kpc)	BB1993 far (kpc)
G 305.199+0.005	4.84	1.7	-1.7	4.84	1.7	-1.7	4.9	4.9
G 305.202+0.208	4.84	1.7	-1.7	4.84	1.7	-1.7	4.9	4.9
G 305.208+0.206	4.14	1.15	-1.15	5.54	1.15	-1.15	3.6	6.3
G 305.248+0.245	3.1	0.75	-0.75	6.6	0.75	-0.75	2.7	7.2
G 305.362+0.150	3.67	0.91	-0.91	6.05	0.91	-0.91	3.2	6.7
G 305.366+0.184	3.28	0.79	-0.79	6.44	0.79	-0.79	2.9	7
G 305.475-0.096	3.48	0.84	-0.84	6.27	0.84	-0.84	3.1	6.9
G 305.563+0.013	3.77	0.94	-0.94	6	0.94	-0.94	3.3	6.6
G 305.573-0.342	4.89	1.69	-1.69	4.89	1.69	-1.69	4.8	4.8
G 305.615-0.344	3.38	0.8	-0.8	6.4	0.8	-0.8	3	7
G 305.634+1.645	4.89	1.69	-1.69	4.89	1.69	-1.69	4.7	4.7
G 305.646+1.589	4.9	1.69	-1.69	4.9	1.69	-1.69	4.7	4.7
G 305.799-0.245	3.56	0.85	-0.85	6.27	0.85	-0.85	3.2	6.9
G 305.822-0.115	4.92	1.69	-1.69	4.92	1.69	-1.69	4.2	5.9
G 305.887+0.017	3.23	0.75	-0.75	6.62	0.75	-0.75	2.9	7.2
G 305.940-0.164	4.93	1.68	-1.68	4.93	1.68	-1.68	4.9	4.9
G 306.322-0.334	2.21	0.66	-0.58	7.74	0.58	-0.66	1.9	8.3
G 307.133-0.477	3.59	0.79	-0.79	6.56	0.79	-0.79	3.3	7.1
G 308.056-0.396	1.14	0.52	-0.51	9.21	0.51	-0.52	0.8	9.8
G 308.651-0.507	0.07	10.87	0.5	10.43	0.51	-0.5	0.5	11.2
G 308.686+0.530	5.25	1.62	-1.62	5.25	1.62	-1.62	5.3	5.3
G 308.715-0.216	1.19	0.51	-0.5	9.32	0.5	-0.51	0.8	9.9
G 308.754+0.549	4.16	0.89	-0.89	6.36	0.89	-0.89	3.9	6.8
G 308.918+0.123	5.28	1.62	-1.62	5.28	1.62	-1.62	5.3	5.3
G 309.384-0.135	4.87	1.22	-1.22	5.79	1.22	-1.22	4.5	6.3
G 309.901+0.231	5.39	1.6	-1.6	5.39	1.6	-1.6	5.5	5.5
G 309.921+0.479	5.39	1.59	-1.59	5.39	1.59	-1.59	5.3	5.3
G 310.144+0.760	5.42	1.59	-1.59	5.42	1.59	-1.59	5.5	5.5
G 310.180-0.122	0.05	11.24	0.49	10.79	0.5	-0.49	0.5	11.5
G 311.230-0.032	12.64	0.58	-0.55	12.64	0.58	-0.55	2.4	13.7
G 311.551-0.055	5.42	1.41	-1.41	5.73	1.41	-1.41	5.2	6.2
G 311.628+0.266	5.58	1.55	-1.55	5.58	1.55	-1.55	5.7	5.7
G 311.643-0.380	13.38	0.62	-0.58	13.38	0.62	-0.58	3.2	14.5
G 311.729-0.735	13.27	0.61	-0.58	13.27	0.61	-0.58	3	14.4
G 311.947+0.142	3.42	0.57	-0.57	7.81	0.57	-0.57	3.3	8.1
G 312.071+0.082	2.68	0.55	-0.51	8.58	0.51	-0.55	2.5	8.9
G 312.108+0.262	3.98	0.67	-0.67	7.28	0.67	-0.67	3.9	7.6
G 312.307+0.661	1.11	0.47	-0.48	10.2	0.48	-0.47	0.8	10.7
G 312.501-0.084	12.69	0.57	-0.54	12.69	0.57	-0.54	2.1	13.6
G 312.598+0.045	5.69	1.53	-1.53	5.69	1.53	-1.53	5.6	5.6
G 312.597+0.045	5.69	1.53	-1.53	5.69	1.53	-1.53	5.8	5.8
G 312.702-0.087	5.41	1.27	-1.27	5.98	1.27	-1.27	5.4	6.2
G 312.698+0.126	13.36	0.61	-0.57	13.36	0.61	-0.57	2.9	14.5
G 313.469+0.190	0.9	0.47	-0.47	10.66	0.47	-0.47	0.5	11.2
G 313.577+0.325	3.59	0.67	-0.55	8	0.55	-0.67	3.5	8.3
G 313.705-0.190	3.07	0.55	-0.5	8.54	0.5	-0.55	3	8.8
G 313.767-0.863	3.32	0.59	-0.52	8.3	0.52	-0.59	3.3	8.6
G 313.774-0.863	4.39	0.69	-0.69	7.23	0.69	-0.69	4.4	7.4
G 313.994-0.084	0.6	0.47	-0.48	11.07	0.48	-0.47	0.2	11.7
G 314.221+0.273	5	0.88	-0.88	6.72	0.88	-0.88	5.1	6.8
G 314.320+0.112	3.18	0.55	-0.5	8.56	0.5	-0.55	3.1	8.8

Table 7.3: – continued

Methanol maser (l, b) (degrees)	Reid09 near (kpc)	Error + (kpc)	Error − (kpc)	Reid09 far (kpc)	Error + (kpc)	Error − (kpc)	BB1993 near (kpc)	BB1993 far (kpc)
G 315.803-0.575	12.37	0.52	-12.2	12.37	0.52	-0.5	0.9	13.1
G 316.359-0.362	0.01	12.63	0.48	12.14	0.5	-0.48	0.5	12.8
G 316.381-0.379	0.3	12.06	0.47	11.86	0.49	-0.47	0.1	12.5
G 316.412-0.308	0.64	0.46	-0.48	11.53	0.48	-0.46	0.3	12.1
G 316.484-0.310	1.02	0.45	-0.46	11.17	0.46	-0.45	0.7	11.7
G 316.640-0.087	1.59	0.44	-0.45	10.63	0.45	-0.44	1.4	11.1
G 316.811-0.057	3.19	0.48	-0.46	9.06	0.46	-0.48	3.2	9.3
G 317.029+0.361	3.32	0.49	-0.46	8.97	0.46	-0.49	3.3	9.2
G 317.061+0.256	3.05	0.47	-0.45	9.25	0.45	-0.47	3	9.5
G 317.466-0.402	2.65	0.44	-0.43	9.73	0.43	-0.44	2.6	10
G 317.701+0.110	2.92	0.45	-0.44	9.5	0.44	-0.45	2.9	9.8
G 318.050+0.087	3.52	0.49	-0.45	8.98	0.45	-0.49	3.6	9.1
G 318.044-1.404	16.25	0.83	-0.75	16.25	0.83	-0.75	5.2	17.9
G 318.472-0.214	1.49	0.43	-0.44	11.09	0.44	-0.43	1.3	11.5
G 318.948-0.196	2.43	0.42	-0.42	10.24	0.42	-0.42	2.3	10.5
G 319.163-0.421	1.61	0.43	-0.44	11.1	0.44	-0.43	1.4	11.5
G 319.836-0.197	0.86	0.45	-0.47	11.98	0.47	-0.45	0.6	12.5
G 320.123-0.504	0.91	0.44	-0.46	11.98	0.46	-0.44	0.6	12.5
G 320.231-0.284	4.08	0.49	-0.45	8.84	0.45	-0.49	4.2	8.9
G 320.244-0.562	3.29	0.43	-0.41	9.63	0.41	-0.43	3.3	9.8
G 320.263-0.534	3.28	0.43	-0.41	9.63	0.41	-0.43	3.3	9.8
G 320.285-0.308	4.54	0.6	-0.49	8.38	0.49	-0.6	4.8	8.4
G 320.427+0.103	1.13	0.43	-0.45	11.82	0.45	-0.43	0.9	12.3
G 320.424+0.089	0.78	0.45	-0.47	12.17	0.47	-0.45	0.5	12.7
G 320.625+0.098	0.75	0.45	-0.47	12.24	0.47	-0.45	0.4	12.8
G 320.780+0.248	0.58	0.46	-0.48	12.43	0.48	-0.46	0.2	13
G 321.033-0.483	3.95	0.46	-0.42	9.11	0.42	-0.46	4.1	9.2
G 321.030-0.485	4.3	0.5	-0.45	8.77	0.45	-0.5	4.5	8.8
G 321.148-0.529	4.26	0.49	-0.44	8.82	0.44	-0.49	4.5	8.8
G 321.704+1.168	2.94	0.4	-0.4	10.24	0.4	-0.4	3	10.4
G 322.158+0.636	4.02	0.44	-0.41	9.25	0.41	-0.44	4.2	9.3
G 322.705-0.331	1.63	0.41	-0.43	11.73	0.43	-0.41	1.5	12.1
G 323.459-0.079	4.17	0.42	-0.39	9.33	0.39	-0.42	4.4	9.3
G 323.740-0.263	3.28	0.38	-0.38	10.26	0.38	-0.38	3.4	10.4
G 323.766-1.370	17.85	1.02	-0.89	17.85	1.02	-0.89	5.9	19.7
G 323.793-0.397	1.69	0.41	-0.43	11.86	0.43	-0.41	1.6	12.2
G 323.799+0.017	3.55	0.38	-0.38	10	0.38	-0.38	3.7	10.1
G 324.716+0.342	3	0.37	-0.38	10.72	0.38	-0.37	3.1	10.9
G 324.789-0.378	14.41	0.6	-0.55	14.41	0.6	-0.55	1.3	15.2
G 324.915+0.158	0.57	0.47	-0.5	13.18	0.5	-0.47	0.3	13.7
G 324.923-0.568	4.73	0.44	-0.4	9.01	0.4	-0.44	5.1	8.9
G 325.659-0.022	16.24	0.8	-0.72	16.24	0.8	-0.72	3.4	17.5
G 326.323-0.393	4.19	0.37	-0.36	9.79	0.36	-0.37	4.4	9.8
G 326.448-0.748	4.14	0.36	-0.35	9.86	0.35	-0.36	4.4	9.9
G 326.475+0.703	2.6	0.37	-0.38	11.4	0.38	-0.37	2.6	11.6
G 326.476+0.695	2.87	0.36	-0.37	11.14	0.37	-0.36	2.9	11.3
G 326.608+0.799	2.94	0.36	-0.37	11.08	0.37	-0.36	3	11.2
G 326.641+0.611	2.82	0.36	-0.37	11.21	0.37	-0.36	2.9	11.4
G 326.662+0.520	2.61	0.37	-0.38	11.42	0.38	-0.37	2.6	11.6
G 326.859-0.677	3.61	0.35	-0.35	10.45	0.35	-0.35	3.8	10.5
G 326.986-0.031	3.74	0.35	-0.35	10.35	0.35	-0.35	3.9	10.4
G 327.120+0.511	5.1	0.43	-0.38	9	0.38	-0.43	5.5	8.8
G 327.282-0.469	0.21	14.26	0.5	13.92	0.55	-0.5	0.2	14.5
G 327.291-0.578	2.53	0.37	-0.38	11.61	0.38	-0.37	2.5	11.8

Table 7.3: - continued

Methanol maser (l, b) (degrees)	Reid09 near (kpc)	Error + (kpc)	Error − (kpc)	Reid09 far (kpc)	Error + (kpc)	Error − (kpc)	BB1993 near (kpc)	BB1993 far (kpc)
G 327.402+0.445	4.84	0.39	-0.36	9.31	0.36	-0.39	5.2	9.2
G 327.392+0.199	4.92	0.4	-0.37	9.23	0.37	-0.4	5.3	9.1
G 327.395+0.197	5.19	0.44	-0.38	8.97	0.38	-0.44	5.6	8.8
G 327.566-0.850	2.08	0.39	-0.41	12.1	0.41	-0.39	2	12.4
G 327.590-0.094	5.03	0.4	-0.37	9.16	0.37	-0.4	5.4	9
G 327.618-0.111	5.75	0.45	-0.45	8.44	0.45	-0.45	6.4	8
G 327.710-0.394	4.57	0.36	-0.35	9.63	0.35	-0.36	4.9	9.6
G 327.808-0.634	2.82	0.36	-0.37	11.4	0.37	-0.36	2.9	11.6
G 327.863+0.098	3.02	0.35	-0.36	11.21	0.36	-0.35	3.1	11.3
G 327.945-0.115	3.29	0.34	-0.35	10.95	0.35	-0.34	3.4	11.1
G 328.140-0.432	2.68	0.36	-0.38	11.59	0.38	-0.36	2.7	11.8
G 328.164+0.587	5.3	0.43	-0.38	8.97	0.38	-0.43	5.8	8.7
G 328.237-0.547	2.94	0.35	-0.36	11.34	0.36	-0.35	3	11.5
G 328.254-0.532	2.56	0.37	-0.38	11.72	0.38	-0.37	2.6	11.9
G 328.385+0.131	16.8	0.88	-0.77	16.8	0.88	-0.77	3.6	18.1
G 328.808+0.633	2.91	0.35	-0.37	11.47	0.37	-0.35	3	11.6
G 328.809+0.633	2.93	0.35	-0.36	11.45	0.36	-0.35	3	11.6
G 328.819+1.704	4.96	0.37	-0.34	9.41	0.34	-0.37	5.3	9.3
G 328.942+0.565	5.19	0.39	-0.35	9.2	0.35	-0.39	5.6	9
G 329.029-0.205	2.55	0.36	-0.38	11.86	0.38	-0.36	2.6	12.1
G 329.031-0.198	3.02	0.35	-0.36	11.39	0.36	-0.35	3.1	11.5
G 329.066-0.308	2.91	0.35	-0.36	11.5	0.36	-0.35	3	11.6
G 329.183-0.314	3.49	0.33	-0.34	10.93	0.34	-0.33	3.6	11
G 329.272+0.115	4.27	0.33	-0.33	10.18	0.33	-0.33	4.5	10.1
G 329.341-0.644	4.7	0.34	-0.33	9.75	0.33	-0.34	5	9.6
G 329.339+0.148	6.09	0.46	-0.46	8.36	0.46	-0.46	7.3	7.3
G 329.407-0.459	4.02	0.33	-0.33	10.44	0.33	-0.33	4.2	10.4
G 329.405-0.459	4.19	0.33	-0.33	10.27	0.33	-0.33	4.4	10.2
G 329.469+0.503	4.26	0.33	-0.33	10.21	0.33	-0.33	4.5	10.2
G 329.526+0.216	5.26	0.38	-0.35	9.22	0.35	-0.38	5.7	9
G 329.556+0.181	6.06	0.44	-0.44	8.42	0.44	-0.44	7.1	7.6
G 329.610+0.114	3.71	0.33	-0.33	10.78	0.33	-0.33	3.9	10.8
G 329.622+0.138	4.87	0.34	-0.33	9.62	0.33	-0.34	5.2	9.5
G 329.719+1.164	4.44	0.33	-0.32	10.06	0.32	-0.33	4.7	10
G 330.070+1.064	2.82	0.35	-0.37	11.73	0.37	-0.35	2.9	11.9
G 330.226+0.290	5.11	0.35	-0.33	9.47	0.33	-0.35	5.5	9.3
G 330.283+0.493	5.03	0.34	-0.32	9.56	0.32	-0.34	5.4	9.4
G 330.878-0.367	3.68	0.32	-0.33	10.99	0.33	-0.32	3.9	11
G 330.875-0.383	4.16	0.31	-0.32	10.52	0.32	-0.31	4.4	10.5
G 330.953-0.182	4.95	0.32	-0.31	9.74	0.31	-0.32	5.3	9.6
G 330.998+0.093	2.13	0.39	-0.41	12.56	0.41	-0.39	2.1	12.8
G 331.059+0.375	4.73	0.31	-0.31	9.98	0.31	-0.31	5.1	9.9
G 331.120-0.118	5.2	0.34	-0.32	9.51	0.32	-0.34	5.6	9.3
G 331.132-0.244	4.8	0.32	-0.31	9.91	0.31	-0.32	5.1	9.8
G 331.134+0.156	4.27	0.31	-0.31	10.45	0.31	-0.31	4.5	10.4
G 331.278-0.188	4.53	0.31	-0.31	10.2	0.31	-0.31	4.8	10.1
G 331.342-0.346	3.96	0.31	-0.32	10.79	0.32	-0.31	4.2	10.8
G 331.425+0.264	5	0.32	-0.31	9.75	0.31	-0.32	5.4	9.6
G 331.442-0.187	4.96	0.32	-0.31	9.8	0.31	-0.32	5.3	9.7
G 331.437-0.304	5.04	0.32	-0.31	9.71	0.31	-0.32	5.4	9.5
G 331.542-0.066	4.87	0.31	-0.31	9.9	0.31	-0.31	5.2	9.8

Table 7.3: – continued

Methanol maser (l, b) (degrees)	Reid09 near (kpc)	Error + (kpc)	Error − (kpc)	Reid09 far (kpc)	Error + (kpc)	Error − (kpc)	BB1993 near (kpc)	BB1993 far (kpc)
G 331.543-0.066	4.79	0.31	-0.3	9.98	0.3	-0.31	5.1	9.9
G 331.556-0.121	5.37	0.34	-0.32	9.4	0.32	-0.34	5.8	9.2
G 331.710+0.603	4.32	0.3	-0.31	10.47	0.31	-0.3	4.6	10.4
G 331.900-1.186	3.09	0.34	-0.35	11.73	0.35	-0.34	3.2	11.8
G 332.094-0.421	3.67	0.31	-0.32	11.18	0.32	-0.31	3.9	11.2
G 332.295-0.094	2.92	0.34	-0.36	11.96	0.36	-0.34	3	12.1
G 332.295+2.280	1.89	0.41	-0.44	12.98	0.44	-0.41	1.8	13.3
G 332.351-0.436	3.41	0.32	-0.34	11.47	0.34	-0.32	3.6	11.5
G 332.352-0.117	3.02	0.34	-0.36	11.86	0.36	-0.34	3.1	12
G 332.364+0.607	3.21	0.33	-0.35	11.67	0.35	-0.33	3.3	11.8
G 332.560-0.148	3.51	0.32	-0.33	11.4	0.33	-0.32	3.7	11.4
G 332.583+0.147	2.79	0.35	-0.37	12.13	0.37	-0.35	2.9	12.3
G 332.604-0.168	3.28	0.33	-0.34	11.64	0.34	-0.33	3.4	11.7
G 332.653-0.621	3.32	0.32	-0.34	11.6	0.34	-0.32	3.5	11.7
G 332.701-0.588	3.88	0.3	-0.31	11.05	0.31	-0.3	4.1	11.1
G 332.726-0.621	3.17	0.33	-0.35	11.77	0.35	-0.33	3.3	11.9
G 332.813-0.701	3.44	0.32	-0.33	11.5	0.33	-0.32	3.6	11.6
G 332.826-0.549	3.84	0.31	-0.32	11.11	0.32	-0.31	4.1	11.1
G 332.854+0.817	3.25	0.33	-0.34	11.7	0.34	-0.33	3.4	11.8
G 332.960+0.135	3.5	0.32	-0.33	11.47	0.33	-0.32	3.7	11.5
G 332.963-0.679	3.1	0.34	-0.35	11.87	0.35	-0.34	3.2	12
G 332.942-0.686	3.39	0.32	-0.34	11.57	0.34	-0.32	3.6	11.6
G 332.975+0.773	3.34	0.32	-0.34	11.62	0.34	-0.32	3.5	11.7
G 332.987-0.487	3.56	0.31	-0.33	11.4	0.33	-0.31	3.7	11.4
G 333.029-0.063	2.81	0.35	-0.37	12.16	0.37	-0.35	2.9	12.3
G 333.029-0.015	3.49	0.32	-0.33	11.48	0.33	-0.32	3.7	11.5
G 333.068-0.447	3.51	0.32	-0.33	11.47	0.33	-0.32	3.7	11.5
G 333.109-0.500	3.8	0.31	-0.32	11.19	0.32	-0.31	4	11.2
G 333.128-0.560	3.43	0.32	-0.34	11.56	0.34	-0.32	3.6	11.6
G 333.130-0.560	3.61	0.31	-0.33	11.37	0.33	-0.31	3.8	11.4
G 333.121-0.434	3.23	0.33	-0.35	11.75	0.35	-0.33	3.4	11.8
G 333.126-0.440	3.01	0.34	-0.36	11.98	0.36	-0.34	3.1	12.1
G 333.128-0.440	3.01	0.34	-0.36	11.97	0.36	-0.34	3.1	12.1
G 333.163-0.101	5.24	0.3	-0.29	9.75	0.29	-0.3	5.7	9.6
G 333.184-0.091	4.69	0.29	-0.29	10.3	0.29	-0.29	5	10.2
G 333.234-0.060	5.1	0.29	-0.29	9.9	0.29	-0.29	5.5	9.7
G 333.315+0.105	2.88	0.35	-0.37	12.13	0.37	-0.35	3	12.3
G 333.387+0.032	4.36	0.29	-0.3	10.66	0.3	-0.29	4.6	10.6
G 333.466-0.164	2.93	0.34	-0.37	12.1	0.37	-0.34	3	12.2
G 333.562-0.025	2.58	0.37	-0.39	12.47	0.39	-0.37	2.6	12.6
G 333.646+0.058	4.92	0.28	-0.28	10.14	0.28	-0.28	5.3	10
G 333.683-0.437	0.67	0.52	-0.58	14.39	0.58	-0.52	0.4	14.9
G 333.761-0.226	3.56	0.31	-0.33	11.5	0.33	-0.31	3.8	11.5
G 333.851+0.527	2.85	0.35	-0.37	12.23	0.37	-0.35	2.9	12.4
G 333.900-0.099	3.76	0.3	-0.32	11.33	0.32	-0.3	4	11.3
G 333.931-0.135	2.67	0.36	-0.39	12.42	0.39	-0.36	2.7	12.6
G 334.138-0.023	2.36	0.38	-0.41	12.75	0.41	-0.38	2.4	12.9
G 334.307-0.079	2.68	0.36	-0.39	12.46	0.39	-0.36	2.8	12.6
G 334.635-0.015	2.32	0.39	-0.42	12.86	0.42	-0.39	2.4	13.1
G 334.933-0.307	5.53	0.28	-0.27	9.69	0.27	-0.28	6	9.5
G 334.935-0.098	1.78	0.43	-0.47	13.43	0.47	-0.43	1.7	13.7
G 335.060-0.427	3.22	0.33	-0.35	12.01	0.35	-0.33	3.4	12.1
G 335.426-0.240	3.41	0.32	-0.34	11.87	0.34	-0.32	3.6	11.9

Table 7.3: – continued

Methanol maser (l, b) (degrees)	Reid09 near (kpc)	Error + (kpc)	Error − (kpc)	Reid09 far (kpc)	Error + (kpc)	Error − (kpc)	BB1993 near (kpc)	BB1993 far (kpc)
G 335.556-0.307	6.06	0.31	-0.29	9.23	0.29	-0.31	6.7	8.8
G 335.585-0.285	3.33	0.32	-0.34	11.97	0.34	-0.32	3.5	12
G 335.585-0.290	3.45	0.32	-0.34	11.84	0.34	-0.32	3.6	11.9
G 335.726+0.191	3.13	0.34	-0.36	12.19	0.36	-0.34	3.3	12.3
G 335.789+0.174	3.28	0.33	-0.35	12.04	0.35	-0.33	3.4	12.1
G 335.824-0.177	2.13	0.41	-0.45	13.19	0.45	-0.41	2.1	13.4
G 336.018-0.827	3.56	0.31	-0.33	11.79	0.33	-0.31	3.8	11.8
G 336.358-0.137	4.43	0.27	-0.28	10.96	0.28	-0.27	4.7	10.9
G 336.409-0.257	4.9	0.26	-0.26	10.49	0.26	-0.26	5.3	10.4
G 336.433-0.262	5.16	0.26	-0.26	10.23	0.26	-0.26	5.5	10.1
G 336.464-0.157	4.9	0.26	-0.26	10.5	0.26	-0.26	5.2	10.4
G 336.496-0.271	2.04	0.42	-0.46	13.37	0.46	-0.42	2	13.6
G 336.526-0.156	5.24	0.25	-0.26	10.17	0.26	-0.25	5.6	10
G 336.703-0.099	2.72	0.37	-0.4	12.71	0.4	-0.37	2.8	12.8
G 336.809+0.119	4.86	0.26	-0.26	10.58	0.26	-0.26	5.2	10.5
G 336.822+0.028	4.57	0.26	-0.27	10.87	0.27	-0.26	4.9	10.8
G 336.825+0.139	5.01	0.25	-0.26	10.44	0.26	-0.25	5.4	10.3
G 336.830-0.375	1.97	0.43	-0.47	13.48	0.47	-0.43	1.9	13.7
G 336.864+0.005	4.55	0.26	-0.27	10.9	0.27	-0.26	4.9	10.8
G 336.916-0.024	6.47	0.34	-0.29	8.98	0.29	-0.34	7.3	8.4
G 336.941-0.156	4.2	0.28	-0.29	11.26	0.29	-0.28	4.5	11.2
G 336.957-0.225	4.23	0.28	-0.29	11.23	0.29	-0.28	4.5	11.2
G 336.958-0.977	3.42	0.32	-0.34	12.04	0.34	-0.32	3.6	12.1
G 336.983-0.183	4.73	0.26	-0.27	10.74	0.27	-0.26	5.1	10.6
G 336.994-0.027	6.4	0.32	-0.28	9.07	0.28	-0.32	7.1	8.5
G 337.052-0.226	4.61	0.26	-0.27	10.86	0.27	-0.26	4.9	10.8
G 337.097-0.929	2.99	0.35	-0.38	12.48	0.38	-0.35	3.1	12.6
G 337.132-0.068	3.94	0.29	-0.31	11.54	0.31	-0.29	4.2	11.5
G 337.153-0.395	3.44	0.32	-0.34	12.04	0.34	-0.32	3.6	12.1
G 337.176-0.032	4.11	0.28	-0.3	11.37	0.3	-0.28	4.4	11.3
G 337.202-0.094	4.23	0.27	-0.29	11.26	0.29	-0.27	4.5	11.2
G 337.201+0.114	3.81	0.3	-0.31	11.68	0.31	-0.3	4	11.7
G 337.258-0.101	4.3	0.27	-0.29	11.2	0.29	-0.27	4.6	11.1
G 337.263-0.070	2.95	0.35	-0.38	12.55	0.38	-0.35	3.1	12.6
G 337.300-0.874	4.98	0.25	-0.26	10.52	0.26	-0.25	5.3	10.4
G 337.404-0.402	2.97	0.35	-0.38	12.54	0.38	-0.35	3.1	12.6
G 337.388-0.210	3.76	0.3	-0.32	11.75	0.32	-0.3	4	11.8
G 337.517-0.348	16.3	0.88	-0.75	16.3	0.88	-0.75	1.4	17.1
G 337.613-0.060	3.08	0.34	-0.37	12.45	0.37	-0.34	3.2	12.5
G 337.632-0.079	3.8	0.3	-0.32	11.73	0.32	-0.3	4	11.7
G 337.686+0.137	4.54	0.26	-0.27	11	0.27	-0.26	4.8	10.9
G 337.705-0.053	3.7	0.3	-0.32	11.84	0.32	-0.3	3.9	11.8
G 337.710+0.089	4.45	0.26	-0.28	11.1	0.28	-0.26	4.7	11
G 337.720+0.065	4.1	0.28	-0.3	11.44	0.3	-0.28	4.4	11.4
G 337.844-0.375	2.94	0.36	-0.39	12.62	0.39	-0.36	3.1	12.7
G 337.920-0.456	2.9	0.36	-0.39	12.67	0.39	-0.36	3	12.8
G 337.966-0.169	3.93	0.29	-0.31	11.65	0.31	-0.29	4.2	11.6
G 337.997+0.136	2.6	0.38	-0.42	12.98	0.42	-0.38	2.7	13.1
G 338.075+0.012	3.23	0.33	-0.36	12.36	0.36	-0.33	3.4	12.4
G 338.075+0.009	2.98	0.35	-0.38	12.61	0.38	-0.35	3.1	12.7
G 338.069+0.011	3.02	0.35	-0.38	12.57	0.38	-0.35	3.2	12.7
G 338.140+0.178	2.73	0.37	-0.41	12.86	0.41	-0.37	2.8	13
G 338.160-0.064	4.22	0.27	-0.29	11.38	0.29	-0.27	4.5	11.3
G 338.287+0.120	3.03	0.35	-0.38	12.58	0.38	-0.35	3.2	12.7
G 338.280+0.542	3.83	0.3	-0.32	11.78	0.32	-0.3	4.1	11.8
G 338.325-0.409	2.22	0.42	-0.46	13.39	0.46	-0.42	2.2	13.6

Table 7.3: – continued

Methanol maser (l, b) (degrees)	Reid09 near (kpc)	Error + (kpc)	Error − (kpc)	Reid09 far (kpc)	Error + (kpc)	Error − (kpc)	BB1993 near (kpc)	BB1993 far (kpc)
G 338.392-0.403	2.69	0.38	-0.42	12.93	0.42	-0.38	2.8	13.1
G 338.396-0.007	3.48	0.32	-0.34	12.14	0.34	-0.32	3.7	12.2
G 338.388+0.162	2.47	0.4	-0.44	13.14	0.44	-0.4	2.5	13.3
G 338.432+0.058	2.5	0.4	-0.44	13.12	0.44	-0.4	2.6	13.3
G 338.461-0.245	3.62	0.31	-0.33	12.01	0.33	-0.31	3.8	12
G 338.472+0.289	2.46	0.4	-0.44	13.17	0.44	-0.4	2.5	13.3
G 338.497+0.207	2.38	0.41	-0.45	13.25	0.45	-0.41	2.4	13.4
G 338.566+0.110	4.57	0.26	-0.27	11.07	0.27	-0.26	4.9	11
G 338.561+0.218	3	0.35	-0.39	12.63	0.39	-0.35	3.1	12.7
G 338.875-0.084	3.14	0.35	-0.38	12.53	0.38	-0.35	3.3	12.6
G 338.850+0.409	3.82	0.3	-0.32	11.85	0.32	-0.3	4	11.8
G 338.902+0.394	2.27	0.42	-0.47	13.4	0.47	-0.42	2.3	13.6
G 338.926+0.634	4.04	0.28	-0.3	11.64	0.3	-0.28	4.3	11.6
G 338.920+0.550	4.06	0.28	-0.3	11.61	0.3	-0.28	4.3	11.6
G 338.935-0.062	3.17	0.34	-0.37	12.51	0.37	-0.34	3.3	12.6
G 339.053-0.315	5.85	0.23	-0.23	9.84	0.23	-0.23	6.3	9.6
G 339.064+0.152	5.05	0.24	-0.25	10.64	0.25	-0.24	5.4	10.5
G 339.204-0.018	1.47	0.51	-0.57	14.24	0.57	-0.51	1.4	14.6
G 339.282+0.136	4.43	0.26	-0.28	11.29	0.28	-0.26	4.7	11.2
G 339.294+0.139	4.6	0.25	-0.27	11.11	0.27	-0.25	4.9	11
G 339.477+0.043	1.09	0.56	-0.63	14.64	0.63	-0.56	0.9	15
G 339.476+0.185	5.07	0.23	-0.24	10.66	0.24	-0.23	5.4	10.5
G 339.582-0.127	2.58	0.4	-0.44	13.17	0.44	-0.4	2.7	13.3
G 339.622-0.121	2.73	0.38	-0.42	13.02	0.42	-0.38	2.8	13.1
G 339.681-1.208	2.01	0.46	-0.51	13.75	0.51	-0.46	2	14
G 339.762+0.054	3.67	0.31	-0.33	12.1	0.33	-0.31	3.9	12.1
G 339.884-1.259	3.07	0.36	-0.39	12.71	0.39	-0.36	3.2	12.8
G 339.909+0.240	1.32	0.54	-0.61	14.45	0.61	-0.54	1.2	14.8
G 339.949-0.539	5.43	0.22	-0.23	10.35	0.23	-0.22	5.8	10.2
G 339.980-0.538	5.15	0.23	-0.24	10.64	0.24	-0.23	5.5	10.5
G 339.986-0.425	5.16	0.23	-0.24	10.63	0.24	-0.23	5.5	10.5
G 340.034-1.110	2.43	0.42	-0.46	13.36	0.46	-0.42	2.5	13.5
G 340.054-0.244	4.05	0.28	-0.3	11.74	0.3	-0.28	4.3	11.7
G 340.118-0.021	6.23	0.23	-0.22	9.56	0.22	-0.23	6.8	9.2
G 340.182-0.047	6.49	0.24	-0.23	9.32	0.23	-0.24	7.1	8.9
G 340.249-0.372	3.71	0.31	-0.33	12.1	0.33	-0.31	3.9	12.1
G 340.249-0.046	6.33	0.23	-0.22	9.48	0.22	-0.23	6.9	9.1
G 340.518-0.152	3.59	0.32	-0.35	12.25	0.35	-0.32	3.8	12.3
G 340.543-0.162	3.75	0.31	-0.33	12.09	0.33	-0.31	4	12.1
G 340.655-0.235	2.08	0.46	-0.52	13.78	0.52	-0.46	2.1	14
G 340.785-0.096	5.78	0.21	-0.21	10.08	0.21	-0.21	6.2	9.9
G 340.970-1.022	2.73	0.4	-0.44	13.15	0.44	-0.4	2.8	13.3
G 341.124-0.361	3.07	0.37	-0.4	12.82	0.4	-0.37	3.2	12.9
G 341.218-0.212	3.12	0.36	-0.4	12.79	0.4	-0.36	3.3	12.8
G 341.238-0.270	3.79	0.31	-0.33	12.12	0.33	-0.31	4	12.1
G 341.276+0.062	4.58	0.25	-0.27	11.33	0.27	-0.25	4.9	11.2
G 341.367+0.336	4.94	0.23	-0.25	10.98	0.25	-0.23	5.3	10.9
G 341.990-0.103	3.13	0.37	-0.41	12.85	0.41	-0.37	3.3	12.9
G 341.973+0.233	1.39	0.57	-0.66	14.58	0.66	-0.57	1.3	14.9
G 342.251+0.308	6.25	0.2	-0.19	9.75	0.19	-0.2	6.7	9.5
G 342.338+0.305	5.96	0.19	-0.2	10.05	0.2	-0.19	6.4	9.8

Table 7.3: – continued

Methanol maser (l, b) (degrees)	Reid09 near (kpc)	Error + (kpc)	Error − (kpc)	Reid09 far (kpc)	Error + (kpc)	Error − (kpc)	BB1993 near (kpc)	BB1993 far (kpc)
G 342.368+0.140	0.98	0.63	-0.74	15.03	0.74	-0.63	0.8	15.4
G 342.446-0.072	2.09	0.49	-0.56	13.93	0.56	-0.49	2.1	14.1
G 342.484+0.183	3.45	0.34	-0.38	12.57	0.38	-0.34	3.7	12.6
G 342.954-0.019	0.57	15.78	0.71	15.5	0.85	-0.71	0.3	16
G 343.354-0.067	6.15	0.18	-0.19	9.94	0.19	-0.18	6.6	9.7
G 343.502-0.472	3.37	0.36	-0.4	12.73	0.4	-0.36	3.6	12.8
G 343.756-0.163	2.92	0.41	-0.47	13.21	0.47	-0.41	3.1	13.3
G 343.929+0.125	18.24	1.61	-1.25	18.24	1.61	-1.25	3.1	19.5
G 344.227-0.569	2.18	0.51	-0.6	13.98	0.6	-0.51	2.2	14.2
G 344.421+0.045	4.87	0.24	-0.25	11.31	0.25	-0.24	5.2	11.2
G 344.419+0.044	4.64	0.25	-0.28	11.55	0.28	-0.25	5	11.5
G 344.581-0.024	0.01	17.25	0.87	16.19	1.07	-0.87	0.4	16.8
G 345.003-0.223	2.51	0.49	-0.56	13.71	0.56	-0.49	2.6	13.8
G 345.003-0.224	2.73	0.46	-0.53	13.5	0.53	-0.46	2.9	13.6
G 345.010+1.792	2.36	0.51	-0.59	13.87	0.59	-0.51	2.4	14
G 345.012+1.797	1.58	0.62	-0.74	14.65	0.74	-0.62	1.5	14.9
G 345.131-0.174	2.93	0.43	-0.5	13.3	0.5	-0.43	3.1	13.4
G 345.198-0.030	0.28	16.73	0.85	15.96	1.05	-0.85	0.1	16.5
G 345.205+0.317	4.67	0.25	-0.28	11.58	0.28	-0.25	5	11.5
G 345.407-0.952	1.81	0.6	-0.71	14.45	0.71	-0.6	1.8	14.7
G 345.424-0.951	1.71	0.61	-0.73	14.55	0.73	-0.61	1.7	14.8
G 345.441+0.205	0.09	17.2	0.89	16.17	1.12	-0.89	0.3	16.8
G 345.487+0.314	2.48	0.5	-0.59	13.79	0.59	-0.5	2.6	13.9
G 345.505+0.348	2.14	0.55	-0.65	14.13	0.65	-0.55	2.2	14.3
G 345.498+1.467	1.82	0.6	-0.71	14.44	0.71	-0.6	1.8	14.7
G 345.576-0.225	6.49	0.16	-0.16	9.78	0.16	-0.16	7	9.5
G 345.807-0.044	0.43	16.48	0.85	15.86	1.05	-0.85	0.1	16.4
G 345.824+0.044	1.46	0.67	-0.81	14.83	0.81	-0.67	1.4	15.1
G 345.949-0.268	2.53	0.51	-0.59	13.77	0.59	-0.51	2.6	13.9
G 345.985-0.020	5.41	0.2	-0.22	10.89	0.22	-0.2	5.8	10.7
G 346.036+0.048	1.04	0.75	-0.92	15.26	0.92	-0.75	0.9	15.6
G 346.231+0.119	5.77	0.18	-0.19	10.55	0.19	-0.18	6.2	10.4
G 346.480+0.221	2.33	0.55	-0.65	14.01	0.65	-0.55	2.4	14.2
G 346.481+0.132	0.96	15.39	0.78	15.38	0.97	-0.78	0.8	15.8
G 346.517+0.117	1.58	0.67	-0.82	14.75	0.82	-0.67	1.5	15
G 346.522+0.085	17.06	1.46	-16.65	17.06	1.46	-1.12	1.3	17.9
G 347.230+0.016	5.1	0.23	-0.25	11.28	0.25	-0.23	5.4	11.2
G 347.583+0.213	6.08	0.16	-0.17	10.32	0.17	-0.16	6.5	10.1
G 347.628+0.149	5.95	0.17	-0.18	10.46	0.18	-0.17	6.3	10.3
G 347.631+0.211	5.83	0.18	-0.19	10.58	0.19	-0.18	6.2	10.4
G 347.817+0.018	2.91	0.5	-0.6	13.51	0.6	-0.5	3.1	13.6
G 347.863+0.019	3.65	0.4	-0.46	12.78	0.46	-0.4	3.9	12.8
G 347.902+0.052	3.17	0.46	-0.55	13.26	0.55	-0.46	3.4	13.3
G 348.027+0.106	6.54	0.14	-0.14	9.9	0.14	-0.14	7	9.7
G 348.195+0.768	0.35	17.05	1	16.09	1.31	-1	0	16.6
G 348.550-0.979	1.65	0.75	-0.95	14.82	0.95	-0.75	1.6	15.1
G 348.550-0.979n	2.67	0.56	-0.68	13.79	0.68	-0.56	2.8	13.9
G 348.579-0.920	2.11	0.66	-0.82	14.36	0.82	-0.66	2.2	14.5
G 348.617-1.162	1.82	0.72	-0.9	14.65	0.9	-0.72	1.8	14.9
G 348.654+0.244	20.72	3.64	-2.32	20.72	3.64	-2.32	6.3	23
G 348.723-0.078	18.88	2.58	-1.76	18.88	2.58	-1.76	3.6	20.3
G 348.703-1.043	0.79	16.13	0.94	15.69	1.22	-0.94	0.6	16.1
G 348.727-1.037	1.34	0.82	-1.05	15.14	1.05	-0.82	1.2	15.4
G 348.884+0.096	5.51	0.2	-0.22	10.98	0.22	-0.2	5.9	10.8
G 348.892-0.180	16.54	1.55	-15.45	16.54	1.55	-1.15	0.5	17.2

Table 7.3: – continued

Methanol maser (l, b) (degrees)	Reid09 near (kpc)	Error + (kpc)	Error − (kpc)	Reid09 far (kpc)	Error + (kpc)	Error − (kpc)	BB1993 near (kpc)	BB1993 far (kpc)
G 349.067-0.017	19.03	2.76	-1.84	19.03	2.76	-1.84	3.8	20.5
G 349.092+0.105	5.6	0.2	-0.22	10.9	0.22	-0.2	6	10.7
G 349.092+0.106	5.74	0.18	-0.2	10.76	0.2	-0.18	6.1	10.6
G 349.151+0.021	20.07	3.41	-2.18	20.07	3.41	-2.18	5.3	22
G 349.579-0.679	3.24	0.5	-0.61	13.28	0.61	-0.5	3.5	13.3
G 349.799+0.108	5.34	0.23	-0.25	11.2	0.25	-0.23	5.7	11.1
G 349.884+0.231	21.29	4.63	-2.73	21.29	4.63	-2.73	7.2	23.9
G 350.011-1.342	3.39	0.5	-0.6	13.15	0.6	-0.5	3.6	13.1
G 350.015+0.433	3.72	0.44	-0.53	12.82	0.53	-0.44	4	12.8
G 350.104+0.084	5.5	0.21	-0.24	11.05	0.24	-0.21	5.9	10.9
G 350.105+0.083	5.68	0.19	-0.22	10.87	0.22	-0.19	6.1	10.7
G 350.116+0.084	5.5	0.21	-0.24	11.05	0.24	-0.21	5.9	10.9
G 350.116+0.220	17.24	2.08	-16.5	17.24	2.08	-1.44	1.3	18.1
G 350.189+0.003	5.33	0.23	-0.26	11.23	0.26	-0.23	5.7	11.1
G 350.299+0.122	5.33	0.23	-0.26	11.23	0.26	-0.23	5.7	11.1
G 350.340+0.141	5.2	0.25	-0.28	11.36	0.28	-0.25	5.6	11.2
G 350.344+0.116	5.45	0.22	-0.25	11.11	0.25	-0.22	5.8	11
G 350.356-0.068	5.53	0.21	-0.24	11.04	0.24	-0.21	5.9	10.9
G 350.470+0.029	1.34	0.94	-1.26	15.22	1.26	-0.94	1.3	15.5
G 350.520-0.350	3.39	0.52	-0.63	13.18	0.63	-0.52	3.6	13.2
G 350.686-0.491	2.36	0.72	-0.94	14.22	0.94	-0.72	2.5	14.3
G 350.776+0.138	488.53	-423.03	-438.3	488.53	-423.03	-438.3	0	0
G 351.161+0.697	1.24	15.55	1.03	15.36	1.42	-1.03	1.1	15.7
G 351.242+0.670	16.94	2.2	-15.8	16.94	2.2	-1.47	0.9	17.7
G 351.251+0.652	1.56	0.95	-1.3	15.05	1.3	-0.95	1.5	15.3
G 351.382-0.181	5.45	0.23	-0.26	11.16	0.26	-0.23	5.8	11
G 351.417+0.645	2.07	0.84	-1.13	14.55	1.13	-0.84	2.1	14.7
G 351.417+0.646	2.18	0.82	-1.09	14.44	1.09	-0.82	2.2	14.6
G 351.445+0.660	1.9	0.88	-1.2	14.71	1.2	-0.88	1.9	14.9
G 351.581-0.353	6.42	0.14	-0.15	10.2	0.15	-0.14	6.8	10
G 351.611+0.172	4.83	0.32	-0.38	11.79	0.38	-0.32	5.2	11.6
G 351.688+0.171	4.45	0.38	-0.46	12.18	0.46	-0.38	4.8	12.1
G 351.775-0.536	16.71	2.23	-15.32	16.71	2.23	-1.47	0.5	17.4
G 352.083+0.167	5.81	0.2	-0.23	10.83	0.23	-0.2	6.2	10.7
G 352.111+0.176	5.43	0.25	-0.29	11.21	0.29	-0.25	5.8	11.1
G 352.133-0.944	1.78	0.98	-1.37	14.87	1.37	-0.98	1.8	15.1
G 352.517-0.155	5.38	0.26	-0.31	11.27	0.31	-0.26	5.8	11.1
G 352.525-0.158	5.46	0.25	-0.29	11.2	0.29	-0.25	5.8	11
G 352.584-0.185	6.41	0.14	-0.16	10.25	0.16	-0.14	6.8	10.1
G 352.604-0.225	6.32	0.15	-0.17	10.34	0.17	-0.15	6.7	10.2
G 352.624-1.077	1.54	15.18	1.1	15.12	1.6	-1.1	1.5	15.4
G 352.630-1.067	0.93	16.72	1.28	15.73	1.92	-1.28	0.7	16.1
G 352.855-0.201	5.47	0.26	-0.3	11.2	0.3	-0.26	5.8	11
G 353.216-0.249	2.46	0.91	-1.29	14.22	1.29	-0.91	2.6	14.3
G 353.273+0.641	1.34	15.91	1.24	15.35	1.9	-1.24	1.2	15.7
G 353.363-0.166	6.41	0.15	-0.17	10.27	0.17	-0.15	6.8	10.1
G 353.370-0.091	5.33	0.29	-0.35	11.36	0.35	-0.29	5.7	11.2
G 353.378+0.438	3.18	0.73	-1	13.5	1	-0.73	3.4	13.5
G 353.429-0.090	5.98	0.2	-0.23	10.71	0.23	-0.2	6.4	10.5
G 353.464+0.562	5.59	0.25	-0.3	11.1	0.3	-0.25	6	10.9
G 353.537-0.091	5.84	0.22	-0.26	10.85	0.26	-0.22	6.2	10.7
G 354.206-0.038	5.2	0.34	-0.43	11.51	0.43	-0.34	5.6	11.3
G 354.308-0.110	43.52	132.28	-19.46	43.52	132.28	-19.46	34	51
G 354.496+0.083	73.41	-12.55	-44.08	73.41	-12.55	-44.08	0	0
G 354.615+0.472	4.48	0.52	-0.7	12.24	0.7	-0.52	4.9	12.1
G 354.701+0.299	5.87	0.22	-0.26	10.85	0.26	-0.22	0	0
G 354.724+0.300	5.55	0.27	-0.33	11.18	0.33	-0.27	0	0

Table 7.3: – continued

Methanol maser (l, b) (degrees)	Reid09 near (kpc)	Error + (kpc)	Error − (kpc)	Reid09 far (kpc)	Error + (kpc)	Error − (kpc)	BB1993 near (kpc)	BB1993 far (kpc)
G 355.184-0.419	0.8	18.66	1.84	15.94	3.52	-1.84	0.6	16.4
G 355.343+0.148	19.93	11.47	-19.26	19.93	11.47	-3.86	5.3	22.3
G 355.344+0.147	0			0			0	0
G 355.346+0.149	25.39	46.51	-7.21	25.39	46.51	-7.21	16.2	33.1
G 355.538-0.105	18.47	8.39	-17.02	18.47	8.39	-3.16	3	20
G 355.545-0.103	5.15	0.43	-0.58	11.6	0.58	-0.43	5.6	11.4
G 355.642+0.398	2.7	1.2	-2.04	14.05	2.04	-1.2	2.9	14.1
G 355.666+0.374	1.51	16.95	1.67	15.24	3.23	-1.67	1.5	15.5
G 356.054-0.095	396.21	-364.43	-369.05	396.21	-364.43	-369.05	0	0
G 356.662-0.263	6.74	0.17	-0.2	10.03	0.2	-0.17	7.1	9.8
G 357.558-0.321	2.53	17.17	1.91	14.26	5.44	-1.91	2.8	14.2
G 357.559-0.321	25.76	41.3	-25.03	25.76	41.3	-9.7	0	0
G 357.922-0.337	3.09	16.14	1.8	13.69	5.54	-1.8	3.5	13.5
G 357.924-0.337	1.91	23.78	2.5	14.88	10.82	-2.5	2	15
G 357.965-0.164	4.34	1.16	-2.71	12.45	2.71	-1.16	4.9	12.1
G 357.967-0.163	2.48	20.1	2.18	14.31	8.26	-2.18	2.8	14.2
G 358.263-2.061	31.42	-7.3	-29.33	31.42	-7.3	-16.72	34	51
G 358.371-0.468	18.07	48.77	-14.09	18.07	48.77	-5.25	3.4	20.4
G 358.386-0.483	4.1	13.51	1.5	12.69	4.92	-1.5	4.8	12.2
G 358.460-0.391	23.72	2.13	-20.44	23.72	2.13	-10.2	24	41
G 358.460-0.393	4.58	1.27	-3.76	12.21	3.76	-1.27	5.3	11.7
G 358.721-0.126	18.71	10.91	-14.55	18.71	10.91	-6.07	0	0
G 358.809-0.085	7.74	0.07	-0.09	9.05	0.09	-0.07	8.1	8.9
G 358.841-0.737	6.83	0.34	-0.59	9.96	0.59	-0.34	7.5	9.5
G 358.906+0.106	6.73	0.4	-0.75	10.07	0.75	-0.4	7.4	9.6
G 358.931-0.030	6.6	0.46	-0.92	10.2	0.92	-0.46	7.3	9.7
G 358.980+0.084	33.43	-29.7	-31.65	33.43	-18.4	-20.36	0	0
G 359.138+0.031	4.55	39.75	1.82	12.25	32.05	-1.82	5.7	11.3
G 359.436-0.104	8.05	0.04	-0.05	8.75	0.05	-0.04	34	51
G 359.436-0.102	8.01	0.05	-0.07	8.79	0.07	-0.05	34	51
G 359.615-0.243	7.53	0.25	-0.59	9.27	0.59	-0.25	0.1	0.1
G 359.938+0.170	6.31	1.82	1.68	10.49	-1.68	-1.82	7.8	24.8
G 359.970-0.457	8.35	0.01	-0.02	8.45	0.02	-0.01	8.1	8.9
G 0.092-0.663	8.27	0.03	-0.06	8.53	0.06	-0.03	34	51
G 0.167-0.446	7.99	0.14	-0.4	8.81	0.4	-0.14	34	51
G 0.212-0.001	8.25	0.02	-0.02	8.55	0.02	-0.02	34	51
G 0.315-0.201	7.86	0.14	-0.28	8.94	0.28	-0.14	8.1	8.9
G 0.316-0.201	7.9	0.12	-0.23	8.9	0.23	-0.12	8.1	8.9
G 0.376+0.040	8.06	0.05	-0.08	8.74	0.08	-0.05	8.2	8.8
G 0.409-0.504	7.87	0.11	-0.19	8.93	0.19	-0.11	34	51
G 0.475-0.010	7.86	0.1	-0.16	8.94	0.16	-0.1	8	9
G 0.496+0.188	2.06	4.56	1.75	14.74	-1.75	-4.56	2.7	14.3
G 0.546-0.852	7.02	0.46	-1.41	9.78	1.41	-0.46	7.3	9.7
G 0.645-0.042	7.98	0.05	-0.07	8.82	0.07	-0.05	34	51
G 0.651-0.049	7.96	0.06	-0.07	8.84	0.07	-0.06	8.1	8.9
G 0.665-0.036	8.04	0.04	-0.05	8.76	0.05	-0.04	8.2	8.8
G 0.666-0.029	8.1	0.03	-0.04	8.7	0.04	-0.03	34	51
G 0.672-0.031	8.02	0.04	-0.05	8.77	0.05	-0.04	34	51
G 0.677-0.025	8.1	0.03	-0.03	8.7	0.03	-0.03	34	51
G 0.695-0.038	8.07	0.03	-0.04	8.73	0.04	-0.03	34	51
G 0.836+0.184	4.09	158.79	2.19	12.71	150.16	-2.19	4.5	12.5
G 1.008-0.237	2.12	35.18	3.48	14.68	22.62	-3.48	2.5	14.5
G 1.147-0.124	4.17	16.5	1.68	12.63	8.04	-1.68	0	0
G 1.329+0.150	0.71	257.62	3.9	16.09	242.24	-3.9	0	0
G 1.719-0.088	72.89	-54.37	-56.08	72.89	-54.37	-56.08	0	0
G 2.143+0.009	7.39	0.1	-0.12	9.4	0.12	-0.1	7.6	9.4

Table 7.3: – continued

Methanol maser (l, b) (degrees)	Reid09 near (kpc)	Error + (kpc)	Error − (kpc)	Reid09 far (kpc)	Error + (kpc)	Error − (kpc)	BB1993 near (kpc)	BB1993 far (kpc)
G 2.521-0.220	28.64	17.4	-28.01	28.64	17.4	-12.48	15.8	32.8
G 2.536+0.198	1.88	19.92	2.22	14.9	6.9	-2.22	2	15
G 2.591-0.029	45.29	-14.4	-27.31	45.29	-14.4	-27.31	34	51
G 2.615+0.134	7.61	0.06	-0.07	9.18	0.07	-0.06	7.8	9.1
G 2.703+0.040	7.58	0.06	-0.07	9.2	0.07	-0.06	7.8	9.2
G 3.253+0.018	1.18	20.18	2.23	15.59	5.77	-2.23	1.2	15.8
G 3.312-0.399	0.25	24.18	2.7	16.52	7.9	-2.7	0.1	16.8
G 3.442-0.348	1.89	16.3	1.65	14.88	3.31	-1.65	0	0
G 3.502-0.200	6.35	0.23	-0.29	10.42	0.29	-0.23	6.6	10.3
G 3.910+0.001	4.41	0.69	-1.04	12.35	1.04	-0.69	4.7	12.3
G 4.393+0.079	0.83	19.07	1.95	15.92	3.99	-1.95	0.8	16.2
G 4.434+0.129	17.18	5.84	-15.08	17.18	5.84	-2.52	0.7	17.6
G 4.569-0.079	2.83	1.1	-1.81	13.91	1.81	-1.1	3	13.9
G 4.586+0.028	4.9	0.48	-0.66	11.85	0.66	-0.48	5.2	11.8
G 4.676+0.276	1.62	16.29	1.54	15.12	2.79	-1.54	1.7	15.3
G 4.866-0.171	1.79	15.65	1.43	14.95	2.49	-1.43	1.9	15.1
G 5.618-0.082	71.79	-7.48	-42.35	71.79	-7.48	-42.35	0	0
G 5.630-0.294	2.65	0.99	-1.5	14.06	1.5	-0.99	2.8	14.1
G 5.657+0.416	3.91	0.64	-0.87	12.8	0.87	-0.64	4.2	12.7
G 5.677-0.027	24.67	22.16	-5.98	24.67	22.16	-5.98	10.8	27.7
G 5.885-0.393	1.72	15.26	1.25	14.99	1.99	-1.25	1.8	15.2
G 5.900-0.430	2.49	1.01	-1.5	14.22	1.5	-1.01	2.6	14.3
G 6.189-0.358	68.24	13.9	-37.9	68.24	13.9	-37.9	0	0
G 6.368-0.052	7.44	0.07	-0.08	9.26	0.08	-0.07	7.8	9.1
G 6.539-0.108	2.8	0.84	-1.19	13.89	1.19	-0.84	3	13.9
G 6.588-0.192	1.39	15.82	1.25	15.3	1.92	-1.25	1.4	15.5
G 6.610-0.082	0.33	18.67	1.6	16.36	2.63	-1.6	0.1	16.7
G 6.795-0.257	3.14	0.73	-0.99	13.54	0.99	-0.73	3.3	13.5
G 6.881+0.093	17.27	3.2	-15.99	17.27	3.2	-1.88	1	17.8
G 7.166+0.131	6.44	0.14	-0.16	10.23	0.16	-0.14	6.8	10.1
G 7.601-0.139	7.44	0.08	-0.09	9.22	0.09	-0.08	7.8	9
G 7.632-0.109	7.46	0.09	-0.09	9.19	0.09	-0.09	7.9	9
G 8.139+0.226	3.2	0.62	-0.8	13.43	0.8	-0.62	3.4	13.4
G 8.317-0.096	4.99	0.3	-0.35	11.64	0.35	-0.3	5.3	11.5
G 8.669-0.356	4.51	0.36	-0.43	12.1	0.43	-0.36	4.8	12
G 8.683-0.368	4.72	0.33	-0.39	11.89	0.39	-0.33	5	11.8
G 8.832-0.028	17.44	2.47	-16.66	17.44	2.47	-1.62	1.3	18.1
G 8.872-0.493	3.36	0.55	-0.69	13.24	0.69	-0.55	3.6	13.2
G 9.215-0.202	4.72	0.31	-0.37	11.86	0.37	-0.31	5	11.8
G 9.621+0.196	0.38	17.44	1.17	16.19	1.64	-1.17	0.2	16.6
G 9.619+0.193	1.09	15.72	0.99	15.47	1.34	-0.99	1	15.7
G 9.986-0.028	4.4	0.34	-0.4	12.14	0.4	-0.34	4.7	12.1
G 10.205-0.345	1.25	0.91	-1.2	15.29	1.2	-0.91	1.2	15.5
G 10.287-0.125	1.44	0.86	-1.13	15.09	1.13	-0.86	1.4	15.3
G 10.299-0.146	2.79	0.59	-0.73	13.74	0.73	-0.59	2.9	13.8
G 10.320-0.259	4.17	0.37	-0.43	12.36	0.43	-0.37	4.4	12.3
G 10.323-0.160	1.89	0.76	-0.98	14.64	0.98	-0.76	1.9	14.8
G 10.342-0.142	2.34	0.67	-0.85	14.19	0.85	-0.67	2.4	14.3
G 10.35-0.13	4.72	0.29	-0.34	11.81	0.34	-0.29	4.9	11.8

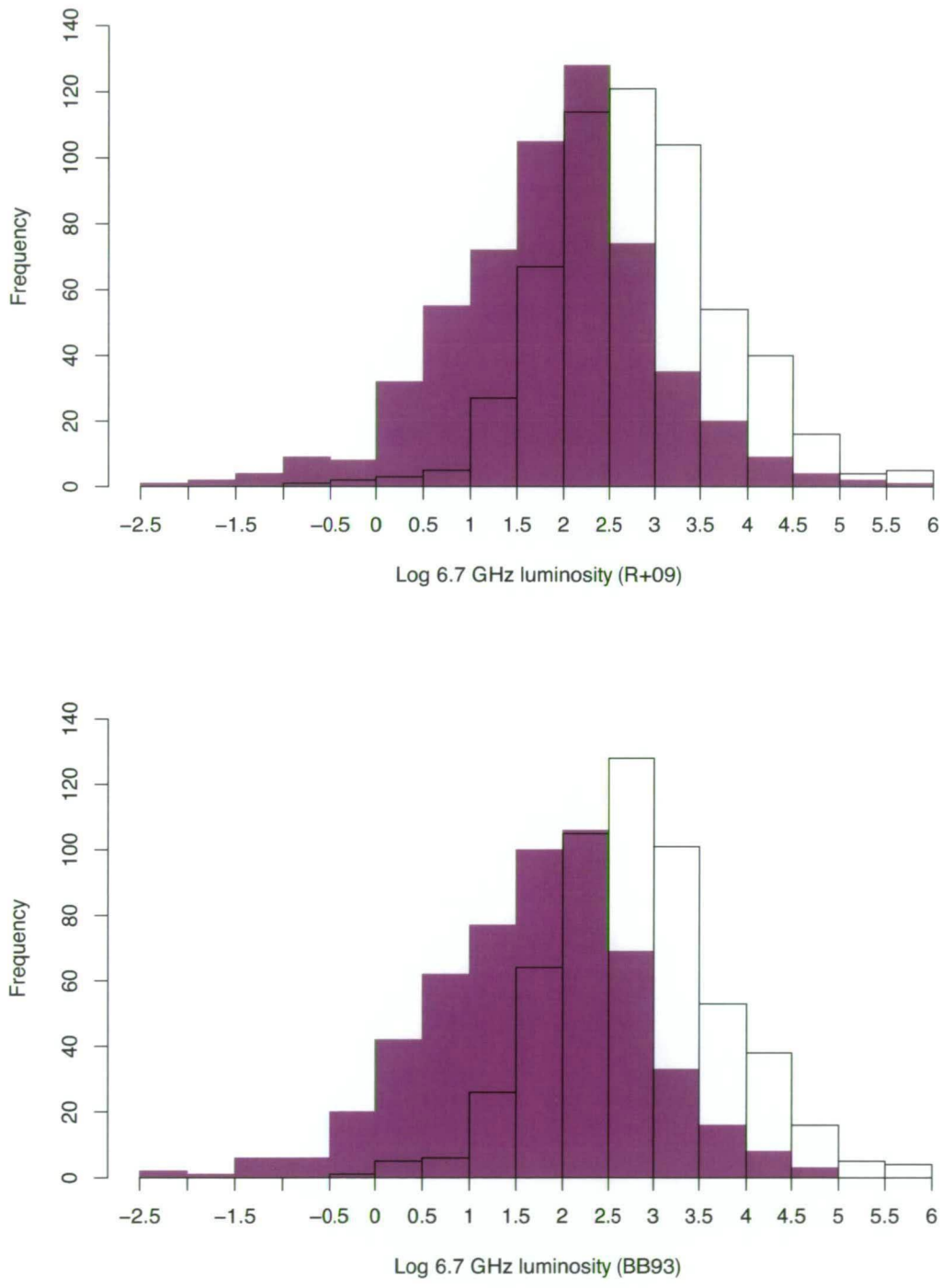

Figure 7.11: *Histogram of the log 6.7 GHz methanol maser integrated luminosity using the near (purple) and far (black outline) distances calculated using Reid et al. (2009) (top) and Brand & Blitz (1993) (bottom).*

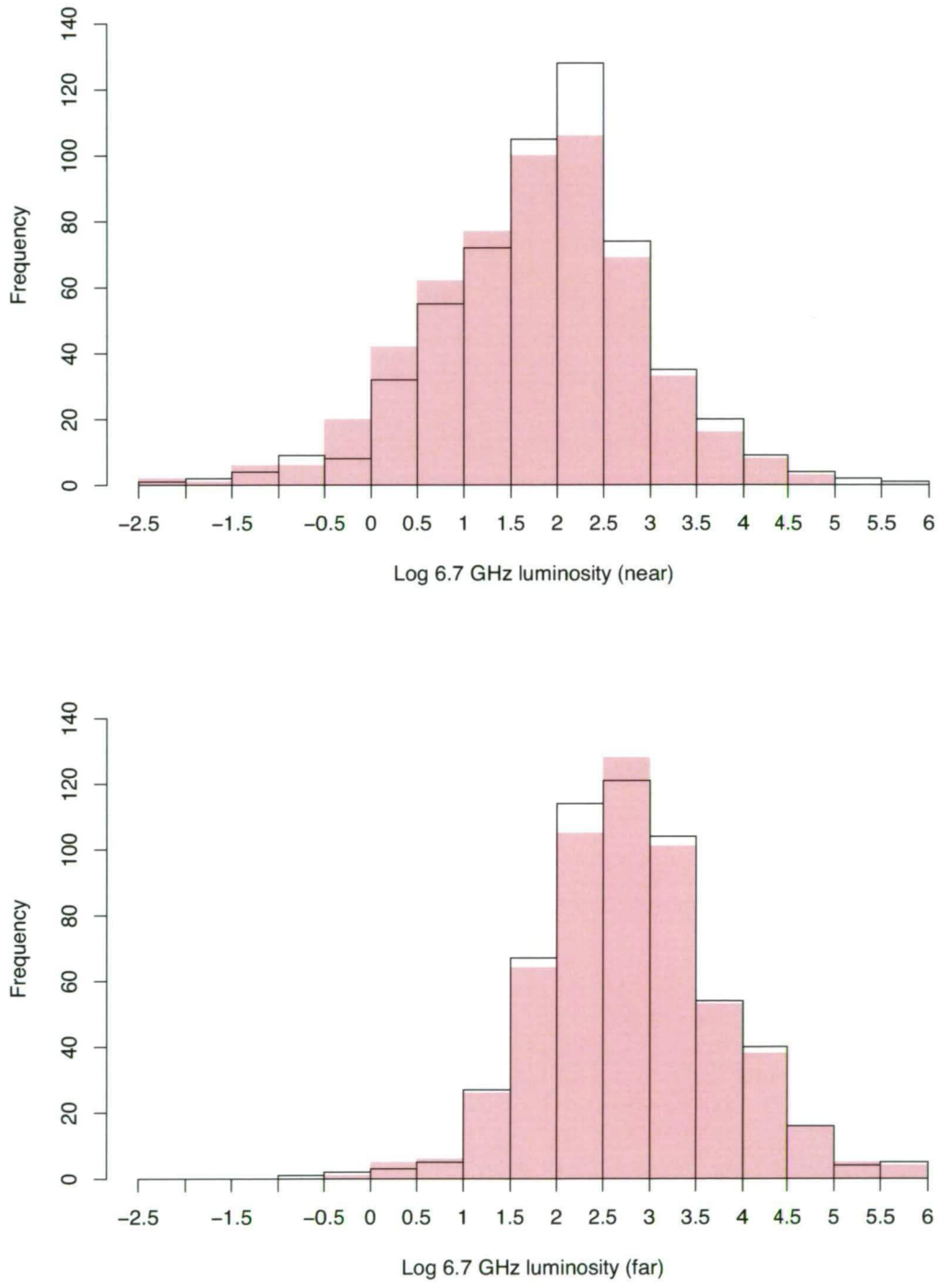

Figure 7.12: *Histogram comparing the 6.7 GHz methanol maser integrated luminosities using near (top) and far (bottom) distances calculated using Brand & Blitz (1993) (pink) and Reid et al. (2009) (black outline).*

It is therefore clear that once this information becomes available, our analysis would gain significantly from being repeated with the more confident distance estimates.

In Chapter 4 we found that there was a relationship between the H_2 number densities of 1.2 mm dust clumps (Hill et al. 2005) and the presence of UCHII regions, with the more evolved 1.2 mm dust clumps (i.e. those with associated UCHII regions) showing lower densities than the younger dust clumps. Plots of 6.7 GHz peak luminosity versus H_2 number density (Fig. ?? of Chapter 4) showed that the more luminous 6.7 GHz methanol masers were associated with the less dense 1.2 mm dust clumps, implying a relationship between 6.7 GHz methanol source luminosity and evolution. Unfortunately, only the peak flux densities of the 6.7 GHz sources were readily available and these were used to calculate the luminosities used in that investigation. Fig. 7.13 shows a similar plot to Fig. ?? of Chapter 4) but uses the integrated flux densities as measured from the MMB observations (Note: for 12 sources no integrated flux densities were available and these have been omitted from this plot). Since the H_2 number densities were calculated using kinematic distances for each source as presented in Hill et al. (2005), we have used these distances to calculate the integrated 6.7 GHz luminosities for this plot for consistency.

Linear regression analysis was carried out on the data contained in Fig. 7.13 and showed that the negative slope of the line of best fit of the distribution is statistically significant, with a weak correlation between individual data points (correlation coefficient of 0.39). The null hypothesis that the line of best fit has a slope of zero can safely be rejected (p-value 0.007). The line of best fit has the equation

$$\log(6.7\text{ GHz lum}) = -0.72[0.25](\log(\text{H}_2\text{density})) + 5.52[1.17],$$

where '6.7 GHz lum' is the integrated luminosity of the 6.7 GHz methanol maser (Jy km s^{-1} pc^2) and 'H_2density' is the H_2 number density (cm^{-3}) of the associated 1.2-mm dust clumps. The numbers contained in the square brackets are the standard errors of the slope and the y-intercept respectively. It is likely that at least some of the scatter present in the distribution of data points can

be explained by the use of the near kinematic distances, which is an assumption prone to introducing errors. A further contributor is likely to be the variable nature of the maser sources (see e.g. Goedhart, Gaylard & van der Walt, 2004). The correlation between data points is slightly lower for sources shown in Fig. 7.13 than those in Fig. ?? of Chapter 4. However, given the smaller sample size in Fig. 7.13 (46 compared to 113) it is difficult to draw meaningful conclusions about what this may mean. The much smaller sample size is a result of the fact that the a large portion of Hill et al. (2005) sample (where the observations of Chapter 4 were targeted) lie north of the declination cut-off imposed on the target sources in this chapter. Regardless, this analysis shows that the result derived in Chapter 4 holds when the 6.7 GHz integrated luminosities are used, confirming that, in general, 6.7 GHz methanol masers increase in luminosity as they evolve.

In Chapter 4 a relationship between the ratio of 6.7 to 12.2 GHz peak flux densities with the luminosities of the respective data was identified. This relationship showed that the ratio of 6.7 to 12.2 GHz peak flux density increased with increasing 6.7 GHz peak luminosity, implying that as the source evolved, the 6.7 GHz methanol maser increased in flux density more rapidly than the associated 12.2 GHz methanol maser. Here we repeat this analysis on our much larger and complete sample using not only the peak flux densities of the sources, but also comparing the integrated flux densities.

Fig. 7.14 shows a log-log plot of the 6.7 GHz to 12.2 GHz peak flux density ratio versus the 6.7 GHz integrated luminosity, while Fig. 7.15 shows a log-log plot of the ratio of 6.7 GHz to 12.2 GHz methanol maser integrated flux densities versus the 6.7 GHz integrated luminosities. The linear regression results for these two plots are almost identical, with the main difference being the values of the calculated y-intercept for the line of best fit which is greater for the ratio of integrated flux densities. This is a direct result of the larger ratios seen in the integrated rather than the peak flux densities of the methanol sources, as outlined in Section 7.6.3. In both cases the linear regression shows a statistically significant positive slope. However, there is little correlation between individual data points. Table 7.5 shows a summary of the results from the linear regression analysis for the data presented in both Fig. 7.14 and Fig. 7.15.

Given that these plots imply that as the luminosity of the 6.7 GHz source

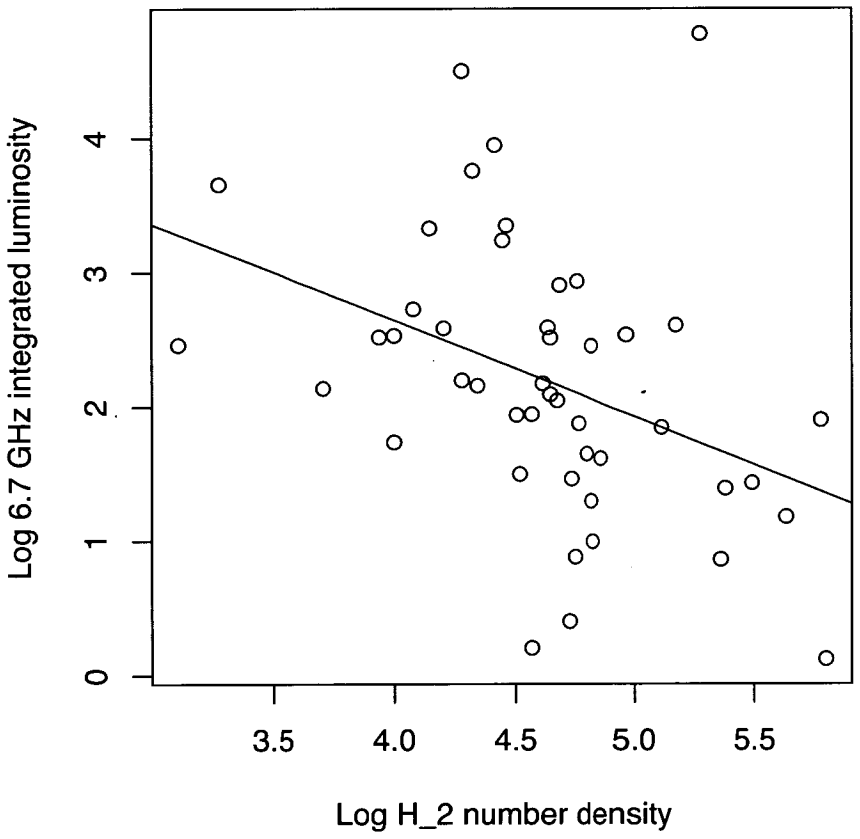

Figure 7.13: *Log of the 6.7 GHz integrated luminosity versus the log of the H_2 number density of the associated 1.2 mm dust clump in cm^{-3}. The line of best fit is also plotted.*

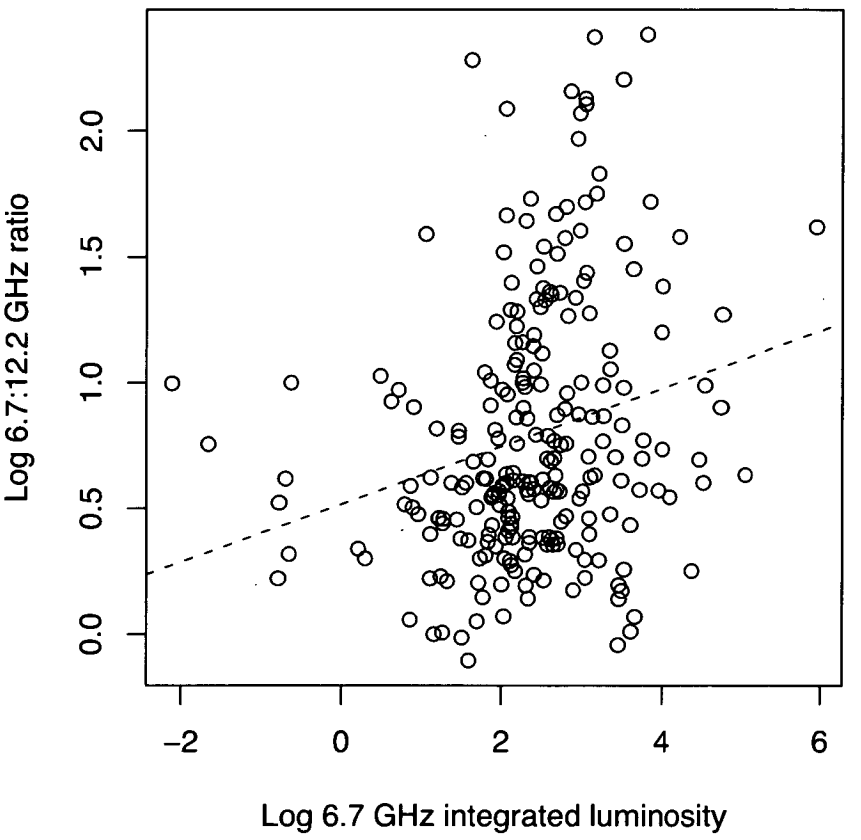

Figure 7.14: *Log of the 6.7 GHz peak flux density divided by the 12.2 GHz peak flux density versus the log of the 6.7 GHz methanol maser integrated luminosity, overlaid with the line of best fit. The characteristics computed in the linear regression are given in Table 7.5.*

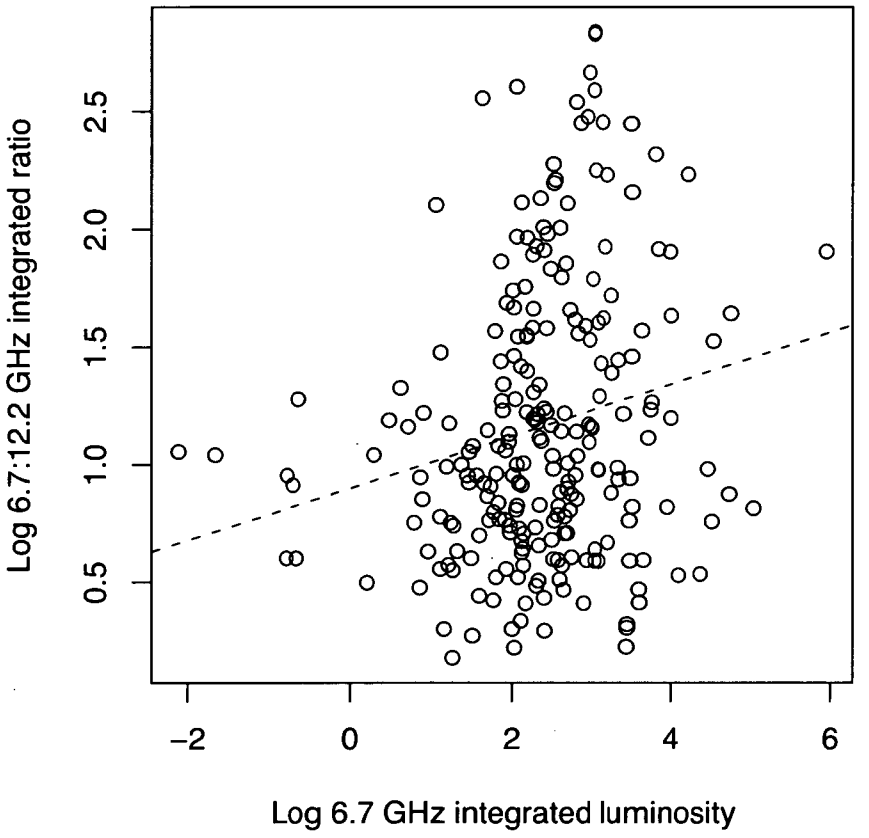

Figure 7.15: *Log of the 6.7 GHz integrated flux density divided by the 12.2 GHz integrated flux density versus the log of the 6.7 GHz methanol maser integrated luminosity, overlaid with the line of best fit. The characteristics computed in the linear regression are given in Table 7.5.*

Table 7.5: *Summary of results from linear regression analysis for data presented in Figs 7.14, 7.15 and 7.16. Column 1 shows the corresponding figure, column 2 shows the slope of the line of best fit, column 3 shows the standard error associated with the slope of the line, column 4 shows the* p*-value relating to the null hypothesis that the line has a zero slope, and column 5 gives the correlation coefficient.*

Figure	Slope	Error	*p*-value	R
Fig. 7.14	0.11	0.03	2.28e–4	0.23
Fig. 7.15	0.11	0.03	1.79e–3	0.19
Fig. 7.16	–0.12	0.03	6.24e–05	0.25

increases so does the ratio of 6.7 to 12.2 GHz peak and integrated flux densities, it would be expected that a log-log plot of the 6.7 GHz to 12.2 GHz peak flux density ratio versus the 12.2 GHz integrated luminosity would show a slope of the opposite sign to Fig. 7.15 which it does (see Fig. 7.16). A summary of the linear regression analysis for this plot is presented in Table 7.5. Re-plotting the integrated ratios of the two methanol transitions against the integrated 12.2 GHz luminosity is not necessary since it is just plotting the same information that is present in Fig 7.15. Fig. 7.16 also shows a statistically significant negative slope and a poor correlation between individual data points.

The large amount of scatter in the data sets plotted in Figs 7.14, 7.15 and 7.16 can largely be accounted for by the inaccuracies introduced by the assumption that all of the methanol masers lie at the near kinematic distance. Comparison between the scatter in these plots compared to Figs. 4.4 and 4.5 in Chapter 4 lends credence to this notion as even though the sample size of the figures in Chapter 4 are much smaller, the correlation between data points is better. Given the incomplete and biased (towards stronger 6.7 GHz sources) nature of the sources presented in Chapter 4, we would expect that the near distance assumption would be more often correct for these sources than our complete sample observed in a sensitive and unbiased manner (where we would expect a more even split between near and far distances).

A comparison between the 6.7 GHz and 12.2 GHz luminosities calculated

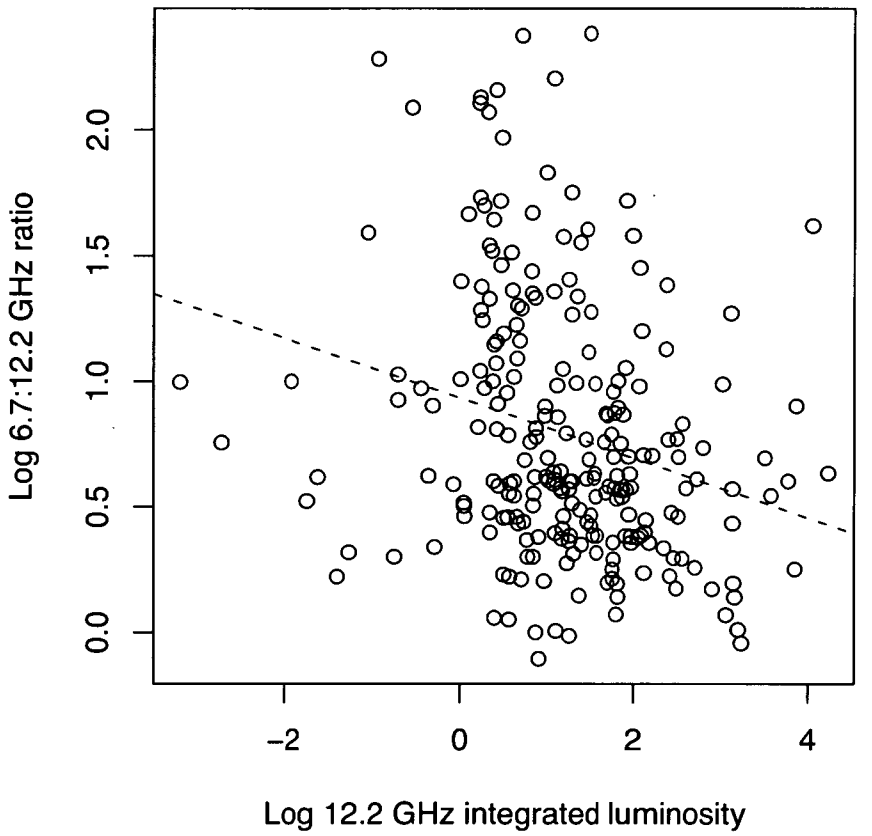

Figure 7.16: *Log of the 6.7 GHz peak flux density divided by the 12.2 GHz peak flux density versus the log of the 12.2 GHz methanol maser integrated luminosity, overlaid with the line of best fit. The characteristics computed in the linear regression are given in Table 7.5.*

from their integrated flux densities is shown in Fig. 7.17. This plot shows that the relationship between the 6.7 and 12.2 GHz methanol maser luminosities is well estimated by the line of best fit as it shows a relatively tight correlation (correlation coefficient is 0.85) between individual data points, with no extreme outliers. This plot similarly shows that for higher 6.7 GHz luminosities, the 12.2 GHz methanol maser luminosity becomes comparatively weaker. The line of best fit has the equation

$$\log(\text{12.2 GHz lum}) = 0.89[0.03](\log(\text{6.7 GHz lum})) - 0.90[0.09],$$

where '12.2 GHz lum' is the integrated luminosity of the 12.2 GHz methanol maser and '6.7 GHz lum' is the integrated luminosity of the 6.7 GHz methanol maser. The numbers contained in the square brackets are the standard errors of the slope and the y intercept respectively. The p-value of <2e-16 allows the null hypothesis that the line has zero slope to be unequivocally rejected.

We have further investigated this relationship by splitting the data into two categories. The first category includes all 6.7 and 12.2 GHz methanol masers with associated OH masers (Caswell, 1998) and the second includes those sites with both 6.7 and 12.2 GHz methanol masers but no associated OH maser. Fig. 7.18 presents a plot similar to Fig. 7.17 but with methanol sources with associated OH masers distinguished from those without. Methanol sources that have not been sensitively searched for OH masers have been excluded from the plot (a total of 58 sources). Interestingly, the methanol sources with OH maser counterparts tend towards the higher luminosities, lending further support to the idea that methanol masers tend to increase in luminosity as they evolve.

The summary of the linear regression analysis carried out on the three categories of sources displayed in Fig. 7.18 (all sources, sources with OH and sources with no OH counterpart) are presented in Table 7.6. The characteristics computed in the linear regression analysis for all sources shown in Fig. 7.18 are almost identical to those derived for the complete sample (Fig. 7.17). Sources with associated OH masers seem to have a slightly more positive slope ($\sim$1) than the sources with no OH maser counterparts that have a slope equal to that of the full sample (0.90). Taking into account the standard errors associated with these

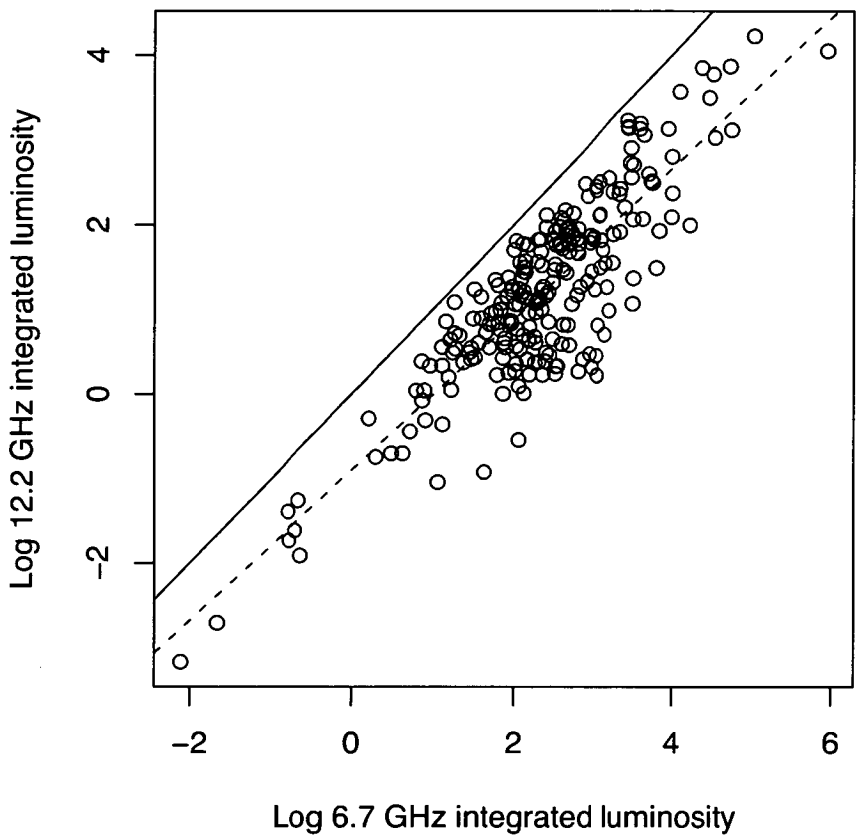

Figure 7.17: *Log 12.2 GHz integrated luminosity versus the log of the 6.7 GHz integrated luminosities. Overlaid is the line of best fit (dashed) and line with a slope of 1 (solid).*

Table 7.6: *Summary of results from linear regression analysis for data presented in Fig. 7.18. Column 1 gives the category of the sources in the sample, column 2 shows the slope of the line of best fit, column 3 shows the standard error associated with the slope of the line, column 4 shows the* p*-value relating to the null hypothesis that the line has a zero slope, and column 5 gives the correlation coefficient.*

Category	Slope	Error	*p*-value	R
full sample	0.90	0.05	<2e–16	0.82
with OH	1.01	0.08	<2e–16	0.80
no OH	0.90	0.06	<2e–16	0.83

two lines shows that they could have the same slope (i.e. both less than one), although the possibility that this is a real difference is intriguing. If the difference is real, it implies that although the methanol maser luminosity increases more rapidly in the 6.7 GHz tranisition as the source evolves, towards the evolutionary stage where OH masers are present this effect lessens.

Preliminary analysis of the luminosity of individual maser features

A preliminary analysis has been carried out on individual features of 6.7 GHz masers with respect to their 12.2 GHz counterparts. Future studies of these sources, together with the MMB sources that lie north of our cutoff declination of –20 degrees, will include an analysis of the individual features of a much large group of sources. Section 7.6.6 contains much discussion of the luminosities of 6.7 GHz sources compared to their 12.2 GHz counterpart, including ratios of the two transitions calculated from both the integrated and peak flux densities of the respective sources.

Analysis of the individual features associated with each maser source has the potential to reveal much more about the sources, as well as the individual features, which show emission at both methanol transitions, or are devoid of a 12.2 GHz counterpart. Since the age of the exciting star will be common to individual maser features, the analysis of individual features associated with each site where both 6.7 and 12.2 GHz emission is detected will reap greater information on the study

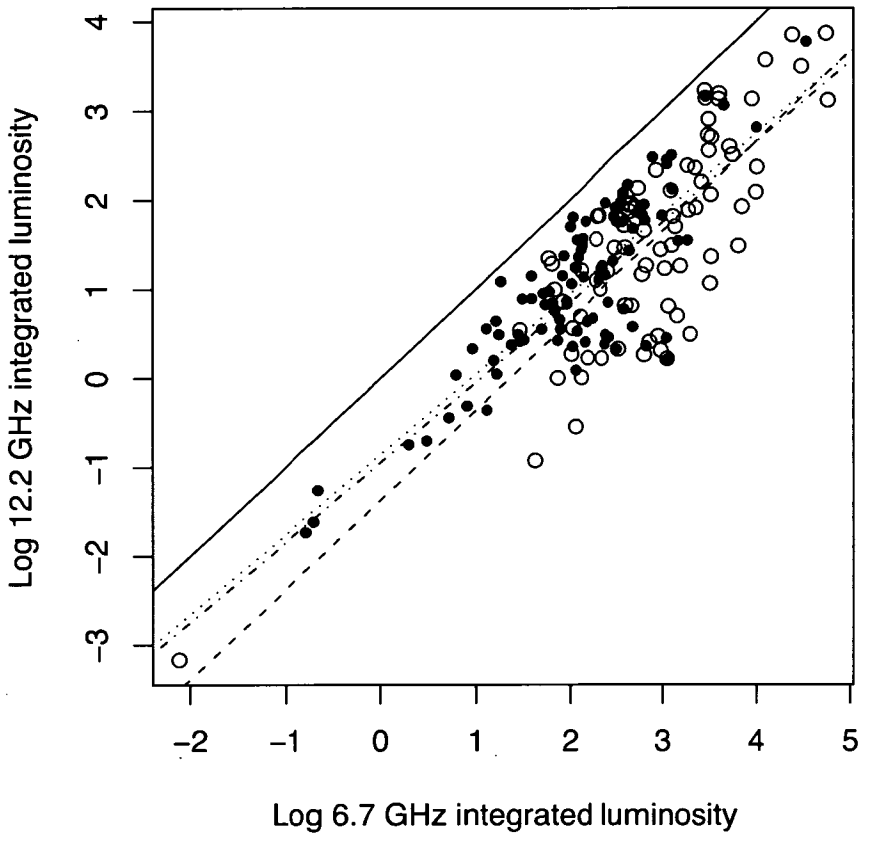

Figure 7.18: *Log 12.2 GHz integrated luminosity versus the log of the 6.7 GHz integrated luminosities. The open circles represent those sources with an associated OH maser and the closed circles show the sources with no OH maser counterpart. Overlaid is the line of best fit for sources with OH masers (dashed), sources without OH masers (dotted), the full sample with OH information (dot-dashed) and line with a slope of 1 (solid) for comparison. A summary of the linear regression analysis for each of the source categories is shown in Table 7.6.*

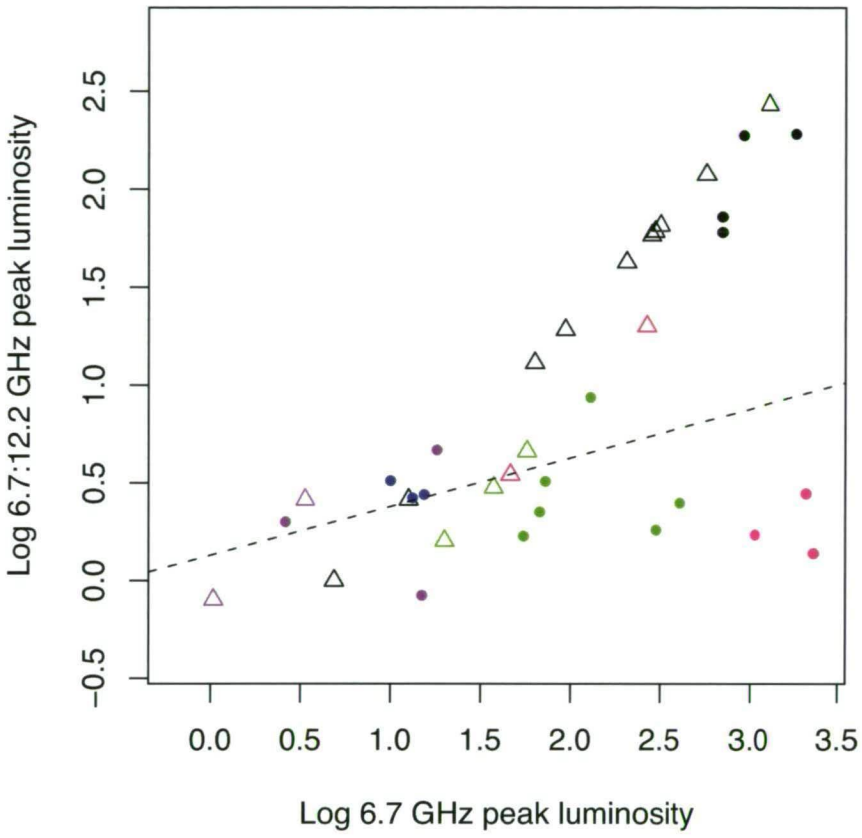

Figure 7.19: *Log of the 6.7:12.2 GHz individual feature ratio versus the log 6.7 GHz peak luminosity for every spectral feature associated with five methanol maser sources. Dots represent 6.7 GHz features with a 12.2 GHz counterpart, while triangles show features with no detectable 12.2 GHz counterpart, thus showing the lower limit of the 6.7:12.2 GHz feature ratio. Colours distinguish between individual maser sites and are as follows; purple: G 319.163–0.421; green: G 331.425+0.264; pink; G 339.986–0.425; black: G 341.218–0.212; and blue: G 6.588–0.192. The dashed line shows the line of best fit from the sample of sources presented in Chapter 4, Fig. 4.4, where a plot of 6.7 GHz peak luminosity versus 6.7:12.2 GHz peak ratio is shown for the peak 6.7 GHz feature associated with each source.*

of the relative evolutionary stage that each methanol transition is associated with. Furthermore, insights into the conditions favourable to both transitions can be achieved by carrying out the analysis on such a large sample of sources.

Fig. 7.19 displays the peak luminosity of each feature associated with five 6.7 GHz methanol masers, versus the ratio of 6.7 to 12.2 GHz luminosity of the corresponding feature. The five sources presented in this plot all exhibit in excess of three 12.2 GHz spectral features and were chosen randomly from this population. In addition to the ratios calculated from detections at both transitions (in individual features), upper limits on the ratios of 6.7 GHz features with no 12.2 GHz counterpart, are shown. The individual features of the five sources are colour-coded, revealing several trends. Firstly, the 6.7 GHz luminosity versus the ratio of 6.7 to 12.2 GHz luminosity of each spectral feature are clustered together in groups containing all the features associated with the same source. It is expected from Section 7.6.6 (in conjunction with results presented in Chapter 4) that the ratio of 6.7 to 12.2 GHz luminosity will increase with 6.7 GHz luminosity, and therefore evolution of the source. The clustering of the features associated with each source supports this idea since the exciting source will be the same, and therefore at the same evolutionary stage, for all spectral features.

The second major implication from Fig.7.19 comes from the location of the upper limits for the ratios. It can be seen that, while the features which show emission at both 6.7 and 12.2 GHz are clustered, the upper limits for features with no detectable 12.2 GHz counterpart lie on the outskirts of the cluster, and since these are upper limits if anything they are likely to lie even further from the cluster. This implies that many of the features with no 12.2 GHz counterpart that are present on this plot are unlikely to just be below the detection limits of the search.

Also shown in Fig. 7.19 is the line of best fit calculated from the linear regression carried out on the larger group of sources shown on a similar plot in Chapter 4, Fig. 4.4 which shows only the peak feature for each of the methanol maser sources. The plotted line is the same (to within the errors) as the line of best fit calculated using the points plotted on Fig. 7.19 (omitting the upper limits).

Methanol maser luminosity and velocity range comparison

Both the luminosity and velocity range has been investigated for the 6.7 GHz and 12.2 GHz methanol maser sources. We find that there is a striking difference in the values of these characteristics for the 6.7 GHz sources devoid of both 12.2 and OH maser counterparts, those with associated 12.2 GHz emission but not OH, and those with both 12.2 and OH maser counterparts. Likewise we find that the 12.2 GHz methanol maser sources with associated OH masers have higher luminosities and velocity ranges than those with no OH counterpart. OH maser associations (or lack thereof) with the methanol masers have been determined from Caswell (1998). Distance estimates are the near distances calculated using Reid et al. (2009). Methanol maser sources with calculated distances of less than 0.5 kpc or more than 20 kpc have been removed from this analysis as they are likely to be erroneous.

Table 7.7 shows the average and median velocity ranges and luminosities of both the 6.7 and 12.2 GHz methanol masers broken up in categories according to their associations. In the top half of the table the characteristics of the 6.7 GHz methanol masers are given and show a progressive widening of velocity range and increasing luminosity from the category which includes 6.7 GHz methanol masers with no 12.2 GHz methanol or OH maser counterpart; to 6.7 GHz methanol masers with associated emission at the 12.2 GHz transition but no associated OH maser; and finally those 6.7 GHz methanol masers with both 12.2 and OH maser counterparts. The bottom half of the table gives the characteristics of the 12.2 GHz methanol masers with and without associated OH masers. In this case, a similar trend is seen, with the sources without OH masers showing smaller 12.2 GHz maser velocity ranges and lower luminosities than those 12.2 GHz sources with associated OH masers.

Figs 7.20 and 7.22 show plots of log 6.7 GHz luminosity versus 6.7 GHz velocity range and log 12.2 GHz luminosity versus 12.2 GHz velocity range, respectively. Fig. 7.20 shows that there is an overall trend between increasing 6.7 GHz methanol maser luminosity and velocity range, with a significantly positive slope and a moderate correlation between data points. This plot also highlights the segregation of the values corresponding to the different association categories. In

Table 7.7: *Average and median velocity ranges and luminosities of 6.7 and 12.2 GHz methanol masers broken into categories on the basis of their methanol and OH maser associations. In the top half of the table, characteristics of the 6.7 GHz methanol masers are shown, broken into their association categories, while the second half of the table presents the characteristics of the 12.2 GHz methanol masers. Column 1 specifies the association category for the 6.7 (top) and 12.2 GHz (bottom) methanol masers; column 2 gives the average velocity range (km s^{-1}); column 3 gives the median velocity range (km s^{-1}); column 4 gives the average luminosity (Jy km s^{-1} kpc^2); and column 5 gives the median luminosity (Jy km s^{-1} kpc^2).*

Associations	$\mathbf{A}_{vel\_range}$ (km s^{-1})	$\mathbf{M}_{vel\_range}$ (km s^{-1})	$\mathbf{A}_{luminosity}$ (Jy km s^{-1} kpc^2)	$\mathbf{M}_{luminosity}$ (Jy km s^{-1} kpc^2)
6.7 GHz				
no 12.2 or OH	5.2	3.9	70	25
12.2 but no OH	8.3	7.6	465	142
12.2 and OH	10.0	9.4	3819	892
12.2 GHz				
no OH	3.1	1.6	35	17
OH	4.7	3.0	667	73

both Chapter 4 and previously in this Chapter we argue that, in general, more evolved 6.7 GHz methanol masers exhibit higher luminosities. The values reported in Table 7.7 along with the data shown in Fig. 7.20 support this idea. This plot offers additional insight, with a clear tendency for the more evolved 6.7 GHz methanol masers to show larger velocity ranges. This suggests that the gas volume conducive to 6.7 GHz methanol maser emission also increases as the source evolves.

There is, of course, the possibility that this relationship is influenced by sensitivity, i.e. for example, that the 6.7 GHz sources with associated 12.2 GHz methanol and OH masers have higher flux densities, increasing the likelihood that a more extensive velocity range would be identified. However, Fig. 7.19 suggests that sensitivity biases are not the culprit for the difference between the sources. Even if this is the case for some sources, it shows that the characteristics of the 6.7 GHz methanol masers change with evolution regardless (since this shows that the flux density increases). Furthermore, if sensitivity limitations were precluding us from observing the full extent of the 6.7 GHz methanol maser velocity range, then we would expect this to affect all of the association categories equally since the different categories will be interspersed through a range of distances in the Galaxy. A sample of the outlying sources shown in Fig. 7.20 have been investigated, specifically those sources represented by purple dots and black triangles centred on $\sim$1 on the x-axis and $\sim$17 on the y-axis. These sources show unexpectedly large velocity ranges for their calculated luminosities. An investigation of these sources shows that they all have low flux densities ($<$4 Jy) and this together with their location on the plot implies that they might actually lie at the far distance rather than the near distance that has been assumed. Therefore, a comparison between the integrated flux densities and velocity ranges of sources may provide a viable, indirect way of resolving near/far distance ambiguities.

There is a group of sources that are missing from Fig. 7.20 and Table 7.7, and these are those 6.7 GHz methanol masers with associated OH maser emission but no 12.2 GHz methanol maser emission. These sources do not fit in with the evolutionary sequence that seems to describe the majority of our sources. The 6.7 GHz methanol sources in this category have average and median velocity ranges and luminosities that fall in between the categories of 'no 12.2 or OH' and

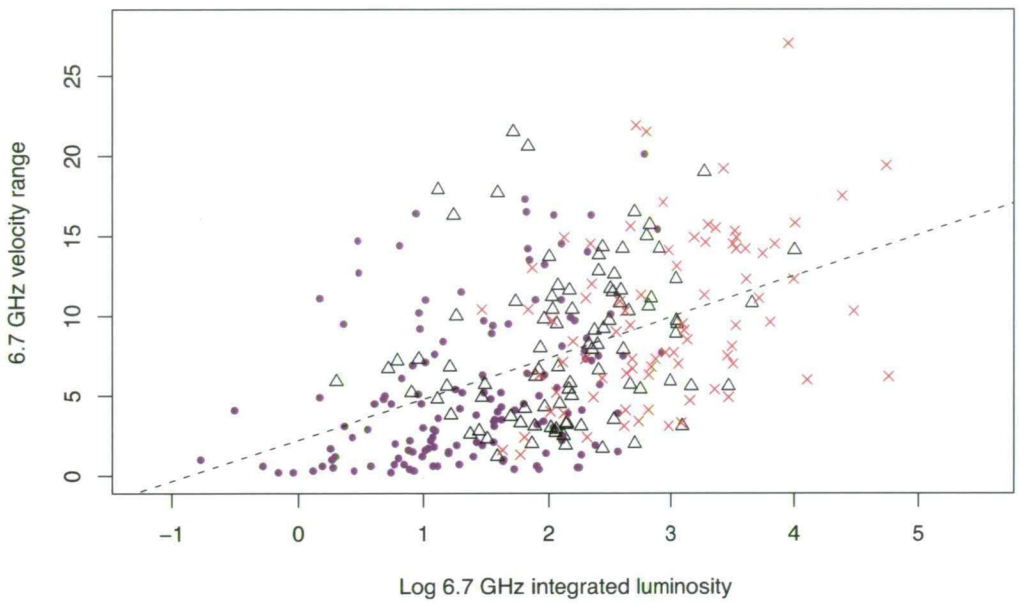

Figure 7.20: *Log of the 6.7 GHz integrated luminosity versus the 6.7 GHz methanol maser velocity range. Shown on the plot are 6.7 GHz sources with no associated 12.2 GHz methanol or OH masers (purple dots); 6.7 GHz methanol masers with detectable 12.2 GHz methanol masers but no associated OH masers (black triangles); and 6.7 GHz methanol masers with both 12.2 methanol and OH maser counterparts (red crosses). Overlaid is the line of best fit that corresponds to all of the 6.7 GHz masers presented on the plot (linear regression gives; slope=2.57[0.27],* p*-value=< 2e-16, and a correlation coefficient of 0.48).*

'12.2 but no OH' (average velocity range: 6.1 km s^{-1}; median velocity range: 5.5 km s^{-1}; average luminosity: 269 (Jy km s^{-1} kpc^2); median luminosity: 64 (Jy km s^{-1} kpc^2)). It seems, therefore, that for some sources, the OH masers switch on prior to the 12.2 GHz methanol masers. Fig. 7.21 shows the log 6.7 GHz luminosity versus 6.7 GHz velocity range, like Fig. 7.20, with the addition of these sources that have associated OH masers but no 12.2 GHz emission (green asterisks). It can be seen that these sources basically populate the same range as the that of the two categories of 'no 12.2 or OH' and '12.2 but no OH'. These sources need further investigation to understand their nature. Of particular interest would be to compare the abundances of methanol in these sources compared to the other categories, as well as determining their associations with UCHII and hyper-compact HII regions.

Fig. 7.22 displays the characteristics of the 12.2 GHz methanol masers, broken into the categories of sources associated with an OH maser (red crosses) and sources with no OH maser counterpart (black triangles). This plot similarly shows evidence for the 12.2 GHz methanol masers to increase in luminosity, and also velocity range, as the source evolves. The congregation of a number of sources with small velocity ranges and the log of the integrated luminosity to be between 0 and 2, perhaps shows that the 12.2 GHz sources are more effected by sensitivity limitations prohibiting the full velocity ranges to be identified. The sensitivity limits of the 6.7 and 12.2 GHz searches were similar, and together with the expectation that the associated 12.2 GHz methanol masers sources are weaker, means that this is not unexpected. However, analysis of individual features associated with five 6.7 and 12.2 GHz methanol masers shown in Section 7.6.6 implies that, at least for these sources, the 6.7 GHz features with no detectable 12.2 GHz counterpart are unlikely to be a result of sensitivity limitations. Both scenarios are probably true for some number of sources.

From analysis of the ratio of integrated flux densities of the two methanol transitions in Section 7.6.3, it was suggested that there was a larger volume of gas that was conducive to 6.7 GHz methanol than their 12.2 GHz counterparts. Data presented in Table 7.7 and Figs 7.20 and 7.22 supports this, with a clear tendency for the 12.2 GHz methanol maser sources to have less extensive velocity ranges. In addition, this table and figures show strong evidence for the gas volume to increase

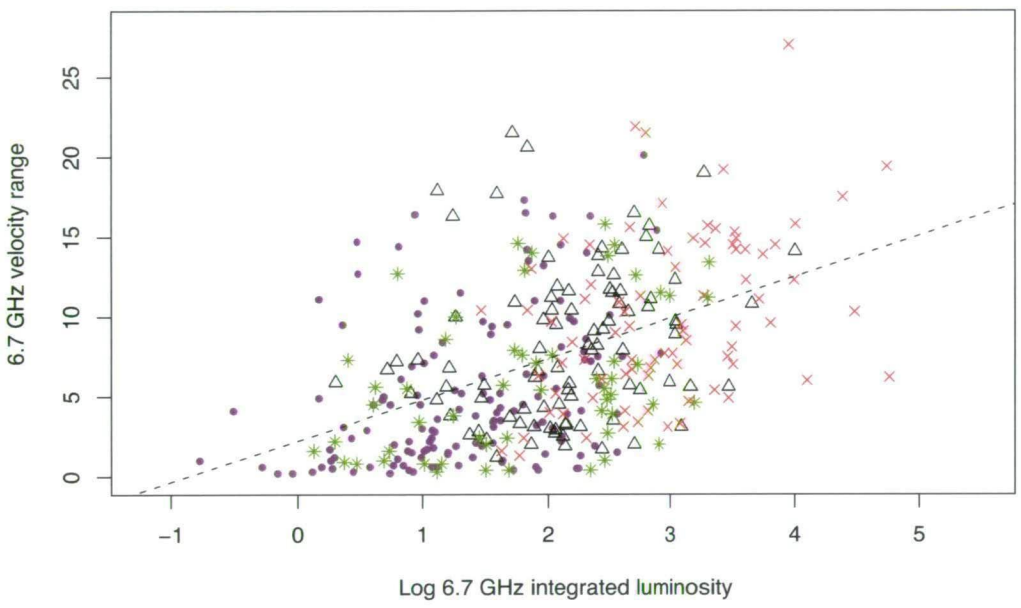

Figure 7.21: *As for Fig. 7.20 with the addition of green asterisks, which represent 6.7 GHz methanol masers with no 12.2 GHz methanol maser counterpart but with OH maser emission.*

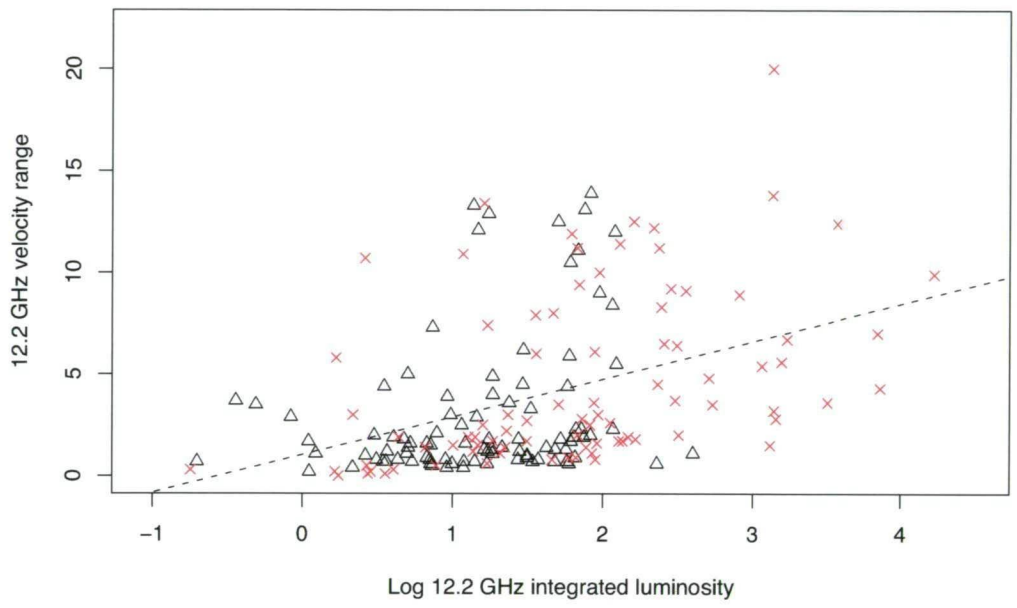

Figure 7.22: *Log of the 12.2 GHz integrated luminosity versus the 12.2 GHz methanol maser velocity range. Shown on the plot are 12.2 GHz sources with no associated OH masers (black triangles); and 12.2 methanol masers with OH maser counterparts (red crosses). Overlaid is the line of best fit that corresponds to all of the 12.2 GHz masers presented on the plot(linear regression gives; slope=1.86[0.31],* p-*value=1.72e-08, and a correlation coefficient of 0.40).*

as the sources evolve (for both the 6.7 and 12.2 GHz sources. In Fig. 7.17, and discussion thereof, we show that the luminosities of both the 6.7 GHz methanol maser and the 12.2 GHz methanol masers increased with evolution, but the rate of increase was much greater for the 6.7 GHz sources. The slopes of the lines derived from linear regression analysis of the data presented in Figs 7.20 and 7.22 show that a similar effect is seen in the velocity ranges of the two methanol transitions. The slope associated with the 6.7 GHz methanol sources is 1.4 times that associated with the 12.2 GHz sources, showing that the velocity range of the 6.7 GHz methanol sources increases more rapidly than that of their 12.2 GHz methanol maser counterpart.

These findings support the idea that the different combinations of 6.7 GHz methanol, 12.2 GHz methanol and OH masers, trace differing evolutionary stages of high mass star formation in the following sequence (starting from youngest); 6.7 GHz methanol masers devoid of both 12.2 GHz counterparts and OH masers; 6.7 GHz methanol masers with 12.2 GHz counterparts but no associated OH maser emission; and finally, 6.7 GHz methanol masers with both 12.2 GHz counterparts and associated OH masers. This interpretation is self consistent with all other analyses completed in this Chapter and also with independent analyses shown in Chapter 4. Further to this result, we find that not only the luminosity of the 6.7 GHz methanol maser increases more rapidly than that of the associated 12.2 GHz maser, but also the velocity range. This supports an evolutionary scenario whereby both the luminosity and the gas volume conducive to the 6.7 and 12.2 GHz masers increases as they evolve (although at a lesser rate for the 12.2 GHz sources).

7.6.7 Association with GLIMPSE sources

The locations of the detected 12.2 GHz methanol masers, along with the 6.7 GHz sources with no detectable 12.2 GHz counterpart have been compared to both the GLIMPSE point source catalogue and the catalogue of Extended Green Objects (EGOs) presented in Cyganowski et al. (2008). The characteristics of infrared sources have long been regarded as an excellent determinant of relative source ages and the investigation of such a large number of methanol maser sources is

important in comparing the relative evolutionary stages associated with different maser species.

Association with GLIMPSE point sources

520 of our target 6.7 GHz methanol fall within either the GLIMPSE I or GLIMPSE II regions (GLIMPSE region I: $10° < l < 65°$ and $295° < l < 350°$, $b = \pm 1°$; and GLIMPSE region II: $5° < l < 10°$ and $350° < l < 355°$, $b = \pm 1$; $2° < l < 5°$ and $355° < l < 358°$, $b = \pm 1.5°$; and $0° < l < 2°$ and $358° < l < 360°$, $b = \pm 2$). Using an association threshold of 2 arcsec, 316 of our target methanol maser sources are coincident with a GLIMPSE point source (a detection rate of 61 %). The association rate for 6.7 GHz methanol masers without associated 12.2 GHz emission is higher (192 of 291, or 66 %), than for sites exhibiting the two methanol maser transitions (127 of 229, or 55 %). Methanol maser sources coincident with OH masers have a similar association rate as for the sources showing emission at 12.2 GHz, a rate of 57 % (75 of 132). The similarity of the detection rates for sources with 12.2 GHz methanol masers or OH masers is expected given the high rate of coincidence for 12.2 GHz masers towards sites of 6.7 GHz methanol and OH masers.

Ellingsen (2006) found a GLIMPSE point source coincidence rate of 56 % for a subset of their 6.7 GHz sources that were detected in a complete search, and this rate dropped to 52 % when their full sample was considered. These association rate statistics, considered in conjunction with our own, suggests that the relatively more evolved star formation regions have fewer associations with GLIMPSE point sources. Evidence for this includes the fact that our sample of 6.7 GHz methanol masers yield the highest association rate (thereby including a high number of weak, possibly younger, sources) and this rate gets progressively less when stronger 6.7 GHz methanol masers or those associated with 12.2 GHz or OH maser emission, are considered. Since we expect the more evolved sources to no longer be a point source in the GLIMPSE bands a lower association rate is expected.

Fig. 7.23 shows a sample of GLIMPSE colour-colour and colour-magnitude diagrams for the 6.7 GHz methanol masers coincident with GLIMPSE point sources. We find similarly to Ellingsen (2006) that the maser associated sources are signif-

icantly redder than the majority of the comparison sources (all of the GLIMPSE point sources within 30 arcmin of $l = 326.5°$, $b = 0°$) on the plot, lying in significantly different regions in each case. Evident from the [5.8]–[8.0] versus [3.6]–[4.5] colour-colour plot, the methanol maser associated sources appear to have a large relative excess of 4.5 μm flux. Interestingly this plot along with the [3.6]–[4.5] versus 8.0 μm colour-magnitude diagram show that the majority of the sources that have similar 3.6 and 4.5 μm magnitudes are without associated 12.2 GHz emission. Aside from this, there are few obvious difference between the GLIMPSE point sources associated with both 6.7 and 12.2 GHz methanol maser emission and those associated with only 6.7 GHz methanol maser emission.

Fig. 7.24 shows the same plots presented in Fig. 7.23 except that, in Fig. 7.24, the sources with associated OH masers have been distinguished from those with no reported emission. OH masers have been taken from Caswell (1998) and given that some of our 6.7 GHz methanol masers lie outside the regions completely searched by Caswell (1998), some number of the sources that have been presented as having no associated OH maser may still have an associated OH maser. It can be seen in Fig. 7.24 that the sources with associated OH masers are relatively brighter in the 4.5 and 8.0 μm bands than those 6.7 GHz methanol masers with no OH maser emission. Ellingsen (2006) similarly noted that 6.7 GHz methanol masers with OH maser counterparts tended to have brighter 8.0 μm magnitudes.

Ellingsen (2006) commented that the majority of masers associated with GLIMPSE point sources meet the criteria [3.6]–[8.0] > 1.3 and 8.0 μm mag < 10 as well as [3.6]–[8.0] > 4.0 mag. From Figs 7.23 and 7.24 it can be seen that these criterion are met by most of our methanol maser sources, although perhaps fail to include some of the methanol maser sources, particularly a number of sources with no OH or 12.2 GHz maser counterpart. From our investigation it seems that these criterion could be refined to [3.6]–[8.0] > 0.8, 8.0 μm mag < 10 and [3.6]–[8.0] > 2.0 mag. This may imply that a number of the younger sources have a less excessive 4.5 to 3.6 μm flux and likewise for 8.0 μm band.

Analysis of the GLIMPSE properties associated with the somewhat smaller sample presented in Chapter 4 resulted in the conclusion that the masers themselves are much more sensitive to evolutionary changes than the associated mid-infrared emission. Apart from a few trends mentioned above, we similarly draw

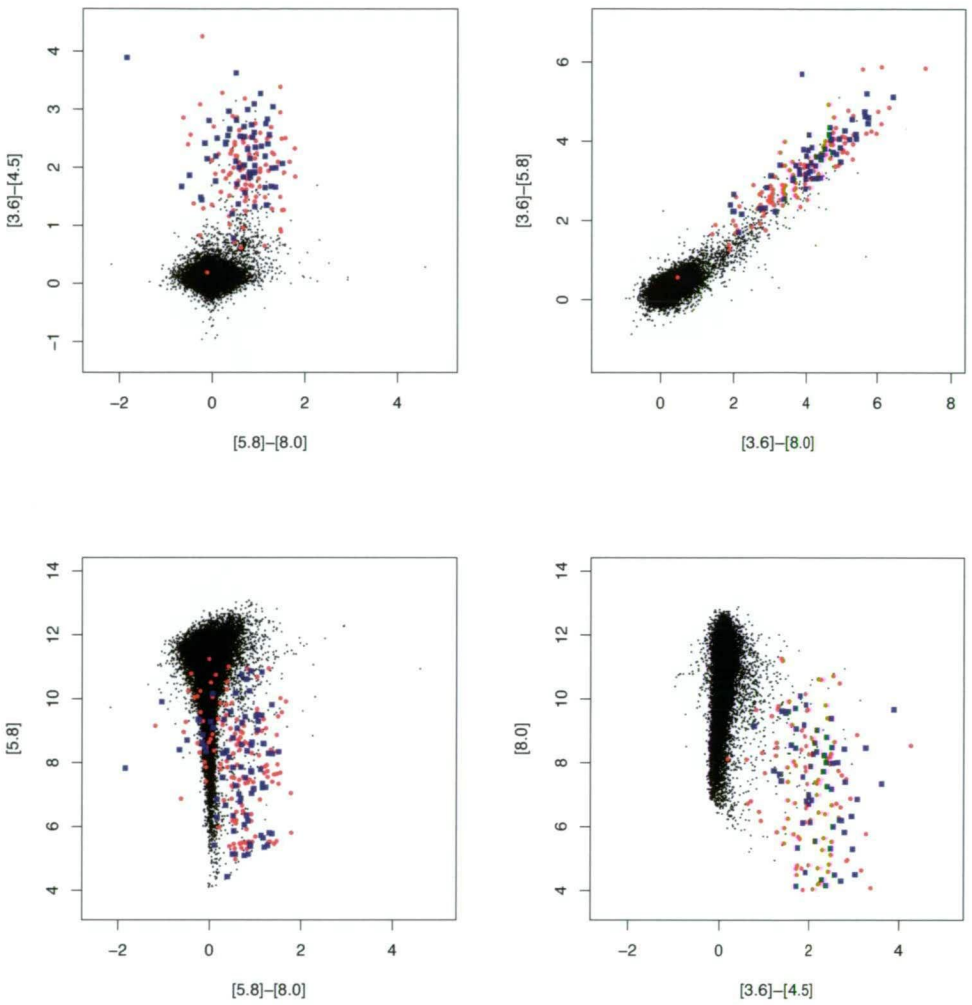

Figure 7.23: *GLIMPSE colour-colour and colour-magnitude diagrams. Clockwise from top left: [5.8]–[8.0] versus [3.6]–[4.5] colour-colour diagram; [3.6]–[8.0] versus [3.6]–[5.8] colour-colour diagram; [3.6]–[4.5] versus 8.0 μm colour-magnitude diagram; and [5.8]–[8.0] versus 5.8 μm colour-magnitude diagram. GLIMPSE point sources associated with sources showing emission at both the 6.7 and 12.2 GHz methanol maser transitions are represented by blue squares and those associated with only the 6.7 GHz transition are represented by red circles. In each plot the black dots represent all of the GLIMPSE point sources within 30 arcmin of* $l = 326.5°$, $b = 0°$.

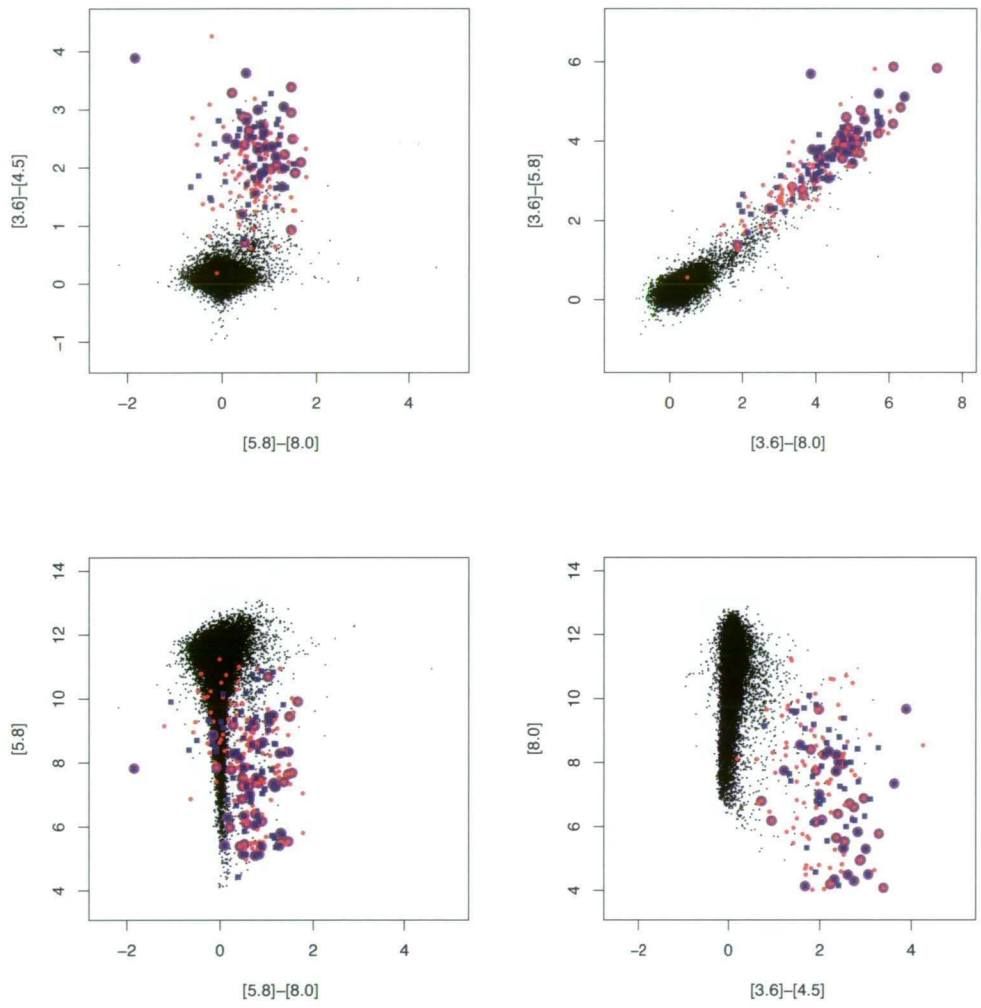

Figure 7.24: *As for Fig. 7.23 with the exception that sources showing OH maser emission (Caswell, 1998) have been differentiated from sources with no reported OH emission with the addition of purple circles.*

this conclusion.

Association with Extended Green Objects (EGOs)

The locations of the 6.7 GHz methanol maser sources were compared with the positions of EGOs presented in Cyganowski et al. (2008). We have adopted an association threshold of 10 arcsec for consistency with analysis carried out in Chapter 6 and to ensure that all associations were captured while minimising the number of chance associations. We find that 97 of the 580 6.7 GHz MMB methanol masers are associated with EGOs, and of these sources 48 have 12.2 GHz methanol counterpart. This equates to an overall 12.2 GHz detection rate of 50 % (49 of 97) for 6.7 GHz methanol masers associated with EGOs and 42 % (121 of 287) towards those without (after discarding 6.7 GHz sources that lie outside the regions inspected by Cyganowski et al. (2008) for EGOs; 10° <l< 65° and 295° $< l <$ 350°, $b = \pm 1°$). This result means that if you have a 6.7 GHz methanol maser that is associated with an EGO you are more likely to detect a 12.2 GHz methanol maser than towards a 6.7 GHz methanol maser that is not associated with an EGO. The 12.2 GHz detection rates towards EGOs is statistically significantly different than the detection rate for the entire 6.7 GHz sample which is 43 %.

These comparisons also show that when taking into account only those 6.7 GHz methanol masers that fall within the regions inspected by Cyganowski et al. (2008) that 25 % (97 of 384) of 6.7 GHz methanol masers have associated EGOs while this increases to 29 % (49 of 170) when you take into account only those 6.7 GHz masers that have associated 12.2 GHz methanol masers. 69 of the 6.7 GHz methanol masers that are associated with EGOs have been searched for OH masers by Caswell (1998). 39 of these sources have an associated OH maser, an association rate of 57 %. In the case where an EGO is associated with both a methanol and an OH maser there is a 74 % chance that there will also be a 12.2 GHz methanol maser, this 12.2 GHz detection rate falls to 43 % for EGOs with associated 6.7 GHz methanol masers but without OH masers. In comparison, comparing the locations of EGOs with water masers in Chapter 6 has shown that 35 of the 89 water-methanol-OH sources that fell within the regions Cyganowski et al. (2008) inspected for the presence of EGOs, equating to an association rate

of 39 %. From these statistics it was concluded that EGOs persist into the stage of star formation that is evolved enough to have produced an OH maser, but not far past the stage where the developing UCHII region has caused the methanol maser emission to cease. Our results support this hypothesis along with the idea that 12.2 GHz methanol masers are present well after the onset of the associated 6.7 GHz methanol maser emission.

7.7 Summary

We have detected 250 12.2 GHz methanol masers towards a complete sample of 580 6.7 GHz methanol masers detected in the MMB survey, equal to a detection rate of 43.1 %. This detection rate is lower than that of other large surveys of comparable sensitivity but this discrepancy can be attributed to the biases introduced from the nature of the target sources in these searches.

Both the velocity ranges and the flux densities of the target 6.7 GHz sources surpass that of their 12.2 GHz companion in almost all cases. 80 % of the detected 12.2 GHz methanol maser peaks are coincident in velocity with the 6.7 GHz maser peak and the peaks of the remaining 12.2 GHz sources are usually associated with a close secondary feature.

Our data is in support of the evolutionary scenario present in Chapter 4, whereby both the 12.2 GHz sources are associated with a somewhat latter evolutionary stage than the 6.7 GHz sources devoid of this transition. Furthermore we find that the 6.7 GHz and 12.2 GHz methanol sources increase in luminosity as they evolve albeit more rapidly for the 6.7 GHz transition. Our new data will allow a slight refinement to the evolutionary plot shown in Fig. 4.6 in light of our new confident detection rates (shown in Chapter 8). In addition to this, evidence for an increase in velocity range as the sources evolve, is presented, and this also occurs at a greater rate for the 6.7 GHz sources. This implies that it is not only the luminosity, but also the volume of gas conducive to the different maser transitions, that increases as the sources evolve.

Comparison with GLIMPSE sources has revealed a similar coincidence rate between the locations of the masers and sources presented in the GLIMPSE point source catalogue. It is evident that the GLIMPSE point sources that are associ-

ated with methanol maser have a large relative excess of 4.5 μm flux. We find little difference between the point source properties associated with the different maser categories (i.e. solitary 6.7 GHz sources, those with 12.2 GHz counterparts, and those associated with OH masers). There is a higher 12.2 GHz detection rate towards those 6.7 GHz methanol masers that are coincident with EGOs.

8

Discussion, conclusion and future work

In this chapter, we discuss the implications of the combined results of Chapters 3 - 7. In particular, we focus on the results that relate to the relative evolutionary stage that each of the investigated maser transitions are tracing. More extensive discussion of the results of each of the individual projects can be found in their corresponding chapters.

From observations targeted towards: OH and 6.7 GHz methanol masers; 1.2 mm dust clumps; and two regions of a GMC; we have reported the detection of hundreds of 12.2 GHz methanol and water masers. A significant fraction of the detected maser sources are reported here for the first time. In the case of the 12.2 GHz sources, we present a complete catalogue of sources south of $-20°$ declination (and b=$\pm$2°). This very large, complete sample has enabled as to definitively report detection statistics for these sources for the first time. While the water masers that we report do not constitute a complete, unbiased sample of sources, they do represent the largest sample of water masers with accurately determined positions. From these large samples of maser sources, we are able to make meaningful investigations of the properties of the sources that they are associated with, as well as the characteristics of the the masers themselves.

The level of variability in the detected maser sources is often acute, especially in the case of the water masers. The observations of 207 water maser sites over two epochs, revealed that 17 % of sources were only above a detection limit of 0.2 Jy on one of these occasions. There is evidence to suggest that weak 12.2 GHz methanol masers are more variable, in general, than the total population of these sources.

We therefore suggest that completing two (or more) epochs of observations, even at a lower sensitivity, allows a more complete sample of both maser species to be gained than can be achieved from a single epoch.

We have compared the properties of the 1.2 mm dust clumps from Hill et al. (2005) with the 8 GHz radio continuum observations of Walsh et al. (1998) and find that the more evolved sources, i.e. those with associated radio continuum emission, have lower H_2 number densities than those 1.2 mm dust clumps without detectable radio continuum. We therefore suggest that the H_2 number densities decrease as the sources evolve (as discussed in Chapter 4, this is likely to be at least partly due to the constant temperature assumption and may therefore indicate that a rise in temperature has occurred in the more evolved sources). Using this, we are able to compare the luminosities of the 6.7 methanol, 12.2 GHz methanol and water masers with the H_2 number densities and recognise a trend between the luminosity of the maser sources and evolution. Fig. 8.1 shows a plot of the luminosity of the maser species versus the H_2 number densities of the associated sources. It can be seen that for all maser species, the more luminous sources are associated with the 1.2 mm dust clumps with lower H_2 number densities and we therefore assert that the maser species increase in luminosity as the sources evolve.

Closer inspection of Fig. 8.1 shows, not only that the fitted lines of best fit have different slopes, but that there is a tighter correlation for some species than for others. In particular, the water maser sources show a much smaller scatter in luminosity than the two methanol maser transitions. There is strong evidence to suggest the that 12.2 GHz methanol masers increase in luminosity at a slower rate than their associated 6.7 GHz methanol sources. Given the much smaller scatter in the values associated with the water masers, we can confidently assert that the water masers increase in luminosity at a slower rate than the 6.7 GHz methanol masers according to their H_2 number densities.

A better test of how the ratios of 6.7 GHz methanol masers to 12.2 GHz methanol maser flux is to calculate the ratio of the two sources and compare these to the luminosity of one of the sources. From this comparison, we show that the ratio of the 6.7 GHz methanol maser to 12.2 GHz methanol maser emission increases with increasing 6.7 GHz methanol maser flux density. A higher

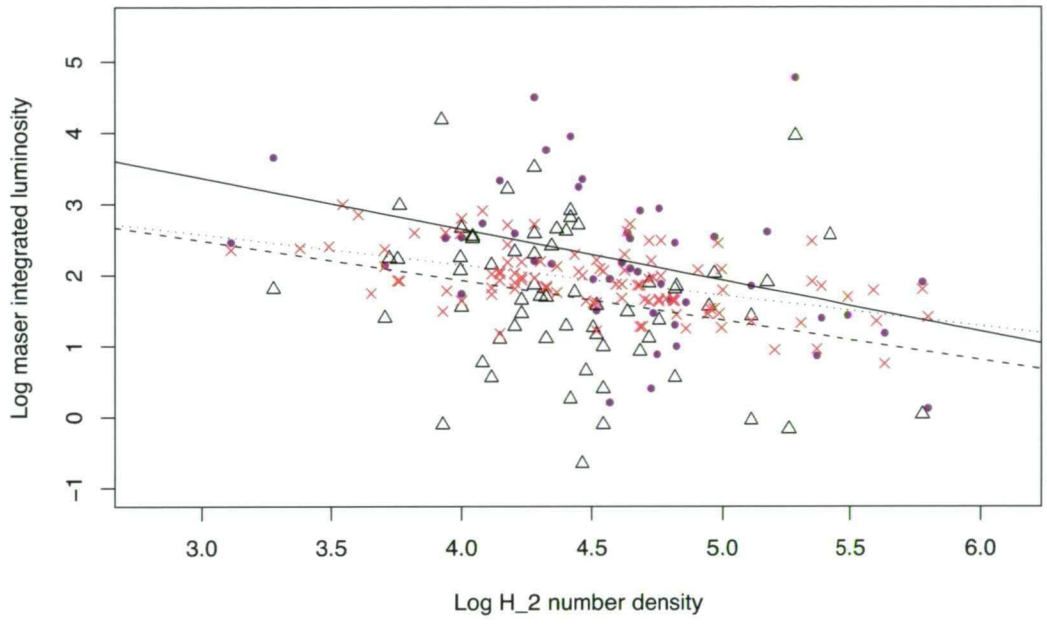

Figure 8.1: *Log integrated maser flux densities (Jy km s^{-1}) versus log of the H_2 number densities (cm^{-3}) of the associated 1.2 mm dust clump. On the plot the different maser species are represented by different symbols and these are as follows: purple dots show the values associated with 6.7 GHz methanol masers; black triangles show the values associated with 12.2 GHz methanol masers; and the red crosses show the values associated with water maser sources. Overlaid are the lines of best fit associated with each of the maser species: 6.7 GHz methanol masers (solid), 12.2 GHz methanol masers (dashed line) and water masers (dotted line).*

coincidence rate of 12.2 GHz methanol maser sources with 6.7 GHz methanol masers with associated OH masers and radio continuum implies that the 12.2 GHz sources are present in the latter half of the lifetime of the 6.7 GHz methanol maser emission.

A further comparison between the flux densities of the different maser sources, broken into categories according to their association with other maser species and radio continuum, shows that those sources associated with OH masers and radio continuum (known traces of more evolved star formation regions) have higher flux densities than those without. In particular, water masers increase in flux density from the categories of solitary, to those with methanol, to those with OH masers and radio continuum. However, a comparison with water masers with 8 GHz radio continuum emission, but no OH masers, shows a decrease in flux density, possibly suggesting that in some sources, weak water maser emission is able to survive into the later stages of evolution, and may imply that the water masers experience a 'turn over' in this increasing flux density trend near the end of their lifetime.

Comparisons between the 6.7 GHz, 12.2 GHz and water maser luminosities with their respective velocity ranges shows that the masers not only increase in luminosity as the sources evolve, but also in velocity range. This implies that for all species the volume of gas conducive to the maser emission also increases as the sources evolve.

Analysis of the water maser sources we detect towards 1.2 mm dust clump emission shows that the water maser sources are associated with bigger, more massive dust sources with higher peak and integrated flux densities. A model for water maser presence towards 1.2 mm dust clumps has been created and tested. The original model was created from complete observations of a GMC with a well determined distance. However, the original search on which this model was based suffered from relatively poor sensitivity and therefore it is sensible to expect that some refinement from a large search of higher sensitivity would be required. Testing this model with observations towards a larger sample of 1.2 mm dust clumps shows that this model is extremely promising. We have shown that the use of the kinematic distance, particularly where distance ambiguities exist, are severely limiting our ability to confidently test and therefore refine this model.

We have compared the locations and characteristics of the detected masers with the locations and the characteristics of mid-infrared emission detected in the GLIMPSE survey. The relative locations of the difference maser species in the G 333 GMC with respect to the main axis of star formation, as revealed by a three-colour GLIMPSE image of the region, lent support to an evolutionary sequence for the different maser species in high-mass star formation regions. Comparisons between the characteristics of GLIMPSE point sources that are coincident with the locations of our maser species shows that there is little difference between the mid-infrared characteristics of the sources associated with different combinations of maser species. This suggests that the masers themselves are much more sensitive to the evolutionary changes in the star formation regions than the associated mid-infrared emission. However, a couple of trends are worth noting:

- 6.7 and 12.2 GHz methanol masers are associated with GLIMPSE point sources that have a relative excess of 4.5 μm flux.

- There is little difference between the GLIMPSE point sources associated with only 6.7 GHz methanol maser, compared to those sources that also exhibit 12.2 GHz methanol maser sources or those that additionally are associated with OH masers.

- GLIMPSE point sources associated with solitary water masers have steeper spectrums below 5 μm than above, compared to water maser associated GLIMPSE point sources that are also coincident with other maser species. We suggest that this means that they are either associated with colder sources, or sources with a relative excess of 4.5 μm flux.

By comparing the coincident rate of the maser species with EGOs, we find that there is a higher 12.2 GHz detection rate towards those 6.7 GHz methanol masers that are coincident with EGOs. Further to this, we find a lower association rate between the solitary water masers and EGOs, suggesting that these sources are too young to have an extended outflow. This therefore implies that EGOs persist into a later stage of the star formation, and are not associated with the majority of sources that are in the pre-maser phases.

8.1 Revised evolutionary sequence for the maser species in high-mass star formation regions

We find strong evidence to suggest that the common maser species are generally associated with slightly different evolutionary stages and hence may be used as an 'evolutionary clock' for high-mass star formation. In Chapter 4 we present an evolutionary sequence for the common maser species in high-mass star formation regions. With the benefit of subsequent investigations, Fig. 8.2 presents a slightly refined evolutionary sequence with greater detail.

We note that in all of our evolutionary analysis, we have considered the mass of the object to be a secondary effect to the evolution of the sources. We find evidence to suggest that this is not an invalid assumption. For example, analysis of 1.2 mm dust clump properties shows that the sources which we consider to be more evolved have lower H_2 number densities. We also note that the due to the manner in which Hill et al. (2005) computed these H_2 number densities, that this effect is closely tied in with the temperature of the sources.

A number of our findings are self consistent and as such we have great confidence in them. For some findings, however, there are minor contradictions with what we see in some of our own sources and from previous observations. Below we summarize a number of the main findings and present arguments which indicate our level of confidence in the conclusions, or conversely, present examples that are in contradiction.

- The basis of our quantitive evolutionary sequence is the lifetime of the 6.7 GHz methanol masers as presented in van der Walt (2005) and the lifetimes of the other masers and characteristics are relative to this number. Therefore, a refinement to the lifetime of 6.7 GHz methanol masers would result in the need for the timeline attached to our proposed sequence to be scaled accordingly. However, all of the lifetimes that we have inferred are not inconsistent with previous proposals, so we would expect this effect to be minimal.

- From the tendency of 12.2 GHz methanol masers to be preferentially associated with sources harboring OH masers and/or UCHII regions, we are

confident that masers of this transition are prevalent towards the end of the 6.7 GHz methanol maser lifetime. This is supported by the fact that very few highly luminous 6.7 GHz methanol masers are without detectable 12.2 GHz counterparts. The characteristics of the associated infrared and 1.2 mm dust continuum emission further support this conclusion.

- The luminosity of both the 6.7 GHz and 12.2 GHz methanol masers show evidence that they increase with evolution. This effect is evident by comparing the methanol masers with known traces of more evolved sources (e.g. OH masers and 8 GHz radio continuum). A comparison between luminosity and velocity range shows that the velocity range (and therefore the volume of gas conducive to the maser emission) also increases with evolution. An investigation of the individual spectral feature of some of the maser shows that this is unlikely due to a sensitivity bias. Comparison between the ratio of the two methanol maser species with evolution shows that the emission from the 12.2 GHz transition increase in both properties at a slower pace. The ratio of the 6.7 to 12.2 GHz sources follows a trend whereby the 6.7 GHz source is stronger at the beginning and then gets progressively comparatively stronger as the sources evolve. There are several cases where the 12.2 GHz emission is as strong, or sometimes possibly even stronger than the associated 6.7 GHz emission. Since maser generation is stochastic, then some stronger 12.2 GHz sources should be expected. However, our scenario is unable to accommodate these sources. Our understanding of these sources may be aided by investigating their chemistry.

- The lifetime of the water maser sources offers further confusion since it cannot be confidently determined if solitary sources are tracing an evolutionary stage prior to the 6.7 GHz methanol masers, or alternatively are associated with lower mass objects. Our interpretation is that, for some sources, relatively weak water maser emission can be present prior to the onset of associated methanol maser emission. We suggest that the water maser emission present at this time may be particularly variable and intermittently disappear (to below flux densities of $\sim$0.2 Jy). We find evidence to suggest that the water masers increase in both flux density and velocity

range as the sources evolve, but at a slower rate to the 6.7 GHz sources. There is some additional evidence to suggest that the water masers experience a 'turn over' towards the end of their lifetime, but this is based on fairly small numbers and needs further investigation. Furthermore, it is surprising that the water masers would increase in flux density at a slower rate than the 6.7 GHz sources as this implies that the lifetime of the water masers must be significantly longer in order for them to achieve the higher luminosities (than the methanol maser sources) that we expect from previous observations.

- We find evidence for small changes in the characteristics of the mid-infrared sources associated with the different maser species, consistent with changes that would be expected with evolution.

- As discussed in Chapter 4 the presence of associated radio continuum is particularly dependent on the mass of the object and is therefore difficult to constrain the timeline shown in Fig. 8.2.

We expect that our proposed evolutionary scheme overlaps with the 'hot molecular core' phase shown in the evolutionary diagram of Purcell (2006) (Fig. 2.8). Therefore, we suggest that prior to the start of our timeline, sources would chiefly be in the 'cold core' phase and at the end of the timeline we expect that the maser emission is ceased by the evolution of the UCHII region.

8.2 Future work

A number of the analyses that have been completed throughout this thesis are subject to poorly determined distances. Due to this, one of the most important pieces of followup work that should be completed is to redo a number of the analyses once better distance estimates are known. Some of this work is currently in progress using HI self absorption to discriminate between the near and far kinematic distances to the methanol masers detected in the MMB survey (Green et al., in prep). While it is extraordinarily unlikely that more accurate distance measurements would act to weaken any of the results that we have found, our analysis

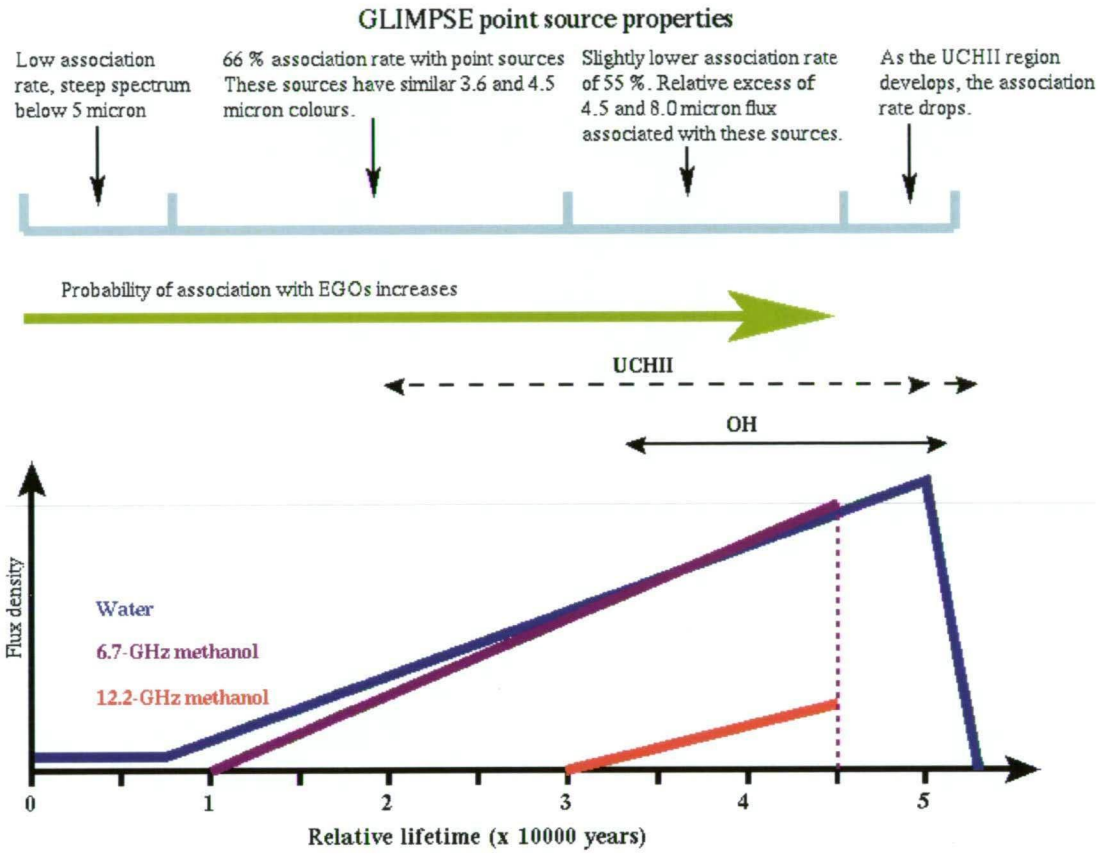

Figure 8.2: *Proposed evolutionary scheme for the common maser species in high mass star formation regions, together with some of the mid-infrared properties and UCH*II *regions. For the 6.7 and 12.2 GHz methanol and water masers, the relative lifetimes are shown, together with the approximate relative flux densities of the sources, represented by the slopes of the lines. In the case of the OH masers, no investigation of the flux densities has been completed, so only the proposed lifetime is shown. Properties and association rates between the combinations of maser sources and GLIMPSE sources are shown (GLIMPSE point source properties shown at the top of the figure, above the cyan line). We note that the detectability of an associated UCH*II *region is dependent on the mass of the associated object which is why it is shown with a dashed line. Furthermore, the lifetime of the associated UCH*II *region will extend beyond the timeline and we use a double arrow head to distinguish this.*

would benefit immensely from better determined measurements, by significantly reducing the scatter in the relationships.

A number of the results presented in this thesis have opened up a lot of new questions that can now be investigated and results that can be tested on larger, more complete samples. In particular, comparison between the data collected in large surveys, such as complete searches for water masers (HOPS (Walsh et al., 2008)), methanol masers (MMB (Caswell et al., 2010; Green et al., 2010)), dust emission (APEX Telescope Large Area Survey of the Galaxy), and large molecular line surveys at 12, 7 and 3mm (HOPS, MALT45 and MALT90), will offer tremendous advancement in understanding the best tracers of high-mass star formation at the different stages of evolution. Furthermore, some advancements in the understanding of the earliest phases of high-mass star formation have been derived from comparison with infrared dark clouds and MIPSGAL data (especially in the 24 μm band) and other data. An extension of our analysis to include these properties may offer significant additional insight.

Below we summarize a number of the more specific questions that have arisen in this work that will constitute the basis for a number of subsequent investigations.

- Further investigate the maser association dependence on mass of the object versus the dependence on evolutionary stage.

- Some thermal lines have been shown to have different characteristics during different phases of evolution (e.g. Longmore et al., 2007; Purcell et al., 2006, 2009). Would the evolutionary sequence for our sources determined from these characteristics agree with ours?

- There is a small group of sources that exhibit 6.7 GHz methanol masers, OH masers but no 12.2 GHz methanol masers, while most 6.7 GHz sources that are associated with OH masers also have 12.2 GHz sources. This raises the question, why? Are there 12.2 GHz sources here that were below our detection limits at the time of our search? Or is there something more complex going on? Is there a difference in the abundances of methanol between these sources and those showing the 12.2 GHz transition?

- It has been suggested that water maser sources with dominant blue-shifted emission are at an early evolutionary phase. Our observations of water masers towards 1.2 mm dust clump sources lends some evidence to support this theory by detecting more examples of these sources. If this is the case, it would be expected that complete searches for water masers will reveal even more of this class of source, is this the case? Does this imply that the emission associated with more evolved water masers are no longer dominated by emissions associated with outflows?

- What is the effect of the metallicity in the Galaxy on the abundances of masers? Does lower metallicity have a greater effect on methanol masers than water masers in our Galaxy just like the LMC (Green et al., 2008)? Our detection statistics show that there is a lower detection rate of 12.2 GHz methanol masers in the Galactic longitude range G 270 - G 305 than in the range G 315 - G 350 (as well as a smaller population of 6.7 GHz methanol masers). However, in a similar region, G 213 - G 333 we find a higher detection rate of water masers towards 1.2 mm dust clumps than in the longitude range G 0 - G 38. Comparing the 6.7 GHz and 12.2 GHz methanol maser populations with the water masers of HOPS should allow us to accurately determine if the water maser detection rate is relatively higher in these regions. Further investigation is required to determine if the detection rates in large portions of the Galaxy are dependent on metallicity gradients, or some other localised effects.

- The mass range of young stellar objects that are able to produce luminous water masers is not well constrained. This is something that requires further investigation before the relative evolutionary stage that the water maser species are tracing can be confidently determined. Are solitary water masers representative of an evolutionary phase that proceeds methanol masers, are they associated with lower mass objects, or are both effects at play?

- While some of our investigations have compared the locations of the maser sources with 8 GHz radio continuum sources, and some with 22 GHz continuum sources (albeit with comparatively low sensitivity), would a comparison with sensitive, millimetre observations reveal support for our maser

species evolutionary scheme by hilighting those sources associated with hyper-compact HII regions?

- Water masers are considered the most luminous maser species, but this is not reflected in the sample of sources that have been detected towards the Hill et al. (2005) sample of 1.2 mm dust clumps. Why is this? Is this sample missing the more evolved sources and therefore the most luminous water masers? Does this imply that the rate in which the water maser luminosity increases accelerates at some stage during their lifetime in order to acheive the higher luminosities that are observed?

8.3 Concluding remarks

One of the current difficulties in understanding high-mass star formation is the lack of sequential signposts in identifying the different evolutionary stages of their formation, particularly during the stage where the objects are still deeply imbedded within their natal molecular clouds. Through the observation of hundreds of masers towards star formation regions, we have found that the common maser species have immense potential to be excellent evolutionary tracers of high-mass star formation regions. We present our proposed evolutionary scenario and note several areas that will be the subject of future investigations.

Bibliography

Argon A. L., Reid M. J., Menten K. M., 2003, ApJ, 593, 925

Baart E. E., Cohen R. J., 1985, MNRAS, 213, 641

Bains I., Wong T., Cunningham M., Sparks P., Brisbin D., Calisse P., Dempsey J. T., Deragopian G., Ellingsen S., Fulton B., Herpin F., Jones P., Kouba Y., Kramer C., Ladd E. F., Longmore S. N., McEvoy J., Maller M., Minier V., Mookerjea B., Phillips C., Purcell C. R., Walsh A., Voronkov M. A., Burton M. G., 2006, MNRAS, 367, 1609

Bains I., Breen S. L., Burton M. G., Cunningham M. R., Jones P. A., Kawamura A., Lo N., Rowell G. P., Walsh A., 2009, PASA, 26, 110

Bally J., Zinnecker H., 2005, AJ, 129, 2281

Barrett A. H., Schwartz P. R., Waters J. W., 1971, ApJL, 168, L101

Batchelor R. A., Caswell J. L., Haynes R. F., Wellington K. J., Goss W. M., Knowles S. H., 1980, Aust. J. Phys., 33, 139

Batrla W., Matthews H. E., Menten K. M., Walmsley C. M., 1987, Nature, 326, 49

Becklin E. E., Frogel J. A., Neugebauer G., Persson S. E., Wynn-Williams C. G, 1973, ApJ, 182,125

Beuther H., Walsh A., Schilke P., Sridharan T. K., Menten K. M., Wyrowski F., 2002, A&A, 390, 289

Beuther H., Shepherd D., 2005, in Nanda Kumar M. S., Tafalla M., Caselli P., eds., Cores to Clusters: Star formation eith Next Generation Telescopes, Astronomy and Space Science Library, 324, Springer, New York, p. 105

Beuther H., Churchwell E. B., McKee C. F., Tan J. C., in Protostars and Planets V, eds. Reipurth B., Jewitt D., Keil K., Tucson: Univ. of Arizona Press, p. 165

Błaszkiewicz L., Kus A. J., 2004, A&A, 413, 233

Boland W., de Jong T., 1981, A&A, 98, 149

Bonnell I. A., Bate M. R., Zinnecker H., 1998, MNRAS, 298, 93

Bourke T. L., Myers P. C., Robinson G., Hyland A. R., 2001, ApJ, 554, 916

Brand J., Blitz L., 1993, A&A, 275,67

Brand J., Cesaroni R., Comoretto G., Felli M., Palagi F., Palla F., Valdettaro R., 2003, A&A 407, 573

Braz M. A., Scalise Jr. E., 1982, A&A., 107, 272

Braz M. A., Epchtein E., 1983, A&AS, 54, 167

Breen S. L., 2005, Honours Thesis, Univ. Tasmania

Breen S. L., Ellingsen S. P., Johnston-Hollitt M., Wotherspoon S., Bains I., Burton M. G., Cunningham M., Lo N., Senkbeil C. E., Wong T., MNRAS, 2007, 377, 491

Breen S. L., Ellingsen S. P., Caswell J. L., Lewis B. J., 2010, MNRAS, 401, 221

Breen S. L., Caswell J. L., Ellingsen S. P., Phillips C. J., MNRAS, *in press*

Bronfman L., Nyman L. A., May J., 1996, A&A., 115, 81

Burnham K. P., Anderson D. R., 2002, Model Selection and Multimodel Inference, A Practical Information - Theoretic Approach, Second Edition, Springer, New York

Caswell J. L., Batchelor R. A., Haynes R. F., Huchtmeier W. K., 1974, Aust. J. Phys., 27, 417

Caswell J. L., Haynes R. F., Goss W. M., 1980, Aust. J. Phys., 33, 639

Caswell J.L., Batchelor R.A., Forster J.R., Wellington K.J., 1983, Aust.J.Phys., 36, 401

Caswell J.L., Batchelor R.A., Forster J.R., Wellington K.J., 1983, Aust.J.Phys., 36, 443

Caswell J. L., Haynes R. F., 1987, Aust. J. Phys., 40,215

Caswell J.L., Batchelor R.A., Forster J.R., Wellington K.J., 1989, Aust.J.Phys., 42, 331

Caswell J. L., Gardner F. F., Norris R. P., Wellington, K. J., McCutcheon W. H., Peng, R. S., 1993, MNRAS, 260, 425

Caswell J.L., Vaile R.A., Forster J.R., 1995, MNRAS, 277, 210

Caswell J. L., Vaile R. A., Ellingsen S. P., Whiteoak J. B., Norris R. P., 1995a, MNRAS, 272, 96

Caswell J. L., Vaile R. A., Ellingsen S. P., Norris R. P., 1995b, MNRAS, 274, 1126

Caswell J. L., 1997, MNRAS, 289, 79

Caswell J. L., 1998, MNRAS, 297, 215

Caswell J. L., 1999, MNRAS, 308, 683

Caswell J. L., 2001, MNRAS, 326, 805

Caswell J. L., 2001, MNRAS, 341, 551

Caswell J. L., 2004a, MNRAS, 351, 279

Caswell J. L., 2004b, MNRAS, 352, 101

Caswell J. L., 2004c, MNRAS, 349, 99

Caswell J.L., Phillips C.J., 2008, MNRAS, 386, 1521

Caswell J. L., 2009, PASA, 26, 454

Caswell J. L., Kramer B. H., Reynolds J. E., 2009, MNRAS, 398, 528

Caswell J. L. et al., 2010, MNRAS, 404, 1029

Caswell J. L., Breen S. L., 2010, MNRAS, (*in press.*)

Caswell J. L., Breen S. L., Ellingsen S. P., 2010, MNRAS, (submitted)

Catarzi M., Moscadelli L., Panella D., 1993, A&AS, 98, 127

Cesaroni R., Walmsley C. M., Koempe C., Churchwell E., 1991, A&A, 252, 278

Cesaroni R., Walmsley C. M., Churchwell E., 1992, A&A, 256, 618

Cesaroni R., Hofner P., Walmsley C. M., Churchwell E., 1998, A&A, 331, 709

Chambers E. T., Jackson J. M., Rathborne J. M., Simon R., 2009, ApJS, 181, 360

Chen X., Ellingsen S. P., Shen Z.-Q., 2009, MNRAS, 396, 1603

Cheung A. C., Rank D. M., Townes C. H., Thornton D. D., Welch W. J., 1969, Nature, 221, 626

Churchwell E., Walmsley C. M., Cesaroni R., 1990, A&AS, 83, 119

Claussen M. J., Wilking B. A., Benson P. J., Wootten A., Myers P. C., Terebey S., 1996, ApJS, 106, 111

Clegg A. W., Cordes J. M., 1991, ApJ, 374, 150

Codella C., Felli M., Natale V., Palagi F., Palla F., 1994 A&A, 291, 261

Codella C., Felli M., 1995 A&A, 302, 521

Comoretto G., Palagi F., Cesaroni R., Felli M., Bettarini A., Catarzi M., Curioni G. P., Curioni P., di Franco S., Giovanardi C., Massi M., Palla F., Panella D., Rossi E., Speroni N., Tofani G., 1990, A&AS, 84, 179

Cook A. H., 1968, Nature, 220, 44

Cragg D. M., Sobolev A. M., Ellingsen S. P., Caswell J. L., Godfrey P. D., Salii S. V., Dodson R. G., 2001, MNRAS, 323, 939

Cragg D. M., Sobolev A. M., Godfrey P. D., 2002, MNRAS, 331, 521

Cragg D. M., Sobolev A. M., Godfrey P. D., 2005, MNRAS, 360, 533

Cyganowski C. J. et al., 2008, AJ, 136, 2391

Cyganowski C. J., Brogan C. L., Hunter T. R., Churchwell E., 2009, ApJ, 702, 1615

Darling J., Giovanelli R., 2002, AJ, 124, 100

Deacon R. M., Chapman J. M., Green A. J., Sevenster M. N., 2007, ApJ, 658, 1096

Dodson R. G., Ellingsen S. P., 2002, MNRAS, 333,307

Elitzur M., de Jong T., 1978, A&A, 1978, 323

Elitzur M., Hollenbach D. J., McKee C. G., 1989, ApJ, 346, 983

Ellingsen S. P., von Bibra M. L., McCulloch P. M., Norris R. P., Deshpande A. A., Phillips C. J., 1996, MNRAS, 280, 378

Ellingsen S. P., Cragg D. M., Minier V., Muller E., Godfrey P. D., 2003, MNRAS, 344, 73

Ellingsen S. P., Cragg D. M., Lovell J. E. J., Sobolev A. M., Ramsdale P. D., Godfrey P. D., 2004, MNRAS, 354, 401

Ellingsen S. P., 2005, MNRAS, 359, 1498

Ellingsen S. P., 2006, ApJ, 638, 241

Ellingsen S. P., Voronkov M. A., Cragg D. M., Sobolev A. M., Breen S. L., Godfrey P. D., 2007, in Chapman J. M., Baan W. A., eds., Proc. IAU Symp., 242, Astrophysical Masers and their Environments. Cambridge Univ. Press, Cambridge, p. 213

Ellingsen S. P., Breen S. L., Caswell J. L., Quinn L. J., Fuller G. A., 2010, MNRAS, 404, 779

Elmegreen B. G., 1998, ASP Conf. Ser. 148: Origins, ed. C. E., Woodward, J. M. Shull, H. A., Thronson, 150

Felli M., Brand J., Cesaroni R., Codella C., Comoretto G., di Franco S., Massi F., Moscadelli L., Nesti R., Olmi L., Palagi F., Panella D., Valdettaro R., 2007, AAP, 476, 373

Fish V. L., Reid M. J., Argon A. L., Menten K. M., 2003, ApJ, 596, 328

Fish V. L., Reid M. J., 2007, ApJ, 656, 952

Fontani F., Cesaroni R., Furuya R. S., A&A, (*in press*)

Forster J.R., Caswell J.L., 1989, A&A, 213, 339

Forster J.R., Caswell J.L., 1999, A&ASuppl., 137, 43

Forster J.R., Caswell J.L., 2000, ApJ, 530, 371

Fuller G. A., Williams S. J., Sridharan T. K., 2005, A&A, 442, 949

Furuya R. S. et al., 2003, ApJS, 144, 71

Garay G., Lizano S., 1999, PASP, 111, 1049

Garay G., Faúndez S., Mardones D., Bronfman L., Chini R., Nyman L.-Å, 2004, ApJ, 610, 313

Gaume R. A., Goss W. M., Dickel H. R., Wilson T. L., Johnston K. J., 1995, ApJ, 438, 776

Gaylard M. J., MacLeod G. C., van der Walt D. J., 1994, MNRAS, 269, 257

Genzel R., Downes, D., 1977, A&AS, 30, 145

Genzel R., Reid M., Moran J. M., Downes D., 1981, ApJ, 244, 884

Gillespie A. R., Huggins P. J., Sollner T. C. L. G., Phillips T. G., Gardner F. F., Knowles S. H., 1977, A&A, 60,2 21

Goedhart S., Gaylard M. J., van der Walt D. J., 2004, MNRAS, 355, 553

Goedhart S., Minier V., Gaylard M. J., van der Walt D. J., 2005a, MNRAS, 356, 839

Goedhart S., Gaylard M. J., Walt D. J., 2005b, A&AS, 295, 197

Goedhart S., Langa M. C., Gaylard M. J., van der Walt D. J., 2009, MNRAS, 398, 995

Goss W. M., Haynes R. F., Knowles S. H., Batchelor R. A., Wellington K. J., 1977, MNRAS, 180, 51

Green J. L. et al., 2008, MNRAS, 385, 948

Green J. A. et al., 2009, MNRAS, 392, 783

Green J. L. et al., 2010, MNRAS (accepted)

Hanslow L. A., 1997, Honours Thesis, Univ. Tasmania

Hill T., Burton M. G., Minier V., Thompson M. A., Walsh A. J., Hunt-Cunningham M., Garay G., 2005, MNRAS, 363, 405

Hill T., Pinte C., Minier V., Burton M. G., Hunt M. R., 2009, MNRAS, 392, 768

Hoffman I. M., Goss W. M., Palmer P., Richards A. M. S., 2003, ApJ, 598, 1061

Hofner P., Churchwell E., 1996, A&AS, 120, 283

Houghton S., Whiteoak J. B., 1995, MNRAS, 273, 1033

Huang M. et al., 1999, ApJ, 517, 282

Jaffe D. T., Gusten R., Downes D., 1981, ApJ, 250, 621

Johnston K. L., Robinson B. J., Caswell, J. L., Batchelor R. A., 1972, ApL, 10, 93

Kalenskii S. V., Johansson L. E. B., Bergman P., Kurtz S., Hofner P., Walmsley C. M., Slysh V. I., 2010, MNRAS, 405, 613

Karnik A. D., Ghosh S. K., Rengarajan, T. N., Verma R. P., 2001, MNRAS, 326, 293

Kaufmann P. et al., 1976, Nature, 260, 360

Kemball A. J., Gaylard M. J., Nicolson G. D., 1988, ApJ, 331, L37

Kim K.-T., Koo B.-C., 2001, ApJ, 549, 979

Knowles S. H., Mayer C. H., Cheung A. C., Rank D. M., Townes C. H., 1969, Science, 163, 1055

Koo B. C., Williams D. R. D., Heiles C., Backer D. C, 1988, ApJ, 326, 931

Krumholz M. R., Klein R. I., McKee C. F., Offner S. S. R., Cunningham A. J., 2009, Science, 323, 754

Kurtz S., 2005, in Cesaroni R., Felli M., Churchwell E., Walmsley C. M., eds., Proc. IAU Symp., 227, Massive Star Birth: A crossroads of Astrophysics. Cambridge Univ. Press, Cambridge, p. 111

Kurtz S., 2006, in Lis D. C., Blake G. A., Herbst E., eds., Proc. IAU Symp., 231, Astrochemistry: Recent Successes and Current Challenges. Cambridge Univ. Press, Cambridge, p. 47

Lewis B. E., 2007, Honours Thesis University of Tasmania

Lo K. Y. Burke B. F; Haschick A. D., 1975, ApJ, 220, 81

Lo N., Cunningham M. R., Jones P. A., Bains I., Burton M. G., Wong T., Muller E., Kramer C., Ossenkopf V., Henkel C., Deragopian G., Donnelly S. Ladd E. F., 2009, MNRAS, 395, 1021

Lockman F. J., 1979, ApJ, 232, 761

Longmore S. N., Burton M. G., Barnes P. J., Wong T., Purcell C. R., Ott J., 2007, MNRAS, 379, 535

Longmore S. N., Burton M. G., Purcell C. R., Barnes P., Ott J., 2008, ASPCS, 387, 58

MacLeod G. C., Gaylard M. J., Kemball A. J., 1993, MNRAS, 262, 343

Mac Low M., Kleesen R. S., 2004, Rev. Mod. Phys., 76, 125

Mader G. L., Johnston K. J., Moran J. M., 1978, ApJ, 224, 115

McCullagh P., Nelder J. A., 1989, Generalized linear models, Chapman and Hall, London

Mehringer D. M., Menten K. M., 1996, ApJ, 474, 364

Menten K. M., Walmsley C. M., Henkel C., Wilson T. L., 1986, A&A, 157, 318

Menten K. M., Melnick G. J., 1989, ApJL, 341, 91

Menten K. M., 1991, in Atoms, ions and molecules: New results in spectral line astrophysics, eds. Haschick A., Ho P. T. P., ASP, San Francisco, p. 119

Menten K. M., 1991, ApJ, 380, L75

Menten K. M., Reid M. J., Pratap P., Moran J. M., Wilson T. L., 1992, ApJ, 401, L39

Minier V., Ellingsen S. P., Norris R. P., Booth R. S., 2003, A&A, 403, 1095

Mookerjea B., Kramer C., Nielbock M., Nyman L., 2004, A&A, 426, 119

Moscadelli L. et al., 2002, ApJ., 564, 813

Müller H. S. P., Menten K. M., Mäder H., 2004, A&A, 428, 1019

Murphy T., Cohen M., Ekers R. D., Green A. J., Wark R. M., Moss V., 2010, MNRAS, 405, 1560

Norris R. P., Caswell J. L., Gardner F. F., Wellington K. J., 1987, ApJ, 321, L159

Norris R. P., Whiteoak J. B., Caswell J. L., Wieringa M. H., Gough R. G., 1993. ApJ, 412, 222

Palagi F., Cesaroni R., Comoretto G., Felli M., Natale V., 1993, A&AS, 101, 153

Palla F., Brand J., Comoretto G., Felli M., Cesaroni R., 1991, A&A, 246, 249

Palla F., Cesaroni R., Brand J., Caselli P., Comoretto G., Felli M., 1993, A&A, 280, 599

Pandian J. D., Menten K. M., Goldsmith P. F., 2009, ApJ, 706, 1609

Pestalozzi M. R., Minier V., Booth R. S., 2005, A&A, 432, 737

Purcell C. R., 2006, PhD. Thesis, Univ. New South Wales

Purcell C. R., et al., 2006, MNRAS, 367, 553

Purcell C. R., Longmore S. N., Burton M. G., Walsh A. J., Minier V., Cunningham M. R., Balasubramanyam R., 2009, MNRAS, *in press*

R Development Core Team, 2006, R: A Language and Environment for Statistical Computing. R Foundation for Statistical Computing, Vienna. Available online from http://www.r-project.org

Radhakrishnan V., Goss W. M., Murray J. D., Brooks J. W., 1972, ApJS, 24, 49

Rathborne J. M., Jackson J. M., Chambers E. T., Stojimirovic I., Simon R., Shipman R., Frieswijk W., 2010, ApJ, 715, 310

Reid M. J., Schneps M. H. Moran J. M. Gwinn C. R. Genzel R., Downes D., Roennaeng B., 1988, ApJ, 330, 809

Reid M. J., Menten K. M., Zheng X. W., Brunthaler A., Moscadelli L., Xu Y., Zhang B., Sato M., Honma M., Hirota T., Hachisuka K., Choi Y. K., Moellenbrock G. A., Bartkiewicz A., 2009, ApJ, 700, 137

Robishaw T., Quataert E., Heiles C., 2008, ApJ, 680, 981

Rodgers A. W., Campbell C. T., Whiteoak J. B., 1960, MNRAS, 112, 103

Roman-Lopes A., Abraham Z., Lepine J. R. D., 2003, Astron. J., 126, 1896

Sakellis S., Taylor M. I., Taylor K. N. R., Vaile R. A., Han T. D., 1984, PASP, 96, 543

Sato M., et al. 1008, PASJ, 60, 975

Sault R. J., Teuben P. J., Wright M. H., 1995, ASP Conf. Ser. 77, Ed. Shaw R. A., Payne H. E., Hayes J. J. E., 433

Sault R. J., 2003,"ATCA flux density scale at 12mm", (http://www.atnf.csiro.au/observers/docs/12mm/calibrators.html)

Sewiło M., Churchwell E., Kurtz S., Goss W. M., Hofner P., 2004, ApJ, 605, 285

Sewiło M., Churchwell E., Kurtz S., Goss W. M., Hofner P., 2008, ApJ, 681, 350

Shu F. H., Adams F. C., Lizano S., 1987, ARA&A, 25, 23

Simon R., Jackson J. M., Clemens D. P., Bania T. M., Heyer M. H., 2001, ApJ, 551,747

Smits D. P., Cohen R. J., Hutawarakorn B., 1998, MNRAS, 296, L11

Smits D. P., 2003, MNRAS, 339, 1

Sobolev A. M., Ostrovskii A. B. Kirsanova, M. S. Shelemei, O. V., Voronkov, M. A., Malyshev A. V., 2005, in Cesaroni R., Felli M., Churchwell E., Walmsley C. M., eds., Proc. IAU Symp., 227, Massive Star Birth: A crossroads of Astrophysics. Cambridge Univ. Press, Cambridge, p. 174

Stark D. P., Goss W. M., Churchwell E., Fish V. L., Hoffman I M., 2007, ApJ, 656, 943

Sullivan, W. T., 1971, ApJ, 166, 321

Sutton E. C., Sobolev A. M., Ellingsen S. P., Cragg D. M., Mehringer D. M., Ostrovskii A. B., Godfrey P. D., 2001, ApJ, 554, 173

Szymczak M., Hrynek G., Kus A. J., 2000, A&AS, 143, 269

Szymczak M., Kus A. J., Hrynek G., Kepa A., Pazderski E., 2002, A&A, 392, 277

Szymczak M., Pillai T., Menten K. M., 2005, A&A, 434, 613

Tan J. C., McKee C. F., 2004, ApJ, 603, 383

Torrelles J. M., Gomez J. F., Rodriguez L. F., Curiel S., Anglada S., Ho P. T. P. 1998, ApJ, 505, 756

Torrelles J. M., Patel N. A., Gómez J. F., Anglada G., 2002, in Revista Mexicana de Astronomia y Astrofisica Conference Series, Ed. Henney W. J., Steffen W., Binette L., Raga A., 13, 108

Valdettaro R., Palla F., Brand J., Cesaroni R., Comoretto G., Di Franco S., Felli M., Natale E., Palagi F., Panella D., Tofani G., 2001, A&AS, 368, 845

Val'tts I. E., Ellingsen S. P., Slysh V. I., Kalenskii S. V., Otrupcek R., Voronkov M. A., 1999, MNRAS, 310, 1077

van der Walt J., 2005, MNRAS, 360, 153

Venables W. N., Ripley B. D., 2002, Modern applied statistics with S, Fourth Edition, Springer, New York

Voronkov M. A., Brooks K. J., Sobolev A. M., Ellingsen S. P., Ostrovskii A. B., Caswell J. L., 2006, MNRAS, 373, 411

Voronkov M. A., Caswell J. L., Ellingsen S. P., Sobolev A. M., 2010, MNRAS, 405, 2471

Voronkov M. A., Caswell J. L., Britton T. R., Green J. A., Sobolev A. M., Ellingsen S. P., 2010, MNRAS, (in press)

Walsh A. J., Hyland A. R., Robinson G., Burton M. G., 1997, MNRAS, 291, 261

Walsh A. J., Burton M. G., Hyland A. R., Robinson G., 1998, MNRAS, 301, 640

Walsh A. J., Burton M. G., Hyland A. R., Robinson G., 1999, MNRAS, 309, 905

Walsh A. J., Macdonald G. H., Alvey N. D. S., Burton M. G., Lee J.-K., 2003, A&A, 410, 597

Walsh A. J., Lo N., Burton M. G., White G. L., Purcell C. R., Longmore S. N., Phillips C. J., Brooks K. J., 2008 PASA, 25, 105

Weaver H., Williams D. R. W., Dieter N. H., Lum W. T., 1965, Nature, 208, 29

White G. J., Macdonald G. H., 1979, MNRAS, 188, 745

Williams J. P., de Geus E. J., Blitz L., 1994, ApJ., 428, 693

Wong T., Ladd E. F., Brisbin D., Burton M. G., Bains I., Cunningham M. R., Lo N., Jones P. A., Thomas K. L., Longmore S. N., Vigan A., Mookerjea B., Kramer C., Fukui Y., Kawamura A., 2008, MNRAS, 386, 1069

Wood D. O. S., Churchwell E., 1989, ApJS, 69, 831

Xu Y., Li J. J., Hachisuka K., Pandian J. D., Menten K. M., Henkel C., 2008, A&A, 485, 729

Xu Y., Menten K. M., Voronkov M. A., Pandian J. D., , Li J. J., Sobolev A. M., Brunthaler A., Ritter B., 2009, A&A (in press)

Zavagno A., Deharveng L., Comerón F., Brand J,. Massi F., Caplan J., Russeil D., 2006, A&A, 446, 171

Zinchenko I., Mattila K., Toriseva M., 1995, A&AS, 111, 95

Zinnecker H., Yorke H. W., 2007, ARA&A, 45, 481